

Morphological and Spectrochemical Characterization of Pyroxene- and Spinel-bearing Lithologies and Impact Cratering Mechanics of the Moon: Implications for Lunar Endogenic and Exogenic Processes

A thesis submitted
in partial fulfillment for the award of the degree of

Doctor of Philosophy

by

Thesniya P. M.



**Department of Earth and Space Sciences
Indian Institute of Space Science and Technology
Thiruvananthapuram, India**

March 2022

Certificate

This is to certify that the thesis titled *Morphological and Spectrochemical Characterization of Pyroxene- and Spinel-bearing Lithologies and Impact Cratering Mechanics of the Moon: Implications for Lunar Endogenic and Exogenic Processes* submitted by **Thesniya P. M.**, to the Indian Institute of Space Science and Technology, Thiruvananthapuram, in partial fulfillment for the award of the degree of **Doctor of Philosophy** is a bona fide record of the original work carried out by her under my supervision. The contents of this thesis, in full or in parts, have not been submitted to any other Institute or University for the award of any degree or diploma.

Dr. Rajesh V. J.

Supervisor (Associate Professor)

Department of Earth and Space Sciences

IIST

Prof. Rama Rao Nidamanuri

Professor & HOD

Department of Earth and Space Sciences

IIST

Place: Thiruvananthapuram

Date: March 2022

Declaration

I declare that this thesis titled *Morphological and Spectrochemical Characterization of Pyroxene- and Spinel-bearing Lithologies and Impact Cratering Mechanics of the Moon: Implications for Lunar Endogenic and Exogenic Processes* submitted in partial fulfillment for the award of the degree of **Doctor of Philosophy** is a record of the original work carried out by me under the supervision of **Dr. Rajesh V. J.**, and has not formed the basis for the award of any degree, diploma, associateship, fellowship, or other titles in this or any other Institution or University of higher learning. In keeping with the ethical practice in reporting scientific information, due acknowledgments have been made wherever the findings of others have been cited.

Place: Thiruvananthapuram

Date: March 2022



Thesniya P. M.

SC17D028

Acknowledgements

First and foremost, I would like to extend my sincere gratitude to my Ph.D. supervisor Dr. Rajesh V. J., for introducing me to this exciting field of Planetary Geoscience. I sincerely thank him for guiding me in my research and mentoring me to keep myself motivated throughout my Ph.D. I greatly appreciate all his contributions of time, ideas, patience, fruitful advice, encouragement, and constant support on a professional and personal level, which made my Ph.D. experience productive and stimulating. The joy and enthusiasm he has for research were contagious and motivational for me, even during tough times in the Ph.D. pursuit. This Ph.D. would not have been possible without him as my supervisor.

I gratefully acknowledge the funding source that made my Ph.D. work possible. I was funded by the Indian Space Research Organization (ISRO) through the DoS grant ISRO/SSPO/Ch-1/2016-17 under the Chandrayaan-1 AO (Announcement of Opportunity) program. I also acknowledge the LROC (NASA), Chandrayaan-1 (ISRO), and TC (JAXA/Japan) data teams for providing the data in the public domain.

I will forever be thankful to the Director (IIST) for the generous support and encouragement. I sincerely thank my doctoral committee members Prof. A. P. Pradeep Kumar, Dr. L. Gnanappazham, and Dr. K. Prabhakaran, for their insightful comments and encouragement and the hard questions that incited me to widen my research from various perspectives. I express my immense gratitude to Prof. Jessica Flahaut (CRPG/CNRS, France) for her valuable suggestions and help in my research work, particularly her valued contributions to improving the Grimaldi basin manuscript. I thank Prof. Chandrasekhar A. (Dean Acad.), Prof. Raju K. George (Dean R&D), Dr. Y.V.N. Krishna Murthy (Registrar), Prof. Kuruvilla Joseph (Dean S&A), Prof. Anandmayee Tej (Former HOD), Dr. Samir Mandal (Former HOD, ESS), Prof. Rama Rao Nidamanuri (HOD), and Dr. Babitha Justin in IIST for their support during different stages of my Ph.D. I would like to extend my sincere gratitude to Dr. Prakash Chauhan (IIRS, Dehradun), Satadru Bhattacharya (SAC, Ahmedabad), Dr. Mamta Chauhan (IIRS, Dehradun), Dr. Sajeev Krishnan (IISc, Bangalore), Dr. Vijayan S., Dr. Rishitosh K. Sinha, and Dr. Neeraj Srivastava from PRL, Ahmedabad for their valuable advice during my research work. My heartfelt thanks go to Dr. Hrushikesh Hari (Geological Survey of India) for his indispensable

inputs in my Ph.D. work. His valuable comments and suggestions during the preparation of several manuscripts in my Ph.D. are greatly appreciated. I especially thank Dr. Satyakumar (NGRI, Hyderabad) for clearing my doubts in planetary data analysis. His help in different stages of my Ph.D. is appreciated.

Besides, the Earth Science Lab members have contributed immensely to my personal and professional time at IIST. My sincere thanks go to Ms. Haritha A., Dr. Sam Uthup, Shri. Muhammed Faisal, Mr. Asif Iqbal Kakkassery, Ms. Saranya R, and Mr. Deepchand Balamani, for their role as fellow labmates. I am particularly indebted to Ms. Haritha A. my fellow lab mate and loving friend, for helpful discussions and unconditional help during my Ph.D. Other past and present group members that I have had the pleasure to work with or alongside are grad students Ms. Jappji Mehar, Ms. Sai Neelu Harishchandran, Mr. Juda Benhur, Mr. Shubhonkar Paramanick, and the many project students who have come through the lab. I also acknowledge the staff members in the ESS department (IIST), Ms. Aswathy S. for her help during hyperspectral measurements and Mr. Sai, Ms. Shalini, and Mr. Ashwin for their help in administrative affairs.

I sincerely thank my colleagues Dr. Harish Nandal and Ms. Tanu Singh from PRL, Ahmedabad, and Ms. Nabamita Chaudhary (Pondicherry University) for their valuable help related to my research. I am grateful for the time spent with my friends in IIST, Sajith Sadashivan, and Sarath. Lastly, I would like to thank my family and friends for all their love and encouragement. And most of all for my loving, supportive, encouraging, and patient partner, Dr. Hrushikesh Hari whose faithful and unconditional support during my Ph.D. is appreciated. My heartfelt thanks to him. Lastly, I take this opportunity to extend my sincere gratitude and appreciation to all those who made this Ph.D. possible.



Thesniya P. M.

Abstract

The knowledge about endogenic and exogenic processes on the Moon is imperative to understanding the evolutionary history of our nearest neighbour. This Ph.D. work focuses on understanding these processes by studying the spectrochemical characteristics and geological context of pyroxene- and spinel-bearing lithologies and morphology of impact craters on the Moon. The research primarily utilized orbital remote sensing datasets from various lunar exploratory missions, particularly ISRO's Chandrayaan-1 mission. The investigation of the Grimaldi and Humorum basins based on pyroxene chemistry and crater chronology provided new insights into the Main-phase and Late-phase volcanic history of the Moon. The estimated long span of volcanism in the Grimaldi and Humorum basins (3.5 Ga – 1.5 Ga) indicates the extended history of lunar thermal evolution. Multiple volcanic episodes have occurred in the Mare Humorum. The older mare basaltic units that erupted during the Imbrian period crystallized from a more fractionated magma, whereas the younger unit crystallized from Mg and Ca-rich magma. The younger basaltic unit's longward shift in Band I and Band II centres indicates a higher Ca^{2+} -rich parental magma composition. The older units' shortening of Band I and Band II centres indicates that the older basaltic magma formed more Fe^{2+} -rich pyroxenes or clinopyroxenes with lower Ca^{2+} concentrations during cooling. It has been concluded that magmas of diverse chemical nature originating from different source regions have erupted in the Humorum basin during the Imbrian to Eratosthenian periods. In addition to discoveries that fit prior identifications of older mare basalts in the Grimaldi basin, the current investigation has revealed younger basaltic units in the Mare Grimaldi and Mare Riccioli with greater FeO and TiO_2 concentrations. The chemical variations in these volcanic basalts were determined using their pyroxene compositions, hinting at the heterogeneous lunar mantle and multiple eruptions in the basins. The wide variations in FeO and TiO_2 contents of basalts and the presence of younger, olivine-bearing, high-Ti basalts point to the chemical evolution of the magma over time and their diverse source regions in the lunar mantle. The Late Imbrian low to intermediate-Ti basalts erupted in the Mare Grimaldi and Mare Riccioli at ~3.5 Ga are derived from, melting of early cumulate materials caused by radioactive heating, or from molten zones that remained in the mantle after initial global melting in the hybrid source region

of the post-overturn upper mantle, which erupted through dikes. The Eratosthenian high-Ti magma that erupted at ~2.5 Ga in the Mare Grimaldi is suggested to have been formed through partial melting caused by a hot plume rising from the deeper clinopyroxene-ilmenite-rich cumulates near the core-mantle boundary. The intermediate-Ti basalts (~1.5 Ga event) in the Mare Riccioli formed through a different process where the ilmenite-clinopyroxene cumulates remained in the upper mantle after the mantle overturn remelted to generate high-Ti magmas. The origin of these mare basalts at different depths in the mantle favour the idea of a possible lunar mantle overturn following the LMO (Lunar Magma Ocean) crystallization. In addition, the long span of volcanism in the Grimaldi and Humorum basins (3.5 Ga – 1.5 Ga) suggests the extended history of the thermal evolution of the Moon.

The investigation of compositional variations of spinels in diverse rock types on the Moon showed that lunar spinels are generally chromites, ulvospinels, pleonaste, and Mg-Al compositions. The comparison of lunar magmatic spinels with terrestrial spinel compositional fields showed an affinity to boninites and komatiites for lunar Cr-spinels, and hence suggested a mantle origin for Cr-spinels on the Moon. The comparison of lunar spinels with the terrestrial spinel from Sittampundi Anorthosite Complex (SAC) based on their spectrochemical characteristics has put significant constraints on the remote identification of lunar spinel chemistry. The Cr-spinels in SAC have a Fe- and Al-rich composition, with Cr₂O₃ concentrations and Cr# ranging from 32–37 wt percent and 0.44–0.53, respectively. The conspicuous Raman peak associated with Cr-spinels' A_{1g} mode ranges from 703 to 714 cm⁻¹, with a shoulder about 671 cm⁻¹. The coexistence of (Mg, Fe) in the tetrahedral site and (Al, Cr) in the octahedral site causes the A_{1g} peak position near 705 cm⁻¹. Because of the increased Al content (Al₂O₃ ~25 wt%) in the SAC Cr-spinels, the 2 μm band position is at shorter wavelengths than conventional Cr-spinels. The Cr# and Cr₂O₃ contents have a positive association with the 2 μm band location, but the Al₂O₃ concentration has a negative correlation. The replacement of Al and Cr for one another in the octahedral site explains the linear relationship. Based on their spectrochemical features, the observed linear connection between 2 μm band position and Cr/Al abundances can be used to distinguish Al-spinels from Cr-spinels. Through an integrated and comparative investigation of spectroscopic and chemical data, the study has unambiguously demonstrated the relationship between the spectral pattern and the chemistry of Cr-spinels. The interpretation of possible occurrences of Fe- and Cr-bearing spinels in the Sinus Aestuum on the Moon was made possible by comparing the spectral properties of SAC Cr-spinels with those of previously detected spinels from Sinus Aestuum. The established spectral-chemical relationships will serve as a reference for separating lunar Al spinels from Cr-spinels. If limited knowledge on their formation processes

involving melt-wall rock interaction on both the planetary bodies is addressed, the SAC-hosted Cr-spinels could serve as a potential functional analogue for lunar Fe- and Cr-bearing spinels. Further, the spectrochemical data of terrestrial spinels derived in this study will greatly add to the lunar analogue database that could be utilized for instrument calibration in future exploration missions.

Impact cratering mechanics of the Moon have been understood by studying the cratering mechanics of Copernican craters (<1 Ga old). The Ohm and Das craters are Copernican craters on the farside of the Moon, which records the diverse processes of impact cratering events on the Moon. Starting with the sharp and scalloped rim, an alcove of wall terraces, the distinct scarp-tread system with steep slopes on the scarp, wall slumping, impact melt deposits, flat floor with hummocky texture, slump hillocks on the floor, melt platform, and central mounds with bedrock exposures, the morphological mapping interior to the crater cavity revealed the characteristic geological features of this complex impact crater. These diverse morphological elements show that the Das crater began as a simple bowl-shaped crater that evolved into a complex crater over time. In less than 4 seconds, the transient crater cavity for the Das crater was excavated. The greatest excavation depth is predicted to be 3 kilometers. The transient crater diameter is expected to be 30.4 kilometers, with a depth of 7.6-9.12 kilometers. The crater was excavated at the same time as shocked and melted debris was ejected outward as impact ejecta. Even before the central mounds developed from depths of maximally compressed materials at roughly 3.2 km, the crater was being modified. The consequent gravitational collapse of the rim resulted in terraced, steeper walls, resulting in a widening of the crater rim along W-E and enlargement of the final diameter to 38 km. On the western inner wall, the wall slumping was more severe, and the slumped materials fell to form heaps of hillocks, mostly in the western half of the floor. The eastern crater floor has sunk, most likely as a result of structural collapse and/or the cooling of the first melt column. The impact melts line the temporary crater cavity throughout its expansion, forming ponds in the wall terraces, vast melt sheets along the inner wall slopes, and melt-draped floor units, among other topographic features. Melt breccia, shattered impact melt deposits with boulders at their edges, and characteristic flow features like melt fronts or flow lobes centered on the inner wall of the crater are all diagnostic of impact-generated melts. Solid and melt phase ejecta are scattered around the crater rim outside the crater cavity, with highly shocked debris components occurring at radial distances beyond the rim and melted debris preferentially occupying topographic lows and slopes both inward and outward from the crater rim. The infilling of secondary crater chains and subsequent overprinting by the contiguous ejecta blanket resulted

from the ground-hugging flow of heterogeneous materials. Within 7 km radial extents from the rim crest, melt-bearing ejecta is spread as rim veneer deposits, ponded melt, and lobate deposits, which entirely overlie the adjacent ejecta blanket. Ballistic ejecta facies have a non-uniform distribution across the crater, with the greatest radial extents in the northwestern and southeastern quadrants compared to the less extensive deposits in the southwest and NNE quadrants, exhibiting asymmetric ejecta with bilateral symmetry along the NNE-SSW line going across the crater's centre. The occurrence of a forbidden zone to the NNE that is free of distal ejecta rays and secondary crater chains shows that the impact was NNE-SSW. The crater's nearly circular shape, together with a well-defined forbidden zone in the uprange, imply that the impact happened at a 15° - 25° inclination to the horizontal. The findings of this study show that studying Copernican craters is critical for furthering our understanding of the Moon's impact dynamics and cratering mechanics.

The discovery of the Late-Imbrian and Eratosthenian volcanic events on the lunar nearside, the compositional diversity of lunar spinels and possible mantle origin of Cr-spinels, and the interpretations on cratering processes and impact dynamics on the Moon during the Copernican epoch reveal that the geological history of the Moon is as vast as we have known yet, and our Moon could still be evolving.

Contents

List of Figures **xvii**

List of Tables **xxxiii**

1	Introduction	1
1.1	Significance and scope of study.....	4
1.1.1	Volcanic and thermal history of the Moon.....	4
1.1.2	Spinel compositions on the Moon and lunar functional analogues	7
1.1.3	Impact cratering mechanics of the Moon	10
1.2	Objectives	13
2	Approach used	15
2.1	Utilization of orbital remote sensing data.....	16
2.1.1	Reflectance spectroscopy	17
2.1.1.1	Reflectance spectroscopy of the Moon.....	18
2.1.1.2	Hyperspectral data analysis for identifying the minerals and their chemistry.....	20
2.1.1.2.1	Integrated Band Depth (IBD).....	20
2.1.1.2.2	Continuum removal	22
2.1.1.2.3	Band parameters.....	23
2.1.1.3	Dating of the lunar surface from crater statistics	24
2.1.1.4	Techniques used for spectroscopic and chemical analyses of Cr-spinels.....	28

	i) Fourier Transform Infrared Spectroscopy.....	28
	ii) Laser Raman spectroscopy.....	29
	iii) X-ray Diffraction.....	31
	iv) Electron Probe Micro – Analysis (EPMA)	33
3	Evidence for Late-Imbrian and Eratosthenian Mare Volcanism in the Grimaldi Basin on the Nearside of the Moon: Implications for the Lunar Mantle Heterogeneity and Thermal Evolution.....	35
	3.1 Introduction.....	36
	3.1.1 Geological background of the study area.....	38
	3.2 Datasets and methods.....	41
	3.3 Results.....	43
	3.3.1 Spectral and compositional diversity of the Mare Grimaldi and Mare Riccioli units.....	44
	3.3.2 FeO and TiO ₂ abundance map.....	45
	3.3.3 Compositional variations from color composite images.....	47
	3.3.4 Mineralogical signatures from M3 spectra.....	50
	3.3.5 Determining the composition of the pyroxenes based on their band parameter analysis.....	55
	3.3.6 Model ages of Mare Grimaldi and Mare Riccioli using CSFD.....	60
	3.4 Discussions.....	63
	3.4.1 Possible origin and emplacement history of the Mare Grimaldi and the Mare Riccioli.....	65
	3.4.1.1 Basin-forming impact event (>3.9 Ga, Pre-Nectarian).....	65
	3.4.1.2 Emplacement of the older low- to intermediate-Ti basalts during the first phase of volcanism in Late Imbrian Epoch (3.5–3.2 Ga).....	66
	3.4.1.3 Emplacement of the younger high-Ti basalts during the second phase of volcanism in the Eratosthenian period (~2.05 to 1.5 Ga).....	69
	3.5 Conclusions.....	71

4	Pyroxene chemistry and crystallization history of basaltic units in the Mare Humorum on the nearside of the Moon: Implications for the volcanic history and heterogeneity of the lunar mantle.....	75
	
4.1	Introduction.....	76
4.1.1	Study area.....	78
4.2	Datasets and methods.....	79
4.3	Results.....	82
4.4	Discussions.....	86
4.5	Conclusions.....	89
5	Compositional variations in spinels on the Moon	91
5.1	Introduction.....	91
5.2	Datasets and methods.....	94
5.3	Results.....	96
5.3.1	Spinel in diverse lithologies on the Moon.....	99
5.3.1.1	Basalt.....	99
5.3.1.2	Breccia.....	101
5.3.1.3	Lunar meteorites.....	104
5.3.1.4	Meteorites from returned samples.....	106
5.3.1.5	Soil.....	108
5.3.1.6	Troctolite.....	110
5.3.1.7	Composite.....	112
5.3.1.8	Crustal cataclasite.....	114
5.3.1.9	Unclassified.....	116
5.4	Discussion and Conclusion.....	118
5.4.1	Comparison with compositional fields of terrestrial spinels and possible origin of lunar spinels.....	119
	
6	Compositional and spectrochemical analyses of chromium spinels in the Sittampundi Anorthosite Complex, southern India: Implications for remote observation of spinels on the Moon.....	123
	
6.1	Introduction.....	124
6.2	Geological setting.....	130

6.2.1	Mode of occurrence of chromitites in the SAC.....	131
6.3	Methodology.....	132
6.3.1	Sample preparation.....	132
6.3.2	Chemical and spectral analyses.....	133
6.4	Results and discussions.....	134
6.4.1	Petrography.....	134
6.4.2	Mineral chemistry.....	136
6.4.3	Spectral analyses.....	140
6.4.3.1	Laser Raman analysis.....	140
6.4.3.2	Hyperspectral analysis.....	143
6.4.3.3	Fourier Transform infrared spectroscopic analysis....	150
6.4.4	Implications for the characterization of spinels on the Moon..	152
6.5	Summary.....	158
7	Morphology and ejecta emplacement dynamics of the selected Copernican craters on the lunar farside: Insights into cratering mechanics of the Moon.....	161
7.1	Introduction.....	162
7.2	Morphology of the Ohm crater on the farside of the Moon.....	165
7.2.1	Data acquisition.....	167
7.2.2	Methodology.....	168
7.2.3	Results.....	168
7.2.3.1	Central peak.....	169
7.2.3.2	Mounds.....	171
7.2.3.3	Crater floor units.....	172
7.2.4	Summary.....	182
7.3	Morphology and ejecta distribution of the Das crater.....	185
7.3.1	Datasets.....	187
7.3.2	Methods.....	188
7.3.3	Results.....	189
7.3.3.1	Geomorphic units interior to the Das crater cavity.....	191
i.	Crater rim and terraced walls.....	191
ii.	Crater floor–Lower Hummocky unit and Elevated Hummocky unit.....	199

iii. Central mounds or peaks.....	206
7.3.3.2 Identification of the distinct ejecta facies and their distribution both interior and exterior to the crater cavity.....	208
i) Continuous and Discontinuous ejecta.....	209
a) Facies A.....	213
b) Facies B.....	219
c) Facies C.....	220
d) Facies D.....	224
7.3.4 Discussions.....	225
7.3.4.1 Cratering mechanics involving the stages in the development of the complex Das crater.....	225
7.3.4.2 Emplacement mechanism of distinct ejecta facies.....	228
i. Ballistic ejecta (Facies A and D).....	228
ii. Melt-phase ejecta (Facies B and C).....	230
7.3.4.3 Determining the direction and angle of the impact event..	231
7.3.5 Conclusions.....	235
8 Summary and conclusions.....	237
8.1 Summary.....	237
8.2 Conclusions.....	240
8.3 Future scope of the work.....	241
Bibliography	243
List of Publications	293

List of Figures

1.1	Lunar Reconnaissance Orbiter Camera –Wide Angle Camera (LROC WAC) mosaic of the nearside and farside of the Moon	2
1.2	The schemata showing the lunar magma ocean crystallization (Source: scientific report, 2007, NASA)	3
1.3	The schemata depicting the outline of the Ph.D. work	4
1.4	LROC WAC-derived TiO ₂ abundance map of the lunar surface. Varying titanium contents in the mare basaltic units are visible	5
1.5	Schemata representing the mechanism of lunar mantle overturn post-magma ocean crystallization	6
1.6	Schemata showing the current understanding of the volcanic evolution of the Moon	7
1.7	(A) Image of the Apollo 16 rake sample, 65785, with a pink-spinel troctolite clast in it (labeled as PST) (Credits: NASA S72-48821). Scale bar is in mm. (B) Thin-section image of the lunar meteorite ALHA81005 showing the pink spinel (pink-grains) in polarized light (From Gross and Treiman, 2011). (C) Spinel detections on the lunar farside and nearside (pink filled circles) (Dhingra et al., 2011; Prissel et al., 2014)	8
1.8	Schemata showing the methods involved in studying the lunar analogues	9

1.9	Impact crater morphologies on the Moon. (a) Microcrater ($D < 1$ mm) found in returned lunar samples. (b) LROC NAC mosaic of the Lichtenberg B crater ($D \sim 5$ km) representing a simple bowl-shaped crater. (c) LROC NAC DTM of the Hell Q crater ($D \sim 3.75$ km). (d) LROC WAC mosaic of the Tycho crater representing a complex impact crater ($D \sim 86$ km). (e) LOLA DEM overlaid on the LOLA hillshade showing the multiring Orientale basin (Barker et al., 2016). North is up in images	11
1.10	Left image: LROC nearside view of the Moon, highlighting the Tycho crater with bright ejecta rays. Right image: A complex crater on the lunar surface having bright radial ejecta rays	12
1.11	Schemata showing the methodology followed for understanding the impact cratering mechanics of the Moon	12
2.1	Schemata depicting the approach used for studying the attributes of endogenic and exogenic processes on the Moon	15
2.2	Depicting the remote observation of the Moon based on reflectance spectroscopy	16
2.3	Wavelength ranges of electromagnetic radiation. The range of wavelengths used to study morphology, mineralogy, and bulk composition is labelled in the figure	17
2.4	Laboratory reflectance spectra of the (A) low-calcium and high-calcium pyroxenes and (B) spinels	18
2.5	Schemata showing the outline of research carried out in the Ph.D. work	19
2.6	Illustration of the M3 continuum removal procedure. The continuum slope is drawn between the tangent points on both sides of the absorption bands	22
2.7	A mare region on the nearside of the Moon. The delineated mare units (Red and blue polygons) have experienced distinct formation history	25

2.8	Top image: Cumulative crater frequency. Bottom image: Cumulative PF fitting (Source: Greg Michael, 2012)	26
2.9	Schemata showing the steps involved in age determination using crater statistics	27
2.10	The FTIR instrument used for measuring the absorbance spectra	29
2.11	The Laser Raman instrument used for measuring the spectra	31
2.12	The XRD instrument used for measuring the spectra	32
3.1	(A) LROC-WAC mosaic of the western limb of the Moon in stereographic projection, centered on the Grimaldi basin at 5°S, 68°W. The white rectangle on the image outlines the area chosen for the present study. (B) WAC grayscale mosaic image of the Grimaldi basin. (C) Color-coded LRO-LOLA & Kaguya Terrain Camera Merge DEM of the Grimaldi basin showing the major topographic units in the basin. The mare basaltic units, namely Mare Grimaldi and Mare Riccioli, have also been labeled in the figure	39
3.2	Simplified geomorphologic map of the Grimaldi basin (modified after Lunar Geologic Renovation; Fortezzo and Hare, 2013)	40
3.3	The schemata showing the methodology adopted for carrying out the studies related to the volcanic and thermal evolution of the Moon	43
3.4	M3 R1578 nm albedo map of the (A) Mare Grimaldi and (B) Mare Riccioli (stretched from 0.057 to 0.184)	44
3.5	(A) Kaguya-MI derived FeO abundance map of the Mare Grimaldi. (B) LROC WAC derived TiO ₂ abundance map of the Mare Grimaldi. (C) Kaguya-MI-derived FeO abundance map of the Mare Riccioli. (D) LROC WAC TiO ₂ abundance map of the Mare Riccioli	46

3.6	(A) M ³ color composite image (red: stretched between 0.572 and 2.660, green: stretched between 0.38 and 0.98, blue: stretched between 0.049 and 0.095) of the Mare Grimaldi showing the mineralogical variations among the predefined basaltic units. (B) M ³ color composite of the Mare Riccioli. (C, D) Clementine color ratio image of the Mare Grimaldi and Mare Riccioli showing the presence of basaltic units having compositional differences	48
3.7	Color-coded IBD1000 parameter map of the (A) Mare Grimaldi and (B) Mare Riccioli. (C) Kaguya MI-derived olivine abundance map (wt%) of the Mare Grimaldi. (D) Kaguya MI-derived olivine abundance map of the Mare Riccioli	49
3.8	(A–D) Representative reflectance spectra of the basaltic units in the Mare Grimaldi. (A, B) Normal and continuum removed spectra for G1, G2, G3, and G4 units in the Mare Grimaldi. (C, D) Normal and continuum removed spectra for the R1 and R2 units in Mare Riccioli. The black dashed lines are drawn at 1000 and 2000 nm. (E, F) Representative reflectance spectra of pure anorthosite (PAN) and crystalline plagioclase obtained from the Grimaldi S crater located along the inner ring of the Grimaldi basin. The spectra collected locations have been labeled in Fig. 3.7A & B	52
3.9	(A–H) Normal and continuum removed reflectance spectra of the clinopyroxenes collected from G1 (A–B), G2 (C–D), G3 (E–F), and G4 (G–H) units of the Mare Grimaldi. The black dashed lines are drawn at 1000 and 2000 nm. The spectra collected locations have been shown in Fig. 3.7A	53
3.10	(A–D) Normal and continuum removed reflectance spectra of the clinopyroxenes collected from the R1 (A, B) and R2 (C, D) units in the Mare Riccioli. The black dashed lines are drawn at 1000 and 2000 nm. The spectra collected locations have been shown in Fig. 3.7B	54
3.11	Pyroxene quadrilateral plot showing the relative abundance of the endmember compositions in the Mare Grimaldi and Mare Riccioli	56

3.12	(A) BAR versus Band I center plot of the compositions sampled from the Mare Grimaldi and Mare Riccioli (after Gaffey et al., 1993). (B) BAR versus Band I displacement plot of the compositions from Mare Grimaldi and Mare Riccioli. (C) Band II centers are plotted against the corrected Band I centers of the pyroxene bearing spectra from the Mare Grimaldi and Mare Riccioli. (D) Mole % compositions of pyroxenes in Mare Grimaldi and Mare Riccioli projected onto the pyroxene quadrilateral along with the equilibrium pyroxene temperatures based on the graphical thermometer developed by Lindsley and Anderson (1983)	58
3.13	Model ages of the Mare Grimaldi and Mare Riccioli basaltic units determined based on the CSFD technique. (A) Kaguya TC image of the Mare Grimaldi showing the crater count areas for each basaltic unit, G1, G2, and G3. (B) TMC image of the Mare Riccioli showing the crater count area for the R1 and R2 units	60
3.14	Cumulative frequency plots of the G1–G2 (merged) and G3 unit in the Mare Grimaldi along with isochron and error for the data points. The younger age of 2.05 Ga corresponds to the age of the merged unit, that is, G1 and G2 (high-Ti basalts). The older age of 3.47 Ga shows the age of the G3 unit (low to intermediate-TiO ₂ basalts)	61
3.15	Cumulative frequency plot of the R1 unit along with age isochron and error for each data point	62
3.16	Cumulative frequency plot of the R2 unit along with age isochron and error for each data point	62
3.17	Schematic representation showing the stages involving emplacement of mare basaltic units in the Grimaldi basin. (A) The early stage of the Grimaldi basin consisting of a transient crater cavity in the pre-Nectarian period. The impact-generated heat would have caused the rising of isotherms and triggered melting up to several kilometers depth, often exceeding the depth of the transient crater cavity. (B) The upliftment of deep-seated lithologies onto the surface by isostatic rebound followed by	67

the impact event. The eruption of the low to intermediate-Ti basalts from the early cumulates in the upper mantle during ~3.5 to 3.2 Ga period (Late Imbrian), which filled the low-lying interior of the basin and forms the lower Mare Grimaldi and Mare Riccioli units. (C) Younger events of intermediate to high-Ti magmas erupted at ~2.05 Ga and ~1.5 Ga ago (Eratosthenian) in the Mare Grimaldi and Mare Riccioli, respectively. The high-Ti magma erupted in the Mare Grimaldi, possibly sourced from a hot plume, risen from ilmenite–clinopyroxene cumulate layer near the core-mantle boundary. In contrast, the youngest intermediate-Ti Riccioli basalt formed from the magma generated through partial melting of pods of early ilm-cpx cumulates that remained in the upper mantle after mantle overturn

3.18	(A) LRO DIVINER-derived crustal thickness map of the Grimaldi basin. (B) Crustal thickness profile across the basin (NW-SE)	70
4.1	(A) LROC-WAC mosaic of the western limb of the Moon in stereographic projection. (B) WAC grey-scale mosaic image of the Humorum basin. (C) Color-coded LRO-LOLA & Kaguya Terrain Camera Merge DEM of the Humorum basin showing the topography of the basin	77
4.2	M3 1578 nm albedo map showing the albedo variations in different basaltic units in the Mare Humorum. The boundary of the distinct basaltic units previously defined by Hackwill et al. (2006) in the Mare Humorum has been redrawn over the M3 albedo image. The ages available for the individual basaltic units have been labelled	81
4.3	(A) Kaguya MI-derived FeO abundance map of the Mare Humorum. (B) TiO ₂ abundance map derived from LROC-WAC data.	83
4.4	(A) M3 colour composite image of the Mare Humorum generated by assigning IBD1000, IBD2000, and R1578 to the red, green, and blue channels, respectively (Mustard et al., 2011). (B-C) Normal and continuum removed reflectance spectra from the different basaltic units within the Mare Humorum	84
4.5	(A) Band II centre vs Band I centre plot of pyroxenes from individual	86

	basaltic units within the Mare Humorum. (B) Band II centre vs Band I centre plot focused on the data of the analyzed pyroxenes	
4.6	Pyroxene quadrilateral plot showing the mole % compositions of endmember pyroxenes from individual basaltic units within the Mare Humorum along with the equilibrium pyroxene temperatures based on the graphical thermometer developed by Lindsley and Anderson (1983)	87
4.7	(A) Age vs Band I center plot of individual basaltic units within the Mare Humorum. (B) Age vs Band II center plot of the basaltic units within the Mare Humorum.	88
5.1	Known locations of spinels (marked as triangles) identified on Moon using remote sensing techniques. The base image is the LOLA-KAGUYA merged DEM in Equidistant cylindrical projection ($<60^\circ$), showing the topography of the lunar surface	92
5.2	Schemata showing the methodology followed for carrying out the present research on spinel compositions and origin	95
5.3	The histograms depicting the oxide concentrations, Mg#, and Cr# in spinels from different rock types on the Moon	97
5.4	The compositional variations of lunar spinels represented on a magnetite triangle projection, ulvospinel triplot, and bivariate plots of #Mg vs #Cr, #Fe ³⁺ vs TiO ₂ , #Fe ²⁺ vs #Fe ³⁺ , and #Fe ²⁺ vs #Cr. The compositional field and trend lines of terrestrial spinels are overlaid in the plots	98
5.5	The histogram showing the oxide concentrations in spinels from basalts	99
5.6	Spinel compositional diagrams plotted for spinel compositions from various basalts in the returned samples	100
5.7	Histogram showing the oxide concentrations of the spinels in breccia	102
5.8	Compositional diagrams for spinels from various breccia samples	103

5.9	Histogram showing the oxide concentrations of the spinels in lunar meteorites	104
5.10	Compositional diagrams for spinels from various lunar meteorites	105
5.11	Histogram showing the oxide concentrations of the spinels in meteorites from returned samples	106
5.12	Compositional diagrams for spinels in meteorites from returned samples	107
5.13	Histogram showing the oxide concentrations of the spinels in soil samples	108
5.14	Compositional diagrams for spinels in soil samples	109
5.15	Histogram showing the oxide concentrations of the spinels in troctolite samples	110
5.16	Compositional diagrams for spinels in troctolites	111
5.17	Histogram showing the oxide concentrations of the spinels in composite samples	112
5.18	Compositional diagrams for spinels in composite samples	113
5.19	Histogram showing the oxide concentrations of the spinels in crustal cataclasites	114
5.20	Compositional diagrams of spinels in crustal cataclasite	115
5.21	Histogram showing the oxide concentrations of the spinels in unclassified samples	116
5.22	Compositional diagrams of spinels in crustal cataclasite	117
5.23	Data density plots for spinels from soil, troctolite, and unclassified rocks	119

5.24	Data density plots for spinels from basalts, breccia, crustal cataclasite, composite, lunar meteorites, and meteorites from returned samples	120
5.25	Ternary plot showing the comparison of lunar spinel compositions with fields of terrestrial spinels from komatiites, boninites, and layered intrusions	122
6.1	Generalized geological map and tectonic framework of the Southern Granulite Terrain (modified after the Geological Survey of India, 2001; Karmakar et al., 2017). Abbreviations: SZ, Shear Zone; LC, Layered Complex (B) Detailed geological map of the Sittampundi Anorthosite Complex showing the distribution of various lithologies (after Subramaniam, 1956)	128
6.2	(A) Field photograph of chromitite-rich amphibolite outcrop in SAC. (B) Photographs of the massive type (C) disseminated type, and (D) layered type chromitites collected from the SAC	132
6.3	(A) Photomicrograph of the Cr-spinels from the SAC showing cumulate texture. The Cr-spinel grains are subhedral to anhedral. (B-C) The Back Scattered Electron (BSE) images of the Cr-spinel grain with inclusions of amphiboles. (D-F) X-ray elemental maps of the Cr-spinel grain showing the distribution and abundance of Cr, Fe, and Mg. Abbreviation: Chr - Cr-spinel	135
6.4	Cr-spinels in the present study plotted in Cr-Al-Fe ³⁺ ternary discrimination diagram for spinels (after Stevens, 1944)	136
6.5	Variation diagrams of (A) Al ₂ O ₃ vs Cr ₂ O ₃ (B) Al ₂ O ₃ vs TiO ₂ and (C) Mg# vs Cr# for the Cr-spinels in the present study plotted along with the previously published data from Sittampundi Anorthosite Complex. An elliptical shape in the figure outlines the Cr-spinels used in the present study. (D) Cr ₂ O ₃ vs Al ₂ O ₃ diagram for Cr-spinels from SAC	138
6.6	X-ray Diffraction spectra of the Cr-spinels from SAC	140

6.7	(A) Laser Raman spectra of Cr-spinels from the present study showing the diagnostic Raman intensity lines corresponding to E_g , F_{2g} , and A_{1g} symmetries. The Al_2O_3 content increases from bottom to top in the figure (in ascending order from SR17 to SR6). (B) Raman A_{1g} peak position vs molar ratio $(Cr + Fe^{3+})/(Cr + Fe^{3+} + Al)$ plot of Cr-spinels from the present study along with the reference data from Malezieux and Piriou (1988)	142
6.8	(A) Normal reflectance spectra of Cr-spinels from the present study. The laboratory reflectance spectra of Cr-spinel, (Mg, Fe) Al spinel, and Cr-bearing Mg-spinel have also been shown for comparison (top). (B) Continuum removed reflectance spectra of the Cr-spinels from the present study along with the reference laboratory spectra. The dashed vertical lines are drawn at 0.49 μm , 0.55 μm , 0.59 μm , 0.93 μm , 1.28 μm , and 2 μm wavelengths	145
6.9	Plot showing the 1.3 μm band position against (A) wt% FeO and (B) wt% MgO of the Cr-spinels from the present study	147
6.10	Plot showing the 2 μm band position against (A) wt% Cr_2O_3 , (B) wt% Al_2O_3 , and (C) Cr# of the Cr-spinels from the present study	149
6.11	FTIR spectra of the Cr-spinels from the present study. (A) Absorbance and (B) Transmittance	151
6.12	(A) The A_{1g} peak position of the SAC Cr-spinels and their corresponding cation distribution in the tetrahedral and octahedral sites of the spinel structure (modified after Wang et al., 2004). (B) The absorption band centres of Cr-spinels in SAC and their corresponding cations of tetrahedral and octahedral sites (after Cloutis et al., 2004)	153
6.13	The absorption band centres in SAC Cr-spinels are compared with those from the spinels in the Sinus Aestuum region on the Moon (Yamamoto et al., 2013)	154
7.2.1	Location of the Ohm crater on the farside of the Moon.	165

7.2.2	Clementine UV-VIS color ratio satellite image covering the Ohm crater and the extension of its ejecta material on the lunar highlands. (Red = 750 nm/415 nm, Anorthosite; Green = 750 nm/950 nm, Iron-rich, low TiO ₂ ; Blue = 414 nm/750 nm, Iron-rich, high TiO ₂)	165
7.2.3	(A) WAC mosaic showing the major geomorphic units in the Ohm crater. (B) DEM of the Ohm crater with the contours labelled. (C) Topographic profile across A-B in Figure 7.2.3.A	166
7.2.4	Detailed morphological map of the Ohm crater	169
7.2.5	(A) WAC mosaic of the Ohm crater showing the central peak of the crater, evidence for impact melting are marked as rectangles. (B-C) Impact melt deposits and boulders on the central peak. (D) Melt pond on the summit of the central peak	170
7.2.6	(A) WAC mosaic of the Ohm crater with the locations of the isolated mounds marked as rectangles. (B-D) LROC-NAC images of the isolated mounds identified from the crater floor	171
7.2.7	Detailed morphological map of the floor of the Ohm crater draped over WAC mosaic	173
7.2.8	a) 3D view of the floor of the Ohm crater. (b) Topographic profile across NE-SW section of the crater floor	174
7.2.9	Sinuous rille observed in the southeastern edge of the central peak	175
7.2.10	(A) WAC mosaic of the Ohm crater with the selected locations of the cooling cracks, marked as rectangles. (B-C) Polygonal cooling cracks were identified in association with dome-like features on the crater floor. (D) Polygonal cracks and associated domes mapped on the NAC image	176
7.2.11	(A) WAC mosaic of the Ohm crater with the selected locations of the domes, marked as rectangles. (B-F) NAC images showing the domes in different parts of the crater	177

7.2.12	Left image: LROC NAC image showing the western crater wall. Right image: Topographic profile across A-B in the left figure	179
7.2.13	(A) LRO WAC image showing the locations of channelized flows. (B) Basaltic flow with smooth texture. (C) Basaltic flow with a rough texture. (D) Basaltic flow with ropy texture	179
7.2.14	(A) WAC mosaic of the Ohm crater with the locations of the melt ponds marked as rectangles. (B-E) NAC images of the melt ponds identified in the crater. (F) Lava pool in spiral form due to the falling of clasts into the pooled lava	181
7.2.15	(A) LRO WAC image showing the locations of the ejecta boulders. (B) Linearly distributed boulders. (C) Larger boulders. (D) Highly weathered boulders	182
7.2.16	3D view of the Ohm crater and the associated unnamed crater towards the east of the Ohm crater	183
7.3.1	(A) Colour-coded Kaguya-LOLA DEM merge overlaid on LOLA global hillshade, showing the location of the Das crater on the farside of the Moon. The enlarged image shows the Hapke WAC colour ratio image displaying the Das crater and its bright ejecta rays. (B) WAC mosaic of the Das crater showing its basic morphology. (C) Topographic profile across the line A-B in Fig. 7.3.1B	186
7.3.2	(A) Color LOLA-Kaguya DEM marge of the Das crater showing the elevation differences in the region. (B) The topographic profile across the line is shown in the inset image. The inset image is the WAC mosaic of the Das crater	190
7.3.3	(A) Colour-coded slope map of the Das crater derived from LOLA-Kaguya DEM marge. (B) LOLA hillshade view of the Das crater showing the major geomorphic units in the crater. (C) Detailed geological map of the Das crater showing the distinct geomorphic units interior to the crater cavity	192

7.3.4	(A) TC mosaic of the western section of the Das crater. (B) The wall terraces are mapped (brown shades) on the LOLA hillshade view of the Das crater. (C) Enlarged view of the white rectangular box in Fig. 7.3.4A. (D) Terraces on the inner wall grading narrower, closely spaced faults towards the crater centre.	193
7.3.5	(A) TC mosaic of the western section of the Das crater shows impact melt deposits on the wall and floor. (B-C) Melt lobe identified on the wall terrace. (D) Melt platform on the crater floor	194
7.3.6	(A-G) Impact melt flow fronts identified along the western and eastern inner wall slopes. (E & G) The enlarged view of the yellow rectangle in Figs 6D & F, respectively	195
7.3.7	(A-J) The fractured impact melt deposits identified on the sloping wall of the Das crater. (F) The enlarged view of the region inside the yellow rectangle in Fig. 7.3.7E. (K) The boulders eroded out of the fractured impact melt deposits and reached the adjoining floor. (L) The enlarged view of the area inside the yellow rectangle in Fig. 7.3.7K. (M-O) Fractured impact melt deposits with boulders distributed on its margins. (N) The enlarged view of the region inside the yellow rectangle in Fig. 7.3.7M	196
7.3.8	(A) Locations of the melt ponds identified in the crater. (B-F) The smooth melt ponds on the wall terraces. (G-I) Melt breccia melt on the inner wall of the crater	198
7.3.9	(A) Locations of the slump hillocks. (B) Enlarged view of the slump hillock on the crater floor. (C-E) Fractured impact melt deposits on the slump hillock surfaces. (F) Eroded boulders are reaching the adjoining floor of the crater. (G) Cooling cracks on the melt-draped hillocks. (H) Heaps of wall slumps on the northwestern edge of the floor. (I) Small superposed impact crater at the summit of the slump hillock is marked using the yellow arrow	199
7.3.10	(A) Color-coded DEM of the crater floor. (B) Hummocky floor units in the crater. (C) The 3D view of the crater floor. (D) Topographic profile	200

- 7.3.11 (A) NAC mosaic of the Das crater floor shows the hummocky unit marked by the yellow polygon. Surface morphology of the elevated hummocky unit (B) and lower hummocky unit (C) in the crater floor. (D-F) Showing the circular uprisings or mounds in the hummocky floor. (G) Fractured impact melt deposits and eroded boulders on the top of a mound on the hummocky floor 201
- 7.3.12 (A) NAC mosaic of the crater. (B-F) NAC mosaic displaying the domes in the elevated hummocky floor. (G-O) NAC mosaic showing the domes identified in the lower hummocky floor 202
- 7.3.13 (A) NAC mosaic of the crater interior. (B-F) Enlarged views of the cooling cracks in the northern and southern sections of the hummocky floor 203
- 7.3.14 (A) LOLA hillshade view of the crater interior. (B) The topographic profile across line A-B in Fig. 7.3.14A. (C) Colour-coded DEM of the eastern floor region. (D) 3D representation of the NAC mosaic manifesting the subsided floor resulting in the elevated hummocky floor and lower hummocky floor. (E) The diagram illustrates the perspective described in Fig. 7.3.14E. (F-G) The topographic profile across lines A-A', B-B', and C-C' in Fig. 7.3.14C 204
- 7.3.15 (A) NAC mosaic of the crater interior. (B-F) NAC mosaic of the intersecting grabens trending NW-SE along the elevated and lower floor regions. (G) LOLA hillshade view of the crater interior overlaid with colour-coded DEM of the floor region, showing the elevated terrain (black dashed polygon) comprising the melt platform in the western section of the floor. (H) TC mosaic showing the elevated terrain with melt platform 205
- 7.3.16 (A) NAC mosaic shows the central mounds of the Das crater. (B) The topographical profile across line A-A' in Fig. 7.3.16A. (C) NAC mosaic showing the melt fronts on central mounds. (D) The flanks of the central mounds with bedrock exposures (purple arrow). (E) NAC mosaic shows several intersecting channels trending NW-SE near the base of the central mound. (F) NAC mosaic shows a prominent channel near the base (to the northeastern part) of the mound. (G) The topographic profile across line B-

B' in Fig. 7.3.16F, showing the cross-section of the channel. (H) NAC mosaic showing the path of flows along the flanks of the mound

- 7.3.17 (A) Hapke WAC mosaic shows the Das crater and its ejecta rays on the equidimensional surface of the lunar farside. (B) Hapke WAC colour ratio image displaying the bright ejecta rays (Bright blue) of the Das crater 210
- 7.3.18 (A) LOLA DEM of the region surrounding Das crater. (B-C) WAC farside mosaic showing the enlarged view of the Das crater, highlighting the western section wherein the remnant ridge (pointed by arrows) of the SPA ring is seen 211
- 7.3.19 A) Ejecta facies map of the Das crater, overlaid on WAC farside mosaic. (B) SW part of the crater displaying the radial striations of the Facies A ejecta. (C-D) Facies A ejecta appears as radial ridges and troughs intertwined in a chaotic terrain to the SE of the crater. (E) The distinctive pattern of Facies A ejecta to the north and northwest of the crater. (F) Enlarged view of the region inside the red rectangle in Fig. 7.3.19E, showing Facies A ejecta to the northwest of the crater. (G) Facies A ejecta to the northeast of the crater. (H) Colour-coded DEM view of the same perspective as in Fig. 7.3.19G, showing the Orientale grooves to the northeast of the crater. (I) Enlarged view of the region covering the radial facies to the northeast of the crater 214
- 7.3.20 (A) The northwestern quadrant of the crater, showing the surface texture of the Facies A and Facies D deposits. (B) The western side of the crater shows the pre-existing topography of the region. (C) The same perspective as Fig. 7.3.20B, showing the interaction of Facies A deposits with the pre-existing topography. (D-E) The interaction of radial facies with the northeastern slopes of the SPA basin ring (S.R.1 and S.R.2 regions). (F) Facies A deposits to the southeast of the crater, beyond the extent of the Das G crater. (G) Hillshade view of the S and SE parts of the crater. (H) Enlarged view of the region inside the yellow rectangle in Fig. 7.3.20G, showing the distinction between chaotic Facies A deposits and discontinuous ejecta 218

7.3.21	The southern part of the Das crater ejecta	220
7.3.22	The Facies B and Facies C deposits to the east of the crater	221
7.3.23	Colour-coded DEM of the same region as in Fig. 7.3.22, showing the east-sloping topography of the area where Facies B and Facies C deposits co-occur	222
7.3.24	(A) Enlarged view of the region in Fig. 7.3.23. The black dashed line demarcates the rim summit. (B) Enlarged view of the flow lobe (marked by the yellow arrow in Fig. 7.3.24a). (C) The rim veneer deposit (Facies C) is interspersed with ejecta blocks in the northwestern part of the crater. (D-E) Blocky ejecta is seen to the north (D) and east (E) of the crater	223
7.3.25	Radially oriented secondary crater chains and grooves to the northwest (A-B) and southeast (C-D) of the Das crater.	225
7.3.26	Distribution pattern of ejecta facies around Das crater.	233

List of Tables

3.1	Estimated band parameters (avg.) of the pyroxenes from G1, G2, G3, G4, R1, and R2 units along with the absolute model ages of these distinct units in the Mare Grimaldi and Mare Riccioli.	60
5.1	List of returned lunar samples from Apollo and Luna series missions and lunar meteorites.	92
5.2	Diverse rock types identified in the returned lunar samples.	94
6.1	Representative electron microprobe analyses of Cr-spinel samples from the Sittampundi Anorthosite Complex.	137
6.2	Band positions of the SAC Cr-spinel samples in comparison with their chemistry.	146

Chapter 1

Introduction

The Moon is our closest neighbour in the solar system and has always been a celestial object of countless mysteries that have fascinated explorers for millennia. The exploration of the Moon began in the 17th century when the Italian astronomer Galileo Galilei made the first telescopic observation of the Moon. The lunar exploration took a giant leap with the launch of Sputnik 1 in 1957, marking the arrival of the space age. The scientific missions in the space age solved several mysteries about the Moon, including its origin, surface morphology, and evolution on the geological time scale (Hartmann and Davis, 1975; Cameron and Ward, 1976; Cameron, 2000; Canup and Asphaug, 2001). In 1964, NASA's Ranger probe revealed that the holes widely seen on the lunar surface are essentially craters formed by meteorite impacts (Fig. 1.1). Series of Surveyor missions showed that the dark mare plains are similar to terrestrial basaltic composition and the brighter highlands (undulated terrain) are rich in aluminium (Kuiper, 1959; Urey, 1962; Storm and Fielder, 1968; Barricelli and Metcalfe, 1969). Later on, the analyses of samples brought back from the Apollo and Luna missions made several path-breaking discoveries, including the identification of highlands as the anorthositic primary crust, hypothesizing lunar magma ocean concept, chemical variations and wider titanium ranges in mare basalts, effects of space weathering on surface rocks, peak in mare volcanism from 3.2-3.8 Ga, presence of KREEP lithology, and information on the interior structure of the Moon (Wood et al., 1970; Turkevich, 1971; Rhodes et al., 1975; Hapke et al., 1975; May et al., 1976; Metzger and Parker, 1979; Warren and Wasson, 1979; Davis, 1980). The Clementine and Lunar Prospector missions launched in the last decade of the twentieth century provided the first global (both nearside and farside) elemental, mineralogical, and topographical views of the Moon (Nozette et al., 1994; Binder, 1998; Lucey et al., 1995; Blewett et al., 1997; Lucey et al., 1998; Lucey et al., 2000; Jolliff et al., 2000; Thesniya and Rajesh, 2020a, b). The scientific missions in the last two decades, especially ISRO's Chandrayaan-1, China's Chang'E,

NASA's LRO, and JAXA's SELENE, gave fresh insights into the origin and subsequent evolution of the Moon (Clark, 2009; Pieters et al., 2009; Sunshine et al., 2009; Ohtake et al., 2009; Haruyama et al., 2009; Sridharan et al., 2010; Yamamoto et al., 2010; McCord et al., 2011; Whitten et al., 2011; Zhu et al., 2013; Bhattacharya et al., 2013; Donaldson Hanna et al., 2014; Braden et al., 2014; Varatharajan et al., 2014; Prissel et al., 2014; Pieters et al., 2014; Chauhan et al., 2015; Yamamoto et al., 2015; Wohler et al., 2017; Milliken and Li, 2017; Bandfield et al., 2018).

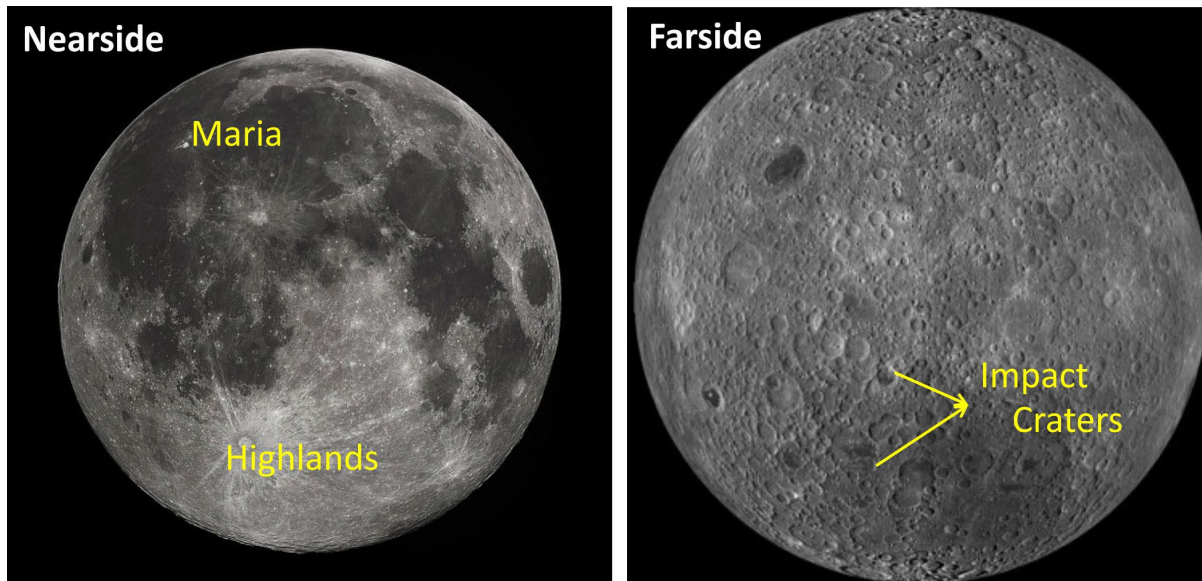


Figure 1.1: Lunar Reconnaissance Orbiter Camera –Wide Angle Camera (LROC WAC) mosaic of the nearside and farside of the Moon.

The formation of the Moon is believed to have occurred as a result of the collision of a Mars-sized body called 'Theia' with the proto-Earth at around 4.5 Ga ago (Hartmann and Davis, 1975; Cameron and Ward, 1976; Cameron, 2000). The Lunar Magma Ocean (LMO) model suggests that the Moon was melted up to a considerably greater depth following its accretion (e.g., Smith et al., 1970; Wood et al., 1970). As the magma ocean crystallized, the cumulate pile of denser mafic minerals and anorthosite were formed as products of differentiated magma (Shearer et al., 2006). Early formed olivine sink to the bottom and formed a part of the lunar mantle (Fig. 1.2). Later formed, less dense, plagioclase crystals floated upward and formed the lunar crust, rich in anorthosite (e.g., Wood et al., 1970; Charlier et al., 2018 and references therein). The last liquid to crystallize would have consolidated into a thin layer (referred to as the UrKREEP layer), sandwiched between the lower crust and mantle, and enriched in incompatible elements such as K, REE, and P (e.g., Warren et al., 1979) (Fig. 1.2). This model is widely accepted today and adapted to the formation of larger planetary bodies in general,

but many fundamental unknowns (e.g., depth of the original magma ocean, presence of volatiles such as water, possible mantle overturn) remain.

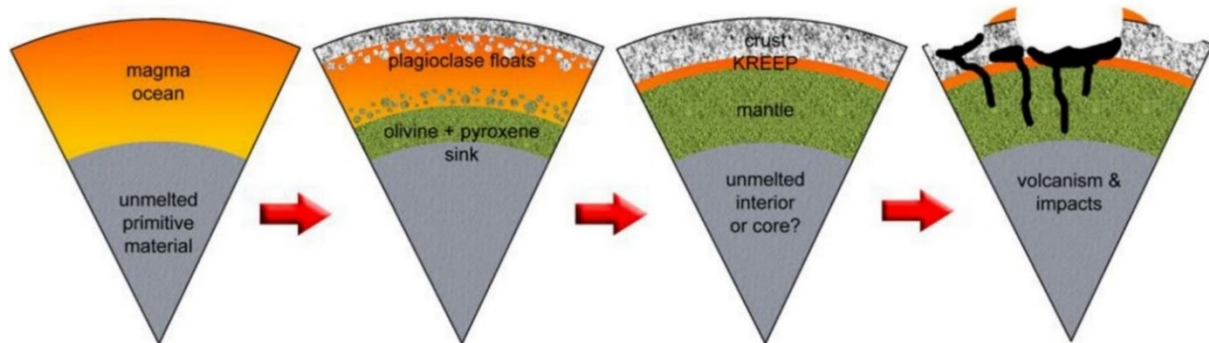


Figure 1.2: The schemata showing the lunar magma ocean crystallization (Source: scientific report, 2007, NASA).

The impact craters and basins are formed by asteroidal impacts on the lunar surface after its formation. The large-scale impact cratering events in the Pre-Nectarian and Imbrian periods considerably weakened the primary crust of the Moon and made way for the eruption of magma from the lunar interior (Head and Wilson, 1992). The eruption of the magma generated by remelting of the lunar interior after the initial differentiation episode formed the Mare basalts on the Moon. The serial magmatism began at ~ 3.9 - 4.0 Ga ago and peaked between ~ 3.2 to 3.8 Ga (Hiesinger et al., 2000). Some observations contrast with this simplistic view of the lunar crust, as inherited from the LMO crystallization. Some lunar anorthosites, at places, are closely associated with magnesium-rich rocks such as dunite, norite, and troctolite and evidence serial magmatism processes, which intruded and modified the crust after its formation (e.g., Spudis and Davis, 1986; Elardo et al., 2011). Lunar rocks, in general, contain several important primary minerals such as olivine, pyroxene, chromian spinel, and Mg-Al spinel, which are useful to track the geological processes on the Moon. The pyroxene minerals are abundant in Mare basalts, while spinels are found in association with anorthosites and basalts. The recent detection of Mg-Al spinel on the lunar surface indicates that spinels have played a significant role in the lunar crustal evolution (Pieters et al., 2011; Dhingra et al., 2011a; Dhingra et al., 2011b; Dhingra and Pieters, 2011; Kaur et al., 2012; Pieters et al., 2011; Pieters et al., 2014; Prissel et al., 2014; Dhingra et al., 2017). Spinel may form in a wet magma ocean in specific conditions (e.g., Lin et al., 2017) and in other settings such as plutonic intrusions (e.g., Pieters et al., 2011). The study of spinel is important to understand the mantle and crustal processes as they specifically crystallize from mafic-ultramafic magmas over a wide range of conditions.

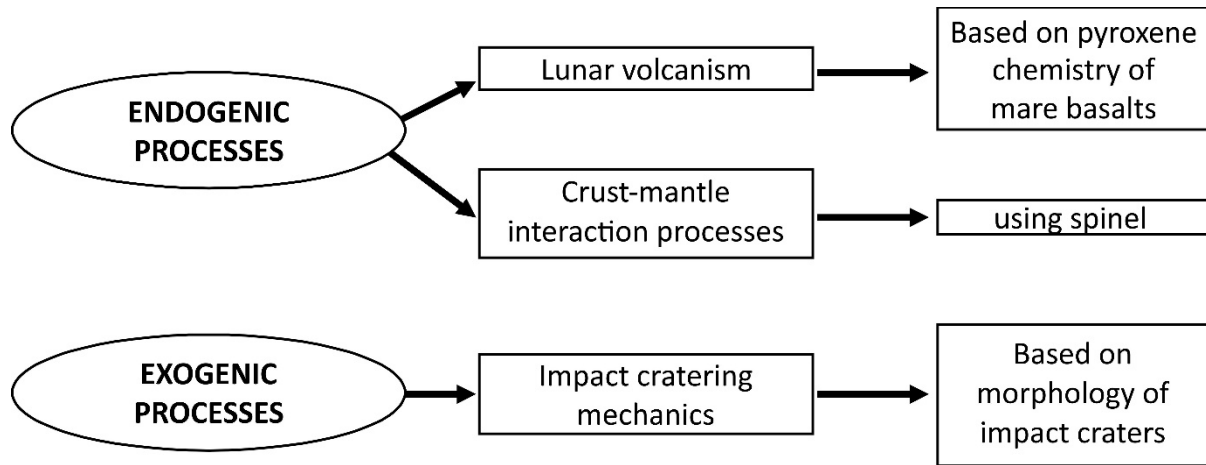


Figure 1.3: The schemata depicting the outline of the Ph.D. work.

The processes responsible for lunar volcanism, differentiation of lunar interior, and crust-mantle interactions constitute endogenic processes on the Moon. Whereas the processes that operate on or above the Moon's surface, involving large-scale impact cratering events and associated surface readjustments, are considered exogenic processes. The knowledge about these endogenic and exogenic processes on the Moon is imperative to understanding the evolutionary history of our nearest neighbour. Therefore, our research focuses on understanding the lunar endogenic and exogenic processes by studying lunar volcanism, spinel chemistry, and impact cratering mechanics (Fig. 1.3). The scope of studying lunar volcanic and thermal history, spinel compositions and lunar functional analogues, and impact cratering mechanics are discussed further.

1.1 Significance and scope of the study

1.1.1 Volcanic and thermal history of the Moon

Rocks record the thermal history as their mineralogy and chemical composition result from the processes that have occurred during the thermal evolution of a planetary body. The thermal evolution of the Moon can be understood from the ages and distribution of magmatic and/or volcanic rocks on the lunar surface. Mare basalts are the volcanic rocks formed by remelting of the lunar interior. Mare basalts cover 17% of the lunar surface and display wide variations in iron and titanium contents (Fig. 1.4). Variations in Ti content in mare basalts erupted over a long period of time suggests lateral chemical heterogeneity in the lunar mantle (e.g., Morota et al., 2011). The low-Ti and high-Ti basalts having considerably varying titanium contents must

have been derived from different source regions in the lunar mantle. Therefore, studying the chemistry of these different mare basaltic units will allow us to understand the source composition of their parent magmas.

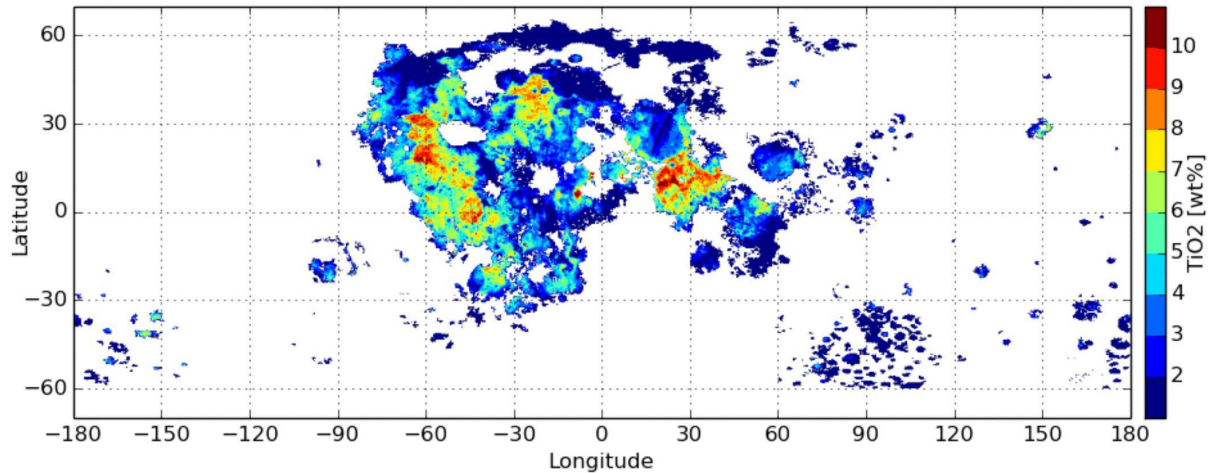


Figure 1.4: LROC WAC-derived TiO_2 abundance map of the lunar surface. Varying titanium contents in the mare basaltic units are visible.

Scientists believe that a lunar mantle overturn occurred soon after the crystallization of the lunar magma ocean, producing a hybrid lunar mantle with olivine-orthopyroxene materials in the bottom of the mantle while ilmenite-clinopyroxene materials on the top of the mantle (Kato et al., 2017) (Fig. 1.5). Though the concept of mantle overturn is still debated, scientists claim that the varying chemical nature of the mare basaltic units across the lunar surface is attributed to the source region and depth of origin of the parent magma (e.g., Morota et al., Kato et al., 2017). The nature of source regions, as well as the reasons and mechanisms of lunar interior remelting for the creation of mare basaltic magmas, are yet unknown. Therefore, studying the compositional variations in mare basalts would help us interpret the depth of origin of the basaltic magma and thereby shed more light on the lunar mantle overturn concept.

Furthermore, the volcanism on the Moon started at around ~ 3.9 to 4.0 Ga ago and continued until ~ 1.2 Ga, with a peak in the volcanic activity at ~ 3.2 to 3.8 Ga (Main-phase volcanism) (Head and Wilson, 1992; Hiesinger et al., 2000) (Fig. 1.6). It was believed that the volcanism on the Moon had ceased at around 1.2 Ga (Late-phase volcanism), and the Moon being a smaller body, cooled much early in its history, unlike the Earth (Fig. 1.6). However, recent findings of volcanic events on the Moon that occurred less than 1 Ga ago (Topical phase) have fascinated the scientists on knowing the extended volcanic history of the Moon (e.g., Singh et al., 2020).

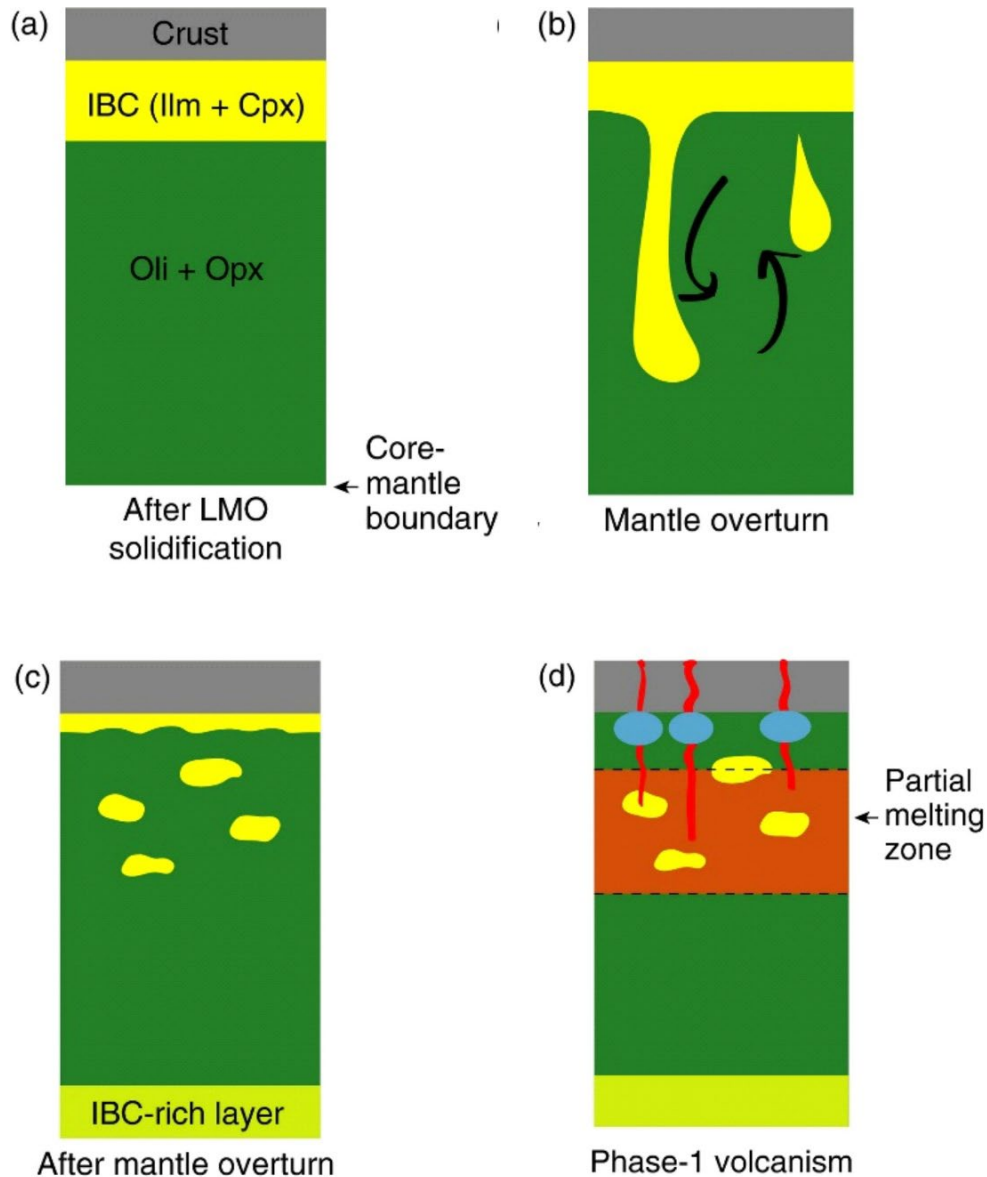


Figure 1.5: Schemata representing the mechanism of lunar mantle overturn post-magma ocean crystallization (Source: Kato et al., 2017). IBC: Ilmenite-bearing clinopyroxene.

The long span of the eruption of mare basalts and wide range of compositions over the lunar surface hint at the lunar interior's heterogeneous nature, making them potential candidates for understanding variations in compositions, source regions, processes, and temperatures over time (Head and Wilson, 1992; Giguere et al., 2000; Morota et al., 2011; Kato et al., 2017; Thesniya and Rajesh, 2020c). Therefore, identification and chemical characterization of the mare basalts formed during the main-phase and late-phase history of the Moon is vital to better comprehend the Moon's volcanic history and thermal evolution. This Ph.D. work investigates the chemistry and ages of selected mare basaltic units on the lunar nearside in order to

understand their time of formation, origin, emplacement mechanism, source composition, and depths, which in turn will give insights into the volcanic evolution of the Moon.



Figure 1.6: Schemata showing the current understanding of the volcanic evolution of the Moon.

The chemistry of mare basaltic units is investigated mainly using their constituent pyroxene group minerals. Basalts contain pyroxenes as major components. The chemistry of pyroxenes in the Mare basalts will give us information about the nature and crystallization history of magma. The iron and titanium contents of basalts and ages would reveal the history of volcanism and heterogeneity of the magma source regions in the lunar interior.

1.1.2 Spinel compositions on the Moon and lunar functional analogues

Spinel is an oxide group mineral with divalent Fe, Mg in the tetrahedral site, and trivalent Fe, Cr, Al in the octahedral site of the spinel structure. Magmatic spinels directly crystallize from ultramafic magma, and therefore, their chemical composition provides information about its source composition and history. Magmatic spinels of varying compositions were detected using orbital remote sensing data and returned lunar samples data from Earth's Moon. The lunar spinels were identified from different source rocks such as basalts, high alumina basalts, pyroxene-phyric basalt, gabbro, anorthosite, pink spinel anorthosite, breccia, and so on. Most of these spinel compositions were Fe-rich and showed a compositional range between chromite and ulvospinel. In addition, the wide orbital detections of spinels across the lunar surface using Moon Mineralogy Mapper (M^3 onboard ISRO's Chandrayaan-1 mission) and Spectral Profiler (aboard JAXA's Kaguya mission) in recent years shed new light on their significant role in the evolution of the lunar crust (Fig. 1.7). Most of the orbital detections of spinels are

Mg- and Al-rich with limited occurrences of Cr- or Fe- rich compositions associated with pyroclastic deposits in Sinus Aestuum.

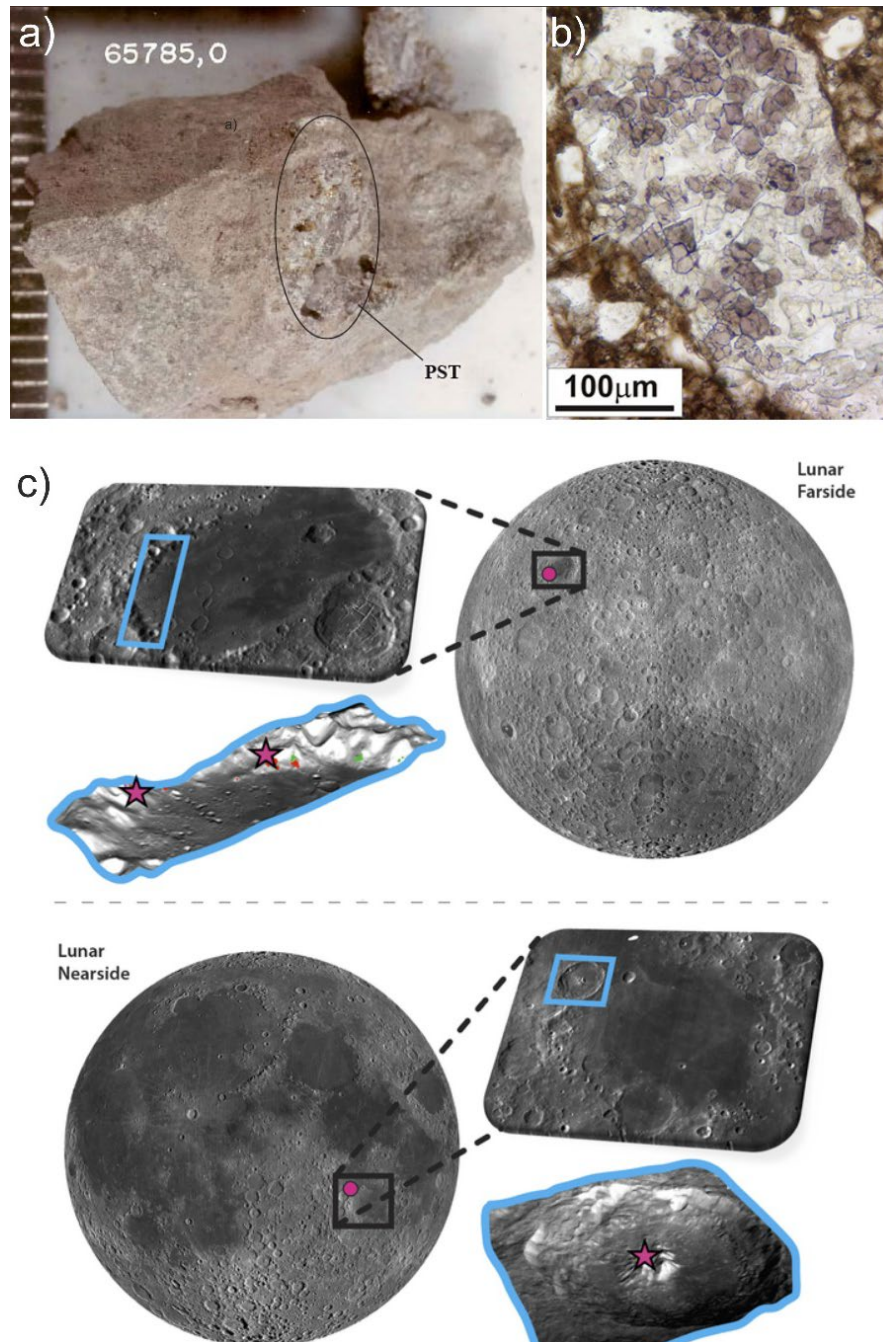


Figure 1.7: (A) Image of the Apollo 16 rake sample, 65785, with a pink-spinel troctolite clast in it (labeled as PST) (Credits: NASA S72-48821). Scale bar is in mm. (B) Thin-section image of the lunar meteorite ALHA81005 showing the pink spinel (pink-grains) in polarized light (From Gross and Treiman, 2011). (C) Spinel detections on the lunar farside and nearside (pink filled circles) (Dhingra et al., 2011; Prissel et al., 2014).

A new rock type named "Pink Spinel Anorthosite" (PSA) enriched in $MgAl_2O_4$ spinel with a low modal abundance of mafic silicates was found to occur in low Fe- terrains dominated by plagioclase feldspar on the Moon. The global occurrence of PSAs has been explained by the interaction between Mg-suite parental melts and the ancient anorthositic crust. Another distinctive rock type, dominated by high concentrations of olivine, orthopyroxene, and Mg-rich spinel (OOS: Olivine- Orthopyroxene-Spinel), has also been reported using M^3 data. The differentiation of magma from plutons intruded into the lower crust or at the crust-mantle interface was suggested for the formation of these unusual lithologies. Recent experimental work suggests that spinel-bearing materials could also be formed from the last liquids crystallized in the Lunar Magma Ocean. The above-discussed models for spinel formation point to their importance in understanding the lunar differentiation as well as crust-mantle interaction processes. Therefore, this Ph.D. work aims to understand the possible origin of spinels on the Moon by examining the compositional variations in spinels from diverse rock types on the Moon. The lunar spinel chemical data are obtained from the previous literature on chemical analyses of returned lunar samples and some lunar meteorites.

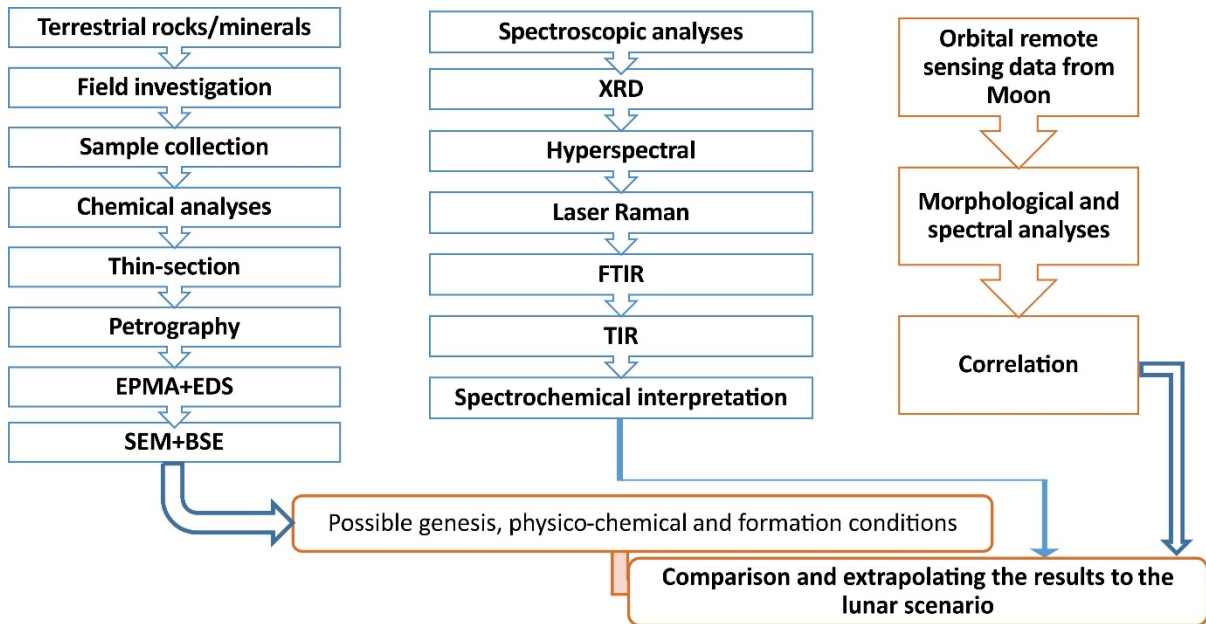


Figure 1.8: Schemata showing the methods involved in studying the lunar analogues.

Further, the orbital detections of spinels depend greatly on their spectrochemical characteristics. Hence, comparative spectral-chemical studies of terrestrial spinels will help identify compositionally similar lunar spinels from their reflectance spectra and thereby refine the constraints on the compositional diversity of remotely observed lunar spinels. This Ph.D. work attempts to investigate the compositional diversity of lunar spinels and examine their

spectrochemical analogy with those of terrestrial spinel composition from the Sittampundi Anorthosite Complex in southern India (Figs 1.7 and 1.8).

The study uses a combination of VNIR, Laser Raman, and FTIR spectroscopic techniques to investigate the chemical-spectral relationship of terrestrial chromian spinels from the Sittampundi Anorthosite Complex, and to compare their spectrochemical characteristics to those of remotely detected Fe- and Cr-bearing spinels on the Moon. The effects of changing chemistry and crystal structure on the spectral pattern and absorption or peak centres of SAC Cr-spinels have been explored. As an approximation to orbital observations of lunar surface compositions, we apply our findings to spectral data of Sinus Aestuum spinels on the Moon. The present comparative spectral-chemical technique will aid in the identification of compositionally similar lunar spinels from their reflectance spectra, thus refining the compositional diversity of remotely detected lunar spinels. Because in-situ observations of lunar spinels are limited in the current scenario, orbital remote sensing measurements of the lunar surface will continue to take precedence, and our findings will serve as a reference for remote identification of compositionally comparable lunar spinels.

1.1.3 Impact cratering mechanics of the Moon

The impact craters on the Moon are of varying dimensions, and the fundamental processes of impact cratering leave characteristic surface features that remain unerased for millions of years, unlike the Earth (Fig. 1.9). Scientists believe that impact cratering has played a major role in the formation and subsequent history of the planets and their satellites, specifically in hypothesized impact origin of the Moon, Late Heavy Bombardment, impact-induced volcanism, etc. Therefore, understanding the fundamental processes of impact cratering is crucial in studying planetary evolution.

The cratering mechanics of lunar impact craters with distinct morphology and ejecta emplacement are primarily comprised of three processes: first, contact of the projectile on the lunar surface and compression of the target materials below the impact point, followed by excavation of the transient crater cavity and simultaneous ejection of a proportion of excavated materials, and finally, the gravitational collapse of the transient crater (Shoemaker, 1962). In general, the gravitational collapse of a basic bowl-shaped crater produces complex craters with a distinct increase in crater diameter. The high-velocity components emplace as patchy and discontinuous distal ejecta, typically reaching higher radial distances beyond the range of the continuous ejecta blanket, whereas the proximal ejecta blanket seems to be contiguous and

gradually thins away from the crater rim (Fig. 1.10). Finer ejecta deposits show as noticeable "rays" that reach further radially out from the source crater (Fig. 1.10).

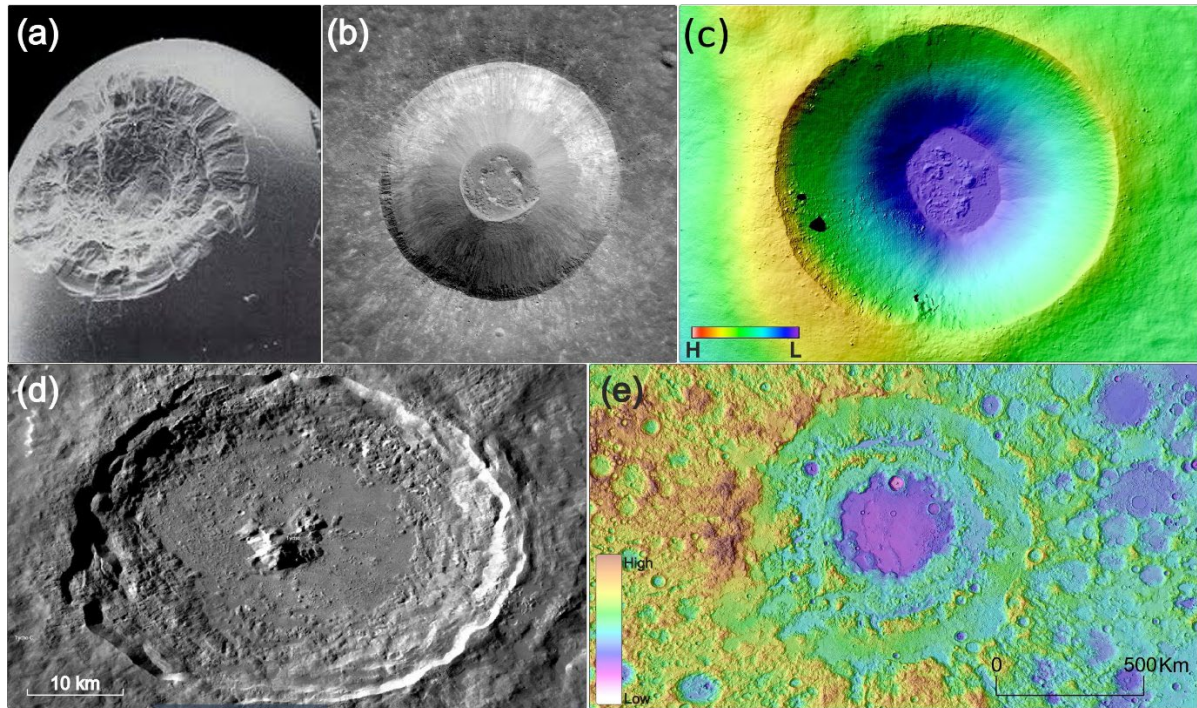


Figure 1.9: Impact crater morphologies on the Moon. (a) Microcrater ($D < 1$ mm) found in returned lunar samples. (b) LROC NAC mosaic of the Lichtenberg B crater ($D \sim 5$ km) representing a simple bowl-shaped crater. (c) LROC NAC DTM of the Hell Q crater ($D \sim 3.75$ km). (d) LOLA DEM overlaid on the LOLA hillshade showing the multiring Orientale basin (Barker et al., 2016). North is up in all the images.

In an airless body like the Moon, cratering processes result in only minor degradations, which are exacerbated by later impact events and lava infillings. By eroding the sharp rim, steep walls into gentle slopes, floor fills, and fading of impact ejecta, these primary degradational processes cause dramatic changes in the overall morphology of the crater. Depending on the temporal duration of their exposure to the lunar environment and the impact flux of the Moon, craters are frequently obscured by later infillings and overlapping craters. Lunar craters are allocated different time units based on their amount of deterioration, ranging from Pre-Nectarian (4.1 Ga) to Copernican (1 Ga) systems. The older Copernican craters are often more degraded than the younger Copernican craters. As a result, Copernican craters retain their original form, which is often characterized by bright ejecta rays surrounding the crater. Because of their contrasting brightness and pure nature in an airless Moon, the ejecta rays of Copernican craters can be seen on the lunar surface (Fig. 1.10).

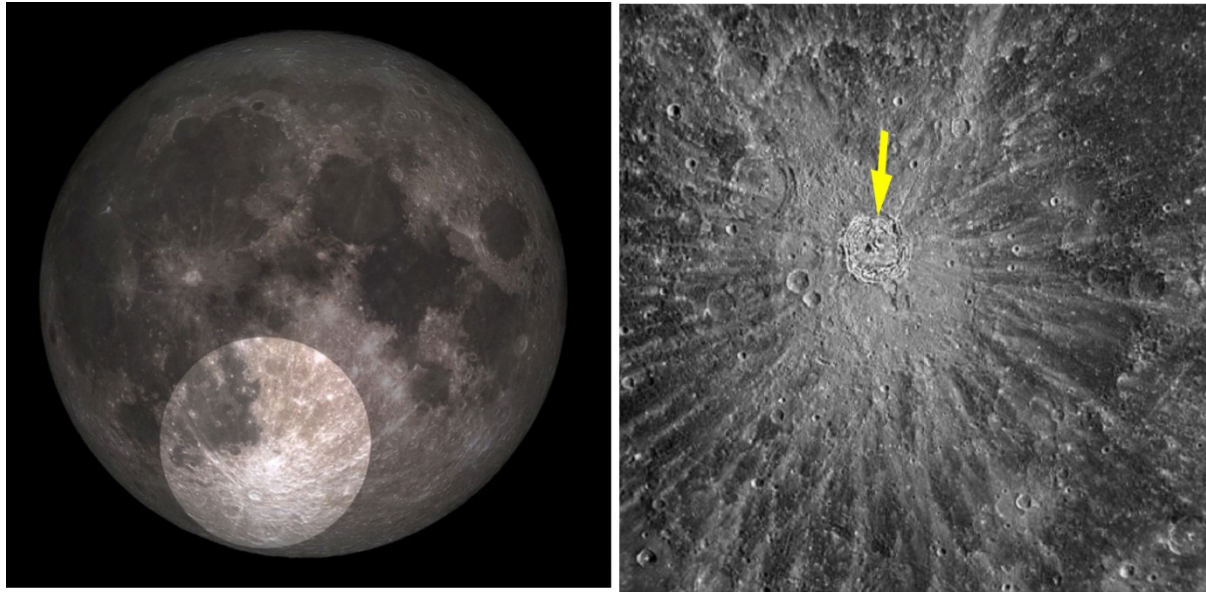


Figure 1.10: Left image: LROC nearside view of the Moon, highlighting the Tycho crater with bright ejecta rays. Right image: A complex crater on the lunar surface having bright radial ejecta rays.

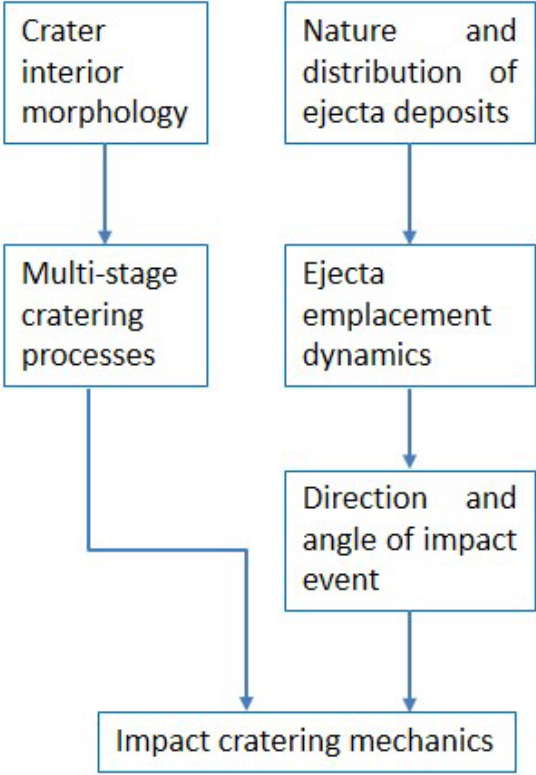


Figure 1.11: Schemata showing the methodology followed for understanding the impact cratering mechanics of the Moon.

Furthermore, the markedly higher surface albedo of ejecta rays is thought to be a representation of their emplacement in the lunar chronostratigraphic record not earlier than 1 billion years ago. The Copernican craters are a natural laboratory for studying the impact cratering mechanics of the Moon because they have relatively undamaged and younger surfaces in the crater interior, as well as a largely undisturbed ejecta blanket and ray system. This Ph.D. work investigates the various morphological features and the nature and distribution of distinct ejecta deposits of the Copernican craters, Ohm and Das, on the farside of the Moon to get insights into the multi-stage cratering processes, as well as ejecta emplacement dynamics on the Moon (Gault, 1973; Stoßfler et al., 1975; Gault and Wedekind, 1978; Holsapple and Schmidt, 1987; Schultz and Gault, 1990) (Fig. 1.11).

1.2 Objectives

This research investigates the spectrochemical characteristics and geological context of pyroxene- and spinel-bearing lithologies and morphology of impact craters on the Moon. The work primarily utilized orbital remote sensing datasets from various lunar exploratory missions, particularly ISRO's Chandrayaan-1 mission. The primary objectives of this research are as follows,

- I. To understand the volcanic and thermal evolution of the Moon based on mare basalts in the Grimaldi and Humorum basins on the lunar nearside.
- II. To better understand the compositional variations and origin of spinels on the Moon.
- III. To determine the spectrochemical characteristics of Cr-spinel from Sittampundi Anorthosite Complex (southern India) for understanding its analogous nature to similar lunar spinel compositions on the Moon.
- IV. To understand the impact cratering mechanics and impact dynamics on the Moon based on morphology and ejecta distribution of the Copernican Ohm and Das craters on the lunar farside.

Chapter 2

Approach used

This Ph.D. work hinges on orbital remote sensing data from various lunar exploratory missions. The lunar lithologies and impact cratering mechanics have been investigated using orbital data, while the analogue work used various analytical techniques (Fig. 2.1). The detailed procedures of utilizing orbital remote sensing data and spectroscopic and chemical techniques have been given in the respective chapters of the thesis.

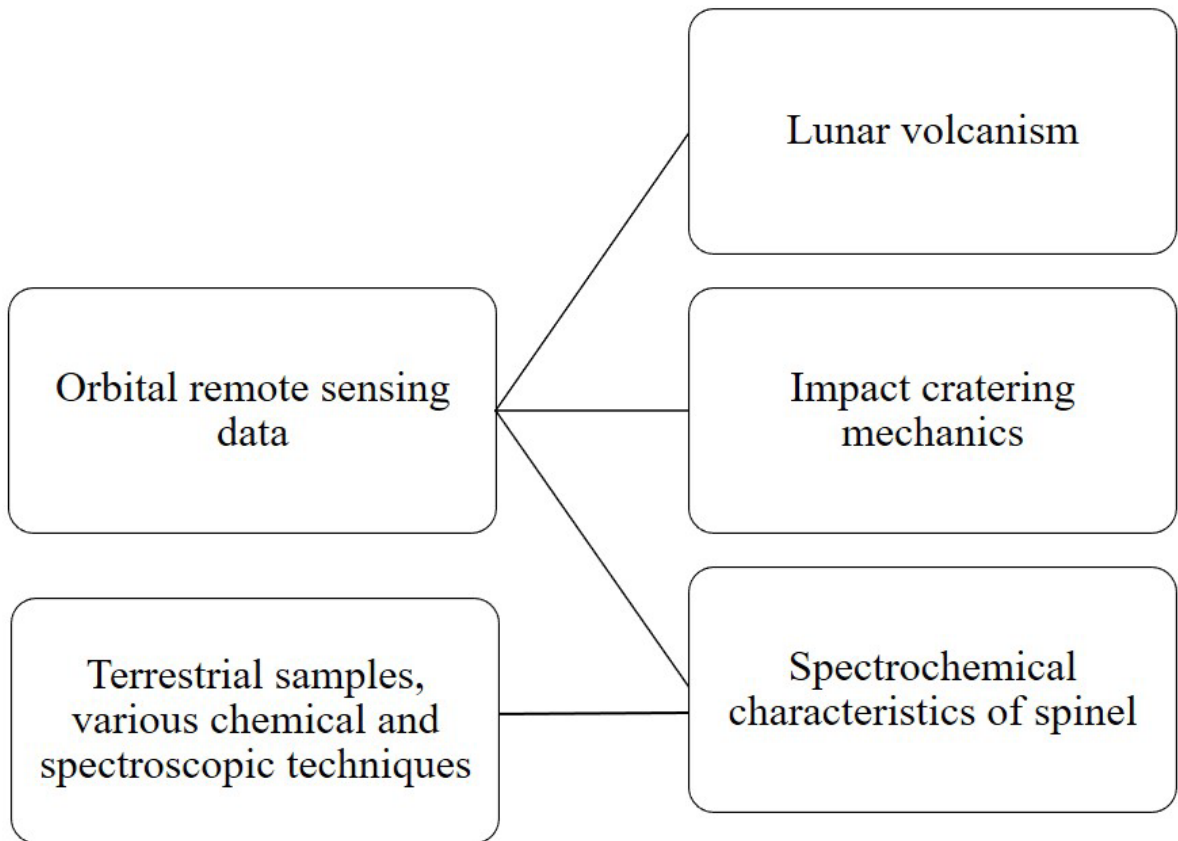


Figure 2.1: Schemata depicting the approach used for studying the attributes of endogenic and exogenic processes on the Moon.

2.1 Utilization of orbital remote sensing data

Remote Sensing is the process of scanning an area/object without being in physical contact with the object. The remote sensing technique relies on measuring the reflected and emitted radiation from an object at a distance (from a satellite or aircraft). The Moon is a distant planetary body and exploring the Moon from the Earth is quite challenging. Remote sensors set up in spacecrafts orbiting the Moon allow us to scan the lunar surface in greater detail. The remote sensors in orbiters comprise spectrometers as well as high-resolution panchromatic cameras. Both types of payloads rely on the technique called spectroscopy. Spectroscopy is the method applied in remote sensing, in which the detectors receive reflected or emitted radiation from an object and record the data in digital format (Fig. 2.2). When many materials interact with light (electromagnetic radiation), they impose a characteristic signature on that light. The most obvious manifestation is colour. Spectroscopy provides a means of quantitatively assessing the nature of the material which interacted with the light. Reflectance spectroscopy involves the measurement of reflected light in different wavelengths of the electromagnetic spectrum. The measured light intensity is recorded in a graph of spectral reflectance as a function of wavelength. The nature of the spectral reflectance of an object depends on its chemistry and crystal structure. The chemical composition of each material differs, and therefore, the target objects produce a spectral reflectance curve unique to its chemistry and structure, which is called a spectral signature. The materials (minerals and rocks) can be identified based on their unique spectral signature (Fig. 2.2).

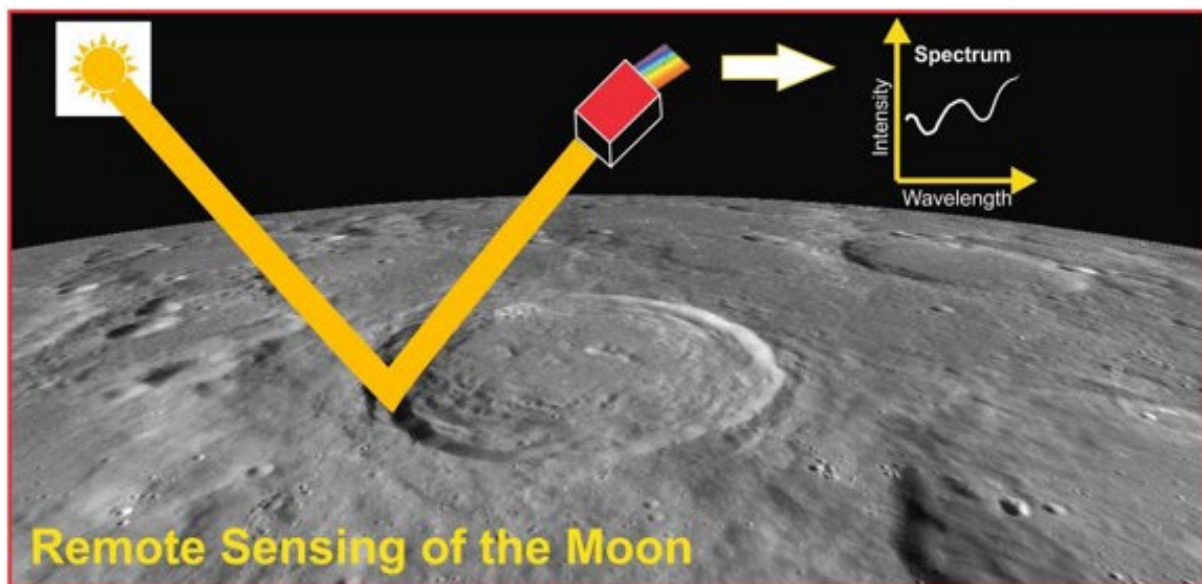


Figure 2.2: depicting the remote observation of the Moon based on reflectance spectroscopy.

2.1.1 Reflectance spectroscopy

Visible and near-infrared (VNIR) regions of the electromagnetic spectrum are generally used for the remote sensing applications of the Moon (Fig. 2.3). The mafic minerals on the Moon, particularly pyroxenes and spinels, exhibit diagnostic absorption features in the VNIR region due to electronic transition absorptions in the transition group elements of these minerals.

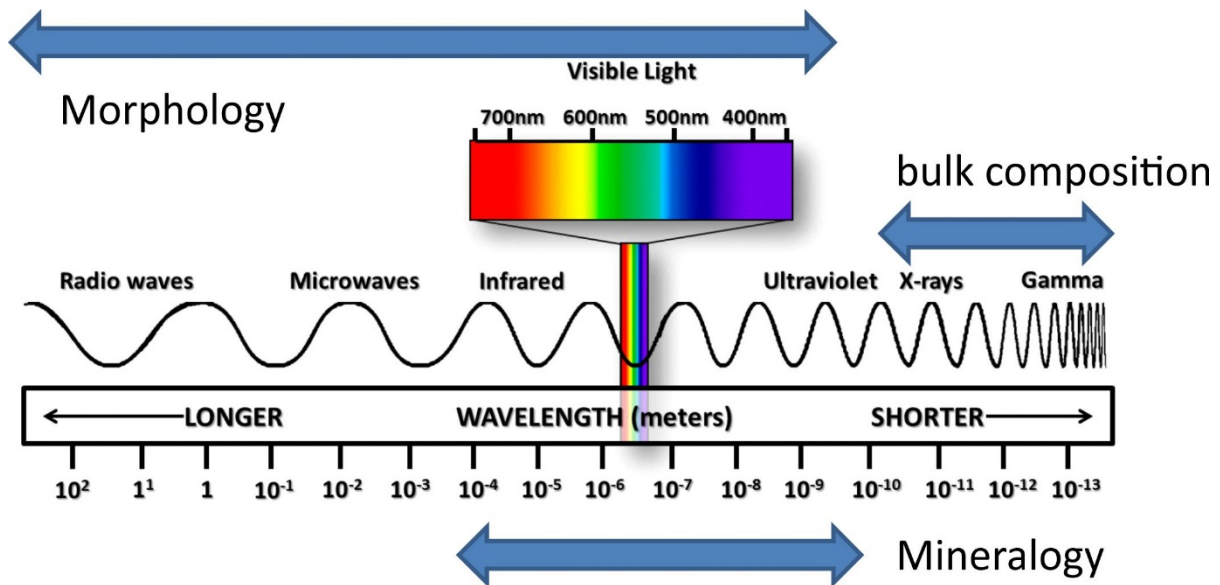


Figure 2.3: Wavelength ranges of electromagnetic radiation. The range of wavelengths used to study morphology, mineralogy, and bulk composition is labelled in the figure.

Reflectance spectroscopy records the properties of solid materials when radiation (light) is directed at a surface, and a detector collects the photons reflected off the surface. The spectrum depends on the material's optical properties and the energy absorbed by excitations of atoms or molecules in the structure. Minerals are identified using reflectance spectroscopy through the “bands,” or dips in reflectance that occur at wavelengths where energy is absorbed, which are often unique to a given mineral structure. The intensity of these spectral bands is, in general, related to the abundance of the exciting phase.

Electronic Absorptions

Electronic transitions from crystal field theory (CFT), metal-to metal intervalence charge transfers, and ligand-to-metal charge transfers cause electronic absorptions due to Fe or other metals. Pyroxenes have symmetrical CFT absorption bands at 1 μm (Band I) and 2 μm (Band II) (Fig. 2.4a). The major Fe^{2+} absorption bands of pyroxenes (from 0.9 μm -1.05 μm and 1.8 μm -2.3 μm) are a function of Fe^{2+} and Ca^{2+} content (Adams, 1974). High Calcium Pyroxenes

(HCP; e.g., augite, diopside) exhibit a 1 μm absorption band centred between 0.91-1.06 μm with a 2 μm band centred at 1.97-2.35 μm . Low Calcium Pyroxenes (LCP; e.g., enstatite, hypersthene) also show both 1 μm and 2 μm absorption bands with band centres that vary from 0.90-0.93 μm and 1.80-2.10 μm respectively (Cloutis and Gaffey, 1991a; Cloutis and Gaffey, 1991b). In addition, the 1 μm and 2 μm band centres of LCP systematically shift to longer wavelengths with an increase in Ca^{2+} content (Adams, 1974; Cloutis and Gaffey 1991b). This shift in the band centres to longer wavelengths as a function of Ca^{2+} content is owing to a change in crystal field sites in which Fe^{2+} ions are located. (Burns, 1970; Adams, 1974). As a result, pigeonites, which are of intermediate Ca composition, show absorption bands near 0.93 μm and 2 μm , sub-calcic augites have bands near 0.99 μm and 2.18 μm , whereas absorption bands of the Ca-rich diopside are near 1.04 μm and 2.3 μm (Adams, 1974). Spinel exhibits a prominent absorption feature in the 2 μm region. The 1 μm feature is either very weak or absent in spinels (Cloutis et al., 2004) (Fig. 2.4b).

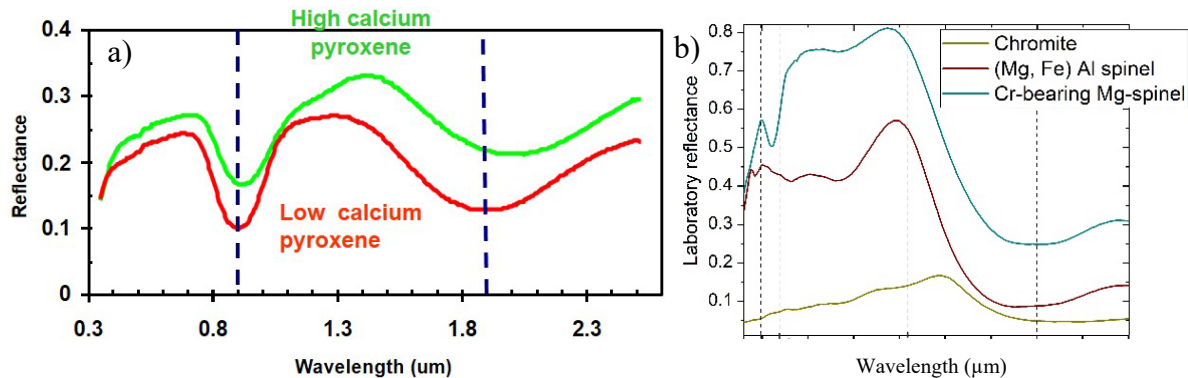


Figure 2.4: Laboratory reflectance spectra of the (A) low-calcium and high-calcium pyroxenes and (B) spinels.

2.1.1.1 Reflectance spectroscopy of the Moon

Remote sensing studies of the Moon are done mainly through spectroscopic analysis of the lunar surface (Fig. 2.5). The returned lunar samples during Apollo and Luna missions were studied in laboratories using reflected VNIR radiation (Adams and McCord, 1970). Electronic mineral absorption bands determined by crystal field theory through measurements of transmitted light from terrestrial minerals were identified in the reflectance spectra of all returned lunar samples. The soils exhibit weaker bands, while crystalline materials showed the strongest bands. These spectroscopic measurements confirmed that remotely recorded reflectance spectra could be used to characterize the mineral properties of the Moon. The laboratory spectra of the returned lunar soil, rock, glass, and mineral samples revealed their

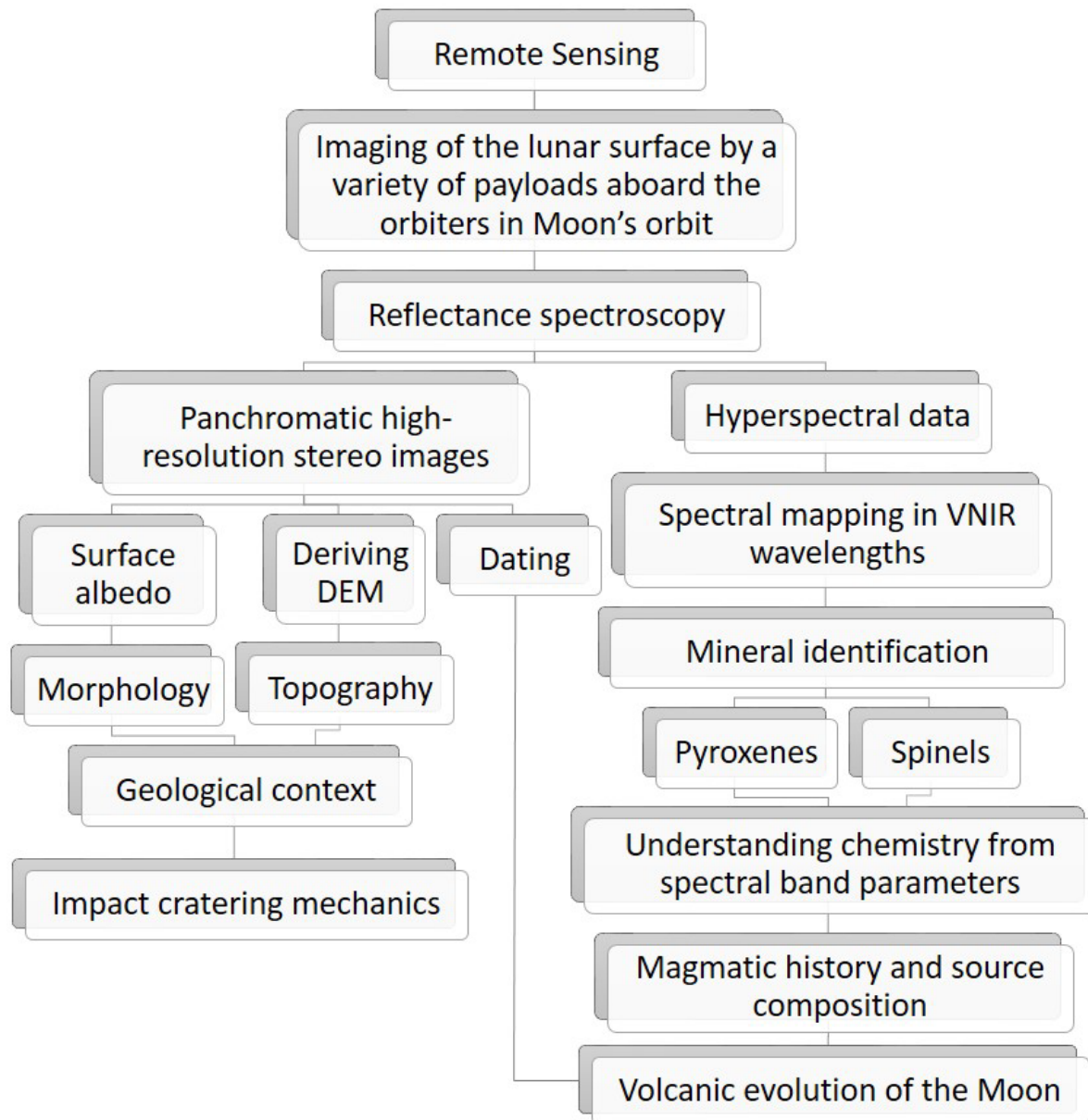


Figure 2.5: Schemata showing the outline of research carried out in the Ph.D. work.

diagnostic absorption bands produced by electronic transitions in transition metal ions (incompletely filled d orbitals) in a crystal structure. When a light photon is absorbed, excitation of electrons takes place from a lower-energy to a higher-energy orbital state (Burns, 1993). The wavelength of the energy or photon being absorbed depends on the coordination and symmetry of anions and transition metals in the crystal structure. The pyroxenes and spinels having transition metal ions in their crystal structure produce diagnostic absorption features in the reflectance spectra.

The panchromatic images, mainly in the visible region, provide the albedo of the surface (Fig. 2.5). The stereo images can also be used to derive the Digital Elevation Model (DEM) of the surface that will provide the topographic information. The high-resolution panchromatic images are useful in determining the ages of the surface using the crater counting technique. The crater size-frequency distribution technique requires counting primary craters on the target surface, and hence the high-resolution images facilitate the estimation of ages using this technique. The morphological data combined with the topography provides the physical characteristics and geological context of the region of interest. The impact cratering mechanics is understood based on an integrated morphology, surface albedo, and topography analysis. The hyperspectral data in the VNIR region are used for spectral mapping and mineral identification (Fig. 2.5). The chemistry of pyroxene minerals derived from band parameters is useful for understanding the magmatic history, source composition, and volcanic evolution of the Moon.

2.1.1.2 Hyperspectral data analysis for identifying the minerals and their chemistry

Lunar minerals and soils commonly exhibit absorption features at 1000 and 2000 nm (e.g., Pieters, 1998). Besides, space weathering effects tend to induce a positive (red) slope in the surface spectra and cause “optical maturation” (evidenced by a decrease in the average reflectance level and the absorption band strengths, e.g., Adams and McCord, 1970; Pieters et al., 1993, 2000). Olivine can be identified by three overlapping broad absorption bands near 1 μm (0.83, 1.05, and 1.3 μm) and the absence of features at higher wavelengths (Burns, 1970, 1993; Burns et al., 1972, 1973; Adams, 1975; King and Ridley, 1987). Two major Fe^{2+} absorption bands from 0.9 to 1.05 μm and 1.8–2.3 μm in pyroxenes vary as a function of Fe^{2+} and Ca^{2+} content (Adams, 1974). The band depths and positions of these absorption features can be used as a diagnostic parameter for discriminating the lunar lithologies.

2.1.1.2.1 Integrated Band Depth (IBD)

Integrated Band Depth (IBD) is a parameter used in the VIS-NIR spectroscopy for the spectral mapping of lunar mafic lithologies based on their ferrous absorption bands (e.g., Besse et al., 2011; Isaacson et al., 2011; Mustard et al., 2011; Staid et al., 2011). This parameter is sensitive to the abundances of pyroxenes, olivine, ilmenite, etc., in the surface lithologies. The band

depth (BD) is the depth of an absorption band and is defined relative to the continuum (Clark and Roush, 1984).

Band depth = 1 – continuum removed reflectance

$$\text{IBD1000} = \sum_{N=0}^{26} 1 - R(789 + 20n)/Rc(789 + 20n) \quad \text{–Eq. 1}$$

$$\text{IBD2000} = \sum_{N=0}^{21} 1 - R(1658 + 40n)/Rc(1658 + 40n) \quad \text{–Eq. 2}$$

where R represents reflectance at a given wavelength, Rc denotes reflectance relative to a local continuum defined between the inflection points on both sides of the absorption band, and n denotes the bandwidth.

IBD at 1000 and 2000 nm was generated to discriminate between mafic-rich regions and anorthositic highland areas. The IBD1000 parameter map has been generated by integrating the band depths between 789 and 1308 nm relative to the local continuum formed between 789 and 1308 nm. The IBD1000 parameter is sensitive to the presence of both olivines and pyroxenes. The IBD2000 parameter map has been generated by summing up the band depths between 1658 and 2498 nm relative to a local continuum drawn between 1658 and 2498 nm and is commonly used to map pyroxene occurrences. An M³ color composite image was generated using IBD parameter maps. The IBD1000 parameter was assigned to the red channel, while the green and blue channels were assigned the IBD2000 and R1578 bands, respectively.

Reflectance spectra were collected from spectrally distinct regions using the color composite images generated for both units. The soil spectra from each unit were extracted by averaging the number of pixels in that region. Apart from this, pyroxene-bearing spectra were also collected from smaller superposed craters within each unit. These spectra are obtained from a single representative pixel in that location. The constituent mineral phases in the average soil spectra were identified based on their characteristic band parameters such as band center (BC), relative band strengths, and the overall spectral pattern.

2.1.1.2.2 Continuum removal

The spectra are a convolution of multiple components present on the target surface. In the case of basalts, the 1000 and 2000 nm absorption bands of pyroxene group minerals are the dominant features. The dominant pyroxene-related features will superimpose the effects of other mixed components such as plagioclase and/or olivine on the reflectance spectra. However, the presence of mixed phases may also impart a slope to the spectra and cause a shift in the 1000 (Band I) and 2000 nm (Band II) apparent band minima. The wavelength-dependent scattering would also cause a greater continuum slope to the spectra, and consequently, the dominant 1000 and 2000 nm absorption bands would have negligible band minima (Clark and Roush, 1984). Therefore, continuum removal of the spectra has to be performed to reduce these effects of continuum slope on the major absorption bands before their band parameter analysis (Clark and Roush, 1984). For the continuum removal, the local maxima on both sides of the absorption bands were determined for each analyzed spectrum, and a straight line tangent was drawn between the local maxima points to define the continuum slope (Fig. 2.6). Continuum removal of the spectra has been done by dividing the spectra by the straight-line continuum drawn between inflection points on both sides of the absorptions for Band I and Band II.

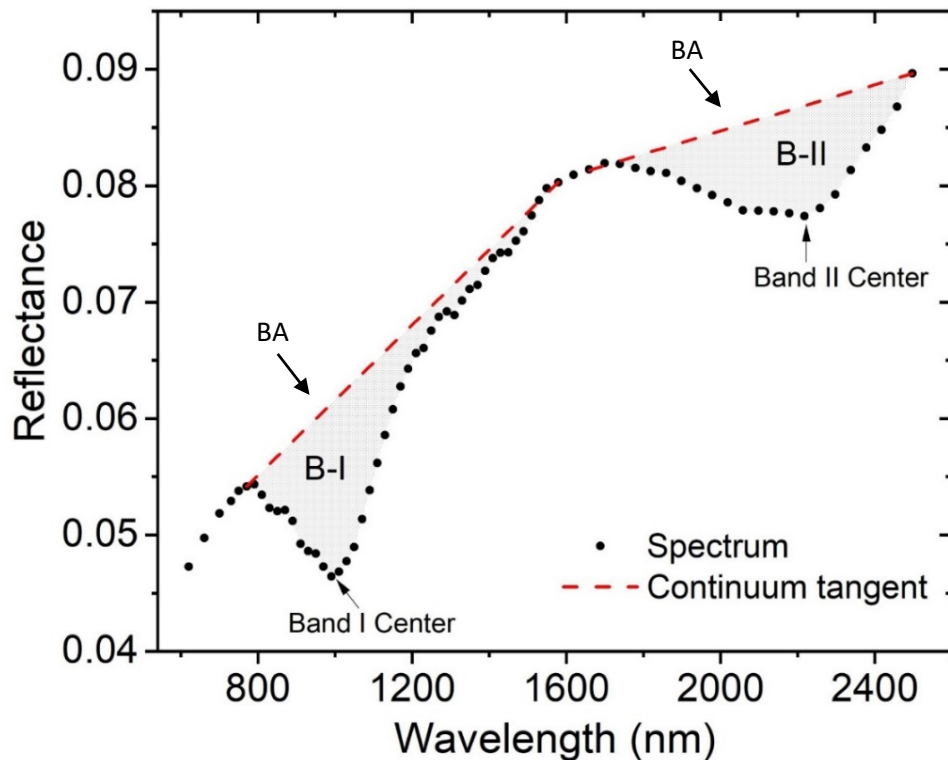


Figure 2.6: Illustration of the M^3 continuum removal procedure. The continuum slope is drawn between the tangent points on both sides of the absorption bands.

2.1.1.2.3 Band parameters

The BC, band area (BA), and band strength (BS) are calculated for each endmember spectra based on the method described in Cloutis et al. (1986) and Gaffey et al. (2002), which was later adopted and successfully applied by Kaur et al. (2013) and Chauhan et al. (2018) for estimating the chemical composition of pyroxenes within the mare basalts on the Moon.

i. Band Centre (BC)

The BC is calculated as the band minima after the removal of the continuum slope. A third- to fourth-order polynomial function was fitted to the bottom of the absorption features, and the BC is calculated as the minimum point of the fitted polynomial. The error associated with the BC calculation was determined through an iterative process by changing the number of points on either side of a visually determined band minimum five to six times, and BCs are calculated each time. The calculated BC values are averaged, and the average BC value is used for further analysis. Standard deviation was also determined using the estimated BC values.

ii. Band Strength (BS) and Band Area (BA)

The Band Strength is the depth of the absorption feature relative to the continuum. BA is calculated as the area between the continuum line and the data points in the absorption band of the spectra. The band area ratio (BAR) is the ratio of Band II area to Band I area of pyroxenes. Band I is sensitive to the relative abundances and composition of pyroxenes and/or olivine, while Band II is sensitive to the abundance of pyroxenes in the spectra (Cloutis et al., 1986). BAR is calculated to determine the relative abundances of olivine and pyroxenes in the mare basalt spectra. Increased BAR value suggests the higher abundance of pyroxenes in the spectra, and lower values indicate the presence of mixed olivine phase in the spectra (Cloutis et al., 1986; Gaffey et al., 1993).

iii. Olivine correction and estimating the molar Ca, Mg, and Fs of the pyroxenes

The effect of olivine in the spectra was removed using the calibration given in Cloutis et al. (1986) and Gaffey et al. (2002). A correction factor was applied to the Band I center to remove the potential contribution of olivine from the spectra before determining the pyroxene composition. The correction factor was derived by calculating the displacement in the Band I center using BAR versus Band I center calibration. The calculated Band I displacement was later applied for olivine correction of Band I center. The estimated Band I center (olivine

corrected) and Band II center values are applied for calculating the molar Ca, Fe, and Mg content in pyroxenes using a set of equations given by Gaffey et al. (2002).

$$Wo (\pm 3) = 347.9 * BI \text{ Center } (\mu\text{m}) - 313.6$$

(Fs < 10; Wo ~5-35 excluded)

$$Wo (\pm 3) = 456.2 * BI \text{ Center } (\mu\text{m}) - 416.9$$

(Fs = 10-25; Wo ~10-25 excluded)

$$Wo (\pm 4) = 418.9 * BI \text{ Center } (\mu\text{m}) - 380.9$$

(Fs = 25-50)

$$Fs (\pm 5) = 268.2 * BII \text{ Center } (\mu\text{m}) - 483.7$$

(Wo < 11)

$$Fs (\pm 5) = 57.5 * BII \text{ Center } (\mu\text{m}) - 72.7$$

(Wo = 11-30, Fs < 25 excluded)

$$Fs (\pm 4) = -12.9 * BII \text{ Center } (\mu\text{m}) + 45.9$$

(Wo = 30-45)

$$Fs (\pm 4) = -118.0 * BII \text{ Center } (\mu\text{m}) + 278.5$$

(Wo > 45)

The estimated molar contents of endmember pyroxene compositions are projected onto a pyroxene quadrilateral plot to understand the relative abundances of endmember compositions. The crystallization trend of basaltic magma was determined based on the pyroxene compositional trend observed in the quadrilateral plot (Lindsley and Anderson, 1983).

2.1.1.3 Dating of the lunar surface from crater statistics

The lunar surface accumulates craters over time depending on the impact flux. The age of any geological unit or feature with a homogenous history can be understood from the crater population-age relationship (Fig. 2.7). The craters of different sizes form at different rates.

Production Function (PF): This parameter is defined as the size-frequency distribution of craters produced at the surface. i.e., the number of craters of a particular diameter expected for each one of a particular size.

Chronology Function (CF): Formation rate of craters with time, for a reference crater of 1 km.

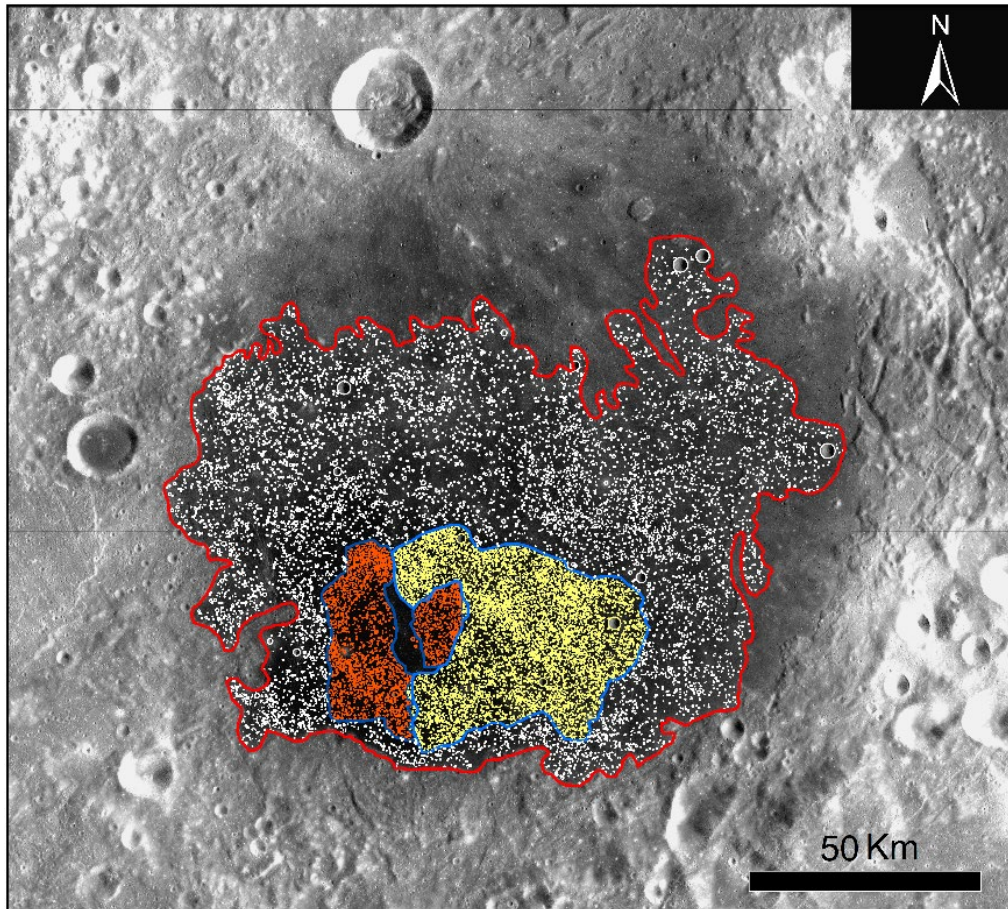


Figure 2.7: A mare region on the nearside of the Moon. The delineated mare units (Red and blue polygons) have experienced distinct formation history, and therefore, the ages of the formation of distinct mare units can be determined based on their crater population-age relationship.

The production and chronology functions allow the construction of an isochron diagram, which represents the expected crater densities for a surface (Fig. 2.8). The method primarily involves the measurement of the surface area of the target unit as well as the diameter of each primary crater within the unit. The counting of any secondary craters (often as a clustering) would give erroneous estimates of age and impacting population. The obtained crater diameters will be plotted as cumulative distribution in the Craterstats 2 software. The crater population data will be imported to the craterstats and divided into bins. The production function is fit into binned crater counts, and age will be obtained from the chronology function. The isochrons are plotted, and resurfacing correction will be applied (Neukum et al., 1975; Neukum, 1983; Neukum and Ivanov, 1994) (Fig. 2.8).

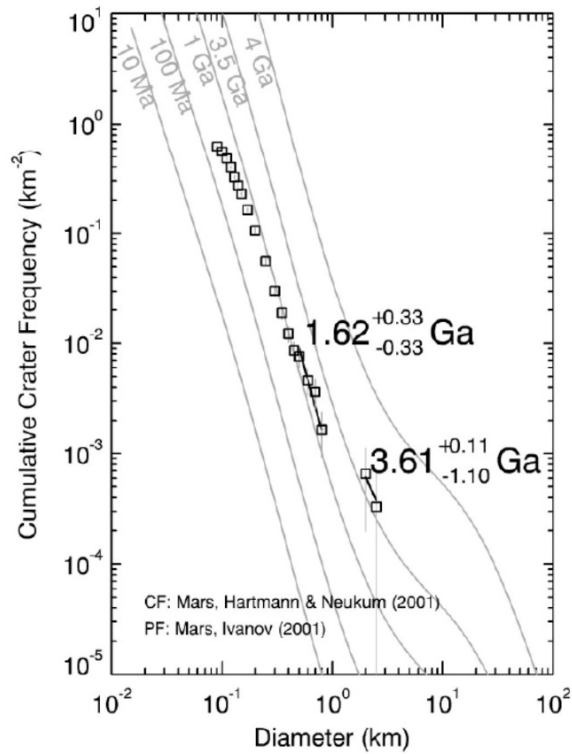
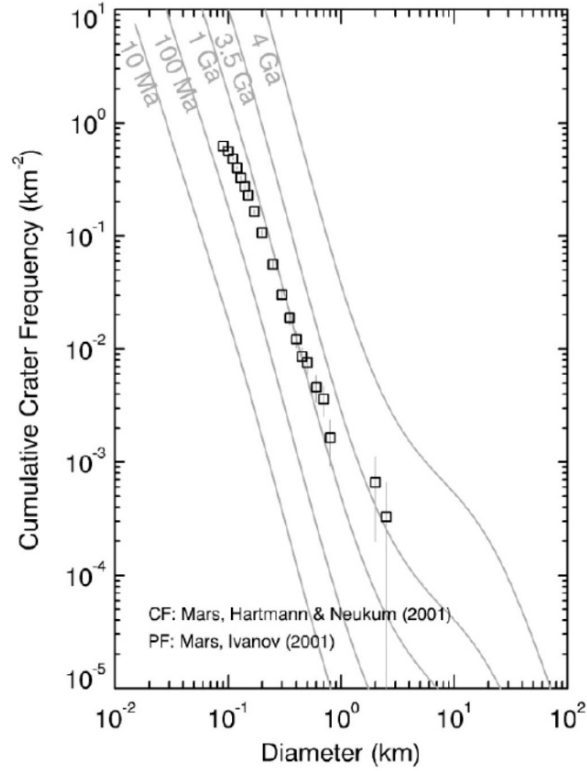


Figure 2.8: Top image: Cumulative crater frequency. Bottom image: Cumulative PF fitting (Source: Greg Michael, 2012).

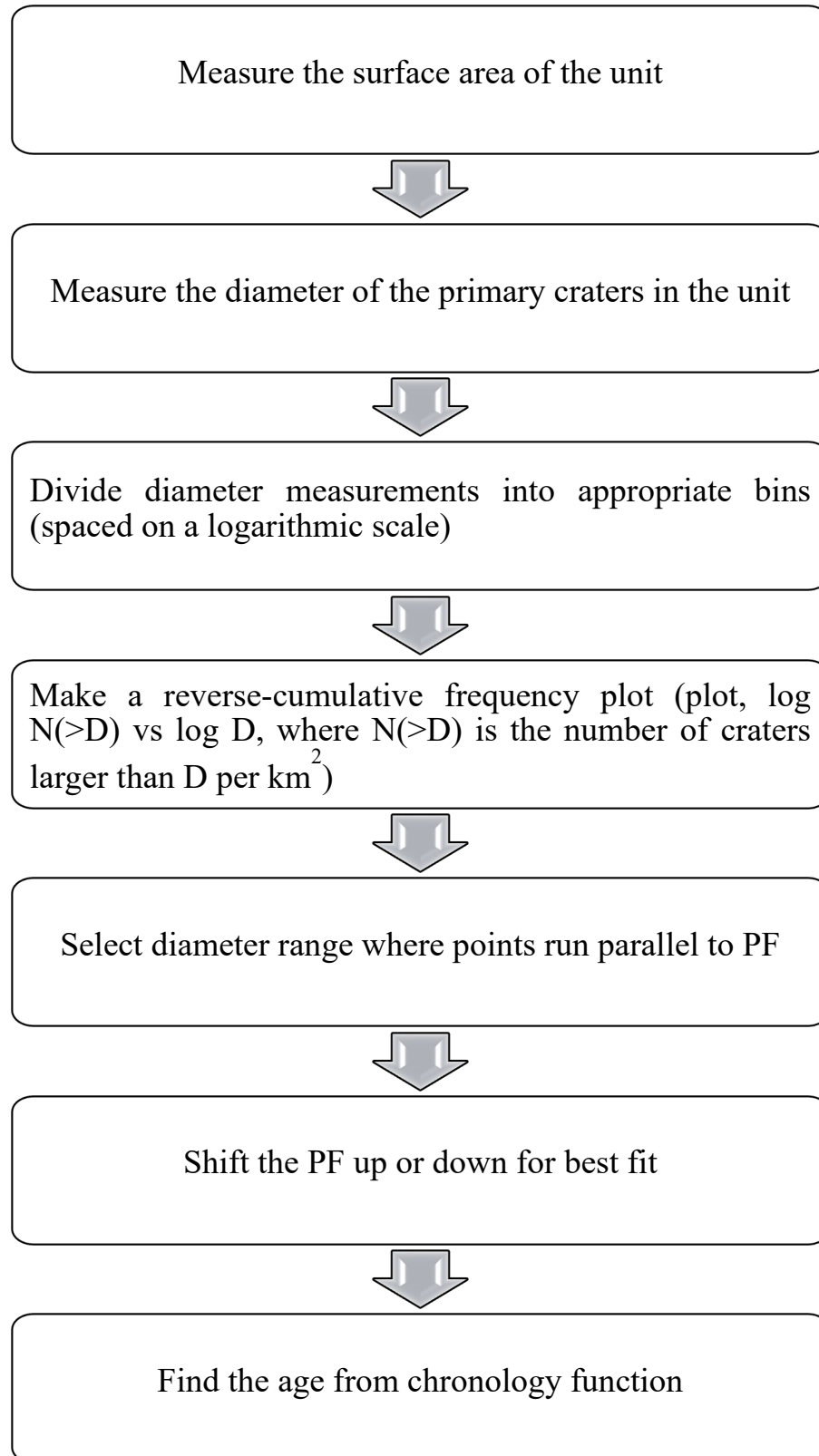


Figure 2.9: Schemata showing the steps involved in age determination using crater statistics.

2.1.1.4 Techniques used for spectroscopic and chemical analyses of Cr-spinels

i) Fourier Transform Infrared Spectroscopy

A PerkinElmer Spectrum 100 Fourier Transform Infrared (FTIR) spectrometer was used to acquire spectra for fine powdered and solid flake samples in the mid-IR band (about 4000–400 cm^{-1}) (PerkinElmer Inc.). The optical module has a HeNe laser that emits a continuous wave (CW) at 633 nm with a maximum output power of 1 mW. The spectra were acquired using a Harrick 'Golden Gate' diamond anvil ATR instrument in both transmission (which can be converted to absorbance) and attenuated total reflectance (ATR) modes. The Deuterated Tri-Glycine Sulphate (DTGS) mid-infrared detector was employed to detect the mid-IR band. The spectra were taken with a KBr beam splitter in the 400 to 4000 cm^{-1} range, with a spectral resolution of 0.5 cm^{-1} and a wavelength accuracy of 0.1 cm^{-1} at 1600 cm^{-1} . In the transmission mode, all of the samples were embedded in a KCl pellet and inspected. The samples were crushed at a pressure of roughly 55 pounds per square inch.

The FTIR technique is used to obtain the sample's IR spectrum of absorption or reflectance (ATR mode). The Fourier Transform (FT) is used to convert raw data to actual output spectra, hence the name. Instead of flashing a monochromatic beam, this technique shines a beam with different frequencies once and then measures the sample's absorption. The reflectance or absorbance/transmittance is then measured after another modified beam with a different set of frequencies is incident. To obtain multiple datasets, the following procedure is repeated multiple times. Some infrared radiation is absorbed by the sample, while others are transmitted. The FTIR method can be used to identify unknown materials and detect the other components in a mixture. The frequency of vibrations between the various energy (vibrational) levels in the molecular bonds that make up the material correlates to the absorption peaks. The interferometer arrangement solves this difficulty. At various wavenumbers, the reflectance or absorbance/transmittance is calculated. The raw data represents light absorption at various positions of the moveable mirror, and the output data represents absorption at various wavelengths.

The Michelson interferometer divides the incident light beam into two mutually perpendicular directions, resulting in differing path lengths for the two beams. After reflecting off the mirrors, the two beams are recombined (two mirrors, one movable and the other are stationary). The intensity difference between the two beams is measured as a function of path difference by the detector. The non-polarizing beam splitter 50 – 50 is used to transmit half of the electric field

amplitude while reflecting the other half. The reflected and transmitted fields collide with the moveable and fixed mirrors. The two light beams recombine at the beamsplitter after being reflected by the mirrors.

The following components are required for a simple setup:

1. Infrared energy source;
2. Interferometer with mirror and beam splitter (KBr);
3. Sample to be analysed;
4. Detector
5. A computer that can do fourier transformations.

The background spectrum is assessed when there is no sample in the light beam (absorption by the air in the beam path). The percentage transmittance/absorbance is then calculated by comparing it to the sample.



Figure 2.10: The FTIR instrument used for measuring the absorbance spectra.

ii) Laser Raman spectroscopy

Raman spectroscopy is a powerful tool for observing vibrational, rotational, and low-energy modes in a molecule or crystal lattice, and it is widely used for molecular identification. Because the energy and momentum of the photons and molecules before and after the interaction are not the same, it involves inelastic scattering / Raman scattering of laser light (here visible light). The laser photons interact with the polarizable electron cloud (selection

rule), which causes a shift in the energy of the photons to a high or low energy state due to variations in bond polarizability with bond length and vibrations of the molecular bonds. The vibrations in the molecular system correlate to the energy shift. The incidence of monochromatic laser light on the sample is the working principle. The Rayleigh scattered radiation (elastic scattering) that corresponds to the laser wavelength is filtered out with filters (an edge pass filter was utilised), and the remaining radiation is sent to the detector.

Rayleigh scattering is a type of elastic scattering in which the dispersed light has the same frequency as the incident laser photons. The molecule in the ro – vibronic state interacts with the laser photon (rotational and vibrational energy state, ground, as well as excited state). After interacting with laser photons, the molecule enters a virtual energy state, which is followed by inelastic photon scattering. In comparison to the entering photon, the inelastically scattered photon has either lower vibrational energy (Stokes Raman scattering) or higher vibrational energy (Anti – Stokes Raman scattering). As a result of the interaction with the laser photons, the molecule's rotational and vibrational energy states change. With reference to the laser line or the Rayleigh line, the energy difference between the beginning state and the end resulting state causes a shift in the frequency of emitted photons (usually given in wavenumbers) (excitation wavelength).

Raman shifted lines are a combination of Stokes and anti-Stokes lines. The scattered photon is shifted to a lower frequency, corresponding to the energy difference between the original and final ro – vibronic state, when the molecule reaches a vibrational energy state with greater energy (after interaction) than the initial state. This is known as a Stokes shift (energy lost). The scattered photon after the interaction is shifted to a higher frequency for the total energy of the system to stay balanced if the molecule enters a vibrational energy state with less energy than the starting state. This is known as anti – Stokes shift (energy gained). The intensity of Raman scattering is proportional to the difference in polarisation before and after the interaction.

Because there is no change in dipole moment, symmetric vibrations produce higher Raman signals with no IR signals, but asymmetric stretching produces weak Raman peaks with strong IR signals. Bending modes produce weak Raman signals and a strong IR peak in the same way. At the same frequency, a molecule can exhibit both IR and Raman activity, but if the Raman intensity is high, the corresponding IR intensity will be low, and vice versa. Stokes Raman light is typically employed since it is more intense than anti-Stokes Raman light; however, the equivalence of both scattering cannot be determined.

The following components make up a laser Raman setup:

1. The monochromatic Laser Source;
2. The Telescope and Lenses for collecting scattered radiation;
3. The Rayleigh Scattering Filters;
4. The Detector;
5. The computer for material analysis and investigation.



Figure 2.11: The Laser Raman instrument used for measuring the spectra.

The Raman measurements of the powdered Cr-spinel samples were obtained in the ReniShaw Laser Raman spectrometer (Renishaw plc, U.K.) using Cobolt's continuous wave (CW) Diode Pumped Solid State (DPSS) laser as the excitation source with air-cooled plasma filter. Raman signals were measured in a broader range of 100 cm^{-1} – 4000 cm^{-1} with a spectral resolution of 0.3 cm^{-1} . The exposure time of the analysis was 10 s for a laser beam with a power of 500 mW. The laser spot was adjusted from $10\text{ }\mu\text{m}$ to $200\text{ }\mu\text{m}$ using a beam expander. The measured Laser Raman spectra were analyzed further, and the chemical phases were identified using the RRUFF library (Lafuente et al., 2015) and literature references.

iii) X-ray Diffraction

X-ray Diffraction (XRD) is a technique that uses the dual nature of radiation (wave and particle) to reveal the structure of crystalline materials. Amorphous materials do not have a long-range periodic structure and do not form a diffraction pattern. The minerals are identified and analysed based on the diffraction pattern. The distinctive peaks are unique to each crystalline material and can be used as a "fingerprint" for mineral identification.

Many crystallites can be found in a powder (minor and finely crushed crystals). In most cases, the crystallites are orientated in a random pattern with regard to one another. Diffraction occurs from the crystallite planes if the powder sample is placed in the path of X-ray radiation to satisfy the Bragg requirement (orientation at the right angle). With the incident beam, the diffracted rays form a 2θ angle. The diffractometer is positioned in the diffracted beam's path. As a result, 2θ is also the angle formed between incident x-rays and detector. The wavelengths of incident radiations must be equivalent to the spacing between the atoms in diffraction. Diffraction (XRD) investigations are most commonly performed with X-rays. The scattering happens in a specular pattern. The degree of texturing, which distinguishes powder from crystal diffraction, is determined by the size of crystallites. Different orientations are represented equally in powder diffraction, resulting in isotropy.



Figure 2.12: The XRD instrument used for measuring the spectra.

Powder diffraction is primarily used to identify crystalline materials, and each sample's pattern is unique. The powder sample should have a high number of crystallites that are orientated in a random pattern. To achieve good powder diffraction data, crystallites should be less than 10 microns in size. The position of a diffraction peak is determined by the size and angular orientation of the unit cell of the crystalline sample, which is independent of the position of atoms. The Miller indices are used to describe the individual peaks that make up a lattice plane. The relative intensity of the diffraction peaks in a diffraction pattern is used for quantitative analysis and phase determination. The relative intensity (gives type and position of atoms,

qualitative phase analysis) of the diffraction peaks in a diffraction pattern gives information about the cell parameters and crystal lattice. If the crystallites are orientated randomly in powder diffraction, a continuous Debye cone is generated. When compared to crystal XRD with bigger crystallites, X-Ray Powder Diffraction (XRPD) is an inefficient approach. The observed diffraction pattern is not caused by all of the crystallites in the sample. Diffraction from any lattice plane is impossible because the crystallites are not aligned appropriately.

XRD analysis of the Cr-spinel samples was carried out at the Department of Physics, University of Kerala. Bruker D8 ADVANCE with DAVINCI design XRD system was used for the analysis. The instrument used Cu target and N filter, operated at 40 mA current and 40 kV. The samples are scanned for 10 to 80° 2 θ range with a scanning speed of 0.045 2 θ /s.

iv) Electron Probe Micro – Analysis (EPMA)

The Electron Probe Micro Analyzer (EPMA) is a reliable technique for determining the chemical composition of solid materials in situ without having to destroy them. Scanning electron microscopy (SEM) is comparable to this technology. However, it is used for quantitative microanalysis. EPMA can detect levels as low as 100 parts per million. This EPMA uses the same method as an SEM, in which a solid material is attacked with an accelerated electron beam, which produces X-rays, which are detected by spectrometers linked to the electron probe. Wavelength dispersive spectrometry is used to analyze the X-rays liberated for chemical analysis (WDS). The WDS selects X-rays of specific wavelengths using Bragg diffraction from crystals, then guided to gas-flow or sealed proportional detectors. The chemical composition is determined by comparing the intensity of the sample material's distinctive X-rays to known composition intensities (standards). The counts must be adjusted to account for matrix effects (i.e., absorption and secondary fluorescence). Although electron probes can analyze most elements, they cannot detect the lightest ones (i.e., H, He, and Li).

The spatial scale of analysis combined with the ability to develop precise photographs of the sample makes it possible to examine geological materials in situ and resolve intricate chemical variation within single phases (in geology, mostly glasses, and minerals). Under a light microscope, irresolvable features can be scanned to investigate specific micro textures or offer the fine-scale context of an individual spot analysis. Imaging modes for acquiring 2D element maps include secondary electron imaging (SEI), back-scattered electron imaging (BSE), and cathodoluminescence imaging (CL). The Cr-spinel samples from Sittampundi were analysed using EPMA. The polished thin sections were used for EPMA analysis of the Cr-spinel samples

using a JOEL JXA-8230 Electron Probe Micro Analyzer with WDS spectrometry positioned at the Advanced Facility for Microscopy and Microanalysis (AFMM) Centre of the Indian Institute of Science, Bangalore, India. The accelerating voltage is 15 kV with a probe current of 12 nA. Natural silicates and oxide minerals were used as standards.

Chapter 3

Evidence for Late-Imbrian and Eratosthenian mare volcanism in the Grimaldi basin on the nearside of the Moon: Implications for the lunar mantle heterogeneity and thermal evolution

Overview

Lunar mare basalts represent flood volcanism between ~4.0 and 1.2 Ga, therefore, providing insights into the thermal and volcanic history of the Moon. The present study investigates the spectral and chemical characteristics as well as ages of the nearside mare basaltic units from the Grimaldi basin, namely Mare Grimaldi and Mare Riccioli, using a wealth of orbital remote sensing data. This study delineated distinct basaltic units of varying albedo, mineralogy, and titanium contents in Mare Grimaldi and Mare Riccioli. The crater size-frequency distribution technique revealed that at least two phases of basaltic magmatism spanning ~3.5 to 1.5 Ga (Late Imbrian–Eratosthenian) have occurred in the Grimaldi basin. High-Ti olivine basalts dated at 2.05 Ga are found to be surrounded by the Late Imbrian (~3.47 Ga) low- to intermediate-Ti basalts in Mare Grimaldi. Low- to intermediate-Ti basalts observed in Mare

Riccioli date back to two different volcanic events at ~ 3.5 Ga and ~ 3.2 billion years, while patches of basalts having remarkably higher titanium content within the Mare Riccioli record the youngest age of ~ 1.5 Ga. The chemical trend of the pyroxenes from distinct basaltic units also revealed that multiple events of volcanism have occurred in the Grimaldi basin. The high-Ti basalts in the Mare Grimaldi crystallized from an Fe-enriched late-stage magma while the low-Ti basalts crystallized from an Mg- and Ca-rich initial magma that experienced an ultra-late stage quenching. The low- to intermediate-Ti basaltic magma erupted in both the units was derived by partial melting of early cumulate materials from the hybrid source region in the post-overtun upper mantle and made its way to the surface through dikes that propagated by excess pressures accumulated in the diapirs stalled at the base of the crust due to buoyancy trap. The high-Ti magma erupted in the Mare Grimaldi was generated by a hot plume ascended from the deeper clinopyroxene–ilmenite-rich cumulate layer near the core-mantle boundary. However, the Eratosthenian (~ 1.5 Ga) intermediate-Ti volcanic activity in the Mare Riccioli rather sourced from the ilmenite–clinopyroxene cumulate materials that remained in the upper mantle after mantle overturn. The new results suggest that volcanism had not ceased in the Grimaldi basin at 3.27 Ga, rather it was active and fed by different mantle sources until 1.5 Ga for a period spanning ~ 2 billion years.

3.1 Introduction

Earth's moon is a natural laboratory for studying key planetary processes, including the formation and evolution of rocky planets. Scientific contributions from sample return missions and orbital measurements have greatly improved our understanding of the Moon. According to the Lunar Magma Ocean scenario, the Moon was melted up to a considerable depth following its accretion (Smith et al., 1970; Wood et al., 1970; Wood, 1972, 1975, 1983; Warren, 1985). As this magma ocean crystallized, denser mafic minerals (e.g., olivine) settled to the bottom and formed a part of the lunar mantle, whereas later formed plagioclase crystals floated upward and formed the anorthositic lunar crust (e.g., Warren, 1985; Shearer et al., 2006; Elardo et al., 2011; Charlier et al., 2018). Mare basalts are believed to have been formed by remelting of the lunar interior after this initial differentiation episode through serial magmatism (e.g., Head and Wilson, 1992). They are emplaced as fissure-type eruptions of the low-viscosity basaltic magma through cracks and dikes and cover 17% of the lunar surface area (Wilson and Head, 1981; Head and Wilson, 1992). The nature of source regions and causes and processes of remelting the lunar interior for the generation of mare basaltic magmas are

not yet well understood. The surface dating of the mare basaltic units based on crater size-frequency distribution (CSFD) technique as well as radiometric ages of the returned lunar samples revealed that the mare volcanism on the Moon began ~3.9 to 4.0 Ga ago and continued until ~1.2 Ga, with a peak in the volcanic activity at ~3.2 to 3.8 Ga (Head and Wilson, 1992; Hiesinger et al., 2000). The long time span of the eruption of the mare basalts along with vast diversity in their compositions across the lunar surface hints at the heterogeneous nature of the lunar interior and makes them potential candidates for understanding the variations in compositions, source regions, processes, and temperatures over time (Head and Wilson, 1992; Giguere et al., 2000; Morota et al., 2011; Kato et al., 2017; Thesniya and Rajesh, 2020c; Thesniya et al., 2020a). Therefore, investigating the origin, diversity, and ages of mare basalts on the Moon is vital to understanding its volcanic history and thermal evolution better.

The present study utilizes orbital remote sensing data from various lunar exploration missions to survey mare basalts of the Grimaldi basin on the western limb of the nearside Moon (Fig. 3.1). In the past few decades, the visible near-infrared (VNIR) orbital remote sensing technique emerged as a powerful tool to understand the surface mineralogy and chemical composition of the Moon. Pyroxene, plagioclase, and olivine minerals, which are major components of basalts, can be identified in the VNIR domain due to their diagnostic absorptions (see the Methods section). Among these, pyroxene is a significant component in the basalts. The pyroxene group minerals form in all the stages of the crystallization of basaltic magma (Bence and Papike, 1972; Shearer et al., 2006) and hence record the petrogenetic history of basalts (Bence and Papike, 1972). The chemistry of the pyroxenes present in the mare basalts and the relative abundances of endmember compositions can be determined based on their band parameter analysis, allowing us to retrieve information about the crystallization history of basaltic magma (e.g., Cloutis and Gaffey, 1991a).

In the present study, mare basaltic units in the Grimaldi basin (Fig. 3.1) have been investigated using high-resolution optical and spectral imagery. M³ (Moon Mineralogy Mapper) data have been utilized for determining the mineralogy of mare basaltic units. Detailed chemistry of pyroxenes in the Mare Grimaldi and Mare Riccioli has been analyzed further based on the M³ absorption band characteristics. Moderate to high-resolution spatial data from Terrain Mapping Camera (TMC), Terrain Camera (TC), Lunar Reconnaissance Orbiter Camera (LROC), and topographic data from LOLA (Lunar Orbiter Laser Altimeter) have also been used to study the geological context and CSFD dating of the mare basaltic units in the Grimaldi basin. Based on the results, the origin, age, possible source regions, chemical nature of the crystallizing magma, cooling history, and emplacement mechanism of the basaltic units in the Mare Grimaldi and

Mare Riccioli are discussed. The evolutionary stages of the Grimaldi basin involving the eruption of mare basalts in multiple stages and from diverse sources are also discussed.

3.1.1 Geological background of the study area

Grimaldi basin is a Pre-Nectarian two-ringed, “mascon” impact basin located at 5°S, 68°W on the western limb of the nearside Moon, northeast of the Orientale basin (nearly 290 km away; Hartmann and Kuiper, 1962; Wilhelms et al., 1987; Fig. 3.1A). The basin has a diameter of ~440 km and an inner peak ring of ~230 km in diameter, with an approximate depth estimated to ~2.7 km (Figs. 3.1A and 3.1B; Wood 2004). Lunar mascon (mass concentrations) basins, including the Grimaldi basin, are characterized by positive free-air gravity anomalies in their central low-lying topography (Muller and Sjogren, 1968; Melosh et al., 2013), which might be an indication of a positive density anomaly or excess distribution of mass within the crust or upper mantle (Freed et al., 2014; Zhong et al., 2018). Possibly, dense mare basaltic lavas and upliftment of the crust-mantle interface would have contributed to the buildup of mass concentrations in basin depressions (Bratt et al., 1985; Melosh et al., 2013). Crustal thickness map derived from the GRAIL (Gravity Recovery and Interior Laboratory) data suggests a thickness of ~7 to 43 km for the crust beneath Grimaldi basin (Wieczorek et al., 2013), which is relatively thinner than the average lunar crust and make it, together with the occurrence of a mascon anomaly, a potential site of interest for this study. Mare basalts (Mare Grimaldi, hereafter) of Eratosthenian age (termed as “Elm” unit, Scott et al., 1977) fill part of the basin interior to the inner peak ring of 230 km diameter (Wilhelms et al., 1987). The inner peak ring is prominent toward the SE and NW sides of the basin (Fig. 3.1C). The peak rings have been degraded partially and to some extent in the northeastern and southwestern parts of the basin. The ringed peaks rise to an approximate height of ~4.5 km. The region that is lying between the inner ring and outer rim has been designated as the basin floor (Fig. 3.1B). On the west, this mascon basin is bounded by a regular border, having an average height of 1.21 km, while on the opposite side, it is much broken. Riccioli crater is present on the northwestern side of the basin. Mare basalts (Mare Riccioli, hereafter) have partially filled the floor of the Riccioli crater. In the south of the basin, the wall is broken by a large irregular depression. On the east, several grabens were identified (Fig. 3.2). At the extreme north end, several linear grabens cut through the wall and trend toward the Lohrmann crater. Rimae Havelius is one such linear fracture trending in the NW–SE direction (Fig. 3.2). Wrinkle ridges were also found within Mare Grimaldi, trending in the NE–SW direction (Fig. 3.2). The Grimaldi region was initially mapped by McCauley (1973), later studied with NIR telescopic data by Peterson et al. (1995),

and the stratigraphy of the pre-impact target site was also discussed. Spectral studies revealed that much of the Grimaldi region is covered by the outer facies of Havelius formation (Orientale Group) of noritic anorthosite and anorthositic norite composition. The proximity of the Grimaldi basin to the Orientale basin (~3.8 Ga; Yue et al., 2020) resulted in the blanketing of intact lithologies in the Grimaldi basin by the outer facies of the Orientale ejecta (Fig. 3.2).

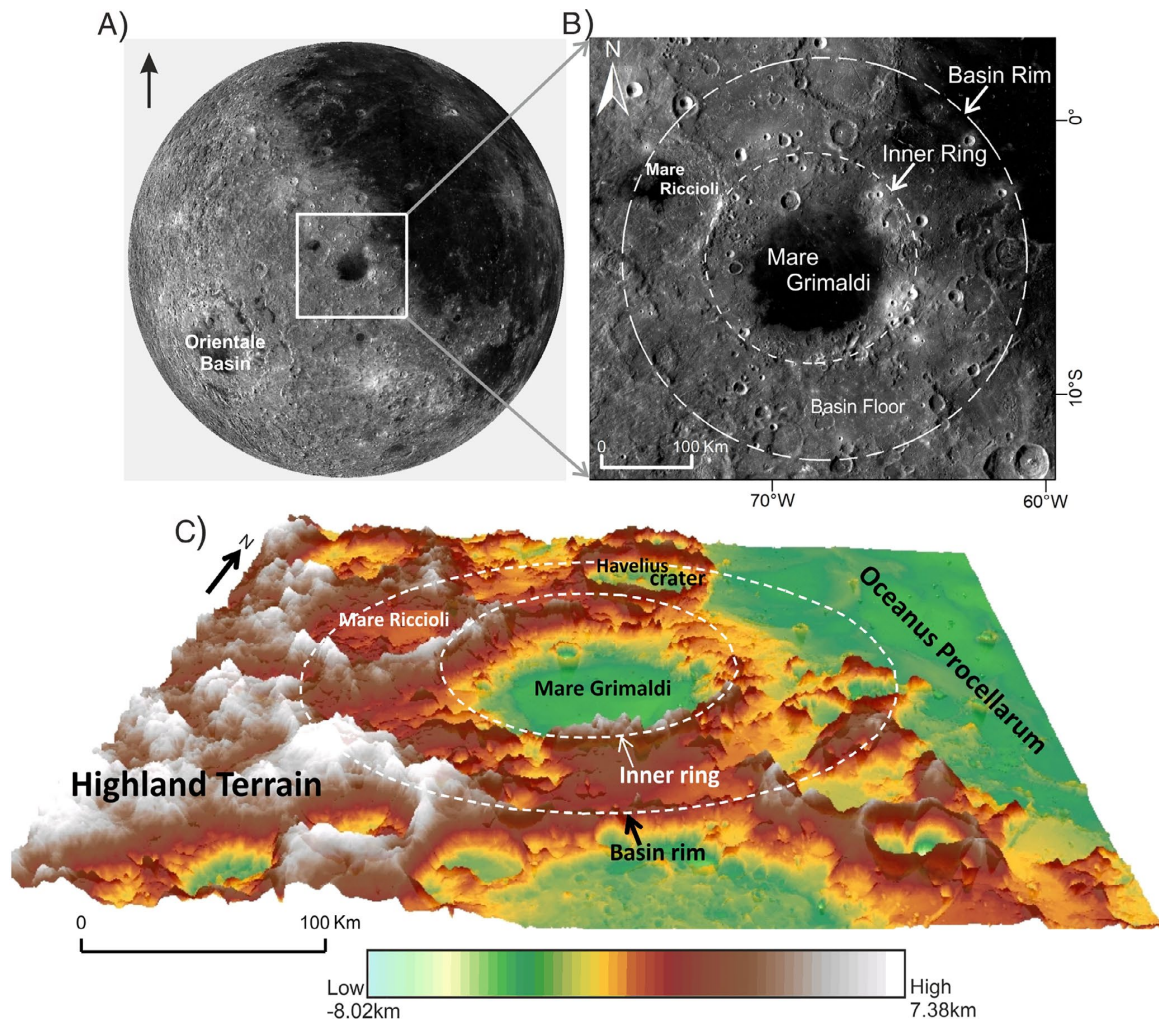


Figure 3.1: (A) LROC-WAC mosaic (Speyerer et al., 2011) of the western limb of the Moon, centered on the Grimaldi basin at 5°S, 68°W. (B) WAC grayscale mosaic image of the Grimaldi basin. The inner ring and basin rim are outlined in white. (C) Color-coded LRO-LOLA & Kaguya Terrain Camera Merge DEM (Barker et al., 2016) of the Grimaldi basin showing the major topographic units in the basin.

The Orientale ejecta also overlies the interior of the Riccioli crater to the northwest. This blanketing of the Orientale ejecta is evident in long linear patterns on the surface of the Riccioli crater. Pure anorthosites were detected in the peak ring and represent the excavated anorthositic crust. The mare basalts within the Grimaldi have mafic assemblages dominated by high

calcium pyroxenes (HCP; Peterson et al., 1995). Gabbroic materials were also identified in excavated materials from beneath the Orientale-related units at the location of three small impact craters (Fig. 3.2). Localized dark mantling deposits (LDMD) of pyroclastic origin were also identified in the outer portion of the Grimaldi basin (McCauley, 1973; Scott et al., 1977; Coombs, 1989; Hawke et al., 1989; Coombs and Hawke, 1992). The compositional and morphological studies of Grimaldi LDMDs were carried out in detail by Gaddis et al. (2003) and Hawke et al. (2012).

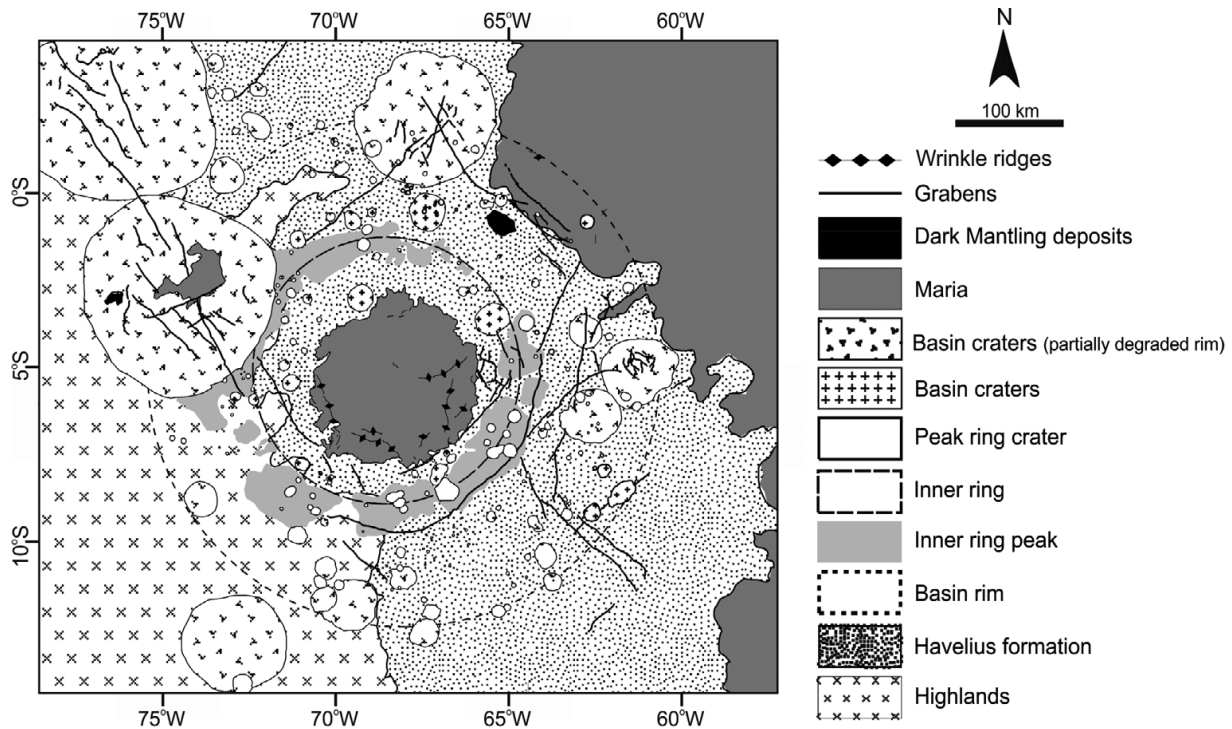


Figure 3.2: Simplified geomorphologic map of the Grimaldi basin (modified after Lunar Geologic Renovation; Fortezzo and Hare, 2013). Major morphologic units are mapped.

Elongated depressions aligned along the NW–SE direction at the center of the Grimaldi deposit were suggested to be probable vents through which pyroclastic debris erupted. These vents have widths ranging from ~3.1 to 3.2 km, lengths from 4.4 to 12.3 km, and depths up to 1007 m (Hawke et al., 2012). The wt% FeO of the dark deposits shows greater values ranging from 10 to 15 compared to that of the surrounding geological units (~4–6 wt%), while the TiO₂ values are ~3.6 wt% (Hawke et al., 2012). As discussed in the previous section, compositional studies of the Grimaldi basin were carried out by previous researchers. The present study investigates the two mare basaltic units in the Grimaldi basin with newly available high-resolution data sets.

3.2 Datasets and methods

3.2.1 Data

Orbital remote sensing data from various lunar missions available in the public domain have been utilized in the present study. Hyperspectral data from Moon Mineralogy Mapper (M^3) onboard ISRO's Chandrayaan-I spacecraft have been used for the identification and mapping of minerals. M^3 is a VNIR hyperspectral imager aboard the Chandrayaan-1 mission, designed for compositional mapping of the lunar surface (Pieters et al., 2009; Klima et al., 2010; Green et al., 2011). The sensor has obtained global images of the Moon at a spatial resolution of 140 m per pixel in global mode and operated in the 446–3000 nm wavelengths range with a spectral resolution of 10 nm. Fifteen Level 2 images from the optical period OP1B have been used in the present study because of their complete coverage in the regions of interest (Boardman et al., 2011). Level 2 data set, consisting of photometrically and thermally corrected reflectance data (Isaacson et al., 2011, 2013; Besse et al., 2013), was downloaded from the Lunar Orbiter Data Explorer Portal (<http://ode.rsl.wustl.edu/moon/>).

Moderate to high spatial resolution optical imagery from TMC, TC, and NASA's LROC has been used for morphological studies. TMC was a panchromatic stereo-viewing camera onboard Chandrayaan-1 with a spatial resolution of 5 m, operating in the spectral range of 0.5–0.75 μm (Bhandari, 2005; Kumar and Chowdhury, 2005; Goswami and Annadurai, 2009). TMC was aimed for topographic mapping of the Moon using high-resolution images acquired in the fore, nadir, and aft directions of the spacecraft movement (Gopala Krishna et al., 2009; Arya et al., 2011; Chauhan et al., 2012). TMC images were downloaded from the ISSDC (Indian Space Science Data Center) portal (<https://webapps.issdc.gov.in>). Full coverage of the mare was only available for Mare Riccioli.

The Kaguya TC is a push broom type stereoscopic imager that flew in the SELENE spacecraft (Haruyama et al., 2008). TC has a spatial resolution of 10 m per pixel from the nominal 100 km SELENE orbit. TC operated in a panchromatic band ranging from 430 to 850 nm. TC data were utilized in addition to TMC data because of its full coverage in the regions of Mare Grimaldi and Mare Riccioli. TC images were downloaded from the SELENE data archive portal (<http://darts.isas.jaxa.jp/planet/pdap/selene/dataset>). Mare Grimaldi units were dated using the mosaic generated from TC images, while TMC images were used for the Mare Riccioli.

LROC is a set of high-resolution stereo-viewing cameras that flew on the LRO (Lunar Reconnaissance Orbiter) mission of NASA (Robinson et al., 2010; Tooley et al., 2010;

Speyerer et al., 2011; Scholten et al., 2012; Wagner et al., 2015). LROC-WAC (Wide-Angle Camera) images with a spatial resolution of 100 m per pixel have been used to understand the broad morphology and local geological setting of the study area. LROC WAC global mosaic of the Moon was downloaded from the Astrogeology Science Centre portal (<https://astrogeology.usgs.gov>).

LOLA and Kaguya TC merged DEM has been utilized in the present study to understand the topography of the study area. This DEM merge was generated at a horizontal resolution of 512 pixels per degree (~59 m at the equator) with ~3–4 m vertical accuracy (Barker et al., 2016). LRO-LOLA and Kaguya TC merge global hillshade map has also been used in the present study. The data were downloaded from the Astrogeology Science Centre portal (<https://astrogeology.usgs.gov>).

Olivine abundance maps of the region were generated using SELENE MI (Multiband Imager) data (Lemelin et al., 2016). The FeO abundance map generated from the SELENE MI data (Lemelin et al., 2016) and TiO₂ abundance map generated from the LROC WAC (Wide Angle Camera; Sato et al., 2017) were also utilized. These three abundance maps were obtained from the QuickMap web interface (<https://quickmap.lroc.asu.edu>).

3.2.2 Methods

3.2.2.1 Mineralogical Mapping

M³ image strips were georeferenced and spatially subset to the boundary coordinates of the basin. The subset of images was then used to produce a reflectance mosaic of the Grimaldi basin. Albedo variations in the lithological units were observed based on the M³ R1578 albedo map. The varying albedo in the 1578 nm band points toward the mineralogical differences in the region. The detailed methodology is described in Chapter 2: section 2.1.1.2.

3.2.2.2 Datation with CSFD Technique

CSFD technique has been adopted for determining the absolute model ages of the distinct basaltic units within Mare Grimaldi and Mare Riccioli. The CSFD method is a widely used technique to estimate the absolute and relative ages of the photogeological units on planetary surfaces (Neukum, 1983; Neukum and Ivanov, 1994; Hiesinger et al., 2000; Neukum et al., 2001). The method primarily involves the measurement of the surface area of the target unit as well as the diameter of each primary crater within the unit. The obtained crater diameters were

plotted as cumulative distribution in Craterstats 2 software. Craters with diameters between 200 m and 2 km have been considered for age estimation. The age is estimated by fitting the lunar production function to the cumulative crater distribution (Neukum et al., 1975; Neukum, 1983; Neukum and Ivanov, 1994).

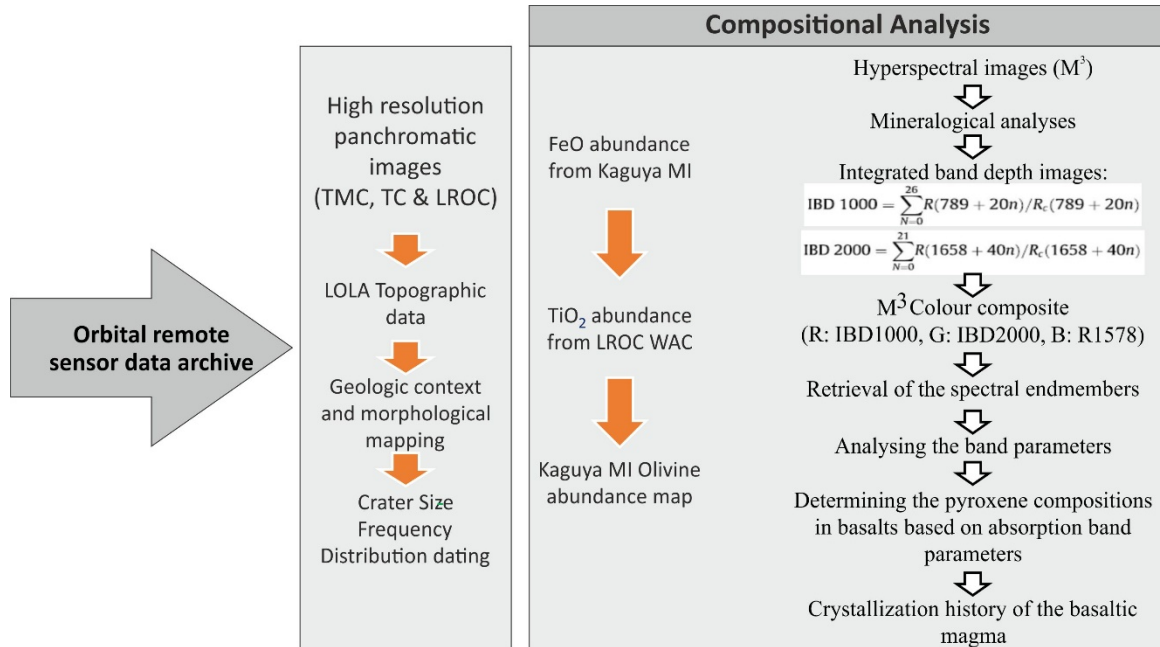


Figure 3.3: The schemata showing the methodology adopted for carrying out the studies related to the volcanic and thermal evolution of the Moon.

3.3 Results

Mare Grimaldi and Mare Riccioli were previously mapped as two basaltic units emplaced during the Imbrian–Eratosthenian period (~3.2–3.48 Ga), consisting of low albedo units with superposed rays and Eratosthenian craters (Fig. 3.5; Wilhelms et al., 1987; Hiesinger et al., 2010). Albedo variations and mineralogy are widely used methods for defining distinct geological units (e.g., Staid et al., 2011; Kaur et al., 2013; Staid and Besse, 2013; Zhang et al., 2014). In the present study, the M³ R1578 albedo map has been used to understand the albedo variations in the Mare Grimaldi and Mare Riccioli basaltic units, while the M³ RGB composite highlights variations in mineralogy (Fig. 3.5). Fresh impact craters that are found to have excavated these basaltic units exhibit spectral signatures of pyroxene group minerals. The albedo variations, chemical composition and mineralogy, FeO and TiO₂ abundances, pyroxene crystallization trend, model ages, and emplacement history of Mare Grimaldi and Mare Riccioli are discussed separately in the following sections.

3.3.1 Spectral and compositional diversity of the Mare Grimaldi and Mare Riccioli units

Unit Mapping from M³ Albedo Variations Mare Grimaldi has occupied the low-lying regions of the basin interior. Within the Mare Grimaldi, notable variations in the R1578 albedo can be observed (Fig. 3.4A). Albedo variations result from the mafic mineral abundances as well as optical maturity of the surface. M³ R1578 albedo in the Mare Grimaldi ranges from ~0.01 to 0.12 (Fig. 3.4A). The measured albedo is less compared to the bright surrounding highlands (>0.09) in the Grimaldi basin due to the presence of mare basalts containing mafic minerals. The bright ejecta rays from the Grimaldi B crater located in the NNW of the Mare Grimaldi are seen to have partially blanketed the top layer of the mare basalt (Fig. 3.4A). The prominent albedo variations in the Mare Grimaldi are attributed to the distribution of ejecta rays from the Grimaldi B crater. The basaltic units toward the northern half of the Mare Grimaldi show higher reflectance because of its proximity to the Grimaldi B crater. The relatively younger superposed craters, which appear to have excavated the basaltic units in the Mare Grimaldi, also display relatively higher albedo values (0.07–0.12). Based on the prominent variations in the albedo, distinct basaltic units have been delineated within the Mare Grimaldi. Four major basaltic units have been defined, namely, G1, G2, G3, and G4 (Fig. 3.4A). These units are labeled in the order of increasing albedo.

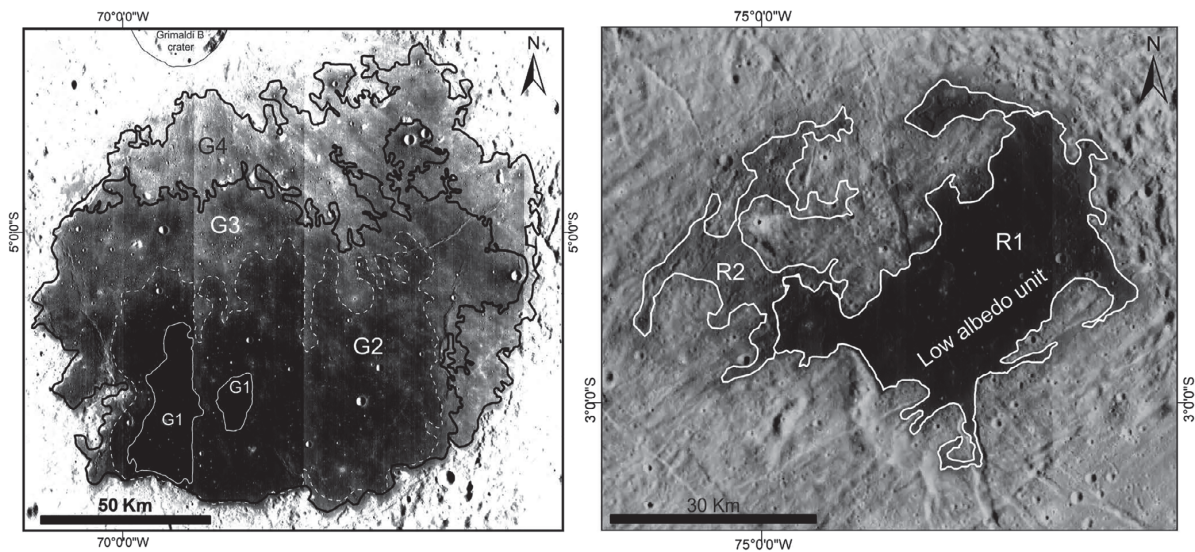


Figure 3.4: M³ R1578 nm albedo map of the (A) Mare Grimaldi and (B) Mare Riccioli (stretched from 0.057 to 0.184). The distinct basaltic units within the Mare Grimaldi (G1, G2, G3, G4) and Mare Riccioli (R1, R2) are delineated based on the albedo variations.

The G1 unit, located in the SW part of the Mare Grimaldi, displays the lowest albedo values (~0.04; Fig. 3.4A). The G1 unit is surrounded by the G2 unit having albedo values in the ~0.05 to 0.06 range. The albedo in the G3 unit ranges from ~0.06 to 0.07. G4 unit exhibits the highest albedo in the Mare Grimaldi ranging from ~0.08 to 0.09. However, the smaller craters within the Mare Grimaldi exhibit a longer range of albedo from 0.01 to 0.12. The lower albedo in these craters, ranging between 0.01 and 0.04, is a manifestation of the mafic mineral exposures on the crater wall, while the higher values (~0.1) indicate less optical maturity of the crater. Mare Riccioli basalts exhibit a slightly varying albedo ranging from ~0.02 to 0.10 (Fig. 3.4B). The low-albedo regions (~0.04 to 0.05) are confined to the central portion of the Mare Riccioli as well as the inner walls of superposed craters. The surrounding regions show albedo values between 0.06 and 0.11. The intermediate to low albedo regions in the central portion of the Mare Riccioli is designated as R1 unit. Within the R1 unit, a few patches of distinctively lower albedo can also be seen toward the north-central region (Fig. 3.4B). These small patches of low albedo regions (0.02) might be attributed to a varying maturity of the surface units and/or later younger eruptions. The surrounding higher albedo region is labeled as the R2 unit (Fig. 3.4B). The Mare Grimaldi units have slightly lower albedo values compared to the Riccioli basalts, possibly due to the more mafic-rich composition of the Mare Grimaldi basalts.

3.3.2 FeO and TiO₂ abundance map

FeO and TiO₂ abundances of the Mare Grimaldi and Mare Riccioli have also been examined to understand the chemical nature of these basaltic units (Fig. 3.5). In the Mare Grimaldi, the G1 unit shows higher FeO (>22.5 wt%) and TiO₂ (>9 wt%) contents, indicating the presence of high-Ti basalts in the region (Thesniya et al., 2020b) (Figs. 3.5A and B). The G2 unit shows FeO and TiO₂ contents between 20–22.5 wt% and 6–10 wt%, respectively. The G3 unit exhibits relatively higher FeO abundance values (15–20 wt%) than the G4 unit and intermediate TiO₂ contents ranging from 4 to 9 wt%. The outer unit, G4 toward the northern part of the Mare Grimaldi, displays medium FeO contents (12.5–15 wt%) and low to intermediate TiO₂ abundance values (2–5 wt%). The varying FeO and TiO₂ contents are consistent with the spectrally defined distinct basaltic units in the Mare Grimaldi. The intermediate to high-Ti basalts (G1 and G2 units) are seen to be surrounded by the low- to intermediate-Ti basalts comprising the G2, G3, and G4 units (Fig. 3.5B).

The G1 unit having the lowest albedo possesses higher FeO and TiO₂ abundance values. The boundary of the G1 unit is delineated based on the distinctly visible extents of the high TiO₂ and FeO contents (Figs. 3.5A and B). It is apparent that the high TiO₂ regions have a greater

spatial extent and are seen as intermixed with the intermediate-Ti unit that overlies one another in the G1 and G2 units. The lower albedo values in the spectrally defined units are linked with the higher TiO₂ and FeO abundance in those units. The mafic-rich composition (higher FeO and TiO₂) of these units causes the observed decrease in their albedo.

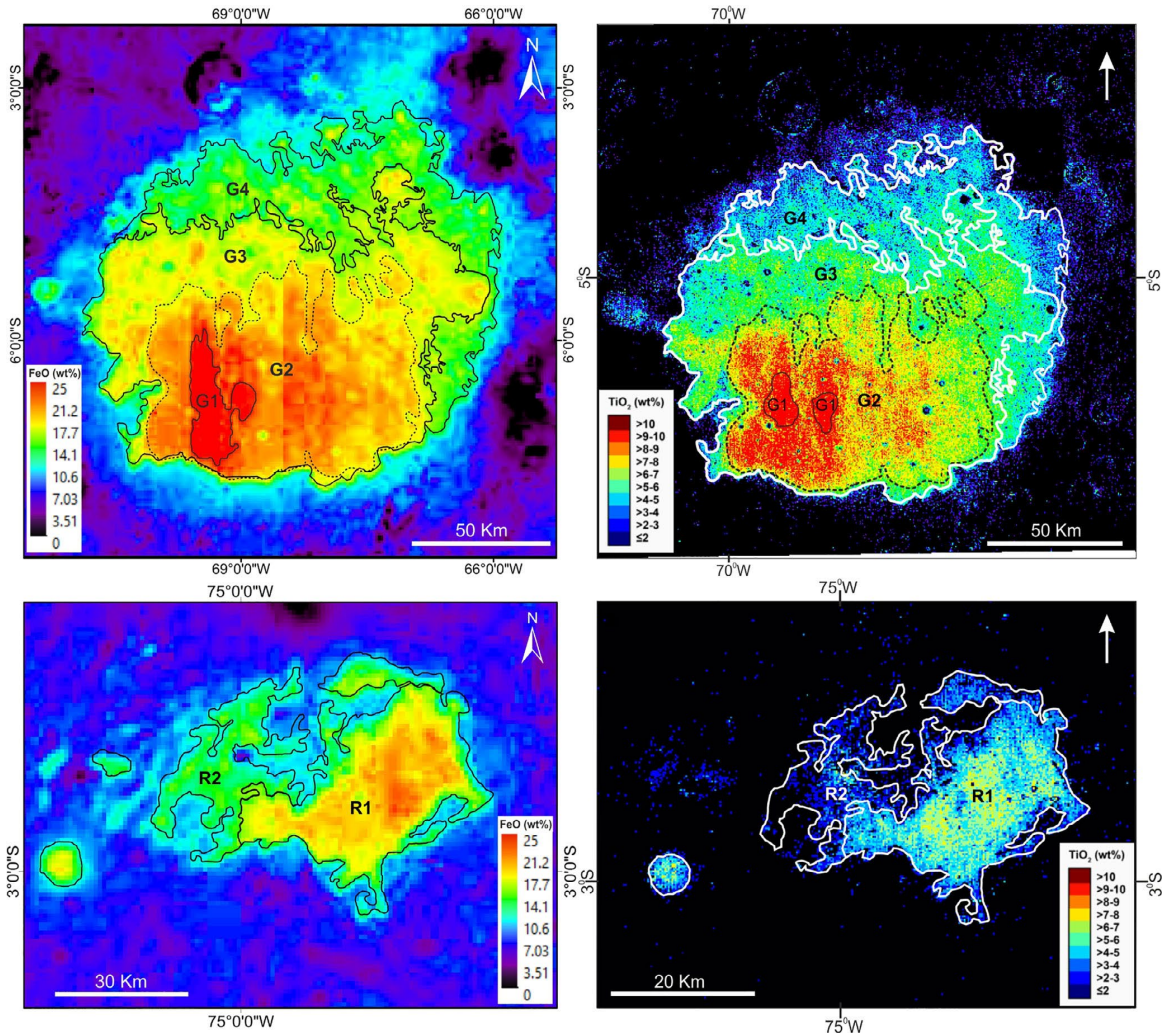


Figure 3.5: (A) Kaguya-MI derived FeO abundance map of the Mare Grimaldi (Lemelin et al., 2016). (B) LROC WAC derived TiO₂ abundance map of the Mare Grimaldi (Sato et al., 2017). (C) Kaguya-MI-derived FeO abundance map of the Mare Riccioli. (D) LROC WAC TiO₂ abundance map of the Mare Riccioli. Distinct basaltic units within Mare Grimaldi and Mare Riccioli have been delineated based on the variations in the FeO and TiO₂ abundances. The basaltic units defined based on the FeO and TiO₂ abundances are consistent with the spectrally defined units in the M³ R1578 albedo map.

In the Mare Riccioli, the FeO content ranges from 12.5 to 22.5 wt% and TiO₂ contents between 2 and 8 wt% (Figs. 3.5C and D). The R1 unit exhibits higher FeO (20–22.5 wt%) and low to intermediate TiO₂ (3–8 wt%) abundance values, while the R2 unit shows relatively lower FeO

(12.5–20 wt%) and low to intermediate TiO₂ (2–5 wt %) abundance values. The R1 unit is surrounded by the R2 unit of relatively low-TiO₂ contents to the northwest. Small patches of higher FeO and TiO₂ concentrations are seen within the R1 unit toward the northern part (Figs. 3.5C and D). The intermediate–low albedo unit (R1) defined in Fig. 3.4B does not display a uniform distribution of FeO and TiO₂ contents in the abundance map (Figs. 3.5C and D). The unit rather shows an uneven distribution of FeO and TiO₂ abundances.

3.3.3 Compositional variations from color composite images

M³ color composite images generated by assigning IBD1000, IBD2000, and R1578 to the red, green, and blue channels, respectively, are shown in Fig. 3.6. In the color composite image, the basaltic units are displayed in the shades of yellow-orange. The varying color shades in the image are attributed to the differences in ferrous band strengths as well as BCs arising from the variations in the mineralogy and/or optical maturity (Cheek et al., 2011; Staid et al., 2011). Distinct basaltic units within Mare Grimaldi and Mare Riccioli were distinguished based on the color differences in the color composite image. The approximate boundary of the G1 unit was delineated based on the spectrally visible spatial extent of TiO₂ abundance in the unit, as the spectral contrast between G1 and the surrounding G2 unit is not very obvious in the color composite image.

In the Mare Grimaldi, the G1 and G2 units exhibit slightly brown-red hues (Fig. 3.6A). The surrounding low-Ti basaltic units, G3, and G4, exhibit yellow-blue shades. The smaller craters within the Mare Grimaldi show brighter yellow tones representing the pyroxene-rich materials of underlying basaltic units exposed on these crater walls (Staid et al., 2011; Fig. 3.6A). The surrounding highlands are displayed in the blue shades resulting from the high feldspathic contents and/or greater maturity of the highland soil (Cheek et al., 2011). Similarly, in the color composite image of the Mare Riccioli, the basaltic units are displayed in the yellow-orange shades. (Fig. 3.6B). The R1 unit exhibits yellow shades, which are consistent with the low-to intermediate-Ti contents in the unit. The relatively low-Ti basalts, R2 unit, are displayed in the light green-orange shades. The smaller craters having pyroxene-rich materials are shown in the bright yellow shades (Fig. 3.6B).

The brown to red-hued basaltic units (G1 and G2) in the Mare Grimaldi exhibit high-FeO and high-TiO₂ contents, as shown in Figs. 3.5A and B. The late-stage high-Ti basalts would have a unique color, composition, and spectral characteristics, and they often represent the younger volcanic materials (Staid et al., 2011). In the Clementine color ratio image, the late-stage high-

Ti basalts in the G1 and G2 units appear blue because of higher spectral reflectance in the blue region of the electromagnetic spectrum (e.g., Pieters 1978; McEwen et al., 1994; McEwen and Robinson, 1997; Lucey et al., 2000) Fig. 3.6C). In the M³ color composite image, the high-Ti basalts in the central portion toward the southern half of the Mare Grimaldi display brown-red hues and are, therefore, thought to represent late-stage younger basalts (Fig. 3.6A).

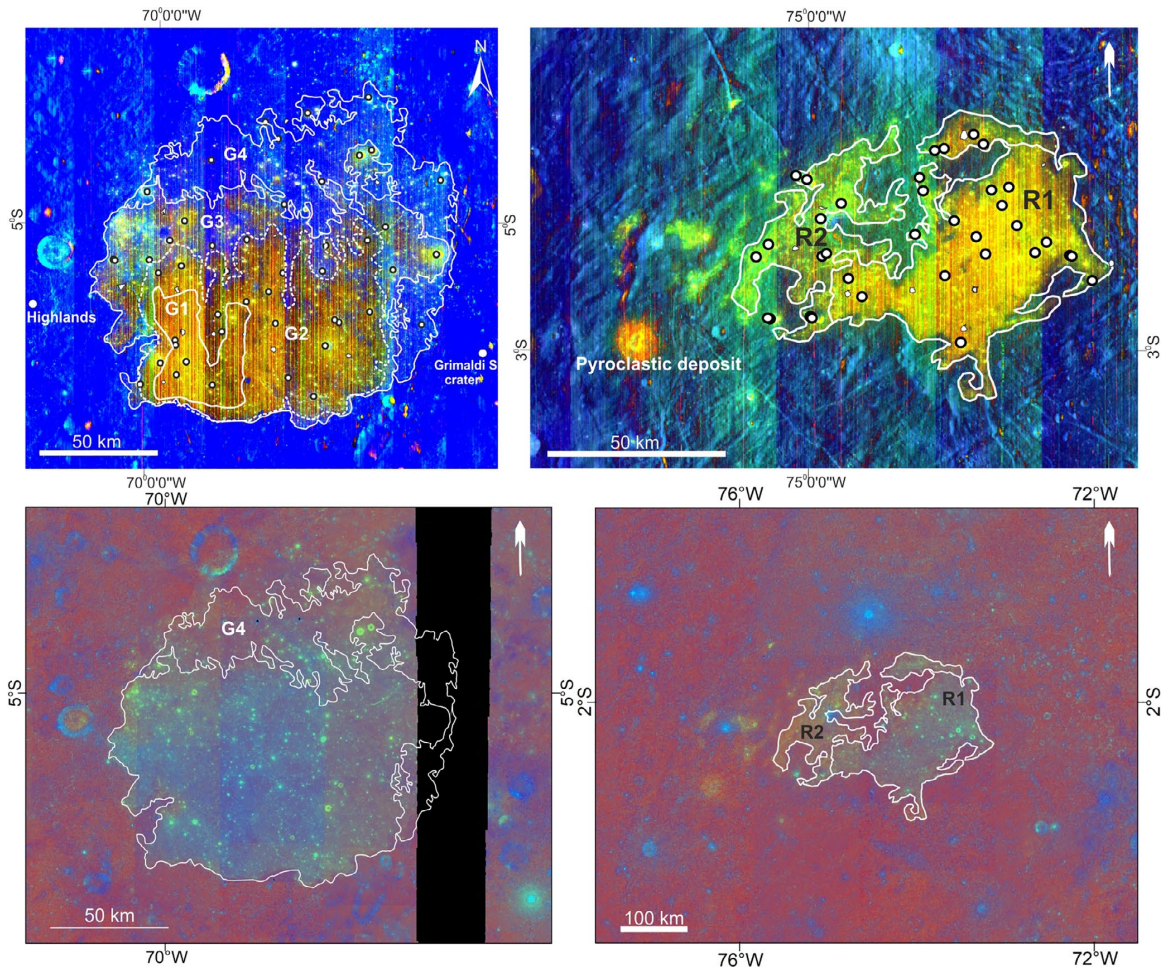


Figure 3.6: (A) M³ color composite image (red: stretched between 0.572 and 2.660, green: stretched between 0.38 and 0.98, blue: stretched between 0.049 and 0.095) of the Mare Grimaldi showing the mineralogical variations among the predefined basaltic units. The solid and dashed white lines demarcate the boundaries of the distinct basaltic units in the Mare Grimaldi. (B) M³ color composite of the Mare Riccioli. The white circles in the image represent the locations where the reflectance spectra have been extracted. The white polygons in the image represent the locations from where the soil spectra were obtained. (C, D) Clementine color ratio image of the Mare Grimaldi and Mare Riccioli showing the presence of basaltic units having compositional differences. The blue shades in the image represent the high-Ti basalts (Pieters, 1978; McEwen et al., 1994). The red regions represent the anorthositic highlands, and the yellow/orange shades correspond to intermediate/low TiO₂ mare units.

The brown-red hues of the high-Ti basalts of the Mare Grimaldi in the M³ color composite are likely caused by the increased band strengths in the 1000 nm region relative to a weaker 2000 nm absorption band, which might indicate the presence of olivine (Staid et al., 2011; Zhang et al., 2016; Fig. 3.6A). The strong and broad absorption feature in the region of 1000 nm might also reflect the presence of FeO-rich glass in basalts (Pieters et al., 1980).

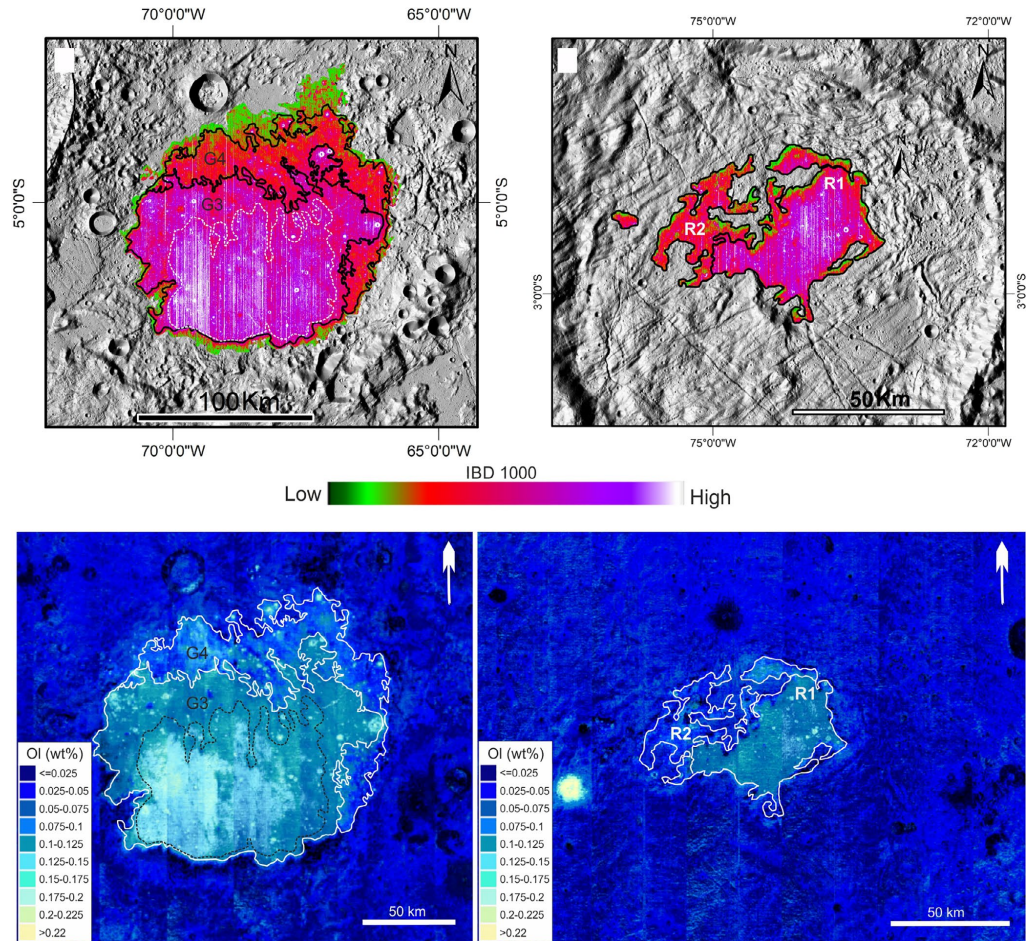


Figure 3.7: Color-coded IBD1000 parameter map of the (A) Mare Grimaldi and (B) Mare Riccioli. The white-purple shaded areas in the central units of the Mare Grimaldi and Mare Riccioli show higher abundance values in the IBD1000 map. The outer G4 unit shows lower abundance values. The solid black lines demarcate the boundaries of the units with distinct abundance values in the IBD1000 parameter map. (C) Kaguya MI-derived olivine abundance map (wt%) of the Mare Grimaldi. (D) Kaguya MI-derived olivine abundance map of the Mare Riccioli (Lemelin et al., 2016). The central basaltic units in the Mare Grimaldi exhibits greater olivine abundance. The solid white line demarcates the boundary of the basaltic units defined based on their olivine abundance.

In the Mare Grimaldi, the brown-red hues are likely to be caused by a higher abundance of olivine. IBD 1000 nm parameter map has been used to estimate the olivine abundance in the

Mare Grimaldi. The IBD1000 parameter is sensitive to the strengths of absorption features in the 1000 nm region of the spectra. Olivine has the diagnostic absorption band only in the 1000 nm region, unlike pyroxenes which have two major diagnostic bands both in the 1000 and 2000 nm regions. Therefore, the abundance of olivine in the basalts can be mapped based on the IBD1000 nm parameter. In the IBD1000 map, the central portion toward the southern half of the Mare Grimaldi exhibits higher abundance values (white and purple hues; Fig. 3.7A). The higher values in this parameter map are consistent with the high Fe-Ti region of the Mare Grimaldi (G1 and G2; Fig. 3.7A). This higher olivine abundance associated with the high-Ti basalts in the Mare Grimaldi is validated by the Kaguya MI-derived olivine abundance map (Fig. 3.7C). The MI olivine abundance map displays greater abundance values in the G1 (0.17–0.22 wt%) and G2 (0.1–0.2 wt%) units of the Mare Grimaldi (Fig. 3.7C). The low- to intermediate-Ti basalts in the Mare Riccioli also show a higher IBD1000 value (Fig. 3.7B). However, the Riccioli units are not showing higher values (0.025–0.15 wt%) in the MI olivine abundance map, contrary to the higher IBD1000 value (Fig. 3.7D). This discrepancy in the olivine abundance of Mare Riccioli units would have been caused by the contribution of other mixed phases to the 1000 nm band strengths that resulted in the increased band strength values in the 1000 nm region and thereby higher abundance values in the IBD1000 parameter map.

3.3.4 Mineralogical signatures from M^3 spectra

Exposure of lunar surface to space weathering reduces the overall reflectance and spectral contrast, weakens the absorption features of different chemical phases, and increases the soil maturity (e.g., Staid and Pieters, 2000). In the Grimaldi basin, materials of highly immature (e.g., the interior of the superposed craters), as well as mature soils, are distributed unevenly. These variations in the optical maturity of the mare units caused by the space-weathering effects are determined based on the relation of R_{950}/R_{750} (ratio of the reflectances at 950 and 750 nm) versus 750 nm reflectance (R_{750}). The reflectance at 750 nm indicates the variations in soil compositions and maturity, while the R_{950}/R_{750} ratio is linked to the mafic absorption band strength, which is sensitive to the optical maturity of the mare and highland soils (e.g., Wöhler et al., 2006). Therefore, the linear relationship between 750 nm albedo and reflectance ratio on the ratio reflectance plot allows us to distinguish the soil materials, and the trends related to soil maturity can be evaluated (Lucey et al., 1995, 1998, 2000). On the ratio-reflectance plot, the pixels occupying low-ratio, brighter end belong to immature materials while high-ratio, dark end represents mature soils (Lucey et al., 1998; Staid and Pieters, 2000). Relatively younger superposed craters within the Mare Grimaldi and Mare Riccioli expose

materials of underlying basaltic units from depth. These smaller craters are subjected to space weathering effects for relatively less time and remain fresh or immature.

Similar mature and immature regions have been distinguished based on the relation of R950/R750 versus R750. Representative soil spectra were extracted from each unit by averaging the reflectance of these immature pixels (Figs. 3.8–3.10). Reflectance spectra from the surrounding highland soils are also shown for comparison (Figs. 3.8A and B). The locations from where the spectra have been obtained are marked as white polygons in Figs. 3.6A and B. Crystalline plagioclase exposures and pure anorthosite-bearing spectra were identified from the wall of the Grimaldi S crater (Figs. 3.8E and F). This anorthosite exposure may represent primary crustal material from the PAN (pure anorthosite) layer (Ohtake et al., 2009; Donaldson-Hanna et al., 2014). The soil spectra collected from the distinct basaltic units exhibit varying spectral slope and absorption characteristics. The soil spectra from the G1 unit display lower average albedo values and a relatively stronger absorption band in the 1000 nm region (Figs. 3.8A and B). A weaker absorption band has been observed in the 2000 nm region. Moreover, the band I absorption is observed to be shifted longward in response to the Fe²⁺ electronic transition absorption. The band strength in the 1000 nm region is higher relative to the 2000 nm band. The presence of olivine would increase the strength of the 1000 nm band relative to the Band II absorption and bring a longward shift in the Band I absorption. The presence of FeO-rich glass might also contribute to the longward shift of the Band I center (Besse et al., 2014). However, the presence of glass will additionally contribute to a shortward shift in Band II center and higher Band II strength relative to Band I, which is contrary to the G1 spectra. Therefore, the observed longward shift in Band I center and a greater band I strength is conclusively consistent with the olivine abundance in the G1 unit of Mare Grimaldi. This evidence favors the occurrence of olivine basalt in the Mare Grimaldi (Fig. 3.7). The soil spectra from the G2 unit exhibit relatively symmetric Band I and Band II absorptions (Figs. 3.8A and B). Band I appears to be narrower compared to a broader Band II absorption.

The spectra from the G2 unit are dominated by pyroxene-rich materials. The G3 unit soil spectra exhibit evident absorption features in the 1000 and 2000 nm regions (Figs. 3.8A and B). However, the Band II absorption is broader relative to narrow Band I absorptions. The average soil spectra from the G4 unit also exhibits absorptions in the 1000 and 2000 nm regions with a relatively stronger and broader Band II absorption (Figs. 3.8A and B). The soil spectra from the R1 unit in the Mare Riccioli have spectral characteristics more or less similar to the G1 unit of Mare Grimaldi (Figs. 3.8C and D). The Band I absorption is relatively stronger and shifted slightly longward. The R2 spectra also show both the Band I and Band II absorptions with a stronger and broader absorption band in the 2000 nm region (Figs. 3.8C and D).

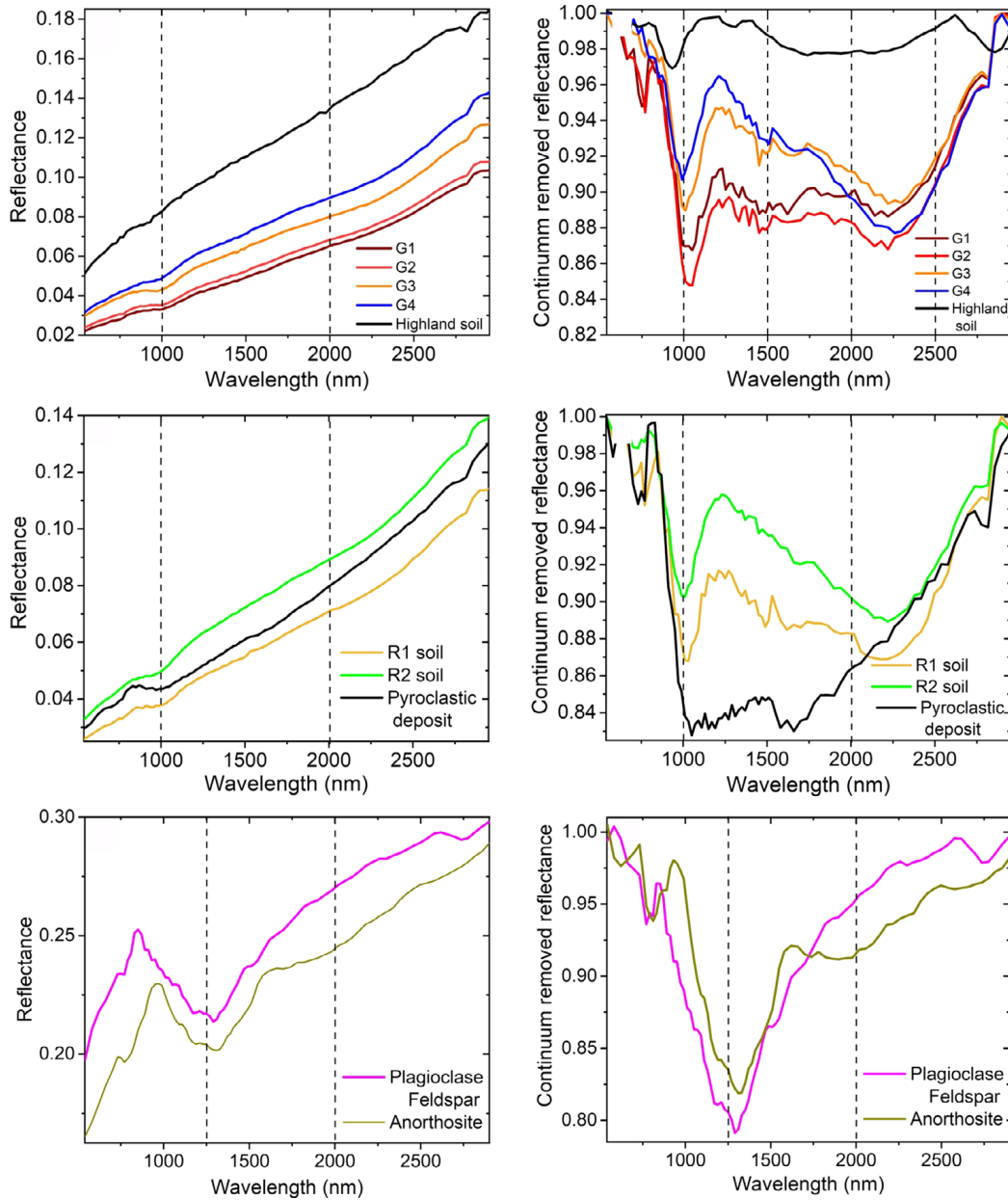


Figure 3.8: (A–D) Representative reflectance spectra of the basaltic units in the Mare Grimaldi. The average reflectance spectra of the soil from each basaltic unit have been plotted. (A, B) Normal and continuum removed spectra for G1, G2, G3, and G4 units in the Mare Grimaldi. The spectrum from the highland soil has also been plotted along with the soil spectra to understand the differences in the spectral slope and pattern among the soil of mare and highlands. (C, D) Normal and continuum removed spectra for the R1 and R2 units in Mare Riccioli. The spectrum of the pyroclastic deposit in the western region of the Mare Riccioli has also been plotted along with the soil spectra. The black dashed lines are drawn at 1000 and 2000 nm. (E, F) Representative reflectance spectra of pure anorthosite (PAN) and crystalline plagioclase obtained from the Grimaldi S crater located along the inner ring of the Grimaldi basin. The spectra collected locations have been labeled in Fig. 3.6A & B.

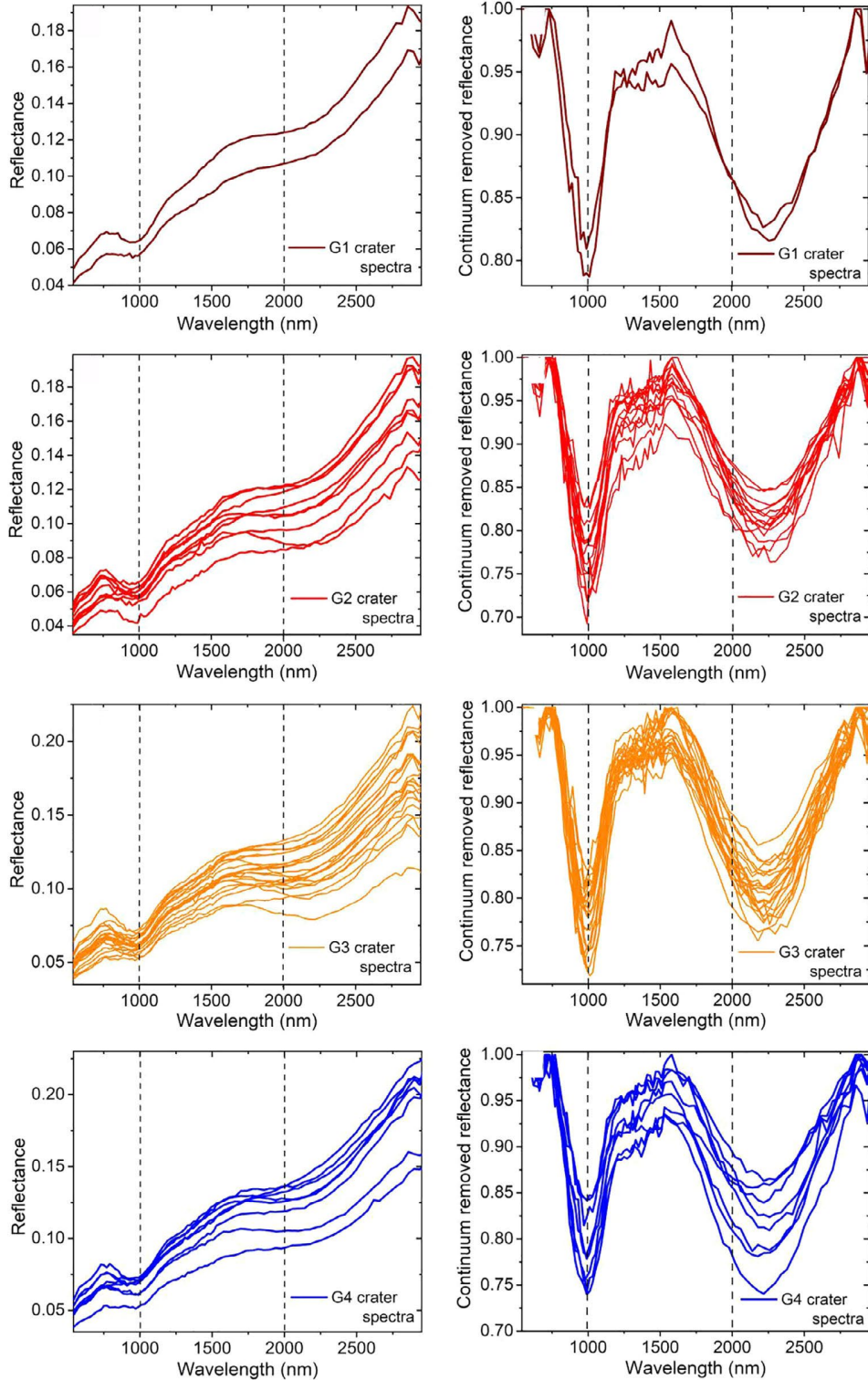


Figure 3.9: (A–H) Normal and continuum removed reflectance spectra of the clinopyroxenes collected from G1 (A–B), G2 (C–D), G3 (E–F), and G4 (G–H) units of the Mare Grimaldi. The black dashed lines are drawn at 1000 and 2000 nm. The spectra collected locations have been shown in Fig. 3.6A.

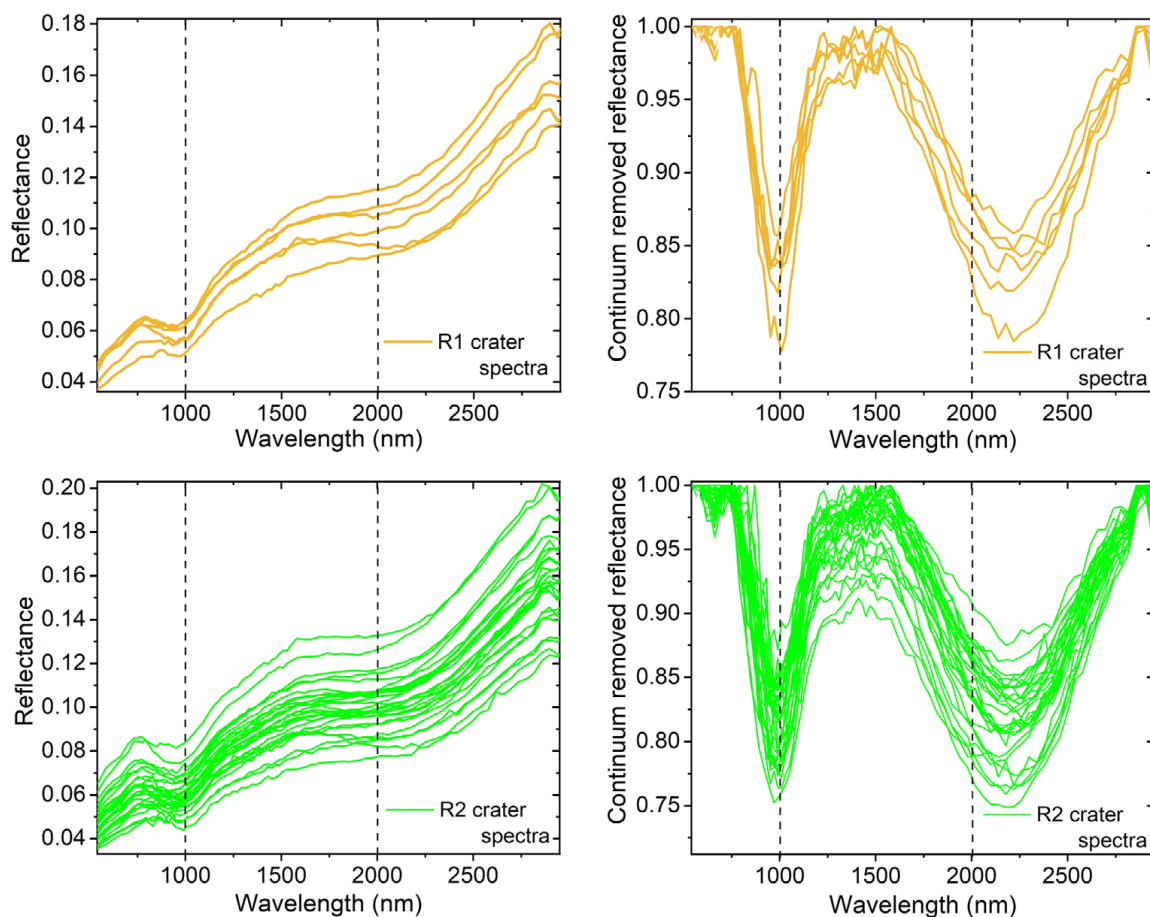


Figure 3.10: (A–D) Normal and continuum removed reflectance spectra of the clinopyroxenes collected from the R1 (A, B) and R2 (C, D) units in the Mare Riccioli. The black dashed lines are drawn at 1000 and 2000 nm. The spectra collected locations have been shown in Fig. 3.6B.

The R2 unit is dominated by pyroxene-rich materials. The pyroxene-bearing spectra obtained from the inner walls of superposed craters in Mare Grimaldi and Mare Riccioli were identified, and found that the clinopyroxenes are the major component present in the spectra (Figs. 3.9 and 3.10). The clinopyroxenes exhibit two major absorption bands at 1000 nm (Band I) and 2000 nm (Band II) in response to the electronic transition absorptions by Fe^{2+} ions in the M1 and M2 sites. The clinopyroxene-rich spectra in the G1, G2, and G3 units exhibit stronger Band I absorption relative to the Band II absorption, suggesting the presence of mixed phases in the spectra (Figs. 3.9A–F). However, the clinopyroxene-rich spectra from the G4 unit, as well as Riccioli units, exhibit more or less symmetrical and stronger Band I and Band II absorptions, which indicate that clinopyroxene is dominating in the reflectance spectra from these regions (Figs. 3.9G–H and 3.10A–D).

3.3.5 Determining the composition of the pyroxenes based on their band parameter analysis

The “Elm” basaltic units in the Mare Riccioli and Mare Grimaldi are dominated by clinopyroxenes (Fig. 3.11). The Band I and Band II absorption features of the pyroxenes would enable us to retrieve relevant information about their chemistry as well as crystallization conditions (Bence and Papike, 1972). Hence, the Band I and Band II parameters such as BC, BS, and BA have been calculated for the collected spectra based on the method described in the Methods section. The Mare Grimaldi units show Band I centers between ~985 and 991 nm while the Band II centers between ~2142 and 2159 nm. The Mare Riccioli units show both the Band I and Band II centers at relatively shorter wavelengths (~969 to 983 nm, ~2074 to 2136 nm). The variations in the BCs are consistent with the TiO₂ and FeO contents of different units. The Band I and Band II centers, are found to have shifted to somewhat longer wavelengths with the enhanced TiO₂ abundances of the basaltic units.

BAR versus Band I center is plotted to understand the mixing of olivine and pyroxenes in the obtained spectra as the olivine abundance is noticeably higher in the high-Ti units (after Gaffey et al., 1993; Fig. 3.12A). The Mare Grimaldi and Mare Riccioli compositions fall in the region of clinopyroxenes and orthopyroxenes (Opx > Ol) in the BAR versus Band I center plot. The BAR for the Mare Grimaldi compositions (fresh craters as well as soil samples) is between 0.4 and 2 (Fig. 3.12A). The Band I center ranges from ~963 to 1032 nm. The Mare Riccioli compositions have BAR in the 0.6–1.7 range, while the Band I center ranges from ~951 to 1016 nm (Fig. 3.12A). The BAR increases as the pyroxene component dominates the reflectance spectra (Cloutis et al., 1986). Mare Riccioli compositions have BAR values greater than the Mare Grimaldi compositions (fresh craters), suggesting the relative dominance of pyroxenes in the Mare Riccioli (Fig. 3.12A). The Band I center shifts longward with the corresponding decrease in the BAR when the olivine content in the spectra increases (Cloutis et al., 1986). The soil sample from the Mare Grimaldi and Mare Riccioli showing lower BAR values and longer Band I centers indicate the mixed olivine content in the spectra. This mixed olivine content yet again validates the observed higher olivine abundance of the high-Ti basaltic units in the Mare Grimaldi. As most of the soil samples show evidence of mixed olivine components, these soil compositions are not included in the further band parameter analysis. Since the mixing of olivine and pyroxene phase in the reflectance spectra is noticed, the displacement in the Band I center of pyroxenes has to be corrected to remove the spectral effects of olivine (see Methods section). The estimated displacement in the Band I center is approximately 23 nm on average (Fig. 3.12B). The estimated Band I (corrected) and Band II parameters for the

pyroxenes from each basaltic unit are given in Table 3.1. The corrected Band I centers and Band II centers have been used for the Band II versus Band I plot. This Band II versus Band I plot is used to understand the compositional variations among the pyroxenes (Fig. 3.12C). The reference data from Adams (1974), later modified by Cloutis and Gaffey (1991a), and synthetic pyroxene data from Klima et al. (2011) are also plotted for comparison (Fig. 3.12C). The Mare Grimaldi and Mare Riccioli pyroxene compositions are falling along the main trend of the reference pyroxene data. The corrected Band I center of the Mare Grimaldi pyroxenes ranges from 937 to 983 nm, while the Band II center ranges between 2097 and 2199 nm (with average values of 959 and 2148 nm).

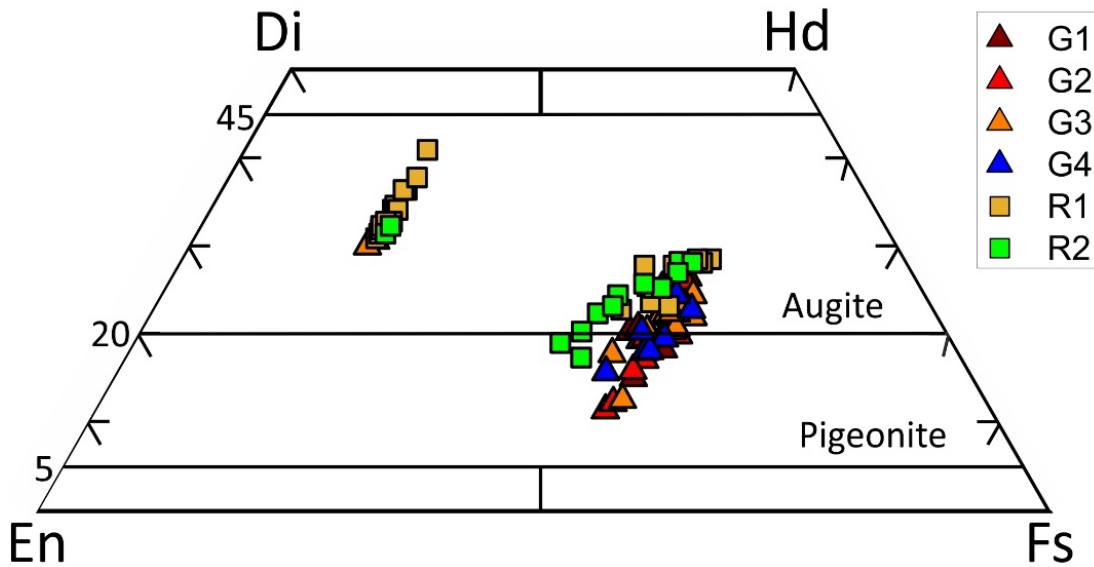


Figure 3.11: Pyroxene quadrilateral plot showing the relative abundance of the endmember pyroxene compositions in the Mare Grimaldi and Mare Riccioli.

Typically, mare basalts contain a stable equilibrium three-phase assemblage of Ca Fe pyroxene- Fe olivine-silica that formed through crystallization from a Fe-enriched late-stage melt (cf. Papike et al., 1991). In some cases, extremely Fe-rich pyroxene or a silicate mineral called pyroxferroite ($\sim\text{Wo}_{14}\text{En}_{11}\text{Fs}_{75}$) crystallizes metastably relative to the typical pyroxene-olivine-silica assemblage due to rapid cooling of the late-stage melts. These metastable iron-rich pyroxenes occupy the “forbidden region” near the Hd- Fe joins of the “pyroxene quadrilateral” (Lindsley and Anderson, 1983). Similar compositions formed metastably at low pressures in lunar basalts by the rapid cooling of magma (to below 990 °C at 2 °C per hour) at or near the surface were reported earlier, particularly in high-K basalts, olivine basalts, pigeonite basalts, ilmenite basalts, feldspathic basalts, and very high-Ti basalts in the Apollo

11, Apollo 12, Apollo 15, Apollo 17, and Apollo 14 samples (Lindsley and Burnham, 1970; Lindsley et al., 1972; Papike et al., 1991).

Mare Riccioli pyroxene compositions exhibit Band I center between 951 and 1004 nm and Band II center in the 1997–2180 nm range (with average values of 976 and 2108 nm). The systematic shift of Band II center to longer wavelengths is owing to the increase in the Ca²⁺ content (Cloutis and Gaffey, 1991a; Klima et al., 2011). The BC values indicate that the pyroxene compositions are mainly pigeonite and augite in the Mare Grimaldi and Mare Riccioli (Fig. 3.12C). The estimated band parameters of pyroxenes can also be used to calculate the relative abundance of endmember pyroxene compositions (Gaffey et al., 2002; Kaur et al., 2013; Chauhan et al., 2018). The abundance of these pyroxenes is determined using the calibration equations described in the Methods section (Gaffey et al., 2002). The estimated pyroxene abundances have been projected onto a pyroxene quadrilateral plot to understand the relative proportions of Ca, Mg, and Fe (Lindsley and Anderson, 1983).

In the quadrilateral plot, the major pyroxene compositions in Mare Grimaldi and Mare Riccioli are pigeonite and augite. However, most of the pyroxene compositions in the Mare Grimaldi and Mare Riccioli fall in the “forbidden zone” of the pyroxene quadrilateral (Fig. 3.12). In the forbidden region, single pyroxene of intermediate composition is unstable at low pressures (Lindsley and Anderson, 1983). However, Fe-rich pyroxene compositions, often zoned to pyroxferroite, falling in the forbidden region, were observed in lunar basalts as a result of metastability and rapid crystallization (cf. Papike et al., 1976; Papike and Vaniman, 1978).

The Mare Riccioli pyroxenes are mostly subcalcic augites to augites, while the Mare Grimaldi pyroxenes comprise pigeonite and augites (Fig. 3.12). The chemical trend of these compositions is commonly the reflection of a combination of factors such as melt composition, crystallization history, and late-stage to subsolidus cooling rate (cf. Bence and Papike, 1972; Papike et al., 1976). The augites from R1 and R2 show a compositional cluster near the Di-Hd join (Fig. 3.12D). This kind of clustering is common in pyroxenes of quickly cooled basalts. The subcalcic-augites from both these units show a clustering towards the forbidden zone.

In the R1 and R2 units, the crystallization commences with primary Mg-rich augite compositions, representing the initial stage of crystallization of the magma. A sudden drop in the calcium content of augites is observed (Fig. 3.12D). This discontinuity in the trend has possibly resulted from the onset of crystallization of plagioclase that preferentially incorporated CaO into plagioclase and thereby depleted calcium content in the residual melt (Bence and Papike, 1972). The Fe-enriched late-stage residual liquid might have crystallized iron-rich subcalcic augites. The intermediate calcium content of these pyroxenes between

pigeonite and augite suggests their crystallization metastably from an iron-rich residual melt that cooled rather quickly in the late stage (e.g., Smith and Lindsley, 1971). The extreme iron enrichment is also indicating a fairly fast cooling rate and thereby violated the “forbidden region” of the pyroxene quadrilateral (Lindsley and Munoz, 1969).

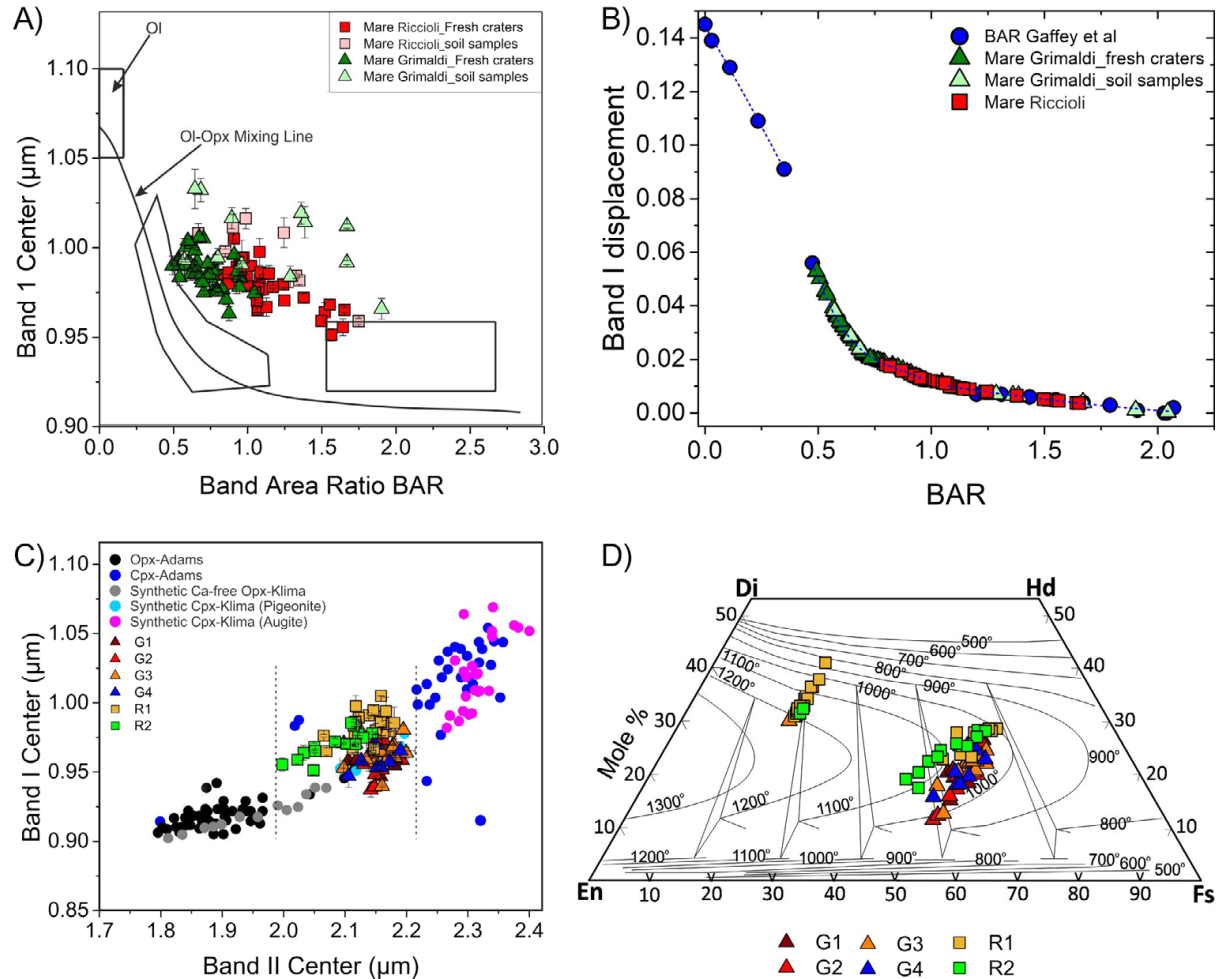


Figure 3.12: (A) BAR versus Band I center plot of the compositions sampled from the Mare Grimaldi and Mare Riccioli (after Gaffey et al., 1993). (B) BAR versus Band I displacement plot of the compositions from Mare Grimaldi and Mare Riccioli. The Band I displacement of each composition has been determined from the BAR versus Band I calibration function originally derived by Gaffey et al. (2002). (C) Band II centers are plotted against the corrected Band I centers of the pyroxene bearing spectra from the Mare Grimaldi and Mare Riccioli. The data are plotted along with the reference data for orthopyroxenes and clinopyroxenes from Adams (1974), modified by Cloutis and Gaffey (1991a). The data of synthetic pyroxenes from Klima et al. (2011) are also plotted for comparison. (D) Mole % compositions of pyroxenes in Mare Grimaldi and Mare Riccioli projected onto the pyroxene quadrilateral along with the equilibrium pyroxene temperatures based on the graphical thermometer developed by Lindsley and Anderson (1983).

The compositions from G1, G2, G3, and G4 units exhibit a lower Ca, and Fe-enrichment trend zoning to the metastable composition in the forbidden region along the Hd-Fs join (Fig. 3.12D). In the G1 unit, the Fe-rich subcalcic augite compositions show tight clustering in the region of metastable pyroxenes in the quadrilateral. The extremely Fe-rich compositions in this unit might be indicative of crystallization from a highly fractionated magma at a fast cooling rate. This compositional clustering might also be the result of the mantling of the olivine by pyroxenes that hindered the former from reacting with the liquid. However, this scenario is beyond the scope of this study. Furthermore, the G2 and G3 units are showing distinct chemical trends starting with the crystallization of Fe-rich pigeonite followed by subcalcic-augite (Fig. 3.12D), although few compositions from G2 and G3 units are seen to have crystallized at the Mg-rich end of the quadrilateral. It is possible that crystallization in the G2 and G3 units started with primary Mg-rich augites in early stages, followed by the incoming of plagioclase and subsequent rapid crystallization of iron-rich subcalcic late-stage augites and pigeonites from the residual melt. This iron enrichment with constant Mg at the expense of Ca is reflected in their occurrence as a metastable phase in the “forbidden region” of the quadrilateral. The compositions in the G4 unit also show calcium content intermediate between pigeonite and augite, suggesting that they crystallized metastably from a quickly cooled late-stage melt (Fig. 3.12D). The compositional break in the augite trend due to preferential incorporation of CaO into plagioclase is not very common in fast-cooled rocks as the plagioclase nucleation is very late or not at all in such rocks. However, the late residual melt in a slowly cooled magma might experience a late-stage rapid cooling (quenching) and crystallize metastable pyroxene compositions, which otherwise are not stable in the forbidden region of the quadrilateral. Therefore, the extremely Fe-rich pyroxenes in these basalts are possibly the result of the crystallization of a fractionated magma under quenching conditions. The possibility of a subsolidus re-equilibration can also not be ruled out as augite–pigeonite exsolution is common in lunar basalts (Ross et al., 1970; Papike et al., 1971; Takeda et al., 1975). However, the remote spectrochemical analysis limits the scope of detection of subsolidus exsolution in pyroxenes, and therefore, this is not understandable using this pyroxene thermometer (e.g., Lindsley and Anderson, 1983).

Based on the observations, it can be inferred that the high-Ti basalts in the Mare Grimaldi crystallized from a Fe-enriched highly fractionated late-stage magma at a fast cooling rate (~2 °C per hour) between ~1100 and 1000°C (Fig. 3.12D). However, the low-Ti basalts in the Mare Grimaldi crystallized from a rather Mg- and Ca-rich initial magma that underwent an ultra-late stage rapid cooling at a rate between 1200 and 1000 °C. The chemical trend of low-Ti basalt in the Mare Riccioli conforms to a similar scenario where the cooling (1200–1000°C) of an

initial high Ca-Mg magma followed a late-stage quenching through rapid crystallization. The intermediate-Ti basalts in the Mare Riccioli also suggest a quenching trend where an initial Ca and Mg-rich magma experienced a late-stage fast cooling (1100–1000°C), resulting in a metastable crystal–liquid equilibration.

3.3.6 Model ages of Mare Grimaldi and Mare Riccioli using CSFD

The Mare Grimaldi and Mare Riccioli basalts were previously dated by Hiesinger et al. (2010) and reported ages of 3.48 and 3.27 Ga, respectively. In the present study, the distinct basaltic units in the Mare Grimaldi and Mare Riccioli have been dated separately to understand the volcanic history of the basin (Figs. 3.13, 3.14, 3.15, and 3.16; Table 3.1).

Table 3.1: Estimated band parameters (avg.) of the pyroxenes from G1, G2, G3, G4, R1, and R2 units along with the absolute model ages of these distinct units in the Mare Grimaldi and Mare Riccioli (age classification is based on Stoffler et al., 2006).

Basaltic units		Band I center (nm; avg.)	Band II center (nm; avg.)	FeO (wt%)	TiO ₂ (wt%)	Age (Ga)	
Mare Grimaldi	G1	958	2142	>22.5	>9	2.05 ± 0.10	Eratosthenian period
	G2	959	2148	20–22.5	6–10	2.05 ± 0.06	
	G3	963	2159	15–20	4–9	3.47 ± 0.08/0.19	Late Imbrian epoch
	G4	959	2146	12.5–15	2–5	n.a.	
Mare Riccioli	R1	983	2136	20–22.5	3–8	1.5 ± 0.07	Eratosthenian period
						3.2 ± 0.2/0.6	Late Imbrian epoch
	R2	969	2080	12.5–20	2–5	3.5 ± 0.05/0.07	

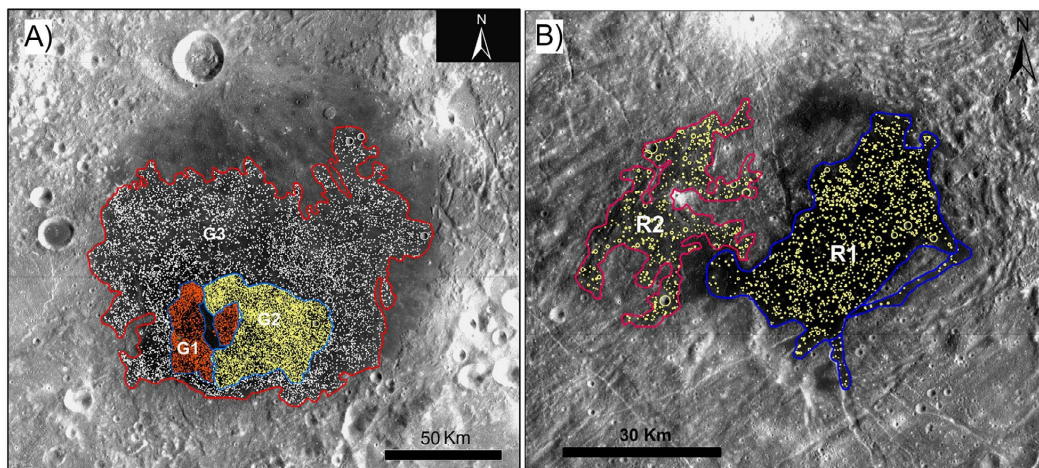


Figure 3.13: Model ages of the Mare Grimaldi and Mare Riccioli basaltic units determined based on the CSFD technique. (A) Kaguya TC image of the Mare Grimaldi showing the crater count areas for each basaltic unit, G1, G2, and G3. (B) TMC image of the Mare Riccioli showing the crater count area for the R1 and R2 units.

The model age for the basaltic unit in G4 could not be determined based on the CSFD technique as the unit is more or less blanketed by ejecta from the Grimaldi B crater. The cumulative crater frequency plot of the G1 and G2 units revealed younger ages, $\sim 2.05 \text{ Ga} \pm 0.06$. Since both the units are showing similar ages, the crater counts of these areas have been merged, and the cumulative frequency plot along with the age isochron for these units is shown in a single plot displaying a common age of 2.05 Ga (Figs. 3.14). The G3 unit in the Mare Grimaldi revealed a model age of $3.47 \text{ Ga} \pm 0.08/0.19$ (Fig. 3.14).

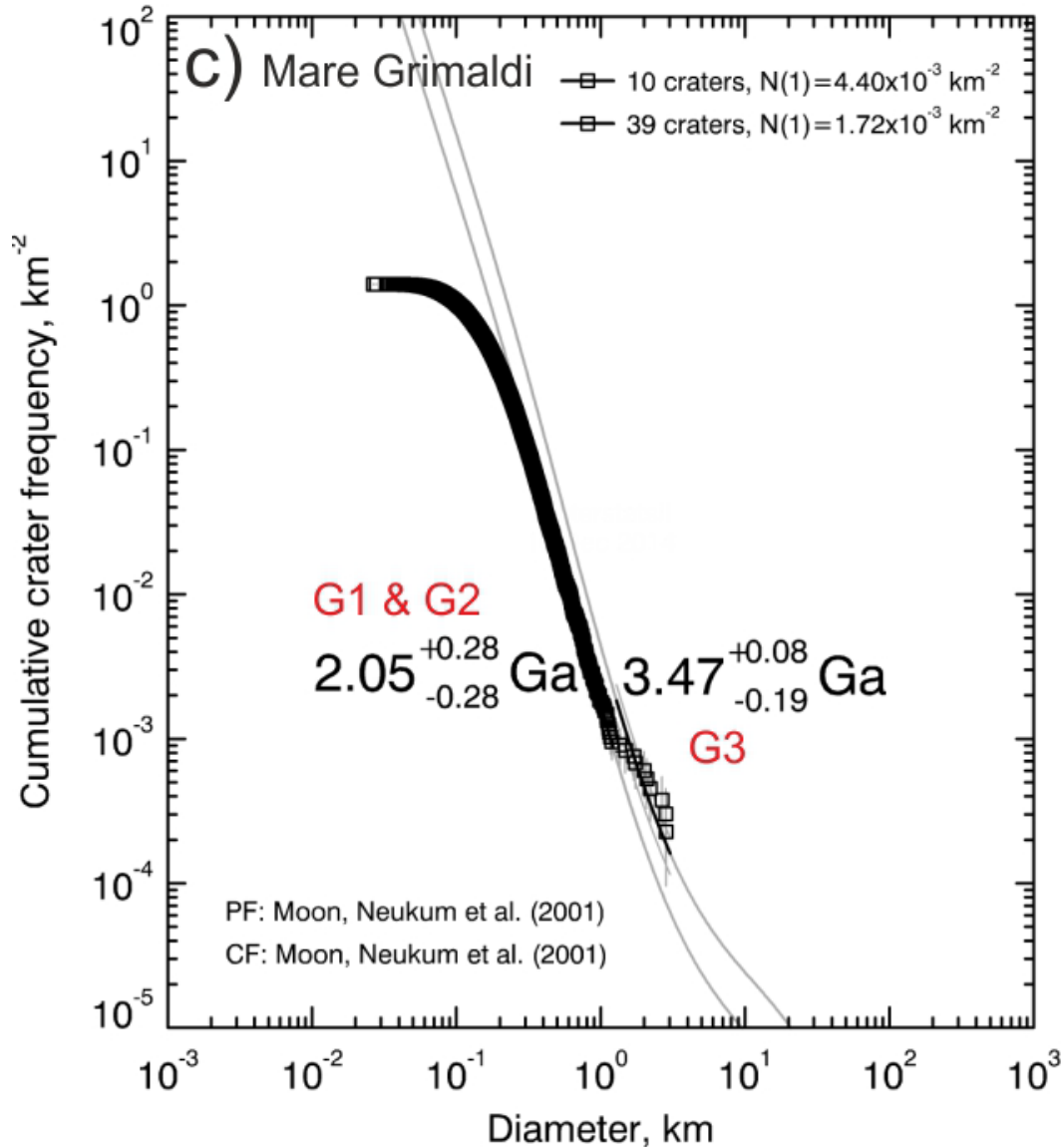


Figure 3.14: Cumulative frequency plots of the G1–G2 (merged) and G3 unit in the Mare Grimaldi along with isochron and error for the data points. The younger age of 2.05 Ga corresponds to the age of the merged unit, that is, G1 and G2 (high-Ti basalts). The older age of 3.47 Ga shows the age of the G3 unit (low to intermediate-TiO₂ basalts).

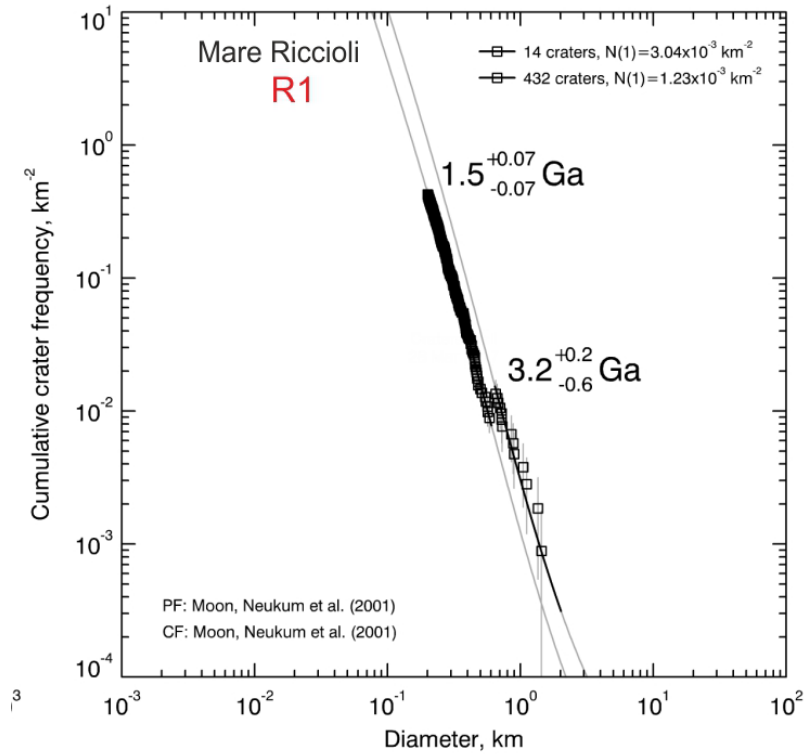


Figure 3.15: Cumulative frequency plot of the R1 unit along with age isochron and error for each data point.

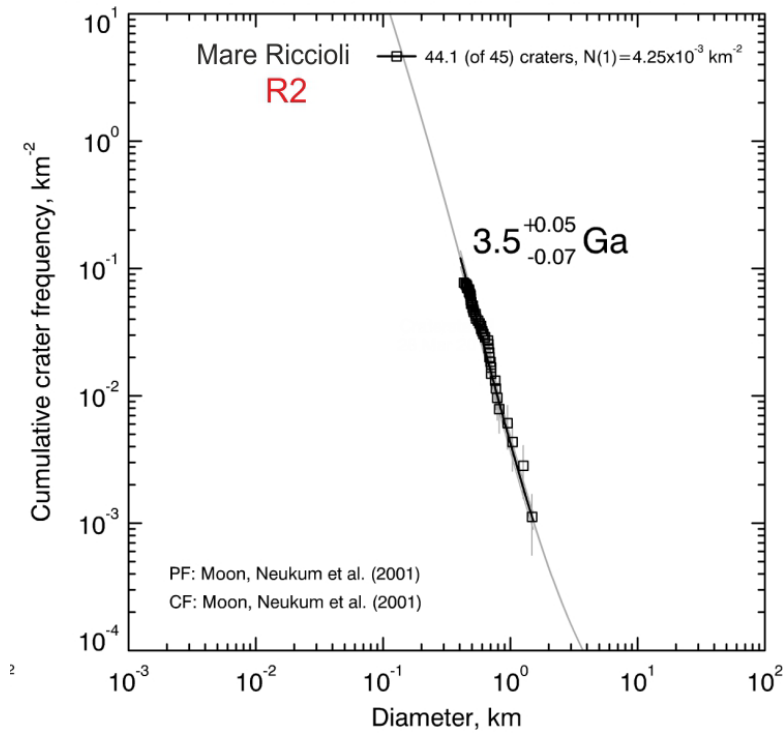


Figure 3.16: Cumulative frequency plot of the R2 unit along with age isochron and error for each data point.

The R1 unit in the Mare Riccioli revealed an older age of $3.2 \text{ Ga} \pm 0.2/0.6$ and a younger age of $1.5 \text{ Ga} \pm 0.07$ (Figs. 3.15). These older and younger model ages suggest at least two volcanic events in the R1 unit. As discussed earlier, few patches of intermediate-Ti, high-Fe basalts are seen within the R1 unit. The younger age of $1.5 \text{ Ga} \pm 0.07$ might be indicative of this late-stage intermediate-Ti magmatic event. It is speculated that the 3.2 Ga volcanic event that occurred in the R1 unit is followed by a younger 1.5 Ga event, identified as small patches of intermediate-Ti basalts within the unit. The R2 unit revealed an age of $3.5 \text{ Ga} \pm 0.05/0.07$ (Fig. 3.16). This older event of 3.5 Ga in the R2 unit coincides with the age of low to intermediate-Ti basalts (G3) in the Mare Grimaldi. The age of the R1 unit in Mare Riccioli and the G3 unit in Mare Grimaldi is consistent with the previous dates reported in Hiesinger et al. (2010). In addition, new results show rather younger events of 1.5 Ga in the Mare Riccioli and $\sim 2.05 \text{ Ga}$ in the intermediate to the high -Ti basaltic units of Mare Grimaldi. These relatively younger volcanic events in the Grimaldi basin have important implications for the thermal and volcanic history of the basin.

3.4 Discussions

In the Mare Grimaldi, the low to intermediate-Ti basalts are widespread, while the high-Ti olivine-bearing basalts are confined to the south-western part (Thesniya et al., 2020b; Figs. 3.5A and B and 3.7A and C). The intermediate-Ti basalts in the Mare Riccioli also appear to have limited spatial extends which have been observed as small patches within the R1 unit (Figs. 3.5C and D). The spectrally visible high-Ti basaltic units are considered to be relatively younger materials based on their intrusive relationship with the surrounding low to intermediate-Ti basalts (Fig. 3.5). The model ages revealed that at least two major volcanic events spanning ~ 3.5 to $\sim 1.5 \text{ Ga}$ (Late Imbrian–Eratosthenian) have occurred in the Grimaldi basin (Fig. 3.13).

The ages further emphasize that an older Late Imbrian volcanic event of $\sim 3.47 \text{ Ga}$ formed the low- to intermediate-Ti basalts in the Mare Grimaldi, followed by the eruption of high-Ti magma at $\sim 2.05 \text{ Ga}$ ago (Eratosthenian period; Fig. 3.14). The Late Imbrian low- to intermediate-Ti basalts in the G3 unit might have filled the entire low-lying region of the Mare Grimaldi while the Eratosthenian high-Ti basalts localized to the extents of G1 and G2 units. Also, the younger high and intermediate titanium basalts in the G1 and G2 units are seen intermixed with each other. This coalescing of high-Ti basalts in the G1 and G2 units with the intermediate-Ti basalts might be the result of impact-induced lateral mixing of high-Ti and

underlying Late Imbrian low-Ti basalts (Giguere et al., 2000). The older event of ~3.5 Ga (Late Imbrian) in the Mare Riccioli is nearly coinciding with the formation age of the Late Imbrian (~3.47) low- to intermediate-Ti basalt in the Mare Grimaldi (Figs. 3.14 and 3.16). This low-Ti magma erupted at ~3.5 Ga has filled the entire Riccioli unit, whereas the low to intermediate-Ti basalts formed at ~3.2 Ga ago are spatially limited to the extent of the R1 unit (Figs. 3.13, 3.15, and 3.16). The youngest volcanic event that occurred in the Mare Riccioli is at ~1.5 Ga ago (Eratosthenian period), which erupted intermediate-Ti basalts within the R1 unit. It is plausible that these Eratosthenian intermediate-Ti basalts formed in the Mare Riccioli (R1 unit) were the result of impact mixing of younger high-Ti basalts with the underlying Late Imbrian low-Ti basalts in the Mare Riccioli (Giguere et al., 2000). Furthermore, a correlation between ages and titanium contents of basalts has been observed (Table 3.1). The late-stage Eratosthenian basaltic units show intermediate to high titanium contents, whereas the low to intermediate basalts erupted during the Late Imbrian epoch. This progressive enrichment of TiO₂ and FeO contents in the Mare Grimaldi and Mare Riccioli with time is consistent with the similar observations from other regions on the Moon, particularly mare basalts in Procellarum KREEP Terrane (PKT) and Mare Imbrium (e.g., Giguere et al., 2000; Bugiolacchi and Guest, 2008).

The crystallization history of the pyroxenes from distinct basaltic units in the Mare Grimaldi and Mare Riccioli also revealed signs of multiple volcanic events in the Grimaldi basin. This observation is consistent with the emplacement of distinct basaltic units that erupted at different periods in the basin (~3.5–1.5 Ga). Based on the results from Hiesinger et al. (2010), it was believed that the volcanic activity occurred at ~3.47 and 3.27 Ga ago and ceased soon after the eruption of Mare Riccioli. However, the results from the present study indicate that volcanism was active in the Grimaldi basin until 1.5 Ga ago.

The variations in the Ti-contents of mare basalts erupted over a long time span and its proportional correlation with time suggests lateral chemical heterogeneity of the lunar mantle (e.g., Morota et al., 2011). It is suggested that the high-Ti basalts in the Mare Grimaldi crystallized from a Fe-enriched highly fractionated late-stage magma at a fast cooling rate while the low-Ti basalts crystallized from a rather Mg- and Ca-rich initial magma that underwent an ultra-late stage rapid cooling under disequilibrium conditions. The possible source regions and emplacement mechanism of the basaltic magma that erupted in the Grimaldi basin during the Late- Imbrian and Eratosthenian period are discussed in the following section.

3.4.1 Possible origin and emplacement history of the Mare Grimaldi and the Mare Riccioli

A schematic model for the evolutionary history of the Grimaldi basin based on evidence from the present study and incorporating the current understanding of the thermal evolution of the lunar interior is proposed. The stages in the evolution of the Grimaldi basin involving the eruption of mare basaltic units are marked by three major events (Fig. 3.17).

3.4.1.1 Basin-forming impact event (>3.9 Ga, Pre-Nectarian)

The basin-forming impact event induces pressure release melting and produces secondary convection following the selenotherm uplift, which causes the melting of the lunar crust and upper mantle to a depth greater than the depth of the transient crater (Fig. 3.17A; Elkins-Tanton et al., 2004). Grimaldi basin-forming impact event would also have generated impact heat and might have triggered the melting of the lunar crust and upper mantle to a considerably greater depth below the impact point. The basaltic magma produced by this pressure release melting might have caused the eruption of older basalts through the fractures in the Grimaldi basin. However, the eruption of the older low-Ti basaltic units presently identifiable in the Mare Grimaldi and Mare Riccioli must not be related to the magma generated by pressure release melting because the basin forming impact event occurred at >3.9 Ga ago, and the oldest visible basalts in the Grimaldi basin are ~3.5 Ga old. An age gap of approximately 700 Ma can be observed between the time of formation of the Grimaldi basin and the low-Ti basalts in the Mare Grimaldi and Mare Riccioli. The impact-generated magma would persist for ~350 Ma following the impact-induced pressure release melting and associated secondary convection (Elkins-Tanton et al., 2004). If the older low-Ti basaltic units in the Mare Grimaldi and Mare Riccioli are formed as a result of the eruption of an impact-generated magma, the magma would not have persisted for such a long period (Whitten et al., 2011). Therefore, it can be inferred that the surface mare basaltic units present in the Mare Grimaldi and Mare Riccioli are not related to the impact-induced decompression melting and subsequent magma generation.

Given the above inferences, different models already proposed by previous workers for the source regions and evolution of the mare basalts on the Moon have been assessed here to understand the origin and emplacement history of the mare basaltic units in the Mare Grimaldi and Mare Riccioli. The magma ocean cumulate model suggests the remelting of Magma-

Ocean cumulates, caused by the influx of a hot, deep (~1000 km) magma that formed during its thermal evolution post-LMO, for the generation of mare basaltic magmas in the lunar upper mantle (Taylor and Jakes, 1974; Solomon and Longhi, 1977). In another model by Wieczorek and Phillips (2000), the presence of higher KREEP levels causes the initiation of partial melting in the lunar mantle directly beneath the KREEP basalt layer in the PKT and leads to the generation of mare basalts in the region. However, this model can be ruled out as the Mare Grimaldi, and Mare Riccioli lies outside the boundary of the PKT, and they do not show any signatures of enhanced heat-producing elements. Furthermore, the differences in crustal thickness would lead to the asymmetric spatial distribution of mare basalts on the nearside of the Moon (Solomon, 1975; Head, 1976; Head and Wilson, 1992). Grimaldi basin is located on the boundary of the thicker farside and thinner nearside. Furthermore, crustal thickness estimates are ~8 km in the region of Mare Grimaldi and ~32 km in Mare Riccioli (Wieczorek et al., 2013, model 1; Fig. 3.18). The observed differences in the crustal thickness between Mare Grimaldi and Mare Riccioli could have led to the non-uniform eruptions of basaltic magma at different periods in the basin. Another model explains that the instabilities in the lunar mantle, followed by large-scale mantle overturn, affect the emplacement and evolution of mare basalts (Hess and Parmentier, 1995). This model is independent of basin formation impact events. The mode of emplacement of Grimaldi basalts would rather support this model.

3.4.1.2 Emplacement of the older low- to intermediate-Ti basalts during the first phase of volcanism in Late Imbrian Epoch (3.5–3.2 Ga)

The petrological models suggest that late-stage ilmenite–clinopyroxene-rich layer (ilm-cpx) formed between the underlying olivine–orthopyroxene cumulate layer (ol-opx) and the primary floatation crust during the final stages of solidification of the Lunar Magma Ocean (e.g., Snyder et al., 1992; Shearer et al., 2006; Elardo et al., 2011). The ilm-cpx-rich layer included a higher abundance of incompatible elements (radiogenic elements) owing to their formation in the later stages of the magma ocean crystallization and has a relatively higher density than the underlying ol-opx cumulate layer.

This gravitational instability in the early formed lunar mantle triggered a solid-state mantle overturn, causing the ilm-cpx cumulate layer to diapirically sink to the bottom, and correspondingly, the ol-opx-rich layer rose to the top of the mantle (Kesson and Ringwood, 1976; Hess and Parmentier, 1995; Shearer et al., 2006; Fig. 3.17B). The mantle overturn occurred at around 4372 ± 35 Ma (Sm-Nd isochron age) during or soon after the solidification

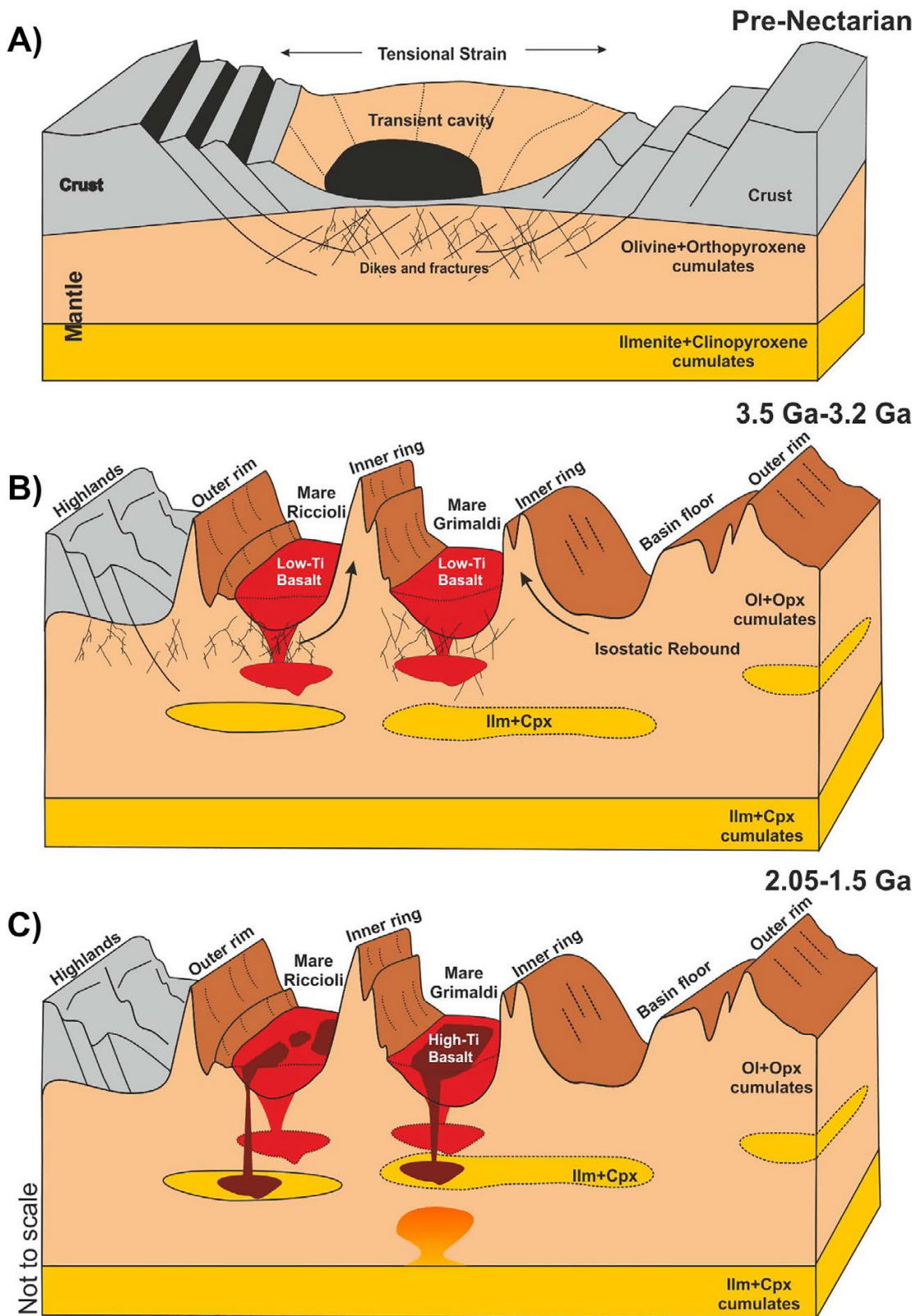


Figure 3.17: Schematic representation showing the stages involving emplacement of mare basaltic units in the Grimaldi basin. (A) The early stage of the Grimaldi basin consisting of a

transient crater cavity in the pre-Nectarian period. The impact-generated heat would have caused the rising of isotherms and triggered melting up to several kilometers depth, often exceeding the depth of the transient crater cavity. (B) The upliftment of deep-seated lithologies onto the surface by isostatic rebound followed by the impact event. The eruption of the low to intermediate-Ti basalts from the early cumulates in the upper mantle during ~3.5 to 3.2 Ga period (Late Imbrian), which filled the low-lying interior of the basin and forms the lower Mare Grimaldi and Mare Riccioli units. (C) Younger events of intermediate to high-Ti magmas erupted at ~2.05 Ga and ~1.5 Ga ago (Eratosthenian) in the Mare Grimaldi and Mare Riccioli, respectively. The high-Ti magma erupted in the Mare Grimaldi, possibly sourced from a hot plume, risen from ilmenite–clinopyroxene cumulate layer near the core-mantle boundary. In contrast, the youngest intermediate-Ti Riccioli basalt formed from the magma generated through partial melting of pods of early ilm-cpx cumulates that remained in the upper mantle after mantle overturn.

of the lunar magma ocean (Sio et al., 2020). As a result of the overturn, the descended ilm-cpx-bearing cumulates formed a layer near the core-mantle boundary (e.g., Hess and Parmentier, 1995; De Vries et al., 2010). It was suggested that small portions of the early ilm-cpx layer remained in the upper mantle in “pods” (~5–20 km dimensions) while several workers argued for dynamic mixing of the descending ilm-cpx cumulates with the rising low-Ti ol-opx cumulates (e.g., Hess and Parmentier, 1995; Giguere et al., 2000; Elkins-Tanton et al., 2004; De Vries et al., 2010). Petrological models also suggest lateral compositional heterogeneity in the lunar upper mantle compositions (up to 500 km depth) as reflected by the variations in titanium contents of mare basalts (Longhi, 1992). This hybrid source region where primordial LMO cumulates mixed during the mantle overturn was suggested to be the source regions of the basaltic magmas (e.g., Shearer et al., 2006; Kato et al., 2017).

Head and Wilson (1992) suggested that zones of partial melt that remained in the lunar mantle after initial global melting or generated by radioactive heating have driven the early mare volcanism spanning the Early Nectarian to Late Imbrian epoch. The buoyancy, crustal thickness, and impact basin topography are the factors that influence the ascent and eruption of these mare basaltic magmas (Head and Wilson, 1992). Due to this mantle heating, magma could be produced at depths up to 400 km (Taylor, 1982), and the buoyancy drives it to rise diapirically through the ductile regions of the lunar mantle. The buoyantly rising magma would be trapped at the base of the crust due to the relatively lower density of the lunar crustal materials. Due to the buoyancy trap, the magma diapirs stall at depths below the crust, and subsequent accumulation of excess pressures in the diapirs leads to the propagation of dikes to the surface and eruption of the magma (Head and Wilson, 1992).

The emplacement of low- to intermediate-Ti basalts has occurred in the Mare Grimaldi and Mare Riccioli in the Late Imbrian Epoch. The low- to intermediate-Ti magma erupted at 3.47 Ga ago in the Mare Grimaldi might have been derived from the dynamically mixed hybrid source region in the mantle through partial melting of early cumulate materials at depths between 200 and 400 km, which subsequently rose diapirically to the surface through dikes (Kesson, 1975; Fig. 3.17B).

The emplacement of Mare Riccioli basalts must not be related to the Riccioli crater forming impact event as the crater is older than the Orientale basin (3.8 Ga). Rather, the low to intermediate titanium magma that erupted at ~3.5 and 3.2 Ga ago in the Mare Riccioli might also have been derived by a similar process where melting of early cumulate materials in the upper mantle caused the generation of magmas. The magma diapirs would have been stalled at the base of the crust, and the excess pressure build-up caused the fracturing of the overlying crust and dike propagation to the surface through which the magma extruded (Fig. 3.17B). The low-lying topography and fractures resulting from basin-forming impact event might have favored the ascent and eruption of magma through hydrostatic effects (Head and Wilson, 1992).

3.4.1.3 Emplacement of the younger high-Ti basalts during the second phase of volcanism in the Eratosthenian period (~2.05 to 1.5 Ga)

The high-Ti basalts ($\text{TiO}_2 > 9 \text{ wt}\%$) having relatively higher ilmenite (FeTiO_3) content are believed to be sourced from the ilm-cpx cumulates in the lunar mantle. This ilm-cpx cumulate source region could either be the ilm-cpx layer that sank to the bottom post overturn or the material concurrently mixed with early ol-opx cumulates in the upper mantle. Each of these scenarios has been explored further. First, radiogenic elements that sank along with the ilm-cpx cumulates to the bottom of the mantle generated radiogenic heat near the core-mantle boundary, which caused the deep ilm-cpx-rich material to rise as a hot plume (Hess and Parmentier, 1995; Zhang et al., 2013). Since the melting temperatures of plume materials (ilm-cpx cumulate materials) are lower than the surrounding ol-opx cumulates (Delano, 1990), the ascended hot plume would undergo decompression melting and generate high-Ti magma. Another scenario is that the early ilm-cpx-rich cumulates that remained in the partially molten zone of the upper mantle post overturn melted to form high titanium magmas (Kato et al., 2017). The hot plume rising from the deeper ilm-cpx cumulate layer and directly generating high-Ti magmas could be the most plausible scenario. The high-Ti magmas that erupted in the

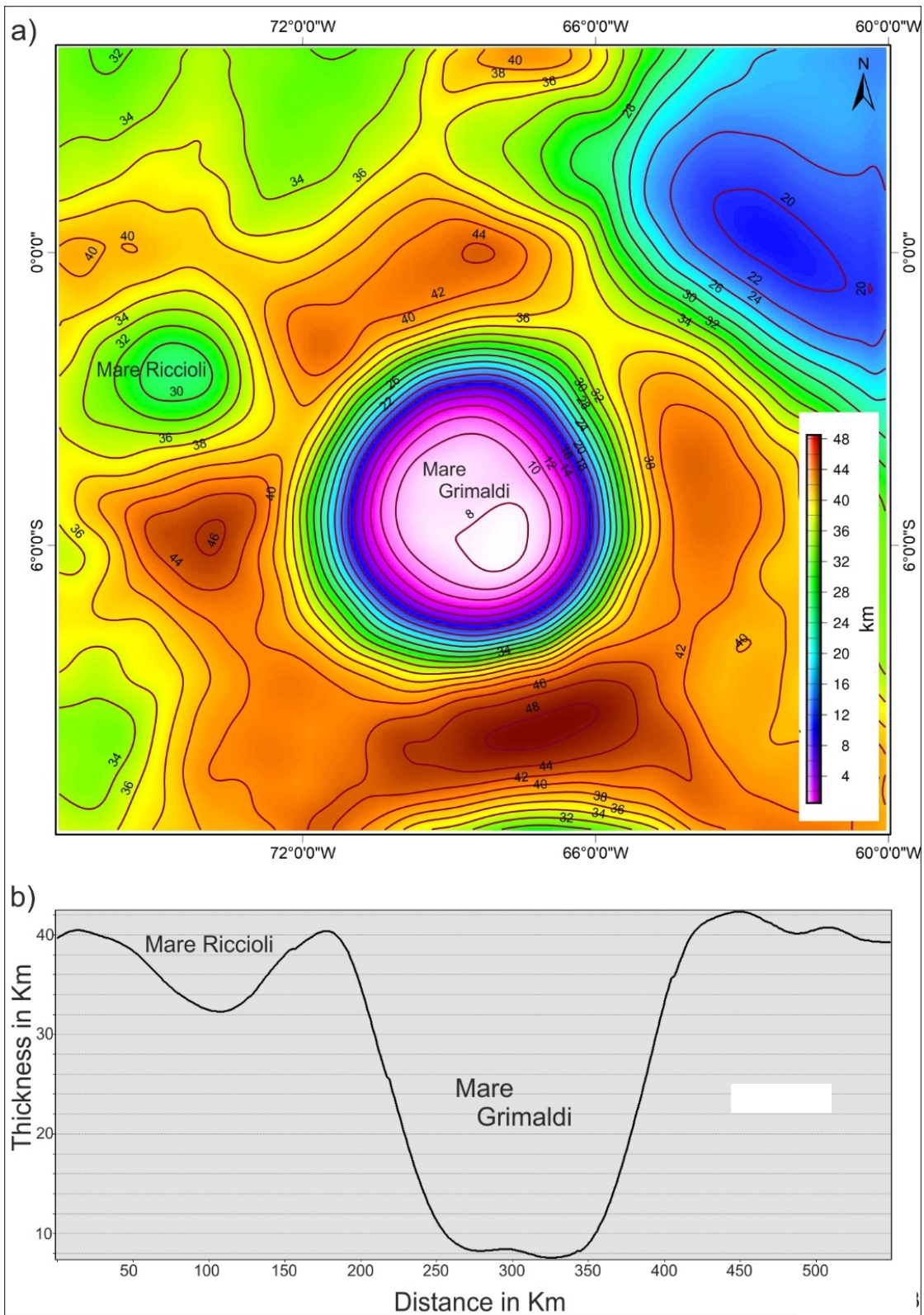


Figure 3.18: (A) LRO DIVINER-derived crustal thickness map of the Grimaldi basin. (B) Crustal thickness profile across the basin (NW-SE).

Mare Grimaldi at 2.05 Ga ago could have been generated by such a hot plume rising from the deeper ilm-cpx layer near the core-mantle boundary (Fig. 3.17C).

The factors such as the abundance of heat-producing elements in the deeper ilm-cpx cumulate layer and the density differences from the overlying mantle control the timing of the rising plume (Hess and Parmentier, 1995). The estimated timing of such a rising plume is ~2 Ga after the overturn of the mantle (Hess and Parmentier, 1995), which is consistent with the timing of the younger ~2.05 Ga volcanic event in the Mare Grimaldi. Furthermore, the rising melts have a relatively higher density (~3000 kg m⁻³) than that of the anorthositic crust (~2750 kg m⁻³), which prevents the magma from making its way to the surface (Wieczorek et al., 2001). The rising magma was not buoyant enough to rise through the lunar crust due to these density differences. In the case of Mare Grimaldi, exposures of pure anorthosites were detected in the peak ring craters of the basin. Although a basin-forming impact event has excavated the primary anorthositic crust to considerably greater depths, the crustal thickness remains at ~8 km in the Mare Grimaldi and ~32 km in the Mare Riccioli (Fig. 3.18). It requires melting at higher temperatures (1800–2000 K) for the high-Ti magmas to escape this density contrast (Wieczorek et al., 2001). The heating induced by ascending hot plume from the core-mantle boundary might have resulted in higher temperatures for the magma, which would allow it to rise through the less dense anorthositic crust (Wilson and Head, 1981; Wieczorek et al., 2001). The intermediate-Ti magma of the younger event of ~1.5 Ga occurred in the Mare Riccioli might have been originated from the hybrid source region in the upper mantle where segregated pods of ilm-cpx cumulates that remained in the upper mantle post-overturn remelted by heating from hot plume to form the intermediate-Ti magma (Fig. 3.17C).

3.5 Conclusions

The present study has investigated the spectral and chemical characteristics and ages of the mare basaltic units, Mare Grimaldi and Mare Riccioli, in the Grimaldi basin on the near side of the Moon.

- Apart from the discoveries that match with the previous identification of mare basalts of older ages in the Grimaldi basin, the present study has identified distinct and younger basaltic units of higher FeO and TiO₂ contents in the Mare Grimaldi and Mare Riccioli. The high-Ti basalts in both the mare units are stratigraphically overlain on the low to intermediate-Ti basalts.

- The higher olivine abundance associated with the high-Ti basalts in the Mare Grimaldi indicates the presence of olivine basalts in the region.
- The dating of these distinct basaltic units has revealed that the Grimaldi basin has experienced at least two phases of volcanic events spanning the Late Imbrian–Eratosthenian period. The first phase of low- to intermediate-Ti basaltic volcanism occurred at ~3.5 Ga ago in both the units, followed by the eruption of low- to intermediate-Ti basalts in the Mare Riccioli at ~3.2 Ga ago. The younger event of intermediate- to high-Ti basaltic volcanism occurred at ~2.05 Ga and ~1.5 Ga ago in the Mare Grimaldi and Mare Riccioli, respectively.
- The crystallization history of the pyroxenes from distinct basaltic units also supports the idea that multiple volcanic eruptions have occurred in the Grimaldi basin. The high-Ti basalts in the Mare Grimaldi crystallized from an Fe-enriched highly fractionated late-stage magma at a fast cooling rate, while the low-Ti basalts crystallized from a rather Mg and Ca-rich initial magma that underwent an ultra-late stage quenching.
- The origin and emplacement of these basaltic units in the Grimaldi basin are predicted to be independent of the basin-forming impact event because of the huge time gap (~700 Ma) existing between the eruptions of Grimaldi basaltic units (~3.5 to 1.5 Ga) and basin-forming impact event (>3.9 Ga). It has been inferred that the origin and emplacement of these basalts are related to the global thermal evolution of the Moon, rather than relying on the basin-forming impact event.
- The Late-Imbrian low to intermediate-Ti basalts in both the Mare Grimaldi and Mare Riccioli is derived from the melting of early cumulate materials caused by radioactive heating or from molten zones that remained in the mantle after initial global melting in the hybrid source region of the post-overtturn upper mantle, and eruption through dikes that propagated to the surface. The Eratosthenian high-Ti magma that erupted in the Mare Grimaldi would have been formed through partial melting caused by a hot plume rising from the deeper clinopyroxene-ilmenite-rich cumulates near the core-mantle boundary.
- The Mare Riccioli intermediate-Ti basalts (~1.5 Ga event) formed through a different process where the ilm-cpx cumulates that remained in the upper mantle after the mantle overturn remelted to generate intermediate-Ti magmas.
- The new results from the present study suggest that volcanism had not ceased in the Grimaldi basin at 3.2 Ga, rather it was active until 1.5 Ga for approximately ~2 billion years spanning Late Imbrian to Eratosthenian period.

This chapter is the reproduction of an article published in the journal Meteoritics & Planetary Science.

P. M., Thesniya, Rajesh V. J., and Flahaut J., 2020. Ages and chemistry of mare basaltic units in the Grimaldi basin on the nearside of the Moon: Implications for the volcanic history of the basin. Meteoritics & Planetary Science 55, Nr 11, 2375–2403. 13579. <http://dx.doi.org/10.1111/maps.13579>.

Chapter 4

Pyroxene chemistry and crystallization history of basaltic units in the Mare Humorum on the nearside of the Moon: Implications for the volcanic history and heterogeneity of the lunar mantle

Overview

Mare basalts are volcanic features on the lunar surface and are vital for understanding the Moon's volcanic and thermal history. The present study investigates the mineralogy and chemical variations of the mare basaltic units in the Mare Humorum on the Moon's nearside using orbital remote sensing data from recent lunar exploration missions. The previous model ages available for the Humorum basaltic units have been utilized in the present study to understand the chemical evolution of these basaltic units with time. Basalts of Imbrian-Eratosthenian periods occur in the Mare Humorum. Hyperspectral data from Moon Mineralogy Mapper onboard Chandrayaan-1 mission showed pigeonites and augites as the major compositions in these basaltic units. The compositional trend between pigeonites and augites point towards the differentiation of the basaltic magma while cooling. The older units crystallized from a Fe-enriched fractionated magma while the younger unit formed from an Mg and Ca-rich magma. The distinct chemical trends in the pyroxene quadrilateral revealed

that multiple volcanic eruptions have occurred in the Mare Humorum. The longward and shortward shifts in the Band I and Band II centres in the younger and older basalts, respectively, also indicate that the older basaltic units crystallized more Fe²⁺-rich, Ca-depleted pyroxenes while the younger basaltic unit was formed from a rather Ca-rich magma. Hence, the basaltic magmas that erupted in the Mare Humorum during Imbrian and Eratosthenian periods were derived from heterogeneous source regions.

4.1 Introduction

The investigations on the compositions and ages of volcanic products on the lunar surface provide insights into the Moon's thermal and geologic evolution (e.g., Head and Wilson, 1992). Basalts are the common volcanic rocks of the Earth and the Moon, produced by the partial melting of the mantle rocks. Basaltic lava flows (known as Mare basalts) on the Moon account for about 17% of the lunar surface and occupy about 1% of the total volume of the lunar crust (Head, 1976). The nearside of the Moon occupies most of these mare basalts with few eruptions on the farside (e.g., Head and Wilson, 1992; Haruyama et al., 2009; Hiesinger et al., 2011). The study of these basalts provides insights into the chemical makeup of their source regions. Earth-based telescopic observations at low resolutions (Pieters and McCord, 1976; Pieters, 1978), returned soil and rock sample analyses, meteorites, and space-borne high-resolution reflectance measurements of the lunar surface in the Visible/Near-Infrared (VNIR) region have greatly expanded our knowledge on the distribution, diversity, mineralogy and emplacement history of the mare basalts on the Moon (e.g., Tompkins and Pieters, 1999; Bussey and Spudis, 2000; Staid and Pieters, 2000; Pieters et al., 2001; Staid et al., 2011). Scientists consider that mare basaltic volcanism on the Moon likely began before 3.9 Ga and peaked between 3.8 Ga and 3.2 Ga (Head, 1976; Ryder and Spudis, 1980; Nyquist and Shih, 1992; Head and Wilson, 1992). Recent studies reveal that episodic eruptions of mare basalts have continued on the Moon till 1.2 billion years (Neukum et al., 1975; Neukum and Horn, 1976; Boyce and Johnson, 1978; Wilhelms et al., 1987; Neukum and Ivanov, 1994; Hiesinger et al., 2000; Wiczorek and Phillips, 2000; Hiesinger et al., 2003, 2010; Haruyama et al., 2009; Morota et al., 2011; Thesniya et al., 2020a,b, and c). The recent datasets, particularly Chandrayaan-1 data, have provided high-resolution spatial images and spectral data with a good spectral resolution, which can be utilized for compositional mapping of the Moon, particularly mare basaltic units exposed on the lunar surface. The present study focuses on the compositional characterization of mare basaltic units in the Humorum basin on the nearside of the Moon, primarily using Chandrayaan-1 data (Fig. 4.1).

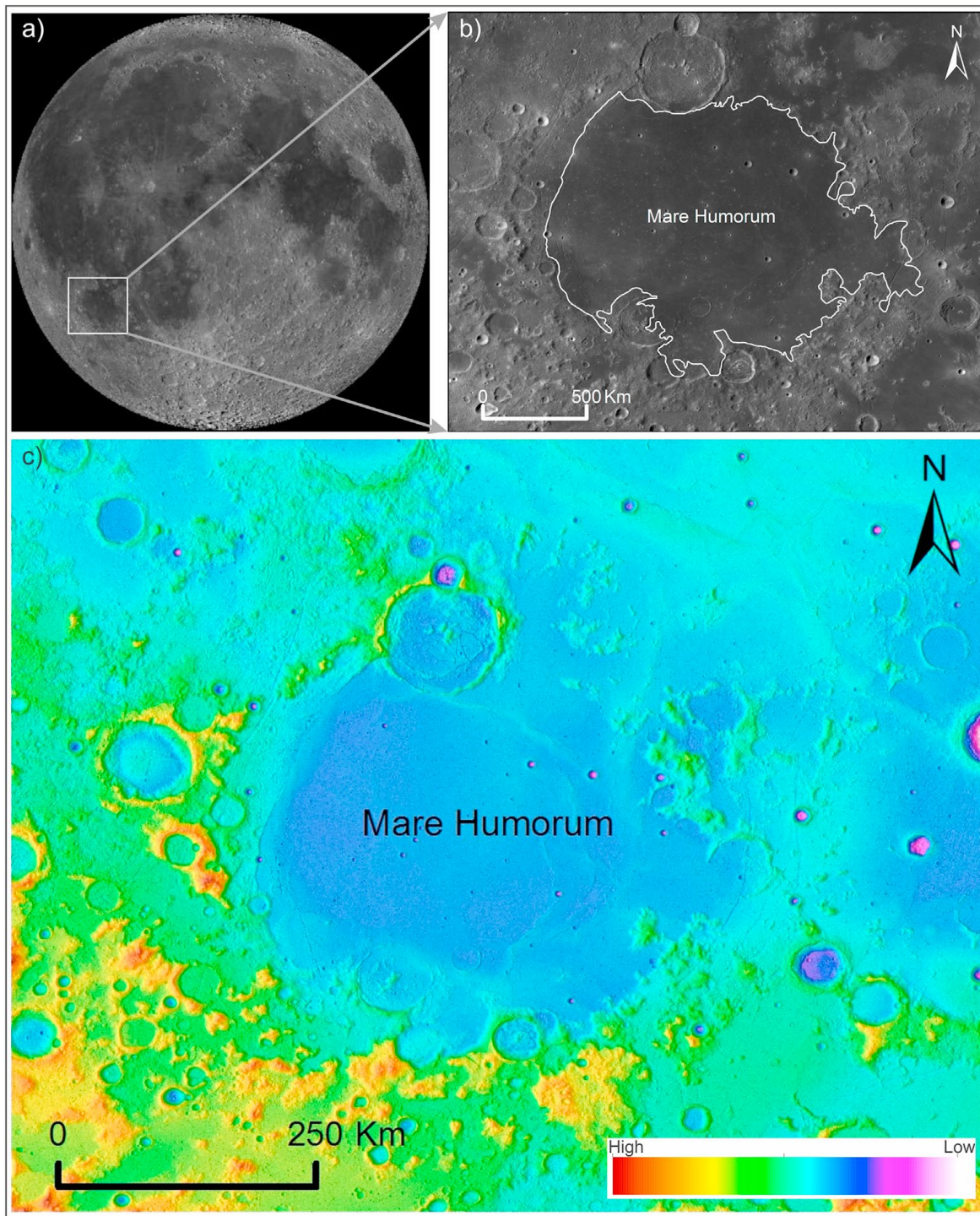


Figure 4.1: (A) LROC-WAC mosaic (Speyerer et al., 2011) of the western limb of the Moon in stereographic projection. The white rectangle on the image outlines the Humorum basin. (B) WAC grey-scale mosaic image of the Humorum basin. The boundary of the Mare Humorum has been outlined in white. (C) Color-coded LRO-LOLA & Kaguya Terrain Camera Merge DEM (Barker et al., 2016) of the Humorum basin showing the topography of the basin. The mare basalts, namely Mare Humorum, have been labeled in the figure.

The Humorum basin is a multi-ring impact basin located on the Moon's western nearside (24.4°S and 38.6°W). Many detailed studies on mineralogy and topography of the Humorum basin have been carried out by previous researchers; however, the pyroxene chemistry of the mare basaltic units in the Mare Humorum has not been explored further. The present study intends to determine the chemical variations among distinct basaltic units in the Mare Humorum based on their pyroxene chemistry and FeO and TiO₂ variations. Pyroxene and plagioclase are the primary minerals present in mare basalts. Of these, pyroxene group minerals are abundant in basalts. Pyroxene exhibits solid solutions, and their diverse compositions form in different stages of the crystallization of basaltic magmas. Therefore, the chemistry of co-existing pyroxenes in basalts reveals the cooling history and evolution of the magma (e.g., Bence and Papike, 1972; Lindsley and Anderson, 1983; Klima et al., 2008). The mineralogical mapping of the mare basaltic units can be performed using orbital reflectance spectroscopic data. The chemical composition of identified pyroxenes could be estimated based on their spectral band parameter analysis. The estimated pyroxene compositions have been used to infer the crystallization history of the parent basaltic magma. The individual basaltic units previously defined in Hackwill et al. (2006) based on FeO and TiO₂ contents and CSFD (Crater Size-Frequency Distribution) ages have been utilized in the present study to delineate the distinct basaltic units in the Mare Humorum (Blewett et al., 1997; Lucey et al., 2000; Hiesinger et al., 2000; Hackwill et al., 2006). The relationship between the pyroxene chemistry and the ages of the mare basaltic units have also been explored, which further provides us information about the chemical evolution of individual basaltic units of distinct ages within the Mare Humorum over time and the cooling history of the magma.

4.1.1 Study area

The Humorum basin is a multi-ringed impact basin located at the southern end of the Oceanus Procellarum on the southwestern nearside of the Moon (Spudis et al., 1992). Humorum basin is of Nectarian-Early Imbrian age (Neukum, 1983; Wilhelms et al., 1987). The Nubium basin surrounds the Humorum basin to the east, the southern end of the Oceanus Procellarum to the north, and the rugged highlands to the south and west (Byrne, 2005). The Humorum basin is younger than the Nubium basin but predates the age of the Orientale basin (Byrne, 2005). Mare Humorum is a near-circular mare that fills the interior of the Humorum basin. The lava that filled the Humorum basin, in some places, expanded to regions outside the basin rim (Fig. 4.1). Several such lava flows extend to the northwest of the southern Oceanus Procellarum. The inner ring (the Doppelmeyer ring) is a concentric ridge of mare deposits in the central portion

of the basin with a diameter of 210 km (Pike and Spudis, 1987) (Fig. 4.1c). The Vitello ring next to the inner ring has a 340 km diameter that borders the filled mare lavas in the basin. This ring consists of ridges, massifs, and arcuate scarps (Spudis et al., 1992). The Vitello ring is encircled by a 425 km diameter rugged ring of massifs that runs through the center of the Gassendi crater in the north. Other exterior rings include three discontinuous rings having diameters of 570 km, 800 km, and 1200 km (Pike and Spudis, 1987). Wilhelms et al. (1987) defined the basin rim as the larger 800 km diameter ring (Letronne ring) outside the Gassendi ring. However, considering the compositional and topographic information, the Gassendi ring (425 km) was interpreted as the outer rim of the Humorum basin (Pike and Spudis, 1987; Spudis et al., 1992). The geological and compositional studies of the Humorum basin were carried out by previous researchers (Spudis et al., 1992; Hawke et al., 1993; Peterson et al., 1993) using telescopic and orbital remote sensing data. The highlands surrounding the basin are feldspathic, predominantly noritic anorthosite with minor amounts of anorthositic norite (Spudis et al., 1992). The inner rings of the basin showed signatures of pure anorthosites (e.g., Peterson et al., 1993).

4.2 Datasets and Methods

4.2.1 Datasets

Orbital remote sensing data from various lunar missions available in the public domain have been utilized in the present study. Hyperspectral data from Moon Mineralogy Mapper (M³) onboard ISRO's Chandrayaan-1 mission have been used to map and identify minerals. High spatial resolution images from NASA's Lunar Reconnaissance Orbiter Camera (LROC) have been used for investigating the geological context of the regions of interest. LOLA data provide a high-resolution global topographical model of the Moon. LOLA and Kaguya Terrain Camera (TC) DEM merge was utilized to understand the study area's topography and elevation differences.

The Moon Mineralogy Mapper (M³) was a NASA-supported guest instrument in ISRO's Chandrayaan-1 mission. M³ has a spatial resolution of ~140 m/pixel from 100 km orbit in the global mode. M³ operates in the spectral range between 430 and 3000 nm at a spectral resolution of 10 nm with a high signal-to-noise ratio (Pieters et al., 2009; Green et al., 2011).

The Kaguya TC is a stereoscopic imager in the SELENE spacecraft (Haruyama et al., 2008). TC operated in the panchromatic band, ranging from 430 to 850 nm from the nominal 100 km

SELENE orbit, and has a 10 m/pixel spatial resolution. TC images were downloaded from the SELENE data archive portal (<http://darts.isas.jaxa.jp/planet/pdap/selene/dataset>).

The Lunar Reconnaissance Orbiter Camera (LROC) is a system of three cameras mounted on the Lunar Reconnaissance Orbiter (Robinson et al., 2010). LROC consists of two Narrow-Angle Cameras (NACs) designed to provide 0.5 m-scale panchromatic images over a 5 km swath, and a Wide Angle Camera (WAC) that produces images at a scale of 100 m/pixel in seven color bands over a 60 km swath.

Lunar Orbiter Laser Altimeter (LOLA) and Terrain Camera (TC) merged DEM (Digital Elevation Model) was designed to produce a high-resolution global topographic model of the Moon (Barker et al., 2016). LROC and LOLA images were downloaded from the Lunar Orbiter Data Explorer Portal (<http://ode.rsl.wustl.edu/moon/>).

4.2.2 Methods

M³ hyperspectral datasets were downloaded from the Orbital Data Explorer portal (<http://ode.rsl.wustl.edu/>). Each of the images was georeferenced and mosaicked to get complete coverage of the basin. The ENVI image processing software is used for processing the image and generating the results. The spatial subset of the M³ reflectance images was taken and mosaicked to the boundary of the basin. The mineralogy is determined from the M³ reflectance spectra. The pyroxene group minerals exhibit two major absorption bands in the 1 μm and 2 μm regions. These absorption bands between 0.9 μm -1.05 μm and 1.8 μm -2.3 μm in pyroxenes vary as a function of Fe²⁺ and Ca²⁺ content (Adams, 1974). The 1 μm band of orthopyroxenes shifts linearly to longer wavelengths with an increase in Fe²⁺ content (Adams, 1974). Also, the 1 μm and 2 μm band centres of orthopyroxenes systematically shift to longer wavelengths with an increase in Ca²⁺ content (Adams, 1974). This shift in the band centres to longer wavelengths as a function of Ca²⁺ content is due to a change in crystal field sites in which Fe²⁺ ions are located (Burns et al., 1972). In the case of orthopyroxenes, the M2 site is occupied by Fe²⁺ ions. In the diopside, Ca²⁺ occupies the M2 site and Fe²⁺ fills the M1 site (Burns, 1970; Cloutis and Gaffey, 1991). Pigeonites (low-calcium clinopyroxene) show absorption bands near 0.93 μm and 2 μm while sub-calcic augite has bands near 0.99 μm and 2.18 μm . The absorption bands of the diopside (high-Ca clinopyroxene) are near 1.04 μm and 2.3 μm (Adams, 1974; Cloutis and Gaffey, 1991). The band centres and strengths of these absorption features can be used to discriminate different lunar lithologies. The Integrated band depth (IBD) images for 1 μm and 2 μm regions have been generated to discriminate between

mafic-rich regions and anorthositic highland areas (e.g., Mustard et al., 2011; Staid et al., 2011).

A color composite image was generated using IBD images for spectral mapping. IBD1000 band was assigned to the Red channel while Green and Blue channels were assigned the IBD2000 and R1578 (M^3 Reflectance at 1578 nm) bands, respectively. The soil spectra from each unit were taken as the average of a few pixels. The clinopyroxene-rich fresh craters in the image appear as bright yellow in the color composite image. Representative spectra were extracted from the corresponding mineral-bearing regions and identified using the reflectance spectra available in the RELAB spectra library (<http://www.planetary.brown.edu/rehab/>). The distinct basaltic units in the Mare Humorum were previously defined by Hackwill et al. (2006) based on Crater Size-Frequency Distribution ages, which is the latest model age data available for this region. This model age has been utilized in the present study as a reference for analyzing the compositional variations among the basaltic units that erupted at different periods in the Mare Humorum.

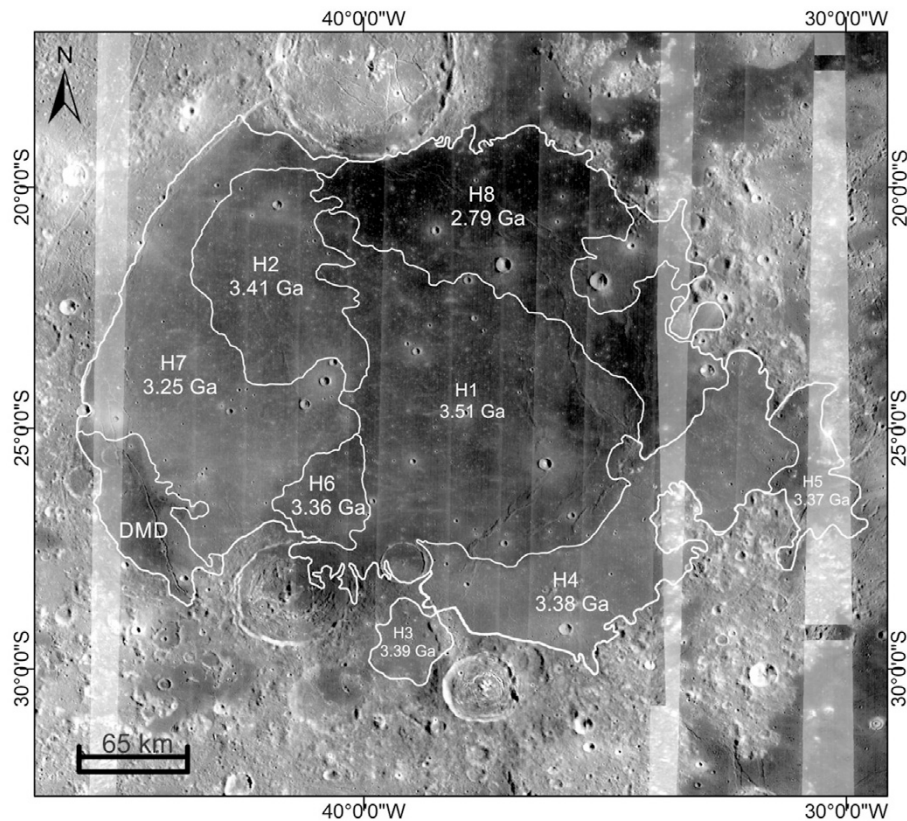


Figure 4.2: M^3 1578 nm albedo map showing the albedo variations in different basaltic units in the Mare Humorum. The boundary of the distinct basaltic units previously defined by Hackwill et al. (2006) in the Mare Humorum has been redrawn over the M^3 albedo image. The ages available for the individual basaltic units have been labeled.

The spectra were collected from the pre-defined distinct basaltic units. These units were defined based on TiO₂ and FeO wt% and absolute model ages (Hackwill et al., 2006). The collected spectra were further analyzed using OriginPro software for determining their band parameters. The continuum removal of the collected spectra has to be performed to reduce the effects of continuum slope arising from other mixed components such as plagioclase and/or olivine as well as wavelength-dependent scattering on the major absorption bands before band parameter analysis (Clark and Roush, 1984). For each band, the continuum removal is done by dividing the spectra by a straight-line continuum drawn between the local maxima on both sides of the absorption band minima. After the continuum removal, the band parameters such as Band Center (BC) and Band Depth (BD) have been determined based on the method described in Cloutis et al. (1986). The minimum reflectance of the absorption feature after the continuum removal is the Band Center. The Band Center was calculated by fitting a 3rd order polynomial to the bottom of the absorption feature, and the minimum point of the fitted polynomial is estimated as the Band Center. The error in Band Center calculations was also determined by an iterative process in which Band Center is calculated each time by changing the number of points on any side of the band minima. The average Band Center value is used for further analysis. Afterwards, the molar Ca, Fe, and Mg content in pyroxenes was calculated using a set of equations given by Gaffey et al. (2002). The method for calculating the mole% concentrations of Ca, Fe, and Mg in pyroxenes using their spectral parameters were originally derived for natural pyroxene compositions (Cloutis and Gaffey, 1991; Gaffey et al., 2002), which later adopted and successfully applied for determining the relative abundance of mole% Ca and Fe in pyroxene group minerals in mare basalts on the Moon (Kaur et al., 2013; Chauhan et al., 2018). The calculated B-I and B-II centre values of pyroxenes from each basaltic unit are plotted in a B-II versus B-I scatter plot. The calculated molar compositions of Wo, En, and Fs were then projected onto a pyroxene quadrilateral to understand the chemical variations among the pyroxenes. The crystallization history and cooling temperatures of pyroxenes were determined based on a graphical two-pyroxene thermometer developed by Lindsley and Anderson (1983).

4.3 Results

The distinct basaltic units mapped by Hackwill et al. (2006) have been used as the reference for selecting the category-wise pyroxene compositions in the present study (Fig. 4.2). The delineated basaltic units have been labeled as H1 (oldest) to H8 (youngest) in ascending order. The units H1–H7 (3.51–3.25 Ga) were formed during the Imbrian period, whereas the H8 unit

(2.79 Ga) was emplaced in the Eratosthenian period (Hiesinger et al., 2000; Hackwill et al., 2006) (Fig. 4.2). The variations in the surface albedo are a manifestation of the maturity of the surface and the mineralogy (e.g., Staid et al., 2011; Cheek et al., 2011). M^3 reflectance at 1578 nm wavelength has been used to understand the albedo variations among the distinct basaltic units, which arise from chemical differences and/or soil maturity. The bright regions within the Mare Humorum correspond to the relatively younger fresh craters that excavated the basaltic units in the regions. The blanketing by the ejecta rays from the surrounding craters has also contributed to the moderately higher albedo towards the southern portions of the Mare Humorum. The older units exhibit albedo ranging between 0.05 and 0.08. The younger units have slightly lower albedo values ranging from 0.04 to 0.07. The lowest albedo (~ 0.04 – 0.05) in the Mare Humorum has been observed in Dark Mantling Deposits (DMD). The superposed craters within the Mare Humorum exhibit distinctively higher albedo (~ 0.19) in the crater interior. The low albedo regions indicate the occurrence of relatively mature and/or mafic compositions within the Mare Humorum (Fig. 4.2).

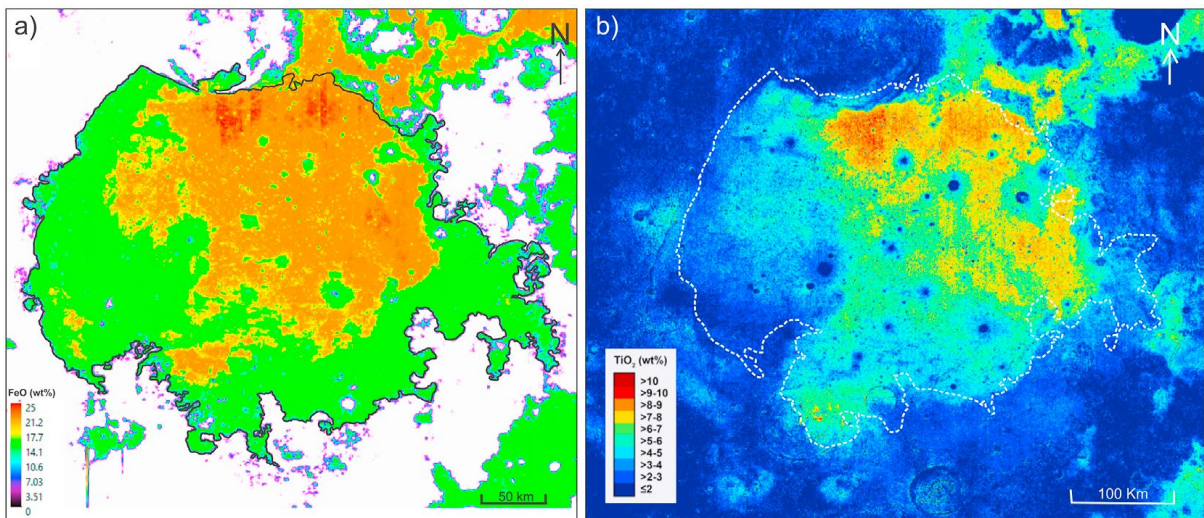


Figure 4.3: (A) Kaguya MI-derived FeO abundance map of the Mare Humorum (Lemelin et al., 2016). (B) TiO₂ abundance map derived from LROC-WAC data (Sato et al., 2017).

The individual basaltic units originally delineated by Hackwill et al. (2006) were based on the variations in the FeO and TiO₂ contents obtained from the Clementine data. As better resolution datasets are available today, the present study utilized FeO abundance maps derived from Kaguya MI data (Lemelin et al., 2016) and TiO₂ map derived from LROC WAC (Sato et al., 2017) for confirming the spatial variations of these oxides within Mare Humorum (Fig. 4.3). The FeO abundance in the Mare Humorum ranges from ~ 7 to 22 wt% (Fig. 4.3a). The TiO₂ contents in the Mare Humorum range from ~ 2 to 10 wt%, suggesting the presence of low-

high Ti basalts in the region (Fig. 4.3b). The high FeO (>22 wt%) and high TiO₂ (~10 wt%) basalts are restricted to the northern margin of the Mare Humorum (H8 unit, youngest).

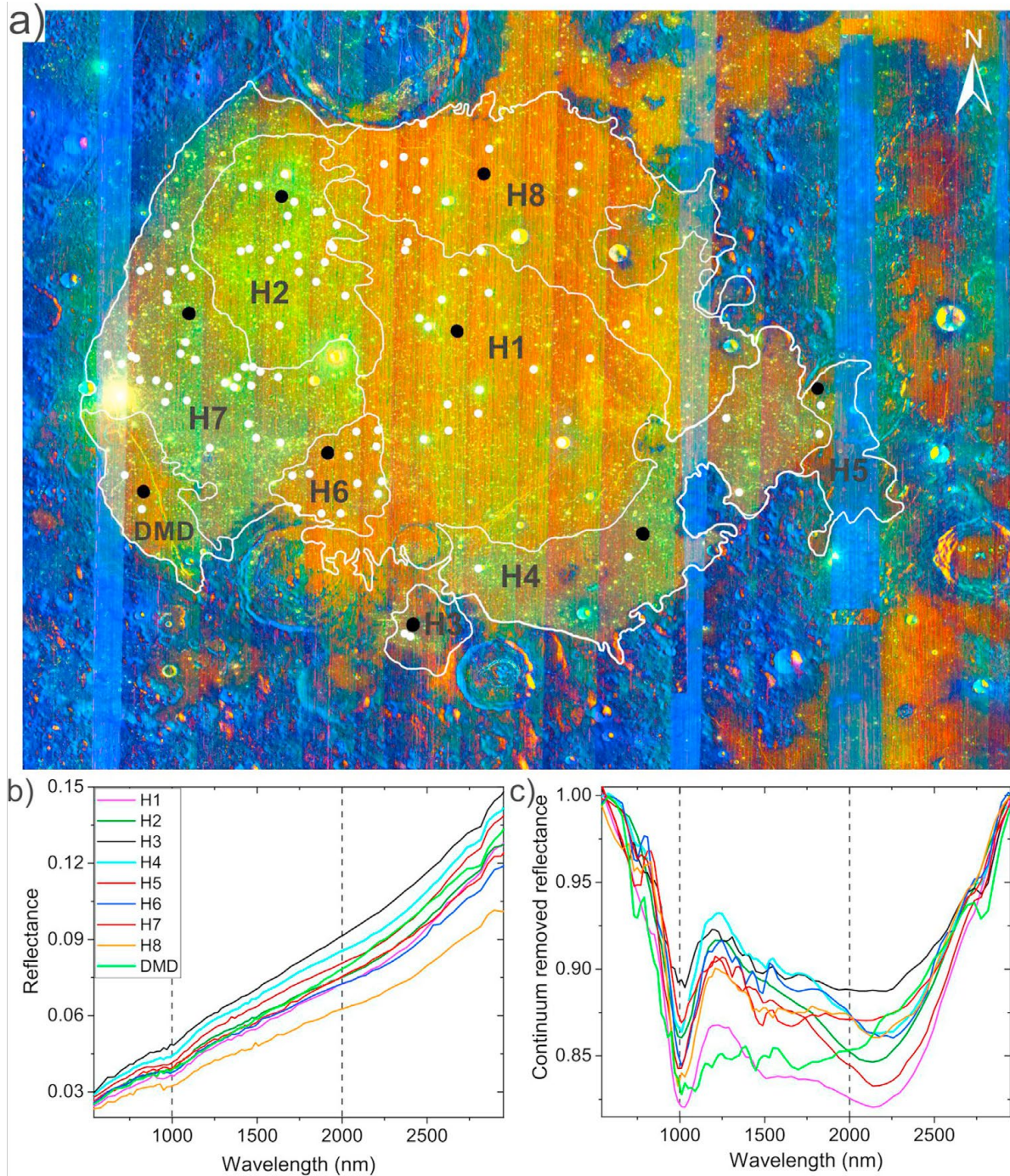


Figure 4.4: (A) M³ colour composite image of the Mare Humorum generated by assigning IBD1000, IBD2000, and R1578 to the red, green, and blue channels, respectively (Mustard et al., 2011). (B-C) Normal and continuum removed reflectance spectra from the different basaltic units within the Mare Humorum.

The remaining areas display low-intermediate FeO and TiO₂ contents. The younger unit of 2.79 Ga age exhibits the higher FeO and TiO₂ contents, which corroborate well with the presence of younger high-Ti basalts in the Mare Humorum (e.g., Staid et al., 2011).

The M³ color composite image shows the mineralogical variations in the basaltic units, which have been manifested by varying hues across Mare Humorum (Fig. 4.4a). The white boundaries in Fig. 4.4a demarcate the extent of various spectral units mapped within the Mare Humorum. The blue regions in the image represent highland terrains. The mare basalt in the Mare Humorum can be clearly distinguished from the surrounding highland terrain by its yellow-orange tone in the image. The pyroxene-bearing regions appear in shades of greenish-yellow to yellow. However, it is to be noted that not all pixels colored in shades of yellow are necessarily pyroxenes. Mixing of regolith with the crater material can add random noise to the spectrum.

Mare units exposed in the south and western side appear yellow to yellowish-green in the color composite, whereas the central and eastern units are displayed in bright orange shades, which might have been caused by increased band strengths in the 1000 nm region. The Dark Mantling Deposit regions appear in yellow shades (Fig. 4.4a).

The representative reflectance spectra from each of these units have been collected separately (Fig. 4.4a). The obtained spectra are shown in Fig. 4.4b and c. The spectra show major absorption bands in the 1000 nm and 2000 nm regions and are characterized by the narrower band I and relatively broader band II absorptions. The spectra from eastern mare units also show a notable absorption feature near the 1500 nm region, while the western mare units, H2, and H7 do not exhibit this feature (Fig. 4.4b). The spectra from pyroxene-bearing locations within the Mare Humorum were also obtained. The presence of pyroxenes in these craters has been identified by their diagnostic absorption bands in the 1 μm and 2 μm regions of the reflectance spectra. The unit spectra show symmetrical band I and band II absorptions corresponding to the electronic transition absorptions in the Fe²⁺ ions in the crystal structure of pyroxenes. The spectra are dominated by clinopyroxenes. The compositional variations of these pyroxenes have been understood using the Band II vs Band I plot (Fig. 4.5). The pyroxene compositions fall in the field of pigeonites and subcalcic-augites in the Band II vs Band I plot. The 2 μm band is centered between 2.05 and 2.22 μm while the 1 μm band centres are in 0.925–1.01 μm range. The mole % concentrations of Ca, Fs, En in these pyroxenes projected onto the pyroxene quadrilateral also reveal the occurrence of pigeonite and augites in the Mare Humorum basaltic units (Fig. 4.6).

4.4 Discussions

The M³ mineralogical map has shown that the clinopyroxenes are present on walls of the relatively younger craters that excavated the basaltic units hundreds of meters deep within the Mare Humorum (DeHon, 1977). The fresh exposures of these pyroxenes appear as bright yellow hues in the color composite image, reflecting the higher strength of Band II and thereby higher abundance of clinopyroxenes in the spectra (Fig. 4.4). The spectra collected from individual units show stronger and broader absorptions at Band I and Band II. The strength of the Band I in Mare Humorum ranges between 8.3 and 12.3%. The strength of the Band II varies from 13.2 to 28.9%. The Band II strength is observed to be higher than the Band I strengths across the Mare Humorum. Further, the spectra exhibit narrower Band I and relatively broader Band II absorptions. This broadness and increased strengths of the Band II also indicate that the clinopyroxene dominates the spectra. The shift in the Band I and Band II centres is a direct consequence of the variation in the composition of the pyroxene in that region.

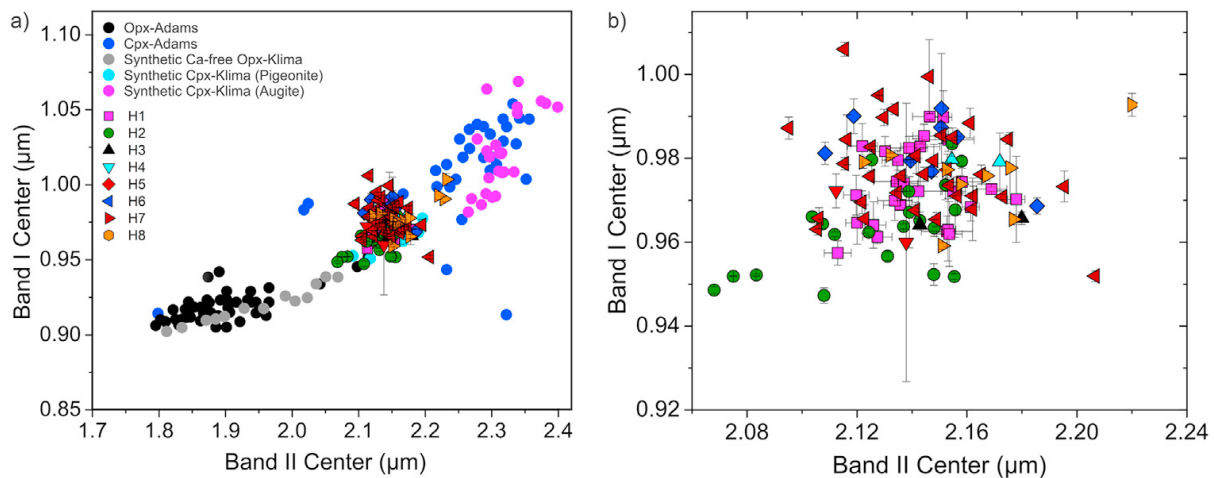


Figure 4.5: (A) Band II centre vs Band I centre plot of pyroxenes from individual basaltic units within the Mare Humorum. The analyzed data are plotted along with the reference data for orthopyroxenes and clinopyroxenes from Adams (1974), modified by Cloutis and Gaffey (1991) and Klima et al. (2011) for comparison. (B) Band II centre vs Band I centre plot focused on the data of the analyzed pyroxenes for unambiguous observation of the shift in band centres.

The Band II vs Band I plot shows compositional variations from low-calcium clinopyroxenes to high-calcium clinopyroxenes (Fig. 4.5). The natural pyroxene data from Cloutis and Gaffey (1991) and synthetic pyroxene data from Klima et al. (2011) were plotted together with the analyzed pyroxene data for comparison and interpretation of the compositional affinity. The analyzed pyroxenes show a trend similar to the reference data (Fig. 4.6). Most of the pyroxenes in the Mare Humorum that cluster between 2.05 μm and 2.2 μm indicate a shift in the band

centres to the longer wavelengths and thereby compositional change from pigeonite to augite. The Band I centres range from 0.94 μm to 1.01 μm while the Band II centres range between 2 μm and 2.3 μm , indicating the presence of pigeonites, sub-calcic augite, and augite compositions in the Mare Humorum. In the Band II vs Band I plot, though the Band II centres are shifted to longer wavelengths, the high-calcium pyroxene data do not fall precisely in the augite field. Instead, it occupies the region along the boundary of the augite and diopside (Fig. 4.6). Therefore, the mole % contents of En, Wo, and Fs of the obtained pyroxenes were determined based on their estimated band centres (see Methods section) to understand the relative proportions of enstatite, calcium pyroxene, and ferrosilite.

In the pyroxene quadrilateral plot, the average composition in the Mare Humorum is $\text{En}_{32}\text{Fs}_{40}\text{Wo}_{27}$, which indicates an augitic nature of the pyroxenes (Fig. 4.6). The chemical trend parallel to the En-Di join of the quadrilateral show subcalcic-augite and augite.

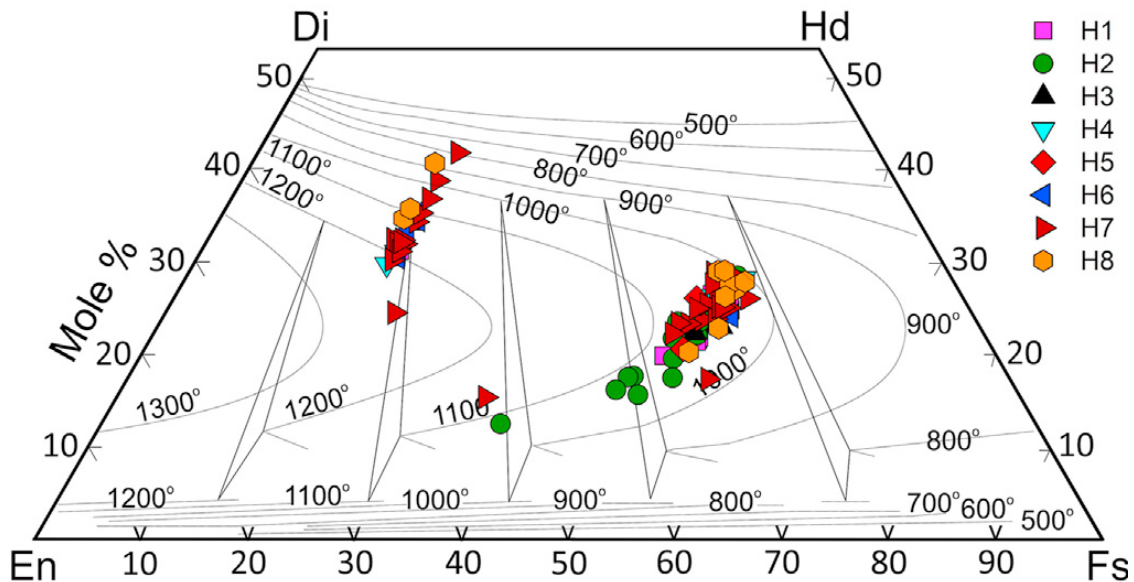


Figure 4.6: Pyroxene quadrilateral plot showing the mole % compositions of endmember pyroxenes from individual basaltic units within the Mare Humorum along with the equilibrium pyroxene temperatures based on the graphical thermometer developed by Lindsley and Anderson (1983).

The crystallization begins with Mg and Ca-rich augitic compositions and proceeds to more Ca-rich endmember as the temperature decreases. A gap in the chemical trend of these pyroxenes is marked by the onset of crystallization of plagioclase, which preferentially incorporates CaO and thereby reduces the Ca content in the residual liquid (Bence and Papike, 1972). As the crystallization proceeds, subcalcic augites followed by extremely Fe-rich pigeonites crystallized from the late-stage Ca-depleted, Fe-enriched melts. These Fe-rich compositions,

representing a quenching trend, occupy the “forbidden region” of the pyroxene quadrilateral (e.g., Lindsley and Munoz, 1969; Papike et al., 1991). The compositions trending from pigeonite to augite in this region are crystallized metastably from the late-stage magma through rapid crystallization (e.g., Smith and Lindsley, 1971). These compositions are metastable with respect to the typical pyroxene-olivine-silica assemblage resulting from the late-stage quenching (cf. Papike et al., 1976; Papike and Vaniman, 1978). It can be inferred that the younger units began to crystallize with an initial Mg and Ca-rich magma at a cooling rate between 800 °C and 1200 °C. The late-stage Ca-depleted Fe-enriched, more fractionated magma cooled rather quickly (1100 °C–1000 °C) and crystallized pyroxene compositions metastably (Fig. 4.6). Whereas the older units formed from a more fractionated magma which crystallized subcalcic augites and Fe-rich pigeonites metastably. The inferred crystallization history of these basaltic units reveals that the magma was not sourced from the single source region; rather, it was generated from different mantle source regions.

The ages available for the Humorum basaltic units suggest that these basalts formed at different periods (Imbrian to Eratosthenian) and probably sourced from a single parental magma and/or different magmatic sources regions. The chemical variations in the basaltic units directly reflect the compositional heterogeneity in its source regions. Therefore, the Band I and Band II centres of pyroxenes which are sensitive to the chemical variations in basalts, are plotted against the age of the basaltic units to understand the chemical nature of magmas that erupted at different periods (Fig. 4.7).

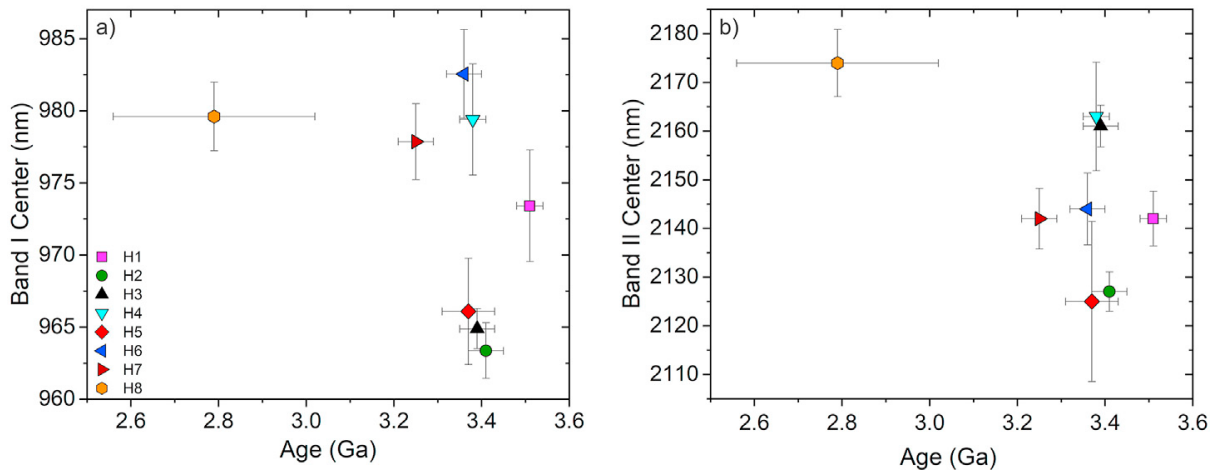


Figure 4.7: (A) Age vs Band I center plot of individual basaltic units within the Mare Humorum. (B) Age vs Band II center plot of the basaltic units within the Mare Humorum.

The individual flow units in the Mare Humorum erupted at periods between 2.79 Ga and 3.51 Ga. The Band I centre of these units is between 0.96 μm and 0.99 μm . In general, a significant

variation in the Band I centres with respect to the ages of the units has not been observed. The weak correlation might be because the pyroxene compositions examined are obtained from superposed craters having varying excavation depths (hundreds of meters). It is likely that these pyroxene compositions are part of different basaltic units and not of a single representative unit. However, the younger unit is clearly distinguished from older units based on their band centres. The youngest unit (2.79 Ga old) shows a Band I centre at 0.98 μm (Fig. 4.7a). The older units show Band I centres between 0.96 μm and 0.98 μm . Therefore, a decreasing trend in the Band I centre values can be noticed as it moves towards older age units. Band I centres in the younger unit is shifted to longer wavelengths, whereas the Band I centres of the older units are located at relatively shorter wavelengths. This shift in the Band I centres with respect to the age of the different basaltic units might correspond to the variations in the Fe^{2+} and Ca^{2+} contents in the pyroxene solid solutions. The Band I centre of the relatively younger basaltic unit moves to longer wavelengths with an increase in the Ca^{2+} and/or Fe^{2+} contents.

Variations in the Band II centres of the pyroxenes with respect to the ages of individual basaltic units have also been observed (Fig. 4.7b). The Band II centres for the units fall between 2.17 μm and 2.12 μm . The youngest unit shows the Band II centre at 2.17 μm . The older units exhibit Band II centres between 2.12 μm -2.16 μm . The Band II centres are also shifted towards shorter wavelengths as the age increases. The Band I and Band II centres are at relatively longer wavelengths in the younger unit compared to the older units. It is inferred that the older basaltic units crystallized more Fe^{2+} -rich pyroxenes or clinopyroxenes with less Ca^{2+} contents, whereas the younger unit crystallized more Ca^{2+} -rich pyroxenes during the cooling of the magma.

4.5 Conclusions

The present study investigated the chemical variations of distinct basaltic units in the Mare Humorum on the nearside of the Moon. The broadness and increased strengths of Band II indicated the dominance of clinopyroxenes in the region. The pyroxene band parameter analysis further showed that pigeonites and sub-calcic augites are the major components in these basaltic units with an average augitic composition. The chemical trend of pyroxene compositions suggests that multiple volcanic events have occurred in the Mare Humorum. The older units that erupted in the Imbrian period were crystallized from a more fractionated magma, while Mg and Ca-rich magma crystallized the younger unit. The observed longward shift in the Band I and Band II centres for the younger basaltic unit indicate a more Ca^{2+} -rich parental magma composition. The shortward shift of Band I and Band II centres in older units

suggest that the older basaltic magma crystallized more Fe²⁺-rich pyroxenes or clinopyroxenes with less Ca²⁺ contents during the cooling of the magma. Hence, it can be concluded that magmas of different chemical nature derived from heterogeneous source regions have erupted in the Humorum basin during Imbrian to Eratosthenian periods.

This chapter is the reproduction of an article published in the journal Planetary and Space Science.

Thesniya P. M. and Rajesh V. J. 2020. Pyroxene chemistry and crystallization history of basaltic units in the Mare Humorum on the nearside Moon: Implications for the volcanic history of the region. Planetary and Space Science 193:105093. 10.1016/j.pss.2020.105093.

Chapter 5

Compositional variations in spinels on the Moon

5.1 Introduction

Spinel is an oxide group mineral with divalent Fe, Mg in the tetrahedral site, and trivalent Fe, Cr, Al in the octahedral site of the spinel structure. Magmatic spinels directly crystallize from ultramafic magma, and therefore, their chemical composition provides information about its source composition and history (e.g., Irvine, 1965; Irvine, 1967; Sack and Ghiorso, 1991; Arai, 1992; Barnes and Roeder, 2001). Chromite is notable within the spinel group because of its role as a petrogenetic indicator (e.g., Irvine, 1965; Irvine, 1967; Arai, 1992; Barnes and Roeder, 2001). After ilmenite, this mineral is the second most prevalent opaque mineral on the Moon (cf. Heiken et al., 1991). One of the first minerals to crystallize from mafic-ultramafic magma is chromite. Chromite is a complex solid-solution of chromium, aluminium, magnesium, ferrous iron, ferric iron, and titanium oxides, similar to magnetite and spinel (Roeder, 1994). Chromite is resistant to post-magmatic changes, such as metamorphism (e.g., Suita and Streider, 1996). Because of its resistance under a variety of geological conditions, chromite can be used to determine magmatic conditions at the time of initial crystallization. Many attempts were made to link the composition of chromite to that of the melt from which it crystallized (Irvine, 1967; Evan and Frost, 1975; Arai, 1980; Sack, 1982; Engi, 1983; Arai, 1994; Barnes and Roeder, 2001; Arai et al., 2011). Chromian spinels and Mg-Al spinels are the most detected spinels on the Moon (Pieters et al., 2011; Yamamoto et al., 2013; Pieters et al., 2014; Prissel et al., 2014; Weitz et al., 2017) (Fig. 5.1). The compositions of lunar spinels were primarily deduced from remote sensing data and chemical investigations of returned lunar materials. Lunar spinels of comparable chemistry to terrestrial Cr-spinels were reported (Thesniya et al., 2021a).

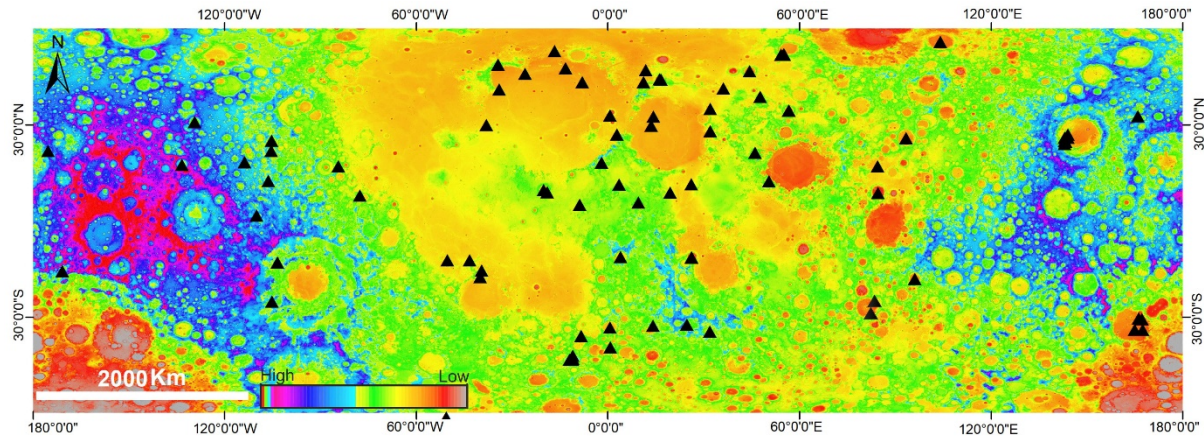


Figure 5.1: showing the known locations of spinels (marked as triangles) identified on Moon using remote sensing techniques (e.g., Martinot et al., 2018; and references therein). The base image is the LOLA-KAGUYA merged DEM in an Equidistant cylindrical projection ($<60^\circ$), showing the topography of the lunar surface.

Though orbital detections of spinels are limited, spinels and other oxide phases were identified from different source rocks in returned lunar samples (Table 5.1).

Table 5.1: List of returned lunar samples from Apollo and Luna series missions and lunar meteorites.

Returned lunar samples	Mission
Apollo samples	A11
	A12
	A14
	A15
	A16

	A17
Luna robot lander samples	Luna 16
	Luna 20
	Luna 24
Lunar meteorites	e.g., Northwest Africa 4734

The diverse rock types identified in the returned lunar samples include basalt, breccia, lunar meteorites, meteorites from returned samples, soil, troctolite, composite, crustal cataclasite, and unclassified materials (Table 5.2). Endmember spinel compositions of varying chemistry were reported from these rock types (e.g., Agrell et al., 1970; Cameron, 1971; Reid, 1971; Haggerty, 1971a, 1971b, 1971c; Taylor et al., 1971; El Goresy et al., 1972; Busche et al., 1972; Haggerty, 1972a, 1972b, 1972c, 1972d, 1972e, 1972f; Roedder and Weiblen, 1972; Taylor and McCallister, 1972; Taylor et al., 1972; Haggerty, 1973a, 1973b; Prinz et al., 1973; McCallister and Taylor, 1973; Dalton et al., 1974; Nehru et al., 1974; Brett, 1975; Haselton and Nash, 1975; Carter et al., 1975; Nehru et al., 1976; Nagasawa et al., 1976; Warner et al., 1976; El Goresy et al., 1976; Haggerty, 1977; El Goresy and Ramdohr, 1977; Haggerty, 1978a, 1978b; Sato, 1978; Schmitt et al., 1981; Haggerty, 1988). The source rocks of spinels are further grouped into different subcategories (Table 5.2).

The compositions of chromite, spinel, and ulvospinel from various rock types in returned lunar samples have been compiled from published and unpublished sources better to understand the compositional variations in lunar spinel-group minerals. This study will look at the different compositions of chromite, ulvospinel, and spinel found in lunar rocks and how the spinels found in rocks on Earth relate to those found on Moon. In the spinel database, there are around 4500 analyses. The composition of spinels in various source rocks is compared. The variation in spinel-group mineral composition from different lunar rocks is then compared to that seen in various terrestrial magma types.

Table 5.2: Diverse rock types identified in the returned lunar samples.

Source rocks of lunar spinels	Subcategory	
Basalt	Ilmenite basalt Basalt/microgabbro Olivine basalt Feldspathic basalt Pigeonite basalt KREEP basalt Olivine-normative basalt	
Breccia	Regolith breccia Fragmental breccia Breccia Crystalline matrix breccia Impact melt breccia Anorthosite breccia Recrystallized breccia	
Lunar meteorites	Unbrecciated basalt Basaltic meteorite Regolith breccia Fragmental breccia Feldspathic breccia Basalt-rich mafic breccia Melt breccia Gabbroic breccia Plutonic_granulitic troctolitic breccia	Plutonic_spinel anorthositic troctolite Plutonic_gabbroic meteorite Plutonic_troctolitic anorthosite
Meteorites_ returned samples	Olivine meteorite Anorthositic meteorite Basalt meteorite	
Soil	Soil Fines	
Troctolite		
Unclassified rock		
Composite		
Crustal cataclasite		

5.2 Datasets and methods

Around 4500 chemical data of lunar spinels from previous literature (Apollo and Luna returned samples and lunar meteorites) are compiled, and the mineral formulae were recalculated for each data (Fig. 5.2). Further, the different spinel compositions are classified based on their source lithologies, and spinel compositional variations in each rock type are plotted. The overall trend of lunar spinels was observed based on ternary and bivariate plots. Data density

contours were drawn on spinel compositional plots to their chemical affinity. The data density strategy entails contouring these multiple plots for data concentration so that the n^{th} percentile contour encloses the data that is most densely packed (Barnes and Roedder, 2001). This method is effective for analyzing very large data populations, such as the one provided above, where there are dense clusters of data points surrounded by a significant number of outliers. Simple x–y plots tend to draw attention to outlier data points rather than providing a clear picture of where the majority of the data points are located. The best strategy to derive a meaningful compositional field from a population is to use the data density approach. The contoured data are compared with the compositional fields of spinels from terrestrial settings.

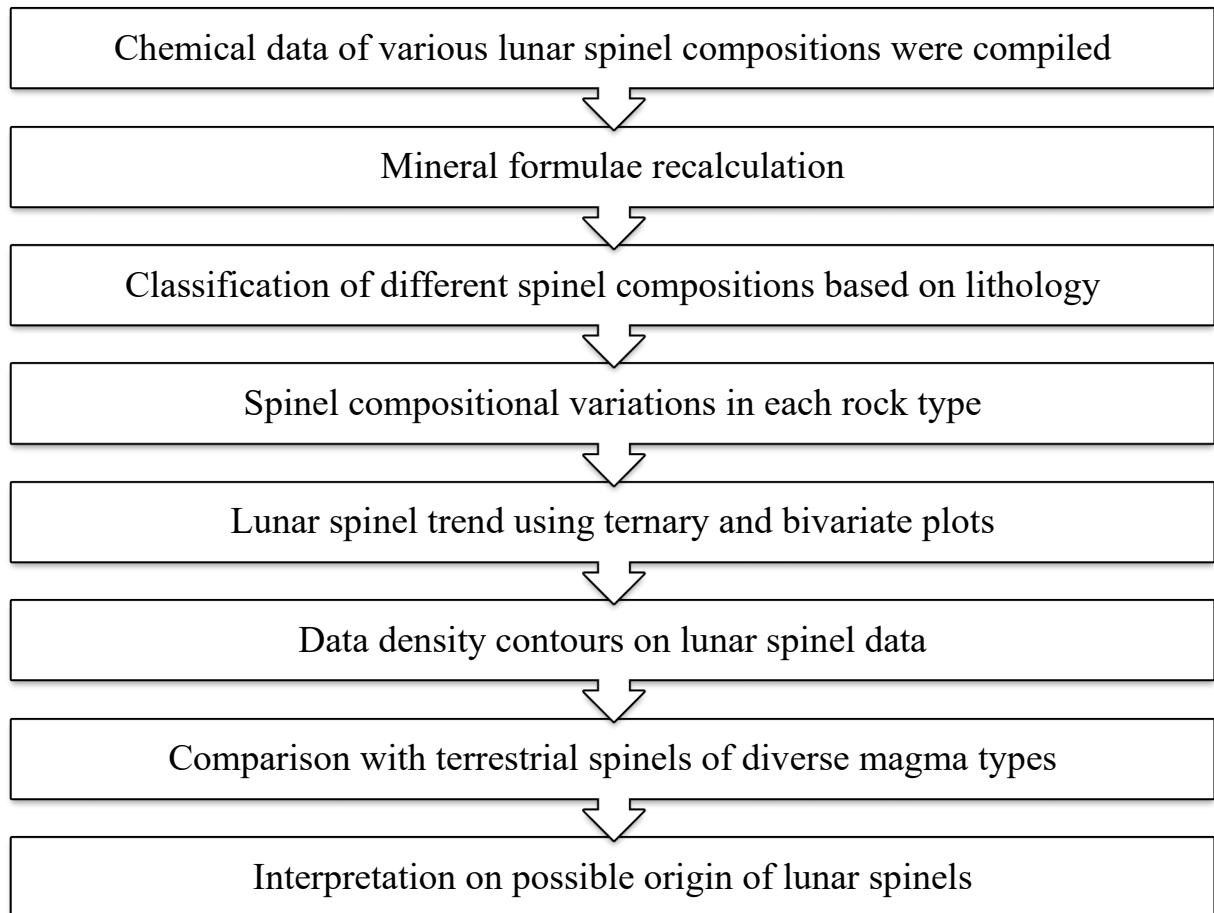


Figure 5.2: Schemata showing the methodology followed for carrying out the present research on spinel compositions and origin.

5.3 Results

The earliest crystallisation products are chromium-rich spinels, followed by chromian

ulvospinel, ulvospinel, and, lastly, ilmenite. With increased crystallisation and lowering temperature, this paragenetic sequence suggests early Cr depletion and enrichment of Fe+Ti in the liquid (Haggerty et al., 1971). The compiled chemical data showed that lunar spinels are mainly chromites or Cr-spinels, ulvospinels, chromian ulvospinels, and Mg-Al spinels.

The FeO content in lunar spinels ranges between 0-65 wt% (Fig. 5.3). The Cr₂O₃ concentration is from 0-55 wt%, while Al₂O₃ shows a wider range (0-70 wt%). The MgO (0-25 wt%) and TiO₂ (0-40 wt%) concentrations are in intermediate ranges. The spinels are dominantly seen in basalts and meteorites from returned samples. Basalts contain spinels with greater FeO (15-65 wt%) and TiO₂ (0-40 wt%), and a low Mg# (0-0.4), Al₂O₃ (<20 wt%) and Cr₂O₃ contents. In breccia, the prominent compositions are of greater Al₂O₃ (up to 70 wt%) TiO₂ (up to ~36 wt%), with FeO contents lesser than 25 wt% and Cr# between 0-0.6. The spinels in crustal cataclasites contain 16-51 wt% Cr₂O₃ and 15-35 wt% FeO contents. The MgO contents are less than 17 wt%, Al₂O₃ (~18 wt%), and TiO₂ less than 5 wt%. In troctolites, the spinels contain Al₂O₃ from 5-70 wt%, MgO between 0.1-26 wt%, TiO₂ less than 25 wt%, and FeO (10-58 wt%) and Cr₂O₃ (3-51 wt%). The spinels in soil samples contain lesser TiO₂ (0-33 wt%) and MgO (0-24 wt%) contents, while the Al₂O₃ (1-67) wt%, Cr₂O₃ (0-54 wt%), and FeO (5-61 wt%) in intermediate ranges (Fig. 5.3). The spinels from composites are more Al₂O₃ (1-65 wt%) and FeO-bearing compositions (10-63 wt%), with TiO₂ (0.2-34 wt%), Cr₂O₃ (0.1-48 wt%), and MgO (0-21 wt%) in lesser amounts. The spinels from lunar meteorites contain greater Al₂O₃ (1-65 wt%) and FeO (6-61 wt%) contents. The Cr₂O₃ content ranges from 0.2-45 wt%, while the TiO₂ and MgO contents are between 0.1-33 wt% and 0-23 wt%, respectively. In meteorites from returned samples, the spinels have FeO contents between (24-65 wt%), TiO₂ up to 51 wt%, Al₂O₃ and Cr₂O₃ contents from 0-55 wt%, and MgO less than 10 wt%. The spinels from the unclassified category contain greater Cr₂O₃ (0.33-47 wt%) and FeO contents (28-62 wt%). The TiO₂ content ranges from 3-33 wt%, while the Al₂O₃ (1-13 wt%) and MgO contents (0.05-6 wt%) are relatively less (Fig. 5.3).

Spinel has been classified into two compositional fields. First, there are the chromite-ulvospinel, titanium chromite, and aluminium chromite compositions, which range from ulvospinel to chromite. Second compositions are found in the transition zone between spinel and hercynite. These spinels are known as chromian pleonastes because they have a minor chromium enrichment. Lunar spinels have four unique compositional trends and three major compositional discontinuities. Between these two endmembers, there is a complete solid solution series, as indicated by the ulvospinel-chromite group (Fig. 5.4).

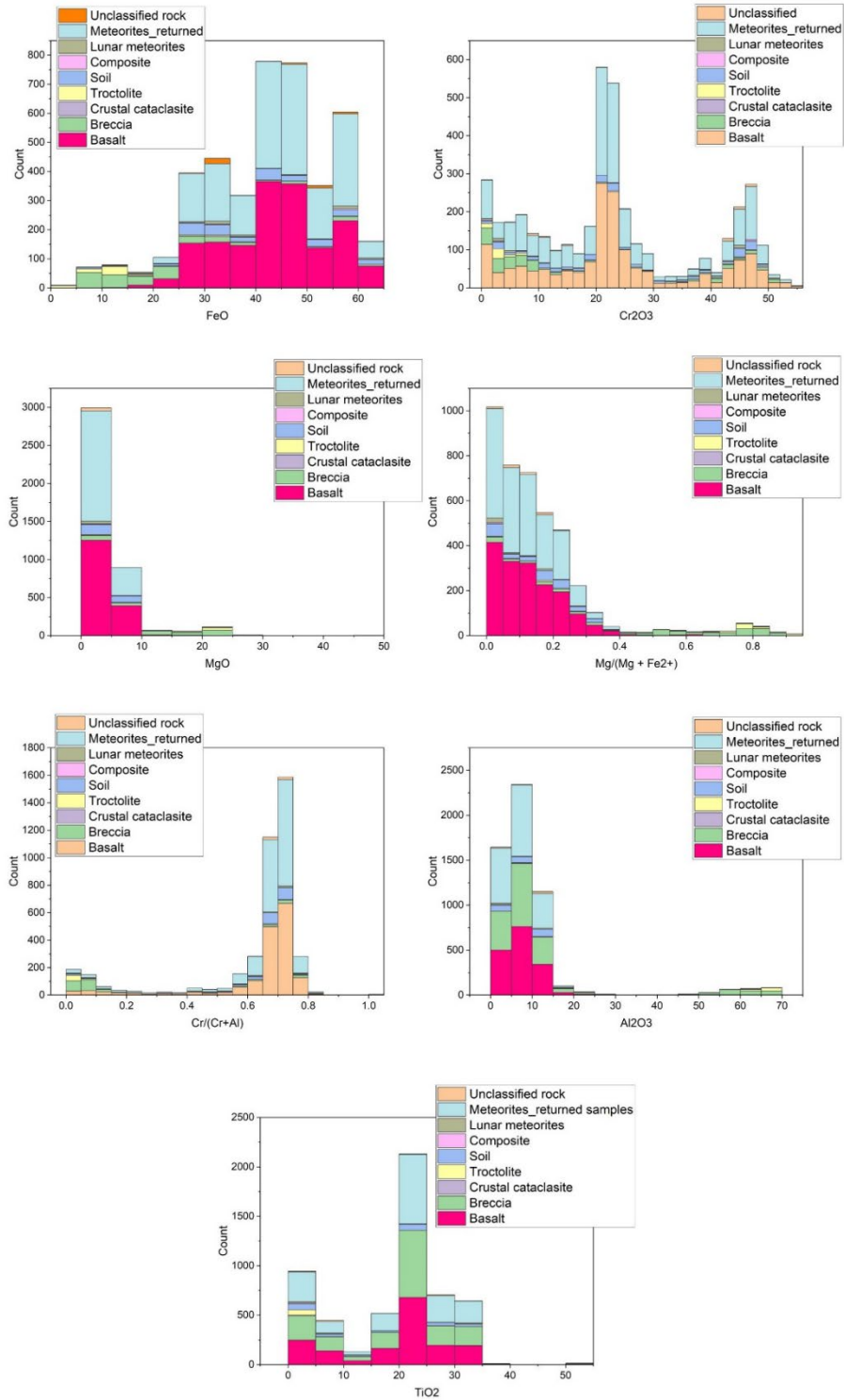


Figure 5.3: The histograms depicting the oxide concentrations, Mg#, and Cr# in spinels from different rock types on the Moon.

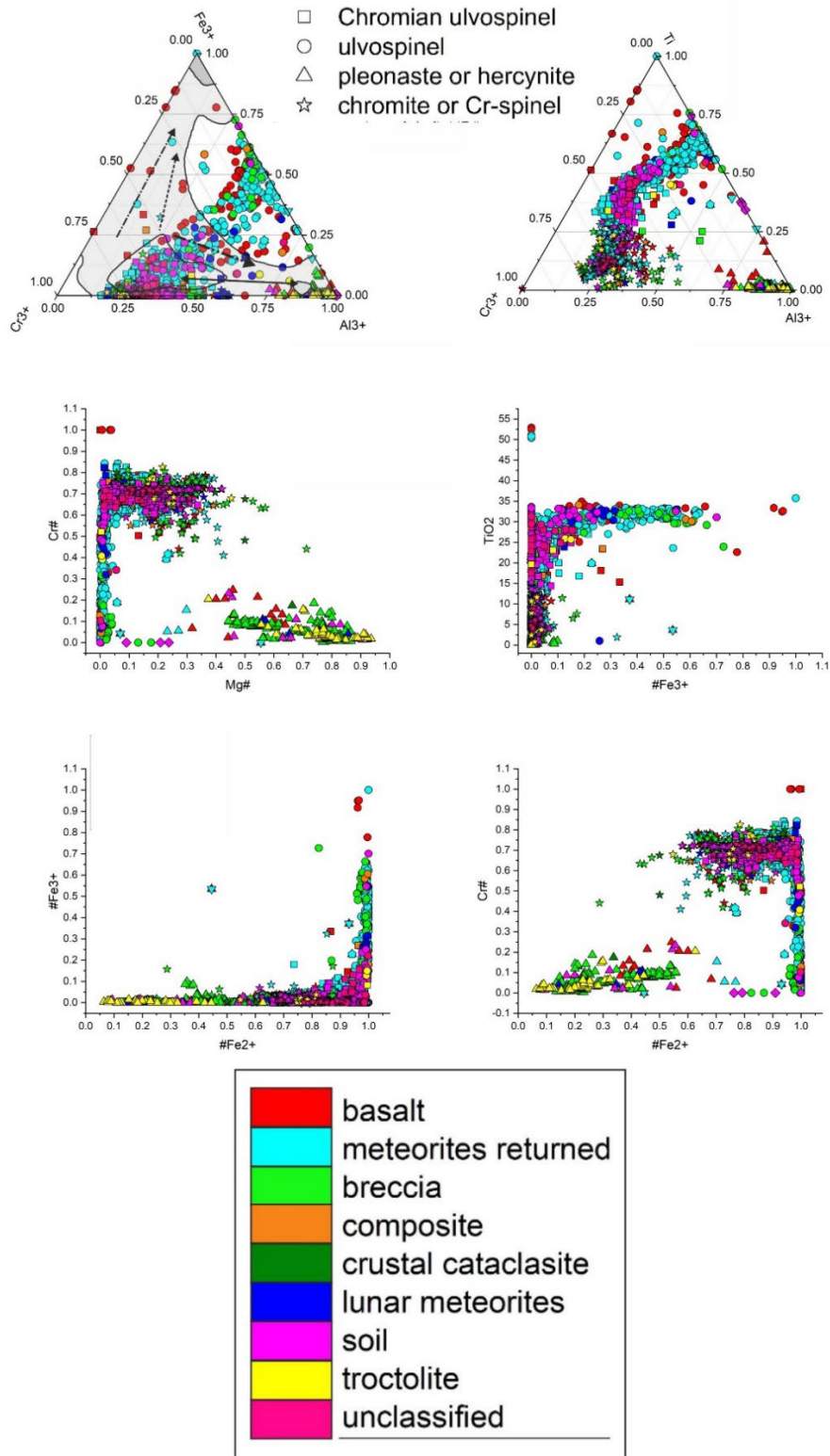


Figure 5.4: The compositional variations of lunar spinels represented on a magnetite triangle projection, ulvospinel triplot, and bivariate plots of $\#Mg$ vs $\#Cr$, $\#Fe^{3+}$ vs TiO_2 , $\#Fe^{2+}$ vs $\#Fe^{3+}$, and $\#Fe^{2+}$ vs $\#Cr$. The compositional field and trend lines of terrestrial spinels are overlaid.

5.3.1 Spinel in diverse lithologies on the Moon

5.3.1.1 Basalt

The basalts in the returned lunar samples contain spinels with TiO_2 (0-35 wt%), Al_2O_3 (0-20 wt%), Cr_2O_3 (0-55 wt%), MgO (0-10 wt%), and FeO (20-65 wt%) in the respective ranges (Fig. 5.5).

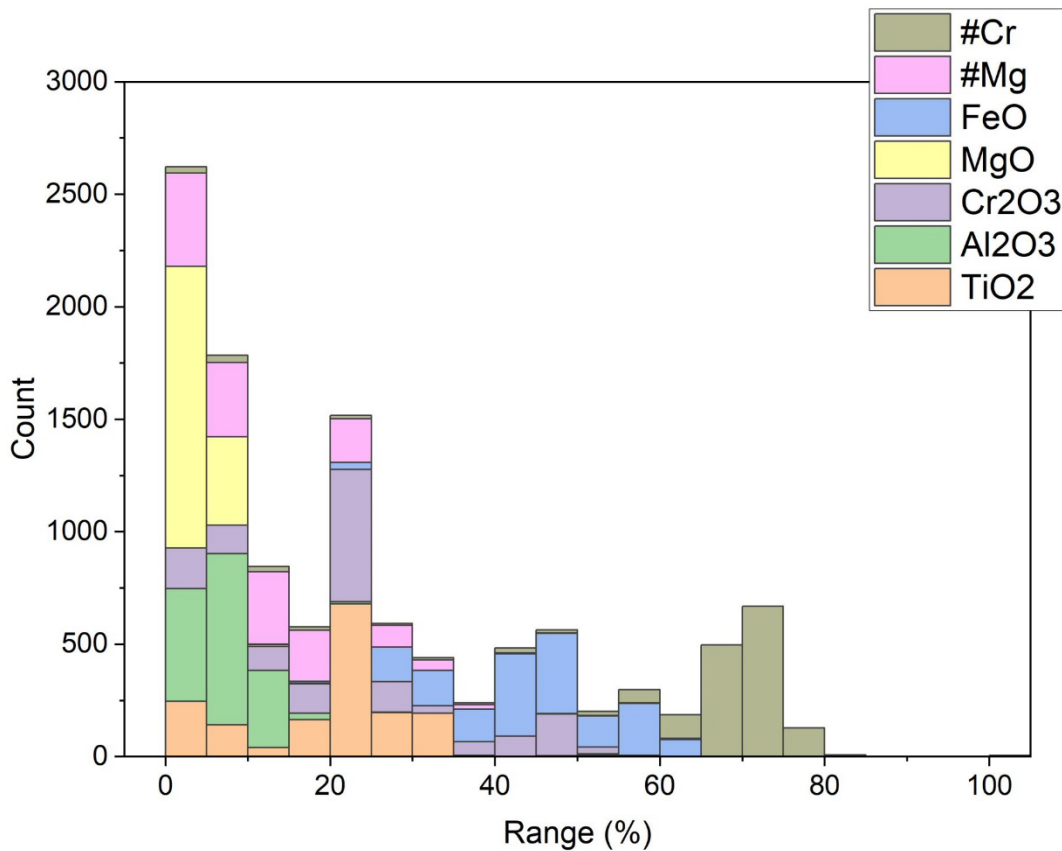


Figure 5.5: The histogram showing the oxide concentrations in spinels from basalts.

The ternary spinel series, ulvospinel (Fe_2TiO_4)-chromite (FeCr_2O_4)-hercynite (FeAl_2O_4) in basalts, are of particular interest. This spinel series is restricted to lunar basalts and is of interest petrogenetically because members of the series appear to precipitate during the crystallisation history of some of these basalts (Haggerty, 1972), with Mg-aluminian chromite crystallising early and Cr-Al-ulvospinel crystallising late. Because most basalts have a characteristic bimodal distribution of early and late-stage products, the series is of importance compositionally.

Spinel with compositions spanning the complete normal-inverse series are found in basalts (Fig. 5.6). A typical trend of Cr-rich spinels to Cr-Al-ulvospinel can be seen in ilmenite basalts.

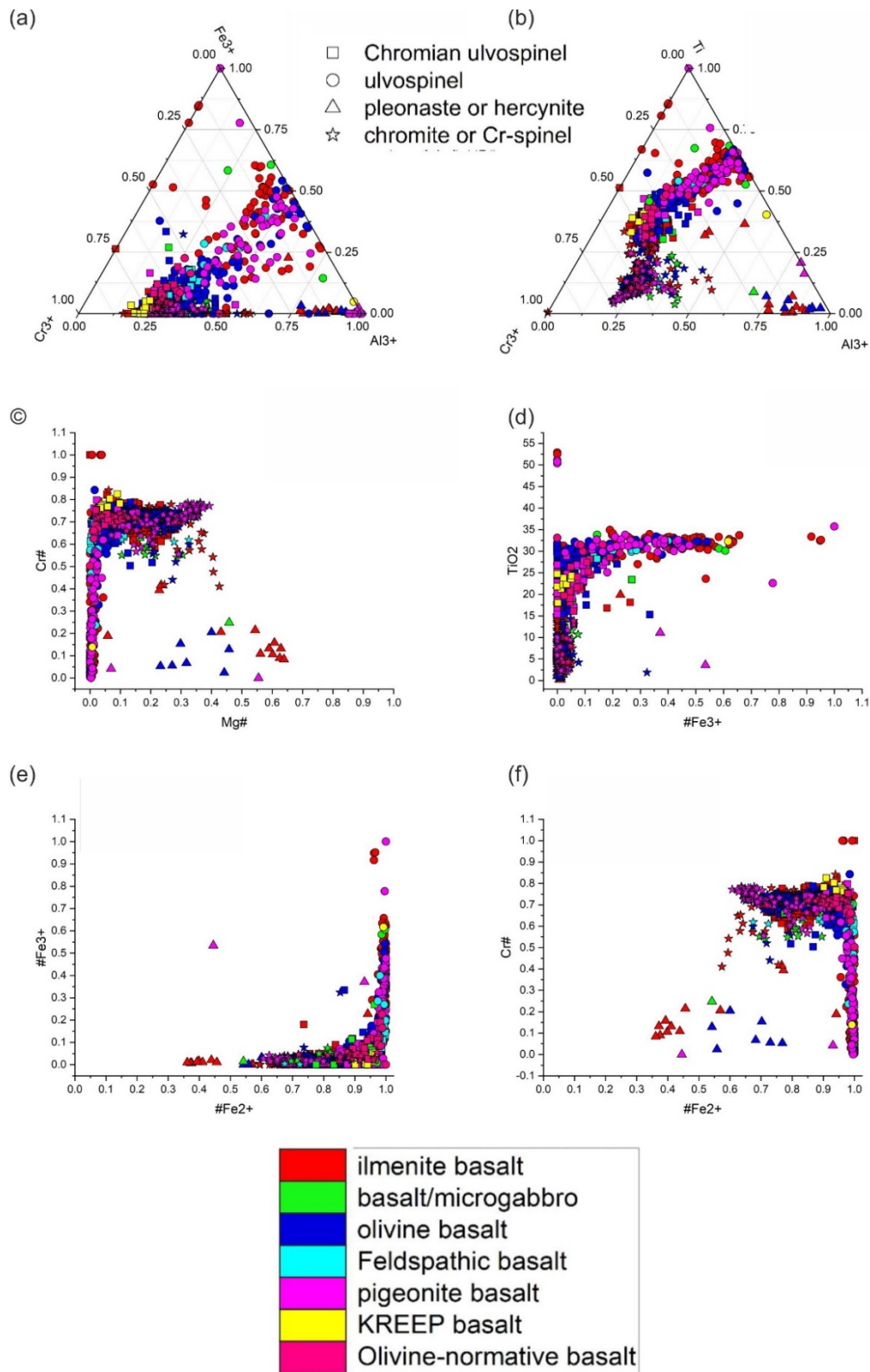


Figure 5.6: Spinel compositional diagrams plotted for spinel compositions from various basalts in the returned samples.

In microgabbro, the compositions are mainly Cr-spinels and chromian ulvospinel. The olivine-vitrophyre basalt samples show a typical bimodal distribution with Cr-spinel and ulvospinel as prominent endmembers. The feldspathic basalts show two distinct compositional fields in Cr-spinel and Cr-ulvospinel. The pigeonite basalts show a distinct compositional trend between Cr-spinel and Cr-Al-ulvospinel. KREEP basalts only contain chromian ulvospinel. Olivine normative basalts show a compositional trend between Cr-spinel and Cr-ulvospinel. The spinels of intermediate compositions in the compositional fields in basalts could have been crystallized metastably (Haggerty, 1971, 1972). Two of the three principal components are structurally classified as normal spinels (chromite and hercynite), whereas the third (ulvospinel) is classified as an inverse spinel. The coordination preference of the transition metal ions, as well as the occupancy of Fe^{2+} (and Mg^{2+}) solely in the A sites in chromite-hercynite and the split occupancy of Fe^{2+} between A and B sites in ulvospinel, are the key differences between these types. Cr+Al are gradually replaced by Fe+Ti as crystallisation progresses, and because Cr, Al, and Ti all have high octahedral (B site) site preference energies, divalent ion occupancy of B sites is structurally restrained and only enters 6-fold coordination to the extent required to maintain electrostatic charge balance. As a result, intermediate spinel members with neither a high normal nor a high inverse character are considered metastable (Haggerty, 1972).

5.3.1.2 Breccia

In spinels from breccia, Al_2O_3 (up to 70 wt%), Cr_2O_3 (up to 50 wt%), and FeO (5-55 wt%) are in greater abundances, while MgO is less than 25 wt% and TiO_2 content is between 0-35 wt% (Fig. 5.7).

The spinels from breccia samples show distinct compositional fields occupying the fields of Mg-Al spinels, Cr-spinels, Cr-ulvospinel, and Cr-Al-ulvospinel (Fig. 5.8). In regolith breccia, compositions are Mg-Al spinels. In fragmental breccia, chromian ulvospinel is prominent. Crystalline-matrix breccia contains Cr-spinel compositions. Agglomerate breccia contains some Cr-spinels and Cr-ulvospinel. Impact melt breccia shows three compositional clustering of Cr-spinels, ulvospinel, and Mg-Al-spinels. Anorthosite breccia samples have Cr-spinel compositions, while recrystallized breccia contains more aluminium compositions. Any distinct compositional trend between spinel endmembers is not observed in breccia samples. Breccia on the Moon is majorly the product of impact events. The impact disintegrates the primary crustal rocks into breccia, and therefore, the spinels in analyzed breccia samples from Apollo sites must have been sourced from different primary rocks. This explains the clustering

of spinels in distinct compositional fields.

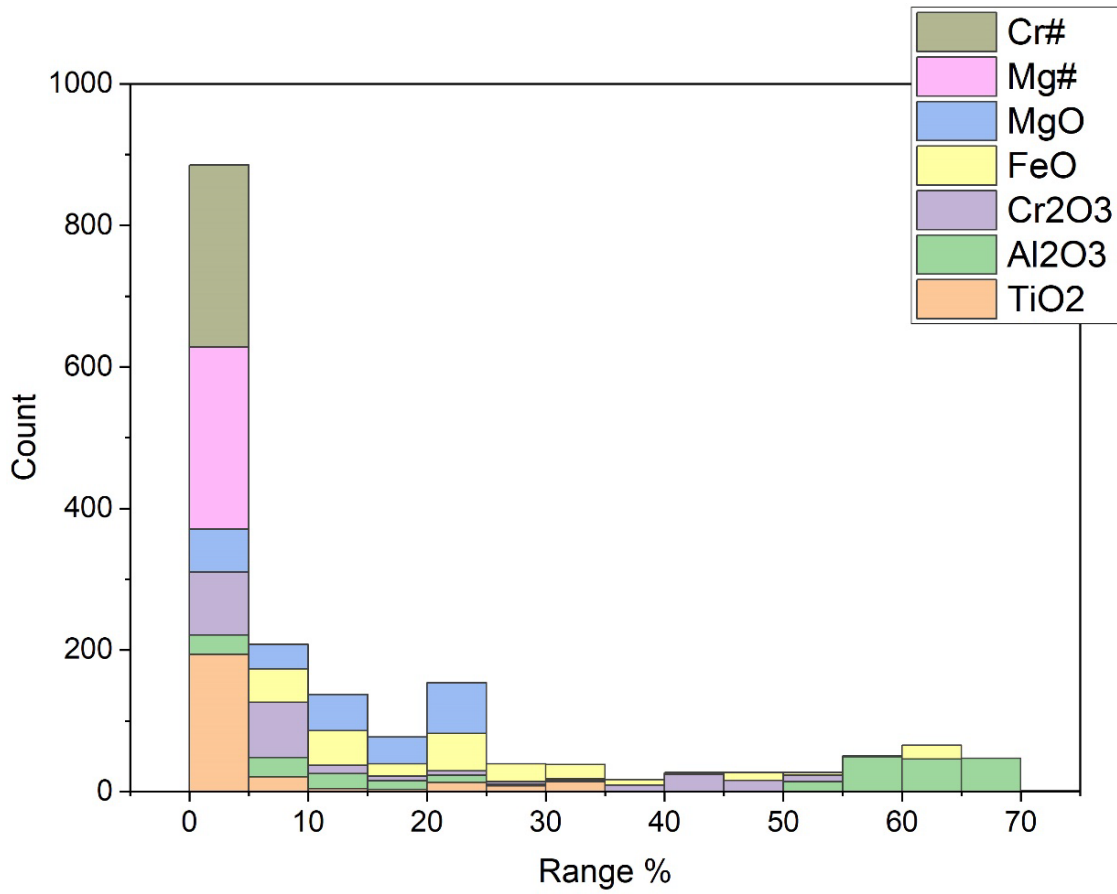


Figure 5.7: Histogram showing the oxide concentrations of the spinels in breccia.

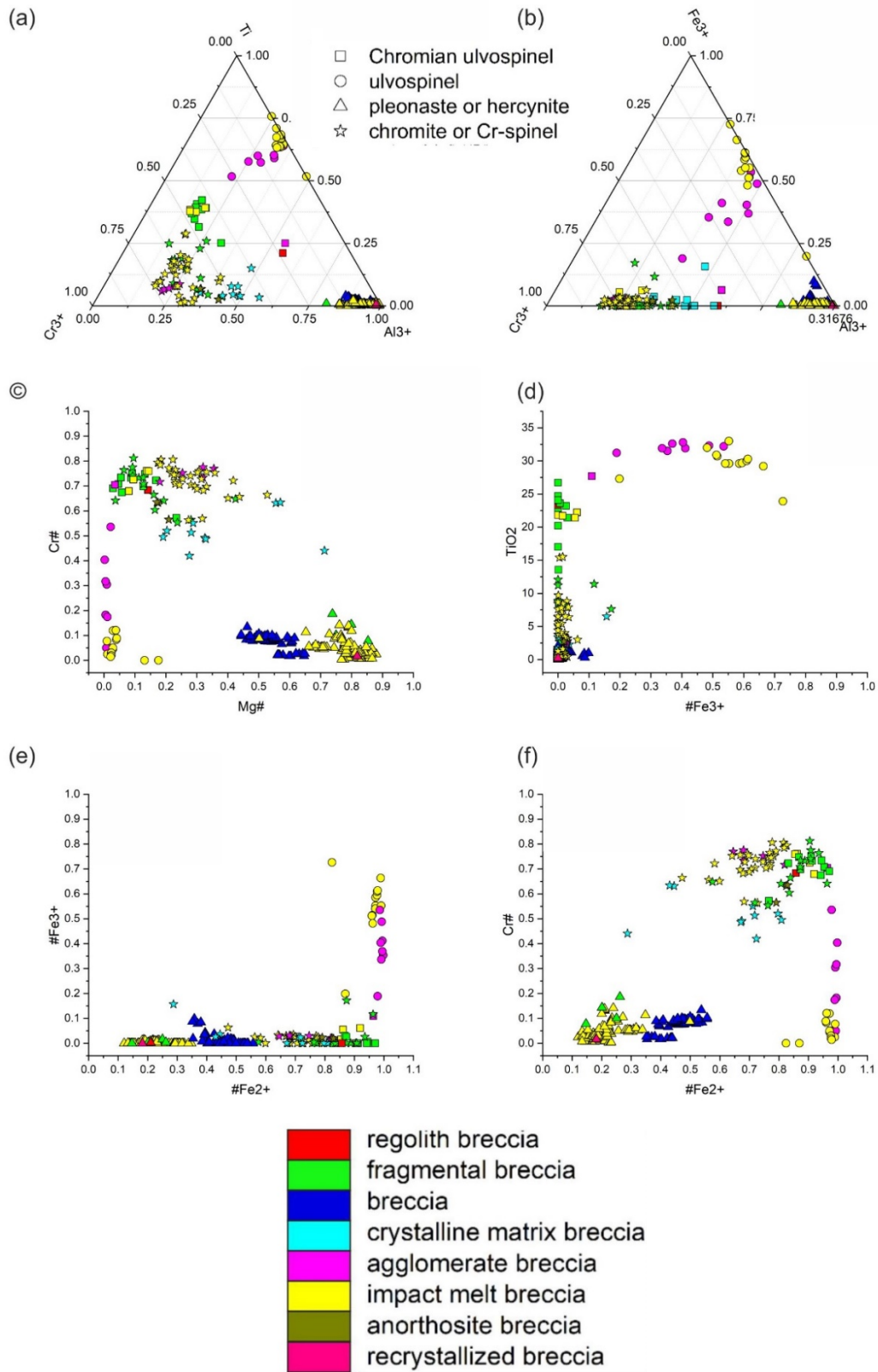


Figure 5.8: Compositional diagrams for spinels from various breccia samples.

5.3.1.3 Lunar meteorites

In spinels from lunar meteorites, Al_2O_3 (up to 70 wt%), Cr_2O_3 (0-50 wt%), and FeO (10-70 wt%) are in greater abundances, with MgO less than 25 wt% and TiO_2 up to 40 wt% (Fig. 5.9).

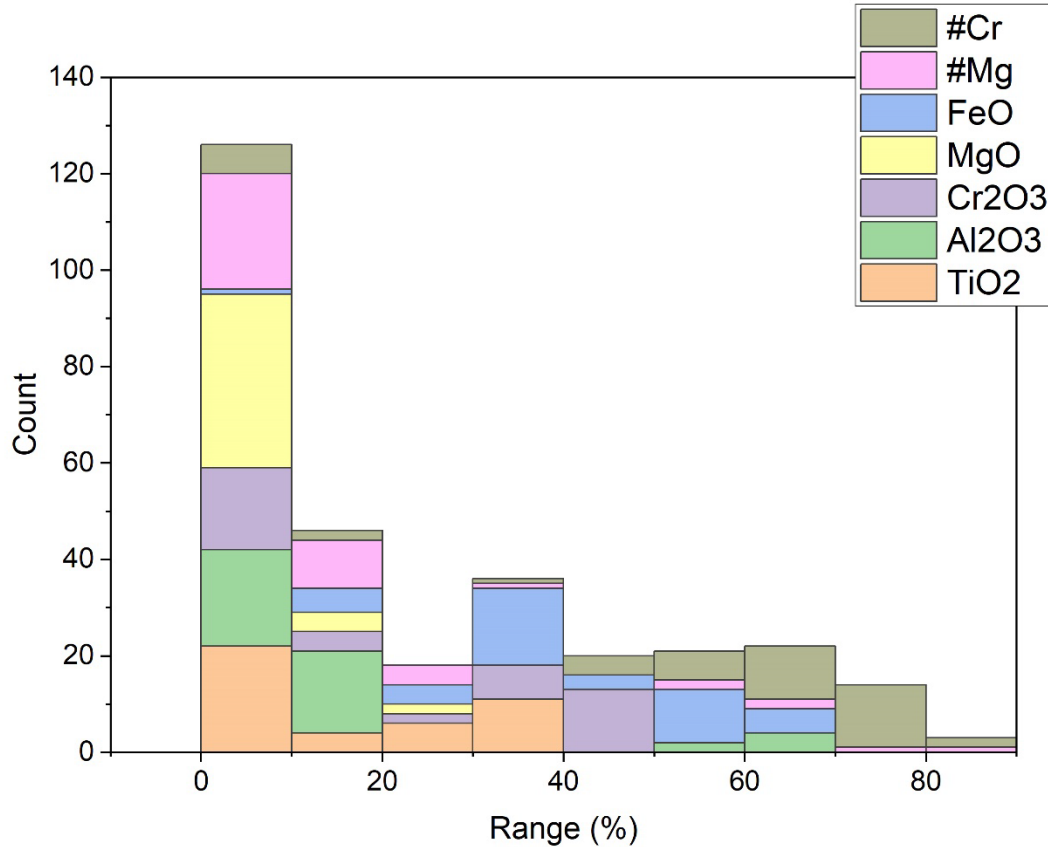


Figure 5.9: Histogram showing the oxide concentrations of the spinels in lunar meteorites.

The spinels in lunar meteorites are mainly Cr-ulvospinel compositions (Fig. 5.10). The spinel-bearing rock types in lunar meteorites include unbrecciated basalts, mare basalt, regolith breccia, fragmental breccia, feldspathic breccia, basalt-rich mafic breccia, melt breccia, gabbroic breccia, plutonic granulitic troctolitic breccia, plutonic spinel anorthositic troctolite, plutonic gabbroic meteorite, plutonic troctolitic anorthosite. Mg-Al-rich compositions are observed in some plutonic rocks and feldspathic breccia samples. Cr-spinels dominate the samples from melt breccia, mare basalt, and regolith breccia. Cr-ulvospinel to ulvospinel compositions are found in basaltic meteorite, mare basalt, gabbroic breccia, and unbrecciated basalt samples.

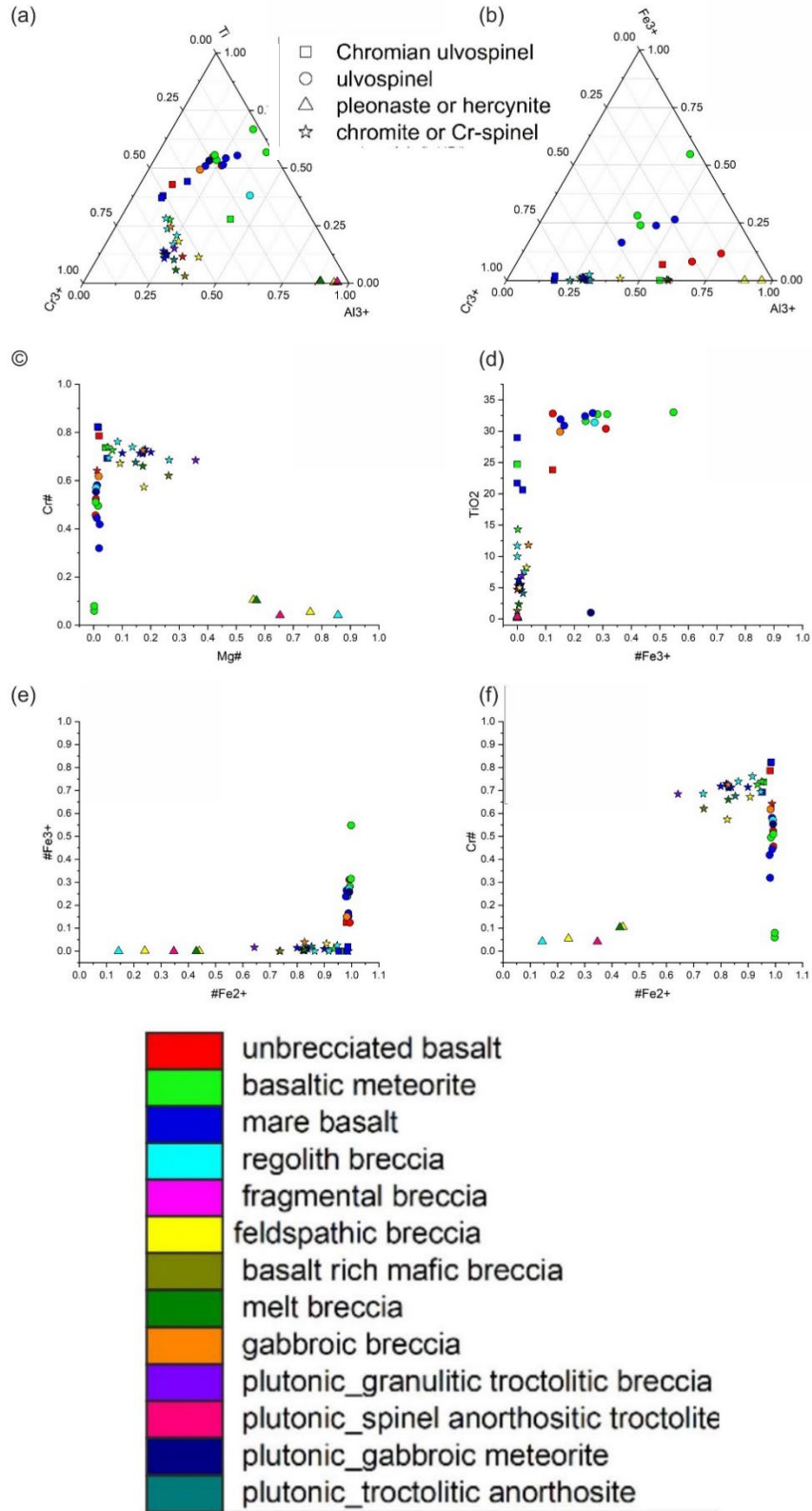


Figure 5.10: Compositional diagrams for spinels from various lunar meteorites.

5.3.1.4 Meteorites from returned samples

In spinels from meteorites in returned samples, Cr₂O₃ (up to 50 wt%) and FeO (up to 65 wt%) contents are in greater abundances, with MgO <10 wt%, TiO₂ <35 wt%, and Al₂O₃ <15 wt% (Fig. 5.11).

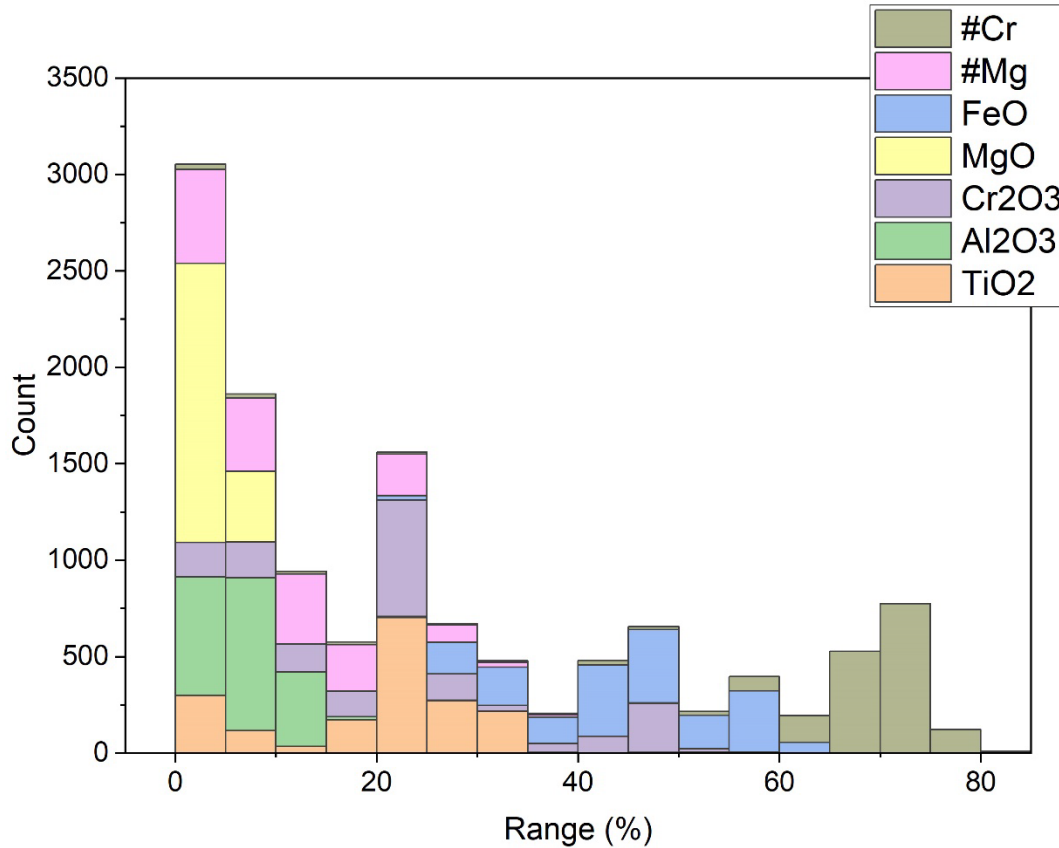


Figure 5.11: Histogram showing the oxide concentrations of the spinels in meteorites from returned samples.

The meteorites in returned lunar samples comprise rock types such as olivine meteorite, anorthositic meteorite, and basaltic meteorite (Fig. 5.12). The spinels from these meteorite samples show a distinct bimodal distribution between Cr-endmember and ulvospinel. In olivine meteorites, a distinct compositional trend is observed between chromites and chromian ulvospinels. Anorthositic meteorites only contain chromite compositions. The basaltic meteorites also show a distinct bimodal distribution between chromites and ulvospinels.

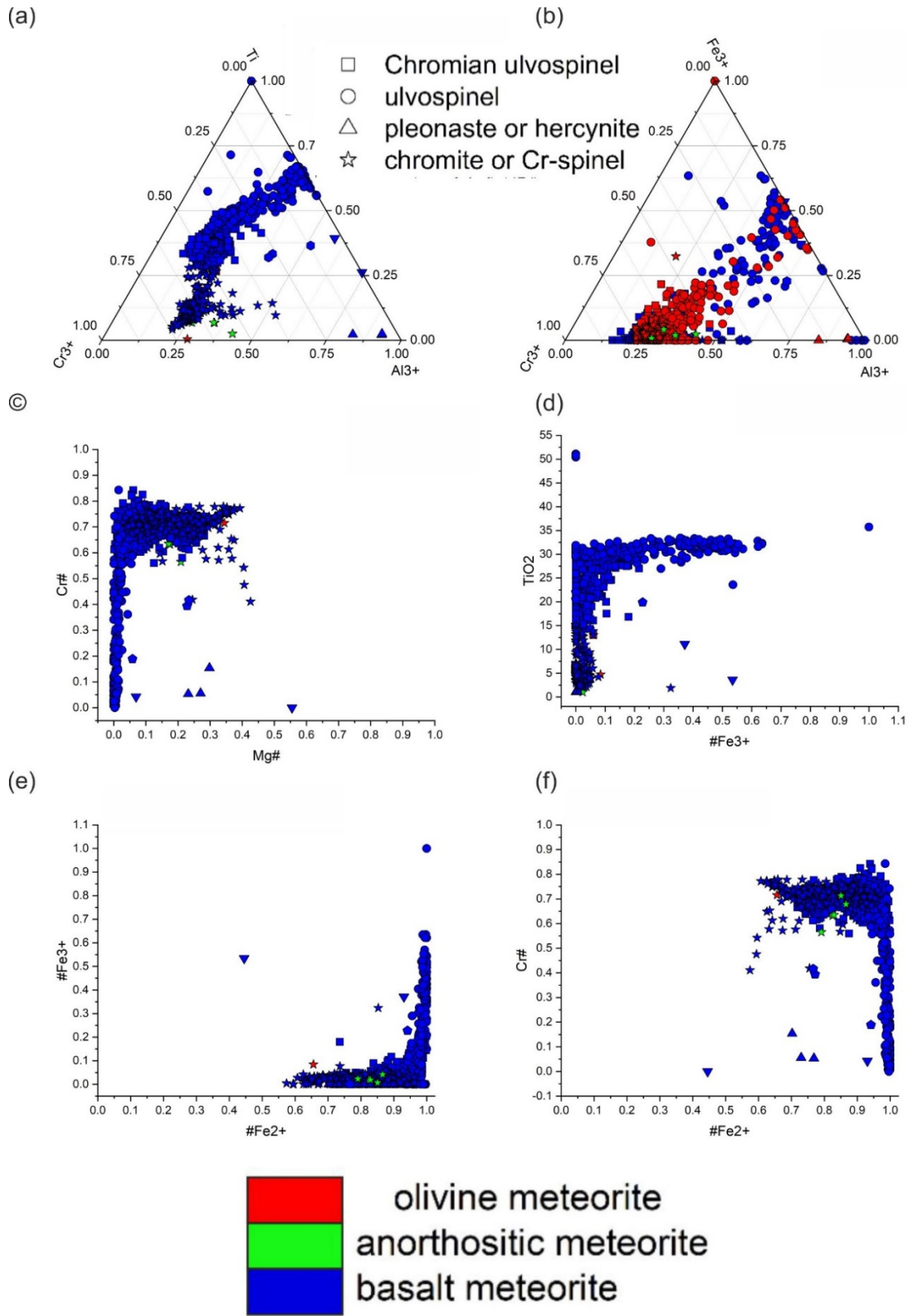


Figure 5.12: Compositional diagrams for spinels in meteorites from returned samples.

5.3.1.5 Soil

In spinels from soil samples, Al_2O_3 (up to 65 wt%), Cr_2O_3 (up to 50 wt%), and FeO (<55 wt%) are in greater contents, while MgO is less than 25 wt% and TiO_2 content is <35 wt% (Fig. 5.13).

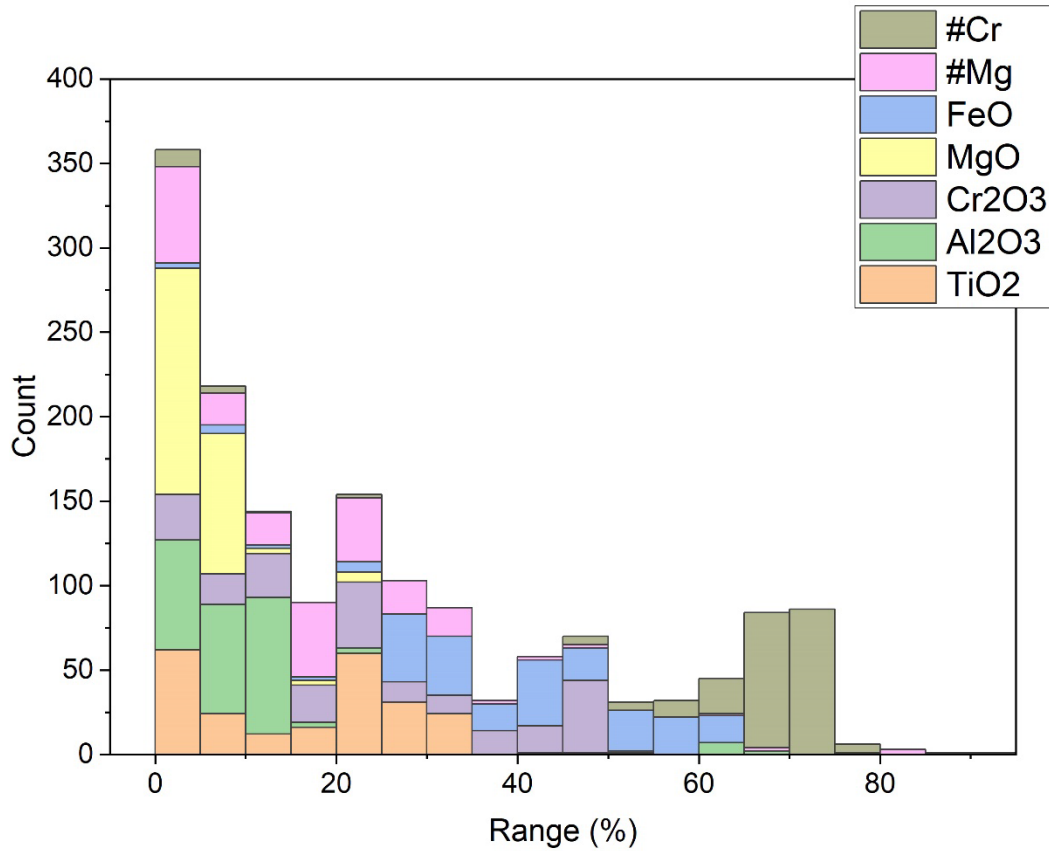


Figure 5.13: Histogram showing the oxide concentrations of the spinels in soil samples.

The soil samples in returned lunar samples contain soil and fine materials. The spinels in soil samples exhibit a compositional trend between chromites and chromian ulvospinel (Fig. 5.14). A cluster near the aluminium end is also observed in soil and fine samples, suggesting the presence of Mg-Al spinels.

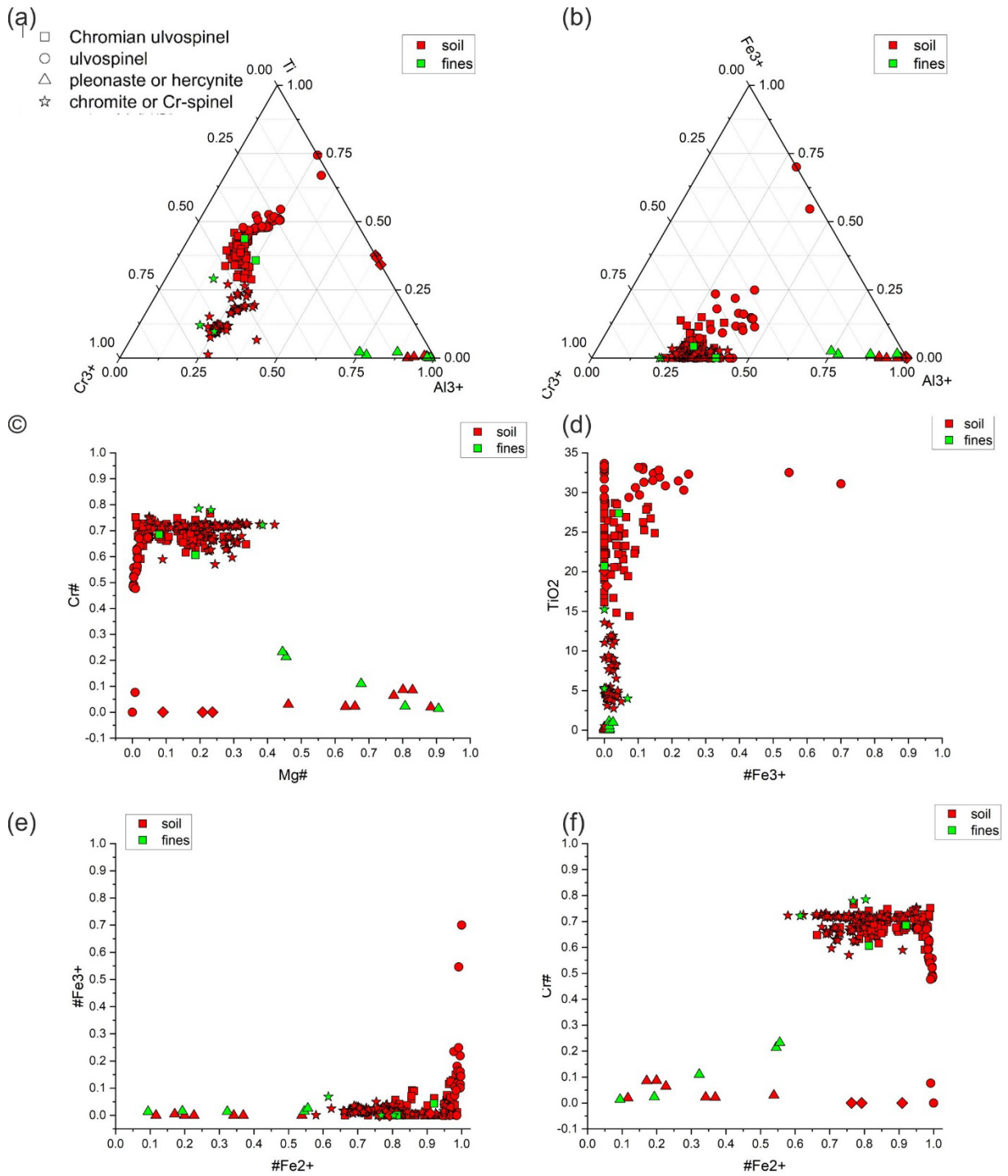


Figure 5.14: Compositional diagrams for spinels in soil samples.

5.3.1.6 Troctolite

In spinels from troctolite, Al_2O_3 (up to 70 wt%), Cr_2O_3 (up to 50 wt%), and FeO (<60 wt%) are in greater contents, while MgO and TiO_2 contents are <30 wt% (Fig. 5.15).

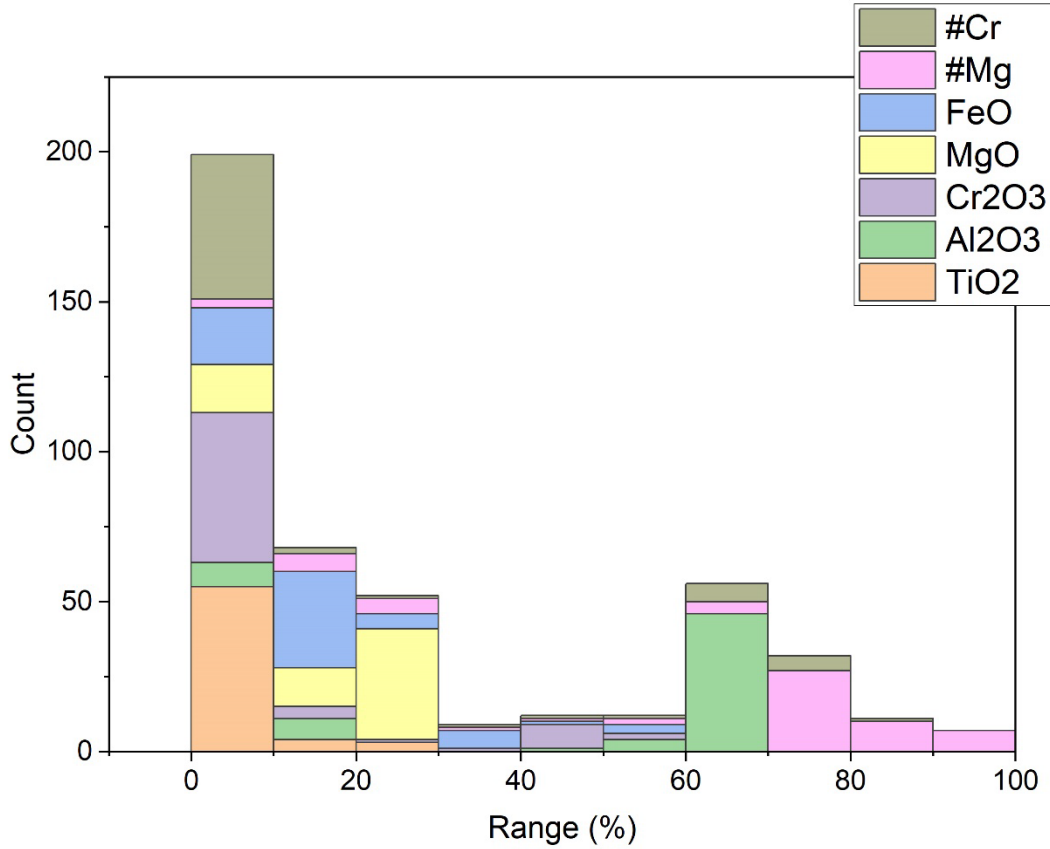


Figure 5.15: Histogram showing the oxide concentrations of the spinels in troctolite samples.

The spinels in troctolites exhibit compositional clusters of Mg-Al spinels, chromites, and some Cr-ulvospinels. Mg-Al spinels are the prominent phases identified in troctolites (Fig. 5.16).

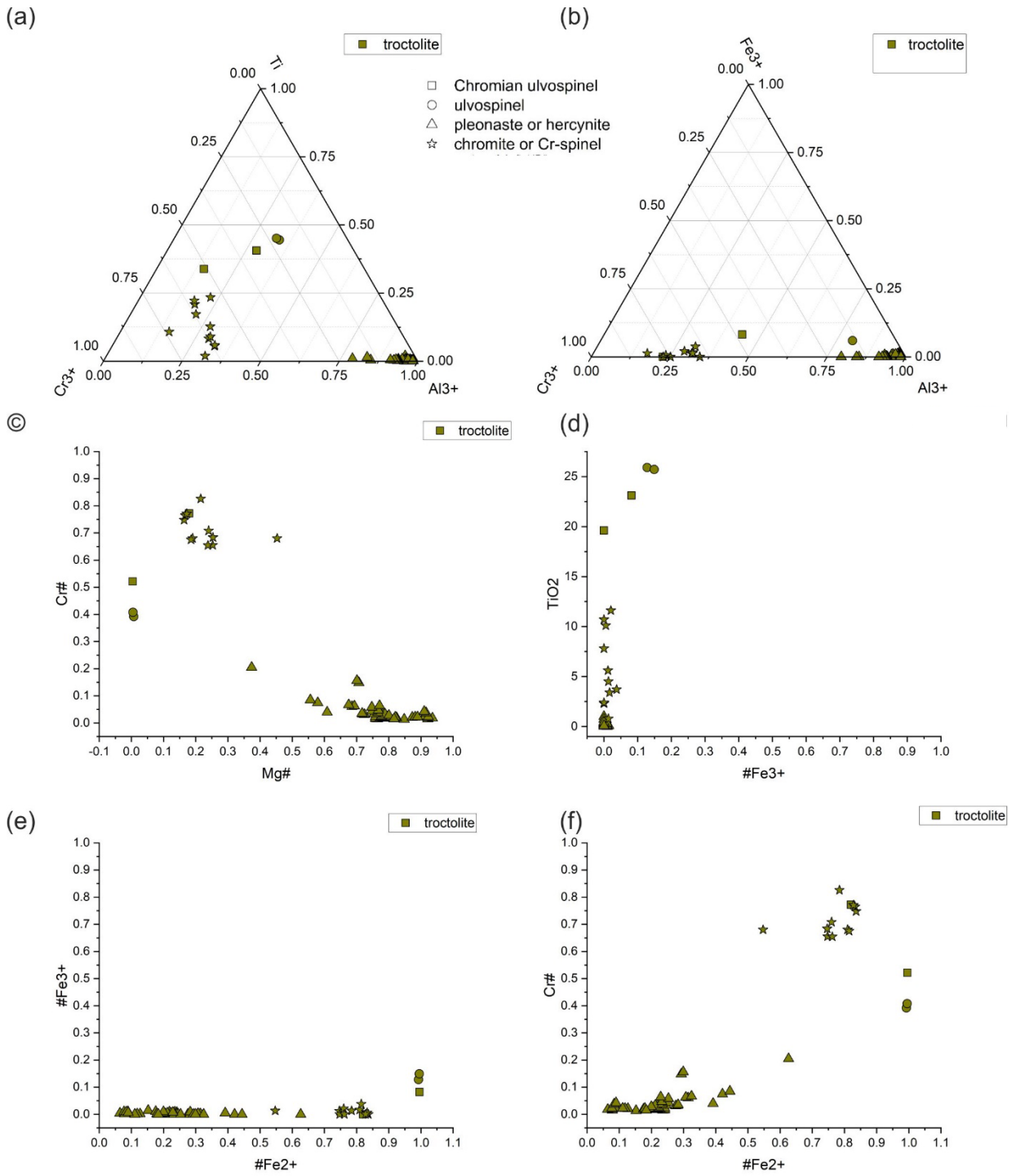


Figure 5.16: Compositional diagrams for spinels in troctolites.

5.3.1.7 Composite

In spinels from composite samples, Al_2O_3 (up to 70 wt%), Cr_2O_3 (up to 50 wt%), and FeO (<70 wt%) are in greater contents, while MgO is <30 wt%, and TiO_2 content is <40 wt% (Fig. 5.17).

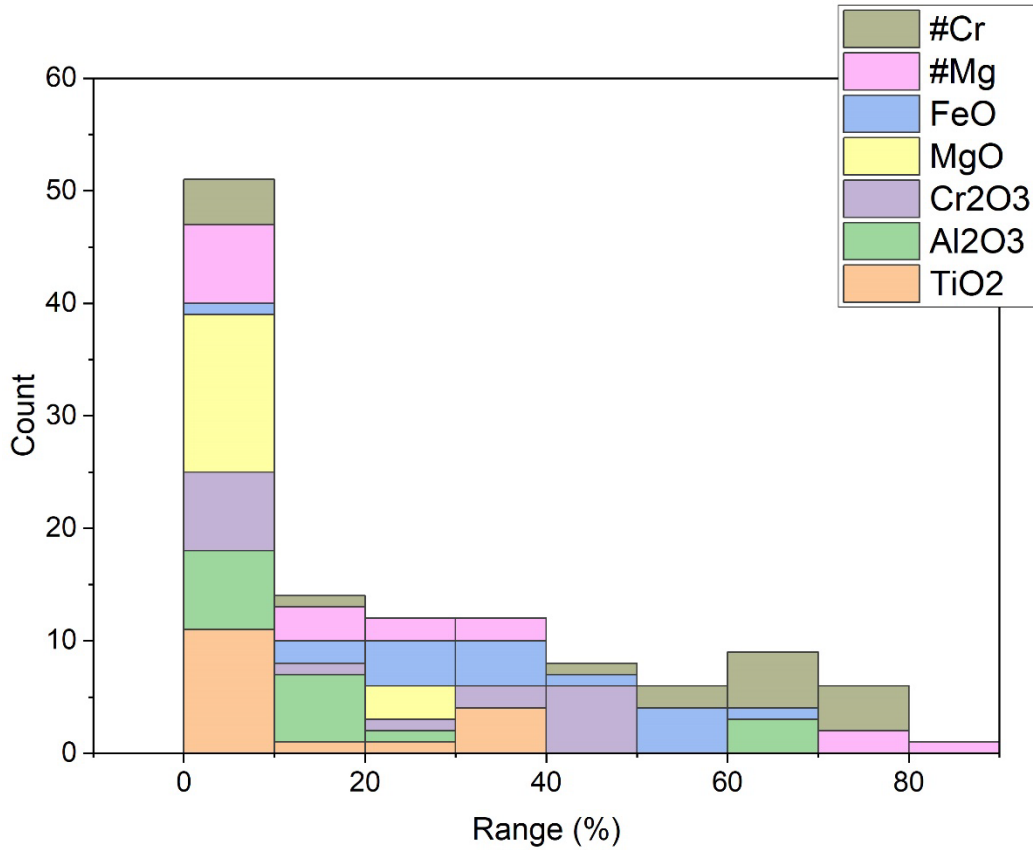


Figure 5.17: Histogram showing the oxide concentrations of the spinels in composite samples.

The composite samples contain some chromites, ulvospinel, and Mg-Al spinels (Fig. 5.18).

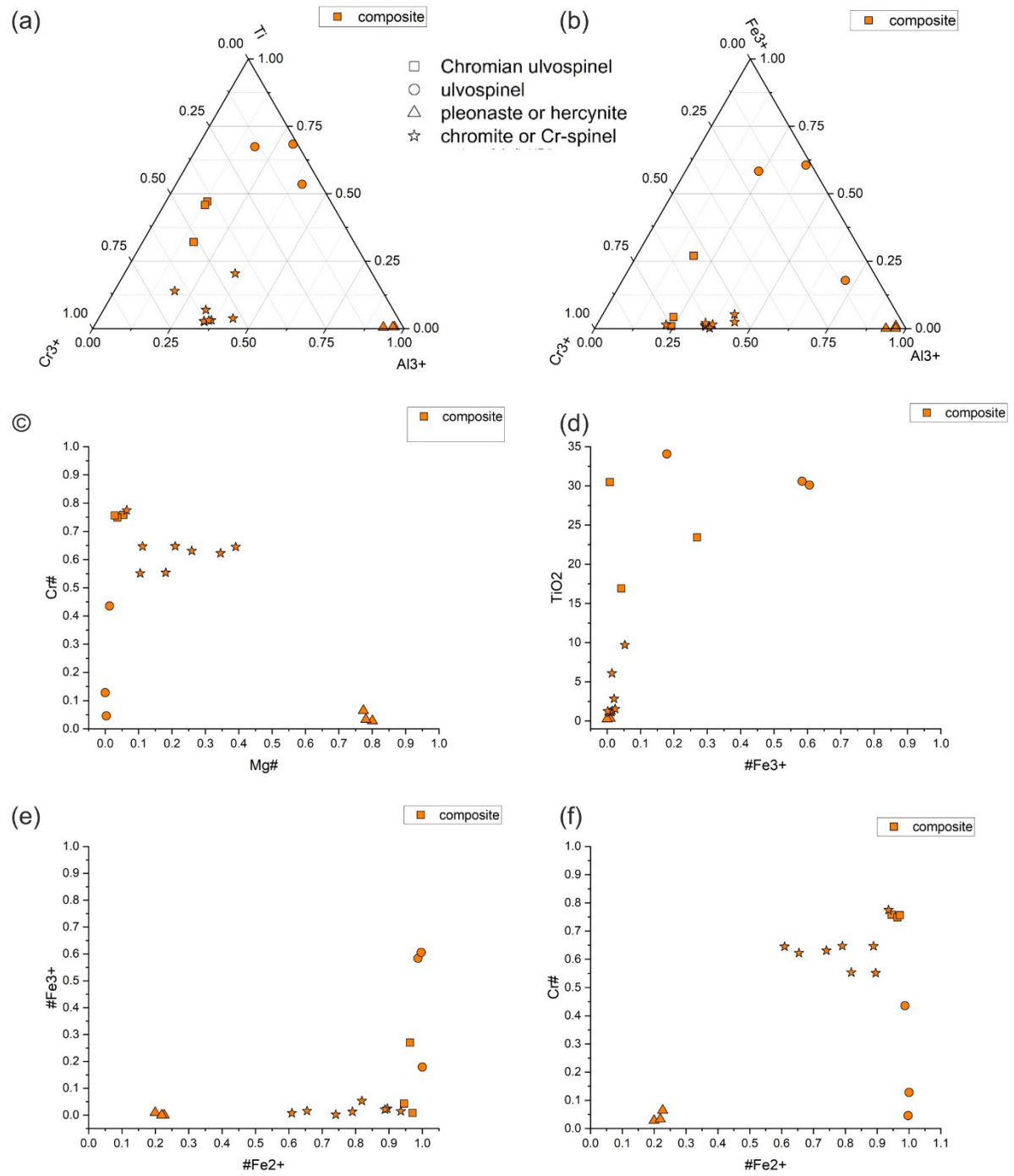


Figure 5.18: Compositional diagrams for spinels in composite samples.

5.3.1.8 Crustal cataclasite

In spinels from crustal cataclasite, Al_2O_3 (up to 60 wt%) and Cr_2O_3 (up to 60 wt%) are in greater contents, while FeO is <40 wt%, MgO is <20 wt%, and TiO_2 content is <10 wt% (Fig. 5.19).

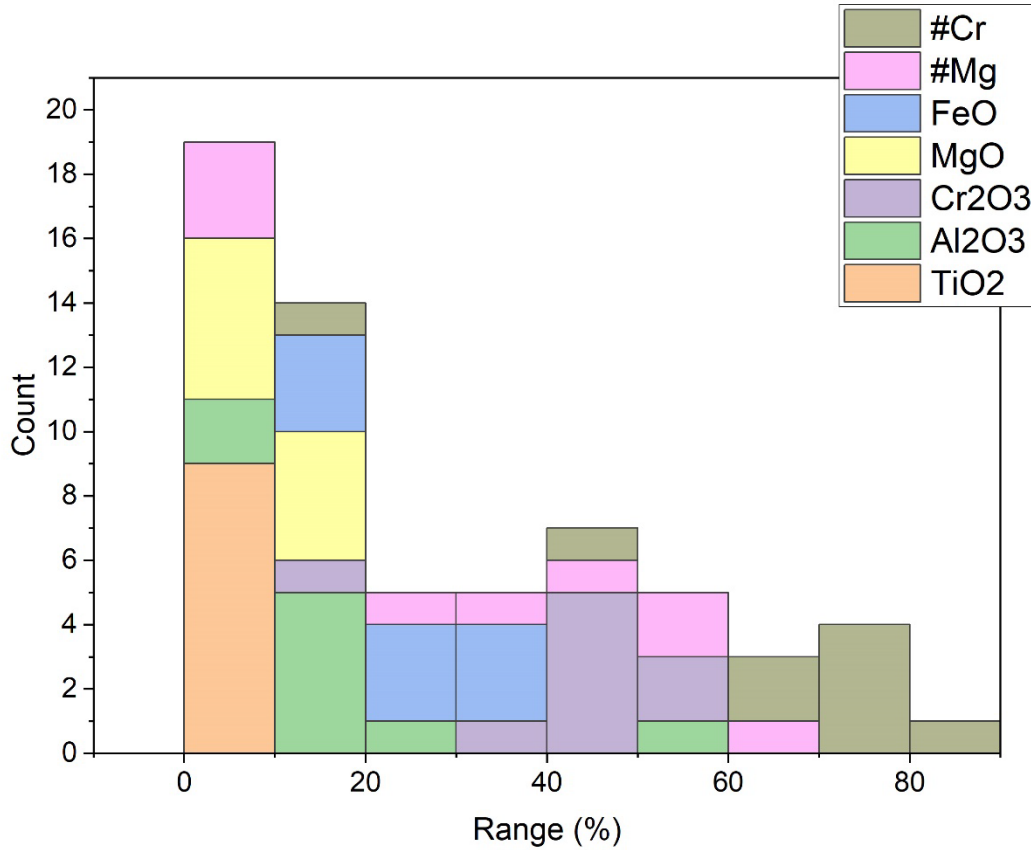


Figure 5.19: Histogram showing the oxide concentrations of the spinels in crustal cataclasites.

In crustal cataclasites, spinels are mostly chromites, with an Mg-Al spinel composition (Fig. 5.20).

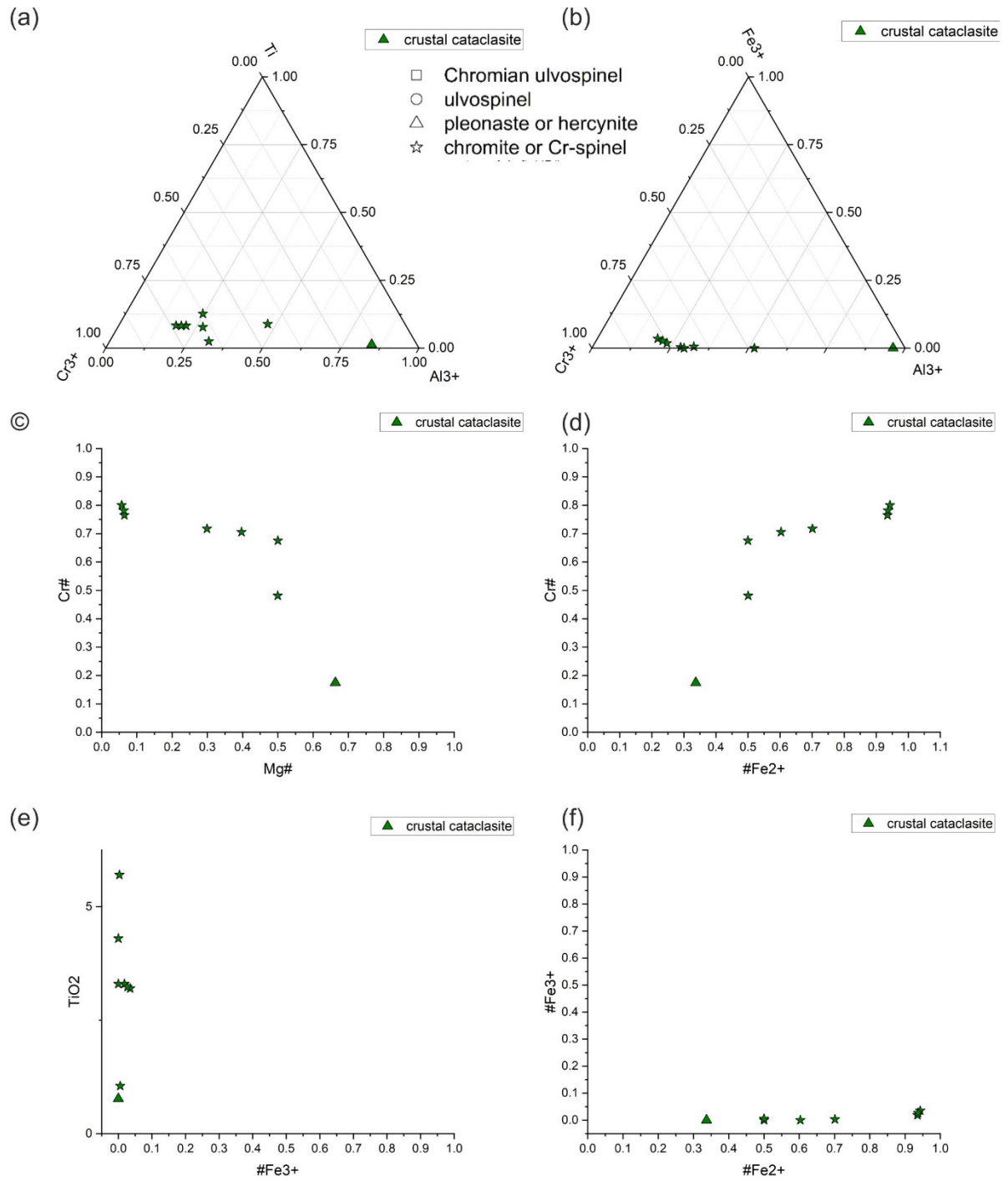


Figure 5.20: Compositional diagrams of spinels in crustal cataclasite.

5.3.1.9 Unclassified

The unclassified materials in returned lunar samples are reported to have spinels. In spinels from unclassified materials, Al_2O_3 (up to 15 wt%) and Cr_2O_3 (up to 50 wt%) are in greater contents, while FeO is <65 wt%, MgO is <10 wt%, and TiO_2 content is <35 wt% (Fig. 5.21).

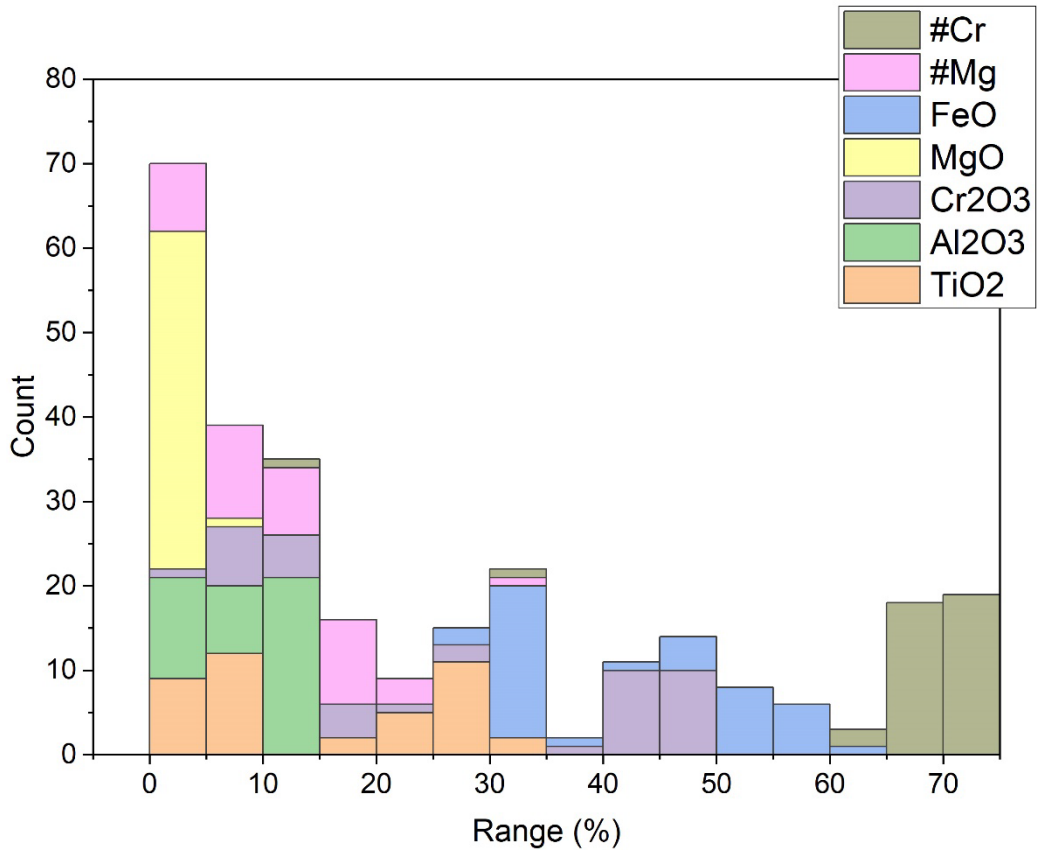


Figure 5.21: Histogram showing the oxide concentrations of the spinels in unclassified samples.

In unclassified materials, compositional clusters of chromites and chromian ulvospinel are observed (Fig. 5.22).

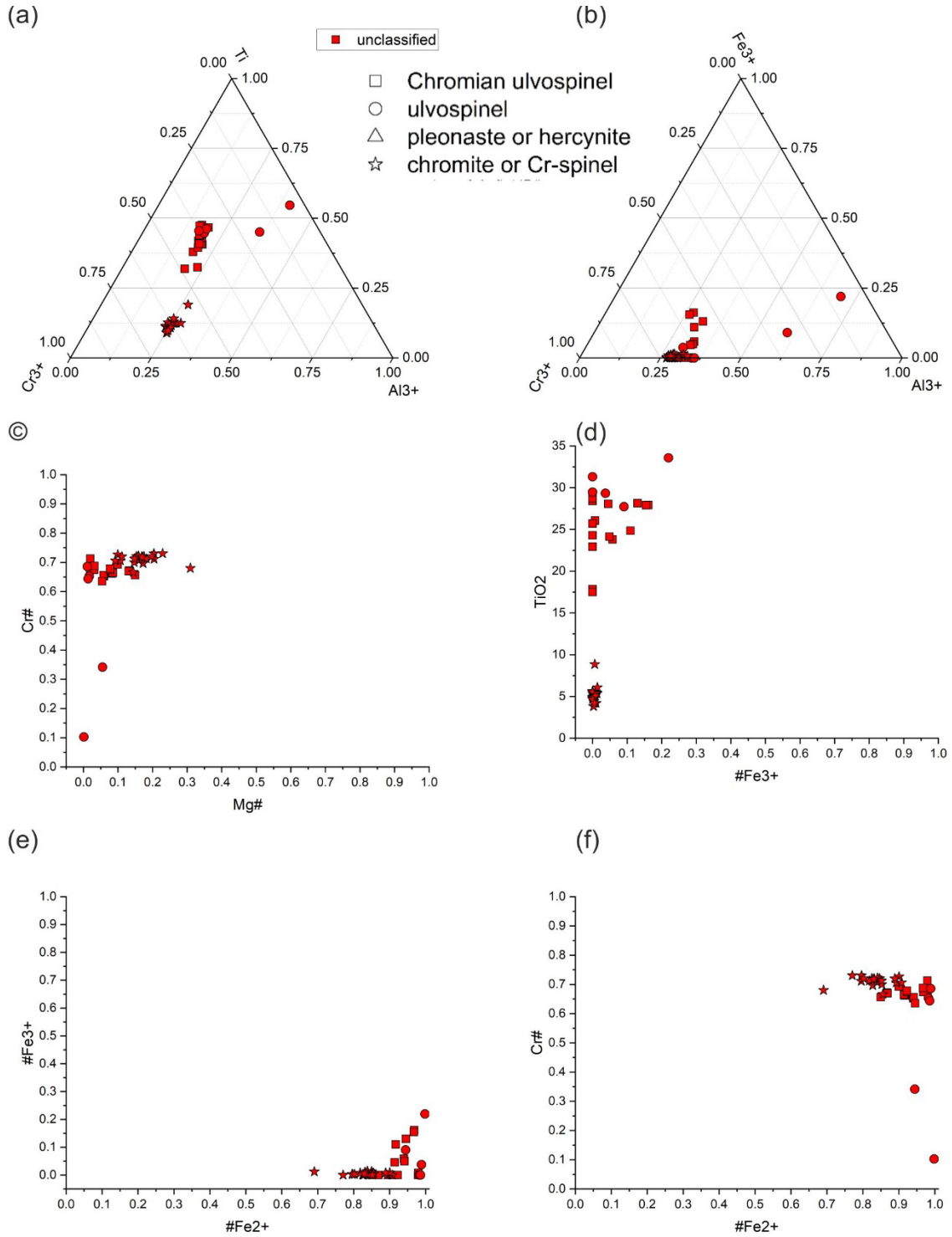


Figure 5.22: Compositional diagrams of spinels in unclassified rock. The legend is the same as Fig. 5.22a for all the plots.

5.4 Discussion and conclusions

Chromite or Cr-spinels and ulvospinels are abundant phases in lunar rocks (Fig. 5.4). Basaltic rocks and soil samples are rich in Cr spinels, whereas breccia and troctolites mostly contain aluminium spinels. The overall trend of lunar spinels is observed using ternary and bivariate plots (Fig. 5.4). Ulvospinel compositions from basalts, meteorites, breccia, and soil samples fall in the terrestrial spinel gap region (Fig. 5.4). The Cr# in ulvospinels vary over a range at nearly constant #Fe²⁺ and vice versa (Fig. 5.4). The #Fe³⁺ contents also vary over a nearly constant TiO₂ for lunar ulvospinels. Aluminium spinels show higher abundances of Mg# (Fig. 5.4).

The TiO₂ content ranges from ~0-40% in all the classified rocks (Fig. 5.3). The Al₂O₃ content (~0-20%) is lowest in spinels from basalts, unclassified rocks, and meteorites of returned lunar samples. Other rock categories show intermediate (~0-30%) to higher Al₂O₃ contents (~60-70%). The chromium content is showing higher abundances (~0 – >90%) in all the rock categories, with breccia, composite, and unclassified rocks showing slightly lesser concentrations (up to 80%). The FeO content is in intermediate ranges (~20-65%) in basalts and meteorites from returned lunar samples. The spinel compositions in other rock categories show FeO contents between ~0-70%, while the crustal cataclasites exhibit slightly lower FeO contents (~10-40%).

The MgO contents range between ~0-10% in basalts, meteorites from returned samples, and unclassified rocks. The spinels from breccia, composite, crustal cataclasite, soil, and troctolites show slightly higher MgO contents (~0-30%). Chromian ulvospinels, ulvospinels, and chromium spinels are the dominant phases in basalts (Fig. 5.4). Certain aluminium spinel compositions are identified from ilmenite- and olivine- basalts. The dominant phases are aluminium spinels in breccia, while fewer chromium spinels, ulvospinels, and chromian ulvospinels compositions are also identified. Ulvospinels and chromium spinels are abundant in meteorites of returned lunar samples, among which basalt meteorites show limited aluminium spinel occurrences. Chromium spinels are the prominent phases in crustal cataclasites. In soil samples, ulvospinels and chromian ulvospinels are prominently identified, along with fewer chromites and aluminium spinel compositions in soil fines. Aluminium spinels are abundantly seen in troctolites, with limited occurrences of chromites and chromian ulvospinels. A uniform distribution of chromites, ulvospinels, and chromian ulvospinels compositions is observed in composites and lunar meteorites. Yet, minor abundances of ulvospinels and chromites are observed in lunar meteorites. In unclassified rock, chromites and chromian ulvospinels are identified, along with some ulvospinels compositions.

The bimodal distribution between chromites and ulvospinel in basalts, soil samples, olivine meteorite, and basalt meteorite indicate that these compositions are primary crystallization products (Haggerty, 1971) (Fig. 5.4). The intermediate compositions can be formed by rapid quenching or metastable crystallization. In general, one of the three methods listed below can produce intermediate members of the spinel series (Haggerty, 1972). 1) first-order crystallization products. 2) when early produced, Mg-aluminium-chromite reacts with liquid, resulting in intermediate compositions at the gradational interface between the Cr-rich core and Ti-rich borders. 3) Cr-Al-ulvospinel re-equilibration via strong subsolidus reduction. Since impact activities are common on Moon, the spinels of intermediate compositions can form by subsolidus recrystallization.

5.4.1 Comparison with compositional fields of terrestrial spinels

The data density contours were drawn for lunar spinel data and are compared with terrestrial spinels of diverse magma types (Figs. 5.23 and 5.24).

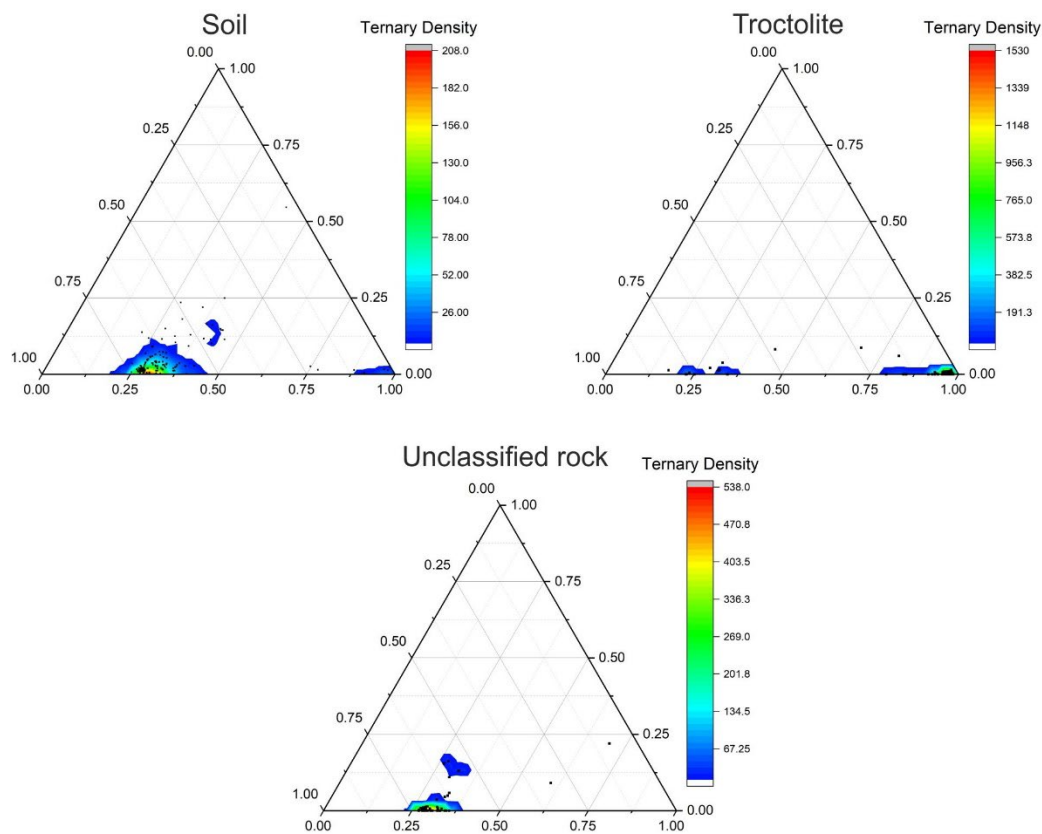


Figure 5.23: Data density plots derived for spinel compositions in soil, troctolite, and unclassified rock.

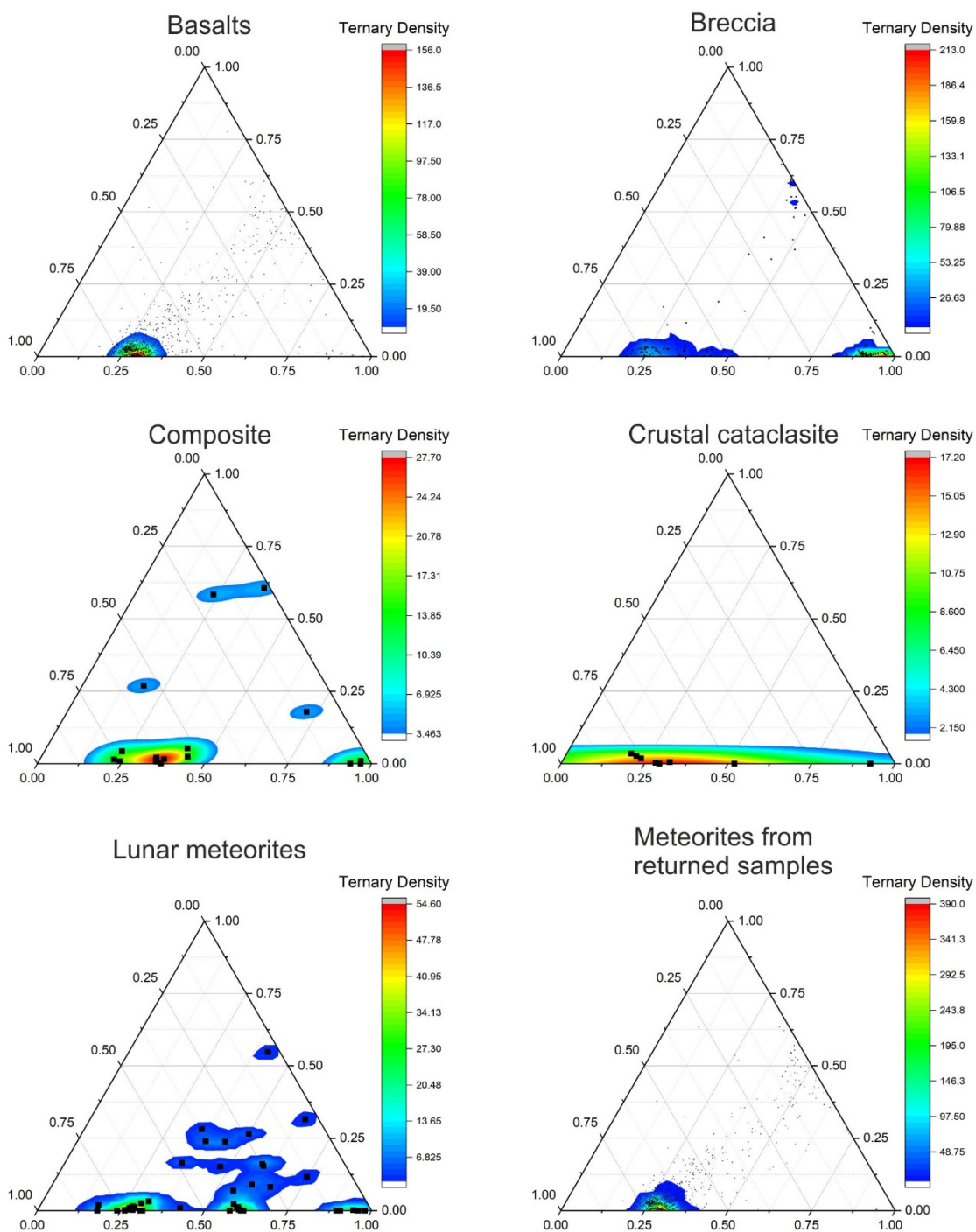


Figure 5.24: Data density plots derived for spinel compositions in basalts, breccia, composite, crustal cataclasite, lunar meteorites, and meteorites from returned samples.

In comparison with the terrestrial spinels, lunar spinel compositions strongly overlap with those from boninites (Fig. 5.25). These lunar compositions have features that fall somewhere between boninite and Komatiite (Fig. 5.25), with a general similarity to boninites but a larger range in Cr³⁺ extending to less Cr-rich compositions. Boninites are the only natural magmas that usually contain Cr-rich spinels (Barnes and Roedder, 2001). This suggests that the average parental magma to these chromite compositions is closer to the boninite end. These chromite compositions are thought to be derived from very depleted and thus Al-poor mantle (Crawford and Cameron, 1985). Komatiites are similarly high-degree partial melts of the depleted mantle, with high Cr/Al ratios in the melt, and should be predicted to produce substantially more Cr-rich chromites than boninites, despite the fact that the spinel populations are nearly identical (Barnes and Roedder, 2001).

Chromites found in komatiites and boninites fields indicate initial crystallisation from primitive, unfractionated mantle-derived magmas (Barnes and Roedder, 2001). The high Cr can be attributed to melt composition in both situations, as both magma forms have high Cr: Al ratios (Barnes and Roedder, 2001). This occurs in boninites due to earlier depletion of the mantle source, whereas it occurs in Al-depleted komatiites due to Al retention in the source by majorite garnet (Ohtani et al., 1988; Fan and Kerrich, 1997; Inoue et al., 2000). The solubility of chromium and iron in basaltic melts is highly dependent on oxygen fugacity (Hill and Roeder, 1974, Roeder and Reynolds, 1991). Because the 2+ oxidation state of chromium, like that of iron, is more soluble than the 3+ state, the low oxygen fugacity of the basaltic melts on the lunar surface resulted in melts with higher chromium and iron levels (Roeder, 1994). The greatly reduced character of these komatiitic chromites is related to magma composition, and it could eventually represent the mantle source (Barnes and Roedder, 2001).

It is to be noted that in igneous rocks, chromite almost usually crystallises in association with olivine (Roeder, 1994). Both chromite and olivine are early cocrystallizing phases, however, both minerals tend to react with the melt and be replaced by pyroxene at some point (Irvine, 1965). Both fayalitic olivine and a spinel phase, magnetite, can return as crystallising phases as the melt produced by fractional crystallisation of basalt becomes higher in iron. Early chromite reacts with melt to form pyroxene, which has a higher chromium content than the melt (Roeder, 1994). Hence, the geological controls on these lunar spinels, such as the interaction between the co-existing olivine and pyroxene phases, are not well understood. This limits a more accurate conclusion on their origin. Future studies using orbital data and future returned samples will put better constraints on these inferences.

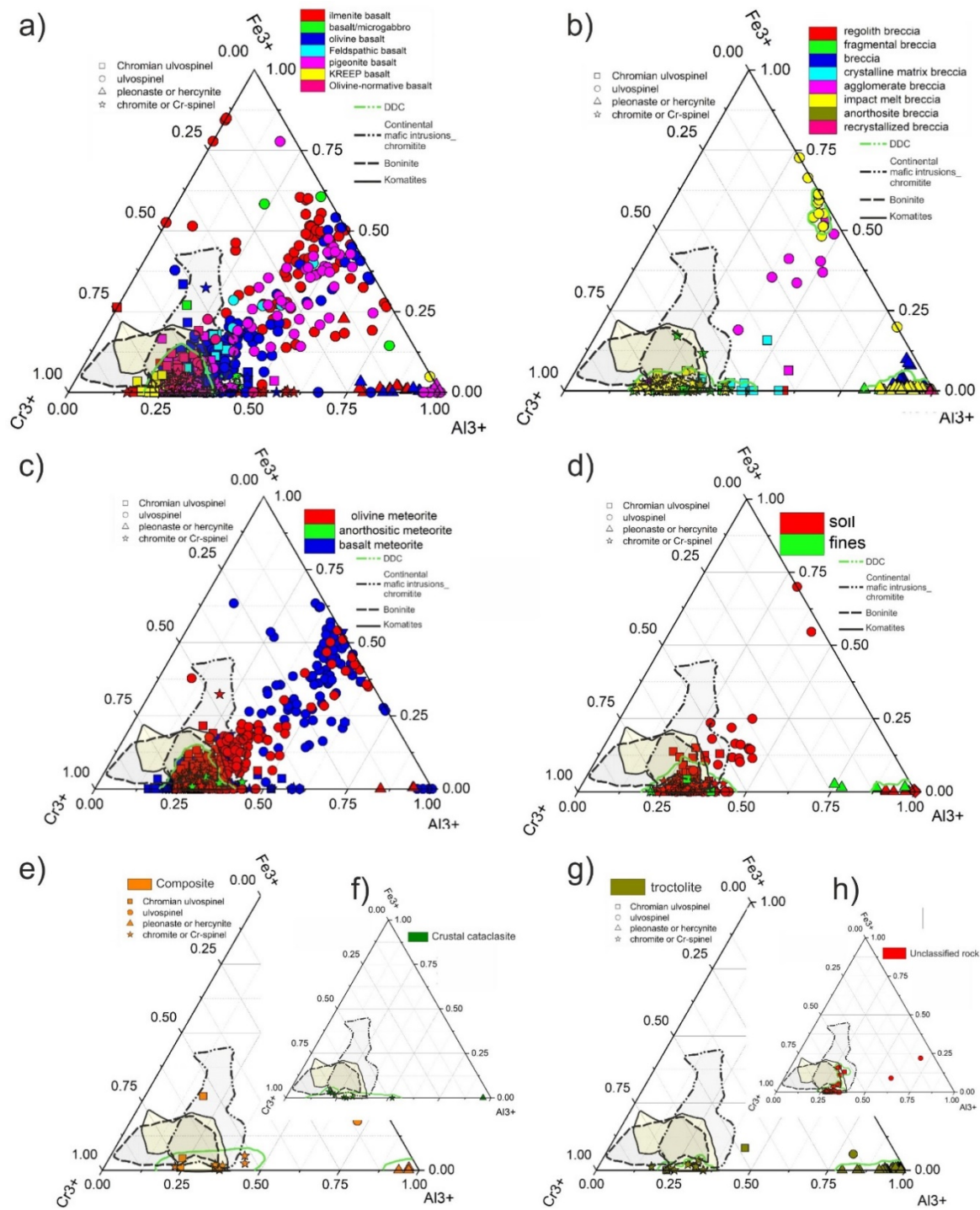


Figure 5.25: Ternary plot showing the comparison of lunar spinel compositions with fields of terrestrial spinels from komatiites, boninites, and layered intrusions.

Chapter 6

Compositional and Spectrochemical Analyses of Chromium Spinel in the Sittampundi Anorthosite Complex, Southern India: Implications for Remote Observation of Spinel on the Moon

Overview

The spectroscopic techniques such as Laser Raman, Fourier Transform Infrared (FTIR), and hyperspectral have been used widely to understand the mineral chemistry and crystal structure and identify the functional phases and organic molecules in geological materials on Earth and other planetary bodies. The present study used these spectroscopic techniques combined with X-ray Diffraction (XRD) and Electron Probe Micro Analysis (EPMA) to understand the spectral-compositional relationships of the Cr-spinel (Chromian spinel) present in chromitite bodies associated with Sittampundi Anorthosite Complex (SAC), southern India. The bands/lenses of Cr-spinel are found as layers (a few centimeters to 6 m thick) intercalated with anorthosites and clinopyroxenites of the SAC. The cumulate Cr-spinels of the study area exhibit compositions ranging between Al-chromite and Cr-spinel. Fe-, Al-rich Cr-spinel is a characteristic of the SAC with Cr₂O₃ content ranging from ~32–37 wt% and Cr# (Cr/[Cr + Al]) in the 0.44 to 0.53 range.

The XRD spectra of these Cr-spinels have shown characteristic peaks corresponding to its constituent phases, with the highest peak at 36.11° . The observed longward shift in the Raman A_{1g} peak ($\sim 705\text{--}714\text{ cm}^{-1}$) is likely to be caused by the substitution of Al^{3+} in the spinel structure. The Raman A_{1g} peak position near 705 cm^{-1} in the spectra is attributed to the coexistence of (Mg, Fe) in the tetrahedral site and (Al, Cr) in the octahedral site. The broader and stronger $2\text{ }\mu\text{m}$ band position in the hyperspectral data is at relatively shorter wavelengths than typical Cr-spinels due to enhanced Al content ($Al_2O_3 \sim 25\text{ wt}\%$) in the SAC samples. The $2\text{ }\mu\text{m}$ band position is observed to have a longward shift with increasing Cr_2O_3 and Cr# abundances and a corresponding shortward shift with enhanced Al_2O_3 content in Cr-spinels. The linear relationship between the $2\text{ }\mu\text{m}$ band position and Cr/Al abundances indicates that this absorption band is significant in distinguishing Cr-spinels from Al-spinels. Based on spectral and compositional resemblance, Fe- and Al-rich Cr-spinels in SAC are considered as probable terrestrial (functional) analogues for similar lunar spinel compositions given that evidence-based correlation of intricate processes involved in their formation under the lunar and terrestrial conditions. The present study demonstrates the approach of applying spectrochemical characteristics of terrestrial analogue spinels for remote identification of lunar spinels and retrieving their compositional ranges from the spectral reflectance parameters.

Keywords: Chemical and spectral analyses, Cr-spinel, Sittampundi Anorthosite Complex, Southern India, Lunar spinels, Terrestrial analogue

6.1 Introduction

The VIS-NIR (VNIR) reflectance, Laser Raman, and FTIR spectroscopy are the widely used and powerful techniques to characterize the geological materials on the Earth and other planetary surfaces. These techniques were effectively employed for identifying the mineralogy, crystal structure, functional phases, and organic molecules on planetary surfaces (Terada and Maekawa, 1964; Malezieux and Piriou, 1988; Cloutis et al., 2004; Wang et al., 2004; Williams et al., 2016; Sarkar et al., 2019; Thesniya et al., 2021b). Laser Raman spectroscopy relies on the scattering of light when monochromatic light of a particular frequency strikes a sample (Raman, 1928; Raman and Krishnan, 1928). Raman spectroscopy has numerous advantages over IR and VNIR spectroscopic techniques in terms of the sharpness of spectral features enabling the detection of certain minerals, rocks, and/or glasses explicitly

(McMillan, 1985; McMillan and Hofmeister, 1988; Nasdala et al., 2004; Dubessy et al., 2012). Scientists successfully used Raman spectroscopy to investigate the presence of organic molecules in frozen ices (Spinella et al., 1991; Ferini et al., 2004) and the detection of homopolar molecules like H₂, N₂, and O₂, which are otherwise IR inactive. Scientists have also used the Raman spectrometer for studying the spectral behavior of CO₂ ices and organic compounds in interstellar ice analogues (Bennett et al., 2013). This technique allows identifying different mineral compounds and mineral mixtures or rocks based on their characteristic peaks at frequencies corresponding to the constituent phases present in the sample. The compositional variations arising from the substitution of cations can also be inferred from Raman spectra. A Deep Ultraviolet (DUV) Raman spectrometer (248.6 nm-laser wavelength) named 'SHERLOC' (Scanning Habitable Environments with Raman and Luminescence for Organics and chemicals) has already flown on NASA's MARS 2020 rover – Perseverance to probe for the detection of minerals, organic molecules, and possibilities of biosignatures on the Mars. Fourier Transform Infrared Spectroscopy (FTIR) has also been used extensively in material characterization as the geologically significant minerals, and inorganic molecules are infrared active. The IR spectrometers operate in the 2.5–15 μm range (4000–500 cm⁻¹). FTIR spectra allow recognizing the functional groups present in the mineral, based on their stretching and bending vibrations that arise from the absorption of light of specific wavenumbers (Lyon and Burns, 1963; Lyon, 1964, 1965; Conel, 1965). The wavenumber at which the light is absorbed is unique and allows us to distinguish different functional groups and thereby understand the structural chemistry of the minerals.

VIS-NIR optical spectroscopy is also a widely used method for the characterization of Earth and planetary materials. Many VNIR spectrometers have flown in various exploration missions to Mars, Moon, Asteroids, and other solar system bodies and provided information about the chemical makeup of these planetary bodies (e.g., Pieters et al., 2011). VNIR spectrometers commonly operate within the wavelengths ranging from 0.4 to 2.5 μm, and their functions are based on electronic transition absorptions in the transition group metallic ions, which allows the identification of minerals or mineral mixtures on planetary surfaces (Hunt and Salisbury, 1970; Burns, 1993). The spectral slope, pattern, and diagnostic absorption features manifest the chemical makeup of the observing materials. The minerals can be identified, and their chemistry can be retrieved based on band parameters such as band center and band strength (Nash and Conel, 1974; Singer, 1981; Clark, 1983; Cloutis et al., 1986; Mustard and Pieters, 1989). VNIR spectroscopic method was also applied to distinguish different textural variants of chromian spinels based on their varying spectral manifestations (Guha et al., 2018; Sarkar et al., 2019). Therefore, a combination of Raman, FTIR, and VNIR spectroscopic analyses will

provide complementary information about the surface composition and chemical buildup of planetary bodies, especially of our Earth's Moon.

Earth's Moon has always been of great interest to planetary scientists because of its proximity to Earth and its spectacular geological diversity. Olivine, pyroxene, spinel, and plagioclase are the typical mafic phases on the Moon. These minerals exhibit unique spectral signatures, making them identifiable through remote sensing observations (Adams, 1974; Hazen et al., 1978; Cloutis and Gaffey 1991; Sunshine and Pieters, 1993; Klima et al., 2007, 2008, 2011a). The spinel has a typical structure with a cubic arrangement of oxygen atoms. The chemical formula of spinels comprises two units ($^{IV}(\text{Fe}^{2+}, \text{Mg}^{2+})^{VI}(\text{Cr}^{3+}, \text{Fe}^{3+}, \text{Al}^{3+})_2 \text{O}_4$) in a primitive unit cell. The divalent cations (Fe^{2+} or Mg^{2+}) in lunar spinels occupy the A site and/or both the A and B sites, whereas the cations of higher charges (Cr^{3+} , Al^{3+} , Ti^{4+}) occupy only the B site in the spinel structure. The spinels (AB_2O_4 , A: $\text{Fe}^{2+}/\text{Mg}^{2+}$, B: $\text{Fe}^{3+}/\text{Al}^{3+}/\text{Cr}^{3+}$) form complete solid solutions due to the substitution of Fe^{2+} and Mg^{2+} ions in tetrahedral sites and Cr^{3+} , Al^{3+} , and Fe^{3+} ions in octahedral sites in their structure. Among the spinel group of minerals, chromian spinel is significant owing to its role as a petrogenetic indicator (e.g., Irvine, 1965; Irvine, 1967; Arai, 1992; Barnes and Roeder, 2001). This primary mineral is recognized as the second most abundant opaque mineral on the Moon after ilmenite (cf. Heiken et al., 1991). Chromian spinels are one of the first minerals to get crystallized from mafic-ultramafic magma. The study of magmatic spinels in mafic-ultramafic rocks discloses information about the mantle and crust-mantle interaction processes (e.g., Irvine, 1965; Irvine, 1967; Sack and Ghiorso, 1991; Arai, 1992; Barnes and Roeder, 2001). Also, the chromian spinels are relatively resistant to post-magmatic alterations, including metamorphism (e.g., Suita and Streider, 1996). Hence, the chemical composition of chromian spinels provides important insight into the geodynamic evolution of the planetary body (Irvine, 1967; Evan and Frost, 1975; Arai, 1980; Sack, 1982; Engi, 1983; Arai, 1994; Barnes and Roeder, 2001; Arai et al., 2011).

On the Moon, commonly reported spinels are chromian spinels and Mg-Al spinels (Pieters et al., 2011; Yamamoto et al., 2013; Pieters et al., 2014; Prissel et al., 2014; Weitz et al., 2017). The lunar spinel compositions were understood mostly through remote sensing observations and chemical analyses of returned lunar samples. Remote identification of Cr- and Mg-Al spinels were possible based on their diagnostic absorption characteristics in the remotely observed reflectance spectra (e.g., Pieters et al., 2011). The identification of remote sensing data was solely based on the comparison with reference spectra obtained from the spectral measurements of terrestrial samples and returned lunar samples. Therefore, understanding the spectral-compositional relationship of terrestrial spinels is essential to infer the chemistry of

spinel group minerals on the Moon using their remotely observed reflectance spectra, which will enable us to infer the Moon's evolutionary history.

The Cr-spinels in chromitite bodies associated with the Sittampundi Anorthosite Complex in southern India are chosen as the potential candidate for the spectrochemical characterization of terrestrial spinels in the present study. The Sittampundi Anorthosite Complex in Tamil Nadu, southern India, is a Neoarchean layered igneous complex emplaced within the Palghat-Cauvery Shear Zone in Southern Granulite Terrain (SGT) of peninsular India (Bhaskar Rao et al., 1996) (Fig. 6.1a). The anorthositic complexes are considered geologically significant, as they represent magmatic rocks of the Archean to Phanerozoic age evolved from the mantle (Ashwal, 1993). The Sittampundi Anorthosite Complex has attracted significant geological consideration for the presence of conformable horizons of chromitite layers in association with highly calcic anorthosites and clinopyroxenites within the SAC (Subramaniam, 1956; Windley et al., 1981; Bhaskar Rao et al., 1996; Dutta et al., 2011; Brandt et al., 2014) (Fig. 6.1b). A magmatic origin was suggested for these intercalated sequences of chromitites, anorthosites, and clinopyroxenites in the complex based on their petrological and tectonic characteristics (Subramaniam, 1956; Dutta et al., 2011; Ghosh and Konar, 2011; Dharma Rao et al., 2013).

The anorthosites in the SAC have been considered chemically analogous to lunar highland anorthositic rocks based on their spectral and chemical analyses (Anbazhagan and Arivazhagan, 2010; Anbazhagan, 2012). Based on similarities in geotechnical and geomechanical properties of the SAC anorthosites with those of lunar highland anorthosites, a lunar highland soil simulant was developed to test the lander and rover in the Chandrayaan-2 mission (Venugopal et al., 2020a; 2020b). The chromite-rich layers (as thick as ~5 m) in the chromitite bodies were composed of about 60–70% granular chromite with 30–40% amphiboles and other accessory phases (Ghosh and Konar, 2011). The chromites and spinels were studied for understanding their mineralogy, textural variations, magmatic and metamorphic history, and petrogenesis (Dutta et al., 2011; Ghosh and Konar, 2011; Ghosh, 2011; Dharma Rao et al., 2013; Karmakar et al., 2017; Talukdar et al., 2017). The chromitite bands were suggested to be crystallized from a Fe, Al-rich basaltic melt, formed by the evolution of an initial basic magma through fractionation of peridotite and pyroxenite (Ghosh and Konar, 2011). At the same time, several authors proposed chromitite crystallization from a parental magma of tholeiitic composition generated by partial melting of aluminous harzburgite (Dutta et al., 2011; Dharma Rao et al., 2013). A recent study by He et al. (2020) suggested that melt injection and subsequent mixing in the anorthositic mush caused the saturation of SAC-hosted Cr-spinels.

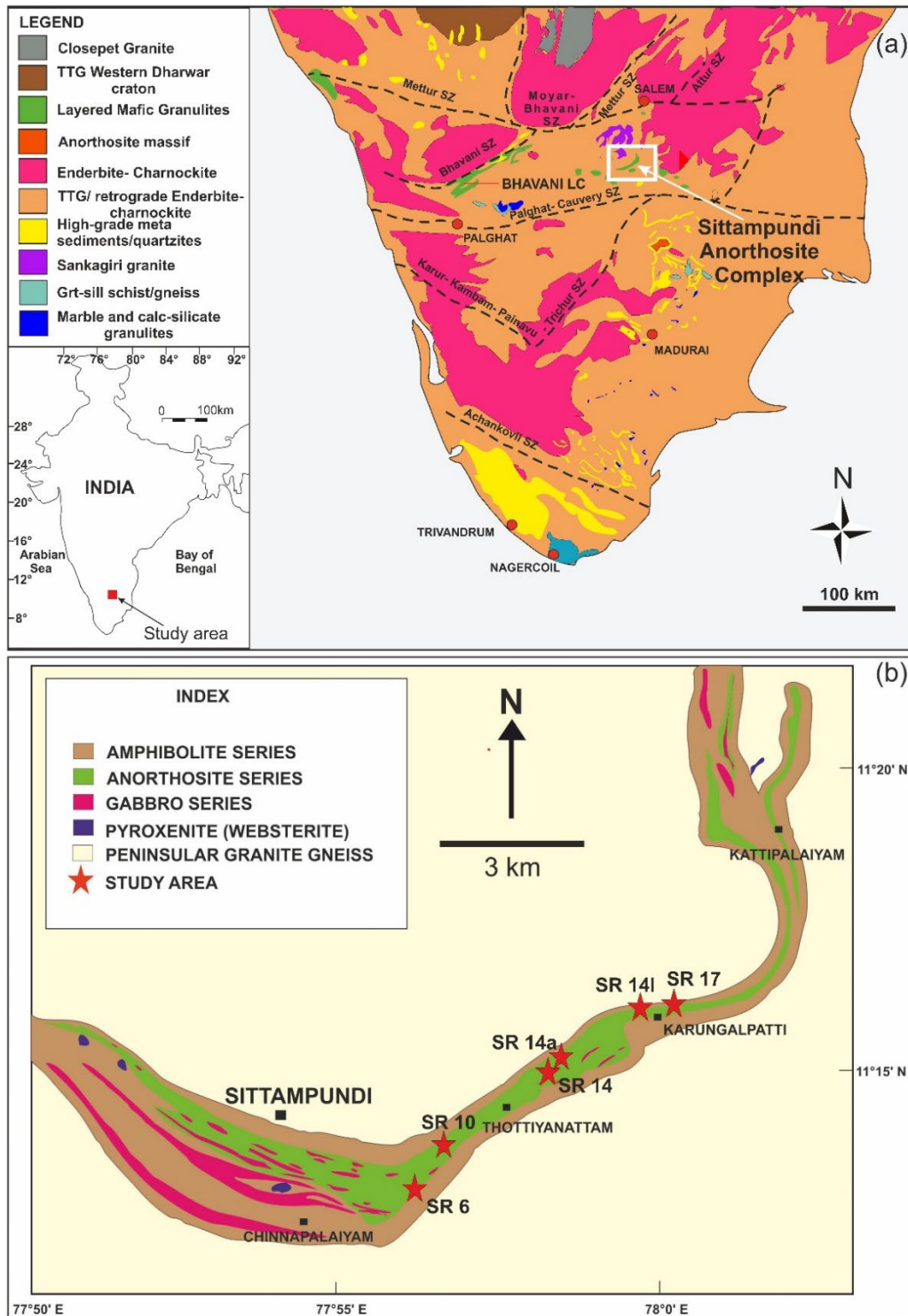


Figure 6.1: (A) Generalized geological map and tectonic framework of the Southern Granulite Terrain (modified after the Geological Survey of India, 2001; Karmakar et al., 2017). Abbreviations: SZ, Shear Zone; LC, Layered Complex (B) Detailed geological map of the Sittampundi Anorthosite Complex showing the distribution of various lithologies (after Subramaniam, 1956). The sample locations of the present study are labeled.

Although comprehensive studies were carried out on the petrological characteristics and origin of the Cr-spinels associated with the SAC, the possibilities of Cr-spinels as a probable functional analogue for similar lunar spinel compositions are yet to be explored. The present study attempts to investigate the chemical-spectral relationship of terrestrial chromian spinels from Sittampundi Anorthosite Complex using a combination of VNIR, Laser Raman, and FTIR spectroscopic techniques and comparing their spectrochemical characteristics with the spectral features of remotely detected Fe- and Cr-bearing spinels on the Moon. Though the SAC is highly metamorphosed, and the chromitite bodies have shown metamorphic imprints, the chromites of magmatic compositions were also found in chromitite bodies (Suita and Streider, 1996; Dutta et al., 2011; Ghosh and Konar, 2011; He et al., 2020). These Cr-spinels in SAC having moderate Cr# (0.44-0.53) are focused on for the spectrochemical characterization in the present study. The changes in the spectral pattern and absorption or peak centers as a function of the varying chemistry and crystal structure of SAC Cr-spinels have been discussed. We also apply our results to the spectral data of Sinus Aestuum spinels on the Moon as an analogue to the orbital measurements of lunar surface compositions.

Though the orbital detections of spinels on the Moon were mainly Mg-Al spinels and limited Fe-spinel, compositions having Cr₂O₃, Al₂O₃, FeO, and Cr# similar to SAC compositions are present on the Moon (14303,50, Roedder and Weiblen, 1972; Yamamoto et al., 2013; Weitz et al., 2017). The identification and compositional interpretation of these types of lunar spinels from their reflectance spectra are generally challenging due to many factors such as space weathering effects, mixing with other components, etc. (Pieters et al., 2011; Gross et al., 2015). Besides, the effects of metamorphism on the Moon are least known except for some granulitic impactite suites found in returned Apollo samples (e.g., Miura and Kato, 1992). Therefore, a direct genetic analogy of the SAC Cr-spinels with those on the Moon would be an oversimplified assumption. Rather, the present approach of the comparative spectral-chemical studies will help identify compositionally similar lunar spinels from their reflectance spectra and thereby refine the constraints on the compositional diversity of remotely observed lunar spinels. Since the in-situ observations of the spinels on the Moon are limited in the current scenario, orbital remote sensing observations of the lunar surface will continue to take precedence, and therefore, the results from our study would be a reference for remote identification of compositionally similar lunar spinels.

6.2 Geological setting

The Southern Granulite Terrain (SGT), constituting the southernmost end of the Indian shield, comprises late Archaean to Neoproterozoic high-grade metamorphic blocks, which are dissected by roughly E-W trending crustal-scale shear zones (Chetty, 1996; Janardhanan, 1999; Meißner et al., 2002; Ghosh et al., 2004; Brandt et al., 2014; Sengupta et al., 2015; Raith et al., 2016) (Fig. 6.1a). The Palghat-Cauvery Suture Zone (PCSZ) is a prominent collisional suture zone (to the direct north of SGT) that marks a tectonic boundary within the SGT between the northern Archaean terrain and the southern Neoproterozoic mobile belt (Cenki et al., 2005; Santosh et al., 2006; Chetty and Bhaskar Rao, 2006; Collins et al., 2007; Santosh et al., 2009; Clark et al., 2009; Naganjaneyulu and Santosh, 2010; Santosh et al., 2011; Ghosh and Konar 2011; Dharma Rao et al., 2013). The PCSZ comprises amphibolite to granulite facies orthogneisses within which anorthositic igneous complexes such as SAC and Kanjamala are emplaced (Subramaniam, 1956; Mukhopadhyay and Bose, 1994; Saitoh et al., 2011) (Fig. 6.1a).

The Neoproterozoic Sittampundi Anorthosite complex (SAC) ($11^{\circ}14'N$, $77^{\circ}54'E$) is a prominent metamorphosed anorthositic complex emplaced within the orthogneisses of the PCSZ (Subramaniam, 1956; Janardhanan and Leake, 1975; Windley and Selvan, 1975; Windley et al., 1981; Bhaskar Rao, 1996) (Fig. 6.1a and b). The SAC is located in the Namakkal district of Tamil Nadu state in southern India. The complex forms an approximately 2 km wide arcuate belt stretching from Cholasiramani in the west to Kottakkalpalaiyam in the east along a 36 km strike length (Fig. 6.1b). While anorthosites are the dominant rock types, the bottom of the complex also contains discontinuous layers of ultramafic rocks (namely pyroxenites, peridotites), gabbro, and granulite/eclogite lenses (Fig. 6.1b). The SAC is surrounded by the older amphibolite grade hornblende-biotite gneisses and migmatitic hornblende gneisses (TTG gneisses), of which the pegmatitic veins and tongues of TTG are intruded into the anorthosites in the complex (Ghosh and Konar, 2011). Stratigraphically, the SAC consists of dunites at the bottom, chromite-layered clinopyroxenite, chromite-layered anorthosite, clinopyroxenite-layered gabbro towards the top (Dutta et al., 2011) (Fig. 6.1b). Several authors investigated the lithological units of this complex for understanding the tectonic history, petrological and mineralogical characteristics, geochronology, geochemistry, and structural relationships (Subramaniam, 1956; Ramadurai et al., 1975; Janardhanan and Leake, 1975; Drury et al., 1984; Bhaskar Rao et al., 1996, 2003; Mukhopadhyay et al., 2003; Ghosh et al., 2004; John et al., 2005; Shimpo et al., 2006; Rao et al., 2006; Sengupta et al., 2009a, b; Ghosh and Konar, 2011; Ghosh and Konar, 2012; Dharma Rao et al., 2013; He et al., 2020). The SAC is

overprinted by granulite-upper amphibolite facies of metamorphism (Bhaskar Rao et al., 1996). The rocks of this complex were compared to Greenland's Fiskenaesset complex (Ghisler, 1970; Windley and Selvan, 1975). The present arcuate pattern of the SAC is demonstrated by the tight isoclinal antiform structure, which was later refolded into an open fold having a N-S trending axial plane (Fig. 6.1b). The SAC comprises repeated stratigraphic sequences resulting from this isoclinal structure (Ramadurai et al., 1975). The earlier fold is sometimes replicated in the anorthosites (Ghosh and Konar, 2011).

The chromitites occur as continuous to discontinuous bands and lenses, hosted by anorthosites and clinopyroxenites in the complex. The chromitite layers in anorthosites are thin (<1 m), while up to 6m thick seams are found in chromiferous amphibolite schist (altered clinopyroxenites) (Subramaniam, 1956; Ghosh and Konar, 2011). The Cr# ($Cr/(Cr + Al)$) in SAC Cr-spinels was estimated to be between 0.44 and 0.53 (Ghosh and Konar, 2011). The Cr₂O₃ content varies between 34 and 40 wt%, while Al₂O₃ ranges from 23 to 28 wt%. The chromitite layers and their host anorthosites and amphibolites have undergone intense post-crystallization deformation (Dutta et al., 2011). The chromite-bearing clinopyroxenites are largely retrograded into amphibole-chlorite schists at several places (Dutta et al., 2011). Dutta et al. (2011) discovered magmatic and metamorphic imprints in the chromite in chromitite bodies hosted by the anorthosites and clinopyroxenite. The metasomatic replacement of chromites under the amphibolite facies conditions gave rise to green spinels having Cr# between 0 and 0.1 (Dutta et al., 2011; Talukdar et al., 2017). At places, the SAC has retained its intact igneous nature despite the high-grade metamorphic overprint (Dharma Rao et al., 2013). Also, a recent study proposed a magmatic origin for amphiboles in chromitites (He et al., 2020). The presence of highly calcic plagioclase (An₉₀₋₁₀₀) in anorthosite and Fe, Al-rich chromites indicate a hydrous tholeiitic parental magma for chromites, generated by partial melting of aluminous harzburgite in a supra-subduction zone oceanic arc environment (Dutta et al., 2011; Dharma Rao et al., 2013).

6.2.1 Mode of occurrence of chromitites in the SAC

The outcrops of hornblende-biotite gneisses, anorthosites, metapyroxenites, and other mafic rocks were found along the arcuate stretch of SAC. The study areas are located in the southern stretches of SAC, where exposures of chromitites and associated rocks are conspicuously present (Fig. 6.1b). The anorthosites host conformable layers of chromitites in varying thicknesses extending from several meters to kilometers along the strike. Chromitites are

observed in lenses and bands between Karungalpatti and Sittampundi regions (Figs. 6.1b and 2a-d). Massive chromitites were found in the area near Karungalpatti (Fig. 6.2a-b). The disseminated and massive forms of chromitites were found in association with amphibolites in the region (Fig. 6.2a-c). Cr-spinels are dark gray to black with a metallic to submetallic luster and have high specific gravity. Cr-spinels in these chromitite layers occur as granular aggregates in close association with amphiboles.

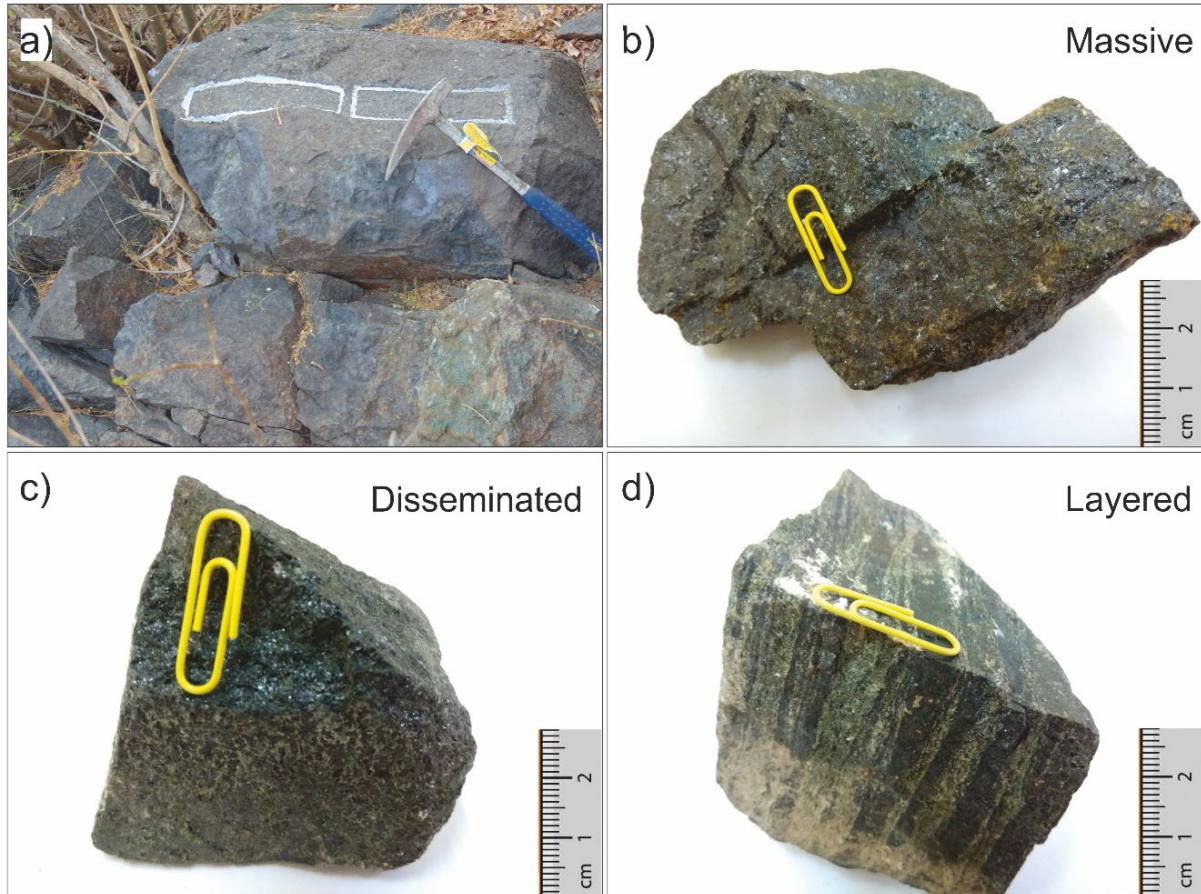


Figure 6.2: (A) Field photograph of chromitite-rich amphibolite outcrop in SAC. (B) Photographs of the massive type (C) disseminated type, and (D) layered type chromitites collected from the SAC.

6.3 Methodology

6.3.1 Sample preparation

The Cr-spinel samples were systematically collected from the field outcrops in Karungalpatti, Thottiyannattam, and Chinnapalaiyam areas of the Sittampundi Anorthosite Complex. The

collected samples were packed in polythene covers to avoid any chemical alterations and carefully numbered based on the sample location. Later, the samples were cleaned adequately in the lab and made into small chips. The thin sections were prepared using the laboratory facility at the National Centre for Earth Science Studies (NCESS, Thiruvananthapuram). The remaining samples were then crushed, ground, and powdered for chemical and spectral analyses (XRD, Laser Raman, hyperspectral, and FTIR).

6.3.2 Chemical and spectral analyses

The X-ray diffraction (XRD) gives information about the structure of crystalline materials analyzed. The characteristic peaks are unique for each crystalline material and can be used as a “fingerprint” for mineral identification. XRD analysis of the Cr-spinel samples was carried out at the Department of Physics, University of Kerala. Bruker D8 ADVANCE with DAVINCI design XRD system was used for the analysis. The instrument used Cu target and N filter, operated at 40 mA current and 40 kV. The samples are scanned for 10 to 80° 2 θ range with a scanning speed of 0.045 2 θ /s. The polished thin sections were used for EPMA analysis of the Cr-spinel samples using a JOEL JXA-8230 Electron Probe Micro Analyzer with WDS spectrometry positioned at the Advanced Facility for Microscopy and Microanalysis (AFMM) Centre of the Indian Institute of Science, Bangalore, India. The accelerating voltage is 15 kV with a probe current of 12 nA. Natural silicates and oxide minerals were used as standards.

The Laser Raman spectroscopic analysis was carried out at the Aerospace Structures Laboratory in the Indian Institute of Space Science and Technology, Thiruvananthapuram. The Raman measurements of the powdered Cr-spinel samples were obtained in the ReniShaw Laser Raman spectrometer (Renishaw plc, U.K.) using Cobolt’s continuous wave (CW) Diode Pumped Solid State (DPSS) laser as the excitation source (laser wavelength is 532 nm) with air-cooled plasma filter. Raman signals were measured in a broader range of 100 cm⁻¹ – 4000 cm⁻¹ with a spectral resolution of 0.3 cm⁻¹. The exposure time of the analysis was 10 s for a laser beam with a power of 500 mW. The laser spot was adjusted from 10 μ m to 200 μ m using a beam expander. The measured Laser Raman spectra were analyzed further, and the chemical phases were identified using the RRUFF library (Lafuente et al., 2015) and literature references.

The hyperspectral measurements were obtained using an ASD field Spectroradiometer in the Department of Earth and Space Sciences in the Indian Institute of Space Science and Technology, Thiruvananthapuram. The FieldSpec® Pro 3 Spectroradiometer by Analytical Spectral Device (ASD) Inc. (calibrated to NIST) operating in the spectral range of 0.35 to 2.5

μm in the visible- near-infrared (VNIR) region was used for obtaining the reflectance spectra of the Cr-spinel samples in the laboratory-based conditions. Spectra from all the three spectral regimes have been collected, i.e., UV/visible-near- infrared (VNIR) from 0.35–0.969 μm and shortwave infrared (SWIR) from 0.969 to 2.5 μm . The spectrometer has a spectral resolution of 3 nm for the Visible-NIR range between 0.35 and 1.0 μm while 10 nm for the rest of the spectral range up to 2.5 μm . A lamp and power supply from Optronic Laboratories Inc. were used as an illumination source. The field of view (FOV) for the probe was 25°. The reflectance measurements were recorded relative to the calibrated reflectance of a Spectralon. RS³™ software has been used for collecting the measured data. At least 20 consecutive measurements were averaged to improve the signal-to-noise ratio of the collected spectra. The recorded spectra were then viewed and splice corrected in ViewSpec Pro software. The reflectance spectra were further analyzed in ENVI software and plotted using OriginPro software.

The FTIR analysis of the Cr-spinel samples was carried out in the Department of Chemistry at the Indian Institute of Space Science and Technology, Thiruvananthapuram. The FTIR spectra were recorded in the mid-IR range between 400 cm^{-1} and 4000 cm^{-1} with a spectral resolution of 0.5 cm^{-1} and wavelength accuracy of 0.1 cm^{-1} at 1600 cm^{-1} using a PerkinElmer Spectrum Fourier transform infrared (FTIR) spectrometer (PerkinElmer Inc.). The FTIR spectra were obtained in transmission mode, which was later converted into absorbance and attenuated total reflectance (ATR) mode using a Harrick ‘Golden Gate’ diamond anvil ATR unit. The obtained spectral data using these spectroscopic techniques were then compared with the mineral chemistry to understand the spectrochemical characteristics.

6.4 Results and discussions

6.4.1 Petrography

The Cr-spinels are more or less homogeneous, characterized by cumulate Cr-spinels in association with amphiboles (Fig. 6.3a). Chlorite and rutile have been observed as inclusions within the Cr-spinel grains (Fig. 6.3a). Minor occurrences of plagioclase can also be seen along with the amphiboles in the matrix. The Cr-spinel grains exhibit cumulus and intercumulus textures typical of magmatic anorthosite complexes (Fig. 6.3a). At places, the minerals also show signs of deformation and recrystallization. The grain fracturing and the consequent rugged boundaries of the Cr-spinel grains embedded in the matrix of amphiboles are likely due to the post-crystallization deformations in the chromitite bodies. The backscattered electron

(BSE) images obtained for the Cr-spinels show the dominant compositional homogeneity of the Cr-spinels (Fig. 6.3b-c).

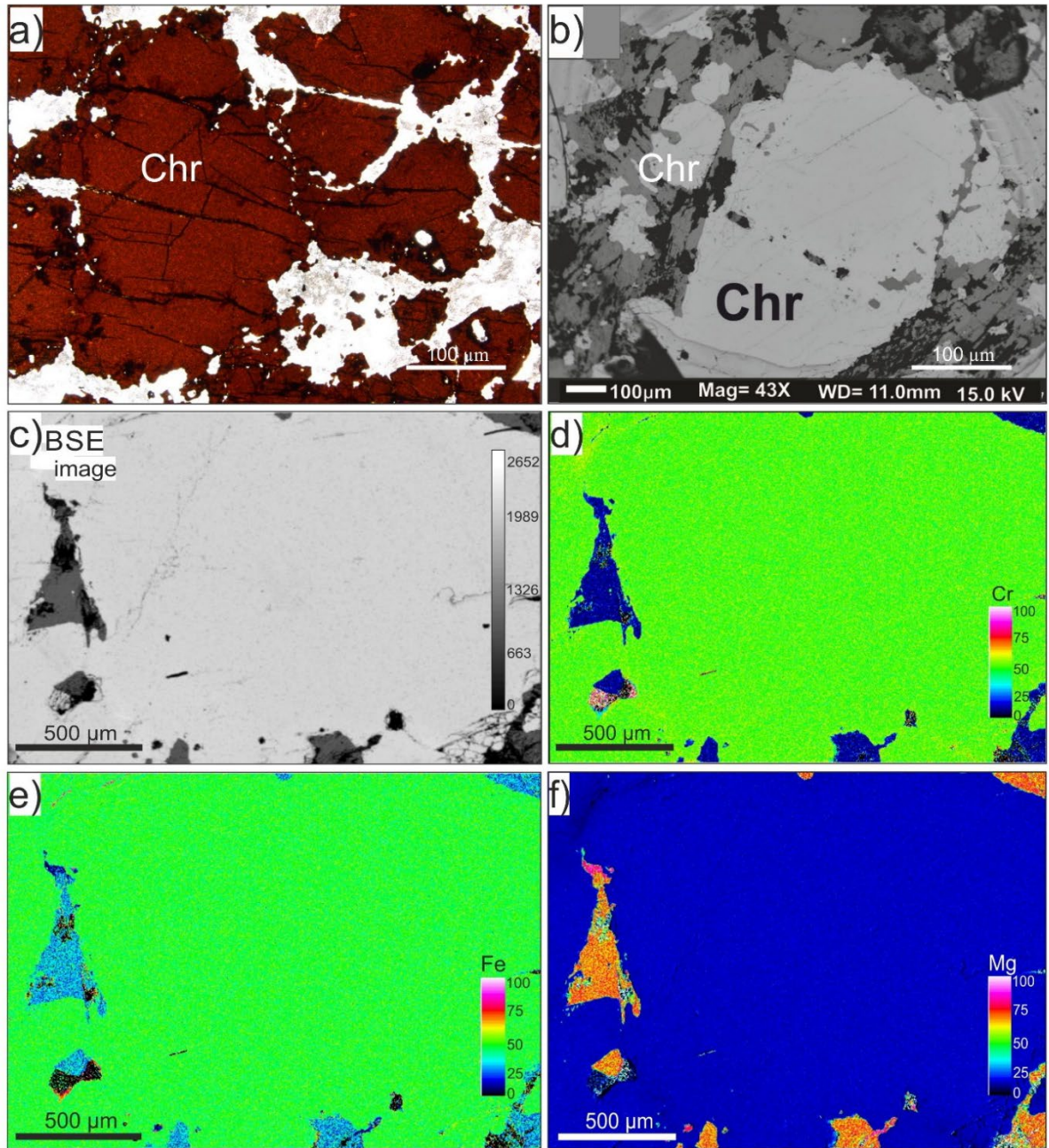


Figure 6.3: (A) Photomicrograph of the Cr-spinels from the SAC showing cumulate texture. The Cr-spinel grains are subhedral to anhedral. (B-C) The Back Scattered Electron (BSE) images of the Cr-spinel grain with inclusions of amphiboles. Note, amphibole also occurs as discrete grains surrounding the spinel. (D-F) X-ray elemental maps of the Cr-spinel grain showing the distribution and abundance of Cr, Fe, and Mg. Note, the variation in Cr, Fe, and Mg is negligible within the grain. Abbreviation: Chr - Cr-spinel.

6.4.2 Mineral chemistry

The representative EPMA data showing the core to rim compositional variations (average) of the Cr-spinel samples are listed in Table 6.1. The EPMA data for all the analyses on Cr-spinel samples are given in Table A5. X-ray elemental maps of selected mineral grains were also obtained, showing the tonal variations in Fe, Mg, and Cr abundances (Fig. 6.3c-f). The X-ray elemental maps showed fairly homogenous compositions from the core to the rim, with negligible variations in the Cr, Fe, and Mg abundances across the grain (Fig. 6.3d-f).

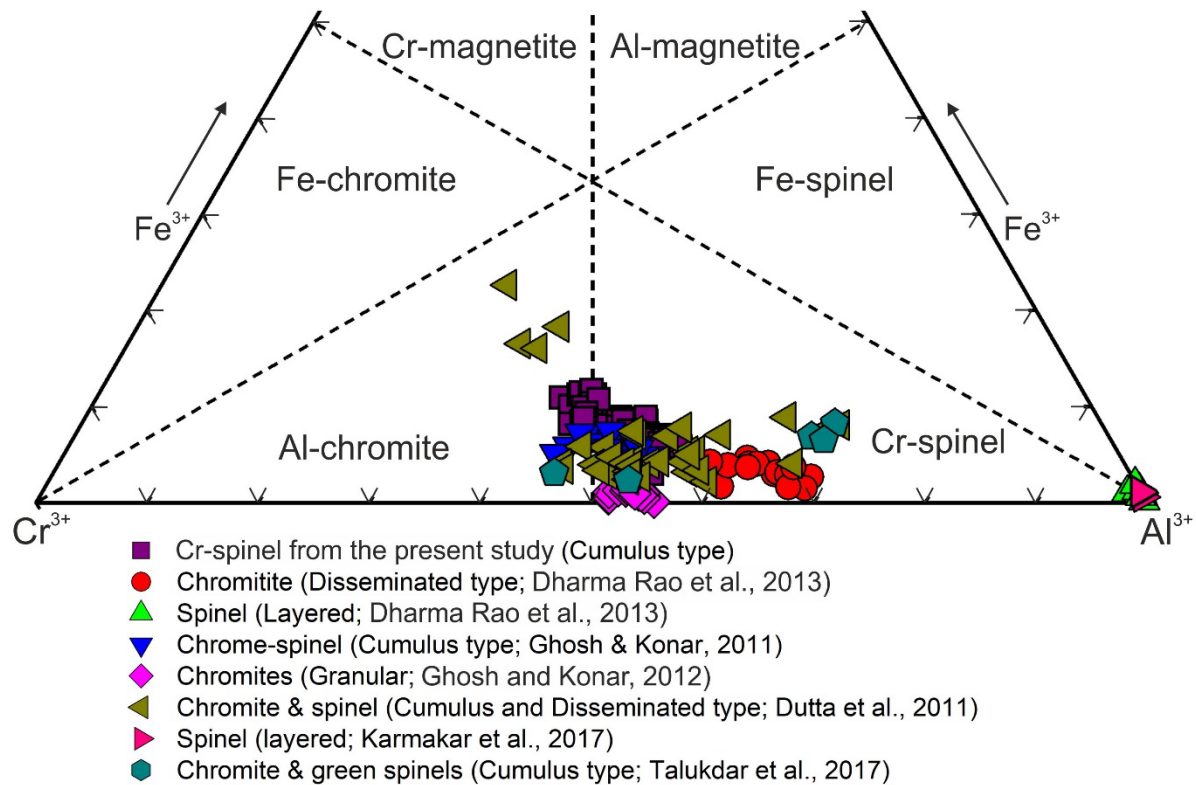


Figure 6.4: Cr-spinels in the present study plotted in Cr-Al-Fe³⁺ ternary discrimination diagram for spinels (after Stevens 1944). The previously published data (compiled) from SAC has also been plotted for comparison.

The Cr₂O₃ content in the Cr-spinels ranges between 32.99 and 37.55 wt%, while Al₂O₃ content varies from 22.08 to 27.70 wt%. The FeO and MgO contents vary between 29.16 and 32.78 wt% and 6.28–7.97 wt%, respectively. The concentrations of SiO₂, TiO₂, and MnO are less than 0.25 wt%. SAC Cr-spinels are considered refractive grade because of their higher Al₂O₃ contents (>20 wt%) and Cr₂O₃ + Al₂O₃ concentrations above 60 wt% (Ghosh and Konar, 2012). The estimated Cr# (Cr/(Cr + Al)) is varying from 0.44 to 0.53, while Mg# (Mg/(Mg + Fe²⁺)) ranges from 0.32 to 0.38.

Table 6.1: Representative electron microprobe analyses of Cr-spinel samples from the Sittampundi Anorthosite Complex.

Oxides (wt%)	SR10		SR6		SR14I		SR14		SR17	
	Core	Rim	Core	Rim	Core	Rim	Core	Rim	Core	Rim
SiO₂	0.03	0.00	0.00	0.00	0.00	0.00	0.02	0.04	0.02	0.01
TiO₂	0.00	0.20	0.22	0.00	0.06	0.06	0.00	0.00	0.18	0.08
Al₂O₃	25.82	25.50	24.75	24.55	23.95	23.94	24.29	24.21	27.73	26.21
Cr₂O₃	35.41	36.12	36.68	35.98	35.17	35.65	36.97	37.55	33.32	34.55
FeO	30.64	30.11	31.59	32.78	31.76	30.96	31.99	30.99	29.37	28.90
MnO	0.28	0.37	0.31	0.32	0.27	0.21	0.34	0.35	0.35	0.25
MgO	7.62	7.54	6.47	6.28	7.99	8.04	7.22	7.25	9.10	8.63
Total	100.05	99.96	100.17	100.00	99.24	98.95	100.97	100.63	100.89	99.42

Formula units based on 4 oxygens

Cr	0.87	0.89	0.92	0.90	0.88	0.90	0.92	0.93	0.81	0.86
Ti	0.00	0.00	0.01	0.00	0.00	0.00	0.00	0.00	0.00	0.00
Al	0.95	0.94	0.92	0.92	0.89	0.90	0.90	0.90	1.01	0.97
Fe³⁺	0.17	0.15	0.15	0.18	0.22	0.21	0.19	0.17	0.18	0.17
Fe²⁺	0.63	0.60	0.69	0.69	0.62	0.62	0.65	0.65	0.58	0.59
Mn	0.00	0.01	0.01	0.01	0.01	0.01	0.01	0.01	0.01	0.01
Mg	0.35	0.35	0.31	0.30	0.38	0.38	0.34	0.34	0.42	0.40
Mg#	0.36	0.36	0.31	0.30	0.38	0.38	0.34	0.35	0.42	0.41
Cr#	0.47	0.49	0.50	0.50	0.50	0.50	0.51	0.51	0.45	0.47

Mg# Mg/Mg+Fe²⁺

Cr# Cr/Cr+Al

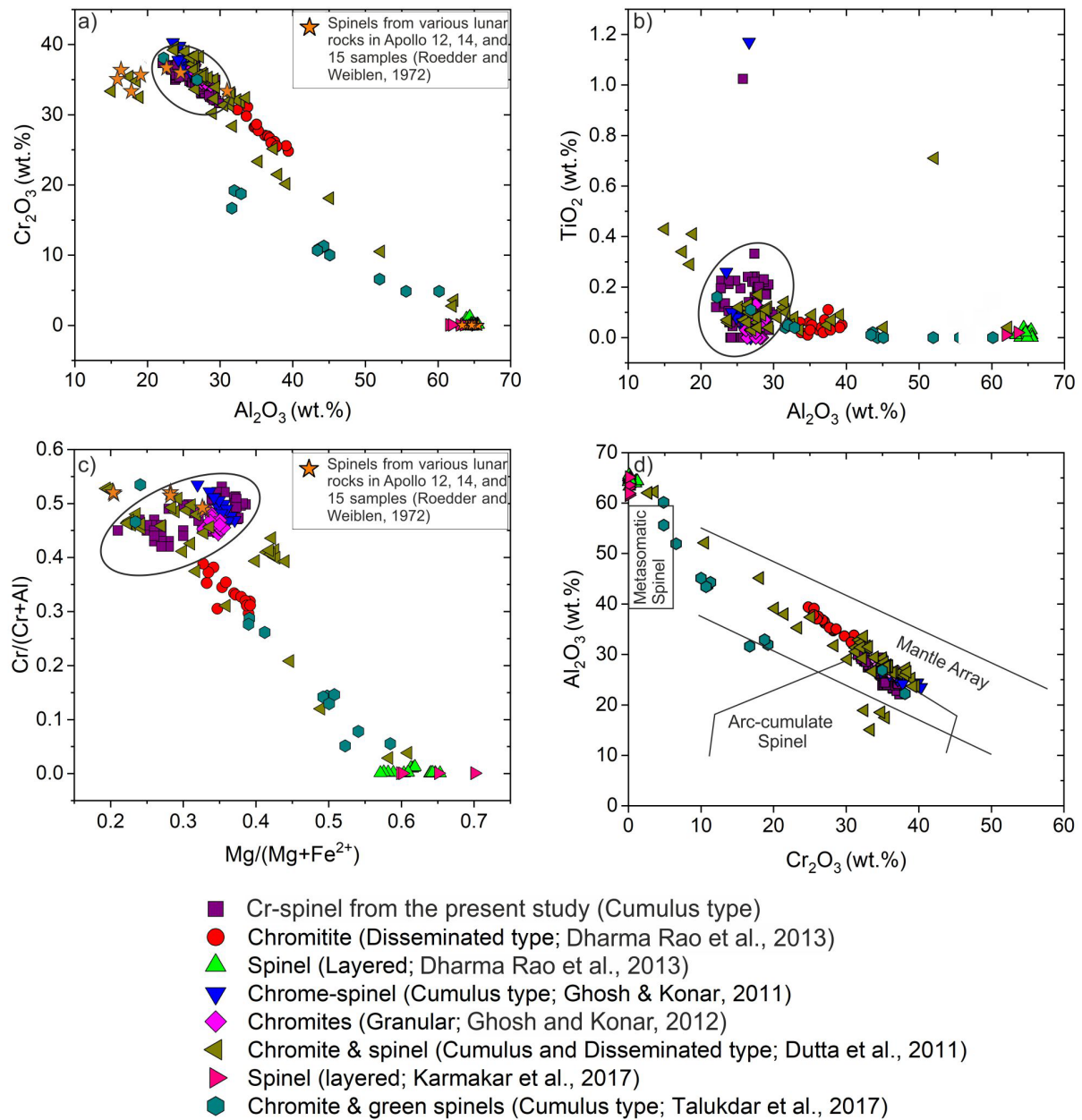


Figure 6.5: Variation diagrams of (A) Al_2O_3 vs Cr_2O_3 (B) Al_2O_3 vs TiO_2 and (C) $\text{Mg}\#$ vs $\text{Cr}\#$ for the Cr-spinels in the present study plotted along with the previously published data from Sittampundi Anorthosite Complex. An elliptical shape in the figure outlines the Cr-spinels used in the present study. (D) Cr_2O_3 vs Al_2O_3 diagram for Cr-spinels from SAC. The fields of mantle array, arc cumulate spinel, and metasomatic spinel have been shown (after Conrad and Kay 1984; Haggerty 1988; Kepezhinskis et al., 1995).

In the Cr–Al–Fe³⁺ ternary discrimination diagram (after Stevens 1944), the Cr-spinels from the present study plot in the compositional region between Al-chromites and Cr-spinels (Fig. 6.4). Most of the compositions in the present study fall in the compositional field of Cr-spinel.

The chemical data of SAC spinel compositions from the published literature have been compiled and plotted along with the Cr-spinel data from the present study for comparison (Fig. 6.5a-c) (Ghosh and Konar, 2011; Ghosh, 2011; Dutta et al., 2011; Dharma Rao et al., 2013; Karmakar et al., 2017; Talukdar et al., 2017). In the ternary plot, the compositions towards the Al-spinel end of the diagram are mainly from the green spinels formed by metasomatic alteration and metamorphic recrystallization of chromites (Dutta et al., 2011; Dharma Rao et al., 2013; Karmakar et al., 2017; Talukdar et al., 2017) (Fig. 6.4). The variation diagrams of Al_2O_3 vs Cr_2O_3 , Al_2O_3 vs TiO_2 , and Mg# vs Cr# for Cr-spinels were also plotted (Fig. 6.5a-c). Both magmatic and metamorphic imprints were discovered in the chromitite bodies hosted by anorthosites and clinopyroxenite in the SAC (Dutta et al., 2011) (Fig. 6.5). The chemical modifications such as subsolidus re-equilibration and hydrothermal processes during metamorphism can significantly alter the high-T primary composition of Cr-spinels (Stowe, 1994; Talukdar et al., 2017). Because of this, the Cr# in the SAC Cr-spinel compositions show a significant variation ranging from 0.04 to 0.54 owing to its textural differences and the nature of associated minerals (Fig. 6.5c). The SAC Cr-spinel grains display alteration features by a gradual increase in the Mg and Al contents (green spinels). The Cr# (0.05–0.15) and Mg# (0.45–0.56) in these green spinels exhibited a reverse relationship (Talukdar et al., 2017) (Fig. 6.5c). However, studies have shown that massive chromitite bodies can retain the igneous chemical composition in the cores of Cr-spinel grains irrespective of the metamorphic changes (Suita and Streider, 1996; Candia and Gaspar, 1997; Proenza et al., 2004). The bivariate plot of Mg# vs Cr# (after Stevens 1944) shows an inverse correlation for the Cr-spinels in the present study (Fig. 6.5c). Also, the inverse relationship of Cr# and Mg# in SAC Cr-spinels corroborates well with the compositional array of magmatic chromites in other metamorphosed Archean anorthosite-hosted chromite deposits of the Fisskenaasset complex and Mangabal complex (Candia and Gaspar, 1997; Rollinson et al., 2010; Talukdar et al., 2017). The Cr_2O_3 vs Al_2O_3 diagram revealed that the Cr-spinel compositions from the present study show proximity to the mantle array and arc-cumulate setting (Fig. 6.5d). He et al. (2020) proposed that the amphiboles in the chromitites are of magmatic origin based on their microtextural, geochemical, and isotopic studies. These Cr-spinels, which are considered magmatic (Cr# ranging between 0.44 and 0.53), are chosen for further spectrochemical characterization in the present study (Fig. 6.5c). The X-ray diffraction analysis has shown characteristic XRD peaks of Cr-spinels in the 2θ positions at 18.58° , 30.59° , 43.85° , 58.06° , and 63.92° with the highest peak occurring at 36.11° (Fig. 6.6).

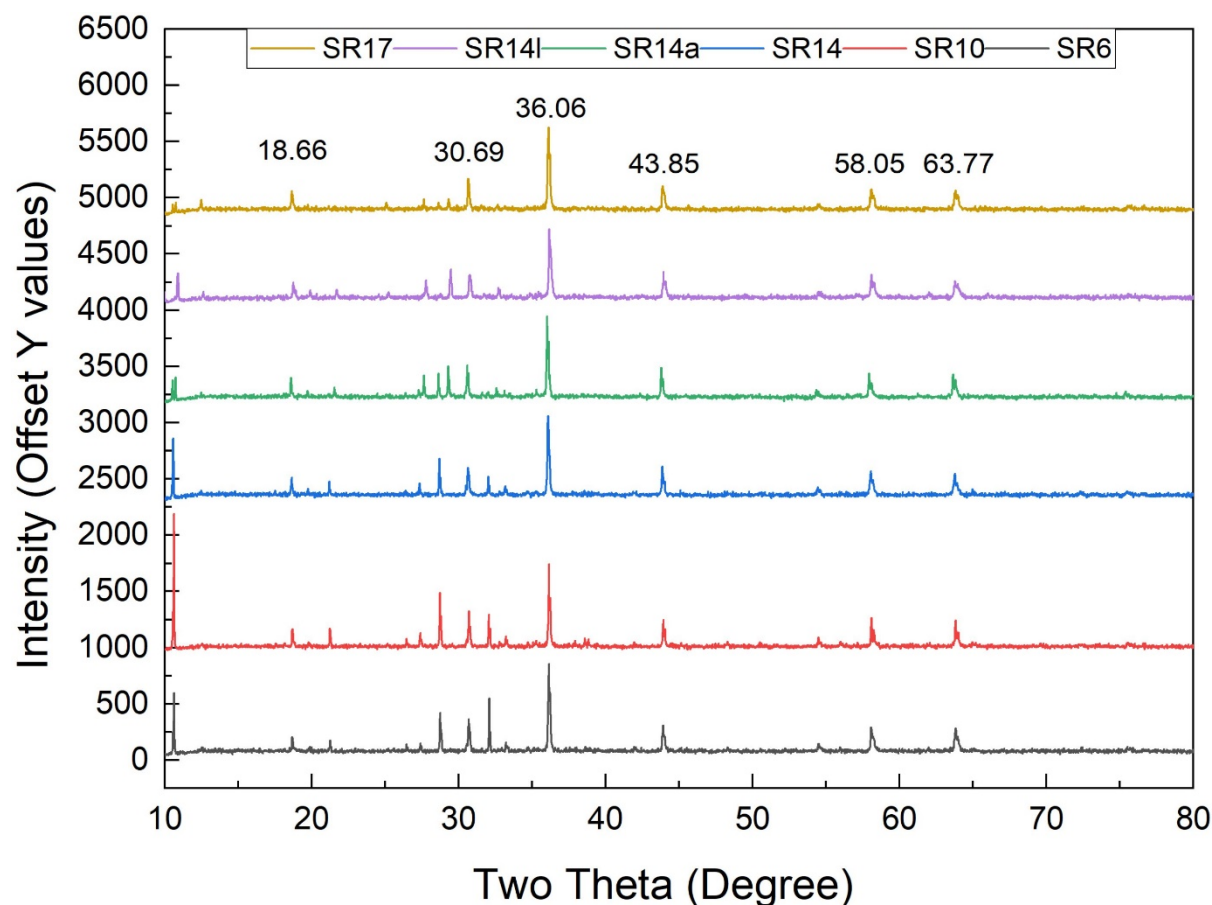


Figure 6.6: X-ray Diffraction spectra of the Cr-spinels from SAC showing the characteristic intensity peaks.

6.4.3 Spectral analyses

6.4.3.1 Laser Raman analysis

The Cr-spinel samples have been characterized using Laser Raman spectroscopy. Previous studies on Fe-Ti-Cr oxides, including Cr-spinels, have described the Raman features of these mineral solid solutions (Malezieux and Piriou, 1988; Cynn et al., 1992; Wang et al., 2002a, 2004; Lenaz and Lughi, 2013; Zhu et al., 2017; Sarkar et al., 2019). $A_{1g} + E_g + 3F_{2g}$ are the symmetries of the five Raman-active vibrational modes for spinels (Chopelas and Hofmeister, 1991). The symmetric stretching of highly covalent bonds associated with trivalent ions in $(Cr^{3+}, Fe^{3+}, Al^{3+})O_6$ octahedra produces a most substantial peak near 685 cm^{-1} and a shoulder near 650 cm^{-1} in the Raman spectra of end-member Cr-spinel. The broader strongest peak near 685 cm^{-1} was designated to the A_{1g} mode (Malezieux and Piriou, 1988), while the minor peak

near 650 cm^{-1} belongs to the F_{2g} symmetry. Other minor peaks near $\sim 450\text{ cm}^{-1}$, $\sim 520\text{ cm}^{-1}$, and $\sim 610\text{ cm}^{-1}$ were assigned to E_g and F_{2g} symmetries, respectively (Busey and Keller, 1964; White and DeAngelis, 1967; Yamanaka and Ishii, 1986; Degiorgi et al., 1987; McMillan and Akaogi, 1987; Ross and Navrotsky, 1987; Chopelas and Hofmeister, 1991; Cynn et al., 1992; Gasparov et al., 2000; Wang et al., 2004; D'Ippolito et al., 2015). The A_{1g} peak in the Raman spectra was assigned to the symmetric stretching vibration of Cr-O in Cr^{3+}O_6 groups (Malezieux and Piriou, 1988; Wang et al., 2004; Marinkovic Stanojevic et al., 2007; Lenaz and Lughi, 2013). Higher Cr_2O_3 ($\geq 63\text{ wt}\%$) contents in some mantle-derived Cr-spinels yield a Raman peak near $\sim 730\text{ cm}^{-1}$ (e.g., Malezieux et al., 1983). Raman peaks vary over a considerable range of frequencies with the substitution of cations in the spinel structure. Malezieux and Piriou (1988) pointed out that the shifts in the major peak of A_{1g} mode over a range of 100 cm^{-1} (from 770 cm^{-1} to 683 cm^{-1}) are a function of the cation ratio $(\text{Cr} + \text{Fe}^{3+})/(\text{Cr} + \text{Fe}^{3+} + \text{Al})$ in the octahedral sites. The A_{1g} peak position linearly shifts to lower frequencies with an increase in the molar ratio $(\text{Cr} + \text{Fe}^{3+})/(\text{Cr} + \text{Fe}^{3+} + \text{Al})$. It was later proved that the major Raman peak of Cr-spinel corresponding to the A_{1g} mode is contributed by the vibration of the trivalent ions (Al^{3+} , Cr^{3+} , Fe^{2+}) in the octahedral site (A^{3+}O_6) of the spinel structure (Wang et al., 2004). Hence, the major Raman peak positions of spinels aid us in retrieving their compositional information. The presence of Al in the octahedral site of the spinel structure produces a strong Raman peak near 770 cm^{-1} . Substitution of Cr in the octahedral site shifts this major Raman peak downward into $\sim 680\text{--}690\text{ cm}^{-1}$. A continuous spread of the major Raman peaks between $\sim 680\text{--}770\text{ cm}^{-1}$ was observed when Al and Cr co-exist in the octahedral site (Wang et al., 2004). The major Raman peak shifts further downward into $\sim 659\text{--}665\text{ cm}^{-1}$ with the substitution of Fe^{3+} , whereas Ti^{4+} in the octahedral site moves the peak to relatively higher wavenumbers, close to 680 cm^{-1} (Wang et al., 2004).

The principal Raman spectral features of the Cr-spinels (in the powdered form) from the SAC have been analyzed. The variation in the spectral patterns and peak positions in response to compositional and structural changes in the mineral has also been discussed. The Raman spectra of the analyzed samples are presented in Fig. 6.7a. The predicted modes of symmetries of the corresponding Raman peaks have also been labeled in the figure. Raman spectra from the analyzed Cr-spinel samples show similar patterns despite the slight shift in the major peak positions from the pre-defined Raman peaks for Cr-spinels (Fig. 6.7a). The samples show four principal Raman peaks. The measured Raman peaks appear to be a continuous spread in the regions between $\sim 430\text{--}500\text{ cm}^{-1}$, $\sim 500\text{--}625\text{ cm}^{-1}$, and $\sim 625\text{--}800\text{ cm}^{-1}$. The prominent peak corresponding to the A_{1g} mode varies from 703 cm^{-1} to 714 cm^{-1} , with a shoulder around 671 cm^{-1} (Fig. 6.7a). The A_{1g} peak position over a range of frequencies suggests compositional

variations. Other peaks are centered near $\sim 468\text{ cm}^{-1}$, 528 cm^{-1} , and $\sim 585\text{ cm}^{-1}$, corresponding to the E_g , $F_{2g}(2)$, and $F_{2g}(3)$ modes, respectively (Fig. 6.7a) (D’Ippolito et al., 2015).

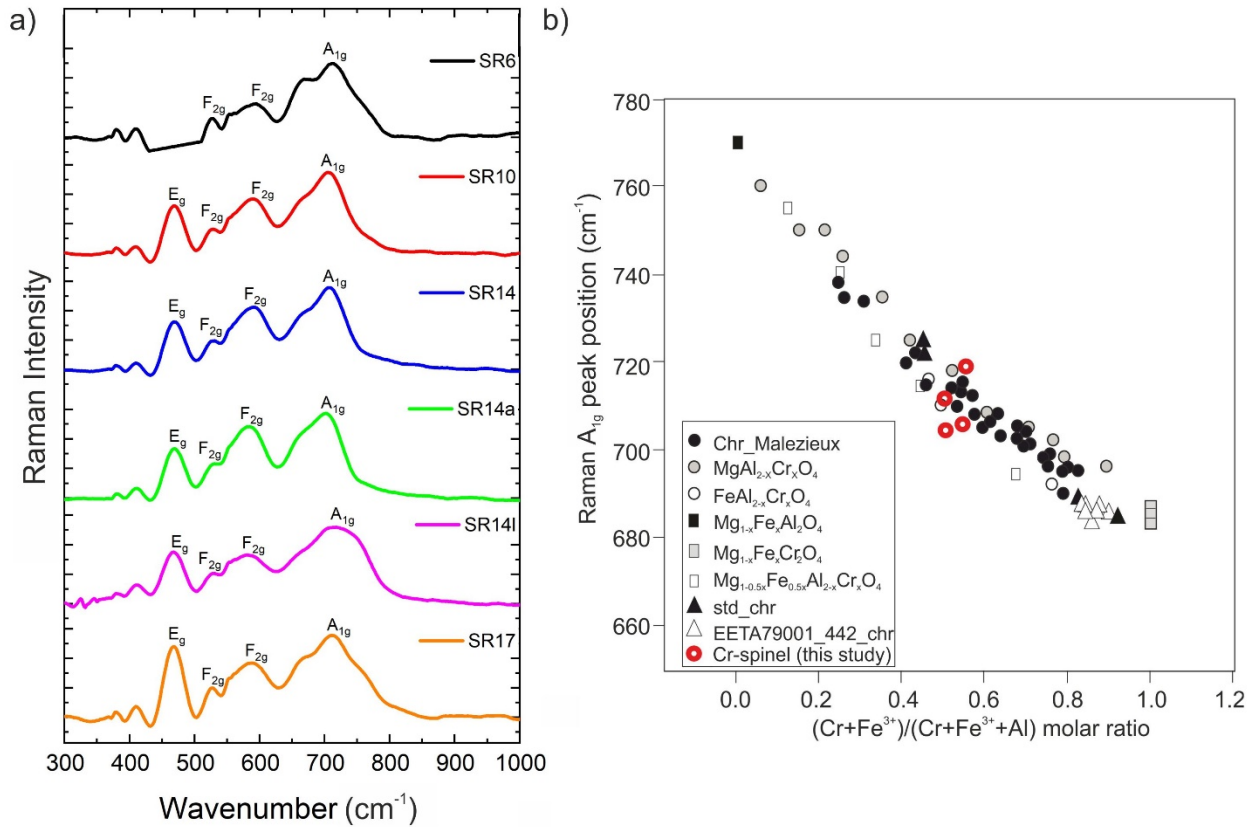


Figure 6.7: (A) Laser Raman spectra of Cr-spinels from the present study showing the diagnostic Raman intensity lines corresponding to E_g , F_{2g} , and A_{1g} symmetries. The Al_2O_3 content increases from bottom to top in the figure (in ascending order from SR17 to SR6). (B) Raman A_{1g} peak position vs molar ratio $(Cr + Fe^{3+})/(Cr + Fe^{3+} + Al)$ plot of Cr-spinels from the present study along with the reference data from Malezieux and Piriou (1988).

The SAC Cr-spinels show composition ranging between Al-chromite and Cr-spinel. Relatively higher Al_2O_3 contents ($\sim 22\text{--}27\text{ wt}\%$) are characteristic of the SAC Cr-spinels with Cr_2O_3 content ranging from $\sim 32\text{--}37\text{ wt}\%$ (Table 6.1). The enhanced Al content in the Cr-spinels causes a shift in the intense and strong A_{1g} position among the analyzed samples. In general, the A_{1g} peak of Cr-spinels ranges between $674\text{ cm}^{-1} - 688\text{ cm}^{-1}$ (D’Ippolito et al., 2015). However, the A_{1g} peak in the analyzed Cr-spinels shows a systematic shift to higher wavenumbers ($\sim 705\text{--}714\text{ cm}^{-1}$) in response to the relatively higher Al content of the SAC Cr-spinels (Fig. 6.7a). As discussed earlier, the type of octahedral cation in the spinel structure determines the type of spinel. Moreover, the major Raman peak of A_{1g} mode is strongly influenced by the kind of octahedral cation (Wang et al., 2004). In Fig. 6.7a, the A_{1g} peak appears to be shifted longward, probably due to the substitution of Al^{3+} in the spinel structure.

The A_{1g} peak position near 705 cm^{-1} in SR10 and SR14 spectra is attributed to the coexistence of (Mg, Fe) in the tetrahedral site and (Al, Cr) in the octahedral site (Wang et al., 2004). The shift in the major peak position to $\sim 712\text{ cm}^{-1}$ in SR17 and SR6 (high Al_2O_3 content of approximately $\geq 49\%$) is also produced by the coexistence of (Al, Cr) in the octahedral site. In the Raman spectra of SR14I, the A_{1g} peak position is at a much higher wavenumber, at $\sim 714\text{ cm}^{-1}$, implied by the coexistence of (Mg, Fe) and (Cr, Al) in their respective sites in the spinel structure (Wang et al., 2004). The trend in the variation in peak position correlates well with the molar ratio $(\text{Cr} + \text{Fe}^{3+}) / (\text{Cr} + \text{Fe}^{3+} + \text{Al})$ of Cr-spinels (Fig. 6.7b). The A_{1g} peak position shifts to higher wavenumbers with a corresponding decrease in the ratio of $(\text{Cr} + \text{Fe}^{3+}) / (\text{Cr} + \text{Fe}^{3+} + \text{Al})$ (Wang et al., 2004). Using this correlation between the molar ratio and A_{1g} peak position, the ratio of $(\text{Cr} + \text{Fe}^{3+}) / (\text{Cr} + \text{Fe}^{3+} + \text{Al})$ is estimated to be between $\sim 0.5\text{--}0.62$ (Fig. 6.7b). However, the molar ratio value obtained by EPMA from the cores and rims of Cr-spinel grains ranges from 0.49 to 0.58. The range of the ratio values estimated using the correlation plot is fairly overlapping with the values obtained from EPMA measurements. The slightly wider range of the values obtained from the correlation plot is likely due to sampling a large area during off-focus Raman point count measurements resulting in measurements from a wider range of compositions (Wang et al., 2004). More systematic and accurate Raman measurements will be required to resolve such minor discrepancies in the spectrochemical analysis.

6.4.3.2 Hyperspectral analysis

In VIS-NIR reflectance spectroscopy of spinels, the spectral pattern is a function of their chemical composition (Cloutis et al., 2004). This relationship between the absorption characteristics of spinels and their chemistry helps us retrieve their compositional information and abundance from the reflectance spectra. Previous studies have discussed the spectral characteristics of common spinel-group minerals (Rossman 1988, Cloutis et al., 2004; Williams et al., 2016; Sarkar et al., 2019). Typically, spinels exhibit a broad and strong absorption band in the $2\text{ }\mu\text{m}$ region of the reflectance spectra (Cloutis and Gaffey, 1993) accompanied by relatively weaker absorption bands in the shorter wavelengths (e.g., Hunt and Wynn, 1979). Inverse spinels like magnetite exhibit a broader absorption band in the $1\text{ }\mu\text{m}$ region (e.g., Adams, 1975). Cloutis et al. (2004) have discussed the variations in the spectral properties of common spinel-group minerals as a function of composition and provided a way of quantitative estimation of the compositions from the VIS-NIR reflectance spectra ($0.3\text{--}3\text{ }\mu\text{m}$) (e.g., Cloutis and Gaffey, 1991). Crystal field transition absorptions in the Fe^{2+} ions in the

tetrahedral site of Cr-spinels are responsible for the diagnostic absorption bands of the spinels, mainly in the 2 μm wavelength region (e.g., Gaffey, 1973; Shankland et al., 1974). The Cr-spinels also have robust and distinctive absorption bands in the visible wavelength, particularly in the 0.5–1 μm range (e.g., Cloutis et al., 2004; Williams et al., 2016). The subtle absorptions present shortward of 1 μm are a function of Fe# and Cr# of spinels. These shorter wavelength bands of Cr-spinels appear at 0.49 μm , 0.59 μm , 0.69 μm , 0.93 μm , and 1.26 μm (Cloutis et al., 2004) (Fig. 6.8). The 0.49 μm absorption band was attributed to the ${}^4\text{A}_2\text{-}{}^4\text{T}_1$ crystal field transition in Cr^{3+} in the octahedral site of the Cr-spinel. It was found that this band can quantify the Cr_2O_3 content to within $\sim\pm 5\%$. The most distinctive absorption feature for Cr-spinels is located at $\sim 0.55 \mu\text{m}$ (Mao and Bell, 1975; Cloutis et al., 2004; Williams et al., 2016). This feature was also identified in the lunar spinel spectra from Apollo 17 sample (70002, 7) (Mao and Bell, 1975). The 0.59 μm absorption feature was assigned to the ${}^4\text{A}_2\text{-}{}^4\text{T}_2$ crystal field transition absorption in the octahedrally coordinated Cr^{3+} ion. The 0.69 μm absorption band was attributed to the ${}^5\text{E-}{}^3\text{T}_1$ spin-forbidden transition in the tetrahedrally coordinated Fe^{2+} ions (Cloutis et al., 2004). The absorption band at 0.93 μm was assigned to the spin-allowed ${}^5\text{T}_2\text{-}{}^5\text{E}$ crystal field transitions in Fe^{2+} ions in the octahedral site (Mao and Bell, 1975). The 0.93 μm band is prominent in the high Fe spinels. This band shifts to longer wavelengths with higher FeO contents. The absorption band present at 1.3 μm is unique to Cr-spinels (e.g., Cloutis et al., 2004). The 1.3 μm band arises from the spin-allowed ${}^5\text{T}_2\text{-}{}^5\text{E}$ crystal field transition in the tetrahedrally coordinated Cr^{2+} ions. This band shifts to longer wavelengths with an increase in the Fe^{2+} content and a decreasing MgO content (Cloutis et al., 2004). The FeO and MgO contents to within $\pm 2\%$ can be constrained using the 1.3 μm band position (Cloutis et al., 2004). The 2 μm band has more intensity than shorter wavelength bands. The 2 μm band is caused by the ${}^5\text{E-}{}^5\text{T}_2$ crystal field transition in Fe^{2+} ions in the tetrahedral site (Slack et al., 1966; Mao and Bell, 1975; Burns, 1993). In Cr-spinels, the 2 μm band center is always at wavelengths beyond 2.1 μm , unlike spinels with a band center shortward of 2.1 μm . Therefore, a 2 μm band position can distinguish between Mg-Fe Al spinels and Cr-spinels (Cloutis et al., 2004).

The diagnostic absorption bands at 0.49 μm , 0.59 μm , 0.69 μm , 0.93 μm , 1.3 μm , and 2 μm have been identified in the SAC Cr-spinel samples (Fig. 6.8a-b). The normal and continuum removed reflectance spectra of the analyzed Cr-spinels have been shown in Fig. 6.8a-b. The laboratory reflectance spectra of the chromite, (Mg, Fe) Al spinel, and Cr-bearing Mg-spinel have also been plotted for comparison with the spectral features of SAC Cr-spinels (Fig. 6.8a-b). The diagnostic absorption characteristics in the laboratory spectra of the chemically diverse spinels unique to different spinel solid solutions have helped to attribute the absorption bands to the constituent chemical phases in the SAC Cr-spinel spectra. The band positions of major

absorption bands in the spectra of analyzed Cr-spinels and their wt% oxide concentrations and Cr# have been given in Table 6.2. The 2 μm band position in all the sample spectra appears to be broader and stronger (Fig. 6.8).

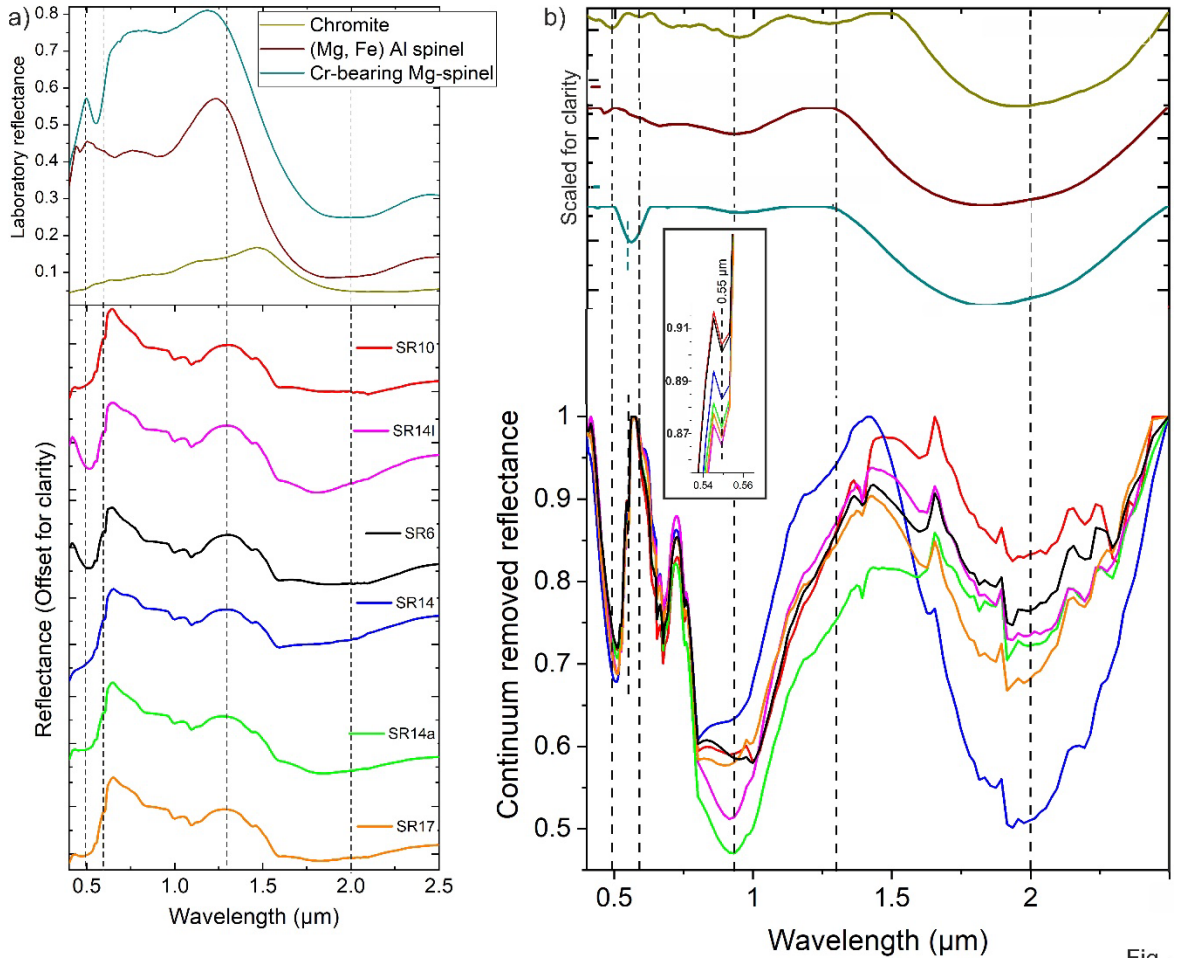


Figure 6.8: (A) Normal reflectance spectra of Cr-spinels from the present study. The laboratory reflectance spectra of Cr-spinel, (Mg, Fe) Al spinel, and Cr-bearing Mg-spinel have also been shown for comparison (top). (B) Continuum removed reflectance spectra of the Cr-spinels from the present study along with the reference laboratory spectra. The dashed vertical lines are drawn at 0.49 μm , 0.55 μm , 0.59 μm , 0.93 μm , 1.28 μm , and 2 μm wavelengths. The 0.55 μm band is focused and shown separately for clarity. The legend is the same as Fig. 6.8A. The laboratory reflectance data were taken from RELAB.

The chemistry of the Cr-spinels has largely been reflected in the position and strength of the diagnostic absorption features. The samples SR14, SR14a, and SR14l show relatively higher band strengths, particularly at 0.5 μm , 1 μm , and 2 μm features compared to the SR10, SR17, and SR6 samples. The 0.93 μm band appears to be relatively stronger in all the samples, apparently due to a relatively higher abundance of Fe^{2+} . Among the minor absorption bands, the bands at 0.49 μm and 0.69 μm are evident in all the analyzed samples. The remaining

absorption bands at 0.59 μm and 1.3 μm are discernible from the spectral broadening and a weak dip in their corresponding wavelength regions (Fig. 6.8). The 0.49 μm band arises from the crystal field transition absorption in the octahedrally coordinated Cr^{3+} ion (Cloutis et al., 2004).

Table 6.2: Band positions of the SAC Cr-spinel samples in comparison with their chemistry.

Sample Name	Band positions (μm)						Oxides (wt. %)			Cr# (Cr/Cr+Al)
	0.49	0.55	0.59	0.93	1.3	2	Al_2O_3	Cr_2O_3	FeO	
SR17	0.5	0.549	0.59	0.93	1.27	1.98	26.97	33.93	29.13	0.45
SR14l	0.5	0.549	0.59	0.93	1.29	2.01	23.53	36.08	31.67	0.5
SR14	0.49	0.549	0.59	0.92	1.3	2.01	24.2	37.21	31.49	0.5
SR10	0.49	0.549	0.59	0.93	1.29	2.06	26.03	35.22	30.07	0.47
SR6	0.5	0.549	0.59	0.93	1.28	2.01	26.57	34.57	31.38	0.46

In the samples SR10, SR14, and SR14a, the 0.49 μm band center is close to 0.495 μm . While SR17, SR14l, and SR6 samples show a 0.49 μm band center at around 0.504 μm (Fig. 6.8). This slight longward shift in the 0.49 μm band position is likely to be caused by the greater Cr contents of the SAC Cr-spinels (Cloutis et al., 2004). The 0.59 μm band center is near 0.597 μm in all the analyzed samples. The 0.59 μm band is attributed to the crystal field transition absorption in the Cr^{3+} ion in the octahedral site. A significant shift in the 0.59 μm band position has not been observed with respect to the varying Cr_2O_3 contents in the samples. Although very subtle, the prominent 0.55 μm absorption feature is noticeable, which is attributed to the Cr^{3+} content in the octahedral site (Fig. 6.8b) (e.g., Williams et al., 2016). A drop in the reflectance shortward of 0.5 μm might result from iron- and chromium-related metal-oxygen charge transfer absorptions (Cloutis et al., 2008). The 0.69 μm band is centered at \sim 0.691 μm (Fig. 6.8). The 0.69 μm band arises from the spin-forbidden transition absorption in the Fe^{2+} ions in the tetrahedral site. This band appears to be a weaker absorption feature with an average band depth of \sim 2.4%. The 0.93 μm band (close to 1 μm) is centered near 0.929 μm . The absorptions in the 1 μm region, linked to the octahedral Fe^{2+} , are characteristic of high iron- and chromium-bearing spinels (Jackson et al., 2014). The 1 μm absorption feature is very prominent, and the high iron content of the SAC Cr-spinels has resulted in the stronger and broader feature in this wavelength region (Fig. 6.8b). The 1.3 μm band in the Cr-spinels is centered near 1.29 μm , and this weaker absorption feature is caused by the spin-allowed crystal field transition in the Cr^{2+} located in the tetrahedral site of the crystal structure (Greskovich and Stubican, 1966; Mao and Bell, 1975; Cloutis et al., 2004). This band is superposed by the

stronger and broader absorption feature in the 1000 nm region, which could be discerned from the flattening of the spectra in the 1.3 μm wavelength region.

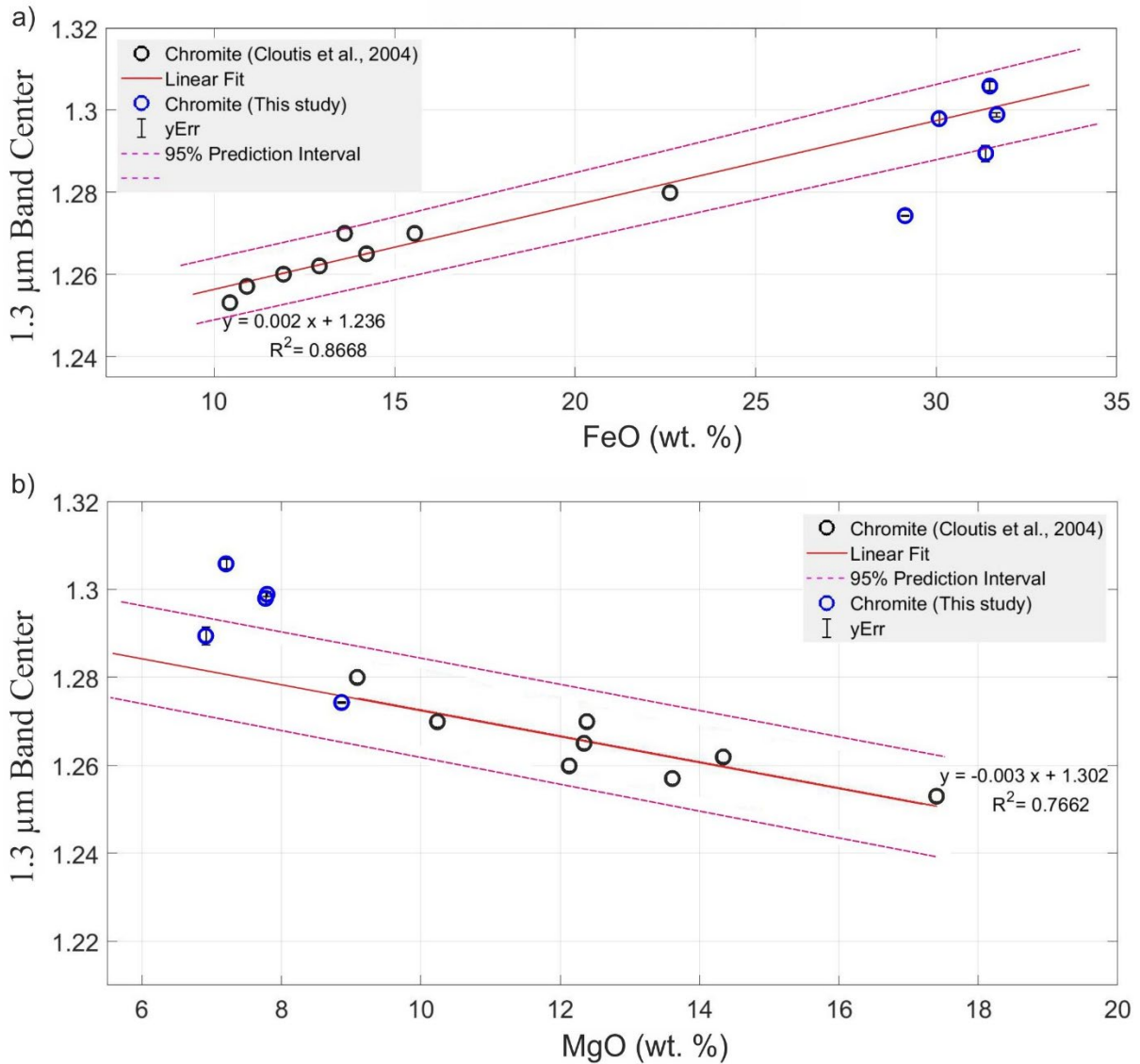


Figure 6.9: Plot showing the 1.3 μm band position against (A) wt% FeO and (B) wt% MgO of the Cr-spinels from the present study. The data from Cloutis et al. (2004) are plotted for comparison. The linear least-squares fit, and the correlation interval (95%) for the chromite data from Cloutis et al. (2004) have also been shown.

The distinctive nature of the shorter Cr^{3+} -related absorption bands, combined with the flattening of the Cr^{2+} absorption at 1.3 μm , indicates that the chromium in the SAC samples is present largely as octahedral Cr^{3+} (Fig. 6.8) (This study; Williams et al., 2016). The 1.3 μm band is sensitive to the FeO and MgO contents in the Cr-spinels. Therefore, the correlation plot of 1.3 μm band center with wt% FeO and MgO has been shown to understand their spectral-

compositional relationship (Fig. 6.9). The chromite data from Cloutis et al. (2004) has also been plotted in the correlation plot for comparison. A linear least square regression fit was given to the reference data, and upper and lower correlation interval for the linear fit has also been derived (Fig. 6.9). This will enable us to understand the shift in the absorption band centres in response to the variations in the wt% oxide concentrations.

The FeO content in the Cr-spinels ranges from 28 to 32%, while the MgO content ranges from 6 to 9%. The Cr-spinels plot along the main trend of reference chromite data from Cloutis et al. (2004) and fall within the 95% prediction interval of the linear fit to the reference data (Fig. 6.9). A positive correlation between FeO content and 1.3 μm band position has been observed (Fig. 6.9a) whereas, the MgO content in the Cr-spinels displays a negative correlation with the 1.3 μm band position (Fig. 6.9b). The 1.3 μm band center moves to longer wavelengths with increased FeO content and a corresponding decrease in the MgO abundances. In SR6, SR14, and SR14l samples, the 1.3 μm band center, appears to have shifted longward due to greater FeO content (Table 6.2). Besides, certain Cr-spinel compositions occupy the space outside the correlation interval, which implies that a decrease in the FeO content can shift the 1.3 μm band center further shortward, as explained by the positive correlation between FeO content and 1.3 μm band center. Similarly, the compositions outside the prediction interval of the reference data in the MgO vs 1.3 μm plot also imply a longward shift in the 1.3 μm band center with a corresponding decrease in the MgO content of the Cr-spinels. The prominent absorptions in the 1 μm and 2 μm regions suggest that the iron is present as both tetrahedral and octahedral Fe^{2+} in the SAC Cr-spinels. The 2 μm band represents the intense and broader absorption feature in the Cr-spinels. The broader absorption band in the 2 μm region with two overlapping absorption features shortward of 2 μm and near 2.2 μm are common in all the analyzed samples. The enhanced Al content in the Cr-spinels has significantly contributed to the overlapping absorption feature shortward of 2 μm (Fig. 6.8b). The central 2 μm band in the SAC Cr-spinels is centered at ~ 2.09 μm . Typically Cr-spinels show 2 μm band positions at longer wavelengths (greater than 2.1 μm). However, the greater Al contents ($\text{Al}_2\text{O}_3 \sim 25$ wt%) in the Cr-spinels from the SAC causes band centers to shift to fairly shorter wavelengths (~ 2.09 μm) (Fig. 6.10, Table 6.2). The 2 μm band depths in the analyzed samples are 22.5% on average. The 2 μm band depth increases with an increase in Fe^{2+} content (Cloutis et al., 2004). The 2 μm band position shows a positive correlation with the Cr# and Cr_2O_3 contents, whereas a negative correlation with Al_2O_3 content (Fig. 6.10). This linear relationship is mainly due to the substitution of Al and Cr for one another in the crystal structure (Cloutis et al., 2004; Sarkar

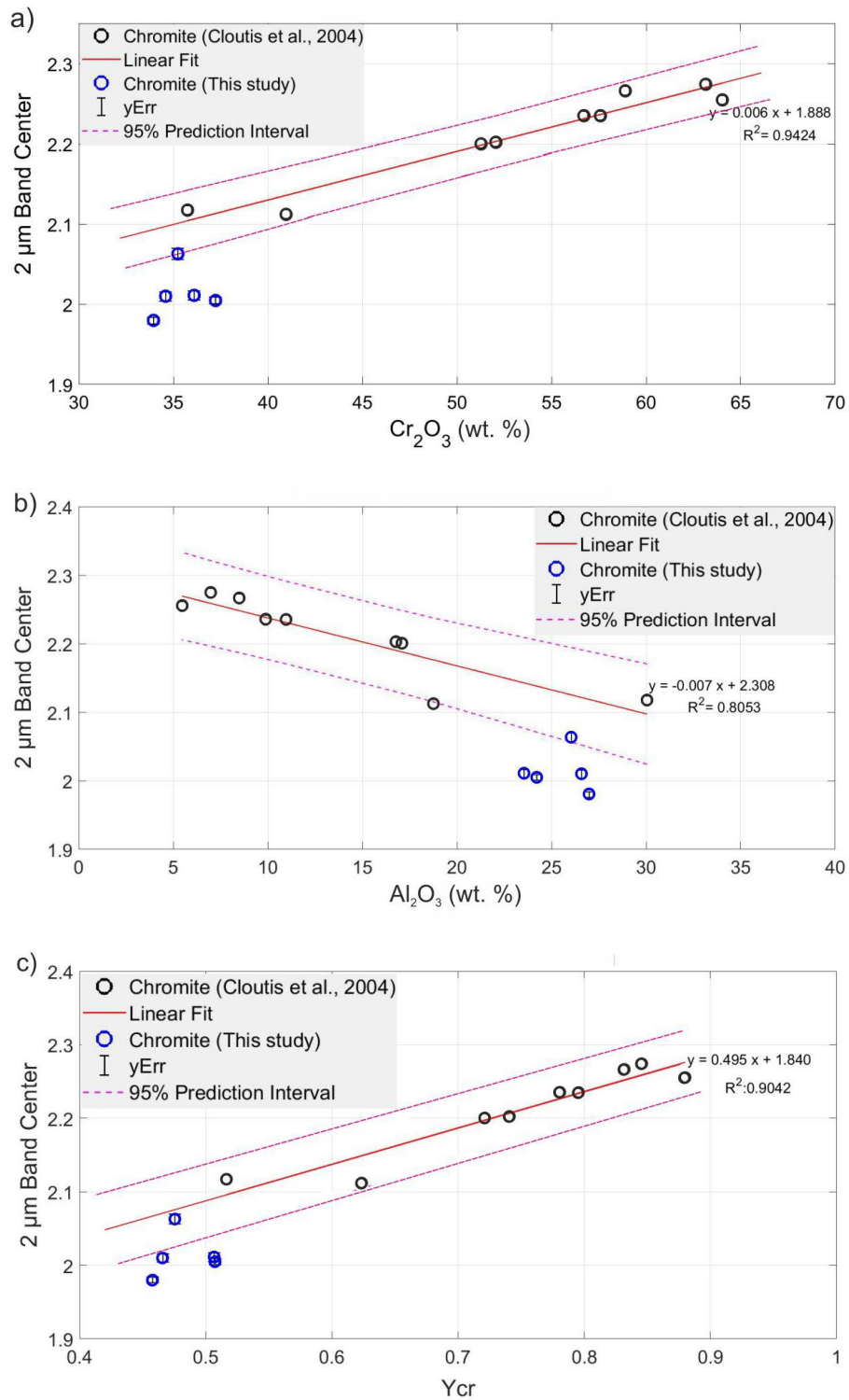


Figure 6.10: Plot showing the 2 μm band position against (A) wt% Cr₂O₃, (B) wt% Al₂O₃, and (C) Cr# of the Cr-spinels from the present study. The data from Cloutis et al. (2004) are plotted for comparison. The linear least-squares fit and the correlation interval (95%) for the chromite data from Cloutis et al. (2004) have also been shown.

et al., 2019). In the Cr₂O₃ vs 2 μm plot, most of the Cr-spinel compositions appear to deviate from the main trend (Fig. 6.10a). This deviation from the trend of reference chromites can be attributed to a combined effect of moderately lower Cr₂O₃ contents and enhanced Al₂O₃ content of the Cr-spinels, which causes an unsystematic shift in the 2 μm band center typically towards shorter wavelengths (Fig. 6.10a, Table 6.2). Similarly, the compositions plotted outside the prediction interval in Al₂O₃ vs 2 μm band center plot can also be attributed to greater Al₂O₃ contents combined with a relatively lesser wt% Cr₂O₃ that collectively lowers the 2 μm band center value to shorter wavelengths which otherwise show a systematic longward shift with the gradual decrease in Al₂O₃ contents (Fig. 6.10b).

The Y_{Cr} value also positively correlates with the 2 μm band center (Fig. 6.10c). The Cr# in the SAC Cr-spinels is 0.48 on average. The 2 μm band center is seen at shorter wavelengths when the Cr# of analyzed Cr-spinels is lesser than reference Cr-spinels (Fig. 6.10c). Though the 2 μm band is commonly attributed to the Fe²⁺ crystal field transitions absorptions in Cr-spinels, the positive correlation with the Cr content is explained by the changes in band positions arising from differences in oxygen-cation bond lengths as Cr substitutes for Al in Cr-spinels (Preudhomme and Tarte, 1971a, b; Farmer, 1974).

Based on these observations, it is inferred that the 2 μm band center is explicitly controlled by the relative abundances of Al₂O₃, Cr₂O₃, and Cr# in the SAC Cr-spinels (e.g., Cloutis et al., 2004; Sarkar et al., 2019). The 2 μm band position moves to longer wavelengths with increasing Cr₂O₃ and Cr# abundances and correspondingly shifts to shorter wavelengths with enhanced Al₂O₃ content in Cr-spinels. This linear relationship between the 2 μm band position and Cr/Al abundance apparently evidence that the 2 μm band center is substantial in discriminating Al-spinels and Cr-spinels.

6.4.3.3 Fourier Transform infrared spectroscopic analysis

The FTIR spectra of Cr-spinels typically show absorptions at around 966 cm⁻¹, 1007 cm⁻¹, and 1052 cm⁻¹. Four active infrared vibration modes were defined for Cr-spinels based on their crystal structure (Terada and Maekawa, 1964; Farmer, 1974; Anki and Lefez, 1996; Cloutis et al., 2004; Reddy and Frost, 2005). The active vibrational modes are attributed to the vibration of oxygen atoms in the (Cr^{VI}O₄)⁻ group along the [111] axis (ν₁), vibrations of oxygen ions perpendicular to the bond axis (ν₂), and the oscillations of metal ions in the isotropic field of their octahedral or tetrahedral environments (ν₃ and ν₄) (Reddy and Frost, 2005). Among these four vibrational modes, the ν₁ and ν₂ are attributed to lattice vibrations of the octahedral ions.

The ν_3 and ν_4 vibrations are controlled by the tetrahedral and octahedral cations synchronously (Reddy and Frost, 2005). The FTIR spectra of the analysed SAC Cr-spinels are shown in Fig. 6.11. The obtained spectra have been compared with the available reference data (Cloutis et al., 2004, and references therein).

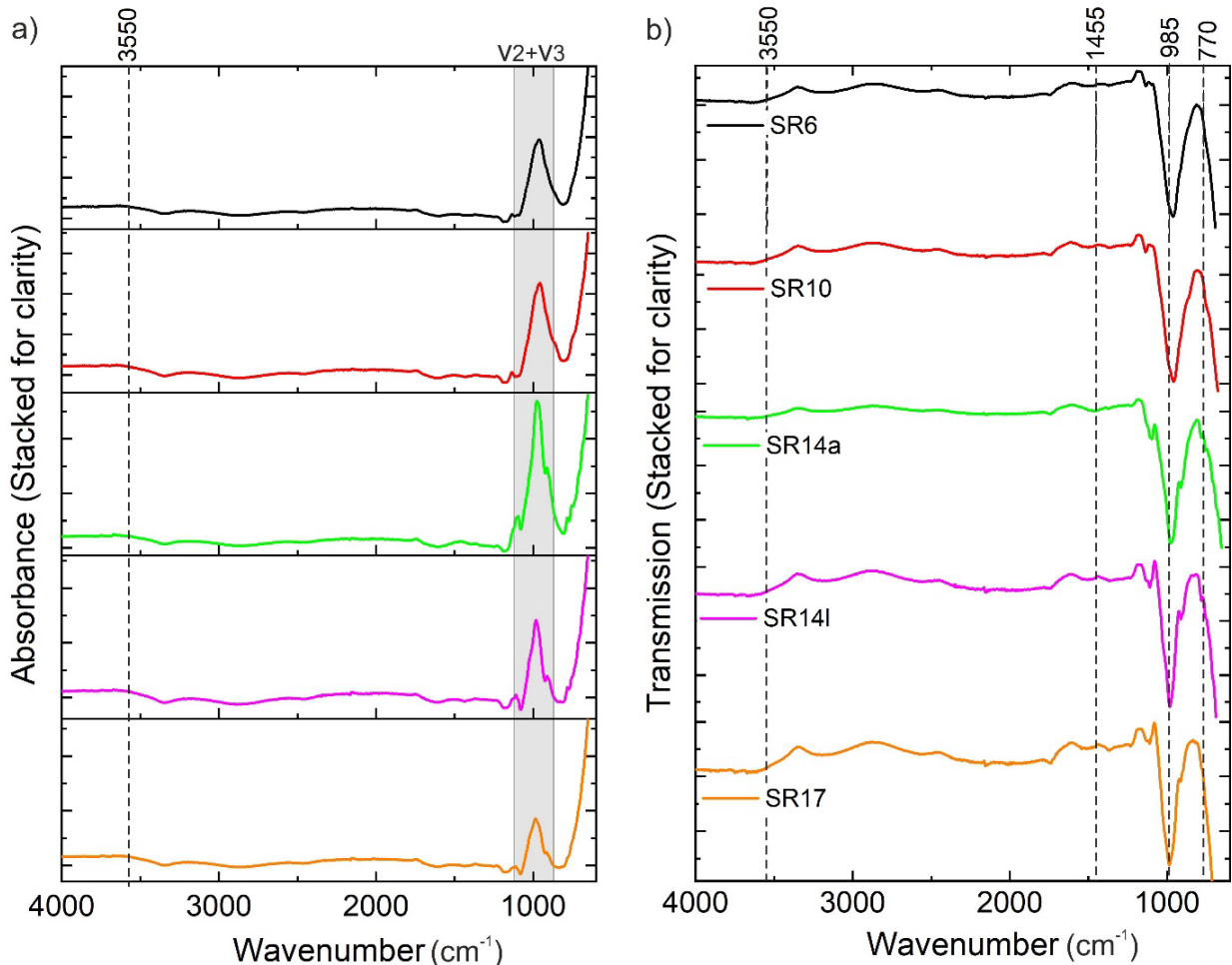


Figure 6.11: FTIR spectra of the Cr-spinels from the present study. (A) Absorbance and (B) Transmittance.

The features between 1000 and 500 cm^{-1} exhibit the fundamental frequencies of Cr-spinel, particularly at around 985, 770, 710, and 650 cm^{-1} (Reddy and Frost, 2005). The observed peaks corresponding to the Cr-spinel vibrational modes are between 913 and 1098 cm^{-1} , which are likely the combined effect of ν_2 and ν_3 vibrations (e.g., Sarkar et al., 2019) (Fig. 6.11a). The 985 cm^{-1} and 650 cm^{-1} bands appear to be strong relative to the other two weak features. The medium-intensity broad infrared absorption bands of the Cr-spinels are around 3550, 3425, 3295, 1455, 985, and 650 cm^{-1} (Reddy and Frost, 2005). The 3550 cm^{-1} feature is attributed to the bonding of the OH group with the octahedral $\text{Cr}^{3+}/\text{Al}^{3+}$ cations. The vibration

feature at 1455 cm^{-1} is assigned to H-O-H bending mode, indicating the presence of molecular water adsorbed in Cr-spinel (Fig. 6.11b).

6.4.4 Implications for the characterization of spinels on the Moon

Planetary geoscientists have applied the VIS-NIR, Laser Raman, and FTIR spectroscopic techniques to understand the mineral chemistry and identify the presence of organic molecules, if any, on planetary surfaces (e.g., Gross and Treiman, 2011; Gross et al., 2014; Jackson et al., 2014; Williams et al., 2016). The present study using this integrated approach on SAC Cr-spinels has enabled the understanding of variations in spinel compositions with respect to their octahedral and tetrahedral cation distribution (Fig. 6.12a-b). This study further attempts to apply the results and interpretations for retrieving the compositional information of analogous spinel compositions on the Moon. Initially, the lunar spinels were identified by analyzing returned samples from the Apollo and Luna missions and lunar meteorites. The spinels were identified from different source rocks such as basalts, high alumina basalts, pyroxene-phyric basalt, gabbro, anorthosite, pink spinel anorthosite, breccia, and so on. Most of these spinel compositions were Fe-rich and showed a compositional range between chromite and ulvospinel (e.g., Taylor et al., 1971; Nehru et al., 1976; El Goresy et al., 1976; Haggerty, 1978). The mare basalts showed an abundance of Cr- and Ti-rich spinels with Al_2O_3 content varying from 2.21 to 61.2 wt%, and Cr_2O_3 and TiO_2 contents in the 0.07 to 47.8 wt% and 0.07 to 32.8 wt% ranges, respectively (Haggerty, 1971, 1972b, c, 1973, Papike et al., 1976; Haggerty, 1977). In contrast, spinels from the ejecta region and highlands, particularly anorthosites, anorthositic gabbros, troctolites, and impact breccia samples, showed a higher proportion of Mg-Fe and Mg-Al spinels (e.g. Papike et al., 1991). Besides these, the wide orbital detections of spinels across the lunar surface using Moon Mineralogy Mapper (M3 onboard ISRO's Chandrayaan-1 mission) and Spectral Profiler (aboard JAXA's Kaguya mission) in recent years shed new light on their significant role in the evolution of the lunar crust (Pieters et al., 2011; Dhingra et al., 2011a, b; Pieters et al., 2011; Bhattacharya et al., 2012a; Kaur et al., 2012; Pieters et al., 2014; Prissel et al., 2014; Dhingra et al., 2017). Most of the orbital detections of spinels are Mg- and Al-rich with limited occurrences of Cr- or Fe-rich compositions associated with pyroclastic deposits in Sinus Aestuum (Fig. 6.13) (Yamamoto et al., 2013; Sunshine et al., 2014; Weitz et al., 2017). A new rock type named "Pink Spinel Anorthosite" (PSA) enriched in MgAl_2O_4 spinel with a low modal abundance of mafic silicates was found to occur in low Fe-terrains dominated by plagioclase feldspar on the Moon. The global occurrence of PSAs has been explained by the interaction between Mg-suite

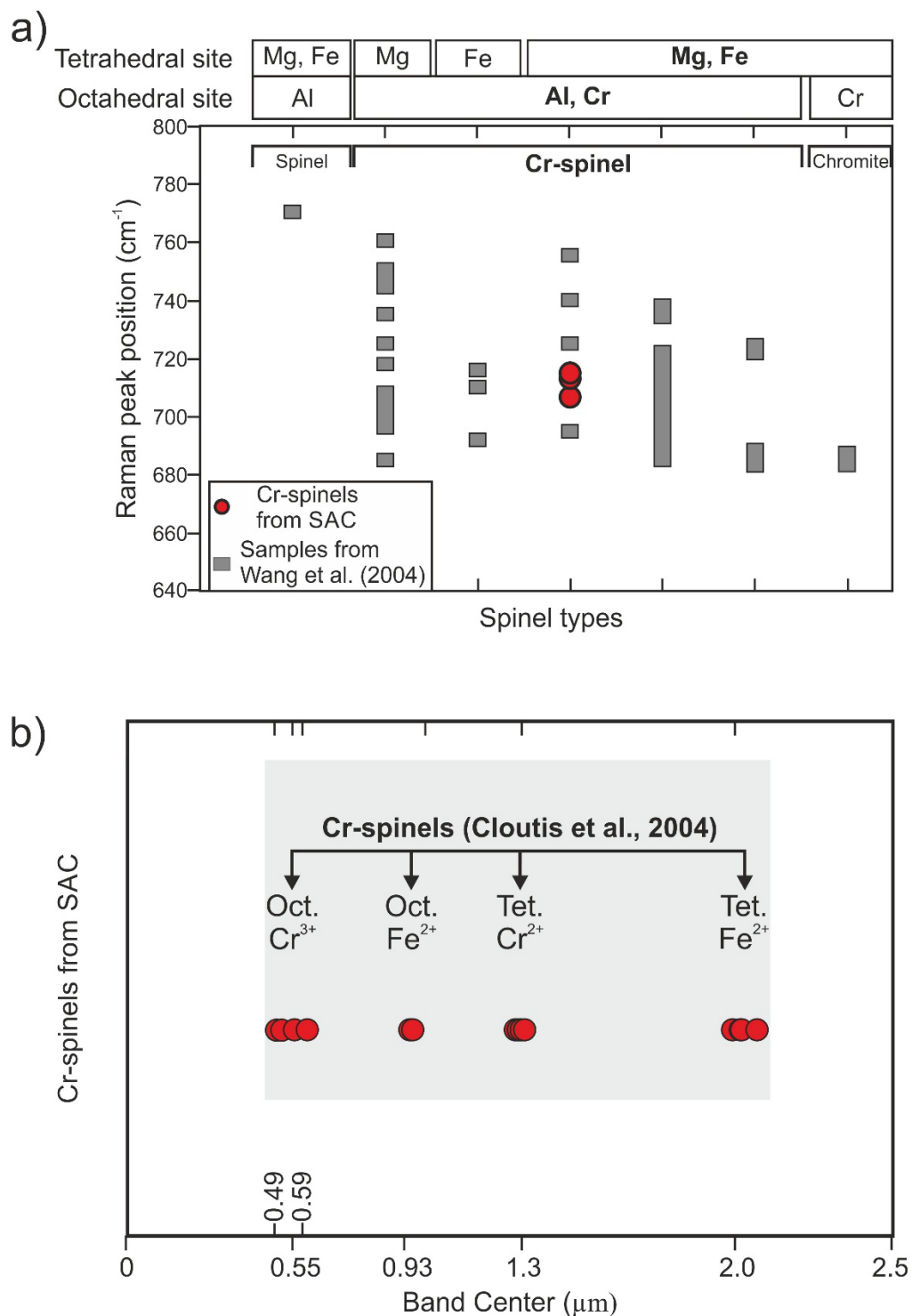


Figure 6.12: (A) The A_{1g} peak position of the SAC Cr-spinels and their corresponding cation distribution in the tetrahedral and octahedral sites of the spinel structure (modified after Wang et al., 2004). The data are plotted in comparison with the A_{1g} peak distribution and their cation assignment from Wang et al. (2004). (B) The absorption band centres of Cr-spinels in SAC and their corresponding cations of tetrahedral and octahedral sites (after Cloutis et al., 2004).

parental melts and the ancient anorthositic crust (Pieters et al., 2014; Prissel et al., 2014). Another distinctive rock type, dominated by high concentrations of olivine, orthopyroxene, and Mg-rich spinel (OOS: Olivine- Orthopyroxene-Spinel) has also been reported using M3 data (Pieters et al., 2011). The differentiation of magma from plutons intruded into the lower crust or at the crust-mantle interface was suggested for the formation of these unusual lithologies (Pieters et al., 2011; Bhattacharya et al., 2012b). Recent experimental work suggests that spinel-bearing materials could also be formed from the last liquids that crystallize in the Lunar Magma Ocean (Lin et al., 2017). Though several models were proposed for the formation of spinel-bearing lithologies detected orbitally on the Moon based on their spectrochemical information and experimental studies (Gross and Treiman, 2011; Yamamoto et al., 2013; Prissel et al., 2014; Gross et al., 2014), constraining their composition from the reflectance spectra for understanding the petrogenesis is still challenging because of the limitations of M3 data and space weathering effects on the spectral response (Isaacson et al., 2014; Pieters and Noble, 2016).

Fe-, Al-rich Cr-Spinels from SAC		Cation Assignment	Spinels from Sinus Aestuum (Yamamoto et al., 2013)
Absorption bands	0.49 (μm)	Octahedral Cr^{3+}	Unidentified
	0.55 (μm)		
	0.59 (μm)		
	1.0 (μm)	Octahedral Fe^{2+}	Present
	1.3 (μm)	Tetrahedral Cr^{2+}	Absent (except certain locations)
	2.0 (μm) ($<2.1\mu\text{m}$ -high Al^{3+})	Tetrahedral Fe^{2+}	Present ($>2.1\mu\text{m}$ -more chromian)

Figure 6.13: The absorption band centres in SAC Cr-spinels are compared with those from the spinels in the Sinus Aestuum region on the Moon (Yamamoto et al., 2013).

Cr-spinels in the SAC show Cr# in the range of 0.44–0.53, and the Al_2O_3 and Cr_2O_3 contents in the ranges of 22–27 wt% and 32–37 wt%, respectively. The compositions having similar Cr_2O_3 (~37 wt%), Cr# (~0.49), TiO_2 (≤ 1 wt%), and Al_2O_3 (~26 wt%) concentrations as the

SAC Cr-spinels were present in Apollo 12, 14 (14303,50), and 15 breccia samples (Fig. 6.5a & c, Roedder and Weiblen, 1972; Papike et al., 1991). This implies the occurrence of spinels on the Moon having chemical similarity with the Cr-spinels of SAC. The compositions of similar chromium levels as SAC Cr-spinels are not detected in remotely observed lunar spinels. Still, they are likely to be present on the Moon. However, unidentified yet probably due to the limited resolution of the instruments and complexities involved in spectral deconvolution (e.g., Papike et al., 1991). Therefore, this study emphasizes comparing the spectrochemical characteristics of SAC Cr-spinels with the available compositionally analogous lunar spinel spectra. This approach could be useful for validating our results and provide a reference for identifying similar compositions (if present) in the remote spectra from the lunar surface. The terrestrial spectra reveal that the short-wavelength absorption bands are mostly governed by the presence of Fe^{3+} , which is insignificant in lunar spectra because of low oxygen fugacity on the Moon (Cloutis et al., 2004). In the lunar sample spectra (Apollo 17 Sample ID: 70002, 7), the 1 μm and 2 μm absorptions corresponding to Fe^{2+} and 0.55 μm feature of octahedral Cr^{3+} were identified (Mao and Bell, 1975; Yamamoto et al., 2013; Williams et al., 2016). Among these bands, the 0.55 μm feature of octahedral Cr^{3+} is common to both lunar (70002, 7) and SAC Cr-spinel spectra (Mao and Bell, 1975; in this study). This feature was not obvious in the remotely observed lunar spinel spectra, except for a very small feature in the M^3 spectra that starts at 0.54 μm , which was not distinguishable to be considered for the presence of octahedral Cr^{3+} content (Pieters et al., 2011; Pieters et al., 2014; Weitz et al., 2017). Among the remotely observed spinels on the Moon, the compositions identified in the Sinus Aestuum region through M^3 spectra were considered to be Fe- and /or Cr-bearing spinels; hence the spectra from this region are compared with those of SAC Cr-spinels (Fig. 6.13). The Sinus Aestuum compositions showed absorptions in visible wavelengths Yamamoto et al., 2013; Weitz et al., 2017). Similar visible wavelength features (0.4–0.56 μm , 0.57–0.72 μm) are observed in the Fe- and Al-rich Cr-spinel spectra of SAC (Fig. 6.13). An experimental study by Jackson et al. (2014) showed that an increase in the Fe content in spinels produces a stronger 1 μm band. Therefore, the spinels in the Sinus Aestuum region displaying the 1 μm band are likely to be of Fe-rich composition when compared with the stronger and broader 1 μm absorption feature (octahedral Fe^{2+}) arising from the increased iron content in the SAC Cr-spinels (Fig. 6.13). The 1.3 μm feature present (though superposed by the 1 μm absorptions owing to high iron content) in high Fe- SAC Cr-spinels is not noticed in the Sinus Aestuum spectra. This indicates the absence of tetrahedral Cr^{2+} in Sinus Aestuum composition, which corroborates well with the previous observations of Fe-rich spinel in Sinus Aestuum (Yamamoto et al., 2013) (Fig. 6.13). The increased iron content in the Sinus Aestuum composition prevents divalent chromium from being stabilized in the spinel structure (Mao and Bell, 1975). This observation is

consistent with the experimental studies revealing the absence of 1.3 μm absorption in lunar compositions since the chromium usually occurs as octahedral Cr^{3+} in spinels on the Moon (Jackson et al., 2014; Williams et al., 2016). Some spectra in the Sinus Aestuum region showed a weaker 1.3 μm band, possibly arising from the tetrahedral Cr^{2+} in spinels formed as a result of low oxygen fugacity conditions (Yamamoto et al., 2012; Williams et al., 2016). The 2 μm band identified in SAC Cr-spinels is also present in Sinus Aestuum, implying the presence of tetrahedral Fe^{2+} in Sinus Aestuum compositions (Fig. 6.13). The 2 μm band in the Sinus Aestuum spectra is centered beyond 2.1 μm (Weitz et al., 2017) in contrary to the SAC Cr-spinels showing 2 μm band centres much shortward ($\sim 2.01 \mu\text{m}$) in response to the increased Al content (Fig. 6.13). This longward shift observed in the 2 μm band center in Sinus Aestuum compositions favors the inference that these spinels are more Fe- and Cr-bearing compositions (Yamamoto et al., 2013; Williams et al., 2016; this study). However, the absence of any octahedral Cr^{3+} feature at 0.55 μm in Sinus Aestuum spinels, unlike the SAC Cr-spinel, might not support the presence of Cr-bearing spinel in the Sinus Aestuum (Fig. 6.13). The 0.55 μm feature is probably unidentified due to the limitations of M^3 data at shorter wavelengths (Weitz et al., 2017). Hence, the possibility for the presence of Fe- and Cr-bearing spinel in Sinus Aestuum cannot be ruled out, and future studies using hyperspectral data of good spectral resolution in the visible range should throw more light on their probable occurrence in the region. Further, the comparison with the Sinus Aestuum spinel spectra favors the idea that the Fe- and Al-rich Cr-spinels from SAC can act as a potential analogue for lunar spinels of similar composition. The 2 μm band center beyond 2.1 μm in Sinus Aestuum compositions limits the interpretation of possible Al content in the Sinus Aestuum compositions, unlike the SAC spinels. However, the 2 μm band center could be affected by the residual thermal components in the M^3 spectra (e.g., Li et al., 2016), and therefore, the possibility for the presence of Al-bearing compositions remains relevant. The data from IIRS (Imaging Infrared Spectrometer) aboard ISRO's Chandrayaan-2 mission will help us address these discrepancies as it covers wavelengths from 0.8 to 5 μm , thereby more unambiguous characterization of the diagnostic 2.8 μm unique to Al-spinels should be possible (Bhattacharya et al., 2020).

The processes involved in the formation of the Cr-spinels in the SAC and those on the Moon shall be taken into account while considering the former as a potential lunar analogue. The wide variations in lunar spinel compositions can be attributed to the different petrogenetic conditions under which they have been formed (e.g., Roedder and Weiblen, 1972; Papike et al., 1991). The minerals like chromite, ilmenite, etc., can form on the Moon through crystal settling in silicate magmas, similar to those found in anorthosite intrusions on the Earth (Papike et al., 1991). On the Earth, slow cooling and physical separation processes cause the accumulation of such minerals. Stillwater Anorthosite complex in Montana, Bushveld Igneous

complex in South Africa, and Sittampundi Anorthosite Complex are examples of anorthosite intrusions containing concentrations of oxide minerals. However, the conditions of the formation of oxide minerals on the Moon are considerably different in terms of higher temperatures and low oxygen partial pressures (Papike et al., 1991). Most of the elements in lunar minerals, including Fe^{2+} , Ti^{3+} , Cr^{2+} , occur in low oxidation states owing to the low oxygen partial pressures on the Moon (Sato et al., 1973; Sato, 1978). The concentration of oxide minerals also depends on crystal settling velocities in melts (cf. Papike et al., 1991). The Moon exhibits 1/6th the gravity of the Earth while the viscosity of melts in the lunar interior is 10 to 100 times less than that on the Earth. The less viscosity in lunar magmas overcomes the effects of low lunar gravity and results in greater crystal settling velocities in melts, thereby increasing the chances of crystallizing minerals accumulating to the bottom of the cooling melt (cf. Papike et al., 1991). Hence, it is possible that the chromites formed in the setting of anorthosite intrusions similar to those on the Earth could be present on the Moon (Taylor and Lu, 1990).

He et al. (2020), based on microtextural, geochemical, and isotopic studies on SAC-hosted Cr-spinels, suggested a process involving melt injection into anorthositic mush and subsequent melting and mixing for the saturation of Cr-spinels in the anorthosite complex. The study assumed a similar mechanism for the Cr-spinel formation in other anorthosite intrusions such as Fiskensæset and Guelb el Azib Complexes (He et al., 2020). In the SAC, the replenished magma in the anorthositic mush remelted the plagioclase that increased the Al^{3+} content in the magma, followed by the addition of SiO_2 and evolved interstitial melt into the replenished melt containing Cr_2O_3 , precipitated high Al Cr-spinels (He et al., 2020). A similar mechanism of crustal assimilation of an Mg-suite parental magma with the ancient plagioclase-rich anorthositic crust was proposed for the formation of widely detected Mg-Al spinels associated with crustal anorthosites on the lunar surface (e.g., Prissel et al., 2014). The experimental study on lunar compositions showed that Fe-rich spinels could also form via the interaction of parental melt of Apollo 15 green glass composition with the crustal anorthositic materials on the Moon (Prissel et al., 2014). The formation of Fe- and Al-rich spinels in the Sinus Aestuum was explained by a similar process in which high-Ti picritic melts interacted with the anorthositic crust at depths before the eruption of pyroclastic deposits, which produced Fe-rich spinels in the region (Prissel et al., 2014; Weitz et al., 2017). The experimental study by Lin et al. (2017) showed that lunar spinels might also form as the final products of Lunar Magma Ocean crystallization and, therefore, should be confined to the base of the lower crust. Several studies are still underway to understand the genesis of spinels on the Moon. Further studies on the effects of oxygen fugacity and chromium levels would provide more insights into the formation of similar spinel compositions on the Moon. Future missions on sample returns,

more sophisticated analyses on the returned samples, and high-resolution orbital data are required to substantiate these inferences.

The spectrochemical characterization of Cr-spinels in the present study would also be helpful to planetary geoscientists for precisely identifying and retrieving compositional information from spectral data of remotely detected spinels on other planetary surfaces. The hyperspectral spectroradiometers have already flown in different interplanetary missions. Many space agencies, including ISRO, ESA, JAXA, and NASA, are planning to deploy Laser Raman and FTIR spectrometers in their future lander-rover missions to Moon. Hence, the data generated from the present study would be a significant addition to the planetary analogue database that could be useful for pre-flight calibration of payloads and data interpretation. The SAC anorthosites were already proposed as an analogue to lunar highland anorthosites based on their chemical, geotechnical, and geomechanical similarities (Anbazhagan and Arivazhagan, 2010; Anbazhagan, 2012; Venugopal et al., 2020a; 2020b). As a result, a lunar highland soil simulant (also known as Indian Moon soil) was manufactured using the analogue anorthosites in the SAC (Venugopal et al., 2020a; 2020b). A testbed was created at ISRO's Lunar Terrain Test Facility in Bangalore using the crushed anorthosite from SAC. The Lander (Vikram) and rover (Pragyan) in the Chandrayaan-2 mission were tested in this "lunar surface terrain testbed" under simulated conditions (Venugopal et al., 2020a; 2020b). The simulant can be used in future missions to test the mobility of rovers and study the geomechanical properties of the lunar soil (Venugopal et al., 2020a; 2020b). The inferences from our study on the analogous nature of SAC Cr-spinels would further affirm the potential of the Sittampundi Anorthosite Complex as a promising lunar analogue site, which will be useful for testing and calibration of instruments in future lunar exploratory missions.

6.5 Summary

The present study has analyzed the spectral and chemical characteristics of Cr-spinels in chromitites of Sittampundi Anorthosite Complex, southern India. Chromitite layers of varying thickness are found to be associated with the SAC. Fe- and Al-rich composition of Cr-spinels are characteristic of the SAC-hosted chromitites, with Cr₂O₃ contents and the Cr# ranging from ~32–37 wt% and 0.44–0.53, respectively. The prominent Raman peak corresponding to the A_{1g} mode of Cr-spinels varies from 703 cm⁻¹ to 714 cm⁻¹ with a shoulder around 671 cm⁻¹. The longward shift in the A_{1g} peak (~705–714 cm⁻¹) is suggested to be caused by the substitution of Al³⁺ in the spinel structure. The A_{1g} peak position near 705 cm⁻¹ in the Raman spectra is caused by the coexistence of (Mg, Fe) in the tetrahedral site and (Al, Cr) in the octahedral site.

The hyperspectral data of the Cr-spinels showed diagnostic absorption bands at 0.49 μm , 0.59 μm , 0.69 μm , 0.93 μm , 1.3 μm , and 2 μm . The 2 μm and 0.93 μm bands appear to be relatively stronger and broader in all the samples, apparently due to a relatively higher abundance of Fe^{2+} in the samples. The 2 μm band position is at relatively shorter wavelengths than that of the typical Cr-spinels due to enhanced Al content ($\text{Al}_2\text{O}_3 \sim 25 \text{ wt}\%$) in the SAC Cr-spinels. The 2 μm band position shows a positive correlation with the Cr# and Cr_2O_3 contents, whereas a negative correlation with Al_2O_3 content. This linear relationship is explained by the substitution of Al and Cr for one another. The observed linear relationship between 2 μm band position and Cr/Al abundances can be used to differentiate Al-spinels and Cr-spinels based on their spectrochemical characteristics. The FTIR analysis revealed peaks corresponding to the Cr-spinel vibrational modes between 913 and 1098 cm^{-1} , which are attributed to the combined effect of ν_2 and ν_3 vibrations arising from the octahedrally coordinated ions in the Cr-spinel structure. The present study has unambiguously established the relationship between the spectral pattern and chemistry of the Cr-spinels through an integrated and comparative analysis of spectroscopic and chemical data. The in-depth analysis of differences in the spectral pattern corresponding to the chemical variations will necessitate the accurate identification and interpretation of chemically similar lunar spinels observed through orbital remote sensing data. The comparison of the spectral features of SAC Cr-spinels with those of the previously identified spinels from Sinus Aestuum has enabled the interpretation of probable occurrences of Fe- and Cr-bearing spinels in the Sinus Aestuum on the Moon. The inferences based on the spectral-chemical relationships will add as a reference for distinguishing lunar Al spinels from the Cr-spinels. The SAC-hosted Cr-spinels could act as a potential functional analogue for lunar Fe- and Al-rich spinels provided that constraints on their formation processes involving melt-wall rock interaction on both the planetary bodies. The data generated from this study would be an addition to the current database of planetary analogue materials that could be utilized for calibration purposes and data interpretation from future missions.

This chapter is the reproduction of an article published in the journal Spectrochimica Acta Part A: Molecular and Biomolecular Spectroscopy.

Thesniya P. M., Saranya R., and Rajesh V. J., 2021. Compositional and Spectrochemical Analysis of Cr-spinels in the Sittampundi Anorthosite Complex, Southern India: Implications for Remote Observation of Spinels on the Moon. Spectrochimica Acta Part A: Molecular and Biomolecular Spectroscopy 255, p.119677. <https://doi.org/10.1016/j.saa.2021.119677>.

Chapter 7

Morphology and Ejecta Emplacement Dynamics of the Selected Copernican craters on the Lunar Farside: Insights into Cratering Mechanics of the Moon

Overview

Impact craters are the most common geological features on planetary surfaces. Studying morphology and ejecta emplacement of impact craters provides important information about the impact dynamics and cratering processes. The present study focuses on the characterization of distinct morphological units in the Ohm and Das craters and ejecta facies of the Copernican-aged Das crater located on the farside of the Moon. The study utilized high-resolution grey-scale images, Digital Elevation Model, and derived data products from various lunar orbiter missions. The mapping of distinct morphological features in the Das crater cavity revealed that the excavation of transient crater cavity to depths of ~3 km took place in less than 4 seconds following the shock wave propagation by the projectile impact. The transient crater depth is estimated to be between 7.6-9.12 km. The displaced materials from the excavating crater cavity were thrown out as highly shocked and melted debris that travelled on a ballistic trajectory, eventually depositing as distinct ejecta facies around the crater. The gravitational collapse of the 30.4 km diameter transient crater triggered a sequence of events in which the initial rim crumbled and walls slumped to develop into a final crater with a

scalloped rim and terraced walls and a subsequent enlargement in the rim-to-rim diameter to ~38 km. The rebound of the crater floor from the depths of ~3.2 km formed the central mounds with a slight offset to the northwest. A western segment of the central mounds is interpreted to have resulted from the rotational slumping of the western wall and subsequent uplift of a small plug in the adjacent crater floor. Impact-generated melts lined the crater interior and cooled down as melt breccia along the inner walls and often overflowed to form melt deposits exterior to the rim. The solidification of impact melts and/or a structural failure along weaker planes in the crater interior likely caused subsidence in the eastern floor section to form elevated and lower hummocky floor units. The target materials from the still-growing crater are embedded in the solidified melt to form the mounds in the hummocky floor. The emplacement of ballistic ejecta facies at varying radial distances from the crater rim followed the deposition of melt-bearing ejecta as rim veneer, ponds in topographic lows, and often as lobate deposits terminal to local topographic slopes within an extent of ~7 km beyond the rim. The ballistic ejecta facies distributed at shorter radial distances form contiguous ejecta blanket, while those deposited farther from the rim are designated to be distal or discontinuous ejecta. The overall asymmetric ejecta pattern with a bilateral symmetry along the line running NNE-SSW through the crater centre suggested an oblique impact for the Das crater formation with the projectile approached from the NNE direction. A nearly circular planform of the crater combined with a well-defined forbidden zone devoid of secondary crater chains and distal ejecta rays in the uprange direction implied that the impact angle was between 15° – 25°. The sequence of events envisaged in the present study and the interpretations on impact dynamics substantiate the significance of studying Copernican craters to better understand the cratering mechanics and impact dynamics of the Moon.

7.1 Introduction

Impact cratering is the excavation of planetary surfaces when hit with meteoroids or cometary bodies in our solar system (Melosh, 1989). Earth's Moon is known to have constantly hit with asteroidal bodies to produce roughly circular depressions called impact craters on its surface (e.g., Shoemaker, 1962; Wilhelms et al., 1987; Pike, 1988; Wieczorek and Philips, 1999). The lunar impact craters are of varying dimensions, and the fundamental processes of impact cratering on the Moon leave characteristic surface features that remain unerased for millions of years, unlike the Earth (Howard, 1974; Pike, 1980a; Pike, 1988; Hörz et al., 1991; Hiesinger and Head, 2006). Simple bowl-shaped craters on the Moon ($D \leq 18$ km) commonly exhibit a nearly circular planform and axisymmetric structure, whereas the onset of complex craters (D

>18 km) are marked by an abrupt change in the crater morphology (e.g., Smith and Sanchez, 1973; Pike, 1974; Pike, 1980a; Melosh, 1989; Kruger et al., 2018). The complex craters characteristically hold a relatively flat floor, steep-sloping walls and terraces, and a typical central peak structure exposing the interior stratigraphic units underneath the impact point (Melosh, 1989). The deposits of ballistic crater interior materials called ejecta thrown out by the target excavation during the impact process are also characteristic of lunar impact craters (Shoemaker, 1962; Oberbeck, 1975; Melosh, 1989; Hörz et al., 1991; Osinski et al., 2011).

Scientists believe that impact cratering has played a significant role in the formation and subsequent history of the planets and their satellites, specifically in hypothesized impact origin of the Moon, Late Heavy Bombardment, impact-induced volcanism, etc. (e.g., Hartmann and Davis, 1975; Cameron and Ward, 1976; Canup and Asphaug, 2001; Canup, 2004; Cohen et al., 2000; Kumar et al., 2016). Therefore, understanding the fundamental processes of impact cratering is crucial in studying planetary evolution. The cratering mechanics of lunar impact craters with distinct morphology and ejecta emplacement principally involves three processes, firstly, the contact of the projectile on the lunar surface and compression of the target materials below the impact point, which is followed by the excavation of the transient crater cavity and simultaneous ejection of the proportion of excavated materials, and eventually, the modification of the transient crater marked by gravitational collapse of the rim and rise of the central peak (e.g., Gault et al., 1968; Stöffler et al., 1975; Shoemaker, 1977; Maxwell, 1977; Orphal, 1977; Croft, 1980; Pike, 1980b; Melosh, 1977; 1982; 1989; Osinski et al., 2011). In general, the gravitational collapse of a simple bowl-shaped crater produces complex craters with a distinguishing enlargement in the final crater diameter (e.g., Melosh, 1977, 1982; Ullrich et al., 1977; Grieve and Robertson, 1979). A proportion of the ejected materials deposit as proximal ejecta blanket appearing to be contiguous and gradually thinning away from the crater rim, whereas the high-velocity components emplace as patchy and discontinuous distal ejecta, often reaching greater radial distances beyond the extent of the continuous ejecta blanket (Shoemaker, 1962; Oberbeck, 1975; Horz et al., 1983; Morse et al., 2018; Morse et al., 2021). The deposits of finer ejecta appear as prominent "rays" extending to greater radial distances away from the parent crater (Hawke et al., 2004).

After the culmination of cratering processes, the craters undergo only limited degradations, specifically by later impact events and lava infillings in an airless body like Moon. These dominant degradational processes bring about noticeable changes in the overall morphology of the crater by eroding their sharp rim, steep walls into gentle slopes, floor fillings, fading of impact ejecta, etc. (Head, 1975). Often the craters fade from their visibility by later infillings and overlapping craters depending on the time span of their exposure to the lunar environment

and the impact flux of the Moon. Based on their level of degradation, lunar craters are assigned different time units ranging from Pre-Nectarian (<4.1 Ga) to the Copernican (<1 Ga) systems (Shoemaker and Hackman, 1962; Wilhelms, 1970; McCauley, 1967). The older craters generally undergo degradation to a greater degree than the younger Copernican craters. Hence, the Copernican craters preserve their pristine morphology, typically marked by bright ejecta rays around the crater (Hawke et al., 2004). The ejecta rays of Copernican craters are discernably visible on the lunar surface because of their contrasting brightness and pristine nature in an airless Moon (Hawke et al., 2004). Additionally, the distinctively higher surface albedo of ejecta rays is considered an expression of their emplacement not earlier than 1 billion years ago in the lunar chronostratigraphic record. Thus, the occurrence of relatively undegraded and younger surfaces in the crater interior and a largely undisturbed ejecta blanket and ray system make the Copernican craters a natural laboratory for studying the impact cratering mechanics of the Moon (Dundas and McEwen, 2007; Li et al., 2017; Dhingra et al., 2017; Morse et al., 2021).

Previous studies have shown that the detailed morphological mapping and an in-depth characterization of the radial extent of ejecta and the physical characteristics of its components are critical for comprehending the impact history and cratering mechanics of the Moon (Osinski et al., 2011; Morse et al., 2018; Morse et al., 2021). The current understanding of the impact cratering mechanics of the Moon is stemmed mainly from such studies on crater interior morphology and ejecta emplacement dynamics (Bray et al., 2010; Van Der Bogert et al., 2010; Kalynn et al., 2011; Kumar et al., 2011; Ashley et al., 2012; Kruger et al., 2016; Dhingra et al., 2017; Zanetti et al., 2017; Plescia and Robinson, 2019; Van Der Bogert et al., 2017; Bray et al., 2018; Morse et al., 2018; Morse et al., 2021). The identification of various morphological features has provided insight into the multi-stage cratering processes, while the nature and distribution of distinct ejecta deposits threw light into the ejecta emplacement dynamics and thereby the direction and angle of the impact event (Gault, 1973; Stoßfler et al., 1975; Gault and Wedekind, 1978; Holsapple and Schmidt, 1987; Schultz and Gault, 1990). Moreover, the reflectance variations in the ejecta blanket might represent the material of multiple compositions excavated by the impact, while the physical characteristics of the ejecta, whether bouldery or smooth deposits, can be a clue to the physical properties of the target material (e.g., solid rock, granular regolith, or a combination of both) (Gillis and Jolliff, 1999; Lakshmi and Kumar, 2020).

We chose to study the Ohm and Das craters on the farside of the Moon to get insights into the impact cratering mechanics of the Moon. The morphological features in the Ohm crater are discussed below.

7.2 Morphology of the Ohm crater on the farside of the Moon

Ohm crater is a Copernican aged crater located in the anorthositic highlands on the farside of the Moon (Fig. 7.2.1). Ohm crater is a complex crater with a well-developed central peak, floor, bright ejecta rays, and terraced wall (Figs. 7.2.2 and 6.2.3). The crater is asymmetric and has a diameter of ~64 km (Fig. 7.2.3).

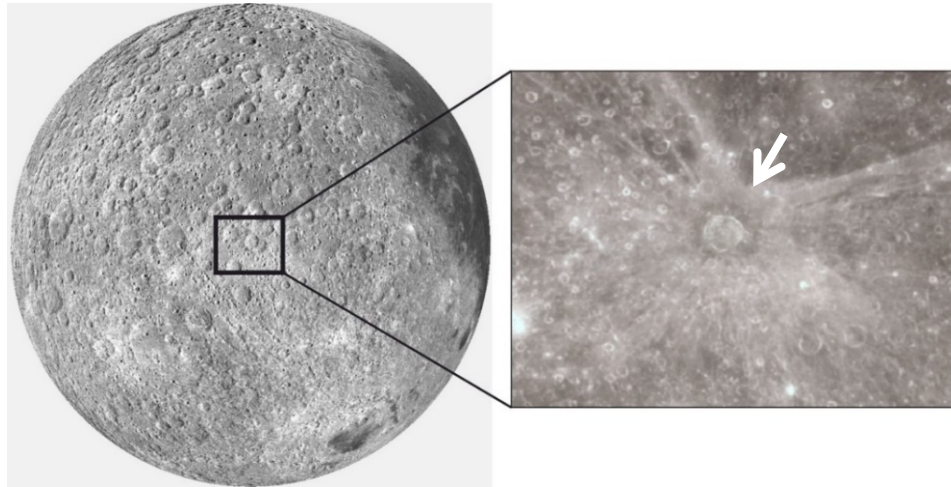


Figure 7.2.1: WAC images showing the location of the Ohm crater on the farside of the Moon. The bright ejecta rays are also visible.

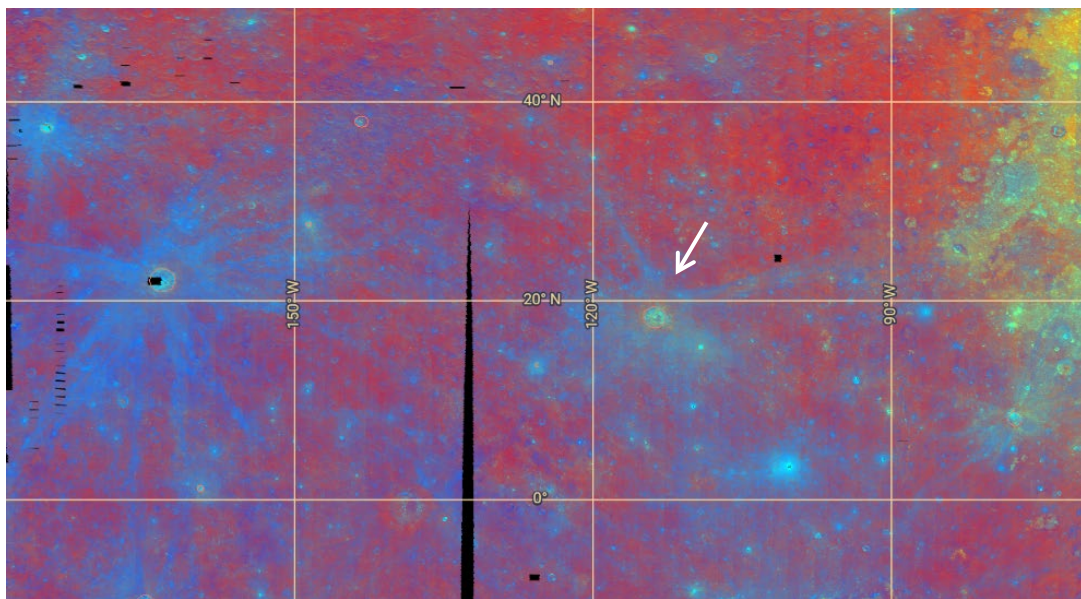


Figure 7.2.2: Clementine UVVIS warped color ratio mosaic (Simple cylindrical, scale-151.5152 pixels/degree) showing the Ohm crater and the extension of its ejecta material on the lunar highlands. (Red = 750 nm/415 nm, Anorthosite; Green = 750 nm/950 nm, Iron-rich, low TiO₂; Blue = 414 nm/750 nm, Iron-rich, high TiO₂).

This young crater dates <1.1Ga, and it has an extensive ray system extending in all directions except the NNE direction, where there is a lack of ray system (Fig. 7.2.2). The asymmetrical distribution of rays indicates an oblique impact event. A bright ray formed in the NNW direction of the crater is extending towards the moon's north pole (Fig. 7.2.2). Another bright ray system formed in the NEE direction of the crater is extending towards the Procellarum terrane. Both of these rays extend over larger distances greater than 1500 km as shown in Figure 7.2.2. These extensive ray systems can be formed if a high-velocity oblique meteorite impacts the feldspathic highlands.

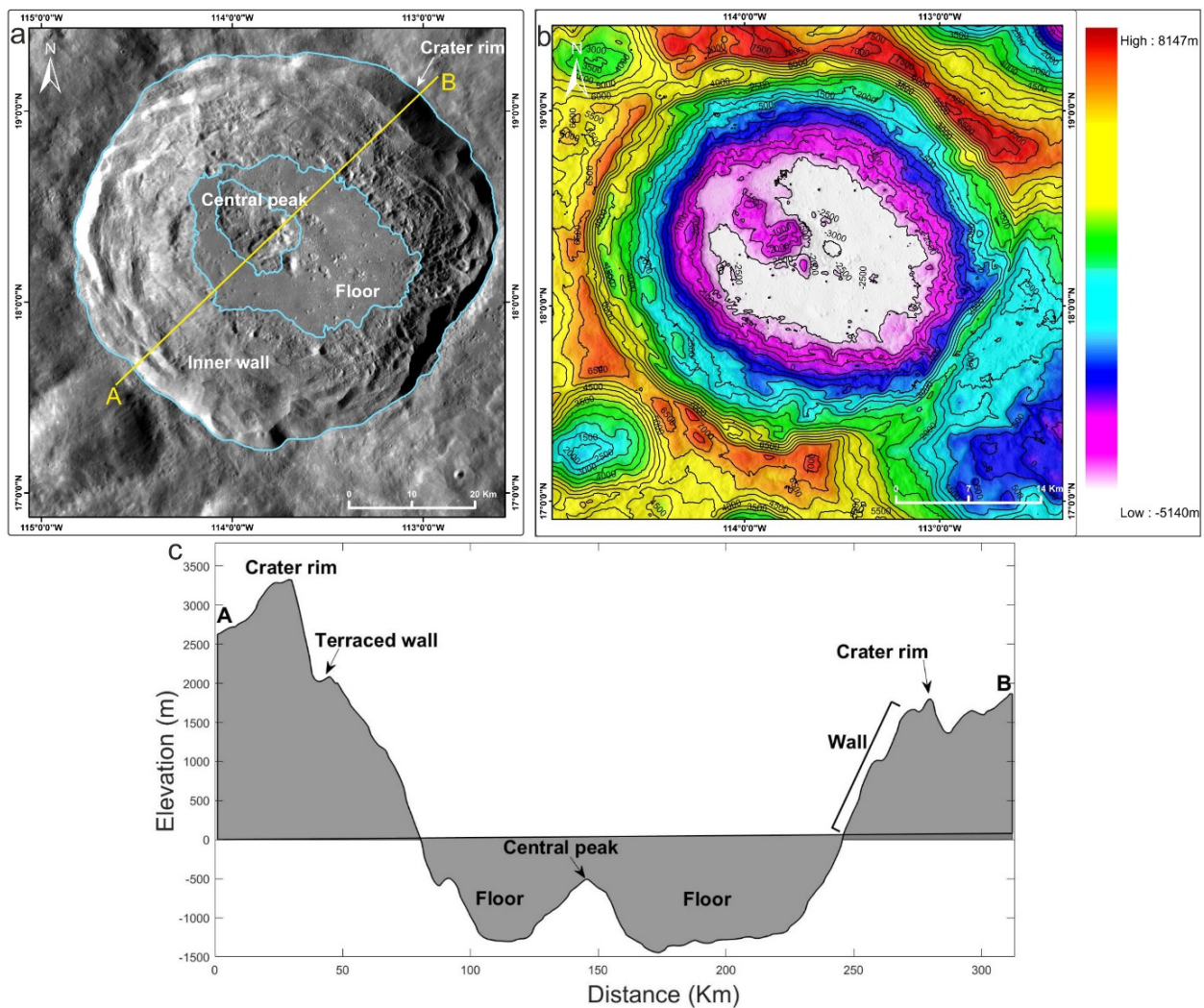


Figure 7.2.3: (A) WAC mosaic showing the major geomorphic units in the Ohm crater. (B) DEM of the Ohm crater with the contours labelled. (C) Topographic profile across A-B in Figure 7.2.3.A.

Previous studies suggest that the Ohm crater was Copernican aged based on the ejecta distribution. M.A. Kreslavsky et al. (2013) showed that Ohm and Jackson craters have the most

prominent albedo ray systems. However, not all distinctive high albedo rays seen on the lunar surface have noticeable roughness expressions. The Ohm crater ray system has a roughness value of ($r=2.5$). Galileo observations of post-Imbrium lunar Craters (McEwen et al., 1993) suggested that the age of the Ohm crater must be Copernican. Since a bright ray from the Ohm crater is superimposed on the nearby Robertson crater, Robertson crater can be inferred as Eratosthenian or Upper Imbrian in age. The present study investigates distinct morphological features in the Ohm crater to understand the impact cratering processes.

7.2.1 Data acquisition

NAC and WAC - Lunar Reconnaissance Orbiter: In this study, the morphological characterization of the complex crater Ohm was carried out using satellite data from Narrow-Angle Camera (NAC), Wide Angle Camera (WAC), and Lunar Orbiter Laser Altimeter (LOLA) of Lunar Reconnaissance Orbiter (LRO) mission of NASA. The preliminary morphologic context of the Ohm crater was studied with the Lunar Reconnaissance Orbiter Wide Angle Camera (LRO WAC) global map at a resolution of 100 m/pixel in seven colour bands. It has over 57 km swath in colour mode and around 105 km swath in monochrome mode (Robinson et al., 2010). NAC orbital datasets were used for detailed morphologic mapping of the crater. The NAC is a pair of two identical, along-track cameras with a high resolution of 0.5 m. They are designated as NAC-Left (NACL) and NAC-Right (NACR), each with 700-mm focal length telescopes providing an instantaneous field of view (IFOV) of 10 micro-radians (Robinson et al., 2010). The calibrated NAC and WAC images were downloaded from the Lunar Orbital Data Explorer (ODE) produced by the PDS Geosciences Node at Washington University. The NAC image data used during the study provides similar illumination conditions to avoid the misinterpretation of albedo conditions of the morphological units.

LOLA – Lunar Reconnaissance Orbiter: LOLA is a multi-beam laser altimeter system with a pulse repetition rate of 28 Hz and an operating wavelength of 1064.4 nm (Smith et al., 2010). The instrument offers remarkable resolution in the along-track direction of ~10 m at the 50 km mean altitude (Chin et al., 2007). The Lunar Orbiter Laser Altimeter (LOLA) investigation provides a precise global lunar topographic model and geodetic grid. The Lunar Orbiter Laser Altimeter - Global Digital Elevation Model (DEM) measures the backscattered energy of an altimetric laser pulse at 1064 nm with a resolution of 20m per pixel. LOLA DEM was used to acquire relative elevation in the various parts of the crater floor to identify distinctive floor units. The LOLA DEM was used to create contour and slope maps. The contour map displayed the overall topography of the crater enhanced the subtle morphologic differentiation in

elevation on the crater floor. The slope map provided the slope gradient along the crater wall to study the discrepancies among crater wall morphologies.

7.2.2 Methodology

Morphological analysis: The Ohm crater was morphologically mapped using LRO WAC and NAC datasets. About one hundred and seventeen NAC images were calibrated/georeferenced and mosaicked using ENVI software. The mosaicked images were sufficient enough to cover the entire Ohm crater. The WAC dataset was used to map major morphological variations, which helped delineate the central peak, crater floor, crater walls, and crater rim. Detailed morphological characterization is done in ArcMap software with the help of NAC images mapped using ArcGIS software. All the morphological characters mapped in this study are dependent on the illumination geometry (0.5 to 2.0m per pixel), which aided in better interpretation of geological features like cooling cracks, domes, isolated mounds, melt platform, channelized flows, ejecta boulders, rille, fault scarp, tread, terraces, and melt ponds and were mapped distinctively. All the morphological features were mapped in vector layers and were combined to produce a morphological map of the entire Ohm crater.

The georeferenced datasets were then mosaicked to produce a single image of the study area. 3D visualization was implemented with hillshade data of Ohm crater draped over the elevation values of each pixel in LOLA DEM to observe and infer the crater from a 3D perspective. From the 3D model, relief variations of the morphological features within the crater and the impact depression caused by the asteroid on the lunar surface are effectively studied. This helps in analyzing the deformation of the lunar surface caused by the impact event. Contour and slope maps are created by using ArcMap software from LOLA DEM. The Slope map was used to display the distribution and steepness of the terraced features ranging from very steep to gentle slopes along the crater wall.

7.2.3 Results

Various morphological units are identified and mapped in the Ohm crater (Fig. 7.2.4). The mapped geomorphic units include central peak, crater floor, crater walls, crater rim, cooling cracks, domes, isolated mounds, melt platform, channelized flows, ejecta boulders, rille, fault scarp, tread, terraces, melt ponds.

7.2.3.1 Central peak

A Central peak is one of the most prominent geomorphic features in complex craters. A central peak complex is formed during the modification stage of impact cratering due to a rarefaction shock wave caused by the primary impact event (Milton et al., 1972). Such a shockwave causes the underlying material to move upwards towards the centre, forming a central peak. Thus, central peaks often expose deep-seated material from below the lunar surface, making them of great importance for the litho-stratigraphic evaluation of the Moon.

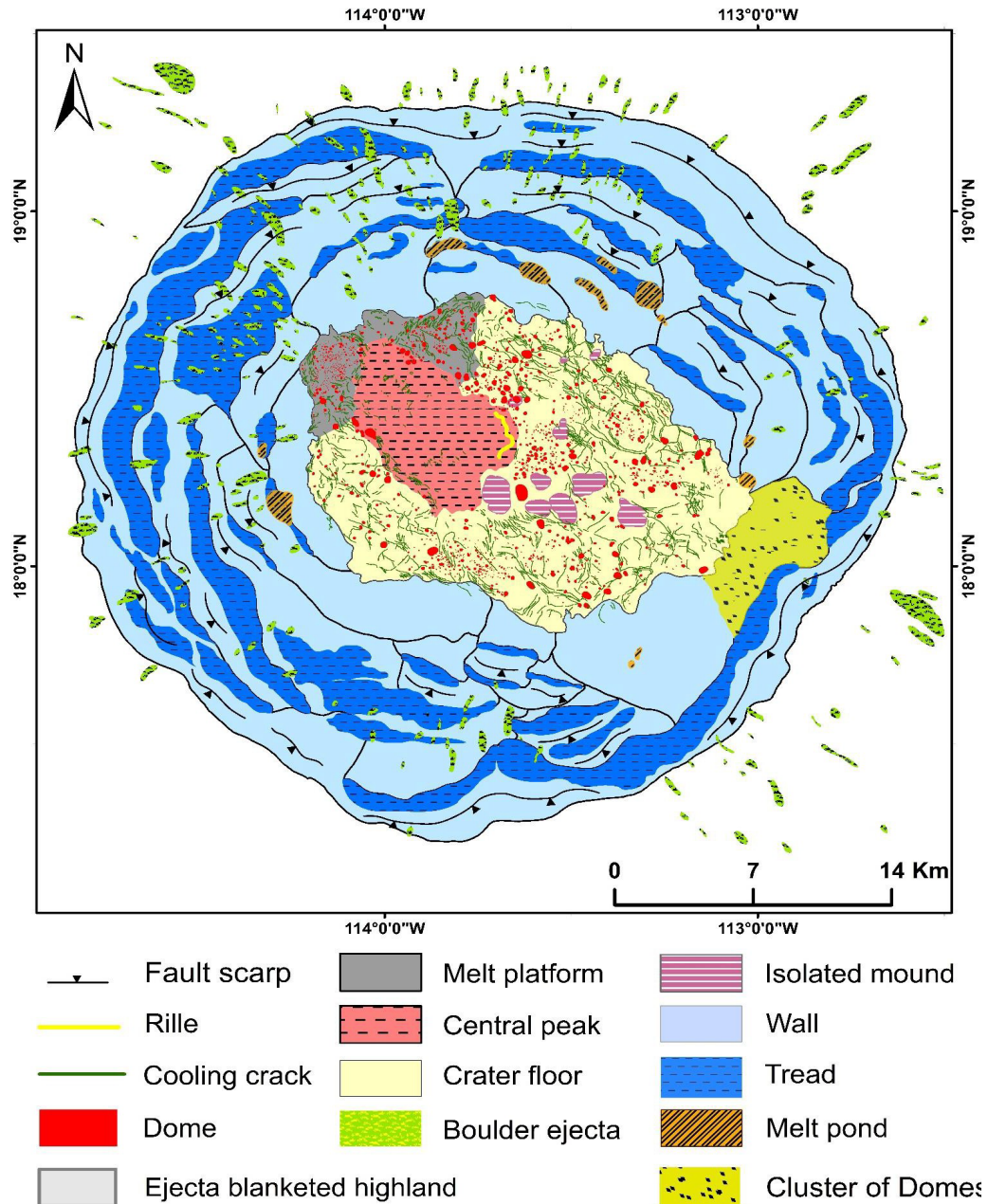


Figure 7.2.4: Detailed morphological map of the Ohm crater.

In the Ohm crater, the central peak rises 1850 m above the crater floor and covers an area of 124.1 km². The elevation of the central peak is low-slung from the crater rim. The top of the central peak is covered by impact melt which is identified by the darker albedo in the NAC images, and impact melts likely cover the gentle sloping surfaces ranging from 0°-7° (Fig. 7.2.5). The morphological framework of the central peak is very complex and elongated in the NW-SE direction. Almost 75% of the central peak is obscured by impact melt. This central peak unit is comprised of boulder fields that are pervasive over the peak region. The melt ponds are flat deposits with usually smooth surfaces (negligible clasts, if any) confined by high-standing topography on all sides (Fig. 7.2.5D).

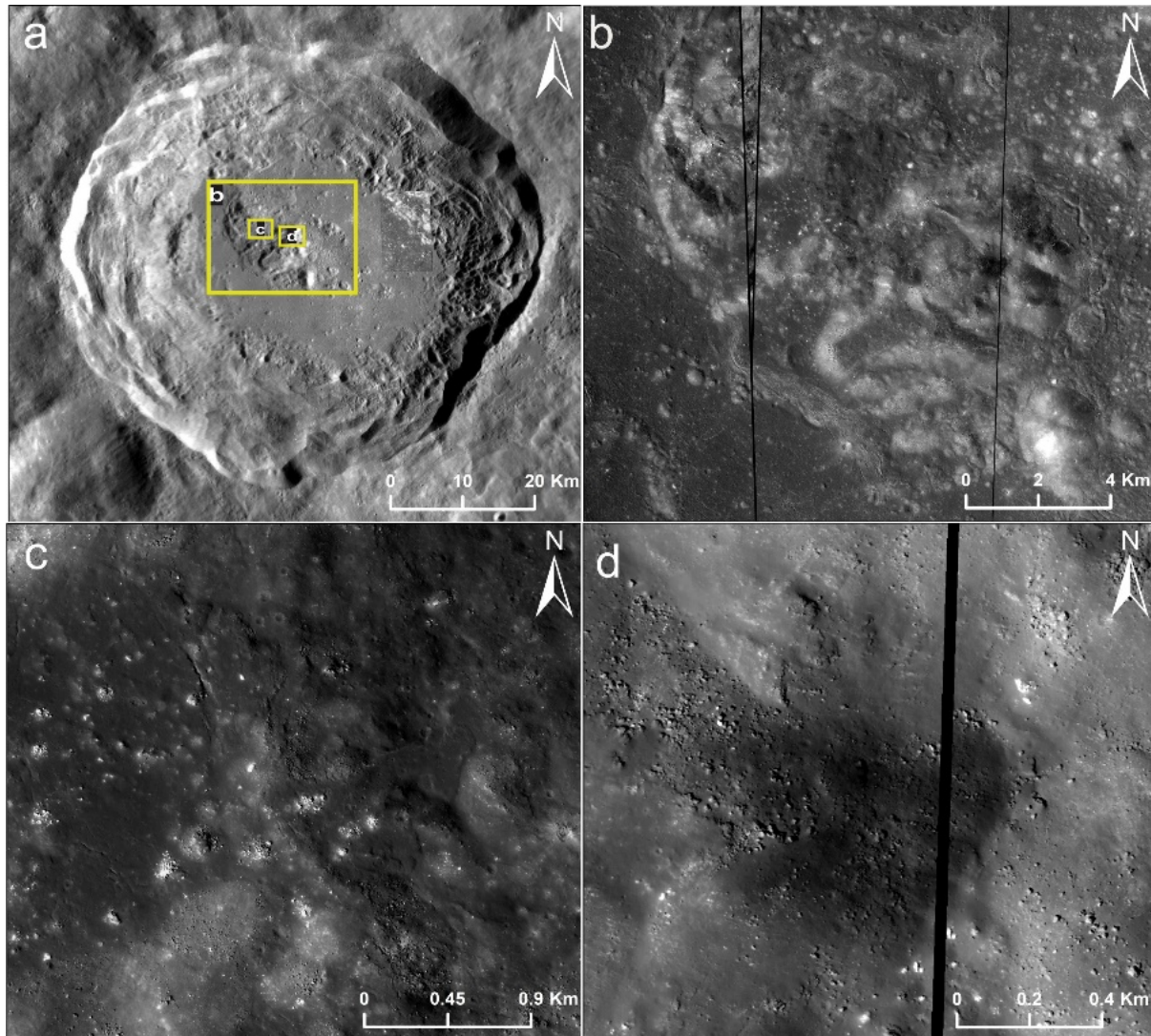


Figure 7.2.5: (A) WAC mosaic of the Ohm crater showing the central peak of the crater, evidence for impact melting are marked as rectangles. (B-C) Impact melt deposits and boulders on the central peak. (D) Melt pond on the summit of the central peak.

7.2.3.2 Mounds

LROC data revealed that Ohm's crater floor exhibits a mass of irregular mounds at the centre of the crater, mostly formed by the low-velocity impact of clustered ejecta material from the primary impact event (Kumar et al., 2011).

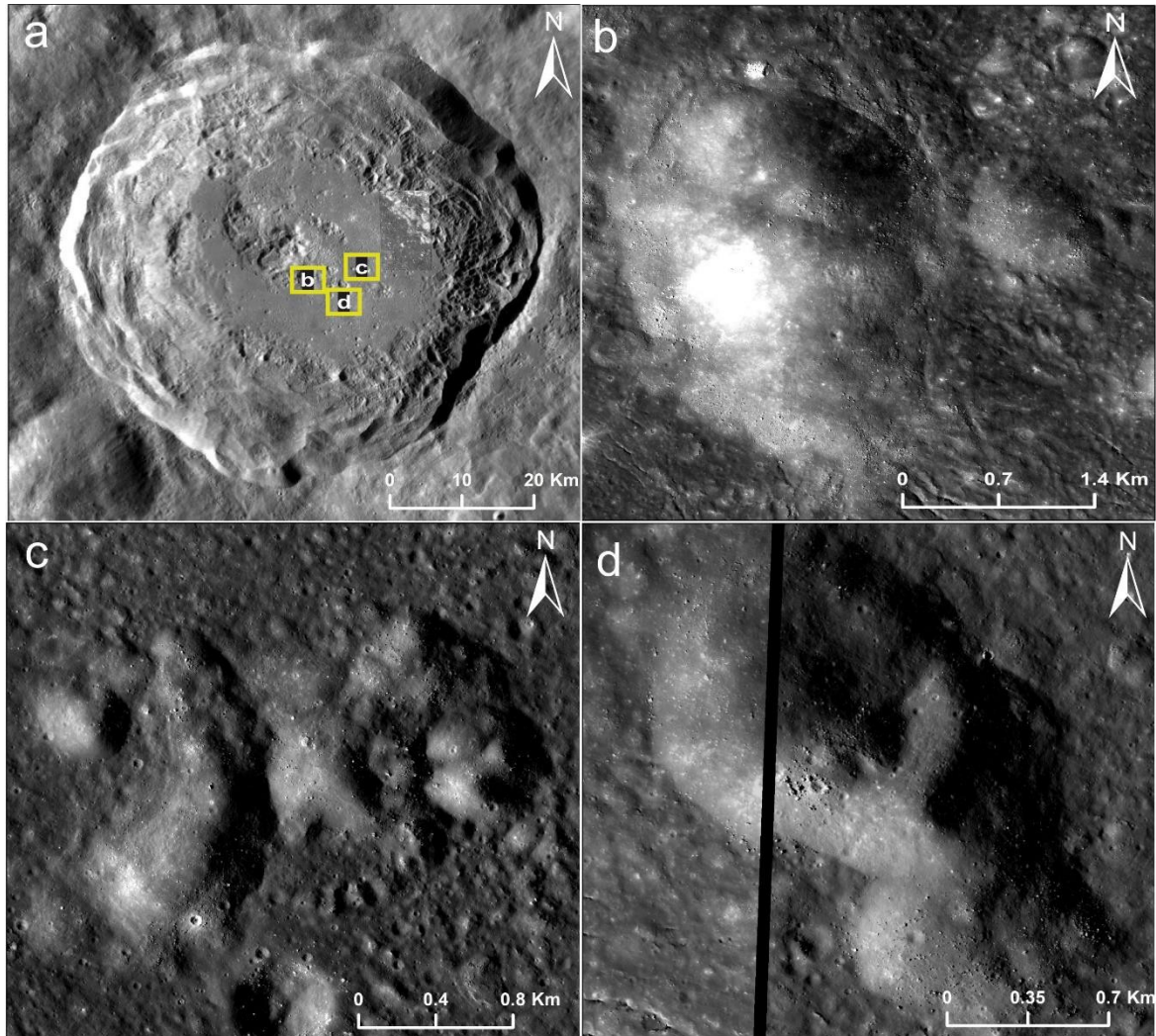


Figure 7.2.6: (A) WAC mosaic of the Ohm crater with the locations of the isolated mounds marked as rectangles. (B-D) LROC-NAC images of the isolated mounds identified from the crater floor.

Usually, they are found in the form of clusters and sometimes also in the form of chains (Fig. 7.2.6). Central mounds show great diversity in their shape and size. According to Kumar et al. (2011), the size of the mounds depends upon the size of the primary crater, and their shape may vary from circular or ellipsoidal to polygonal. This unit comprises megaclasts that stand out distinctively on the crater floor due to their relatively high relief and large spacing between

individual megaclasts (Dhingra et al., 2015, 2016, 2017a). The isolated mounds on the floor of the Ohm crater are larger irregular dome-like features with boulders on the top. The isolated mounds spotted on the crater floor buffer near the central peak are aligned in the SE direction from the central peak. This alignment may be caused during the impact cratering event and not due to later volcanic extrusions like the formation of domes. The isolated mounds are comparatively of lower elevation than the central peak.

7.2.3.3 Crater floor units

The topography of the crater floor is nearly flat and covers an area of 589 km². The average elevation of the crater floor is ~ -2600 m. The impact melt deposits on the floors of the Ohm crater display spectacular diversity in their morphological form (Figs 7.2.7 and 7.2.8). The young age of the crater allows the confident identification of a variety of morphological units located on the crater floor (Fig. 7.2.7).

Detailed mapping of the floor impact melt deposits provides useful information about the character of the melt and the processes controlling impact melt formation and emplacement. The crater floor is classified as a smooth textured, rough-textured, and melt platform. The smooth textured floor has low albedo and is occupied by a smaller number of cracks and domes. The rough textured floor shows high albedo, with many domes of varied dimensions and cooling fractures extending up to longer distances. A possible volcanic vent is identified towards the southern section of the crater floor.

i. Rille

A Rille is a lunar valley, usually long and narrow or sinuous. Sinuous rilles often begin in craters, although the sources of some are not so easily described. The rilles are associated with mare-type material and are absent in the highlands. Most of them are located on the margins of the circular mare basins. They possess conspicuous morphological characteristics of meandering channels or valleys. Normal rilles are straight or gently curved and considered to be graben-type faults.

The rille in the Ohm crater as part of the central peak is sinuous and trending in the NW-SE direction (Fig. 7.2.9). The length of the rille in the Ohm crater is about 4.7 km, and the width is about 160 m. The depth of the rille from the adjacent surface is about 36 m, and the mean elevation is about -2500 m as derived from LOLA DEM. It is a prominent feature in this crater because previous literature highlighted that rilles are generally formed on mare basins, flat topographies, and crater floors. The rille in this crater is assumed to be formed due to fracture expansion resulting from the turbulent flow of low viscosity (very fluid), high-temperature

lavas that erodes the pre-existing surface. The rille is filled with basaltic lava flow and has some boulders in it. The boulders might have been fragmented from the cliff of the rille.

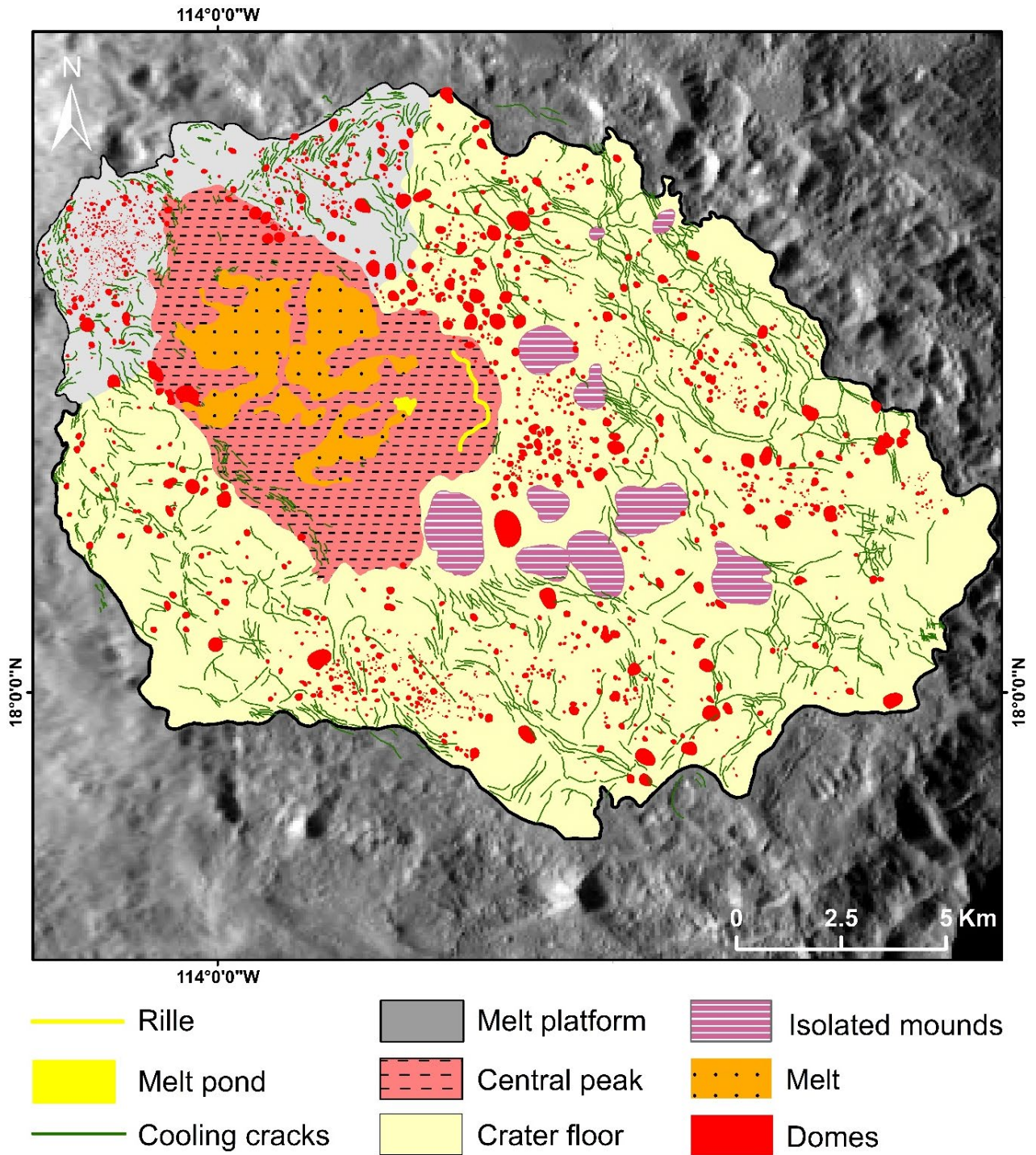


Figure 7.2.7: Detailed morphological map of the floor of the Ohm crater draped over WAC mosaic.

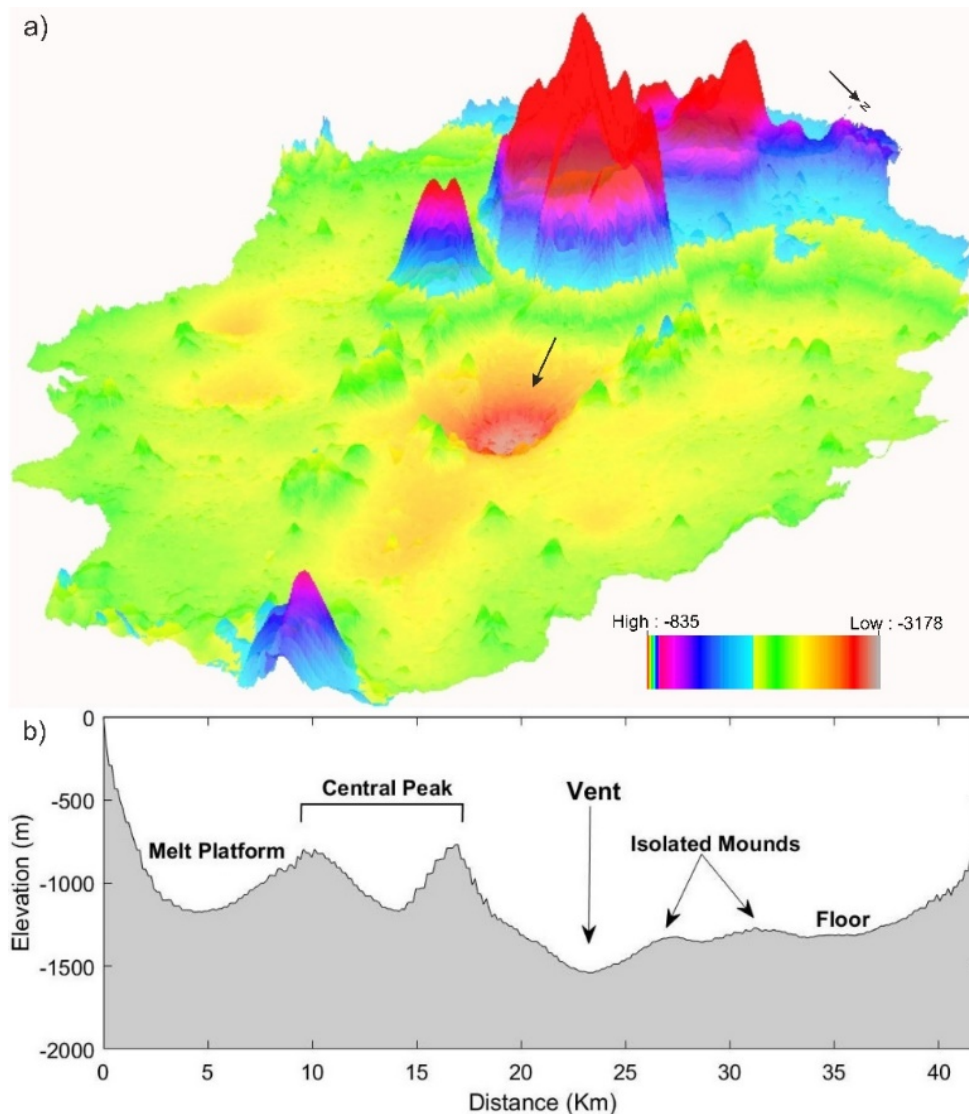


Figure 7.2.8: (A) 3D view of the floor of the Ohm crater. The black arrow points towards a probable volcanic vent. (B) Topographic profile across NE-SW section of the crater floor.

ii. Melt platform

The melt platform is named after the accumulation of impact melt in a large area within the crater floor. This feature is described as a sudden elevation difference above the crater floor but neither part of the crater wall nor the central peak. The melt platform is seen on the NW part of the crater floor, where the central peak divides the feature into two (Fig. 7.2.8b). The melt platform rises to an elevation of -300 m above the crater floor, and the elevation remains unchanged, extending up to the NW crater wall. There is no signature of upliftment of the crater floor supported by fault scarps and fractures along the boundary of the melt platform. So, the sudden elevation change can be caused by the continuous basaltic lava flow in the crater

floor from the adjacent steep sloping crater wall. This lava flow produces a channelized pattern on the crater walls showing the direction of the flow of lava towards the crater floor. The feature is divided into two categories a) area of smooth texture having low albedo accompanied by fewer domes and b) area of rough texture having high albedo showing the irregular pattern and a quite large number of domes. The melt platform is assumed to have formed instantaneously after the impact cratering event. This is evident from the maturity (based on the albedo) of the melt platform compared to other crater features, excluding the crater floor.

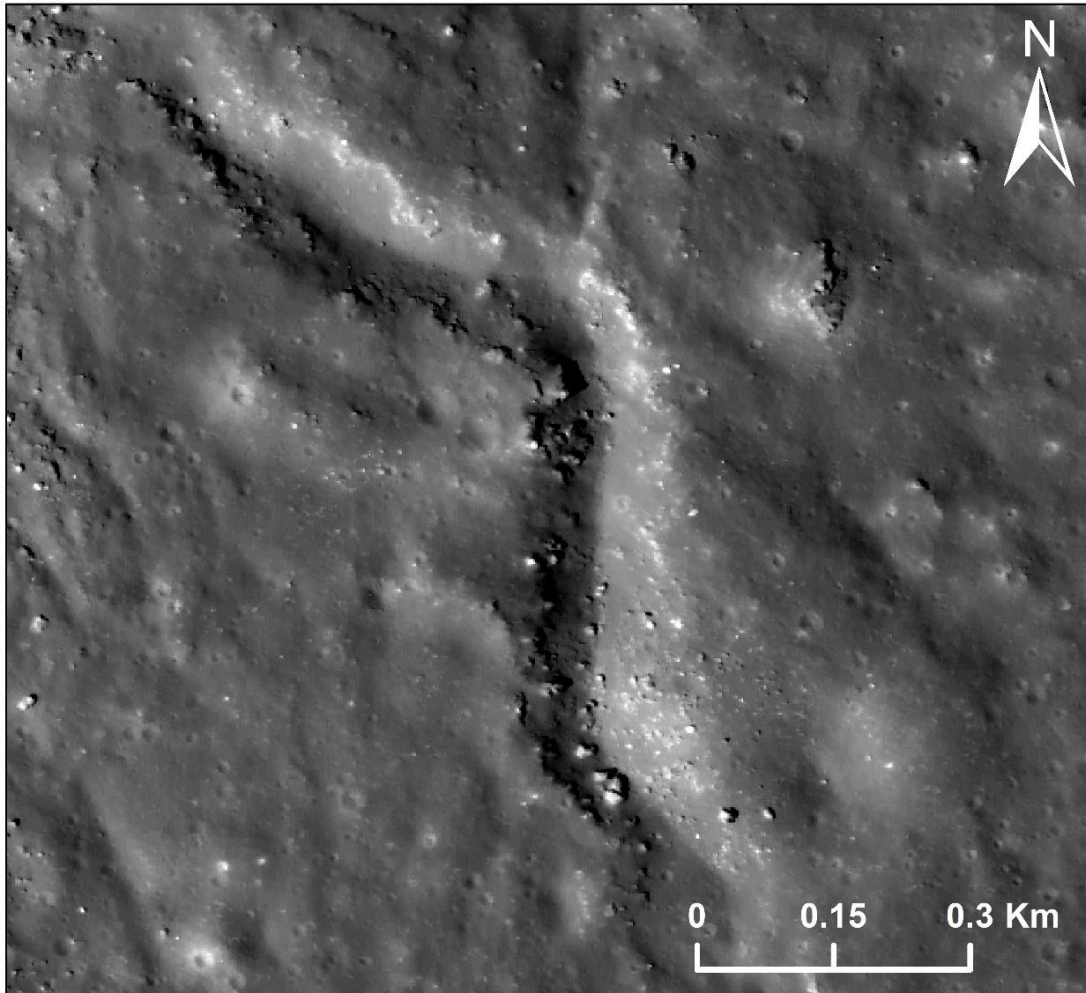


Figure 7.2.9: Sinuous rille observed in the southeastern edge of the central peak.

iii. Cooling cracks

On the surfaces of airless and comparatively dry silicate bodies like the Moon, lava loses heat by thermal radiation to the vacuum of space and by thermal conduction to the underlying and surrounding terrains.

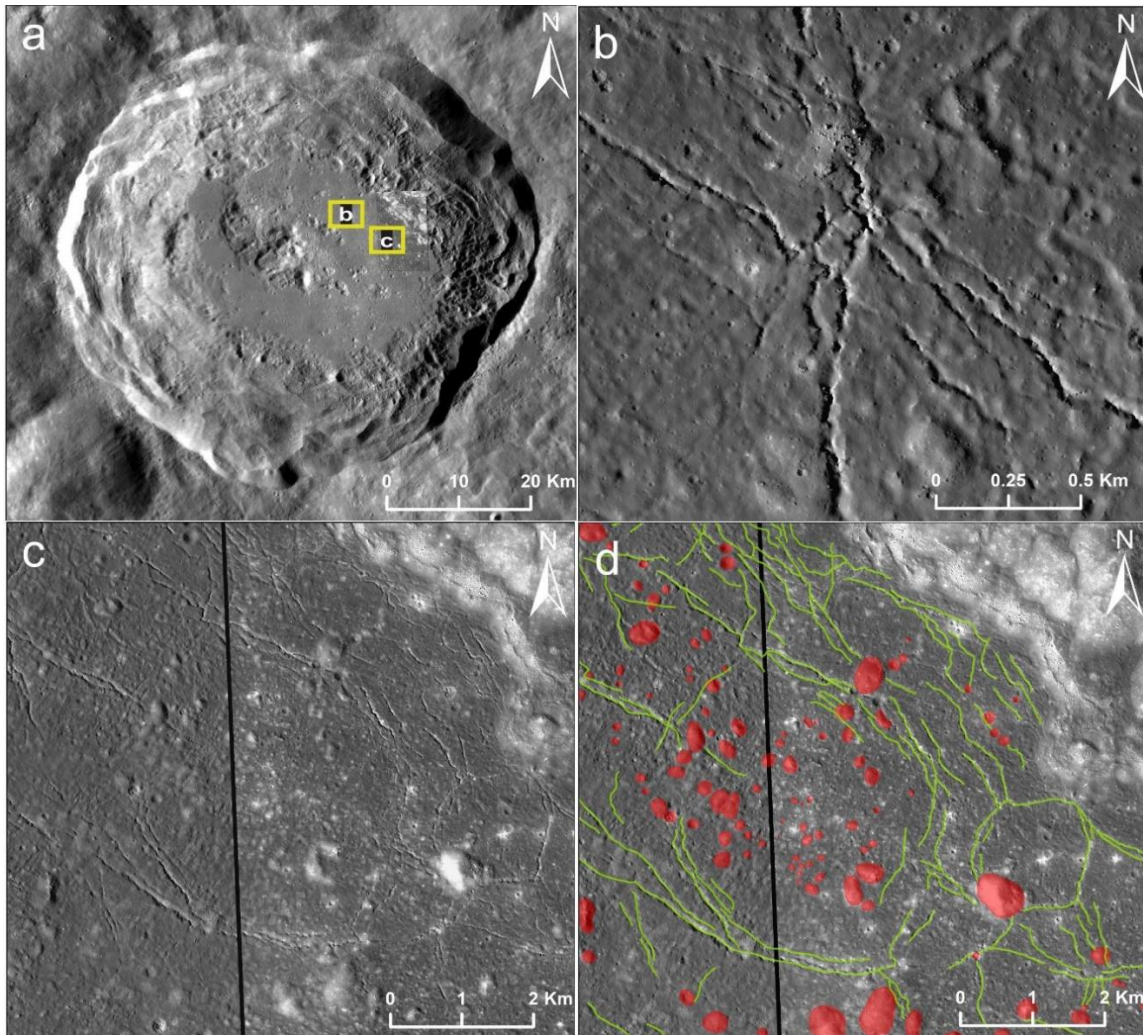


Figure 7.2.10: (A) WAC mosaic of the Ohm crater with the selected locations of the cooling cracks, marked as rectangles. (B-C) Polygonal cooling cracks were identified in association with dome-like features on the crater floor. (D) Polygonal cracks and associated domes mapped on the NAC image.

Cooling fractures observed on the surfaces of the crater floor provide an excellent opportunity for understanding the contribution of thermal radiation to the cooling of lava units. The appearance of polygonal fracture patterns in the Ohm crater is mainly induced by subsidence of the deposits during cooling and solidification (Fig. 7.2.10). Along the boundary of the floor, the marginal cracks are more or less sub-parallel to one another. The length of the cooling cracks ranges from ~ 0.1 km up to ~ 3.1 km.

iv. Domes

The distribution of domes and other probable volcanic features may provide clues to structural

patterns controlling volcanism. The lunar orbiter missions provided good high-resolution photographs of domes on the floor of the Ohm crater and revealed over 1957 numbers of recognized domes on the crater floor.

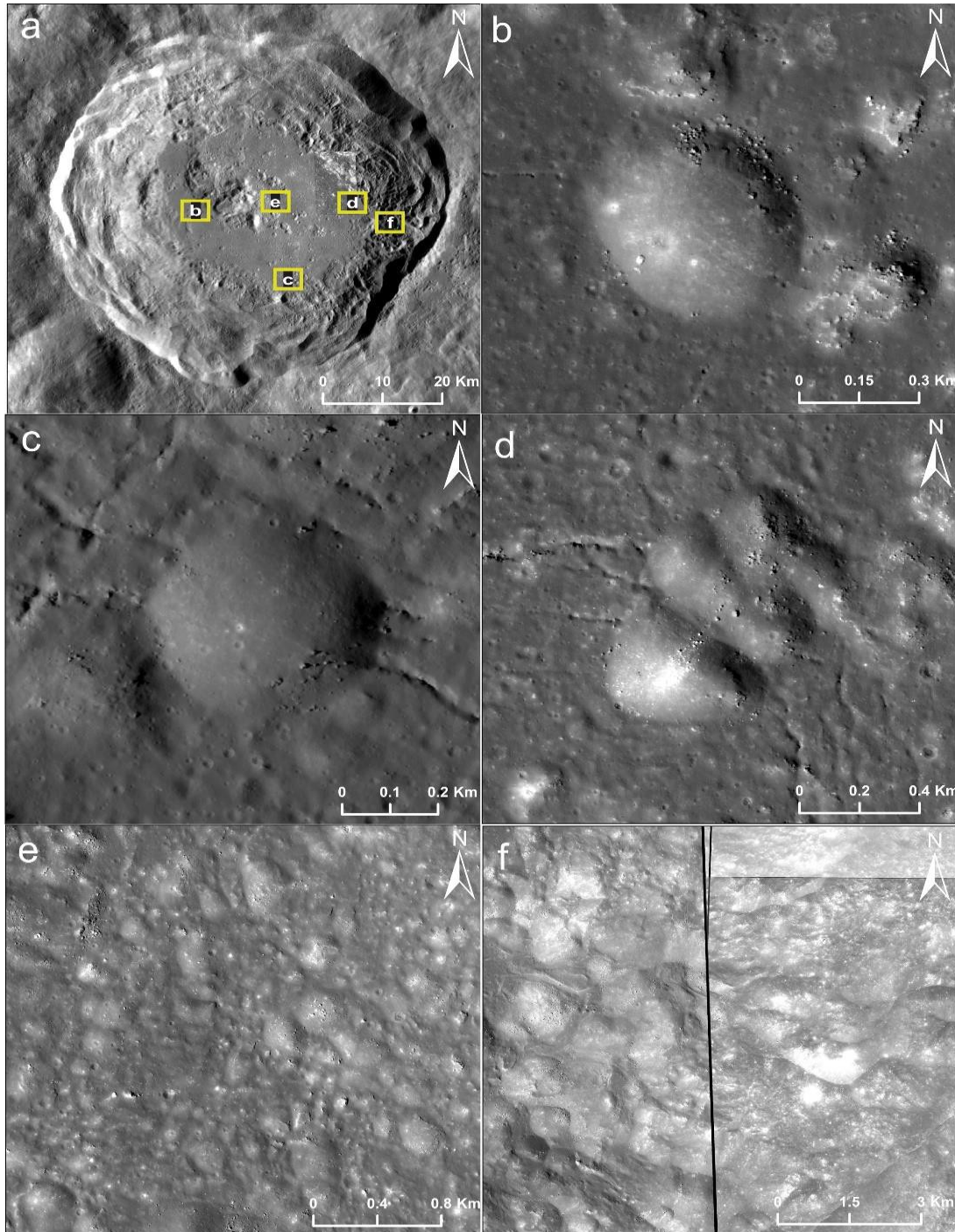


Figure 7.2.11: (A) WAC mosaic of the Ohm crater with the selected locations of the domes, marked as rectangles. (B-F) NAC images showing the domes in different parts of the crater.

The diameter of the domes ranges from the smallest, 50 m, to the largest, 600 m. The smaller domes are mostly found to occur on the smooth textured crater floor (low albedo), and larger domes are observed on the rough-textured part of the crater floor. This localization suggests that the intensity of volcanism is very low on the smooth part of the crater floor and high on the rough part. Moreover, the interpreted domes have boulders with distinct reflectance on the top. This may be due to the brecciation after cooling, consolidation followed by space weathering of the volcanic extrusion. A peculiar orientation is seen in the arrangement of the volcanic domes. Most of the domes on the floor of the Ohm crater are arranged in a curvilinear pattern (7.2.11). Detailed interpretation of the LRO NAC images revealed that domes and cooling fractures are associated with one another. The curvilinear arrangement of the domes is caused by the extrusion of magma along with the underlying fracture system. These fracture units are weaker zones where the magma extrudes onto the surface of the crater floor. A new class of features described as ring-moat dome structures (RMDSs) is distributed near the central mounds and on the margins of the eastern crater floor. These low domes (a few meters to ~20 m height with slopes $<5^\circ$) are typically surrounded by narrow annular depressions or moats. The dome-shaped morphology of RMDS and their association with the lunar maria basaltic flows suggest volcanic landforms. Terrestrial lava flows are known to produce positive features of the scale of RMDS in rootless eruptions (squeeze-ups, formed when lava below the cooling crust becomes cooler and more viscous and extrudes locally onto the deforming chilled layer as bulbous mounds, and hornitos, rootless cones formed of spatter of still-molten lava emerging through local cracks in the deforming lava crust). The process of the RMDS formation appears to be a common product of late-stage lunar mare lava extrusions.

v. Crater wall

The interior side of the crater rim is defined as a crater wall. Such walls are formed during the early stage of modification by deposition of debris. The wall of the Ohm crater is asymmetrical, and the rim of the crater seems to be well developed in the NAC images, but the contour-elevation map derived from LOLA DEM displays a difference in elevation of the crater rim on the eastern part of the crater and the other regions of the crater (Fig. 7.2.12). The elevation of the eastern crater rim is comparatively lower than the rest of the crater rim elevations. There are several collapses and mass wasting movements on the crater wall. Complex crater walls are commonly broken up into a series of terraces: relatively flat ledges, offset by scarps facing the centre of a crater, which step down from the crater rim to the floor. Well-developed terraces with varying widths (~500 m to 3 km) are around the crater wall and define some faults sub-parallel to the terrace boundaries.

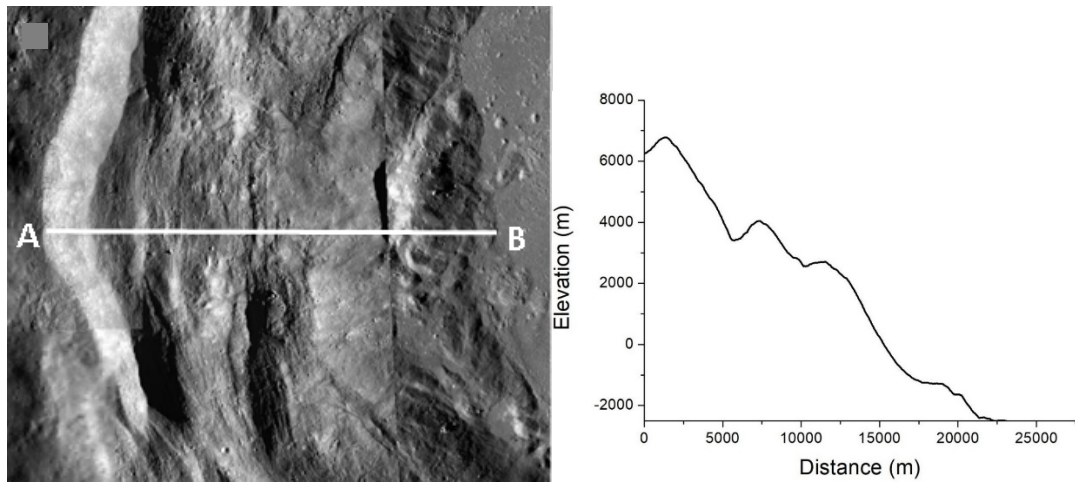


Figure 7.2.12: Left image: LROC NAC image showing the western crater wall. Right image: Topographic profile across A-B in the left figure.

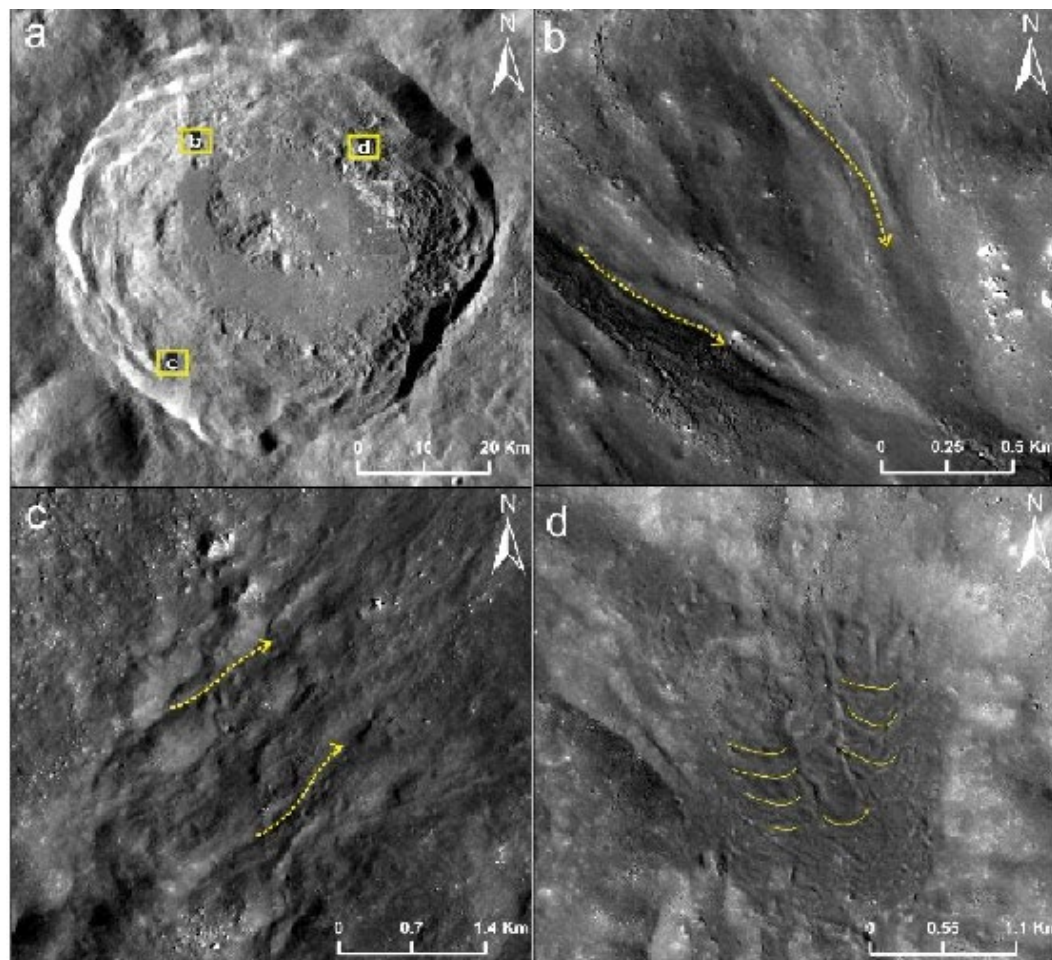


Figure 7.2.13: (A) LRO WAC image showing the locations of channelized flows. (B) Basaltic flow with smooth texture. (C) Basaltic flow with a rough texture. (D) Basaltic flow with ropy texture.

These terraced walls are several hundred meters high and occupy an area of $\sim 320 \text{ km}^2$. Impact melts have flowed down from the surfaces of the terraces and are gathered in the gentle areas between high and low terraces to form several melt ponds (Fig. 7.2.13). Between the channelized flows, there is a relatively smooth surface due to thick veneers of melt materials. This unit has deficiently developed terraces and has a higher albedo than other parts of crater walls. When moving down the slope, impact melts are thought to be both erosive and depositional. The impact melts erode into the walls deeply through mechanical or thermal erosion, or a combination of the two.

vi. Melt ponds

A melt pond is an impact melt deposit that flows from a topographic high into lower basins under the influence of gravity while still in a molten state. In craters, impact melt deposits are a mixture of real melt with breccias and rock fragments that have been merged during melt movement. Melt ponds result from melt flowing to low areas, cooling and solidifying, fracturing the surface. Melt ponds can be easily identified by their relatively darker albedo in contrast with the surroundings. In the Ohm crater, melt ponds are trapped between two adjacent terraces and among the deposits of wall-derived materials near the northern crater floor (Fig. 7.2.14). They have different sizes and are confined by the area available on the terrace and the quantity of melt available when they are formed. The surface of ponds is often smooth and has few superposed craters. Fractures can be found on almost all ponded surfaces. These fractures are probably due to thermal contraction of the surface during cooling but may be related to the extension of the surface. The melt ponds are distributed non-uniformly in the crater, most abundant in the north and NE. The largest melt pond is situated near the northern floor with an area of around $\sim 3.85 \text{ km}^2$, and the smallest one is trapped in between wall terraces in the NE, approximately $\sim 0.17 \text{ km}^2$ in area.

vii. Melt breccia/Ejecta boulders

When the massive impactor hits another object with enough force, it creates a shockwave that spreads out from the impact. The object breaks and excavates into the ground and rock, at the same time spraying this finer material that is known as impact ejecta. The impact ejecta spreads for longer distances based upon the force and size of the impactor. Ejecta boulders are larger brecciated rock fragments distributed outward from the crater centre. The boulders are identified based on the high reflectance observed in the visual interpretation of LRO NAC datasets (Fig. 7.2.15). The concentration of the boulders is high over the crater wall and less on the surrounding regions of the crater.

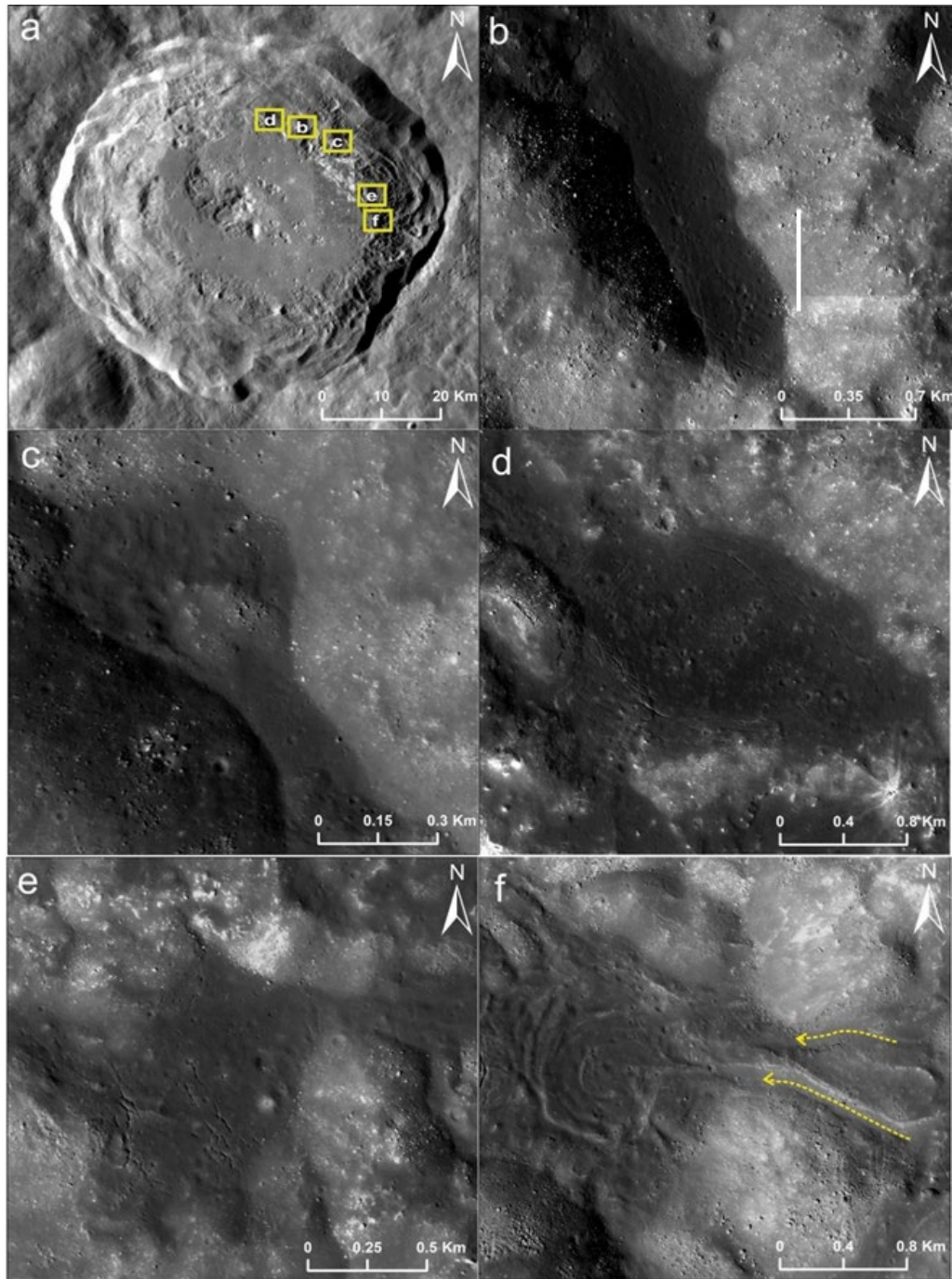


Figure 7.2.14: (A) WAC mosaic of the Ohm crater with the locations of the melt ponds marked as rectangles. (B-E) NAC images of the melt ponds identified in the crater. (F) Lava pool in spiral form due to the falling of clasts into the pooled lava.

The distribution of large ejecta boulders thins out beyond the rim of the crater. The impact melt buries most of the boulders formed during the impact cratering event, and only the larger brecciated boulders are now visible on the crater surface.

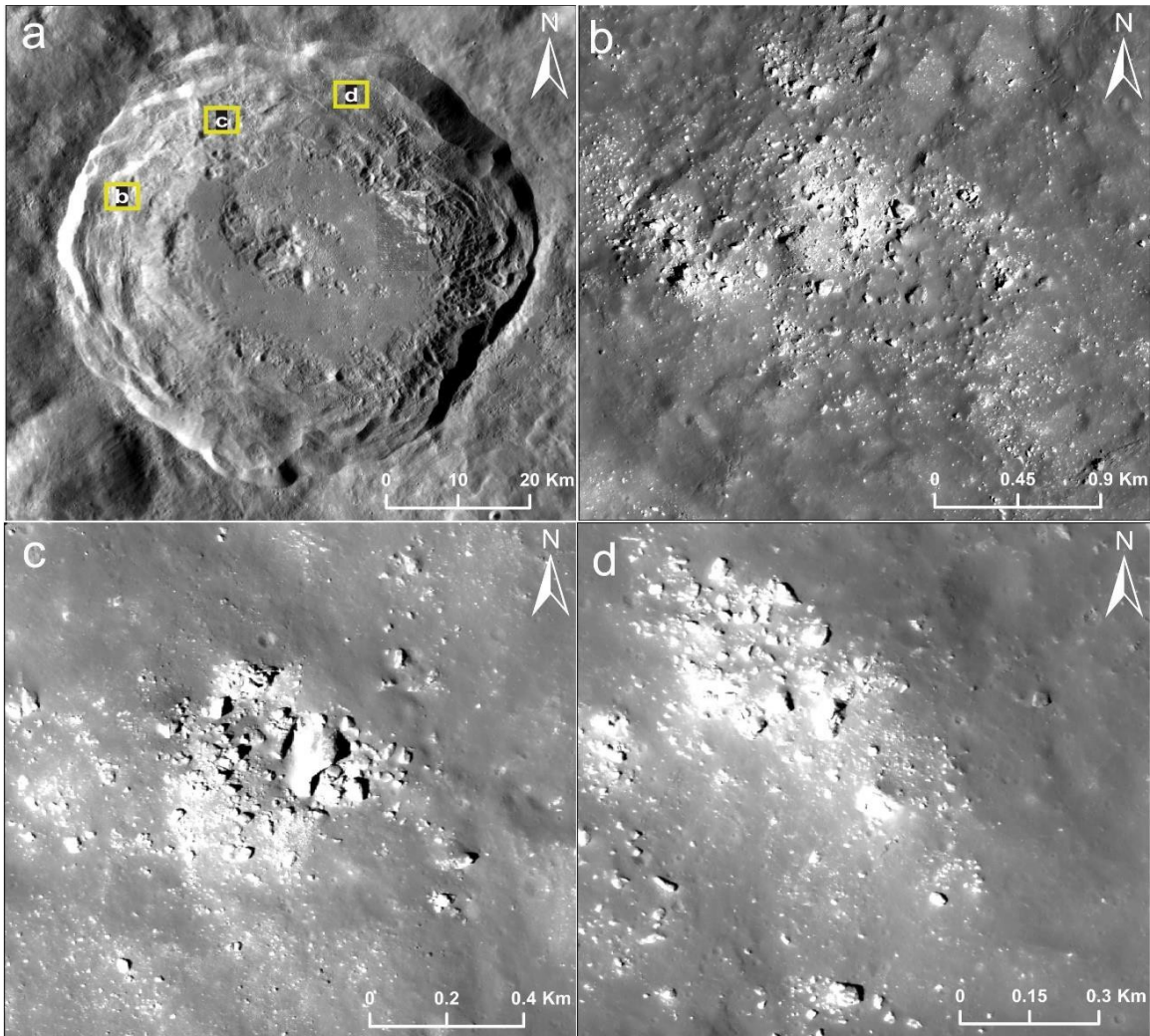


Figure 7.2.15: (A) LRO WAC image showing the locations of the ejecta boulders. (B) Linearly distributed boulders. (C) Larger boulders. (D) Highly weathered boulders.

7.2.4 Summary

The central peak is formed as a result of elastic rebound that happens when an asteroid of large mass and high velocity hits the lunar surface. The boulders interpreted on the central peak are not formed as part of ejecta boulders. It is the disintegration of exposed lithology by the impact weathering. This is confirmed by the lack of radiating pattern or orientation of the boulders on the central peak. The impact melt on the top of the central peak suggests that extreme heat energy would have been released during the cratering event that caused the impact melt to be distributed all over the crater. The morphology of the crater floor is highly complex, as analyzed by the LRO NAC images displayed numerous domes and cooling fractures. As previously mentioned, domes are volcanic extrusions formed on the crater floor by the uprising

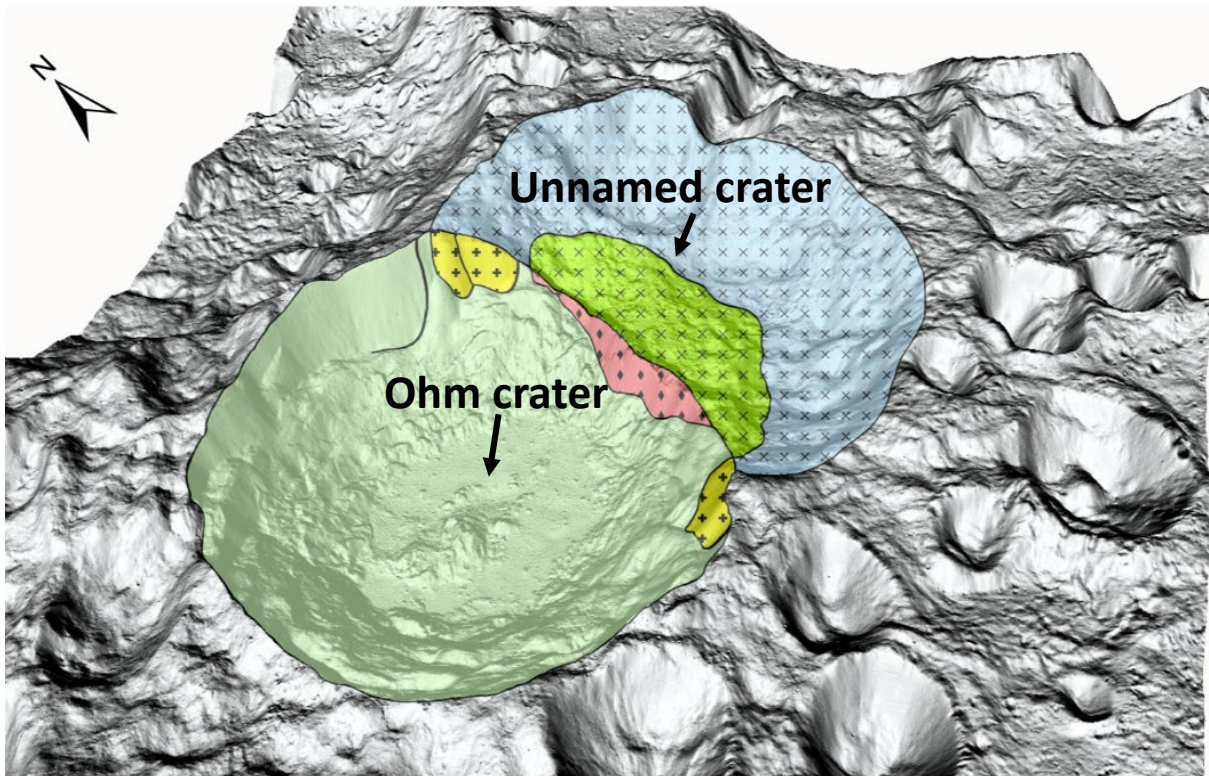


Figure 7.2.16: 3D view of the Ohm crater and the associated unnamed crater towards the east of the Ohm crater. The intact lithologies in the unnamed crater appear to have been excavated by the Ohm crater impact event and exposed these lithologies on the eastern wall of the Ohm crater.

magma. NAC images showed different alignment patterns of the domes in a curvilinear manner along fracture systems. In addition to this, polygonal patterns are seen on the crater floor caused by cooling fractures. Distinctively, the polygonal pattern is formed by the intersection of fractures systems, and the dome is also present at the intersection points of the fractures. This dome is larger in dimension when compared to other domes that developed along the fractures because fracture intersection causes the surface to be much weaker and enable the uprising magma flow in larger concentration. The melt platform is formed by the extensive impact melt flow from the northern crater wall to the floor. The melt ponds are concentrated between the terraces, particularly on the northern crater wall. The crater walls are terraced on the western and northern parts of the crater and the other regions. The crater wall is highly deformed on the eastern part of the crater and relatively lower in elevation. The lower elevation of the wall is due to the obliteration of the crater wall of the nearby unnamed crater during the impact cratering event (Fig. 7.2.16). The overall distribution of ejecta from the NE to the SW is consistent with an oblique impact for Ohm crater formation.

7.3 Morphology and ejecta distribution of the Das crater

The Das crater (25.48° S, 137.00° W) is a Copernican complex impact crater exhibiting a well-developed central peak, fault-bounded terraces, steep-sloping walls, floor deposits, and an asymmetrical ejecta pattern (Jappji et al., 2021) (Fig. 7.3.1b-c). The Das crater is the prime crater on the Moon named after an Indian astronomer Anil Kumar Das. This crater formed on the lunar highland crust, dominated by rugged, uneven topography pockmarked with craters of varying sizes (Fig. 7.3.1a). The crater is surrounded by the South Pole-Aitken basin (SPA) to the east, the Chebyshev crater to the southeast, and the Von der Pahlen crater to the northeast (Fig. 7.3.1a). The diameter of the crater was estimated to be between 32 - 38 km (Fig. 7.3.1b-c). The crustal thickness in the region of Das crater is about 45-50 km, higher than the mean lunar crustal thickness of 34 – 43 km (Blanchette-Guertin et al., 2015). A linearly elongated positive density anomaly interpreted to be Nectarian to Pre-Nectarian aged vertical tabular intrusion or dike, formed by magmatism in combination with the extension of the lithosphere, has been observed near Das crater (Andrews-Hanna et al., 2013). Since the crater is spatially proximate to two large Mascons, i.e., the Apollo and South Pole-Aitken basins, the impacts of those scales may have resulted in formations of ring dikes and ring faults probably manifested as a positive density anomaly in their immediate vicinity (Andrews-Hanna et al., 2018). NASA mentioned Das crater in the LROC featured image dated 22.06.11, in which the presence of impact melt pools was ascertained and distinguished from mare flooded crater by citing slope of flow (downslope) and different elevation of multiple small ponds.

The Das crater holds unaltered, well-preserved morphological units and surface textures, both interior, and exterior, to the crater cavity (Jappji et al., 2021). The crater lies at the centre of a faint ray system (Fig. 7.3.1a). The high albedo ejecta is continuous out to nearly two crater diameters, then forms wispy rays, particularly to the northwest (Fig. 7.3.1a). The present study focuses mainly on the detailed mapping of its morphology and ejecta distribution. The identification and characterization of various morphological units in the crater cavity and their interpreted formation and evolution provide significant insights into the cratering processes that occurred in different stages of crater growth. The precise mapping and identification of distinct ejecta deposits and interpretation of their order of deposition and emplacement dynamics make way for determining the direction and angle of the projectile impact that formed the Das crater. The ejecta blankets also provide an opportunity to sample deeper lunar materials. During impact excavation, the top materials are displaced first and ejected at high velocity and thereby travels farther to eventually fall back and deposit as distal ejecta. As the excavation continues to depths, the impact energy spreads out to more rocks, and the deeper

materials are thrown at a relatively lower ejection velocity. The low-velocity fragments travel only shorter radial distances and deposit as proximal ejecta near the crater rim. Hence, a traverse of the impact ejecta deposits surrounding a crater is an ideal manifestation of the vertical stratigraphy of the region of impact (Shoemaker, 1972; Gault et al., 1968). Therefore, the mapping of ejecta boulders in and around the Das crater and the description of their morphometric parameters in the present study would provide an excellent opportunity for future human explorers to sample the deeper materials of the Moon by taking a traverse along the radial direction of the Das impact ejecta.

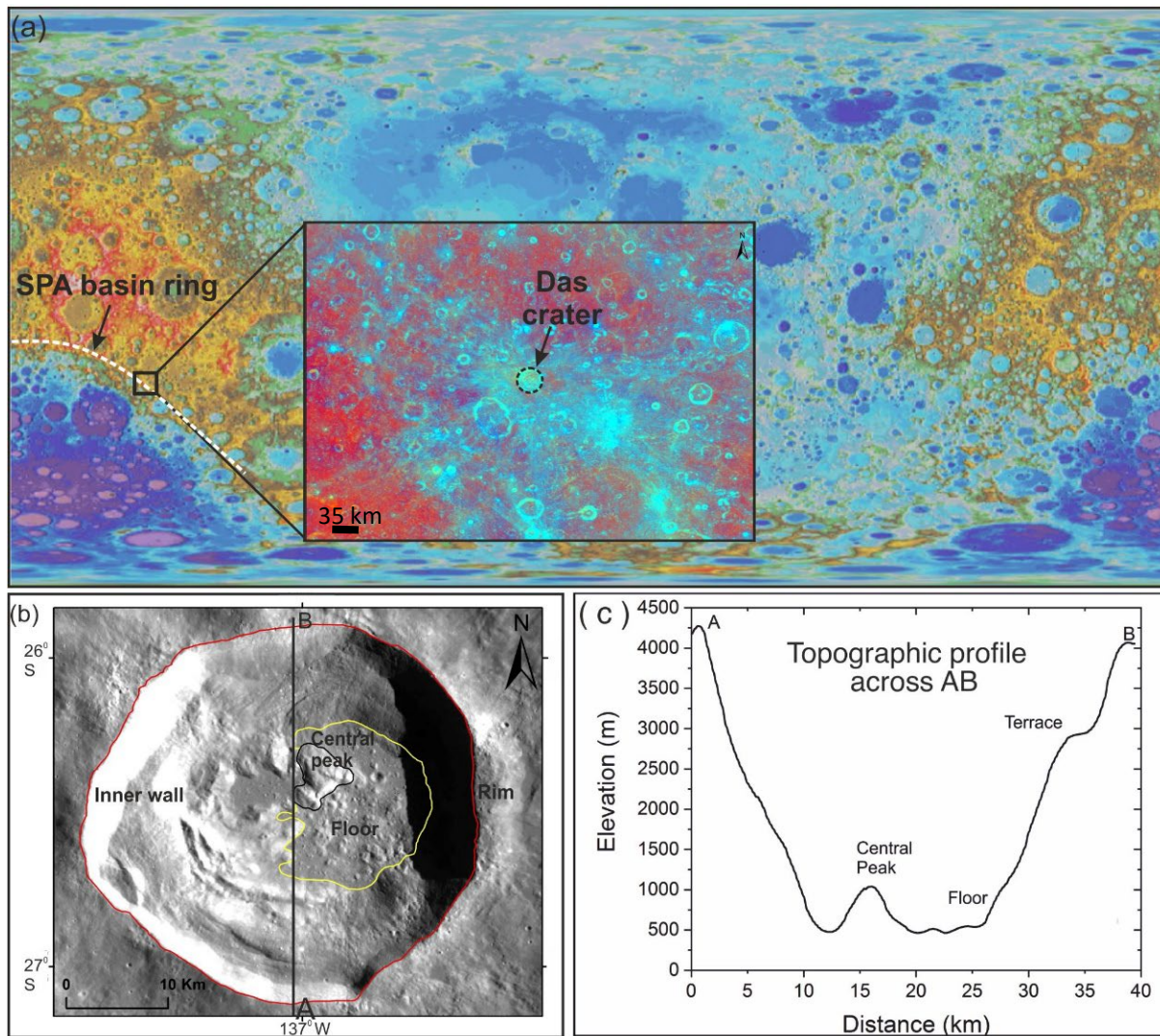


Figure 7.3.1: (A) Colour-coded Kaguya-LOLA DEM merge overlaid on LOLA global hillshade (Global mosaic in Equirectangular projection), showing the location of the Das crater on the lunar farside. The enlarged image shows the Hapke WAC colour ratio image displaying the Das crater and its bright ejecta rays. The white dashed lines represent the SPA basin ring passing through the southwestern region of the Das crater. (B) WAC mosaic of the Das crater showing its basic morphology. (C) Topographic profile across the line A-B in Fig. 7.3.1B.

7.3.1 Datasets

Orbital remote sensing data from various lunar exploratory missions are utilized to investigate the morphology and ejecta deposits of the Das crater. The details are as follows,

SELenological and ENgineering Explorer (SELENE): The SELENE, alternatively known as Kaguya, was a lunar exploration mission launched in 2007 by Japan Aerospace Exploration (JAXA) (Kato et al., 2006; Sasaki et al., 2009). The TC (Terrain Camera) was a push broom type imager flew in SELENE that provides a stereoscopic viewing in the fore and aft directions with slant angles of +/- 15 degrees from the nadir vector (Haruyama et al., 2008). The TC operated in a single monochromatic band ranging from 0.43-0.85 μm and provided high-resolution global mosaicked maps of the Moon at a spatial resolution of 10 m/pixel from the nominal 100 km orbit (Haruyama et al., 2008). The present study used TC low-sun angle images. The TC data corresponding to the regions of interest is downloaded from the SELENE-Kaguya TC online data repository (<http://darts.isas.jaxa.jp/planet/pdap/selene/dataset>).

Lunar Reconnaissance Orbiter (LRO): The LRO mission was launched by NASA on 18 June 2009. The LRO was designed for a one-year base mission at an orbital altitude of 50 ± 20 km. The LROC (Lunar Reconnaissance Orbiter Camera) is a system of three cameras mounted on the LRO that capture high-resolution grey-scale images and moderate-resolution multispectral images of the lunar surface (Robinson et al., 2009). The LROC consists of two Narrow-Angle Cameras (NACs) that provide 0.5 meter-scale panchromatic images over a 5 km swath and a Wide Angle Camera (WAC) that provides images at a scale of 100 meters/pixel in seven bands over a 60 km swath (Robinson et al., 2010). The UV (ultraviolet) bands of the LROC are at 321 nm and 360 nm, and the visible bands are at 415 nm, 566 nm, 604 nm, 643 nm, and 689 nm (Robinson et al., 2010). The NAC images corresponding to the regions of interest are downloaded from the Lunar Orbiter Data Explorer portal (<http://ode.rsl.wustl.edu/moon/>). The WAC global mosaic was downloaded from the Astrogeology Science Centre portal (<https://astrogeology.usgs.gov>). WAC Hapke-photometric normalized colour composite mosaic (3-band image: 689 nm, 415 nm, and 321 nm) is downloaded from <http://wms.lroc.asu.edu> portal (Sato et al., 2014).

Lunar Orbiter Laser Altimeter (LOLA): The LOLA is an altimeter that flew in the LRO mission, aimed at obtaining a high-resolution global topographic model of the Moon. LOLA and Kaguya Terrain Camera merged DEM was generated at a horizontal resolution of 512 pixels per degree (~ 59 m at the equator) with $\sim 3-4$ m vertical accuracy (Barker et al., 2016). The present study utilized both the LOLA-TC merge DEM and LOLA hillshade map to understand the topography of the region of interest. The data were downloaded from the

Astrogeology Science Centre portal (<https://astrogeology.usgs.gov>).

Clementine: The Clementine was launched in 1994 by NASA (Nozette et al., 1994). The Ultraviolet/Visible (UVVIS) camera aboard Clementine was designed to operate at five wavelengths (multispectral) in the ultraviolet and visible spectrum, i.e. at 415 nm, 750 nm, 900 nm, 950 nm, and 1000 nm with bandwidths of 40 nm, 10 nm, 30 nm, 30 nm, and 30 nm, respectively. The Clementine UVVIS warped colour-ratio mineral map was generated using band ratios of the 750/415 nm, 415/750 nm, and 750/1000 nm, which provides better viewing of the compositional differences (Lucey et al., 2000). The colour ratio mosaic has a resolution of 200 meters per pixel and is utilized in the present study to delineate the distinct ray system of the Das crater. The mosaic was downloaded from <https://astrogeology.usgs.gov>.

7.3.2 Methods

The surface morphology of the Das crater has been characterized using high-resolution grey-scale images from LROC – WAC, NAC, and SELENE TC data. The NAC (55 strips) and TC image strips were georeferenced using ArcMap software and mosaicked to obtain complete coverage of the study area. A complementary approach was used with the LROC and TC datasets, with which the morphology was analysed at different solar azimuth and phase angles. The slope map is derived using LOLA-Kaguya merge DEM. The DEM merge has been used for 3D visualization and topographic interpretation of the study area. The crater interior units are demarcated based on similarity in surface texture, topography, and stratigraphic relationships. The mosaic of crater cavity created using NAC images of 0.5-1 m/pixel resolution allowed us to investigate each mapped morphological unit in greater detail. The topographic data overlain on WAC and NAC mosaic gave us a 3D perspective of the crater cavity units and their spatial relationship with the local topographical features. The mapping of proximal and distal ejecta units has been carried out using a combination of datasets of the Clementine colour ratio map, SELENE-TC images, and Hapke-normalized WAC data. Several image enhancements are made to more clearly visualise the extent of the ejecta ray pattern. The Clementine colour ratio image highlighted the distal rays of the crater stretching to about hundreds of kilometers radially from the crater cavity. The Hapke-normalized WAC bands at 321 nm, 415 nm, and 689 nm were used to generate a colour composite that enhances the compositional and albedo contrast between the underlying highlands material and the relatively immature Copernican material (Zanetti et al., 2015). The local topographic setting of each ejecta unit and its interaction with the pre-existing topography has been understood from the elevation map of the region. Shaded relief maps or hillshades are prepared from LOLA-Kaguya

DEM merge to provide a view that combines both the visible morphology and relief of the terrain. The illumination conditions such as altitude and azimuth of a terrain can be varied in a hillshade view to observe the same scene in different illuminations for investigating the textural intricacies in ejecta deposits. The WAC farside images taken at a highly oblique phase angle in the approximate range of 70° - 85° cast large shadows into crater cavities. Though this WAC farside mosaic is not appropriate for studying morphologies of the crater cavity, it is a useful tool for analysing textures and stratigraphic relationships of ejecta deposits around the crater. The viewing geometry of WAC mosaic casting large shadows enhances the textural differences between neighbouring topographic features so that the terrain which otherwise appears similar in images where the Sun is close to the viewing sensor (when the Sun is directly overhead and casts minimal shadows) can be readily distinguished based on their distinctive textural patterns. We used the WAC farside mosaic at very oblique phase angles, the shaded relief map prepared from DEM, and the mosaic generated from TC images acquired at large phase angles to identify and characterize the different types of ejecta units in the proximal and distal deposits of the Das crater. The TC mosaic showed the distinct textures of the crater ejecta deposits at moderately high resolutions of 10 m/pixel. Hence, each recognizable ejecta unit was mapped at TC resolution of 10 m/pixel, and where data gaps were present, the WAC farside mosaic of 100m/pixel resolution was utilised. QuickMap is also utilized in combination with LROC and TC mosaics for morphology and ejecta mapping.

7.3.3 Results

The Das crater exhibits a higher topography in the western and northwestern terrain surrounding the crater while a low-lying topography towards the eastern part (Fig. 7.3.2). The maximum elevation of the terrain surrounding the crater is 5.4 – 6.2 km in the northwest direction, while the lowest elevation of 2.2 – 2.5 km occurs to the east of the crater (Fig. 7.3.2b). This asymmetry likely arose from the topography of the pre-impact terrain along the northwest to east direction of the crater. The Das crater is excavated at the margin of the peak ring structure of the South Pole-Aitken basin. The presence of this peak ring structure in the region, particularly the ridge-like terrain outside the crater rim on the northwest and southwest directions, has largely shaped the underlying terrain or the pre-impact topography in the vicinity of the Das crater leading to the observed elevation differences and subsequent downsloping from northwest to the east (Figs 7.3.1a and 7.3.2).

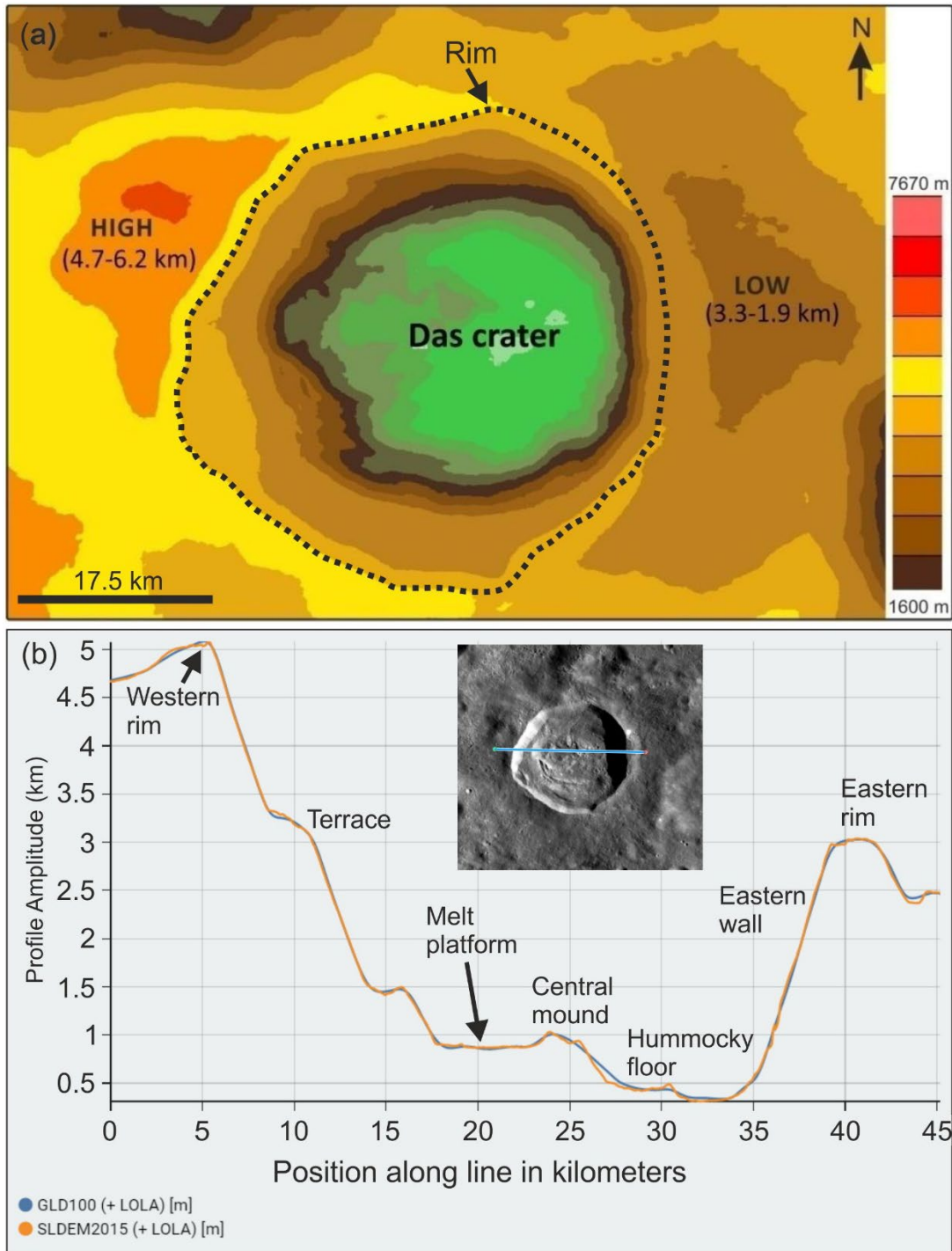


Figure 7.3.2: (A) Color LOLA-Kaguya DEM merge of the Das crater showing the elevation differences in the region. (B) The topographic profile across the line is shown in the inset image. The inset image is the WAC mosaic of the Das crater.

The slope of the crater is such that the wall slopes greater than about 40° from the horizontal plane are shown in shades of orange and red, while the terrain with slopes of less than about 15° from

the horizontal plane is depicted in shades of green (Fig. 7.3.3a). The steep slopes are observed along the inner wall of the crater. The geomorphic units occurring interior and exterior to the crater cavity are discussed separately in the following section. In the crater cavity, the distinct geomorphic units have been mapped and characterized based on the observed surface texture, albedo, topographic setting, and surface slope (Fig. 7.3.3b-c). Within and exterior to the crater cavity, the distribution of the ejecta and its interaction with the pre-existing topography has also been examined. Further details about each mapped unit and its topographical and morphological characteristics are discussed in the following section.

7.3.3.1 Geomorphic units interior to the Das crater cavity

Broadly, the morphology of the Das crater can be divided into ejecta deposits, outermost crater rim region, crater wall region with slump terraces, and the flat floor with a central peak (Fig. 7.3.3b). The observed morphology, typical of lunar complex craters, is a function of crater degradational processes with time (Head, 1975). The crater rim is an elevated crest bordering the outer edge of the crater wall to the interior and the innermost edge of the radial ejecta blanket exterior to the crater, impeccably encircling the transient crater cavity (Fig. 7.3.3a). The rim-to-rim diameter of the crater is approximately 38 km. A slight outward bulge to the western half of the crater is apparent (Fig. 7.3.3b). The overall crater morphology shows a downsloping from southwest to northeast directions (Fig. 7.3.3b).

7.3.3.1.1 Crater rim and terraced walls

The rim of the crater is roughly circular and scalloped in planform and uplifted relative to the surrounding terrain (Fig. 7.3.3b). The western rim appears to be slightly expanded as opposed to the eastern rim having an almost trimmed outcrop to a straight extent (Fig. 7.3.3b). The sharp undegraded edges of the rim crest are a clue to the crater modification processes not earlier than hundreds of million years. The rim crest is highest (5290 km) to the northwest of the crater and lowest (2841 km) to the southeast direction (Fig. 7.3.2). The rim-to-rim elevation difference across the crater equals about 2.44 km, thus sloping from the northwest to the SSE direction of the crater (Fig. 7.3.2). The complex craters form as a result of the collapse of the initial transient crater (Melosh, 1999). The gravitational stability lessens with an increase in the size of the transient crater (Melosh, 1977; 1982; 1989; Pike, 1980b). In such cases, rimmed depressions larger than a

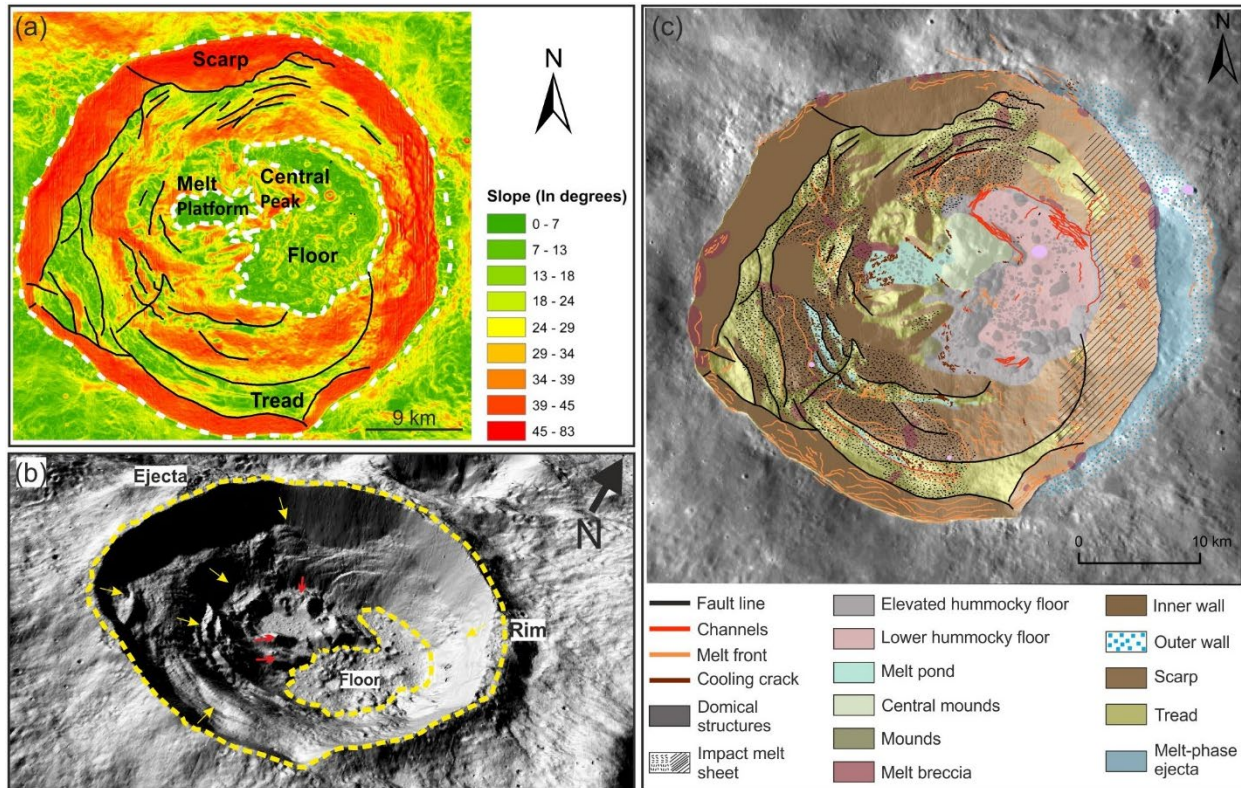


Figure 7.3.3: (A) Colour-coded slope map of the Das crater derived from LOLA-Kaguya DEM merge. (B) LOLA hillshade view of the Das crater showing the major geomorphic units in the crater. The red arrows point to the slumped hillocks on the floor, while yellow arrows denote the wall terracing. (C) Detailed geological map of the Das crater showing the distinct geomorphic units interior to the crater cavity.

threshold size undergoes local collapse and modifies the initial transient cavity to develop into the final crater with a central peak, terraced wall, and flat floor (Dence et al., 1977; Melosh, 1989). The slumping of the inner wall towards the interior during transient crater collapse causes a steeper slope near the rim and reduces the crater rim height as the initial rim slides down to the interior crater cavity (Horz et al., 1991; Smith and Sanchez, 1973).

The crater wall is the steeper, downward-sloping region between the rim and the floor (Fig. 7.3.4a-b). The wall slopes consist of the coalesced scarp (steep-sloped) and tread (gentle-sloped) system known as terraces that appear as a wreath of alcove close to the inner edge of the rim (e.g., Croft, 1985a) (Fig. 7.3.4). The scalloped walls develop as a result of the slumping of masses of rocks and regolith onto the crater floor during crater modification (Smith and Sanchez, 1973, Horz et al., 1991). The slope of the terraced wall ranges from 15° to $>40^{\circ}$, with the most steepness ($>40^{\circ}$ – 80°) in the scarp regions encompassing the crater wall (Fig. 7.3.3a). The total surface area of the crater wall is nearly 936 km^2 . The dimension of the down-sloping crater wall varies vividly, with the rim-to-floor elevation ranging between ~ 5000 – 1800 m and ~ 3000 – 377 m in the northwestern and

eastern parts, respectively (Fig. 7.3.2). The rim-to-floor elevation difference is relatively lower in the northeastern direction (3810-529 m) against an elevation between ~4161-650 in the SSW wall of the crater (Fig. 7.3.2).

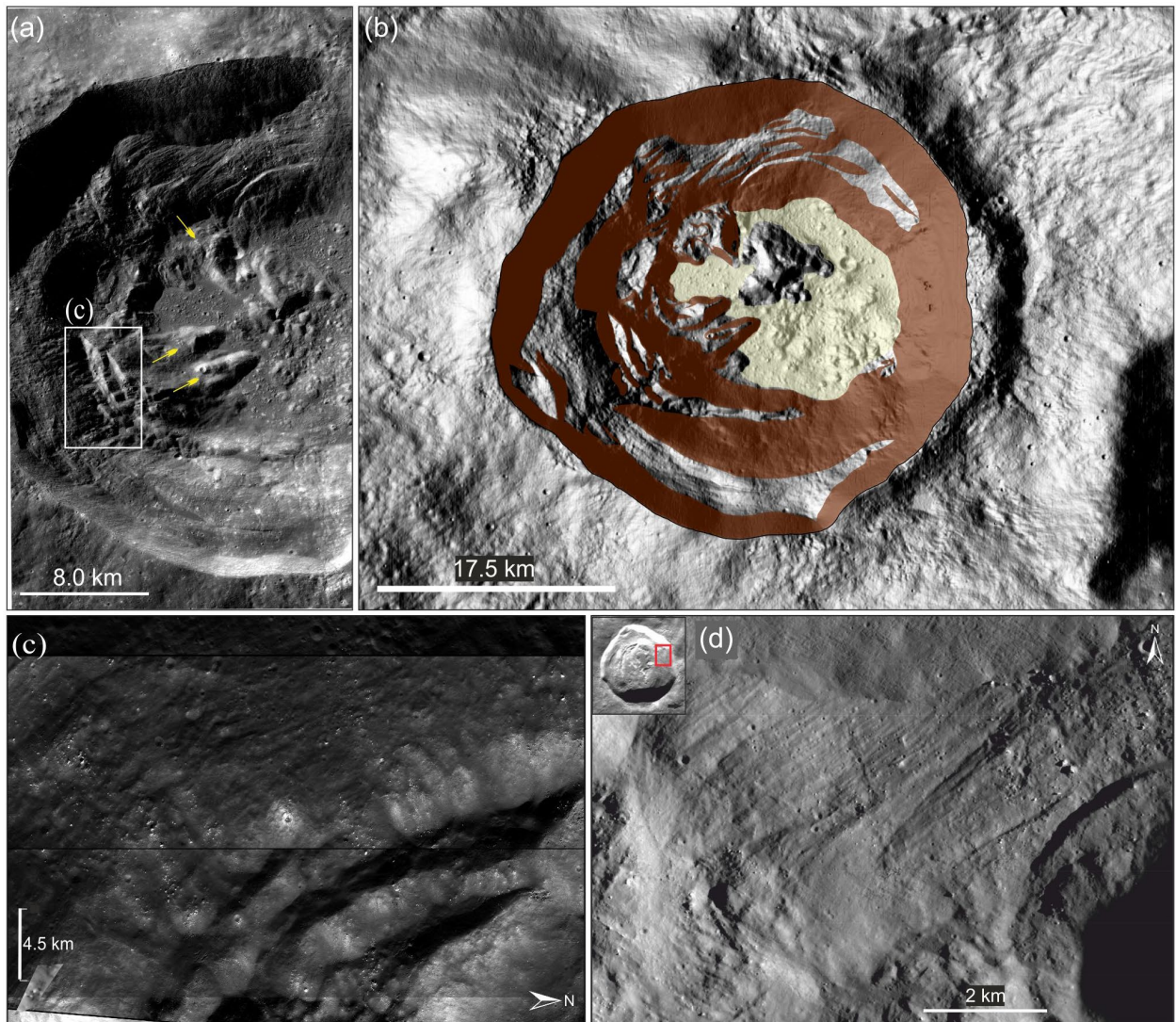


Figure 7.3.4: (A) TC mosaic of the western section of the Das crater. The yellow arrow points to the slump hillocks. (B) The wall terraces are mapped (brown shades) on the LOLA hillshade view of the Das crater. (C) Enlarged view of the white rectangular box in Fig. 7.3.4A. The terraces on the western inner wall are shown. (D) Terraces on the inner wall grading narrower, closely spaced faults towards the crater centre.

The scarp and tread system is generally interlaced by faults that occur when two adjacent blocks of rock are displaced relative to each other. The LOLA hillshade view (vertically exaggerated by a factor of 1.5) of the Das crater shows the sharply defined scarp system of the inner wall and the intervening gently sloped regions, more prominent towards the southwest and northwest of the crater (Fig. 7.3.4c). The terracing of the wall is not well-pronounced on the eastern wall (Fig.

7.3.4b). Terraces progressing to the centre of the crater become narrower and grade to closely spaced faults compared to the wider tread and higher scarp near the rim crest (e.g., Pearce and Melosh, 1986) (Fig. 7.3.4d). The rim collapse and wall terracing have widened the crater producing an outward bulge towards the western half of the crater while the steepness of the wall near the eastern rim increased (Figs 7.3.2 and 7.3.3a).

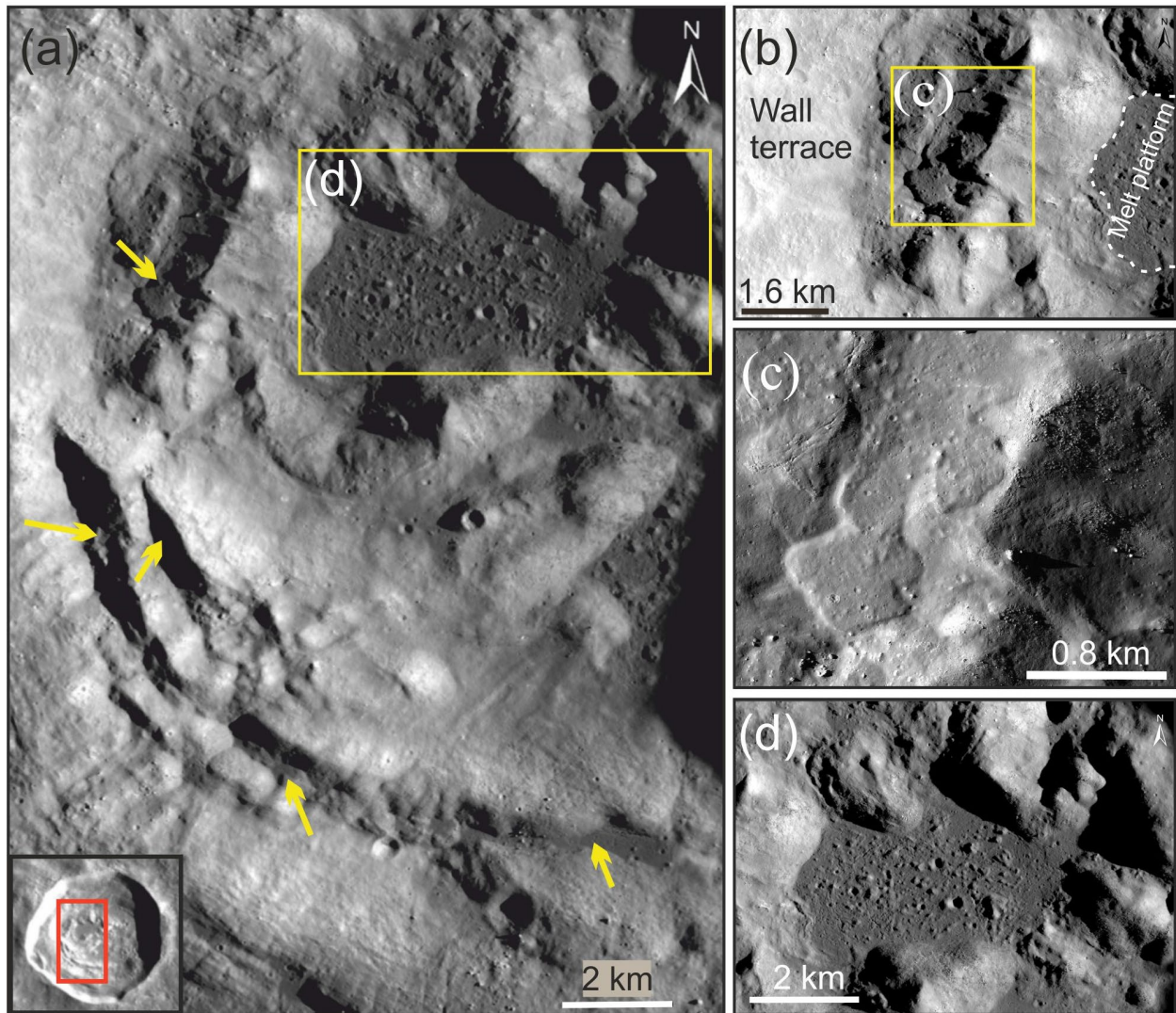


Figure 7.3.5: (A) TC mosaic of the western section of the Das crater shows impact melt deposits on the wall and floor. The yellow arrows point to the melts pooled within topographic lows in the western wall. (B-C) Melt lobe identified on the wall terrace. (D) Melt platform on the crater floor.

Irregular massive slumping features are observed towards the base of the wall close to the outer boundary of the crater floor (Fig. 7.3.4a). The massive slumps form heaps of slumped material that appear to have slid along the western wall and piled up as hillocks or large mounds adjacent to the base of the terraced wall (Fig. 7.3.4a). The slumped blocks partially bound the floor unit in the

west of the crater cavity (Fig. 7.3.4a-b). Impact melts appear to have engulfed the underlying rock/regolith in the inner wall regions and later cooled to form extensive melt sheets, identified as melt fronts and/or flow lobes in several locations along the slopes in terraced walls (Fig. 7.3.5).

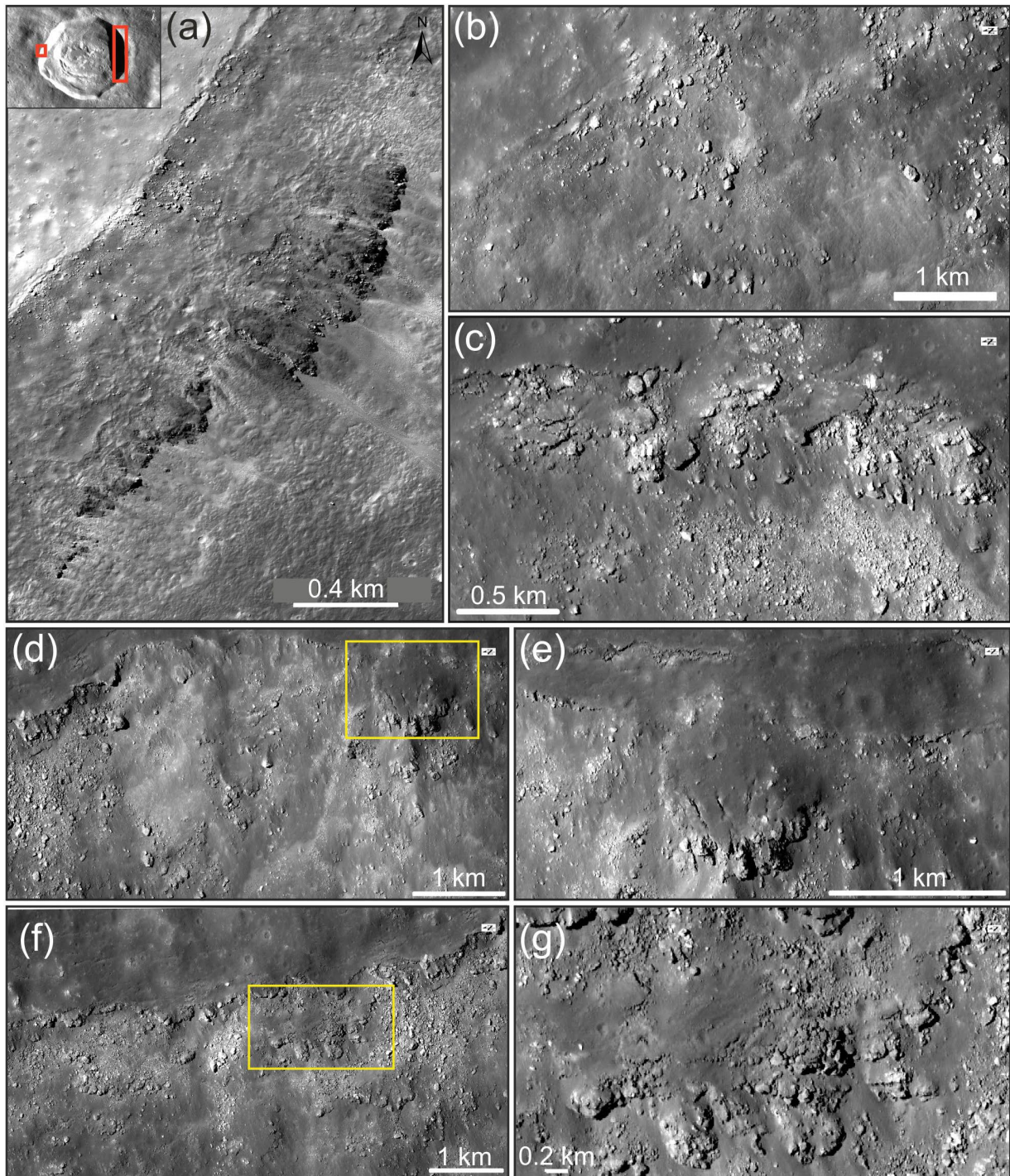


Figure 7.3.6: (A-G) Impact melt flow fronts identified along the western and eastern inner wall slopes. (E & G) The enlarged view of the yellow rectangle in Figs 6D & F, respectively.

The impact melts are believed to have been generated as a result of a large amount of projectile energy being partitioned into the target material during the impact event (Dence, 1971; Hawke and Head, 1977; Melosh, 1989). The generated impact melt can pool in the crater floor, terraces, region outside the crater cavity or flow down the slopes outside the rim (e.g., Ashley et al., 2012; Dhingra et al., 2014; Kruger et al., 2016; Dhingra et al., 2017 (Figs 7.3.5 and 7.3.6).

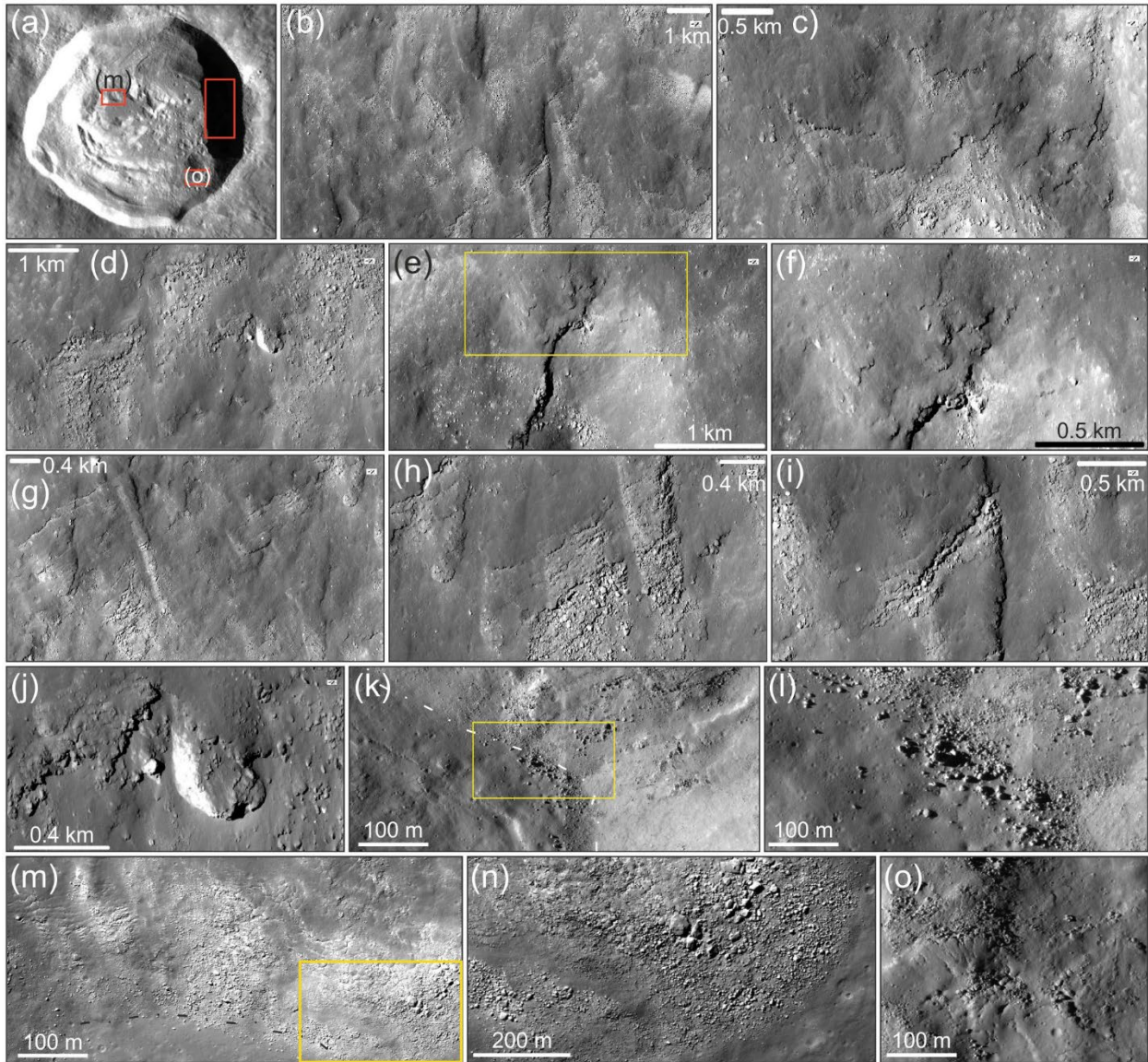


Figure 7.3.7: (A-J) The fractured impact melt deposits identified on the sloping wall of the Das crater. Melt waves can be seen in Figures 7.3.7C, F, and J. (F) The enlarged view of the region inside the yellow rectangle in Fig. 7.3.7E. (K) The boulders eroded out of the fractured impact melt deposits and reached the adjoining floor. (L) The enlarged view of the area inside the yellow rectangle in Fig. 7.3.7K. The tumbled boulders can be seen lying along the wall-floor boundary. (M-O) Fractured impact melt deposits with boulders distributed on its margins. (N) The enlarged view of the region inside the yellow rectangle in Fig. 7.3.7M.

Very often, the impact melts flow down the slopes of the inner wall to form flow fronts resembling melt waves as it cools in time (e.g., Bray et al., 2010; Plescia and Spudis, 2014; Dhingra et al., 2015) (Fig. 7.3.6). The impact melt deposits in the Das crater are identified by their smooth surface texture and low albedo (Fig. 7.3.5). The melt flow fronts or melt waves are identified by an interruption in slope across the flow front, attaining a zigzag margin (Figs. 7.3.6 and 7.3.7). The flow fronts are profuse in the downslopes of the melt-covered eastern inner wall (Fig. 7.3.7). Abundant boulders (~3-15 m across) that appear to have eroded out of the fractured impact melt deposits are dispersed along the margins of the downsloping-melt fronts across the eastern wall (Fig. 7.3.7a-l). These boulders are often tumbled downslope by gravity to arrive at the adjoining floor plains (Fig. 7.3.7k-n). The melt appears to have flowed down the scarp slopes in the northwestern wall to arrive at the tread further down, where it eventually cooled down to form branched flow lobes filling a total surface area of ~5.4 km² (Fig. 7.3.5a-c).

The melt ponds are characterised by smooth low-albedo deposits in topographically low lying areas or gently sloped surfaces (Fig. 7.3.8). In the 0.5m/pixel NAC scale, eight melt pools are found in the crater interior. Ponds of cooled impact melt deposits pooled and later solidified in the plains of wall terraces are evident in the NAC scale (Fig. 7.3.8). The smooth impact melt deposits exhibit curvilinear cracks or fractures across the terrace slopes (Fig. 7.3.8c-d). Such cracks in impact melt deposits would have been developed as a result of a change in volume as the melts solidified (e.g., Xiao et al., 2014).

Impact melt breccia containing rock or mineral fragments in a matrix of crystalline impact melt are ubiquitous in the terrace walls (Fig. 7.3.8g-i). In the melt breccia, the boulders of size varying from <10 m to >100 meters appear partially buried with some edges protruding outward (Fig. 7.3.8g-h). These boulder fragments are most likely the clasts from the target rocks picked up by the impact melts while moving along the crater wall. The weaving boulder trails created when boulder fragments rolled or tumbled down the slopes to leave tracks behind are visible on the terraces along the walls (e.g., Kumar et al., 2016) (Fig. 7.3.8i).

The slumped hillocks at the base of the western wall are draped by smooth impact melt deposits (Fig. 7.3.9). The innermost margins of the wall and the top portion and flanks of the slumped blocks adjacent to the western floor exhibit fractured impact melt developed due to stress that formed the cracks as melt cooled (Fig. 7.3.9d-e). Also, the flanks of the slumped blocks sloping towards the crater floor are covered to a greater degree by clusters of boulders eroded out of the melt deposits over time (Fig. 7.3.9f and h). The boulders could also have resulted partly from the later impact cratering activity over the slumped blocks (Fig. 7.3.9i).

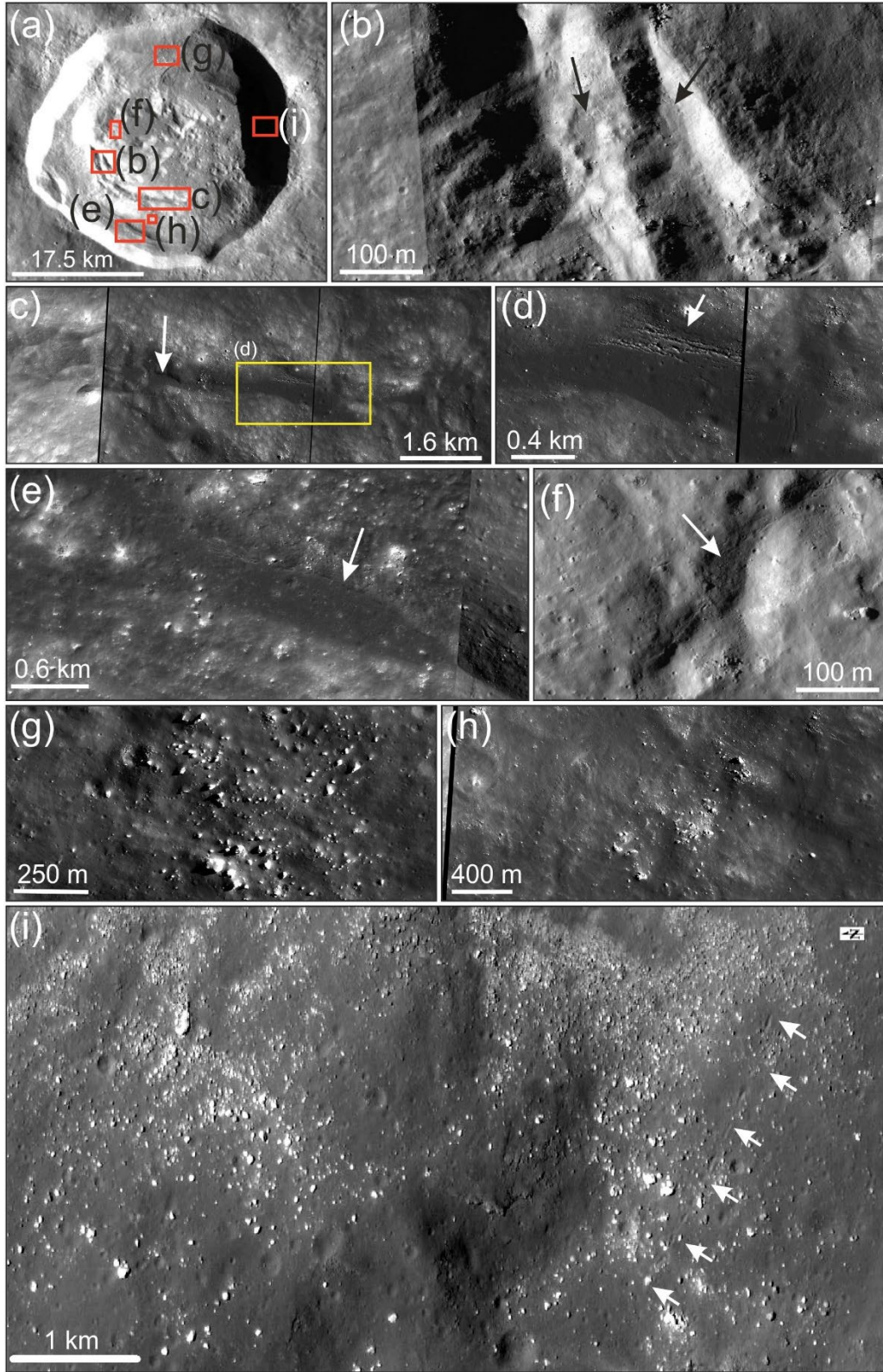


Figure 7.3.8: (A) Locations of the melt ponds identified in the crater. (B-F) The smooth melt ponds on the wall terraces. (G-I) Melt breccia melt on the inner wall of the crater. The white arrows in Fig. 7.3.8I point to the boulder trail.

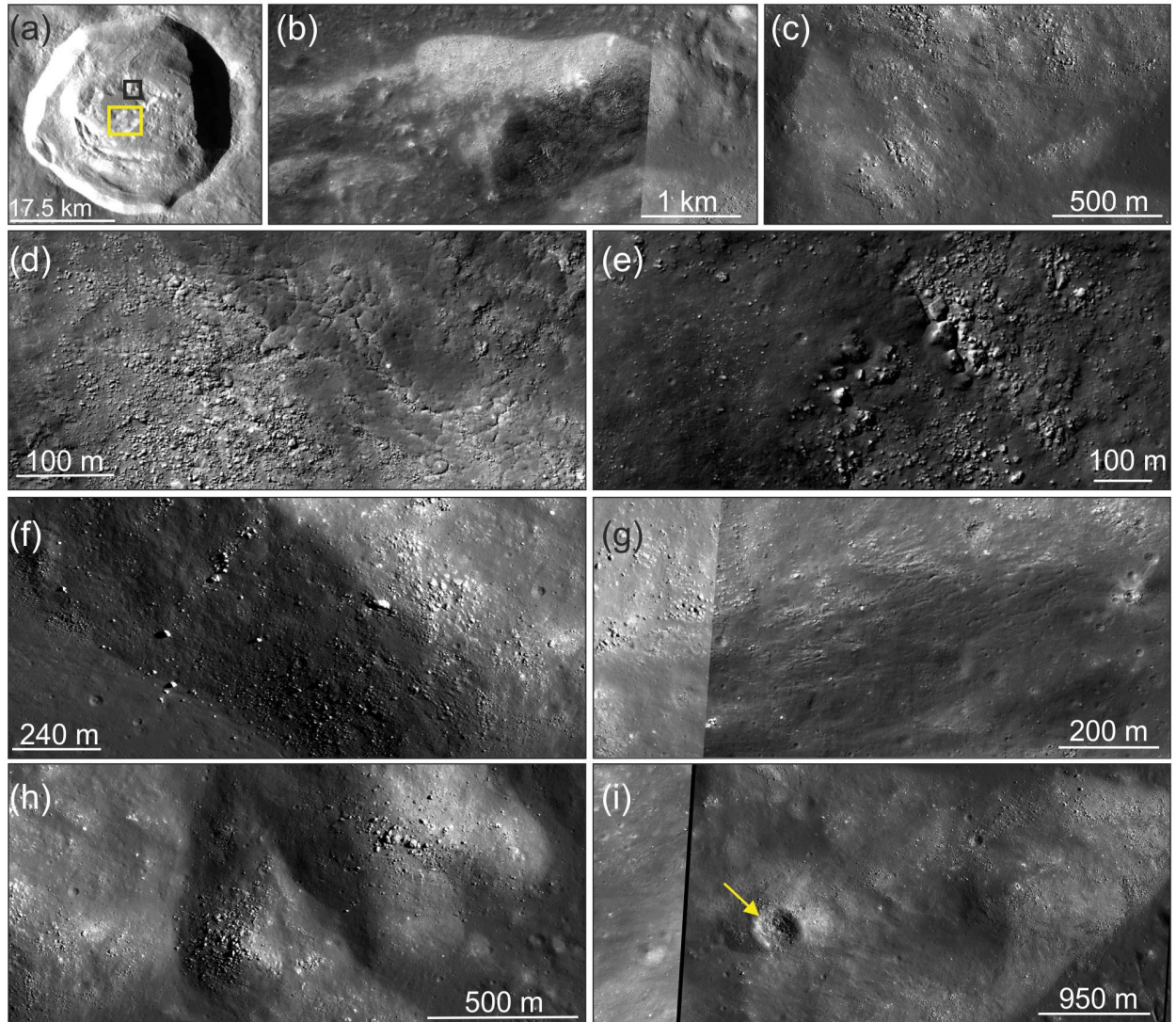


Figure 7.3.9: (A) Locations of the slump hillocks. (B) Enlarged view of the slump hillock on the crater floor. (C-E) Fractured impact melt deposits on the slump hillock surfaces. Eroded boulders at the margins are visible. (F) Eroded boulders are reaching the adjoining floor of the crater. The slope of the flanks is towards the bottom left. (G) Cooling cracks on the melt-draped hillocks. (H) Heaps of wall slumps on the northwestern edge of the floor. (I) Small superposed impact crater at the summit of the slump hillock is marked using the yellow arrow.

7.3.3.1.2 Crater floor–Lower Hummocky unit and Elevated Hummocky unit

The floor region is the bottommost part of the crater extending from the inner edge of the wall-terrace block to the centre of the crater, with a total surface area of $\sim 270 \text{ km}^2$ (Fig. 7.3.10). The crater floor consists of characteristic geologic features representative of crater modification processes. The floor region is marked by a relatively smooth and uneven terrain covered in extensive melt sheets interspersed with several distinct, nearly circular uprisings often bunched

together (Fig. 7.3.10a-b). The geomorphic units in the floor are subdivided into an elevated hummocky floor, a lower hummocky floor, and an elevated melt platform based on topographic and surface textural variations (Figs 7.3.5a and 7.3.10a-c). The elevated hummocky floor (~919 – 1259 m) and the lower hummocky floor (~462 – 919 m) units exhibit a hummocky texture, which is a type of texture commonly seen on the floors of lunar craters except for the largest basins (Cintala and Grieve, 1998) (Fig. 7.3.11). The hummocky texture of the elevated and lower hummocky units is defined by the presence of several domes or boulder-type clasts of size varying from ~100–2000 m embedded in the extensive impact melt sheet (Figs. 7.3.11b-g and 7.3.12). The elevated hummocky unit covers a total surface area of ~170 km², while the lower hummocky unit appears to occupy a fairly lesser spatial extend of ~85 km². The average slope of the hummocky floor is less than 6°.

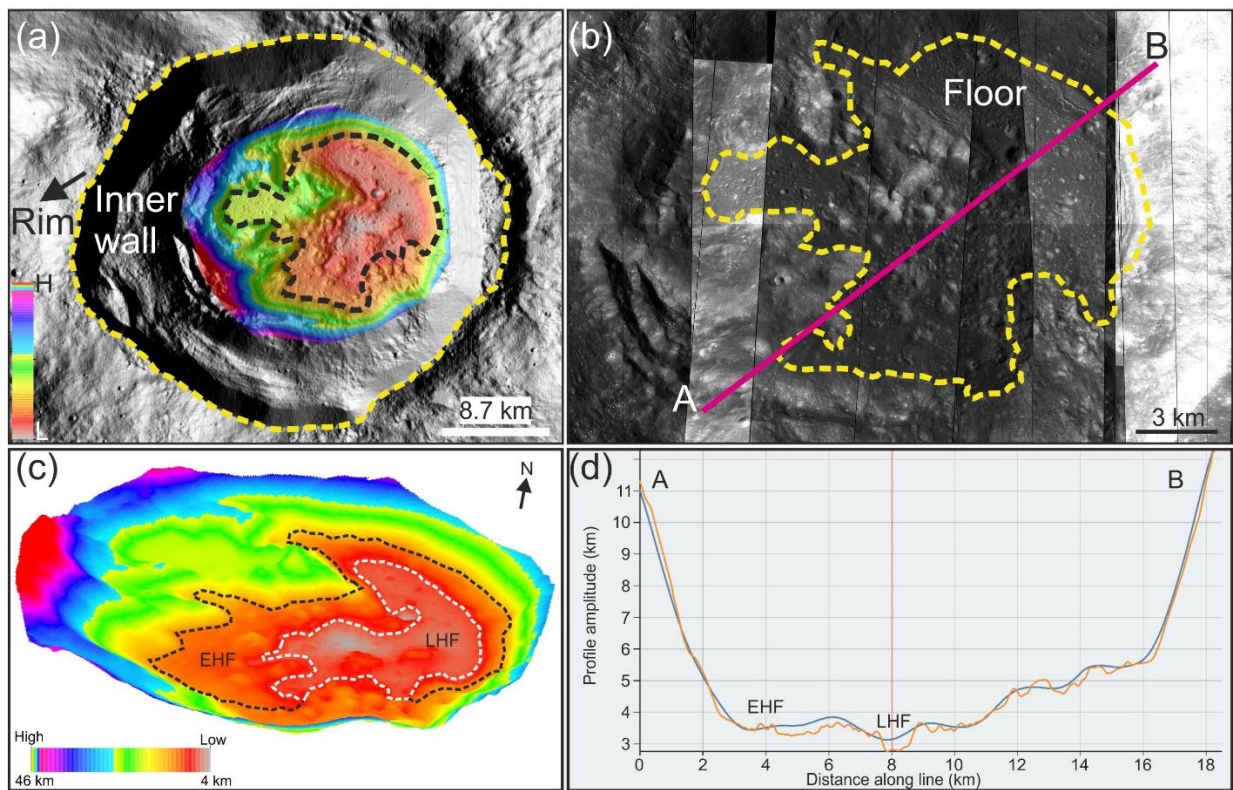


Figure 7.3.10: (A) Color-coded DEM of the crater floor overlaid on the hillshade of the Das crater. (B) NAC mosaic of the hummocky floor units in the crater. (C) The 3D view of the floor section of the crater. The white polygon marks the approximate boundary of the lower hummocky unit, while the black polygon demarcates the elevated hummocky terrain. (D) Topographic profile across the line shown in Fig. 7.3.10B. EHF: Elevated Hummocky Floor, LHF: Lower Hummocky Floor.

The impact melts appear to have draped over the megaclasts seen in the hummocky units (Fig. 7.3.11d-g). The domical structures in the hummocky floor are likely developed by welling up the

target clasts by impact melts. The blocks or clasts in the hummocky units do not protrude from underneath the impact melt nor appear to lie completely above the impact melt. Rather they are embedded in the impact melt such that the lower parts or toes of the blocks from disintegrated target materials disaggregate to form hummocks and clasts, which may or may not be digested by the overlying impact melt depending on the volume and thickness of the impact melt lining the crater cavity (Cintala and Grieve, 1998) (Fig. 7.3.12).

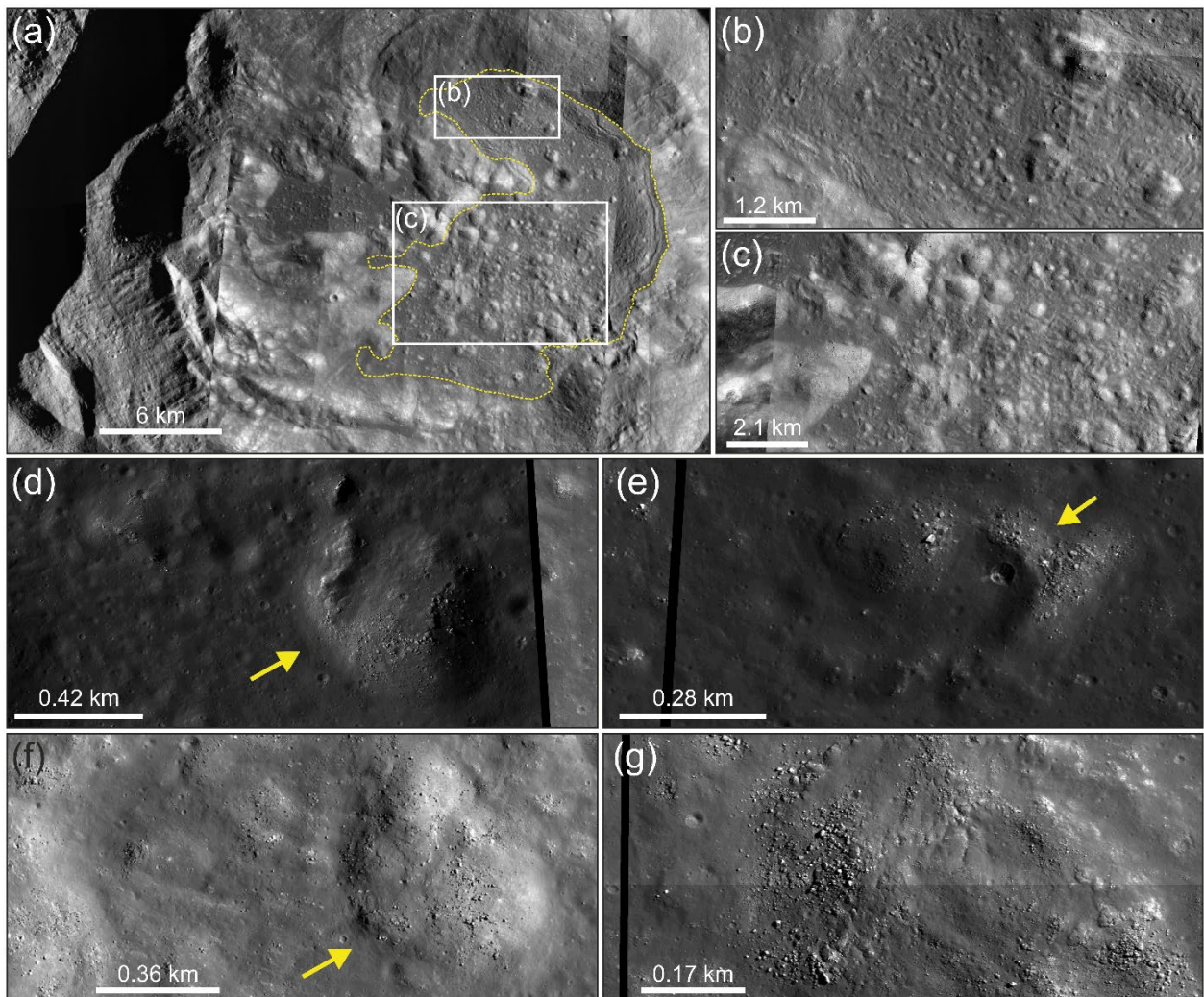


Figure 7.3.11: (A) NAC mosaic of the Das crater floor shows the hummocky unit marked by the yellow polygon. Surface morphology of the elevated hummocky unit (B) and lower hummocky unit (C) in the crater floor. (D-F) Showing the circular uprisings or mounds in the hummocky floor. (G) Fractured impact melt deposits and eroded boulders on the top of a mound on the hummocky floor.

The hummocks are smaller in size (~160 – 200 m) to the northern part of the floor while more pronounced (~1 km in size) and clustered to the southern and western parts (Figs 7.3.11a-c and 7.3.12). The fractured impact melt deposits are seen on the top and flanks of the domes on the

hummocky floor (Fig. 7.3.11g). The clusters of boulder-sized fragments (~3–30 m across) are distributed over, mainly on the brinks and flanks of the melt-swathed domes in the hummocky floor (Fig. 7.3.11f-g). These boulders could be the weathered products of the solidified melt.

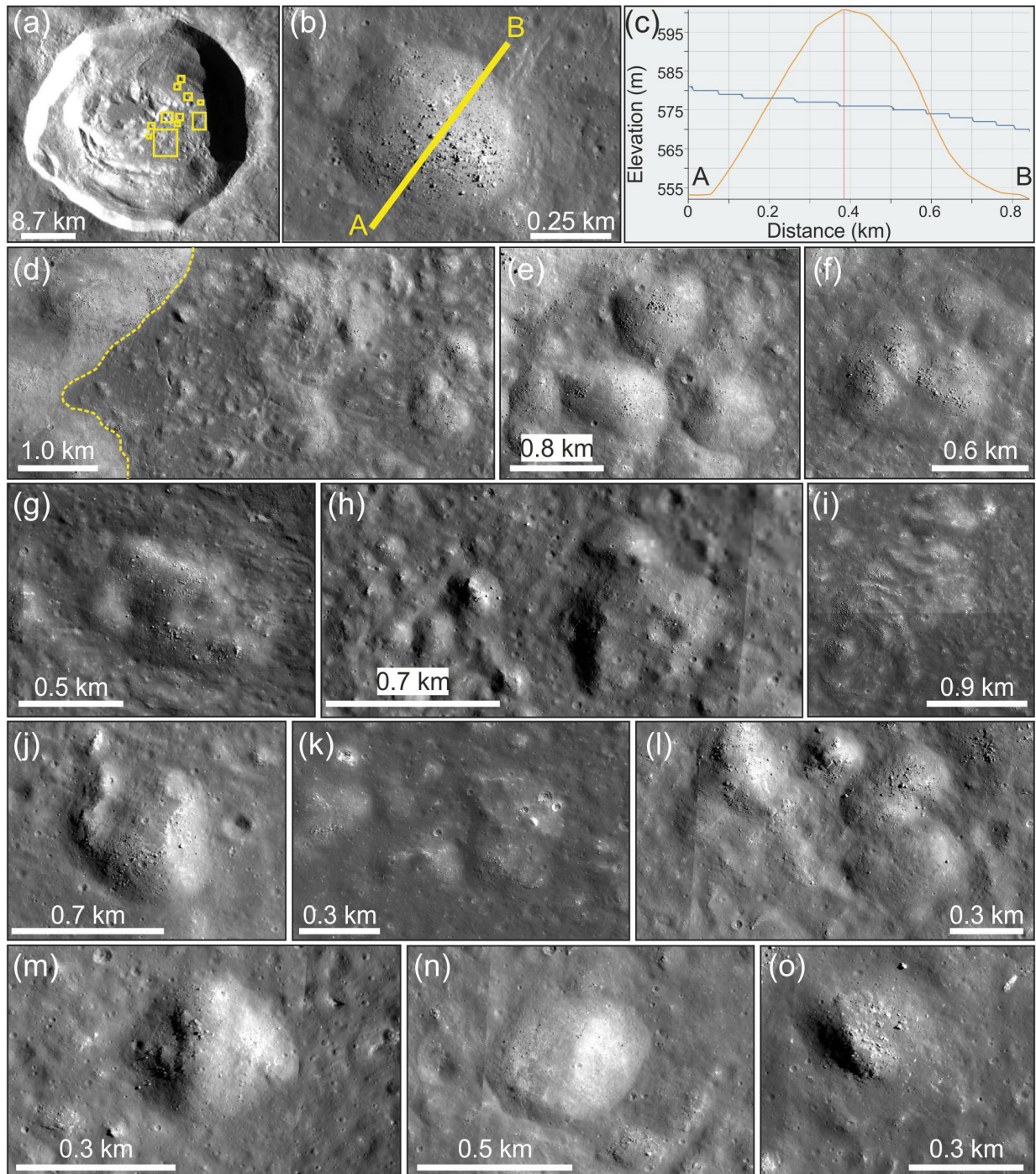


Figure 7.3.12: (A) NAC mosaic of the crater. The yellow rectangles represent the locations of the domical structures identified in the crater floor. (B-F) NAC mosaic displaying the domes in the elevated hummocky floor. Fig. 7.3.12C shows the topographic profile across line A-B in Fig. 7.3.12B. (G-O) NAC mosaic showing the domes identified in the lower hummocky floor.

The near-parallel concentric cooling cracks are visible features on the hummocky floor, mostly towards the margins adjacent to central mounds as well as the inner wall (Fig. 7.3.13). The cooling cracks are formed due to uneven cooling of the impact melt in which the surface of the cooling melt quickly cools than the still-molten flows underneath, promoting crack formation on the exterior part (Xiao et al., 2014).

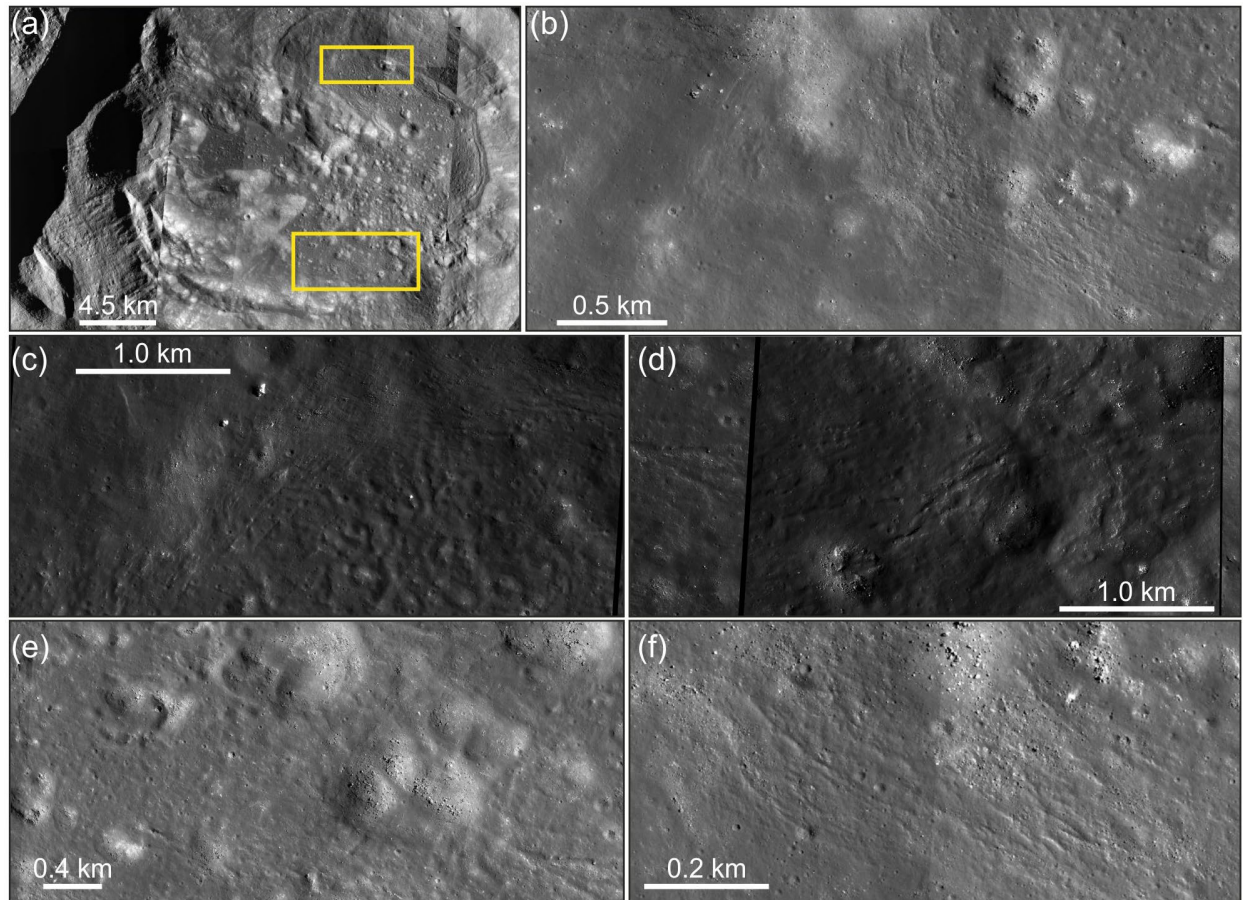


Figure 7.3.13: (A) NAC mosaic of the crater interior. The yellow rectangles represent the locations of the cooling cracks identified in the crater floor. (B-F) Enlarged views of the cooling cracks in the northern and southern sections of the hummocky floor.

The lower hummocky unit appears to have been a collapsed or subsided slab of the initial crater floor (Fig. 7.3.14). The low elevation of this eastern unit has likely resulted from the differential subsidence of the initial floor as the melt column begins to cool down during crater modification processes (Dhingra et al., 2016). Several curvilinear channels of the order of ~10 km running along N-S align with the initial floor adjacent to the innermost margin of the eastern wall that currently stands slightly above the lower hummocky unit formed subsequent to subsidence (Fig. 7.3.15a-f). The channels could originally be grabens developed during floor readjustments (e.g., Sruthi and Kumar, 2014).

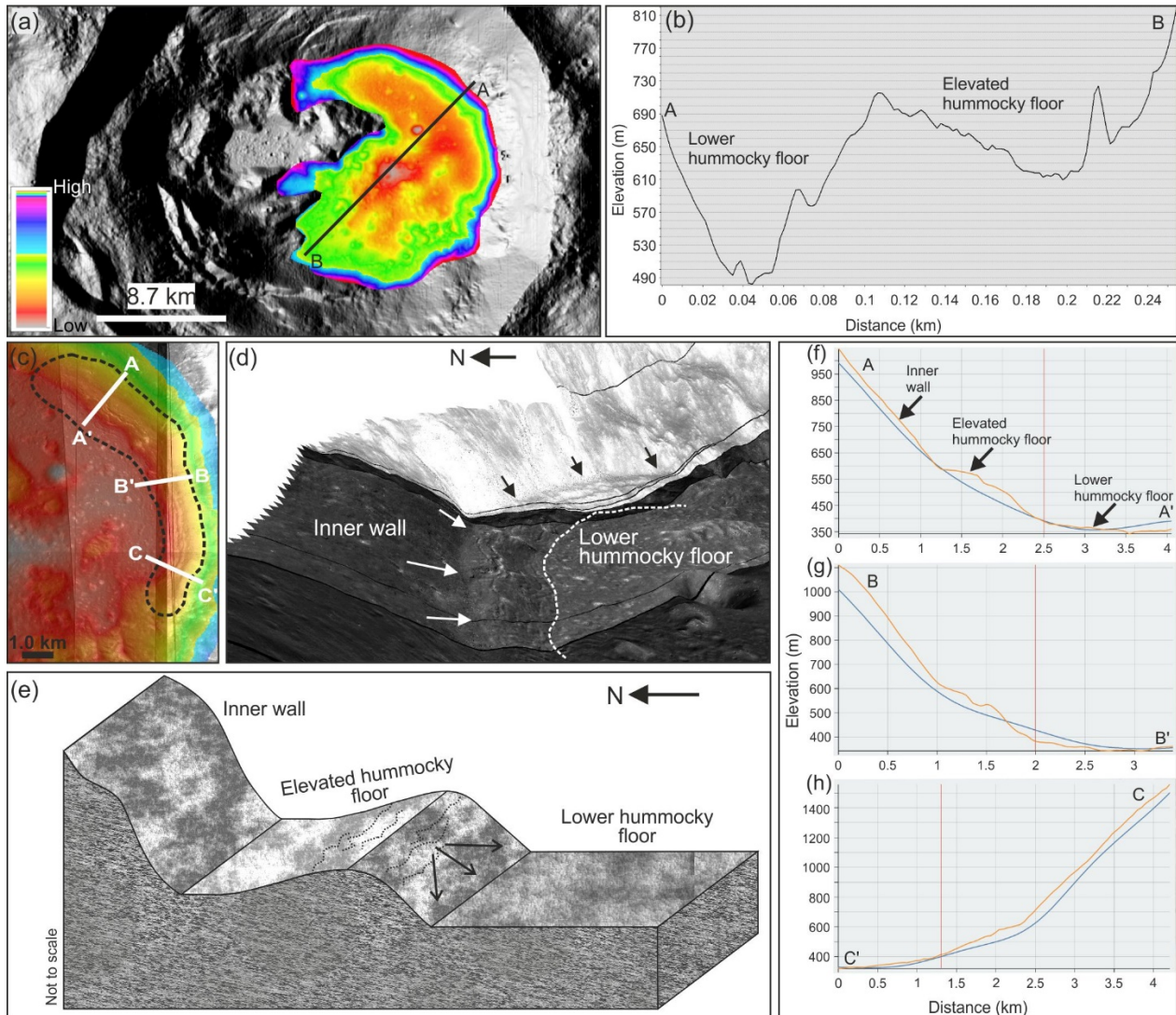


Figure 7.3.14: (A) LOLA hillshade view of the crater interior. The colour-coded DEM encompassing the elevated and lower hummocky floor units is overlaid. The red-orange shaded region represents the lower hummocky floor, while the green regions belong to the elevated hummocky floor. (B) The topographic profile across line A-B in Fig. 7.3.14A. (C) Colour-coded DEM of the eastern floor region. The black dashed polygon marks the region of floor subsidence during the crater modification stage. The dark red regions inside the black polygon denote the plane where subsidence has taken place, while the faded yellow regions represent the elevated floor unit. (D) 3D representation of the NAC mosaic manifesting the subsided floor resulting in the elevated hummocky floor and lower hummocky floor. The arrows point to the boundary between the inner wall and the elevated hummocky floor. The white dashed line represents the boundary between the elevated and lower hummocky floor units. (E) The diagram illustrates the perspective described in Fig. 7.3.14E. (F-G) The topographic profile across lines A-A', B-B', and C-C' in Fig. 7.3.14C. The profiles show the elevation differences across the region where floor subsidence has taken place.

It is also plausible that the structural failure along weaker planes of the crater in the modification

stage could have resulted in floor subsidence and the observed elevation differences between lower and elevated hummocky units (Dhingra et al., 2016). However, it is to be noted that the elevated hummocky unit lying towards the WSW of the floor is shaped largely by the heaps of slumped wall blocks (Figs 7.3.3b and 7.3.4a). The large-scale collapse of the western wall that prompted the wall blocks to slide down and pile up on the neighbouring floor region might have created the elevated platform-like terrain seen on the western half of the crater cavity (Figs 7.3.10a and c and 7.3.14). A practical explanation could be that a combination of the processes mentioned above could have played a role in the observed elevation differences in the floor section of the crater.

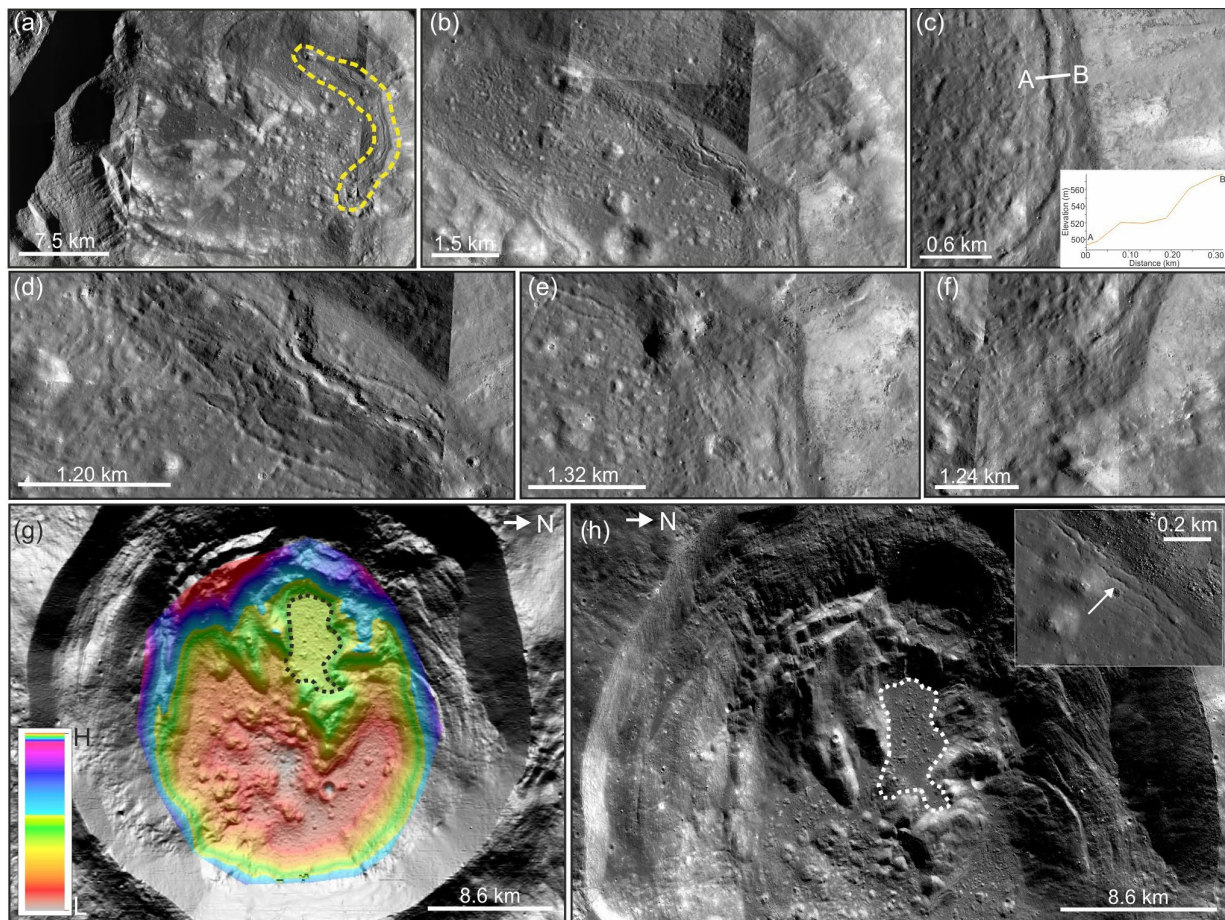


Figure 7.3.15: (A) NAC mosaic of the crater interior. The yellow dashed polygon outlines the location of the grabens. (B-F) NAC mosaic of the intersecting grabens trending NW-SE along the elevated and lower floor regions. The inset image in Fig. 7.3.15C shows the topographic profile across (graben), i.e., line A-B in the figure. (G) LOLA hillshade view of the crater interior overlaid with colour-coded DEM of the floor region, showing the elevated terrain (black dashed polygon) comprising the melt platform in the western section of the floor. The region (black polygon) encompassing the melt platform appears to be an elevated terrain (yellow-green shades) from the surrounding floor region (towards the eastern part of the floor). (H) TC mosaic showing the elevated terrain with melt platform (marked by white dashed polygon). The inset NAC image shows the cooling fractures seen at the periphery of the melt platform.

Further towards the northwestern margin of the crater floor occurs a smooth and relatively flat elevated platform (~1667 - 1995 m) that stands above the surrounding hummocky floor (Fig. 7.3.15g-h). The platform is surrounded by wall slumps except to the east, where it is extending to the summit of central mounds (Fig. 7.3.15g-h). Impact melt deposits peppered with irregular uprisings or blocks ranging between ~50 m to 360 meters occupy the smooth platform (Fig. 7.3.5a and d). This melt platform has slopes of 0° – 4.4° and covers a total surface area of roughly 15 km², only 6% of the total area of the adjacent hummocky floor units. Curvilinear fractures are present near the northern margin of the melt platform, bunched together in a near parallel orientation with an average width of 220 m (Fig. 7.3.15h). The observed melt platform is a part of the larger picture in which a distinct elevated platform-like terrain is formed on the western half of the crater cavity as a result of wall collapse and subsequent slumping during the crater modification stage. The upliftment that took place during the formation of central mounds has also contributed to this elevated section on the west of the crater cavity. The morphology of central mounds is discussed further.

7.3.3.1.3 Central mounds or peaks

The central peak is defined by the isolated hillocks that typically lie at the centre of the crater cavity, often coalesced to form central mounds (Pike, 1980a; Melosh, 1989). The term central mounds would fit the context of the Das crater, wherein a distinct group of irregular hillocks of varying dimensions is located with a slight offset to NNW from the centre of the crater cavity (Fig. 7.3.16a). The central mounds are formed due to the rebound of the crust as the high pressure imparted to the target rock during projectile impact causes it to behave like plastic until it bounces back in a few seconds (Grieve et al., 1981; Melosh, 2011). The gravitational collapse of the crater walls could also give momentum that aids in uplifting material in the centre (Melosh, 2011).

The summit of the central mounds is at an elevation of about 1100 m above the melt platform (Fig. 7.3.16b). The central mounds are covered with solidified impact melts identified as flow fronts and fractured melt deposits on the brinks and downsloping flanks (Fig. 7.3.16c). In addition, the flanks of the mounds are largely degraded to give rise to the boulders that perched over downhill and often rolled down to come to a stop at the plains of the adjoining floor (Fig. 7.3.16c). Sometimes, the nearby cratering events contribute to the large boulders at the summit.

The bedrock exposures are also identified on the brinks of the mounds, exposed possibly by degradation of the draped impact melt sheet (Fig. 7.3.16d). The boulders following the possible bedrock outcrop down the hill could be eroded out of the bedrock itself, making them potential sampling material representative of deeper crustal rocks. The flow of impact melt deposits

downhill from the summit has carved multiple channels near the base along the northeastern boundary of the mound (Fig. 7.3.16e-f). Further, the impact melts that appear to have been sourced from the melt platform have drained down the east-facing slopes of the mounds (Fig. 7.3.16f).

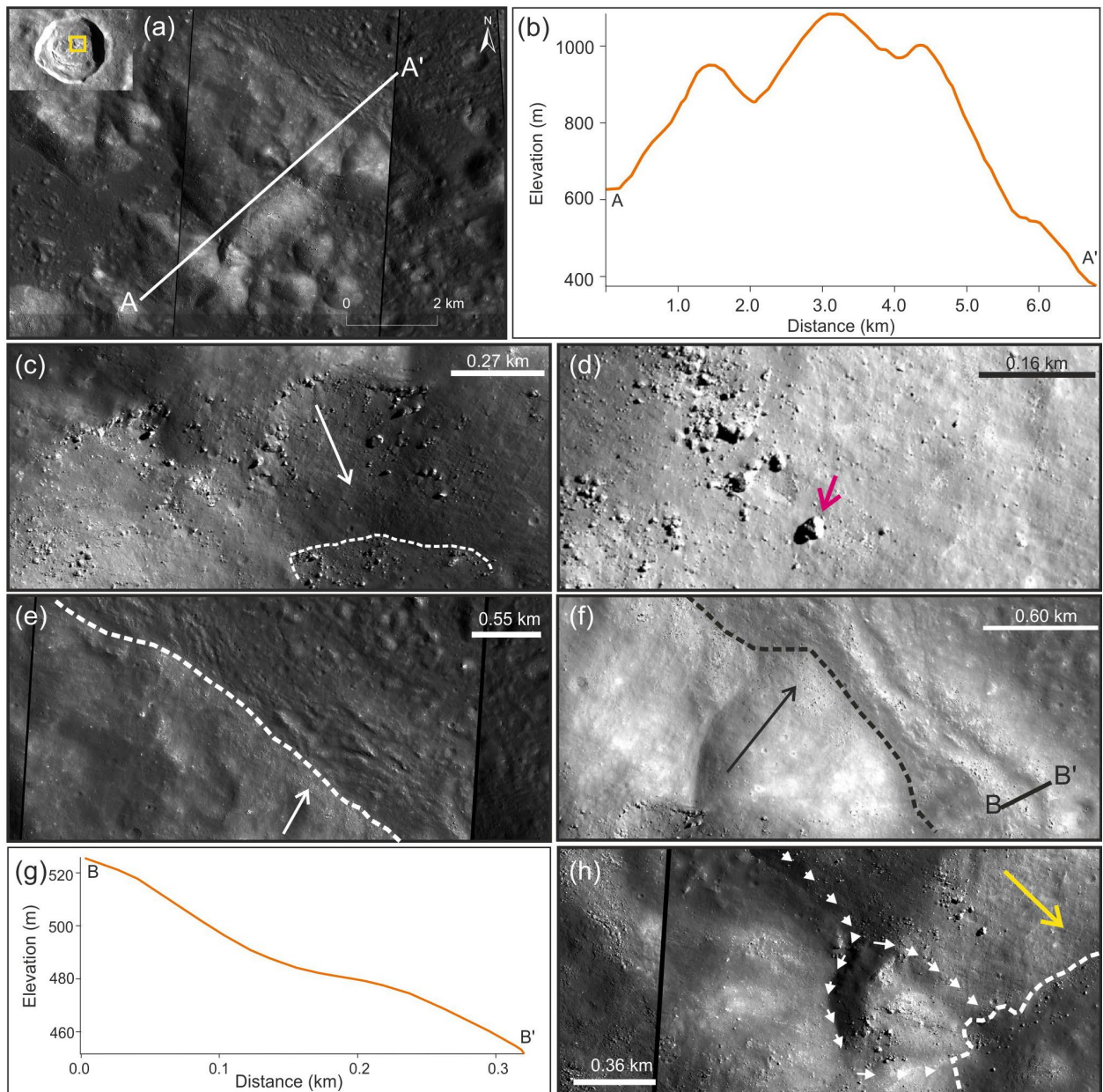


Figure 7.3.16: (A) NAC mosaic shows the central mounds of the Das crater. The inset image shows the location of the central mounds (yellow rectangle) in the crater interior. (B) The topographical profile across line A-A' in Fig. 7.3.16A. (C) NAC mosaic showing the melt fronts on central mounds. The weathered boulders are seen along the downsloping flanks. The white arrow denotes the slope direction. The white dashed line marks the margin of the mound with the surrounding floor region. Several boulders weathered out of the melt sheet appear to have fallen the slopes and settled at the base of the mound. (D) The flanks of the central mounds with bedrock exposures (purple arrow). (E) NAC mosaic shows several intersecting channels trending NW-SE

near the base of the central mound. The white dashed line demarcates the base of the mound. (F) NAC mosaic shows a prominent channel near the base (to the northeastern part) of the mound. The black arrow denotes the slope direction. The black dashed line denotes the region separating the mound and basal platform comprising the channel. (G) The topographic profile across line B-B' in Fig. 7.3.16F, showing the cross-section of the channel. (H) NAC mosaic showing the path of flows along the flanks of the mound. The yellow arrow points to the downsloping direction. The white arrows denote the path of the flows. The white dashed line demarcates the base of the mound from the surrounding floor region.

7.3.3.2 Identification of the distinct ejecta facies and their distribution both interior and exterior to the crater cavity

The hypervelocity high energy impact causes excavation of a cavity (transient crater cavity) which causes the displacement of surface and sub-surface materials in the vicinity of the impact event (Oberbeck, 1975; Osinski et al., 2011; Melosh, 2011). Sub-surface material, approximately one-third of the transient cavity depth, is excavated (thrown out of the cavity) while the remaining is displaced downward (Melosh, 1989; 2011). The excavated material is thrown out of the parent crater as vapour phase, fluidized form, and solid-phase ejecta (Oberbeck, 1975; Morse et al., 2018; Morse et al., 2021). The pressures and temperatures at which the target material is vaporised depend on the composition of the target, and the volume of vapour generated depends on the area exposed to shock pressures sufficient to vaporise the target (Melosh, 2011; Osinski et al., 2019). The fluidic phase of ejecta corresponds to the shocked melt generated as a consequence of the impact event. In contrast, the solid phase ejecta corresponds to the high-velocity spall fragments ballistically transported along a projectile trajectory subject only to retardation by Moon's gravitational acceleration (Oberbeck, 1975; Melosh, 2011). The ejecta deposits surrounding impact craters consist primarily of breccias containing a varying fraction of such fragmental, shocked and melted debris depending on target properties, impact parameters, and distance from the impact crater (e.g., Dence, 1971, Cintala et al., 1977; Horz et al., 1983).

The extent to which ejecta from a particular crater spreads depends on its diameter (Stöffler and Grieve, 2007). Larger-sized craters exhibit a more spatially extensive ejecta field than smaller diameter craters (Moore et al., 1974). Based on their spatial extent, the ejecta field of the crater can be divided into two categories, the continuous (proximal) ejecta blanket and the discontinuous (distal) ejecta blanket (Melosh, 1989). By definition, the continuous and discontinuous ejecta blanket is differentiated based on the presence or absence of continuity in ejecta deposition. Whereas the continuous ejecta blanket is defined to be the portion of the ejecta blanket where the overlying ejecta deposits completely cover or drape the underlying pre-impact topography, the discontinuous ejecta blanket is considered to be the region where the ejecta deposition occurs as

patchy or irregular material, very often manifested as circular or elliptical depressions (secondary craters) (Melosh, 1989). The continuous ejecta completely drapes the underlying terrain and is composed of larger, slower ejected materials, while the discontinuous deposits form from the smaller, faster-ejected materials; both are deposited by ballistic sedimentation (Oberbeck, 1975).

7.3.3.2.1 Continuous and Discontinuous ejecta

The continuous ejecta blanket occurs proximal to the parent crater as sufficiently large volumes of ballistically transported ejecta touchdown the pre-existing terrain to deposit as a contiguous blanket (Oberbeck, 1975; Osinski et al., 2011) (Fig. 7.3.17a and b). The proximal ejecta is located within five crater radius from the rim and comprises 90% of the total emplaced ejecta (Stöffler and Grieve, 2007). The emplaced ejecta form thick blankets closer to the crater rim and progressively degrade to thinner deposits farther from the crater (Melosh, 1989). The discontinuous or distal ejecta is located concurrently or beyond the extent of the continuous ejecta blanket at distances greater than five crater radius from the rim (Melosh, 1989; 2011; Horz et al., 1991) (Fig. 7.3.17a and b). The appearance of discontinuous ejecta is marked by the presence of patchy and irregular deposits often manifested as radial chains of quasicircular depressions or elongated grooves (Melosh, 1989; Morse et al., 2018; Morse et al., 2021) (Fig. 7.3.18a). The fallback of the ballistically transported material ejected from the parent or primary crater in solid-phase results in these pit-like depressions referred to as secondary craters much smaller in size and with rims having a chevron-like shape (>) pointed towards the parent crater (Melosh, 1989). These often occur in clusters (with groupings of 2-3 being very common) oriented radially to the parent crater. The craters in the chains of secondary craters are so closely spaced to appear as a single elliptical trough or a groove embedded on the surface (Fig. 7.3.18a-marked by black dotted lines).

The pulverized materials from the crater often form bright radial rays around the crater (Hawke et al., 2004). The discontinuous or distal ejecta of the Das crater is primarily marked by these distinct rays, which are wispy, filament-type structures having a high albedo (Fig. 7.3.17a and b). The higher albedo of rays is caused by the presence of crystalline silicate materials and/or fracturing of the already present agglutinates in the regolith (Heiken et al., 1991). Though the ray system of the crater is one of the faintest among the category of Copernican craters, a distinctive ray pattern is evident on all sides of the crater except the northeast (Fig. 7.3.17a and b). In the WAC colour composite image, the crater rays are discerned fairly well and are seen to touch the Apollo basin ring, which is around 224 km away (to the SW) from the Das crater in a radial direction (Fig. 7.3.17b). Based on our observations, the ray system of the crater has been divided into two categories. One is the most definitive, distinct ray system closer to the crater, and the other is the

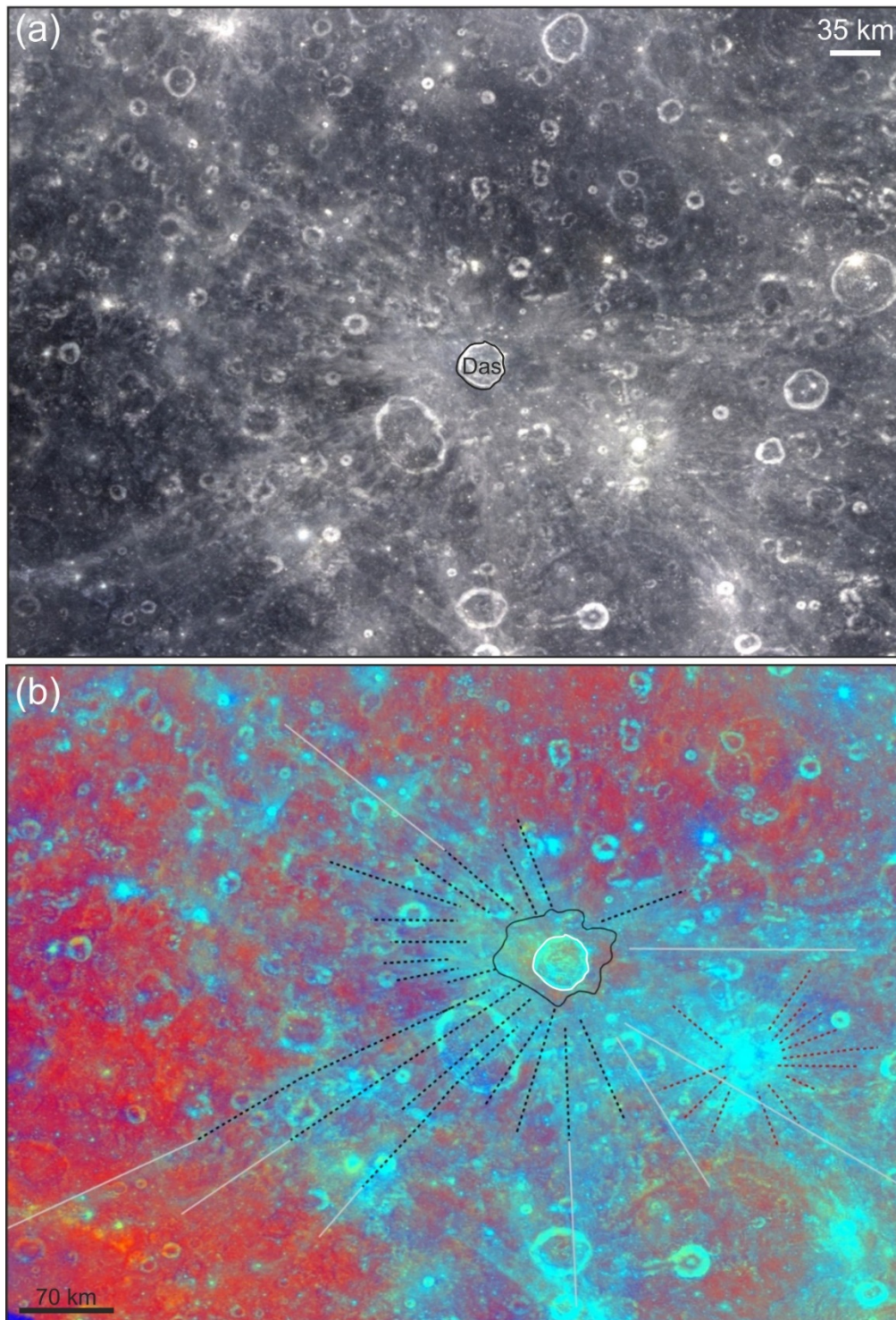


Figure 7.3.17: (A) Hapke WAC mosaic shows the Das crater and its ejecta rays on the equidimensional surface of the lunar farside. (B) Hapke WAC colour ratio image displaying the bright ejecta rays (Bright blue) of the Das crater. The approximate extents of the contiguous (Black solid lines) and discontinuous ejecta (Black dashed lines) are delineated. The prominent rays are marked in dotted black, fainter ones in grey. Discernibly different Crater rays of Chebyshev Z are marked in dotted red.

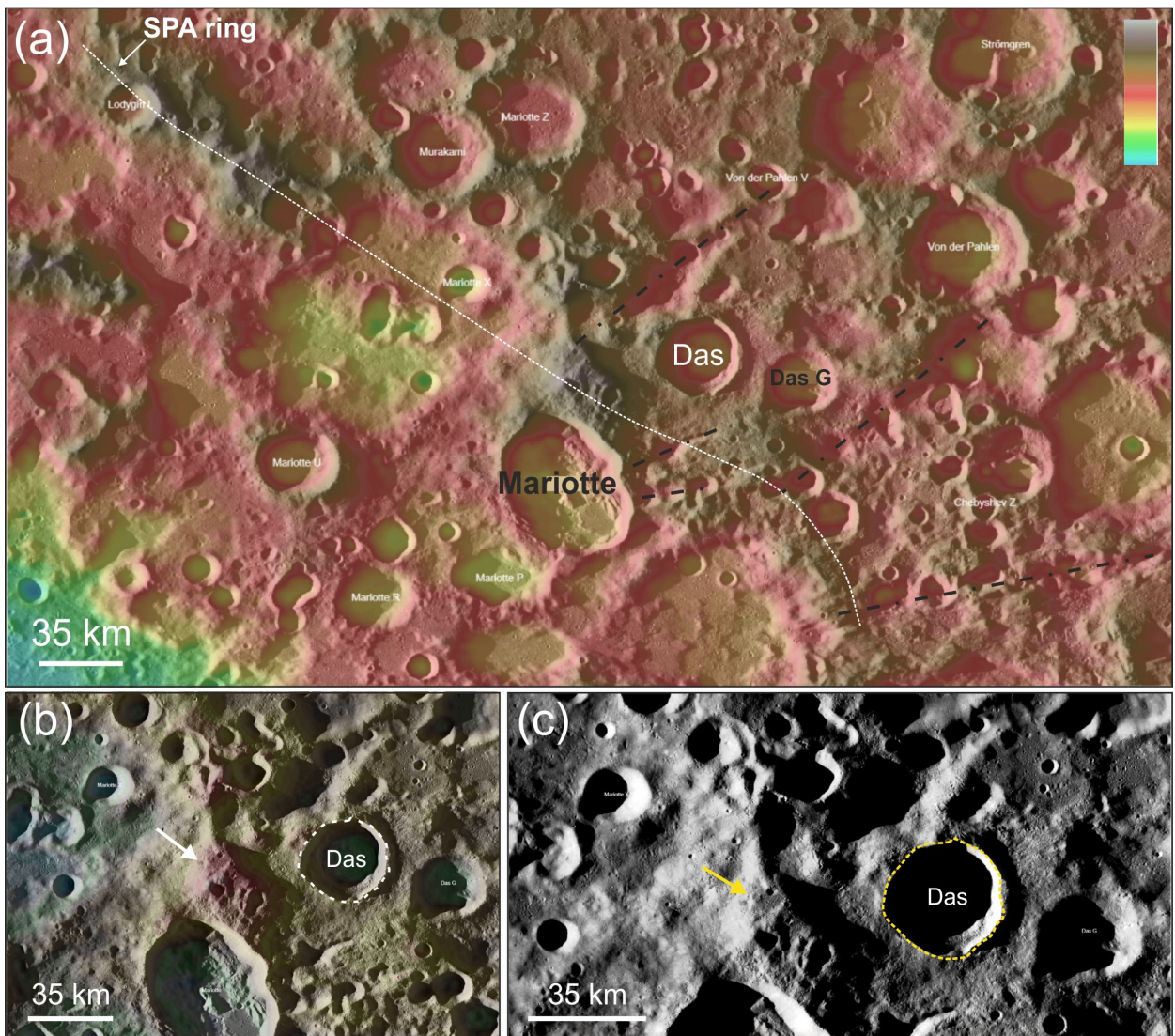


Figure 7.3.18: (A) LOLA DEM of the region surrounding the Das crater. The SPA basin rings pass through western to southern parts of the crater, extending through to the Mariotte and Das G craters. The southeastern and northeastern parts of the Das crater are relatively low-lying, with several older craters and secondary grooves of Orientale ejecta (marked by black dashed line). (B-C) WAC farside mosaic showing the enlarged view of the Das crater, highlighting the western section wherein the remnant ridge (pointed by arrows) of the SPA ring is seen.

fainter, less definitive one away from the crater (Fig. 7.3.17a and b). Often, parts of the same ray degrade into faint wisps at increasing distance from the crater (Fig. 7.3.17a and b). Certain rays are observed to span the greatest radial distances from the crater rim in the southeastern and the northwestern directions, reaching about 225 km and 307 km, respectively. The prominent rays are represented by dotted black lines, whereas grey lines denote the fainter rays (Fig. 7.3.17b). The most prominent rays are distributed in all directions except the NNE and eastern quadrants of the

crater (Fig. 7.3.17a and b). The fainter rays appear to extend predominantly in the northwestern and southeastern quadrants of the crater. Nevertheless, limited occurrences of fainter rays could be observed in the southern and southwestern directions, with the longest ray reaching as far as 380 km (Fig. 7.3.17a and b). It is observed that the prominent rays eventually fade to appear as fainter rays with increasing radial distances from the crater (Fig. 7.3.17b). Another small Copernican crater, Chebyshev Z, 5 km in diameter, is seen to the southeast of the Das crater, distinguished by its bright ray system and exposures of fresh, immature material depicted in bright blue (Fig. 7.3.17b). The prominent rays of Chebyshev Z are marked in dotted red, and a very significant overlap is seen between rays of the Das crater and Chebyshev Z towards the southeast of the Das crater (Fig. 7.3.17a and b).

The continuous ejecta gradually transitions into discontinuous ejecta, marked by the appearance of patchy, irregularly deposited material, partially covering the underlying terrain. Some craters exhibit a distinct herringbone pattern within their ejecta deposits. Though the boundary between the continuous and discontinuous ejecta is subjective, a herringbone pattern is commonly interpreted to mark the boundary between continuous and discontinuous ejecta (Melosh, 1989; 2011). The herringbone pattern is characterised by the presence of several interlocking chevrons (incomplete triangles with just the apex point and the two adjacent sides). A herringbone-type pattern is commonly associated with secondary crater chains of the discontinuous ejecta where the individual crater rims of each of the secondary craters form V-shaped ridges pointing back towards the parent crater. Since the herringbone ridges occur exclusively in the distal ejecta or the discontinuous ejecta blanket, their presence can be used to determine the presence of the discontinuous ejecta blanket. Hence, the appearance of a herringbone pattern is used in conjunction with the appearance of patchy deposits through which the underlying terrain is visible. These patchy deposits display a distinct morphology, such as radial chains of molten material or radially oriented deposits of other textures that can unambiguously be interpreted to have draped over the surface. When interpreted in conjunction with the herringbone pattern, these patchy features can more reliably be used to interpret the approximate boundary between the continuous and discontinuous ejecta blanket (Melosh, 1989; 2011).

Based on the distinct nature of ejecta deposits and surface texture, their occurrence with respect to the radial distance from the crater, spatial extent and distribution pattern in equipotential surfaces, and interaction with the local topographic features, including the terrain slope, the continuous and discontinuous ejecta deposits of the Das crater are mapped into distinct ejecta facies (Fig. 7.3.19a). ‘Facies’ represents an ejecta unit with specified characteristics in terms of its surface texture, pattern, and nature of the deposition. Each ejecta facies unit has been identified and mapped using a combination of datasets discussed in section 2.2, i.e., the WAC farside mosaic at very oblique

phase angles, the LOLA shaded relief map, and a mosaic of Kaguya TC at large phase angles. Our mapping efforts have identified four distinct ejecta facies of the Das crater: Facies A, Facies B, Facies C, and Facies D (Fig. 7.3.19a).

The deposition of each of these facies units in and around the Das crater is largely controlled by the local topographic variations of the terrain. As discussed earlier, the underlying terrain or the pre-impact topography in the region surrounding the Das crater is dominated by the presence of the degraded peak ring structure of the South Pole-Aitken basin (Fig. 7.3.18). Additionally, the Das crater is located in the farside highlands region, and several older craters of comparable dimensions are located in its vicinity (Fig. 7.3.18b-c). The pre-impact topography of the Das crater is shaped by several such older craters of varying sizes and shapes, which enhances the interaction of impact ejecta of Das crater with the surrounding topography and results in non-uniform distribution of the impact ejecta (Fig. 7.3.18b-c). Topographically, a ridge-like feature (thought to be the degraded peak ring of the SPA basin) extends from the WNW part of the crater through to the nearby craters Mariotte and Das G (Fig. 7.3.18). To the SE and NE directions lies a relatively low-lying topography widely disrupted by impact craters and elongated depressions appearing to be secondary grooves from a previous larger impact, likely the Orientale impact (Morse et al., 2018) (Fig. 7.3.18). The description of each ejecta facies unit and its interaction with the encountered topography has been discussed further.

i) Facies A

Facies A is characterised by a chaotic, churned surface showing distinctive radial striation-type texture composed of curvilinear ridges and grooves emanating from the crater rim (Fig. 7.3.19b-d). This unit extends in all directions from the crater rim but at varying radial distances (Fig. 7.3.19a). The lineation type texture grades to a more chaotic terrain and radial striations away from the crater rim (Fig. 7.3.19e-f). The striations are more clearly seen farther from the crater in places where the chaotic terrain is not present. In Fig. 7.3.19f, the Facies A deposits to the northeast of the crater display smooth radial striations near the rim, which grade to a churned deposit (muddy-like) away from the rim in a radial direction. The near-rim deposit has blanketed the eastern slope of the Orientale groove, while the western slope of the groove exhibit the distinct muddy-like deposit (Fig. 7.3.19e and f). It is interpreted that the ballistic ejecta thrown in radial directions hit the western slope of the groove, where the fallen ejecta flowed down the slopes to form the deposit with a mud-splashed pattern (Fig. 7.3.19e-f). The deposition of radial facies here has followed the topography of pre-existing terrain in the region (Figs 7.3.18 and 7.3.19e-f). The presence of radially linear facies extends to greater radial distances in certain directions (Fig. 7.3.19a). The Facies A deposits spreading beyond the rim have the greatest radial extents to the southeastern and

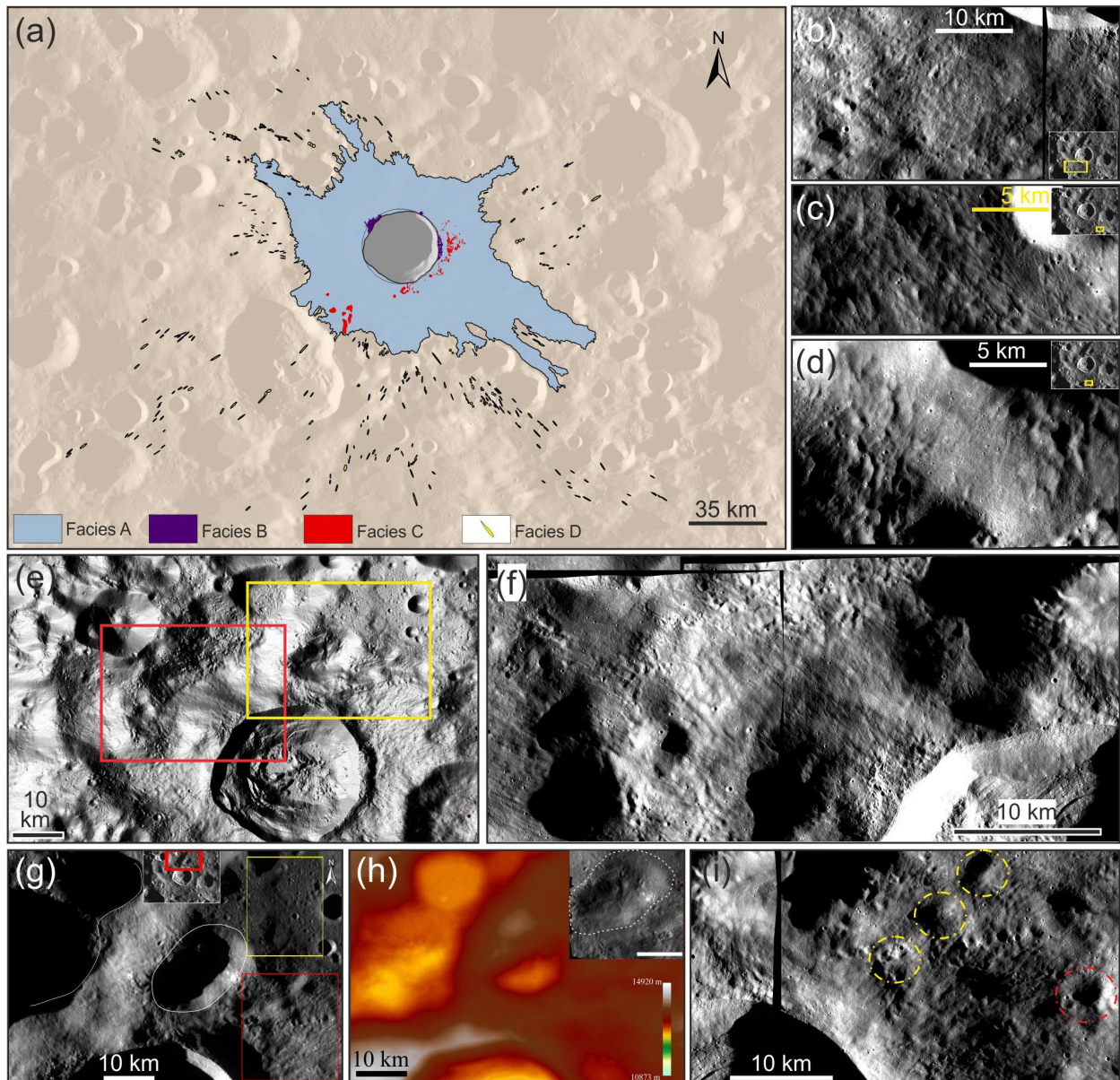


Figure 7.3.19: (A) Ejecta facies map of the Das crater, overlaid on WAC farside mosaic. (B) SW part of the crater displaying the radial striations of the Facies A ejecta. (C-D) Facies A ejecta appears as radial ridges and troughs intertwined in a chaotic terrain to the SE of the crater. (E) The distinctive pattern of Facies A ejecta to the north and northwest of the crater. The red rectangle shows the region of radial striations grading to a distinct mud-splashed pattern. (F) Enlarged view of the region inside the red rectangle in Fig. 7.3.19E, showing Facies A ejecta to the northwest of the crater. The churned surface corresponding to the western slope of the Orientale groove is visible. (G) Facies A ejecta to the northeast of the crater. The shadowed regions represent the cavities or part of the Orientale grooves. The red rectangle marks the maximum extent of Facies A. Beyond this, the radial facies are absent (marked by the yellow rectangle). (H) Colour-coded DEM view of the same perspective as in Fig. 7.3.19G, showing the Orientale grooves to the northeast of the crater. The inset image shows the WAC view of the cavity in Fig. 7.3.19G. (I) Enlarged view of the region covering the radial facies to the northeast of the crater.

northwestern quadrants of the crater, reaching approximately 87 km and 102 km, respectively (Fig. 7.3.19a). In the southwestern and northeastern directions, the deposit reaches maximum radial distances of approximately 35 km and 23-68 km (Fig. 7.3.19a). These ejecta deposits are observed to have draped the underlying terrain entirely in all directions of the crater (Fig. 7.3.19).

The deposition of Facies A also appears to have partly or completely modified the pre-existing topography or rather been influenced by the pre-existing morphology of the terrain surrounding the Das crater, including the topographic lows and highs such as older crater floors, rims, and remnants of SPA peak ring' ridges (Fig. 7.3.19e-f). Fig. 7.3.19g-h shows the Facies A unit spread out to the NNE quadrant of the crater. In the figure, the well-defined, sharp rim of the Das crater is visible towards the bottom of the image, and a smooth surfaced region is visible to a radial distance of about 5 km from the rim. Beyond the radial extent of this surface, a chaotic terrain marked by a combination of linear striations and irregularly shaped blocks of varying sizes is seen (Fig. 7.3.19g). Using an image with high phase angles in the range of 70 – 85 degrees adds to a visual advantage in this scenario as the distinctive nature of the shadows in the chaotic terrain reveals important information regarding the nature of the material in the ejecta deposits of Facies A (Fig. 7.3.19i), e.g., if the shadows in the chaotic terrain were approximately circular, these could have been circular depressions or circular uplifts in the terrain stratigraphically younger than the ejecta deposits of Das crater. Since the planform of the shadows is irregular in appearance, these cannot be circular depressions that are younger than the formation of Das crater, as in that scenario, the planform of the craters would be preserved and not cross-cut by the ejecta deposits of Das crater (Fig. 7.3.19g). Thus, a few of the regions that cast a shadow in the chaotic terrain could be craters older than Das crater, while a few of them could be irregularly shaped ejecta blocks excavated from Das crater cavity. Red circles are older craters, while yellow circles might be irregular blocks ejected from the crater cavity (Fig. 7.3.19i). Several fresh craters younger than the Das crater are also seen in the image marked by the presence of sharp undegraded rims, significantly well-defined relative to the ejecta blanket of the Das crater (Fig. 7.3.19i).

Another point of interest is a marked absence of radially linear striations or any other pattern overlying the highland surface (approximately the image area demarcated by a yellow rectangle) (Fig. 7.3.19g). The area in the yellow rectangle also shows up in Clementine colour ratio image and the colour composite image generated following Zanetti (2015) as well as the Hapke normalised WAC mosaic as having a distinct lack of bright ray material, though the actual area corresponding to the lack of ejecta material is larger in spatial extent than the yellow rectangle and will be discussed in the following sections.

The peculiar deposit of ejecta material towards the north of the crater is visualized in a mosaic of WAC images (Fig 7.3.19g). As shown in the figure, the region corresponding to the peculiar

deposit of ejecta is veiled in shadow (marked by the white circle). The region surrounding the marked circle is also shown in the WAC image, though it is to be noted that the spatial resolution of the WAC images is 100 m/pixel and is significantly less than the spatial resolution of the Kaguya mosaic. Even then, certain features such as the distinct lack of radial facies (approximately demarcated by the yellow rectangle) can be contrasted with the presence of radially linear striations (approximately demarcated by the red rectangle) (Fig. 7.3.19g). More importantly, the presence of shadows to the top left of the WAC image reveals the character of the underlying topographical features of Das crater's pre-impact terrain and is essential to understand the nuances of the interaction of ejecta deposits with the topography of the terrain (Fig. 7.3.19g). From the elevation values of the DEM, it is clear that the shadowed regions are cavities or depressions on the surface (Orientale grooves) (Fig. 7.3.19h). The LOLA hillshade shows the interaction of Facies A ejecta with cavity or depression on the surface (Fig. 7.3.19e). These cavities show similar textural features; a wispy texture towards the centre of the cavity, while the eastern wall of the cavity appears to lack the deposition of ejecta (Figs. 7.3.19e and h-inset image). The western wall of the cavity displays the deposition of radial facies (Fig. 7.3.19h-inset image). According to Melosh (1989), the process of crater cavity excavation proceeds with the simultaneous ejection of different phases of ejecta material at a range of velocities, and the deposition of ejecta material occurs as a blanket whose thickness reduces with distance away from the crater rim. The density of the ejected material closer to the rim ascribes a contiguous texture to this ejecta, while the scarcity of ejected fragments farther away from the rim lends it a discontinuous texture. Thus, ejecta material at a greater radial distance from the rim should essentially have deposition of ejecta material at smaller radial distances relative to itself, but the converse is not true, i.e. for ejecta material deposited at a certain radial distance, it is not apparent that it will certainly have deposition of ejecta material at greater radial distances relative to itself. Cavity 1 thus has the wispy deposit of ejecta towards its centre and western wall, which lies at a greater radial distance from the rim of Das. The eastern wall of Cavity does not show a wispy texture or linear striations similar to that seen at the centre of the cavity (Fig. 7.3.19h).

The distinctive nature of the ejecta deposits is more readily understood from the northwestern part of the crater rim, wherein the presence of linear striations is visible close to the crater around 10 – 30 km radially from the crater rim (Fig. 7.3.20a). This radial pattern changes to a distinctive pattern. The extent of the continuous deposition of ejecta is highly variable depending on the radial direction from the crater. The ejecta pattern under consideration is located at the maximum extent of the Facies A away from the crater (Fig. 7.3.20a). The radial distance corresponding to the presence of this pattern is the maximum radial distance (corresponding to the particular direction), after which no deposition of the radial facies is seen (Fig. 7.3.20a). The distinctive pattern at the boundary is marked by a chaotic appearance significantly different from the radial striation pattern

of ejecta deposits closer to the rim (Figs 7.3.19f and 7.3.20a). The western walls of the Orientale groove display extensive interaction with the ejecta, unlike its floor and eastern slopes (Figs 7.3.19e and 7.3.20a).

When interacting with the underlying topography, the ejecta deposits around Das crater, represented by the radially linear Facies A, exhibit complex patterns. One such pattern is seen to the west of the crater, where deposits that belong to the crater deviate significantly from the radial orientation of the deposition of facies A (Fig. 7.3.20b-e). The farthest of these deposits is located about 35 km radially from the crater rim. The white arrows in the WAC image show the orientation of the radial facies in the region. The expected radial orientation for deposits of Facies A is drawn by extrapolating a line from the approximate centre of the crater outwards to the exterior region. The rim of the Das crater is shown to the right of the image, and a very prominent shadow due to the uplifted rim relative to the depressed crater cavity is seen to cover the entire visible extent of the crater (Fig. 7.3.20b). The other shadows seen in this image represent the remnant ridges of the SPA peak ring (S.R.1 and S.R.2), due to which the ejecta deposits of Das crater were seen to significantly deviate from the expected radial orientation of the proximal radially-oriented Facies A (Fig. 7.3.20b). The S.R.3 region corresponds to an extension of the Orientale groove (Fig. 7.3.20b). The shadow from the ridge falls on its eastern side, and S.R.1 may represent a low-lying region so that the ridge casts a shadow over it. The radial facies in the region of S.R.1 significantly deviates from Facies A's radial orientation and are oriented linearly along the ridge slopes but are not radial to the crater (Fig. 7.3.20c and d). This linear deposition follows the SE-NW orientation of the ridge (Fig. 7.3.20c and d). A similar texture of the ejecta deposit which deviates from the radial orientation, is seen in the region S.R.2 (Fig. 7.3.20e). The Facies A is seen to deposit on the east-facing slopes of this shadowed region (Fig. 7.3.20e). The shadowed region S.R.3 corresponds to the southwestern extent of the Orientale groove, where a distinctive pattern of Facies A deposits cover the ridge crest and slopes facing towards the crater (Fig. 7.3.19e-f).

To the southwest of the crater, uniformly radial facies with a distinctively striated pattern are observed (Fig. 7.3.20g). Unlike the smooth deposits in the 5-10 km closest to the northeastern rim of the crater, the same radial extent to the SW of the crater exhibits a chaotic appearance (Fig. 7.3.20g). Since the Mariotte crater (bottom left in Fig. 7.3.20g) is older than the Das crater, its outer walls are overlaid by impact ejecta from the Das crater. The boundary of the Mariotte crater marks a cessation of the radial Facies A to the southwest. Beyond the radial extent of the rim of the Mariotte crater, its terraced walls and other crater morphology are observed to dominate the terrain, and the prominence of the linear striations on the terrain is lost. Nevertheless, several secondary crater chains are seen on the walls of the Mariotte crater in the proximity of the part of the crater rim.

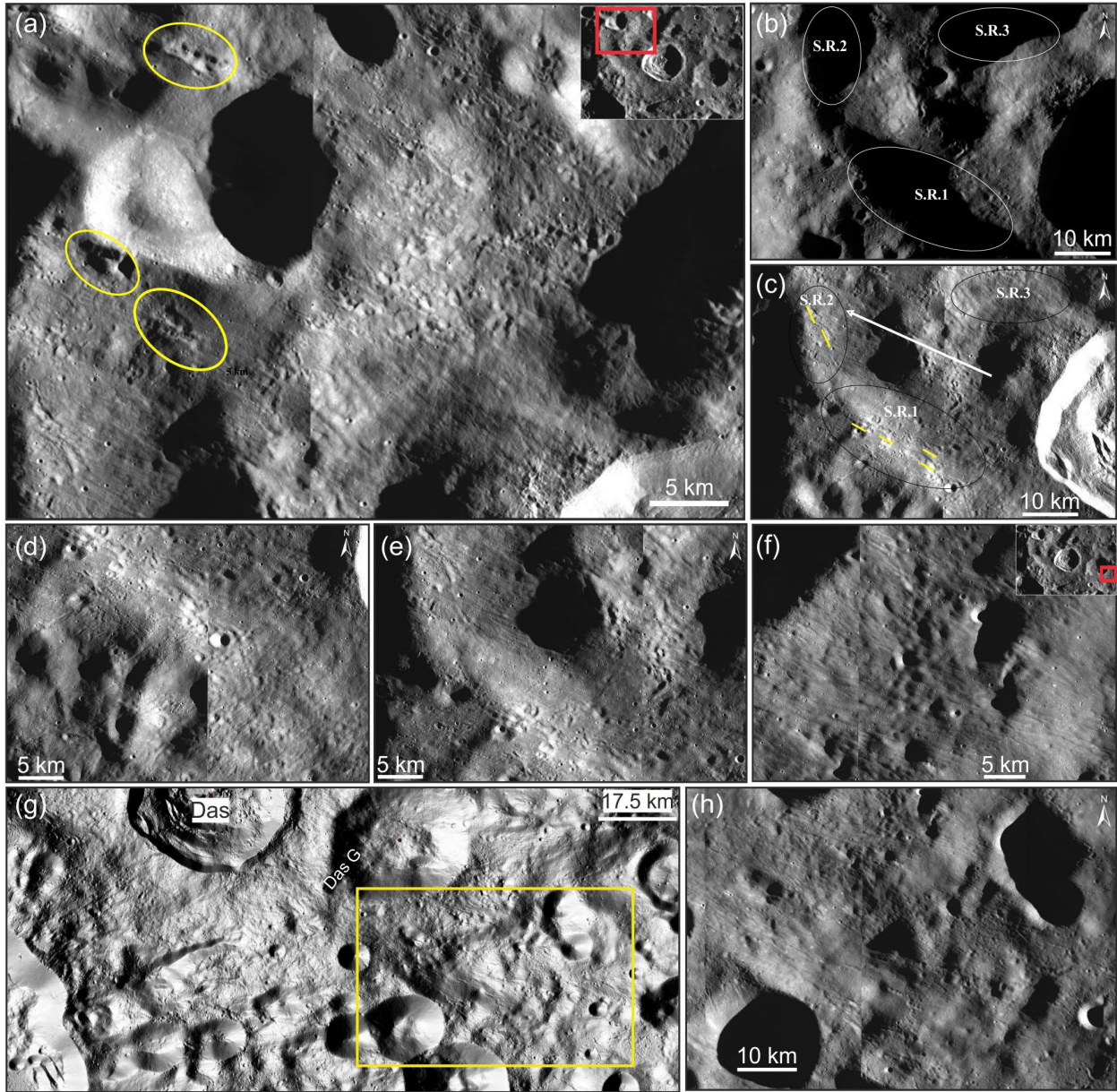


Figure 7.3.20: The northwestern quadrant of the crater, showing the surface texture of the Facies A and Facies D deposits. The yellow polygons denote the secondary crater chains/grooves that are part of the discontinuous ejecta (Facies D). An approximate distinction between radial Facies A and D can be seen in the image. The herringbone pattern that marks the beginning of the discontinuous ejecta is also seen. The inset image shows the location of the region (marked by the red rectangle) using a context image of the Das crater region. The rim is seen in the bottom right corner of the image. The region close to the rim displays smooth linear striations in a radial direction. This striated deposit grades to a more chaotic texture away from the rim. (B) The western side of the crater shows the pre-existing topography of the region. The shadowed features represent part of the SPA ring (S.R.1 and S.R.2) and the linear groove of the Orientale ejecta (S.R.3). (C) The same perspective as Fig. 7.3.20B, showing the interaction of Facies A deposits with the pre-existing topography. Note the peculiar form of the orientation of deposits (yellow lines) with

respect to the radially oriented deposits (marked by white arrow). (D-E) The interaction of radial facies with the northeastern slopes of the SPA basin ring (S.R.1 and S.R.2 regions). (F) Facies A deposits to the southeast of the crater, beyond the extent of the Das G crater. (G) Hillshade view of the S and SE parts of the crater, showing the approximate boundary (region inside yellow rectangle) of the contiguous ejecta blanket and discontinuous ejecta. The radial facies appear to have interacted with the pre-existing linear grooves from Orientale ejecta. (H) Enlarged view of the region inside the yellow rectangle in Fig. 7.3.20G, showing the distinction between chaotic Facies A deposits (top left of the image) and discontinuous ejecta. Note the abundance of secondary crater chains towards the bottom right corner.

The southern and southeastern part of the proximal ejecta deposits are characterised by similar radially linear facies that continue beyond the radial extent of the older Das G crater, unlike the case for the older Mariotte crater (beyond whose radial extent only secondary crater chains and grooves are seen) (Fig. 7.3.20f). The floor and eastern wall of the Das G crater appear to have the deposition of Facies A (Fig. 7.3.20f and g). The boundary between contiguous ejecta and discontinuous ejecta to the southeast of the Das crater is seen in the region inside the yellow rectangle in Fig. 7.3.20g. The enlarged view of this region, as shown in Fig. 7.3.20h, displays the characteristic chaotic texture of the Facies A (top left corner) and the secondary crater chains of Facies D (towards the bottom right corner of the image).

ii) Facies B

Facies B is characterised by smooth melt deposits of low albedo typically collected in topographic depressions (Fig. 7.3.21a). The Facies B deposits have relatively flat surfaces with an average slope of $\sim 2^\circ$. These deposits are of a limited spatial extent and are mostly concentrated as clusters in the terrain bordering the outer slopes of the eastern and northeastern rim (Figs 7.3.22 and 7.3.23). The topographic lows of Facies B are bounded by the higher topography of Facies A and the underlying terrain to some degree (Figs 7.3.21, 7.3.22, 7.3.23). The patchy occurrences of these smooth melt with a few ponded deposits are seen at the southeastern part, approximately 8 km away from the rim crest (Fig. 7.3.21a). The smooth deposits embedded with blocky ejecta to some degree are noticed in the outer slopes of the northern and northeastern rim. The individual deposits range from 0.03 to 3 km², the largest of which is located in the topographic depression just beyond the eastern rim (Fig. 7.3.22 and 7.3.23).

The melt ponds identified in the inner walls of the crater are also part of the Facies B ejecta (Fig. 7.3.8a-f). The deposits in melt ponds inside the crater cavity are enclosed by higher topography of wall terraces (Fig. 7.3.8a-f). Facies B exterior to the east of the crater rim appears to overlie the Facies A deposits. The smooth melt-phase ejecta almost completely overlies the proximal region as far as ~ 7 km to the east from the rim summit (Fig. 7.3.22 and 7.3.23).

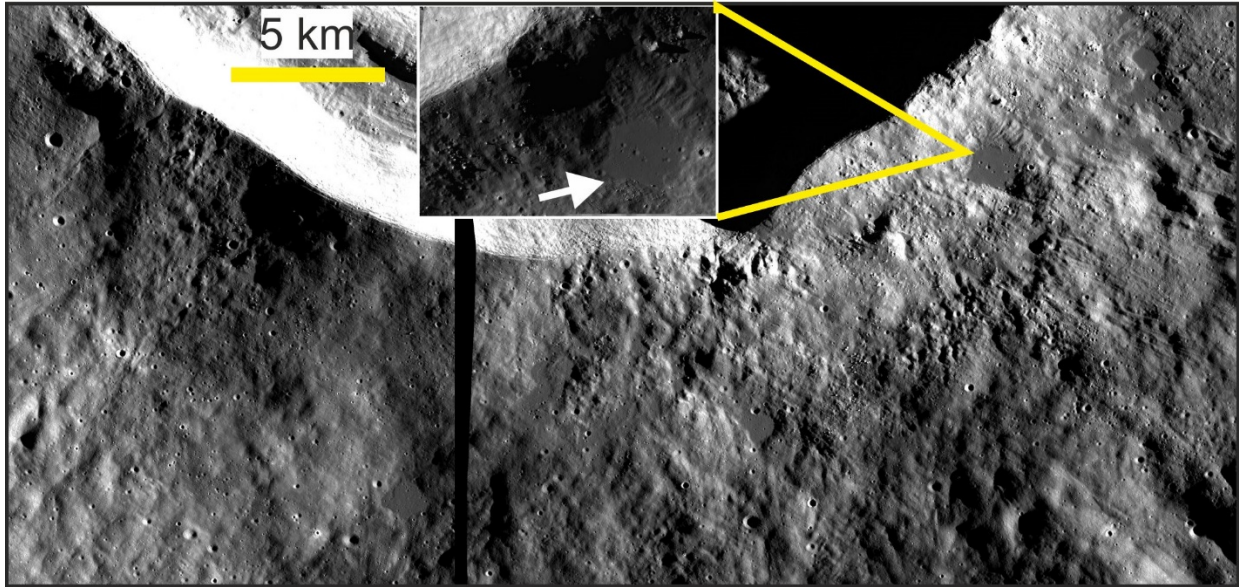


Figure 7.3.21: Southern part of the Das crater ejecta. Several melt ponds could be seen which belong to Facies B deposits. These smooth melt-phase ejecta deposits ponded in depressions are seen to have deposited in conjunction with the radial facies (contiguous ejecta) as they seem to coexist with the contiguous ejecta rather than completely overlying them.

iii) Facies C

Facies C is characterised by the presence of patches of smooth, low albedo melt deposits interspersed with chaotically embedded blocks of varying sizes, extending away from the crater rim and exhibiting a preferential flow to topographically low-lying terrain (Fig. 7.3.21 and 7.3.22). Facies C deposits predominantly occur as rim veneer in the east and northwest parts (Figs 7.3.22 and 7.3.24c). Along the eastern rim crest, a linear stretch of approximately 12 km is prominently occupied by the Facies C melt deposits (Figs 7.3.22 and 7.3.23). The chaotic terrain with blocks of about 30 m – 80 m in diameter in Facies C deposits is restricted to the region radially extending from the eastern rim of the Das crater to a distance of about 1 km (Fig. 7.3.22). These smooth melt deposits, seen interlaced with blocks in this terrain, are observed to have flowed down the outer slopes of the eastern rim towards the low-elevated terrain to further east and froze in time in the topographically low-lying region to manifest in a distinctive lobate pattern (Fig. 7.3.22). These flow deposits are identified by these well-defined flow lobes traversing the topographic slopes of the eastern rim to the low-lying region about 7 km radially from the rim crest, with their tips pointing away from the crater (Figs 7.3.22, 7.3.23, and 7.3.24a). The deposited region is sloped between $\sim 0^\circ$ to 18° . These lobate extensions away from the crater rim combined with low-albedo suggest that the Facies C deposits might have originally been melt-phase ejecta. The individual deposits of Facies C range from $\sim 1 \text{ km}^2$ to 14 km^2 , with a longer flow lobe extending approximately

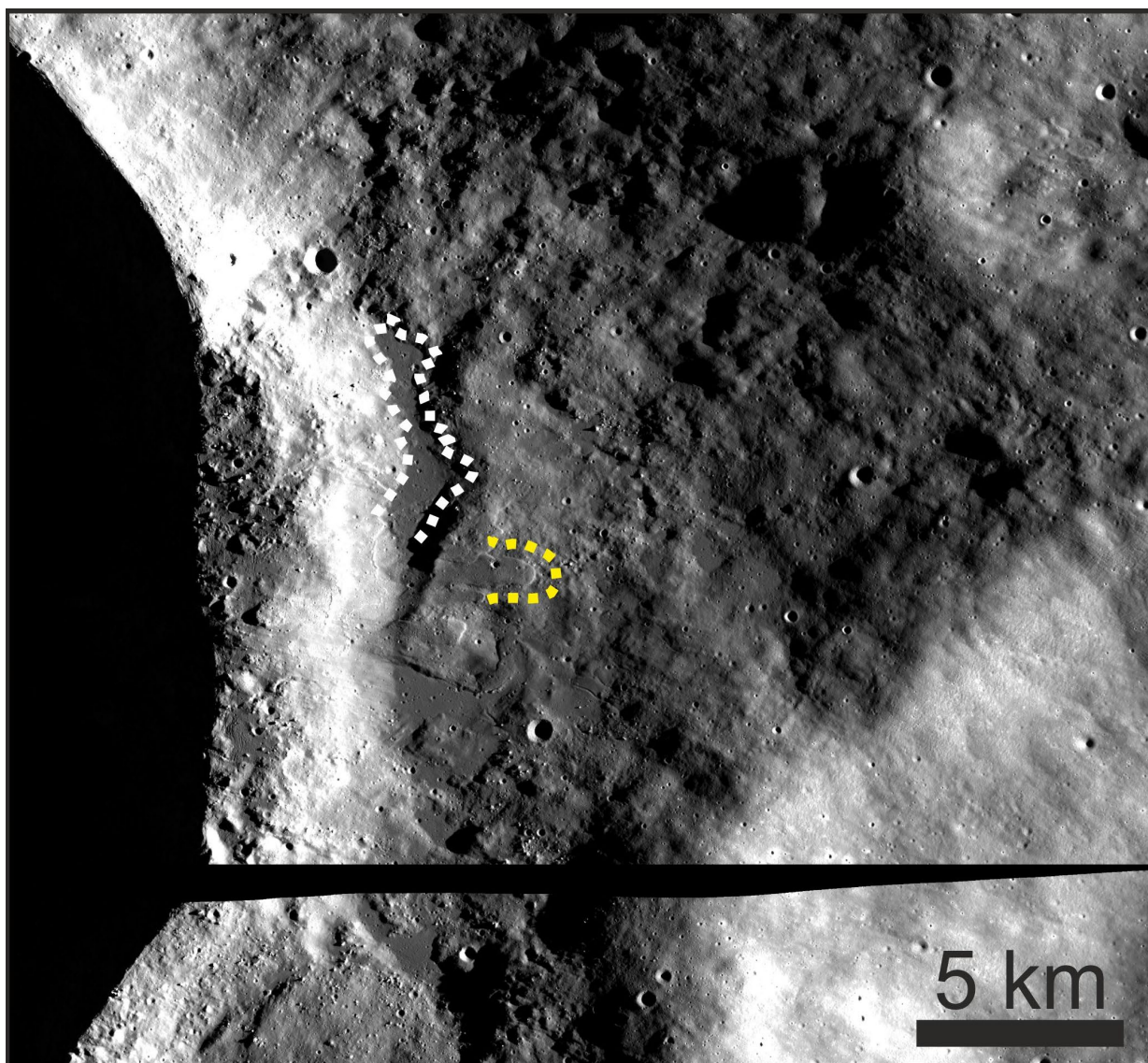


Figure 7.3.22: The Facies B and Facies C deposits to the east of the crater. The rim of the crater is seen to the left of the image. Blocks of varying size are seen at the summit of the crater rim. Note the melt pooling in topographic lows exterior to the rim and the flow lobes pointing away from the crater. The white dashed lines delineate the prominent topographic low with Facies B deposits. The yellow dashed line demarcates the flow lobe (i.e., part of Facies C).

7 km outward from the eastern rim crest (Fig. 7.3.24a). The lobate margin of the Facies C deposit to the east is shown in Fig. 7.3.24a. The topographic profile across the yellow line manifests the outer margin of the lobate deposit (Fig. 7.3.24b).

The Facies C deposit is also observed to have draped the eastern inner walls of the crater (Figs 7.3.6b-g and 7.3.7a-i). The extensive smooth melt flows down the slopes of the inner wall manifest as several melt fronts and flow lobes with extensive boulders dispersed over it (Fig. 7.3.7a-i).

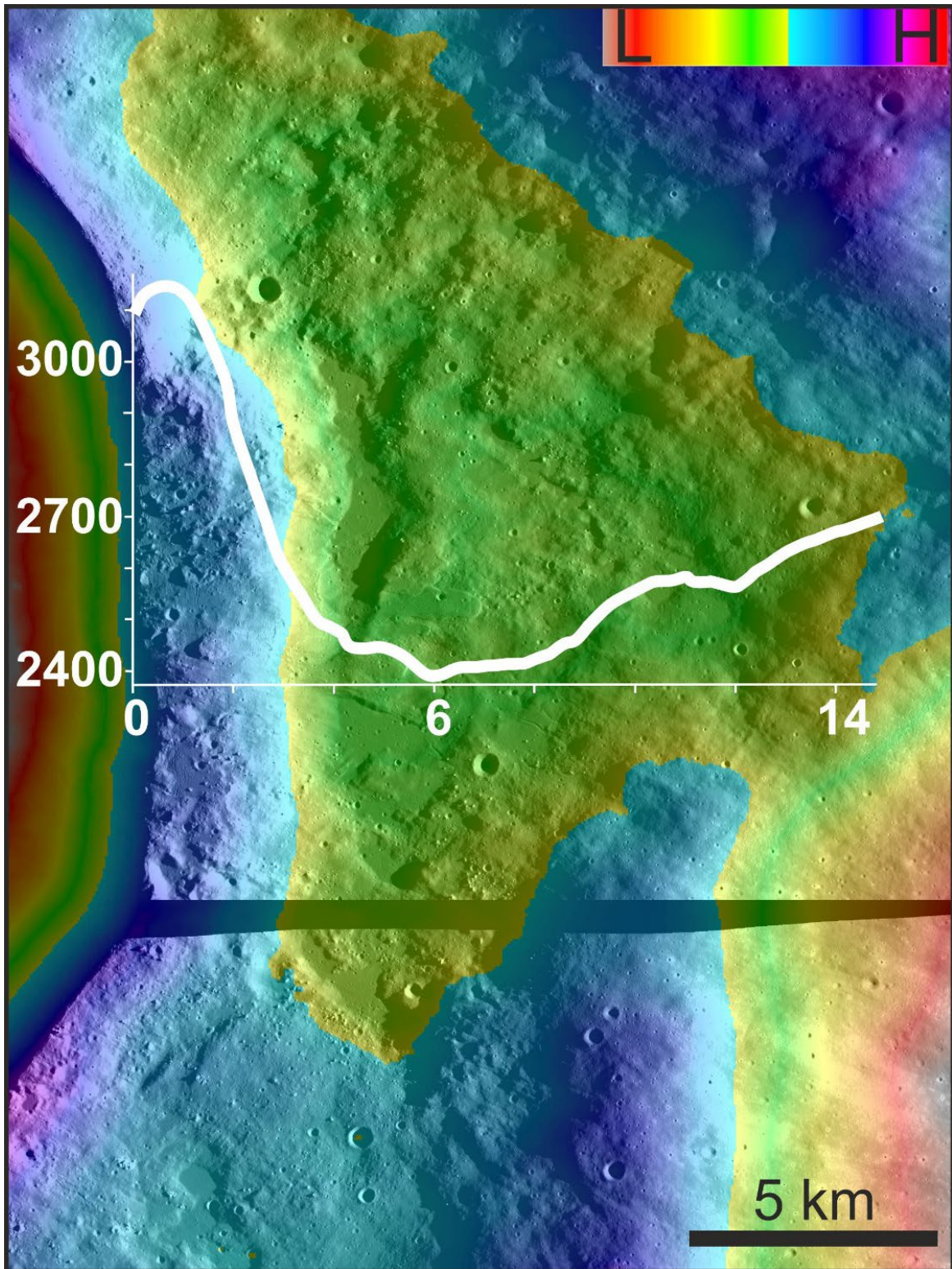


Figure 7.3.23: Colour-coded DEM of the same region as in Fig. 7.3.22, showing the east-sloping topography of the area where Facies B and Facies C deposits co-occur. The topographic profile across the line (corresponding to the X-axis line of the graph) is also shown. X-axis labels are kilometers, and Y-axis labels are in metres.

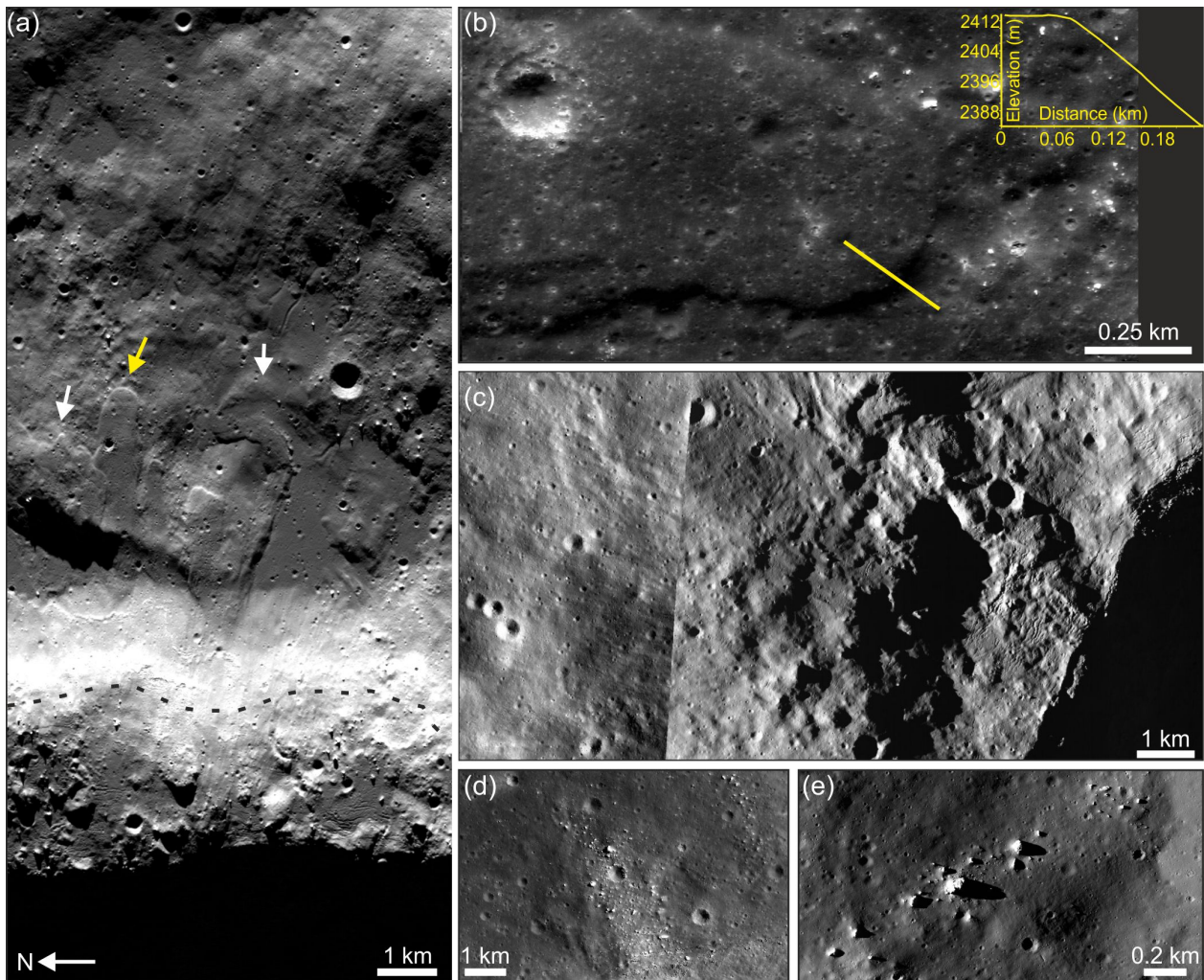


Figure 7.3.24: (A) Enlarged view of the region in Fig. 7.3.23. The black dashed line demarcates the rim summit. The melt pools and flow lobes are seen to co-occur to the east of the crater rim. The co-occurrence of Facies B and Facies C deposits is visible. The arrows point to the flow lobes that have flowed down the slopes. Channelized flow with levees could also be seen (pointed by the white arrow to the right of the image). Here, the melt-phase ejecta deposits appear to have overlaid the contiguous ejecta blanket as the former is bounded mostly by smooth melt-bearing ejecta rather than radial facies. Nevertheless, the exterior melt pools (Facies B) to further east of the image appear to co-exist with the radial facies. (B) Enlarged view of the flow lobe (marked by the yellow arrow in Fig. 7.3.24a). The topographic profile across the yellow line is shown in the inset. The profile reveals the margin of the lobate deposit with the underlying ejecta facies. (C) The rim veneer deposit (Facies C) is interspersed with ejecta blocks in the northwestern part of the crater. Cooling cracks can be seen in the cooled melt-phase ejecta. (D-E) Blocky ejecta is seen to the north (D) and east (E) of the crater.

The closely parallel curvilinear concentric cooling cracks are common in these melt deposits (Fig. 7.3.24a). The well-pronounced veneer deposit on the rim crest to the northwest appears blocky and chaotic (Fig. 7.3.24c). This deposit in the northwest is observed to have draped the higher

topography of the rim. Several boulders, melt fronts, and cooling cracks could be spotted in this chaotically deposited rim veneer deposit (Fig. 7.3.24c). The presence of a chaotic terrain with blocks has not been observed in the northeastern rim veneer; rather, the localised smooth deposits in the region appear to have interacted with pre-existing rocks (blocks) of the underlying terrain.

Facies C materials occur in conjunction with the Facies B deposits (Fig. 7.3.24a). Often, the Facies C deposits embay or are contiguous with the Facies B materials (Fig. 7.3.24a). The ejecta of both the Facies B and C are melt-phase deposits with similar surface texture and albedo, but the former pool in topographic lows while the latter traverse the topographic slopes as flows that often appear to be a lobate extension of the former melt deposit, at places taking a channelized form with levees to the sides (Fig. 7.3.24a). All the deposits of Facies C beyond the crater rim are observed to overlie the Facies A materials (Fig. 7.3.24a). The ejecta boulders thrown out as ballistic ejecta are deposited near the rim (Fig. 7.3.4d-e). These boulders are significant for the sampling of deeper materials and understanding the vertical stratigraphy of the Moon.

iv) Facies D

Facies D is characterised by numerous radially oriented clusters of circular or elliptical depressions farther from the extent of Facies A (Fig. 7.3.25). These quasicircular and/or elongated chains and depressions extend to greater radial distances away from the crater rim (Fig. 7.3.17b).

The careful mapping of these secondary crater chains and radial grooves has been performed to a maximum radial distance of 160 km from the crater rim (Figs 7.3.17b and 7.3.19a). These secondary craters are shallow and irregular in shape (Fig. 7.3.25a). The Facies D deposits reach as far as 157 km to the southeast, 162 km to the southwest, 108 km to the northwest, and 76 km to the northeast quadrant of the crater (Fig. 7.3.19a). The chain of secondary craters is most pronounced in the southeast, southwest, and northwest directions of the crater than the less extensive or absent NNE part (Fig. 7.3.19a).

The radial distribution of the Facies D materials is observed to coincide with the Facies A deposits, often overlie the Facies A and oriented parallel to its curvilinear ridges and grooves in the northwestern and southeastern quadrants (Figs 7.3.19f, 7.3.20a, and h), though the unambiguous interpretation of the stratigraphic relationship of these facies materials is not possible at WAC/TC resolutions due to surface modifications. Additionally, the distribution pattern of Facies D away from the crater match well with that of the Facies A deposits within the 5 crater radii from the rim (Fig. 7.3.19a).

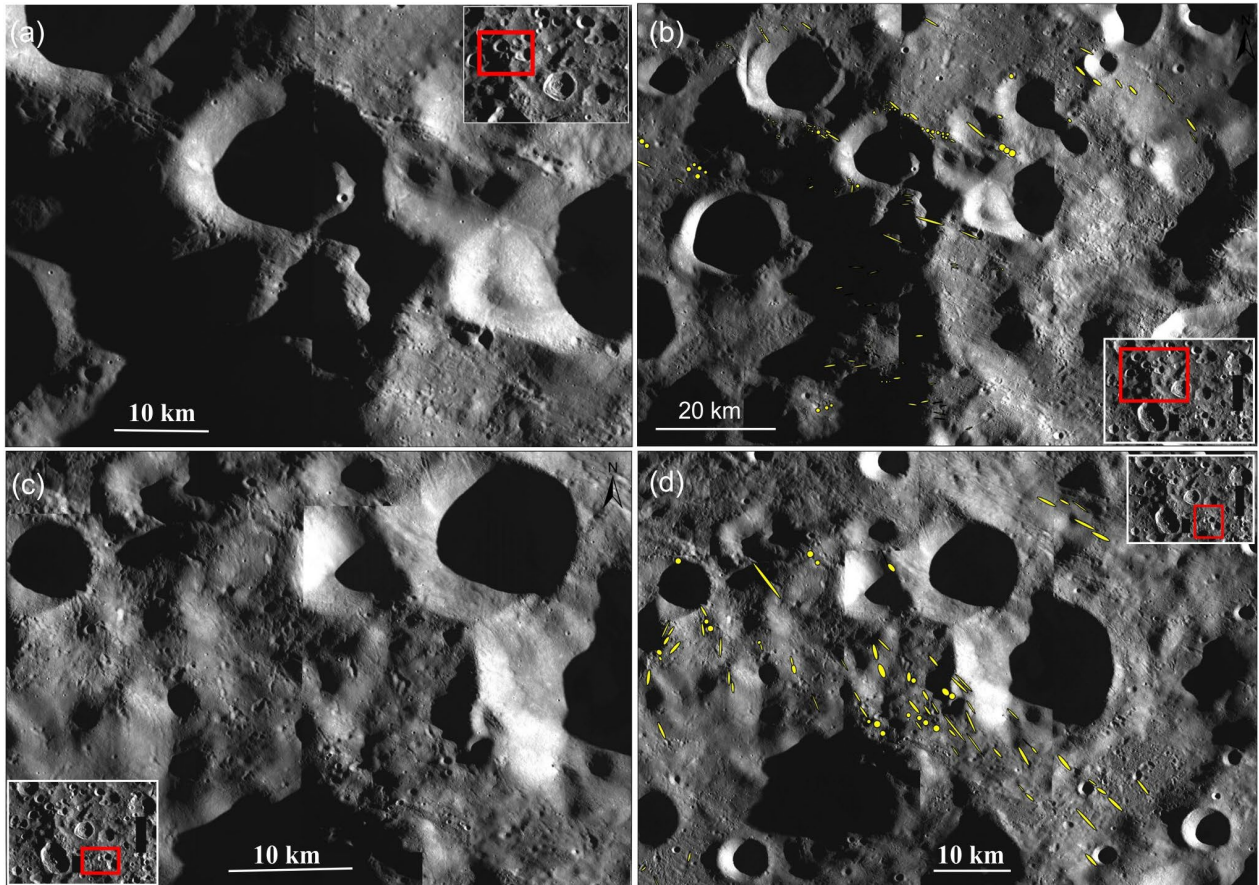


Figure 7.3.25: Radially oriented secondary crater chains and grooves to the northwest (A-B) and southeast (C-D) of the Das crater. The discontinuous ejecta is mapped and shown in yellow in the images. North is up in all the images. The inset images show the WAC mosaic of the Das crater region. The red rectangle in the inset images demarcates the location of the ejecta relative to the crater.

7.3.4 Discussions

7.3.4.1 Cratering mechanics involving the stages in the development of the complex Das crater

The detailed mapping of morphology and ejecta facies both interior and exterior to the crater cavity has revealed the spectacular geological features of this Copernican complex crater, ranging from the bright ray system, exterior radial ridges and grooves, clusters and herringbone chains of secondary craters, sharp and scalloped rim, wall terraces, slumped masses and talus, smooth floor deposits, central mounds, melt platform, and the impact melt deposits being the most prominent feature distributed primarily within the crater and often spilled out of the crater forming exterior melt deposits. These distinct morphological features of the Das crater are expected to have resulted

from a sequence of events accompanied by different physical processes unfolded as the projectile moving at kilometers per second struck the highland surface (Melosh, 1989). The different physical processes following the projectile impact dominate the cratering mechanics involving the contact and compression stage, excavation stage, and modification stage (Melosh, 1989; 2011).

The projectile strikes the highland surface during the contact and compression stage and imparts energy to the underlying target rocks (Holsapple and Schmidt, 1986; O'Keefe and Ahrens, 1977). Following the contact, the high-velocity projectile energetically dives into the underlying target rocks compressing both the target and projectile materials and generating strong shock waves (Melosh, 2011). The shock waves propagate and accelerate into the target further downward and outward by compressing the rocks that come across. The shocked materials form high-velocity jets (Melosh, 1989). The high energy partitioned into the target during this stage is sufficient to open up a cavity and heat the target rocks. This is followed by the transient cavity excavation, during which the shock wave expands away from the impact point to a large volume of rocks and causes a decrease in initial impact energy (Melosh, 1989; 2011). The residual velocity field excavates in a pattern in which the target materials are displaced first downward, then sideways, and eventually upward. The vaporised material moves out of the crater as vapour plumes during this process. The remaining proportions of the excavated materials are displaced in a way that the underlying rocks in the floor region are downwarped, materials are moved out of the crater and deform the surrounding rocks causing upliftment of the surface near the rim, and ejecta is thrown out on ballistic trajectories at angles of about 45° to the rim (Melosh, 1989; 2011). The fast-moving initial ejecta contains more shocked target materials than the slower ejecta as the impact energy spreads to more rocks. The transient cavity is lined with shocked and melted target materials during this excavation growth. The growing transient cavity gradually attains a simple bowl shape to produce the transient crater (Gault et al., 1968; Stöffler et al., 1975). Three to four times the depth of the transient crater will be its diameter which could increase further during subsequent crater collapse (Croft, 1985b; Melosh, 2011). The maximum depth of the excavating materials is one-third the transient crater depth and one-tenth of the transient crater diameter (Melosh, 2011). The materials below this excavation depth are displaced downward by deforming the surrounding rocks. The depth-to-diameter ratio of the transient crater is 1/2.7 (Dence et al., 1977).

Based on the scaling relations given by Melosh (1989), the excavation of the transient cavity of the Das crater took place in approximately 4.8 s. The transient crater diameter for the Das crater is estimated to be ~30.4 km. The maximum depth of excavation of ejected materials in the Das crater was about 3 km. The final depth of the transient cavity lies between 0.25- 0.3 times its diameter (Melosh, 1989), and hence the transient crater depth for Das crater is estimated to be in the 7.6–9.12 km range. The maximum depth of the transient crater cavity is achieved even before the

central uplift begins to rise from the cavity floor where maximally compressed rocks occur and is also the zone of peak shock pressures and maximum impact melt generation (Melosh and Ivanov, 1999). Impact melt lined the transient cavity throughout its growth (Melosh, 1989), the effective thickness of which was 0.4 times the depth of the transient cavity (Cintala and Grieve, 1998) at around 0.03 km.

Soon after the formation of the transient crater, the displacement of target materials upward and sideways stops, and the movement of debris inward the crater begins. This modification of the transient crater is marked by the gravitational collapse of the crater, which brings about major changes in the morphology (Melosh, 1977; 1982; 2011; Pike, 1980b). The probability of a transient crater undergoing such modifications depends on the crater diameter and gravity of the planetary body (Ullrich et al., 1977; Melosh, 1977; 1982; Grieve and Robertson, 1979; Pike, 1980b; Horz et al., 1991). In the Moon, transient craters with diameters greater than 18 km (the transition diameter from simple to complex craters) experience gravitational collapse (Melosh, 1977; 1982; 1989). The major morphological changes that occur during the collapse include uplift of the floor, the rise of central peak, collapse of the temporarily formed structural uplift of the rim to form steep walls and wider terrace zones, and subsequent enlargement of crater diameter (Melosh and Ivanov, 1999). The wall slumps occur along discrete faults. The rise of the floor due to the rebound of the compressed rocks begins even before the rim collapse and eventually forms a central peak (Melosh, 2011). As the floor continues to rise, the wall collapses to develop step terraces (Croft, 1985a). The slumping and sliding of the uplifted rim results in a lense of breccia containing highly shocked impact melt overlying the crater floor (Grieve and Garvin, 1984). The floor hummocks and blocks are common in lunar craters (both simple and complex) (Cintala and Grieve, 1998). The relatively low clast contents or hummocks in the melt platform and certain parts of the Das crater floor may be due to a greater effective melt thickness (Cintala and Grieve, 1998; Melosh and Ivanov, 1999). The solidification of impact melt in Das crater was on the order of several minutes (Melosh and Ivanov, 1999). Since the melt units on the floor are not physically contiguous with the wall and the central uplift, i.e. they do not lap up with the crater collapse units, the melt solidification in those areas have occurred likely before the genetic evolution of the central peak, and steep eastern wall (Melosh and Ivanov, 1999), wherein heavily fractured impact melt (Ohman and Kring, 2012) is observed at their boundary with the elevated hummocky floor unit.

The upliftment of the central peak might also facilitate rim collapse as the central uplift overshoots the stability and triggers gravitational collapse (Ullrich et al., 1977; Grieve and Robertson, 1979). The central uplift of the Das crater rose to approximately 3.2 km from beneath the transient crater depth. A portion of central mounds in the Das crater is likely developed by the rotational slumping along the northwestern inner wall in which the toes of the slumping masses that reach the base of

the crater cause a bulge of the original surface and produces irregular mounds (Melosh, 2011). The timescale for the gravitational collapse of Das crater manifested in the formation of terraced units and rise of central uplift was about 30 s (Melosh and Ivanov, 1999), among which the wall failure resulting in slump blocks closer to the floor occurred sooner than that for blocks near the rim (Melosh, 1989). After the modification stage, the crater only experiences degradational processes and resurfacing events, if any, on its geological timescale (Melosh, 1989; Pierazzo and Melosh, 2000a). The other parameters that govern the final form of the crater other than the cratering processes are the impact angle and direction and the pre-impact topography (Pierazzo and Melosh, 2000a). These parameters are determined based on the order of emplacement and distribution pattern of distinct ejecta facies around the crater, being discussed further.

7.3.4.2 Emplacement mechanism of distinct ejecta facies

7.3.4.2.1 Ballistic ejecta (Facies A and D)

The ejecta debris thrown out of the parent crater with an initial velocity travels on a ballistic trajectory above the surface (Oberbeck, 1975; Osinski et al., 2011). These ballistically transported ejecta materials strike the ground surface upon losing their velocity and deposit as radial ejecta around the primary crater (Osinski et al., 2011). The ejecta emplaced in this manner is referred to as ballistic ejecta. Based on the distribution, depositional character, and radial extent from the rim, the Facies A deposits around the Das crater are interpreted as contiguous ejecta blanket deposited through ballistic sedimentation (Fig. 7.3.19a). According to Melosh (1989), the fragments in the ballistic ejecta curtain strike the ground first near the rim and at greater distances over time. Away from the rim, the proportion of ejecta strikes the ground surface with relatively higher velocity, due to which the surface materials are swept and mixed with the fallen fragments. This intimate mixture moves outward radially as ground-hugging flows to form contiguous ejecta deposits comprising radial ridges and troughs (Melosh, 2011) (Fig. 7.3.19b-d). The interaction with the local topography as the ejecta debris falls back also accounts for their distinct depositional character (Fig. 7.3.20a-f). The observed deviation of the linear striated deposits of Facies A from its radial orientation in certain regions, particularly in the WNE part of the crater, is the result of topographic obstacle by the remnant ridges of the SPA ring lying in the underlying terrain (Fig. 7.3.20b-f). In addition, the thickness of the radial ejecta facies decreases with increasing distance from the crater rim, as observed in the Das crater ejecta blanket, where the linear striated deposits are more pronounced close to the rim (McGetchin et al., 1973; Oberbeck, 1975). The thicker deposits near the rim are manifested by the occurrence of radial facies overlying the neighbouring older craters, almost entirely masking the sharp edges of their rim (Fig. 7.3.20g). The older craters

away from the Das crater are not observed to have entirely been overprinted by radial facies; rather, the ejecta has followed the topographic obstacle arising from these crater morphologies and concealed their sharp features only at depositional interfaces (Fig. 7.3.20g).

Further, based on the herringbone pattern and radial distance from the rim, the Facies D deposits are interpreted as discontinuous deposits formed by ballistic ejecta (Figs 7.3.19a and 7.3.25). The secondary crater chains in Facies D appear as discrete clusters oriented radial to the Das crater (Fig. 7.3.25b and c). These chains of secondary craters are believed to be formed by the high-velocity solid debris ejected in the initial stages of the excavation flow (Oberbeck, 1975). Both the radial ejecta facies are distributed in a radial orientation to the parent crater (Figs. 7.3.19a and 7.3.20a). However, the stratigraphic relationship between these two facies is unclear as the definite boundary between them is not obvious at TC resolutions. The Facies A deposits grade to discontinuous secondary crater chains at varying radial distances from the crater rim (Figs. 7.3.19a and 7.3.20a). Also, the mapping showed that the outermost margins of the continuous ejecta blanket mark the onset of patchy discontinuous ejecta comprising clusters of secondary craters at places grading to linear grooves (Fig. 7.3.20a). Hence, the overlapping of these two radial facies units is not observed at 10m/pixel resolutions. Because of this, the order of emplacement of these two ballistic units is ambiguous. According to Oberbeck (1975), the ballistic ejecta is transported during the initial phases of excavation flow in which the top materials excavated in the initial stage are ejected with high velocity followed by the displacement downward and sideways, spreading out the energy to more volume of rocks and reducing the velocity of later excavated deeper materials. The low-velocity fragments are deposited near the rim and are larger. The high-velocity materials comprising the proportion of highly shocked and glass fragments were rapidly transported farther from the rim. Following this depositional model, the ballistic ejecta units (Facies A and Facies D) of the Das crater were likely deposited simultaneously in which the high-velocity fragments in the ejecta curtain were deposited at greater distances from the rim than the low-velocity larger ejecta fragments. Soon after the ejecta debris struck the surface, mixing with the surface materials and subsequent ground-hugging flow of mixed materials forming an ejecta blanket displaying the intertwining ridges and troughs (Facies A), partially or entirely infilled the secondary crater chains (Facies D) within the radial extents of the continuous ejecta. This overprinting of the Facies D by the emplacement of contiguous ejecta could be the reason for the more pronounced occurrence of secondary crater chains farther from the crater rim (Fig. 7.3.19a).

It is to be noted that the radial facies of the Das crater distributed radially from the crater are more extensive and prominent along the southeastern and northwestern directions (Fig. 7.3.19a). Though distributed in all directions, the continuous ejecta blanket is less extensive in the NNE and southwest parts of the crater (Fig. 7.3.19a). The secondary crater chains are also dispersed

profoundly in almost all directions except the regions along ESE and NNE (Fig. 7.3.19a). However, the lack of discontinuous ejecta in the ESE region is interpreted to be due to overlapping by distal ejecta from the much younger Copernican Chebyshev Z crater southeast of the Das crater (Fig. 7.3.17b). The lack of distal ejecta in the NNE direction of the Das crater is likely related to the direction and angle of the Das crater-forming impact trajectory, being discussed in section 7.3.4.3.

7.3.4.2.2 Melt-phase ejecta (Facies B and C)

The impact melts are believed to be generated by melting both the target and projectile materials due to impact shock heating (Gault and Wedekind, 1978). The melt-bearing ejecta is thought to be deposited by ground-hugging flows of impact-generated melts (Osinski et al., 2011; Neish et al., 2014; 2017; Morse et al., 2018). The deposits of both Facies B and Facies C are smooth low albedo materials representative of melt-bearing ejecta (Figs 7.3.21, 7.3.22, 7.3.24a). The volcanic origin of these melt facies is ruled out as the melt deposits are concentrated along the same direction of ballistic ejecta deposition (cf. Hawke and Head, 1977) (Fig. 7.3.19a). The deposition of the melt-bearing ejecta of the Das crater has largely followed the pre-existing topography of the terrain (Figs 7.3.22, 7.3.23, 7.3.24a). The lobate melt deposits (Facies C) are observed to be directly connected to the ponded Facies B deposits (Fig. 7.3.24a). The stratigraphic position of these melt deposits as rim veneer melt ponds and overlapping with the Facies A deposits link their origin to the impact ejecta (possibly late-stage low-velocity excavation materials) of the Das crater.

The Facies B and C deposits are observed to have overprinted the underlying contiguous ejecta blanket near the rim to the east. However, the pooled melt deposits beyond this extend (farther than ~7 km) in the east as well as the melt ponds in southern and northeastern parts of the crater do not appear to overlie the Facies A radial ejecta similar to the proximal melt deposits (Figs 7.3.21, 7.3.22, 7.3.24a). The melt-phase ejecta pooled in topographic lows is bordered by a thick contiguous ejecta blanket (Fig. 7.3.21). If Facies B were younger than Facies A, then the melt ponds would not have been bordered by the thick blanket of Facies A; rather, it would have appeared as patches of melt peppered over the contiguous ejecta blanket (Figs 7.3.21 and 7.3.24a). The pooled melt belonging to Facies B is seen to have smooth deposits of melt sprinkled with the radial facies (Figs 7.3.21, 7.3.22, and 7.3.24a). Hence, the order of emplacement of Facies B in different parts of the crater may vary. It is interpreted that the Facies B deposits interspersed with the Facies A ejecta were formed as a result of the ground-hugging flows, which later deposited concurrently with the contiguous ejecta blanket, and/or a sprinkling of melt-phase ejecta during the excavation flow. The Facies C deposits that flowed down the slopes of the outer rim

overprinting the contiguous ejecta blanket would have been emplaced specifically in the modification stage of the crater wherein the large volume of impact melts lined the crater cavity overflowed as the rebound and wall collapse occurred (cf. Hawke and Head, 1977; Bray et al., 2010; Osinski et al., 2011; Neish et al., 2014; Zanetti et al., 2017; Morse et al., 2018; Morse et al., 2021). It is possible that the impact melts that were forced out of the crater cavity preferentially pooled in the pre-existing topographic slopes and triggered the outward flow of these melts down the slopes to form Facies C lobate deposits (Bray et al., 2010; Morse et al., 2021). The rim veneer deposits on the northwest and eastern rim crest might have been originated as a part of the main ejecta splashed out of the crater in the initial stages (e.g., Gault and Wedekind, 1978)

Based on the stratigraphic relationship of the identified ejecta deposits of the das crater, the order of emplacement of distinct ejecta facies is as follows, (a) the initial ballistic ejecta blanket comprising Facies A and Facies D materials in the excavation stage of the crater, (b) melt-bearing ejecta, splashed out during the excavation flow and emplaced as ground-hugging flows, and/or melt overflowing the crater cavity near the end of modification stage and flow down the slope to emplace as lobate deposits. The Facies B deposits are emplaced alongside the radial facies, while the Facies C ejecta is deposited after the emplacement of radial facies and Facies B, thereby the former is more or less overprinting the latter two. This observation is consistent with the hypothesized model of multi-stage processes for ejecta emplacement around lunar impact craters proposed by Osinski et al. (2011).

7.3.4.3 Determining the direction and angle of the impact event

The trajectory of the projectile striking the lunar surface typically follows an optimum incidence angle to the horizontal (Pierazzo and Melosh, 2000a). Most of the impacts on the Moon occur at an angle $\leq 45^\circ$ from horizontal and such impacts are referred to as oblique impacts (Schultz and Gault, 1990). The vertical impacts (angle close to 90°) are seldom reported, occurring only 0.8% of the times a projectile strikes the surface (Schultz and Gault, 1990). The oblique impacts on the Moon occur commonly at varying incidence angles ranging from 45° to near-grazing incidence of $<5^\circ$ (Gault and Wedekind, 1978). Experimental studies have shown that the overall crater dimensions, as well as the distribution of impact melts and ballistic ejecta around the primary crater, is a function of the direction and angle of the impact event (e.g., Gault, 1973; Herrick and Taylor, 2003; Schultz and Gault, 1990; Schultz and D'Hondt, 1996; Pierazzo and Melosh, 2000a). The impact trajectory, in particular, has substantial effects on the subsequent cratering processes, cratering efficiency, degree of fragmentation, the fate of the impactor, final depth-to-diameter ratio, etc. (Schultz and Gault, 1990; Schultz, 1992; Schultz and D'Hondt, 1996). Therefore, we

attempt to determine the direction and angle of the Das crater-forming impact event based on the observable characteristics of crater morphology such as its planform shape, symmetry of ballistic ejecta, topographic asymmetry of the rim, and overall melt distribution.

Firstly, the symmetry of ballistic ejecta facies around the primary crater is a defining parameter for the impact angle and direction. In ideal conditions of vertical to 45° angle impacts, the distribution pattern of ballistic ejecta would be symmetrical, with distal ejecta rays spread out uniformly in all directions around the parent crater (Melosh, 1989). A non-uniform distribution of ballistic ejecta marks the oblique impacts at angles $\leq 45^\circ$ (Gault and Wedekind, 1978). The asymmetric ejecta blanket with bilateral symmetry about the path of projectile trajectory is the prime sign of such oblique impacts (Gault and Wedekind, 1978; Melosh, 1989). A forbidden zone appears in the uprange direction at impact angles $\leq 25^\circ$, and a further drop in impact angle to $\leq 15^\circ$ produces a downrange forbidden zone as well (Herrick and Forsberg-Taylor, 2003). At near-grazing impact angles, the displaced materials are ejected only at angles perpendicular to the projectile path and form a butterfly-wing-like pattern with distinct forbidden zones both in the uprange and downrange directions (Gault and Wedekind, 1978). The mapping of ejecta distribution around the Das crater shows that the overall shape of the ejecta blanket is asymmetric (Fig. 7.3.26).

The asymmetric ejecta of the Das crater is marked by the occurrence of ballistic ejecta facies more extensively and at greater radial distances in the northwestern and southeastern quadrants, and conversely, the occurrence of less extensive ejecta at relatively shorter radial distances from the crater rim in the northeastern and southwestern quadrants (Fig. 7.3.26). The ballistic ejecta facies have maximum radial extents in the northwest and southeast directions, with the secondary crater chains almost absent in a zone towards the NNE direction.

The observed pattern with an azimuthal zone devoid of any secondary crater chains mark the occurrence of a bilateral symmetry to the distribution of ballistic ejecta facies along a line running NNE–SSW through the crater centre (Fig. 7.3.26). The contiguous ejecta blanket reaches only up to ~ 35 km to the SW and ~ 23 -68 km to the NNE, compared to their greater radial extents as two major lobes perpendicular to the line of bilateral symmetry (Fig. 7.3.26). Additionally, the distal ejecta rays of the Das crater reach as far as 225 km and 307 in the direction perpendicular to the line of bilateral symmetry (Figs 7.3.17a and b). The observed pattern of overall asymmetric ejecta with a bilateral symmetry along a NNE-SSW line indicates that the Das crater was formed by an oblique impact.

In oblique impacts, the line of bilateral symmetry would be the direction of the impact event (e.g., Gault and Wedekind, 1978). Therefore, the impact direction of the Das crater is proposed to be along NNE–SSW direction (Fig. 7.3.26). In addition, the presence of a forbidden zone with a

distinct lack of secondary crater chains at an azimuthal direction of the crater is also a basis for determining the direction of the oblique impact (Gault and Wedekind, 1978).

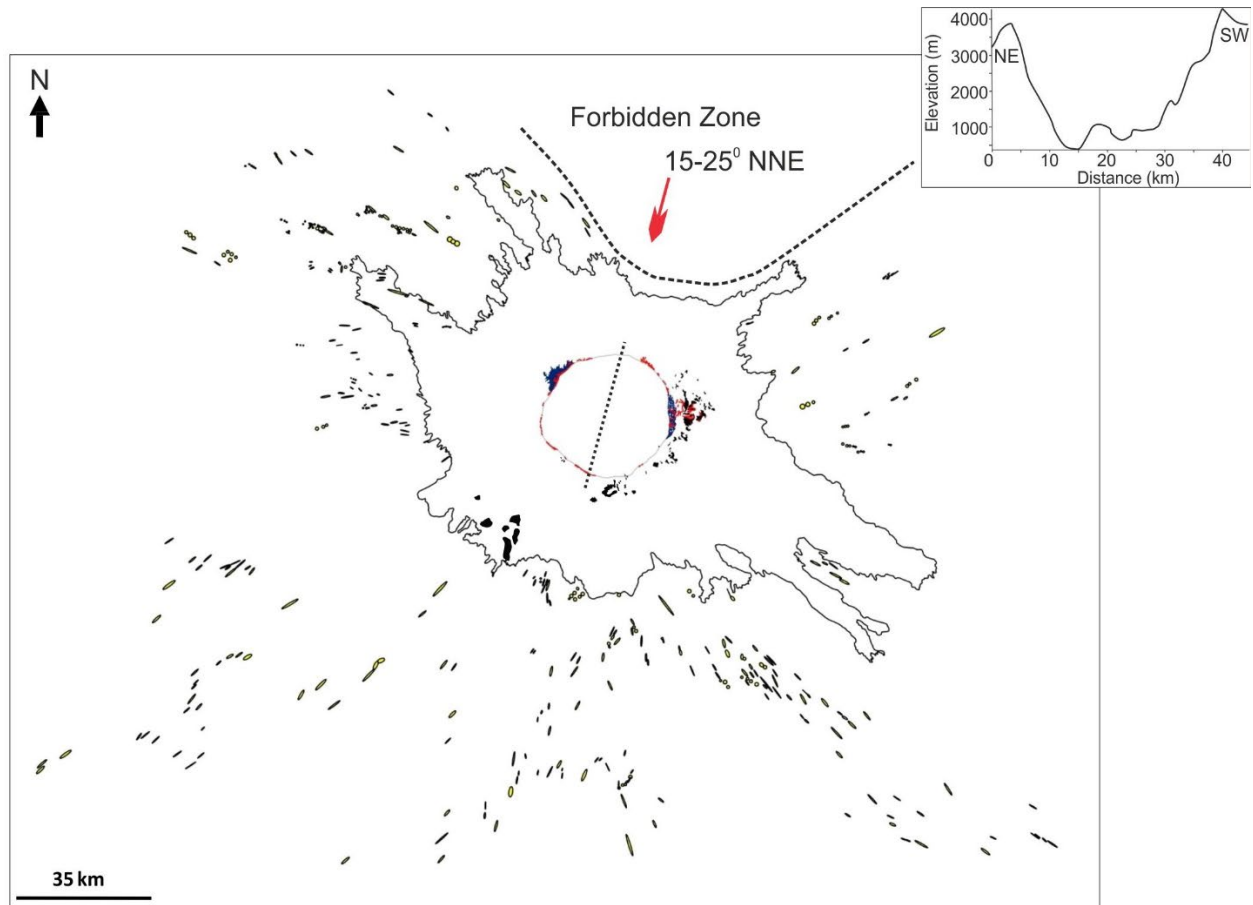


Figure 7.3.26: Distribution pattern of ejecta facies around Das crater. The red arrow points to the proposed direction of the impact trajectory. The proposed angle (to the horizontal) of the trajectory is also labelled. The black dashed line passing through the centre of the crater represents the line of bilateral symmetry. The NNE region devoid of radial facies is labelled the ‘forbidden zone’. The inset image shows the topographic profile across the line of bilateral symmetry. The cross-section reveals the rim asymmetry along the direction of impact trajectory.

The observed absence of secondary crater chains (Facies D) to the NNE of the Das crater is indicative of the well-defined "forbidden zone" or "zone of avoidance" (Fig. 7.3.26). The observed forbidden zone and distribution of longest distal ejecta rays align with the proposed impact direction (Figs 7.3.17 and 7.3.26). The forbidden zone in the NNE is considered the uprange impact direction of the Das crater as the low-angle oblique impacts typically contribute limited ejecta emplacement in the uprange (Gault and Wedekind, 1978; Melosh, 1989; Schultz, 1999; Herrick and Forsberg-Taylor, 2003). The downrange direction of the Das crater impact would be the SSW along which the distal rays and secondary crater chains extend to greater radial distances of approximately 380 km (Figs 7.3.17 and 7.3.26).

The planform shape of the crater is another critical parameter that changes systematically with the impact angle and direction. For impacts of vertical to 30°, the overall shape of the crater remains more or less circular (Gault and Wedekind, 1978; Herrick and Forsberg-Taylor, 2003). For an impact angle less than 30°, the crater geometry begins to deviate from its circular shape depending on the impact velocity and physical properties of the target/projectile (Gault and Wedekind, 1978). The crater shape becomes elongated along the trajectory path with the long axis parallel to the bilateral symmetry line only when the impact angle drops to $\leq 15^\circ$ (Gault and Wedekind, 1978; Pierazzo and Melosh, 2000a; Herrick and Forsberg-Taylor, 2003). The Das crater rim is more or less circular with a bulge in the east-west direction in contrast to the observed bilateral symmetry of ejecta facies (Figs 7.3.3b and 7.3.26). It is noted that the observed elongation of the crater in E-W is not an effect of the oblique impact event, rather resulted from crater modification processes. Hence, the nearly circular form of the Das crater rim suggests its formation from an oblique impact at an angle not lesser than 15°.

Furthermore, the impact angle must be $\leq 25^\circ$ to produce a forbidden zone (Gault and Wedekind, 1978; Pierazzo and Melosh, 2000a; Herrick and Forsberg-Taylor, 2003). In the case of the Das crater, a well-defined forbidden zone devoid of ballistic ejecta facies, along with no observed elongation of the crater rim along the proposed impact direction, indicates that the impact trajectory was from the NNE direction towards SSW at angles between 15° and 25° to the horizontal.

The crater rim is generally depressed and steep in the uprange direction for impact angles less than 25° (Herrick and Forsberg-Taylor, 2003; Kruger et al., 2016). However, the Das crater rim is elevated to the northwest and depressed to the southeast, almost perpendicular to the proposed impact direction (Fig. 7.3.2). This observation is in contrast to the general notion of a topographic asymmetry of the rim along the impact direction. It is inferred that the observed asymmetry in the rim elevations from NW to SE has originally arisen from the pre-impact topographic variation controlled by the remnants of SPA ring ridges to the WNW and southwest parts of the crater (Figs 7.3.1a and 7.3.18). Nevertheless, the rim in the proposed uprange direction of the Das crater is slightly depressed (~4 km), while the downrange rim elevation is ~4.3 km (Fig. 7.3.26).

The impact direction and angle also influence the distribution of impact-melt deposits around the crater (Pierazzo and Melosh, 2000b). The distribution of melt-bearing ejecta is axisymmetric in vertical impacts (Gault and Wedekind, 1978). At impact angles of $\leq 45^\circ$, the melt ejecta deposit preferentially in the downrange compared to their emplacement in reduced amounts in other azimuths, including the uprange (Gault and Wedekind, 1978; Pierazzo and Melosh, 2000a & b). The melt deposits of the Das crater are concentrated mainly in topographic lows inward the crater centre and exterior to the rim (Figs 7.3.21, 7.3.22, and 7.3.24a-c). The lobate melt deposits follow

the local topographic slopes extending from the crater rim. The identified melt deposits are distributed in almost all azimuthal directions except the uprange and show an appropriate amount of melt emplacement in the downrange direction (Fig. 7.3.26). The observed distribution pattern of impact melt deposits in and around the Das crater is consistent with the previous observations suggesting the role of impact direction and local topographic constraints in the overall distribution of melt-bearing ejecta (cf. Hawke and Head, 1977; Melosh, 1989; Neish et al., 2014, 2017; Kruger et al., 2016; Morse et al., 2018; Morse et al., 2021).

7.3.5 Conclusions

Impact cratering is considered the most fundamental geologic process in our solar system. The Copernican impact craters on the Moon are the best sites to study the lunar impact cratering mechanics. The present study attempted to carry out an in-depth mapping of the morphological units and ejecta facies of the Copernican Das crater on the lunar farside to get better insights into the cratering processes associated with projectile impacts on the Moon. The morphological mapping interior to the crater cavity revealed the characteristic geological features of this complex impact crater, starting from the sharp and scalloped rim, an alcove of wall terraces, the distinct scarp-tread system with steep slopes on the scarp, wall slumping, impact melt deposits, flat floor with hummocky texture, slump hillocks on the floor, melt platform, and central mounds with bedrock exposures. These distinct morphological units suggest that the Das crater was originally formed as a simple bowl-shaped crater, which was later modified to become a complex crater. The excavation of the transient crater cavity for the Das crater took place in less than 4 seconds. The maximum depth of excavation is estimated to be 3 km. The transient crater diameter is projected to be 30.4 km, and the transient crater depth ranges between 7.6-9.12 km. The crater excavation was concurrent with the ejection of shocked and melted debris outward as impact ejecta. The modification of the crater began even before the central mounds rose from depths of maximally compressed rocks at around 3.2 km. The subsequent gravitational collapse of the rim produced terraced, steeper walls resulting in a slight widening of the crater rim along W-E and enlargement of the final diameter to 38 km. The wall slumping occurred at a larger scale on the western inner wall, and the slumped materials slid down to form heaps of hillocks, mainly in the western section of the floor. The rotational slumping of the inner wall with their toes reaching the base of the crater to form a small plug has partly contributed to a segment of rising central mounds. The eastern crater floor has undergone subsidence, likely due to structural failure and/or cooling of the initial melt column. The impact melts line the transient crater cavity throughout its growth and is emplaced in a variety of topographic settings ranging from ponds in the wall terraces to extensive

melt sheets along the inner wall slopes and the melt-draped floor units. The melt breccia, fractured impact melt deposits with boulders at their margins, and distinctive flow features appearing as melt fronts or flow lobes concentrated on the inner wall of the crater are diagnostic in determining their origin as impact-generated melts. Exterior to the crater cavity, solid and melt phase ejecta are distributed around the crater, with the highly shocked debris materials occurring at radial distances beyond the rim and melted debris preferentially occupying the topographic lows and slopes both inward and outward the crater rim. Four distinct ejecta facies identified around the crater exhibit similarity in physical characteristics, spatial distribution, and maximum radial extents. The ballistic ejecta facies are emplaced as continuous ejecta blanket (proximal to the crater rim) and discontinuous ejecta (beyond the extent of contiguous ejecta blanket), both distributed at varying radial distances from the rim. The onset of discontinuous ejecta blanket is marked by the appearance of the herringbone pattern consisting of linear clusters of elongated secondary craters or V-shaped depressions pointing back to the crater. The radial facies showed a slight deviation from their expected orientation as a result of interaction with the underlying topography controlled by remnant ridges of the SPA basin ring. The emplacement of the radial ejecta facies, including the contiguous blanket and the secondary crater chains, occurred concurrently during the mixing of fallen ejecta with the surface materials. The resulting ground-hugging flow of mixed materials caused infilling of the secondary crater chains and subsequent overprinting by the contiguous ejecta blanket. The melt-bearing ejecta is distributed as rim veneer deposits and ponded melt and lobate deposits within 7 km radial extents from the rim crest, and they completely overlie the contiguous ejecta blanket. The non-uniform distribution of ballistic ejecta facies around the crater and maximum radial extents to the northwestern and southeastern quadrants than the less extensive deposits towards the southwest and NNE indicates overall asymmetric ejecta with a bilateral symmetry along the line running NNE-SSW through the centre of the crater. The presence of a forbidden zone devoid of distal ejecta rays and secondary crater chains to the NNE suggests that the direction of the impact was NNE-SSW. The near circular form of the crater, along with a clearly defined forbidden zone in the uprange, indicate that the impact occurred at an angle between 15°-25° to the horizontal. The interpretations from the present study demonstrate that studying Copernican craters are crucial for expanding our knowledge on the impact dynamics and cratering mechanics of the Moon.

Chapter 8

Summary and Conclusions

8.1 Summary

The geological evolution of the Earth's Moon is understood mainly through endogenic and exogenic processes operating on this planetary body. The endogenic processes on the Moon include those that cause lunar volcanism and interior differentiation. Exogenic processes operate on or above the Moon's surface and involve large-scale impact cratering events and related surface readjustments. Understanding the evolutionary history of our nearest neighbour requires knowledge of these endogenic and exogenic processes on the Moon. This Ph.D. work focused on investigating lunar volcanism, spinel compositional heterogeneity, and impact cratering mechanics during the Copernican epoch in order to better understand the lunar endogenic and exogenic processes. The study primarily utilized orbital remote sensing data from various lunar exploratory missions. The evidence for a variety of endogenic and exogenic processes on the Moon revealed by this Ph.D. work suggests that the evolution of the Moon is more intricate than we imagined and that our Moon may still be evolving!!

The volcanism on the Moon began around 3.9 to 4.0 Ga ago and lasted until 1.2 Ga, with a peak in volcanic activity between 3.2 and 3.8 Ga. Most of the mare volcanism occurred during the Imbrian epoch, and therefore, the extended volcanic and thermal history of the Moon during the Late-Imbrian and Eratosthenian epochs is yet to be characterized well. Also, the compositional heterogeneity in the mare basaltic units of different ages across the lunar surface suggests their diverse source regions in the lunar mantle. To better understand the volcanic and thermal evolution of the Moon, the chemistry, diversity, ages, and origins of the mare basaltic units in the Grimaldi and Humorum basins are investigated. In the Mare Humorum, Imbrian-Eratosthenian basalts can be found. Pigeonites and augites were the dominant compositions in

these basaltic blocks. The compositional trend between pigeonites and augites points to basaltic magma differentiation as it cools. The older units originated from a Fe-rich fractionated magma, whereas the younger units formed from Mg and Ca-rich magma. Multiple volcanic eruptions in the Mare Humorum were shown by the various chemical patterns in the pyroxene quadrilateral. The younger and older basalts' longward and shortward shifts in the Band I and Band II centres, respectively, suggest that the older basalts crystallised more Fe²⁺-rich, Ca-depleted pyroxenes, whereas the younger basalts were generated from a more Ca-rich magma. Hence, the basaltic magmas that erupted in the Mare Humorum throughout the Imbrian and Eratosthenian periods came from a variety of sources.

In Mare Grimaldi and Mare Riccioli, various basaltic units with varied albedo, mineralogy, and titanium content were identified. The crater size-frequency distribution approach demonstrated that the Grimaldi basin had seen at least two stages of basaltic magmatism spanning 3.5 to 1.5 Ga (Late Imbrian–Eratosthenian). In Mare Grimaldi, high-Ti olivine basalts dated at 2.05 Ga are discovered surrounded by low- to intermediate-Ti basalts dated at 3.47 Ga. Low- to intermediate-Ti basalts found in Mare Riccioli date back to two different volcanic eruptions, 3.5 and 3.2 billion years ago, respectively, while patches of basalts with considerably greater titanium content in the Mare Riccioli have a younger age of 1.5 billion years. The high-Ti basalts in the Mare Grimaldi formed from a Fe-rich late-stage magma, whereas the low-Ti basalts formed from an Mg- and Ca-rich starting magma that was quenched ultra-late. The low- to intermediate-Ti basaltic magma that erupted in both units was derived from partial melting of early cumulate materials from the hybrid source region in the post-overturn upper mantle and made its way to the surface via dikes propagated by excess pressures accumulated in the diapirs stalled at the crust's base due to buoyancy trap. A heated plume climbed from the deeper clinopyroxene–ilmenite-rich cumulate layer near the core-mantle boundary, causing the high-Ti magma to erupt in the Mare Grimaldi. The Eratosthenian (1.5 Ga) intermediate-Ti volcanic activity in the Mare Riccioli, on the other hand, was caused by ilmenite–clinopyroxene cumulate elements that remained in the upper mantle following mantle overturn. The new findings show that volcanism in the Grimaldi basin did not cease at 3.27 Ga but was active and supplied by several mantle sources until 1.5 Ga, spanning a 2 billion-year timeframe.

Spinel is an oxide group mineral with Fe and Mg in the tetrahedral site and Fe, Cr, and Al in the octahedral site. Magmatic spinels crystallise directly from ultramafic magma, hence their chemical composition reveals information about the magma's origins and history. Using orbital remote sensing data and returned lunar samples, magmatic spinels of various compositions were found on Earth's Moon. The compositional differences of lunar spinels are explored in this study, and a comparison with terrestrial spinels is made. According to the accumulated

chemical data, lunar spinels are mostly chromites, ulvospinel, pleonaste, and Mg-Al spinels. Cr spinels are abundant in basaltic rocks and soil samples, whereas Mg-Al spinels are found in breccia and troctolites. When compared to terrestrial spinels, lunar spinels show comparable compositional trends to komatiites, implying a mantle origin for lunar Cr-spinels. Furthermore, terrestrial spinels, specifically Cr-spinels from the Sittampundi Anorthosite Complex (SAC) in southern India, have been chosen as a functional counterpart to lunar spinels and are being studied using a mix of spectroscopic and chemical approaches. The SAC is connected with varied thickness chromitite layers. Cr-spinels have a Fe- and Al-rich composition, with Cr₂O₃ concentrations and Cr# ranging from 32-37 wt percent and 0.44-0.53, respectively, in SAC-hosted chromitites. The major Raman peak associated with the A_{1g} mode ranges between 703 and 714 cm⁻¹, with a shoulder about 671 cm⁻¹. The substitution of Al³⁺ in the spinel structure is thought to be the source of the longward shift in the A_{1g} peak (705-714 cm⁻¹). The coexistence of (Mg, Fe) in the tetrahedral site and (Al, Cr) in the octahedral site is attributed to the A_{1g} peak position near 705 cm⁻¹ in the Raman spectra. Diagnostic absorption bands were found in the Cr-spinels' hyperspectral data at 0.49 μm, 0.59 μm, 0.69 μm, 0.93 μm, 1.3 μm, and 2 μm. The 2 μm and 0.93 μm bands appear to be stronger and wider in all of the samples, which is likely due to a larger amount of Fe²⁺ in the samples. Because of the increased Al content (25 wt%) in the SAC Cr-spinels, the 2 μm band position is at shorter wavelengths than in conventional Cr-spinels. The Cr# and Cr₂O₃ contents have a positive association with the 2 μm band location, but the Al₂O₃ concentration has a negative correlation. The replacement of Al and Cr for one another explains the linear relationship. Based on their spectrochemical features, the observed linear connection between 2 μm band position and Cr/Al abundances can be used to distinguish Al-spinels from Cr-spinels. Through an integrated and comparative investigation of spectroscopic and chemical data, the present study has unambiguously demonstrated the relationship between the spectral pattern and chemistry of Cr-spinels. The spectral signatures of SAC Cr-spinels were compared to those of previously identified Sinus Aestuum spinels, allowing the interpretation of possible Fe- and Cr-bearing spinels in the Sinus Aestuum on the Moon. The conclusions drawn from spectral-chemical relationships will serve as a guide for distinguishing lunar Al spinels from Cr-spinels. The Cr-spinels hosted by the SAC could serve as a possible functional analogue for lunar Fe- and Al-rich spinels. The results of this investigation will be added to the existing library of planetary analogue materials, which can be used for calibration and data interpretation from future missions.

The most prevalent geological feature on planetary surfaces is impact craters. Impact crater morphology and ejecta distribution provide crucial information regarding impact dynamics and cratering processes. The present research focused on identifying discrete morphological units in the Ohm and Das craters, as well as the ejecta facies of the Copernican-aged Das crater on

the Moon's far side. Following the shock wave propagation by the projectile impact, the excavation of the transient Das crater cavity to depths of 3 km occurred in less than 4 seconds. The depth of the transient crater is estimated to be between 7.6 and 9.12 kilometers. The excavated crater cavity's displaced contents were hurled out as severely shocked and melted debris on a ballistic trajectory, finally depositing as various ejecta facies surrounding the crater. The gravitational collapse of the 30.4 km diameter transient crater set in motion a chain of events that resulted in the initial rim crumbling and walls slumping, resulting in the formation of a final crater with a scalloped rim and terraced walls, as well as a subsequent enlargement of the rim-to-rim diameter to 38 km. The centre mounds were created by the rebound of the crater floor from depths of 3.2 km, with a small offset to the northwest. Impact-generated melts lined the inside of the crater, cooled as melt breccia along the inner walls, and frequently overflowed to form melt deposits outside the rim. Subsidence on the eastern floor section occurred as a result of the solidification of impact melts and/or a structural breakdown along weaker planes in the crater core, resulting in elevated and lower hummocky floor units. Ballistic ejecta facies placed closer to the rim create a contiguous ejecta blanket, whilst those deposited farther out from the rim are referred to as distal or discontinuous ejecta. The entire asymmetric ejecta pattern, with bilateral symmetry along the NNE-SSW line across the crater centre, implied an oblique impact for the Das crater formation, with the projectile approaching from the NNE direction. The impact angle was between 15° and 25°, based on the crater's almost circular planform, and a well-defined prohibited zone devoid of secondary crater chains and distal ejecta rays in the uprange direction. The sequence of events depicted in this study and the elucidations on impact dynamics demonstrate the importance of studying Copernican craters to gain a better understanding of the Moon's cratering mechanics and impact dynamics.

8.2 Conclusions

- The long span of volcanism and wide chemical variations of mare basalts in the Grimaldi and Humorum basins (3.5 Ga – 1.5 Ga) shed light on the extended volcanic (Main- and Late-phase) and thermal evolution of the Moon and gave insights into lunar mantle heterogeneity and endogenic processes such as origin and emplacement mechanisms of mare basaltic magmas. The distinct mare basaltic units derived from different source regions in the lunar mantle affirm the occurrence of mantle overturn after LMO crystallization. Based on our results, the Grimaldi basin can be considered a potential site for sample collection and in-situ studies during future Moon landing missions.

- The compositional variations of magmatic spinels in diverse rock types on the Moon showed that lunar spinel compositions could be of mantle origin. The comparison of lunar spinels with the terrestrial spinels based on their spectrochemical characteristics enabled the identification of Fe- and Cr-bearing spinels in Sinus Aestuum on the Moon and put significant constraints on the remote interpretation of lunar spinel chemistry.
- The morphology and ejecta emplacement dynamics of the Copernican Das and Ohm craters (<1 Ga old) provided insights into various exogenic processes operated during- and post the crater formation, particularly about the crater modification processes of the simple bowl-shaped crater to develop into a complex crater, the nature of impact (impactor direction and angle) and the role of pre-impact topography (i.e., SPA basin ridge) in the crater morphology.
- The future of space exploration will be manned and robotic landing on planetary bodies, in-situ analyses and resource extraction, and setting up an interplanetary launch system. Material characterization of planetary field analogue in this study provides a means of scientific backup for methods of in-situ studies, calibration of instruments, and resource utilization in future missions.

8.3 Future scope of this work

- The current understanding of the volcanic history of the Moon encompasses early-phase, main-phase, late-phase, and topical phase volcanism. Results from this Ph.D. work showed evidence of main-phase and late-phase volcanic events on the nearside of the Moon. Additionally, recent studies revealed more evidence of lunar topical phase volcanism, giving more validation to the extended volcanic history of the Moon (e.g., Singh et al., 2020). Therefore, further investigation of chemistry and ages of mare basaltic units on the nearside and farside of the Moon using new remote sensing datasets will shed more light on the volcanic and thermal evolution of the Moon.
- Copernican craters are ideal targets to study the impact cratering mechanics of the Moon, as demonstrated by investigating the Ohm and Das craters on the lunar farside. Probing similar Copernican craters would help us better constrain the late-stage impact cratering dynamics on the Moon.
- Chromite almost always crystallises alongside olivine in igneous rocks (Roeder, 1994). Both chromite and olivine are early cocrystallizing phases; however, they both react with the melt and are eventually replaced by pyroxene (Irvine,

1965). Pyroxene is formed when early chromite reacts with melt and has a higher chromium content than the melt (Roeder, 1994). As a result, geological controls on these lunar spinels, such as the interaction between coexisting olivine and pyroxene phases, remain unknown. This makes it difficult to come to a more exact conclusion on their genesis. These findings can be better constrained in the future by studies that use orbital data and future returning samples. Moreover, the lateral and vertical heterogeneities in spinel compositions on the Moon can be determined by estimating their geological context as well as the depth of occurrence. This will give more insights into the genesis of spinels on the Moon.

- The spectrochemical characterization of terrestrial spinels from other regions in southern India, particularly in the Nugehalli schist belt, can be carried out using various spectroscopic techniques. The Cr-spinel composition slightly varies in Nugehalli with a much higher chromium content; hence, determining their spectrochemical characteristics will be an addition to the database containing spectrochemical information of a wider range of terrestrial spinel compositions. The database will be a reference for remote identification of chemically diverse spinels on the lunar surface.

Bibliography

- Adams J. B., 1975. Interpretation of visible and near-infrared diffuse reflectance spectra of pyroxenes and other rock forming minerals. In *Infrared and Raman spectroscopy of lunar and terrestrial minerals*, edited by Karr C. Jr. Orlando, Florida: Academic Press. pp. 91–116.
- Adams J. B. and McCord T. B., 1970. Remote sensing of lunar surface mineralogy: Implications from visible and near-infrared reflectivity of Apollo 11 samples. *Geochimica et Cosmochimica Acta* 3:1937–1945.
- Adams, J. B., Pieters, C., & McCord, T. B., 1974. Orange glass: Evidence for regional deposits of pyroclastic origin on the moon. *Lunar Science Conference*, 1, 171–186.
- Adams, J., Hörz, F., & Gibbons, R., 1979. Effects of shock-loading on the reflectance spectra of plagioclase, pyroxene, and glass. In *proceedings of the 10th Lunar and Planetary Science Conference* (pp. 5–7).
- Adams, J.B., 1974. Visible and near-infrared diffuse reflectance spectra of pyroxenes as applied to remote sensing of solid objects in the solar system. *Journal of Geophysical Research*, 79(32), pp.4829-4836.
- Agrell S. O., Peckett A., Boyd F. R., Haggerty S. E., Bunch T. E., Cameron E. N., Dence M. R., Douglas J. A. V., Plant A. G., Traill R. J., James O. B., Keil K., and Prinz M., 1970. Titanian chromite, aluminum chromite, and chromian ulvöspinel from Apollo 11 rocks. *Proc. Apollo 11 Lunar Sci. Conf.*, pp. 81–86.

- Anbazhagan, N.K. Sainaba, S. Arivazhagan, 2012. Remote sensing study of Sittampundi anorthosite complex, India, *J. Indian Soc. Remote Sens.* 40, 145–153.
- Anbazhagan, S. and Arivazhagan, S., 2009. Reflectance spectra of analog basalts; Implications for remote sensing of lunar geology. *Planet. Space Sci.*, v.57(12), pp.1346–1358.
- Anbazhagan, S. and Arivazhagan, S., 2010. Reflectance spectra of analog anorthosites: Implications for lunar highland mapping. *Planet. Space Sci.*, v. 58(5), pp.752–760.
- Andrews-Hanna, J.C., Asmar, S.W., Head, J.W., Kiefer, W.S., Konopliv, A.S., Lemoine, F.G., Matsuyama, I., Mazarico, E., McGovern, P.J., Melosh, H.J. and Neumann, G.A., 2013. Ancient igneous intrusions and early expansion of the Moon revealed by GRAIL gravity radiometry. *Science*, 339(6120), pp.675-678.
- Andrews-Hanna, J.C., Head, J.W., Johnson, B.C., Keane, J.T., Kiefer, W.S., McGovern, P.J., Neumann, G.A., Wieczorek, M.A. and Zuber, M.T., 2018. Ring faults and ring dikes around the Orientale basin on the Moon. *Icarus*, 310, pp.1-20.
- Anki, B. Lefez, 1996. Optical constants of various chromites as determined by Kramers-Kronig analysis, *Appl. Opt.* 35, 1399–1403.
- Arai, 1992. Chemistry of chromian spinel in volcanic rocks as a potential guide to magma chemistry, *Mineralogical Magazine* 56 (383) 173–184.
- Arai, 1980. Dunite—harzburgite—chromitite complexes as refractory residue in the Sangun—Yamaguchi zone, western Japan, *J. Petrol.* 21, 141–165.
- Arai, H. Okamura, K. Kadoshima, C. Tanaka, K. Suzuki, S. Ishimaru, 2011. Chemical characteristics of chromian spinel in plutonic rocks: implications for deep magma processes and discrimination of tectonic setting, *Isl. Arc* 20, 125–137.
- Arai, H. Yurimoto, 1994. Podiform chromitites of the Tari-Misaka ultramafic complex, southwestern Japan, as mantle-melt interaction products, *Economic Geology* 89 (6) 1279–1288.
- Arai, Takeda, h., Yamaguchi, a., and Ohtake, m., 2008. A new model of lunar crust: Asymmetry in crustal composition and evolution. *Earth Planets and Space*, v.60(4), pp.433.
- Arvidson, R., Drozd, R., Guinness, E., Hohenberg, C., Morgan, C., Morrison, R., Oberbeck, V., 1976. Cosmic ray exposure ages of Apollo 17 samples and the age of Tycho. In: *7th Proc. Lunar Sci. Conf.*, pp. 2817–2832.
- Arya A. S., Rajasekhar R. P., Thangjam G., and Ajai K. K., 2011. Detection of a potential site

for future human habitability on the Moon using Chandrayaan-1 data. *Current Science* 100:524–529.

Ashley, J.W., Robinson, M.S., Hawke, B.R., Bogert, C.H., Hiesinger, H., Sato, H., Speyerer, E.J., Enns, A.C., Wagner, R.V., Young, K.E. and Burns, K.N., 2012. Geology of the King crater region: New insights into impact cratering dynamics on the Moon. *Journal of Geophysical Research: Planets*, 117(E12).

Ashwal, 1993. *Anorthosites, Minerals and Rocks*, 1st, 21, Springer-Verlag Berlin Heidelberg.

Baker, D.M., Head, J.W., Fassett, C.I., Kadish, S.J., Smith, D.E., Zuber, M.T. and Neumann, G.A., 2011. The transition from complex crater to peak-ring basin on the Moon: New observations from the Lunar Orbiter Laser Altimeter (LOLA) instrument. *Icarus*, 214(2), pp.377-393.

Baldwin, R. B., 1968. Rille pattern in the Lunar Crater Humboldt. *Journal of Geophysical Research*, 73(10),

Bandfield, J.L., Poston, M.J., Klima, R.L. and Edwards, C.S., 2018. Widespread distribution of OH/H₂O on the lunar surface inferred from spectral data. *Nature geoscience*, 11(3), pp.173-177.

Barker M., Mazarico E., Neumann G., Zuber M., Haruyama J., and Smith D., 2016. A new lunar digital elevation model from the LUNAR ORBITER LASER ALTIMETER and SELENE terrain camera. *Icarus* 273:346–355.

Barnes, P.L. Roeder, 2001. The range of spinel compositions in terrestrial mafic and ultramafic rocks, *J. Petrol.* 42, 2279–2302.

Barr D., 2011. The Moon Mineralogy Mapper (M3) imaging spectrometer for lunar science: Instrument description, calibration, on-orbit measurements, science data calibration and on-orbit validation. *Journal of Geophysical Research: Planets* 116:E00G19.

Barricelli, N.A. and Metcalfe, R., 1969. The lunar surface and early history of the earth's satellite system. *Icarus*, 10(1), pp.144-163.

Bence A. and Papike J., 1972. Pyroxenes as recorders of lunar basalt petrogenesis: Chemical trends due to crystal-liquid interaction. *Proceedings, 3rd Lunar and Planetary Science Conference. Proceedings.* p. 431.

Bennett, S.J. Brotton, B.M. Jones, A.K. Misra, S.K. Sharma, R.I. Kaiser, 2013. High sensitivity Raman spectrometer to study pristine and irradiated interstellar ice analogues, *Anal. Chem.* 85, 5659–5665.

- Besse S., Sunshine J. M., and Gaddis L. R., 2014. Volcanic glass signatures in spectroscopic survey of newly proposed lunar pyroclastic deposits. *Journal of Geophysical Research: Planets* 119:355–372.
- Besse S., Sunshine J. M., Staid M. I., Petro N. E., Boardman J. W., Green R. O., Head J. W., Isaacson P. J., Mustard J. F., and Pieters C. M., 2011. Compositional variability of the Marius Hills volcanic complex from the Moon Mineralogy Mapper (M3). *Journal of Geophysical Research: Planets* 116:E00G13.
- Besse S., Sunshine J., Staid M., Boardman J., Pieters C., Guasqui P., Malaret E., McLaughlin S., Yokota Y., Li J.-Y., 2005. A visible and near-infrared photometric correction for Moon Mineralogy Mapper (M3). *Icarus* 222:229–242.
- Bhandari, N., 2005. Chandrayaan-1: science goals. *Journal of Earth System Science*, 114(6), pp.701-709.
- Bhardwaj, A. and Mukundan, V., 2015. Monte Carlo model for electron degradation in methane gas. *Planetary and Space Science*, 111, pp.34-43.
- Bhaskar Rao, 2003. Sm-Nd model ages and Rb-Sr isotopic systematics of charnockite gneisses across the Cauvery Shear Zone, southern India, Implications to the Archean-Neoproterozoic Terrane Boundary in the Southern Granulite Terrain, 297-317.
- Bhattacharya, A.K. Dagar, A. Banerjee, A. Kumar, A. Amitabh, K. Suresh, A. Prashar, A. Patil, A. Roy Chowdhury, A.R. Saxena, S. Gomathi, et al., 2020. Preliminary Observations of Lunar Surface by Chandrayaan-2 Imaging Infrared Spectrometer (IIRS), LPI 2326, 1516.
- Bhattacharya, P. Chauhan, A. Ajai, 2012a. Mg-spinel-rich lithology at crater Endymion in the lunar nearside, 173.
- Bhattacharya, S., Chauhan, M. and Chauhan, P., 2015a. Remote detection of magmatic water in association with olivine of possible mantle origin on the Moon. In *Lunar and Planetary Science Conference (Vol. 46, p. 1396)*.
- Bhattacharya, S., Chauhan, P. and Ajai, A., 2012b. Discovery of orthopyroxene–olivine–spinel assemblage from the lunar nearside using Chandrayaan-1 Moon Mineralogy Mapper data. *Current science*. 103, 21-23.
- Bhattacharya, S., Lal, D., Chauhan, M., Chauhan, P. and Kumar, A.K., 2015b. Detection of hydroxyl-bearing exposures of possible magmatic origin on the central peak of crater Theophilus using Chandrayaan-1 Moon Mineralogy Mapper (M3) data. *Icarus*, 260, pp.167-173.

- Bhattacharya, S., Saran, S., Dagar, A., Chauhan, P., Chauhan, M., Ajai, A., and Kumar, S.K., 2013. Endogenic water on the Moon associated with non-mare silicic volcanism: implications for hydrated lunar interior. *Current Science*, 105, pp.685-691.
- Binder, A.B., 1998. Lunar prospector: overview. *Science*, 281(5382), pp.1475-1476.
- Blanchette-Guertin, J-F., M. Drilleau, T. Kawamura, P. Lognonne, and M. Wieczorek, 2015. Lunar Crustal Thickness and Velocity Model Inversion Using constraints from GRAIL and Apollo Data (and Preparation for the InSight Mission Data Analysis Phase). In *Lunar and Planetary Science Conference*, vol. 46, p. 1867.
- Blewett, D.T., Lucey, P.G., Hawke, B.R., 1997. Clementine images of the lunar sample return stations: Refinement of FeO and TiO₂ mapping techniques. *J. Geophys. Res.* 102, 16,319–16,325.
- Boardman J. W., Pieters C., Green R., Lundeen S., Varanasi P., Nettles J., Petro N., Isaacson P., Besse S., and Taylor L., 2011. Measuring moonlight: An overview of the spatial properties, lunar coverage, selenolocation, and related Level 1B products of the moon mineralogy mapper. *Journal of Geophysical Research: Planets* 116:E00G14.
- Boyce, J.M., Jonnson, D.A., 1978. Ages of flow units in the far eastern maria and implications for basin-filling history. In: *Lunar and Planetary Science Conference Proceedings*, vol. 9, pp. 3275–3283.
- Braden, S.E., Stopar, J.D., Robinson, M.S., Lawrence, S.J., Van Der Bogert, C.H. and Hiesinger, H., 2014. Evidence for basaltic volcanism on the Moon within the past 100 million years. *Nature Geoscience*, 7(11), pp.787-791.
- Brandt, M.M. Raith, V. Schenk, P. Sengupta, C. Srikantappa, A. Gerdes, 2014. Crustal evolution of the Southern Granulite Terrane, south India: New geochronological and geochemical data for felsic orthogneisses and granites, *Precamb. Res.* 246, 91–122.
- Bratt S. R., Solomon S. C., and Head J. W., 1985. The evolution of impact basins: Cooling, subsidence, and thermal stress. *Journal of Geophysical Research: Solid Earth* 90:12,415–12,433.
- Bray, V.J., Tornabene, L.L., Keszthelyi, L.P., McEwen, A.S., Hawke, B.R., Giguere, T.A., Kattenhorn, S.A., Garry, W.B., Rizk, B., Caudill, C.M. and Gaddis, L.R., 2010. New insight into lunar impact melt mobility from the LRO camera. *Geophysical Research Letters*, 37(21).
- Brearley, A. J., and Jones, R. H., 1998. Chondritic meteorites. *Reviews in Mineralogy and Geochemistry*, 36(1), 3–1.

- Bugiolacchi R. and Guest J. E., 2008. Compositional and temporal investigation of exposed lunar basalts in the Mare Imbrium region. *Icarus* 197:1–18.
- Burns R. G., 1993. *Mineralogical applications of crystal field theory*. Cambridge: Cambridge University Press. p. 224.
- Burns R., Vaughan D., Abu-Eid R., Witner M., and Morawski A., 1973. Spectral evidence for Cr³⁺, Ti³⁺, Fe²⁺ rather than Cr²⁺ and Fe³⁺ in lunar ferromagnesian silicates. *Proceedings, 4th Lunar and Planetary Science Conference*. Proceedings. p. 983.
- Burns, 1993. Origin of electronic spectra of minerals in the visible and near-infrared region, *Remote Geochem. Anal.*, 3–29.
- Burns, R.G., 1970. Crystal field spectra and evidence of cation ordering in olivine minerals. *American Mineralogist: Journal of Earth and Planetary Materials*, 55(9-10), pp.1608-1632.
- Burns, R.G., Huggins, F.E., Abu-Eid, R.M., 1972. Polarized absorption spectra of single crystals of lunar pyroxenes and olivines. *Moon* 4 (1–2), 93–102.
- Busche F. D., Prinz M., Keil K., and Bunch T. E., 1972. Spinel and the petrogenesis of some Apollo 12 igneous rocks. *Am. Mineral.*, 57, 1729–1747.
- Busey, O.L. Keller Jr, 1964. Structure of the aqueous pertechnetate ion by Raman and infrared spectroscopy. Raman and infrared spectra of crystalline KTcO₄, KReO₄, Na₂MoO₄, Na₂WO₄, Na₂MoO₄ 2H₂O, and Na₂WO₄ 2H₂O, *J. Chem. Phys.* 41, 215.
- Bussey, D.B.J., Spudis, P.D., 2000. Compositional studies of the Orientale, Humorum, Nectaris, and Crisium lunar basins. *J. Geophys. Res.: Plan* 105 (E2), 4235–4243.
- Byrne, C.J., 2005. Overview of the near side of the moon. In: *Lunar Orbiter Photographic Atlas of the Near Side of the Moon*. Springer, London, pp. 8–10.
- Cahill, J. T. S., Lucey, P. G., & Wiczorek, M. A., 2009. Compositional variations of the lunar crust: Results from radiative transfer modeling of central peak spectra. *Journal of Geophysical Research*, 114, E09001.
- Cameron, A.G. and Ward, W.R., 1976, March. The origin of the Moon. In *Lunar and Planetary Science Conference (Vol. 7)*.
- Cameron, A.G.W., 2000. Higher-resolution simulations of the giant impact. *Origin of the Earth and Moon*, pp.133-144.
- Candia, J.C. Gaspar, 1997. Chromian spinels in metamorphosed ultramafic rocks from Mangabal I and II complexes, Goiás, Brazil, *Mineralogy and Petrology* 60 (1) 27–40.

- Canup, R.M. and Asphaug, E., 2001. Origin of the Moon in a giant impact near the end of the Earth's formation. *Nature*, 412(6848), p.708.
- Canup, R.M., 2004. Simulations of a late lunar-forming impact. *Icarus*, 168(2), pp.433-456.
- Carter J. L., Clanton U. S., Fuhrman R., Laughon R. B., McKay D. S., and Usselman T. M., 1975. Morphology and composition of chalcopyrite, chromite, Cu, Ni-Fe, pentlandite, and troilite in vugs of 76015 and 76215. *Proc. Lunar Sci. Conf. 6th*, pp. 719–728.
- Seni, L.M. Kriegsman, 2005. Tectonics of the Neoproterozoic southern granulite terrain, South India, *Precambrian Research* 138 (1–2) 37–56.
- Charlier B., Grove T. L., Namur O., and Holtz F., 2018. Crystallization of the lunar magma ocean and the primordial mantle-crust differentiation of the Moon. *Geochimica et Cosmochimica Acta* 234:50–69.
- Chauhan M., Bhattacharya S., Pathak S., and Chauhan P., 2018. Remote spectral–compositional analysis of basalt mineralogy at Hansteen-Billy, Moon. *Meteoritics & Planetary Science* 53:2583–2595.
- Chauhan P., Kaur P., Srivastava N., Bhattacharya S., Kumar A., and Goswami J., 2012. Compositional and morphological analysis of high resolution remote sensing data over central peak of Tycho crater on the Moon: Implications for understanding lunar interior. *Current Science* 102:1041–1046.
- Chauhan, M., Bhattacharya, S., Pathak, S., Chauhan, P., 2018. Remote spectral–compositional analysis of basalt mineralogy at Hansteen-Billy, Moon. *Meteoritics Planet Sci.* 53 (12), 2583–2595.
- Chauhan, M., Bhattacharya, S., Saran, S., Chauhan, P. and Dagar, A., 2015. Compton–Belkovich volcanic complex (CBVC): An ash flow caldera on the Moon. *Icarus*, 253, pp.115-129.
- Chauhan, P., Kaur, P., Bhattacharya, S., Dagar, A., Ajai, and Kiran Kumar, A. S., 2014. Detection of OH/H₂O on the central peak of Jackson crater from Moon Mineralogical Mapper (M3) data onboard Chandrayaan-1. In *Lunar and Planetary Science Conference* (Vol. 45, p. 2072).
- Cheek, L. C., & Pieters, C. M., 2014. Reflectance spectroscopy of plagioclase-dominated mineral mixtures: Implications for characterizing lunar anorthosites remotely. *American Mineralogist*, 99(10), 1871–1892.
- Cheek, L. C., Donaldson Hanna, K. L., Pieters, C. M., Head, J. W., & Whitten, J. L., 2013. The

- distribution and purity of anorthosite across the Orientale basin: New perspectives from Moon Mineralogy Mapper data. *Journal of Geophysical Research: Planets*, 118, 1805–1820.
- Cheek, L., Pieters, C., Boardman, J., Clark, R., Combe, J., Head, J., Isaacson, P., McCord, T., Moriarty, D., Nettles, J., 2011. Goldschmidt crater and the Moon's north polar region: Results from the moon mineralogy mapper (M3). *J. Geophys. Res.: Planets* 116 (E6).
- Chetty, Proterozoic shear zones in southern granulite terrain India, 1996. *Archaean Proteroz. Terr. Southern India within East Gondwana* 3, 77–89.
- Chetty, Y.J.B. Rao, 2006. The Cauvery shear zone, Southern Granulite Terrain, India: a crustal-scale flower structure, *Gondwana Res.* 10, 77–85.
- Chin, G., Brylow, S., Foote, M., Garvin, J., Kasper, J., Keller, J., Litvak, M., Mitrofanov, I., Paige, D., Raney, K. and Robinson, M., 2007. Lunar reconnaissance orbiter overview: The instrument suite and mission. *Space Science Reviews*, 129(4), pp.391-419.
- Chopelas, A.M. Hofmeister, 1991. Vibrational spectroscopy of aluminate spinels at 1 atm and of MgAl₂O₄ to over 200 kbar, *Phys. Chem. Miner.* 18, 279–293.
- Cintala M. J., Wood C. A., and Head J. W., 1977. The effects of target characteristics on fresh crater morphology: Preliminary results for the Moon and Mercury. *Proc. Lunar Sci. Conf.* 8th, pp. 3409–3425.
- Cintala, M.J. and Grieve, R.A., 1998. Scaling impact melting and crater dimensions: Implications for the lunar cratering record. *Meteoritics & Planetary Science*, 33(4), pp.889-912.
- Clark R. N. and Roush T. L., 1984. Reflectance spectroscopy: Quantitative analysis techniques for remote sensing applications. *Journal of Geophysical Research: Solid Earth* 89:6329–6340.
- Clark, A.S. Collins, M. Santosh, R. Taylor, B.P. Wade, 2009. The PTt architecture of a Gondwanan suture: REE, U-Pb and Ti-in-zircon thermometric constraints from the Palghat Cauvery shear system, South India, *Precamb. Res.* 174, 129–144.
- Clark, R.N. and Roush, T.L., 1984. Reflectance spectroscopy: Quantitative analysis techniques for remote sensing applications. *Journal of Geophysical Research: Solid Earth*, 89(B7), pp.6329-6340.
- Clark, R.N., 1981. Water frost and ice: The near-infrared spectral reflectance 0.65–2.5 μm . *Journal of Geophysical Research: Solid Earth*, 86(B4), pp.3087-3096.

- Clark, R.N., 2009. Detection of adsorbed water and hydroxyl on the Moon. *Science*, 326(5952), pp.562-564.
- Clark, R.N., Roush, T.L., 1984. Reflectance spectroscopy: Quantitative analysis techniques for remote sensing applications. *J. Geophys. Res. Solid Earth* 89 (B7), 6329–6340.
- Clark, 1983. Spectral properties of mixtures of montmorillonite and dark carbon grains: Implications for remote sensing minerals containing chemically and physically adsorbed water, *J. Geophys. Res. Solid Earth* 88, 10635–10644.
- Cloutis E. A. and Gaffey M. J., 1991a. Spectral-compositional variations in the constituent minerals of mafic and ultramafic assemblages and remote sensing implications. *Earth, Moon, and Planets* 53:11–53.
- Cloutis, E.A. and Gaffey, M.J., 1991b. Pyroxene spectroscopy revisited: Spectral-compositional correlations and relationship to geothermometry. *Journal of Geophysical Research: Planets*, 96(E5), pp.22809-22826.
- Cloutis, E.A., Gaffey, M.J., Jackowski, T.L., Reed, K.L., 1986. Calibrations of phase abundance, composition, and particle size distribution for olivine-orthopyroxene mixtures from reflectance spectra. *J. Geophys. Res. Solid Earth* 91 (B11), 11641–11653.
- Cloutis, J.M. Sunshine, R.V. Morris, 2004. Spectral reflectance-compositional properties of spinels and chromites: Implications for planetary remote sensing and geothermometry, *Meteorit. Planet. Sci.* 39, 545–565.
- Cloutis, K.A. McCormack, J.F. Bell III, A.R. Hendrix, D.T. Bailey, M.A. Craig, S.A. Mertzman, M.S. Robinson, M.A. Riner, 2008. Ultraviolet spectral reflectance properties of common planetary minerals, *Icarus* 197 (1) 321–347.
- Cloutis, M.J. Gaffey, 1993. Lunar regolith analogues: Spectral reflectance properties of compositional variations, *Icarus* 102, 203–224.
- Cohen, B.A., Swindle, T.D. and Kring, D.A., 2000. Support for the lunar cataclysm hypothesis from lunar meteorite impact melt ages. *Science*, 290(5497), pp.1754-1756.
- Collins, C. Clark, K. Sajeev, M. Santosh, D.E. Kelsey, M. Hand, 2007. Passage through India: The Mozambique Ocean suture, high-pressure granulites and the Palghat-Cauvery shear zone system, *Terra Nova* 19, 141–147.
- Conel, 1965. Infrared thermal emission from silicates, Jet Propulsion Laboratory Technical, Memorandum.
- Conrad, R.W. Kay, 1984. Ultramafic and mafic inclusions from Adak Island: crystallization

- history, and implications for the nature of primary magmas and crustal evolution in the Aleutian Arc, *J. Petrol.* 25 (1) 88–125.
- Coombs C. R., 1989. Explosive volcanism on the Moon and the development of lunar sinuous rilles and their terrestrial analogs. PhD dissertation, University of Hawaii, Honolulu.
- Coombs C. R. and Hawke B. R., 1992. Pyroclastic deposits on the western limb of the Moon. *Proceedings, 22nd Lunar and Planetary Science Conference Proceedings*, pp. 303–312.
- Crawford, A.J. and Cameron, W.E., 1985. Petrology and geochemistry of Cambrian boninites and low-Ti andesites from Heathcote, Victoria. *Contributions to Mineralogy and Petrology*, 91(1), pp.93-104.
- Croft S. K., 1980. Cratering flow field: Implications for the excavation and transient expansion stages of crater formation. *Proc. Lunar Planet. Sci. Conf.* 11th, pp. 2347–2378.
- Croft, S.K., 1985. Morphology and mechanics of terraces in lunar craters. *Reports of Planetary Geology and Geophysics Program*.
- Croft, S.K., 1985. The scaling of complex craters. *Journal of Geophysical Research: Solid Earth*, 90(S02), pp.C828-C842.
- Cynn, S.K. Sharma, T.F. Cooney, M. Nicol, 1992. High-temperature Raman investigation of order-disorder behavior in the $MgAl_2O_4$ spinel, *Physical Review B* 45, 500.
- D’Ippolito, G.B. Andreozzi, D. Bersani, P.P. Lottici, 2015. Raman fingerprint of chromate, aluminate and ferrite spinels, *J. Raman Spectrosc.* 46, 1255– 1264.
- Dalton J., Hollister L. S., Kulick C. G., and Hargraves R. B., 1974. The nature of the chromite to ulvöspinel transition in mare basalt 15555 (abstract). In *Lunar Science V*, pp. 160–162. The Lunar Science Institute, Houston
- Davis P. A., 1980. Iron and titanium distribution on the Moon from orbital gamma ray spectrometry with implications for crustal evolutionary models. *J. Geophys. Res.*, 85, 3209– 3224.
- De Vries J., van den Berg A., and van Westrenen W., 2010. Formation and evolution of a lunar core from ilmenite-rich magma ocean cumulates. *Earth and Planetary Science Letters* 292:139–147.
- Degiorgi, I. Blatter-Mörke, P. Wachter, 1987. Magnetite: Phonon modes and the Verwey transition, *Physical Review B* 35, 5421.
- DeHon, R.A., 1977. Mare Humorum and Mare Nubium-Basalt thickness and basin-forming history. *Lunar Planet Sci. Conf.* 8, 633–641.

- Delano J. W., 1990. Buoyancy-driven melt segregation in the earth's moon, I. Numerical results. Proceedings, 20th Lunar and Planetary Science Conference. pp. 3–12.
- Dence M. R., Grieve R. A. F., and Robertson P. B., 1977. Terrestrial impact structures: Principal characteristics and energy considerations. In *Impact and Explosion Cratering* (D. J. Roddy, R. O. Pepin, and R. B. Merrill, eds.), pp. 247– 275. Pergamon, New York.
- Dence, M.R., 1971. Impact melts. *Journal of Geophysical Research*, 76(23), pp.5552-5565.
- Denevi, B.W., Lucey, P.G., Hochberg, E.J. and Steutel, D., 2007. Near-infrared optical constants of pyroxene as a function of iron and calcium content. *Journal of Geophysical Research: Planets*, 112(E5).
- Desai, A.J., Mohan, S. and Murty, S.V., 2016, July. Modelling of lunar crater ejecta extent for highland and mare using Mini-RF data. In *2016 IEEE International Geoscience and Remote Sensing Symposium (IGARSS)* (pp. 1158-1161). IEEE.
- Dhanya, M.B., Bhardwaj, A., Futaana, Y., Barabash, S., Alok, A., Wieser, M., Holmström, M. and Wurz, P., 2016. Characteristics of proton velocity distribution functions in the near-lunar wake from Chandrayaan-1/SWIM observations. *Icarus*, 271, pp.120-130.
- Dhanya, M.B., Bhardwaj, A., Futaana, Y., Fatemi, S., Holmström, M., Barabash, S., Wieser, M., Wurz, P., Alok, A. and Thampi, R.S., 2013. Proton entry into the near-lunar plasma wake for magnetic field aligned flow. *Geophysical Research Letters*, 40(12), pp.2913-2917.
- Dhingra, C.M. Pieters, J.W. Boardman, J.W. Head, P.J. Isaacson, L.A. Taylor, 2011a. Compositional diversity at Theophilus Crater: Understanding the geological context of Mg-spinel bearing central peaks, *Geophys. Res. Lett.* 38.
- Dhingra, D. and Pieters, C.M., 2011b, November. Mg-Spinel rich lithology at crater Copernicus. In *Annual Meeting of the Lunar Exploration Analysis Group* (Vol. 1646, p. 9).
- Dhingra, D., Head, J.W. and Pieters, C.M., 2015, March. Impact Melt Wavefronts at Lunar Complex Craters: Morphological Characteristics and Insights into Impact Melt Emplacement Dynamics. In *Lunar and Planetary Science Conference* (No. 1832, p. 1645).
- Dhingra, D., Head, J.W. and Pieters, C.M., 2016, March. Elevation differences on the floors of complex craters: Insights into the crater evolution processes. In *Lunar and Planetary Science Conference* (No. 1903, p. 2718).

- Dhingra, D., Head, J.W. and Pieters, C.M., 2017a. Geological mapping of impact melt deposits at lunar complex craters Jackson and Tycho: Morphologic and topographic diversity and relation to the cratering process. *Icarus*, 283, pp.268-281.
- Dhingra, D., Pieters, C.M. and Head, J.W., 2011c, December. Large Impact Melt Flow Feature identified across the floor of Copernicus Crater by Moon Mineralogy Mapper (M 3). In AGU Fall Meeting Abstracts (Vol. 2011, pp. P13D-1690).
- Dhingra, J.F. Mustard, S. Wiseman, M. Pariente, C.M. Pieters, P.J. Isaacson, 2011d. Non-linear spectral un-mixing using Hapke Modeling: Application to remotely acquired M3 spectra of spinel bearing lithologies on the moon, 2431.
- Dhingra, R.D., Dhingra, D. and Carlson, L., 2014, March. Evaluating the extent of impact melt on central peaks of lunar complex impact craters. In Lunar and Planetary Science Conference (No. 1777, p. 1754).
- Dhingra, D., Glotch, T.D., Prissel, T.C., Parman, S.W., Pieters, C.M. and Greenhagen, B.T., 2017b, March. Mg-spinel exposures within silica rich setting on Hansteen Alpha: probing the geologic context. In 48th Annual Lunar and Planetary Science Conference (No. 1964, p. 2104).
- Donaldson-Hanna K. L., Cheek L., Pieters C., Mustard J., Greenhagen B., Thomas I., and Bowles N., 2014. Global assessment of pure crystalline plagioclase across the Moon and implications for the evolution of the primary crust. *Journal of Geophysical Research: Planets* 119:1516–1545.
- Drury, N.B. Harris, R.W. Holt, G.J. Reeves-Smith, R.T. Wightman, 1984. Precambrian tectonics and crustal evolution in South India, *The Journal of Geology* 92 (1), 3–20.
- Dubessy, M.C. Caumon, F. Rull, 2012. Raman spectroscopy applied to earth sciences and cultural heritage, *Mineralogical Society of Great Britain and Ireland*.
- Dundas, C.M. and McEwen, A.S., 2007. Rays and secondary craters of Tycho. *Icarus*, 186(1), pp.31-40.
- Dutta, U.K. Bhui, P. Sengupta, S. Sanyal, D. Mukhopadhyay, 2011. Magmatic and metamorphic imprints in 2.9 Ga chromitites from the Sittampundi Anorthosite complex, Tamil Nadu, India, *Ore Geol. Rev.* 40, 90–107.
- Edwin Roedder, Paul.M. Weinblen, 1973. Petrology of some lithic fragments of Luna 20, *Geochemica et Cosmochimica Acta*, 1973, Vol.37, pp.1031 to 1052.
- El Goresy A. and Ramdohr P., 1977. Apollo 17 TiO₂-rich basalts: Reverse spinel zoning as

- evidence for subsolidus equilibration of the spinel-ilmenite assemblage. *Proc. Lunar Sci. Conf. 8th*, pp. 1611–1624.
- El Goresy A., Prinz M., and Ramdohr P., 1976. Zoning in spinels as an indicator of the crystallization histories of mare basalts. *Proc. Lunar Sci. Conf. 7th*, pp. 1261–1279.
- El Goresy, L.A. Taylor, P. Ramdohr, 1972. Fra Mauro crystalline rocks: Mineralogy, geochemistry, and subsolidus reduction of opaque minerals. *Proc. Lunar Sci. Conf. 3rd*, 333–349.
- Elardo S. M., Draper D. S., and Shearer C. K. Jr., 2011. Lunar magma ocean crystallization revisited: Bulk composition, early cumulate mineralogy, and the source regions of the highlands Mg-suite. *Geochimica et Cosmochimica Acta* 75:3024–3045.
- Elkins-Tanton L. T., Hager B. H., and Grove T. L., 2004. Magmatic effects of the lunar late heavy bombardment. *Earth and Planetary Science Letters* 222:17–27.
- Engi, 1983. Equilibria involving Al-Cr spinel: Mg-Fe exchange with olivine. Experiments, thermodynamic analysis, and consequences for geothermometry, *Amer. Jour. Sci.* 283 , 29–71.
- Evans, B.R. Frost, 1975. Chrome spinels in progressive metamorphism—a preliminary analysis, *Geochim. Cosmochim. Acta* 39.
- Fan, J., and Kerrich, R., 1997. Geochemical characteristics of aluminum depleted and undepleted komatiites and HREE-enriched low-Ti tholeiites, western Abitibi greenstone belt: A heterogeneous mantle plume-convergent margin environment. *Geochimica et Cosmochimica Acta*, 61(22), pp.4723-4744.
- Farmer, 1974. *Infrared spectra of minerals*, Mineralogical Society.
- Farr, T.G., Bates, B.A., Ralph, R.L. and Adams, J.B., 1980. Effects of overlapping optical absorption bands of pyroxene and glass on the reflectance spectra of lunar soils. In *Lunar and Planetary Science Conference Proceedings (Vol. 11, pp. 719-729)*.
- Ferini, G.A. Baratta, M.E. Palumbo, 2004. A Raman study of ion irradiated icy mixtures, & *A* 414, 757–766.
- Flahaut, J., Blanchette-Guertin, J.-F., Jilly, C., Sharma, P., Souchon, A., Van Westrenen, W., & Kring, D. A., 2012. Identification and characterization of science-rich landing sites for lunar lander missions using integrated remote sensing observations. *Advances in Space Research*, 50(12), 1647–1665.
- Fortezzo C. M. and Hare T. M., 2013. Completed digital renovation of the 1:5,000,000 lunar

- geologic map series (abstract #2114). 44th Lunar and Planetary Science Conference. CD-ROM.
- Freed A. M., Johnson B. C., Blair D. M., Melosh H., Neumann G. A., Phillips R. J., Solomon S. C., Wieczorek M. A., and Zuber M. T., 2014. The formation of lunar mascon basins from impact to contemporary form. *Journal of Geophysical Research: Planets* 119:2378–2397.
- Freitas Suita, A.J. Strieder, 1996. Cr-spinels from Brazilian mafic-ultramafic complexes: metamorphic modifications, *Int. Geol. Rev.* 38, 245–267.
- Gaddis L. R., Staid M. I., Tyburczy J. A., Hawke B. R., and Petro N. E., 2003. Compositional analyses of lunar pyroclastic deposits. *Icarus* 161:262–280.
- Gaffey M. J., Bell J. F., Brown R. H., Burbine T. H., Piatek J. L., Reed K. L., and Chaky D. A., 1993. Mineralogical variations within the S-type asteroid class. *Icarus* 106:573–602.
- Gaffey M. J., Cloutis E. A., Kelley M. S., and Reed K. L., 2002. Mineralogy of asteroids. In *Asteroids III*, edited by Bottke W. F., Cellino A., Paolicchi P., and Binzel R. P. Tucson, Arizona: The University of Arizona Press. pp. 183–204.
- Gaffey, 1974. A systematic study of the spectral reflectivity characteristics of the meteorite classes with applications to the interpretation of asteroid spectra for mineralogical and petrological information, Doctoral dissertation, Massachusetts Institute of Technology.
- Gaffey, S.J., 1986. Spectral reflectance of carbonate minerals in the visible and near infrared (0.35–2.55 microns); calcite, aragonite, and dolomite. *American Mineralogist*, 71(1-2), pp.151-162.
- Gasparov, D.B. Tanner, D.B. Romero, H. Berger, G. Margaritondo, L. Forro, 2000. Infrared and Raman studies of the Verwey transition in magnetite, *Phys. Rev. B* 62, 7939.
- Gault D. E., Quaide W. L., and Oberbeck V. R., 1968. Impact cratering mechanics and structures. In *Shock Metamorphism of Natural Materials* (B. M. French and N. M. Short, eds.), pp. 87–99. Mono, Baltimore
- Gault D. E., 1973. Displaced mass, depth, diameter, and effects of oblique trajectories for impact craters formed in dense crystalline rocks. *Moon* 6:32–44
- Gault, D.E. and Wedekind, J.A., 1978. Experimental studies of oblique impact. In *Lunar and Planetary Science Conference Proceedings* (Vol. 9, pp. 3843-3875).
- Geological Survey of India (GSI), 2001. Tectonic Map of India, 1:2 Million Scale.
- Ghisler, 1970. Pre-metamorphic folded chromite deposits of stratiform type in the early

- Precambrian of West Greenland, *Miner. Deposita*, 223–236.
- Ghosh, M.J. de Wit, R.E. Zartman, 2004. Age and tectonic evolution of Neoproterozoic ductile shear zones in the Southern Granulite Terrain of India, with implications for Gondwana studies, *Tectonics* 23.
- Ghosh, R. Konar, 2011. Chromites from meta-anorthosites, Sittampundi Anorthosite igneous complex, Tamil Nadu, southern India, *J. Asian Earth Sci.* 42, 1394–1402.
- Ghosh, R. Konar, 2012. Textural developments in chromite deforming under eclogite-facies conditions from the Neoarchean Sittampundi anorthosite complex, southern India, *Geological Journal* 47 (2–3), 253–262.
- Giguere T. A., Taylor G. J., Hawke B. R., and Lucey P. G., 2000. The titanium contents of lunar mare basalts. *Meteoritics & Planetary Science* 35:193–200.
- Gillis, J. J., and Jolliff, B. L., 1999. Lateral and vertical heterogeneity of thorium in the Procellarum KREEP Terrane: As reflected in the ejecta deposits of post-Imbrium craters, in *Workshop on New Views of the Moon II: Understanding the Moon through the Integration of Diverse Datasets*, LPI Contrib. 980, pp. 18-19, Lunar and Planetary Institute, Houston, Texas
- Gopala Krishna B., Sanjay S., Srivastava P., and Kiran Kumar A., 2009. Digital elevation models of the lunar surface from Chandrayaan-1 Terrain Mapping Camera (TMC) imagery—Initial results (abstract #1694). 40th Lunar and Planetary Science Conference. CD-ROM.
- Gores, P.A. and Spray, J.G., 2021. Hypervelocity impact of anorthosite: Excavation, spallation and crater reconstruction. *International Journal of Impact Engineering*, p.104078.
- Goswami, J.N. and Annadurai, M., 2008. Chandrayaan-1 mission to the Moon. *Acta Astronautica*, 63(11-12), pp.1215-1220.
- Goswami, J.N. and Annadurai, M., 2009. Chandrayaan-1: India's first planetary science mission to the Moon. *Current science*, pp.486-491.
- Green, R., Pieters, C., Mouroulis, P., Eastwood, M., Boardman, J., Glavich, T., Isaacson, P., Besse, S., Barr, D., 2011. The Moon Mineralogy Mapper (M3) imaging spectrometer for lunar science: instrument description, calibration, on-orbit measurements, science data calibration and on-orbit validation. *J. Geophys. Res.: Plan* 116 (E10).
- Greg Michael, 2012. Measuring the age of planetary surfaces using crater statistics: Guide to the Craterstats software. Planetary surface dating from crater statistics – PGM Meeting,

USGS Flagstaff, 19 June 2012.

- Greskovich, V.S. Stubican, 1966. Divalent chromium in magnesium-chromium spinels, *J. Phys. Chem. Solids* 27, 1379–1384.
- Grieve R. A. F. and Robertson P. B., 1979. The terrestrial cratering record: I. Current status of observations. *Icarus*, 38, 212–229.
- Grieve R. A. F., Robertson P. B., and Dence M. R., 1981. Constraints on the formation of ring impact structures, based on terrestrial data. In *Multi-Ring Basins, Proc. Lunar Planet. Sci. 12A* (P. H. Schultz and R. B. Merrill, eds.), pp. 37–58. Pergamon, New York.
- Gross, A.H. Treiman, 2011. Unique spinel-rich lithology in lunar meteorite ALHA 81005: Origin and possible connection to M3 observations of the farside highlands, *J. Geophys. Res.* 116, E10009.
- Gross, J. Gillis-Davis, P.J. Isaacson, L. Le, 2015. How rich is rich? Placing constraints on the abundance of spinel in the pink spinel anorthosite lithology on the Moon through space weathering.
- Gross, J., Treiman, A. H., & Le, L., 2011. Unique spinel-rich lithology in lunar meteorite ALHA81005: Origin and possible connection to M3 observations of the farside highlands. *Lunar and Planetary Science Conference*, 42, 2–3.
- Gross, P.J. Isaacson, A.H. Treiman, L. Le, J.K., 2014. Gorman, Spinel-rich lithologies in the lunar highland crust: Linking lunar samples with crystallization experiments and remote sensing, *Am. Mineral.* 99, 1849–1859.
- Guha, B. Ghosh, S. Chaudhury, K. Rani, K.V. Kumar, 2018. Spectral response of few important textural variants of chromitite and its potential in estimating relative grades of chromitite—a case study for chromitite of Nuggihalli Schist Belt, India, *Current Science* 114 (8), 1721.
- Hackwill, T., Guest, J., Spudis, P., 2006. Stratigraphy and evolution of basalts in mare Humorum and south-eastern procellarum. *Meteoritics Planet Sci.* 41 (3), 479–488.
- Haggerty S. E., 1971a. Compositional variations in lunar spinels. *Nature Phys. Sci.*, 233, 156–160.
- Haggerty S. E., 1971b. Subsolidus reduction of lunar spinels. *Nature Phys. Sci.*, 234, 113–117. compositional variations of spinels. *Proc. Lunar Sci. Conf.* 3rd, pp. 305–333.
- Haggerty S. E., 1972a. Chemical characteristics of spinels in some Apollo 15 basalts (abstract). In *The Apollo 15 Lunar Samples* (J. W. Chamberlain and C. Watkins, eds.), pp. 92–97.

The Lunar Science Institute, Houston.

- Haggerty S. E., 1972b. Luna 16: An opaque mineral study and a systematic examination of compositional variations of spinels from Mare Fecunditatis. *Earth Planet. Sci. Lett.*, 13, 328–352.
- Haggerty S. E., 1972c. Solid solutions, subsolidus reduction and compositional characteristics of spinels in some Apollo 15 basalts. *Meteoritics*, 7, 353–370.
- Haggerty S. E., 1973a. Luna 20: Mineral Chemistry of spinel, pleonaste, chromite, ulvöspinel, ilmenite, and rutile. *Geochim. Cosmochim. Acta*, 37, 857–867.
- Haggerty S. E., 1978a. Luna 24: Systematics in spinel mineral chemistry in the context of an intrusive petrogenetic grid. In *Mare Crisium: The View From Luna 24*, (R. B. Merrill and J. J. Papike, eds.), pp. 523–536. Pergamon, New York.
- Haggerty, 1972d. Apollo 14 subsolidus reduction and compositional variations of spinels. *Proc. Lunar Sci. Conf. 3rd*, 305–333.
- Haggerty, 1977. Apollo 14: Oxide, metal, and olivine mineral chemistries in 14072 with a bearing on the temporal relationships of subsolidus reduction. *Proc. Lunar Sci. Conf. 8th*, 1809–1829.
- Haggerty, 1972e. Chemical characteristics of spinels in some Apollo 15 basalts (abstract), in: J.W. Chamberlain, C. Watkins (Eds.), *The Apollo 15 Lunar Samples*, Houston, The Lunar Science Institute, pp. 92–97.
- Haggerty, 1971c. Compositional variations in lunar spinels, *Nature Phys. Sci.* 233, 156–160.
- Haggerty, 1972f. Luna 16: An opaque mineral study and a systematic examination of compositional variations of spinels from Mare Fecunditatis, *Earth Planet. Sci. Lett.* 13, 328–352.
- Haggerty, 1973b. Luna 20: Mineral Chemistry of spinel, pleonaste, chromite, ulvöspinel, ilmenite, and rutile, *Geochim. Cosmochim. Acta* 37, 857– 867.
- Haggerty, 1978b. Luna 24: Systematics in spinel mineral chemistry in the context of an intrusive petrogenetic grid, in: R.B. Merrill, J.J. Papike (Eds.), *Mare Crisium: The View from Luna 24*, Pergamon, New York, pp. 523–536.
- Haggerty, 1988. Upper mantle opaque mineral stratigraphy and the genesis of metasomatites and alkali-rich melts, *J. Geol. Soc. Austr.* 14..
- Halliday, A.N., 2000. Terrestrial accretion rates and the origin of the Moon. *Earth and Planetary Science Letters*, 176(1), pp.17-30.

- Hapke, B., Cassidy, W. and Wells, E., 1975. Effects of vapor-phase deposition processes on the optical, chemical, and magnetic properties of the lunar regolith. *The moon*, 13(1), pp.339-353.
- Hargitai, H. and Kereszturi, Á. eds., 2015. *Encyclopedia of planetary landforms*. Springer New York.
- Hartmann W. and Kuiper G. P. 1962. Concentric structures surrounding lunar basins. *Communications of the Lunar and Planetary Laboratory* 1:51–66.
- Hartmann, W.K. and Davis, D.R., 1975. Satellite-sized planetesimals and lunar origin. *Icarus*, 24(4), pp.504-515.
- Haruyama, J., Matsunaga, T., Ohtake, M., Morota, T., Honda, C., Yokota, Y., Torii, M., Ogawa, Y., Group, L.W., 2008. Global lunar-surface mapping experiment using the lunar imager/spectrometer on SELENE. *Earth Planets Space* 60 (4), 243–255.
- Haruyama, J., Ohtake, M., Matsunaga, T., Morota, T., Honda, C., Yokota, Y., Abe, M., Ogawa, Y., Miyamoto, H., Iwasaki, A., Pieters, C.M., 2009. Long-lived volcanism on the lunar farside revealed by SELENE Terrain Camera. *Science* 323 (5916), 905–908.
- Hawke B., Coombs C., Gaddis L., Lucey P., and Owensby P., 1989. Remote sensing and geologic studies of localized dark mantle deposits on the Moon. *Proceedings, 19th Lunar and Planetary Science Conference*. pp. 255–268.
- Hawke B., Giguere T., Gaddis L., Gustafson O., Lawrence S., Stopar J., Peterson C., Bell J., and Robinson M., 2012. Localized pyroclastic deposits in the Grimaldi region of the Moon. (abstract #1749). 43rd Lunar and Planetary Science Conference. CD-ROM.
- Hawke, B. R., & Head, J. W., 1977a. Impact melt on lunar crater rims. In *Impact and Explosion Cratering: Planetary and Terrestrial Implications; Proceedings of the Symposium on Planetary Cratering Mechanics* (pp. 815–841). Flagstaff, AZ, New York: Pergamon Press, Inc.
- Hawke, B.R. and Head, J.W., 1977b. March. Impact melt in lunar crater interiors. In *Lunar and Planetary Science Conference* (Vol. 8).
- Hawke, B.R., Blewett, D.T., Lucey, P.G., Smith, G.A., Bell III, J.F., Campbell, B.A. and Robinson, M.S., 2004. The origin of lunar crater rays. *Icarus*, 170(1), pp.1-16.
- Hawke, B.R., Spudis, P.D., Taylor, G.J., Lucey, P.G., Peterson, C.A., 1993. The distribution and modes of occurrence of anorthosite on the Moon. *Meteoritics* 28.
- Hazen, P.M. Bell, H.K. Mao, 1978. Effects of compositional variation on absorption spectra

of lunar pyroxenes, 2919-2934.

He, Y.Q. Wang, Z.A. Bao, P.M. George, S. Veni, K. Sajeev, J.H. Guo, M.G. Zhai, 2020. Role of melt injection and mixing in the formation of chromitite in Archean megacrystic anorthosites: Evidence from the Sittampundi anorthosite complex, southern India, *Precamb. Res.* 105914.

Head III, J.W., 1976. Lunar volcanism in space and time. *Rev. Geophys.* 14 (2), 265–300.

Head III, J.W., Wilson, L., 1992. Lunar mare volcanism: stratigraphy, eruption conditions, and the evolution of secondary crusts. *Geochem. Cosmochim. Acta* 56 (6), 2155–2175.

Head, J.W., 1975. Processes of lunar crater degradation: Changes in style with geologic time. *The Moon*, 12(3), pp.299-329.

Head, J.W., 1977. Origin of outer rings in lunar multi-ringed basins-Evidence from morphology and ring spacing. In *Impact and Explosion Cratering: Planetary and Terrestrial Implications* (pp. 563-573).

Heiken GH, Vaniman DT, French BM, 1991. In: Heiken GH, Vaniman DT, French BM (eds) *Lunar source book-a user's guide to the Moon*, Lunar and Planetary Institute. Cambridge University Press, Houston

Herrick, R.R. and Forsberg-Taylor, N.K., 2003. The shape and appearance of craters formed by oblique impact on the Moon and Venus. *Meteoritics & Planetary Science*, 38(11), pp.1551-1578.

Hess P. C. and Parmentier E., 1995. A model for the thermal and chemical evolution of the Moon's interior: Implications for the onset of mare volcanism. *Earth and Planetary Science Letters* 134:501–514.

Hiesinger H., Jaumann R., Neukum G., and Head J. W. III, 2000. Ages of mare basalts on the lunar nearside. *Journal of Geophysical Research: Planets* 105:29,239–29,275.

Hiesinger, H., 2003. Ages and stratigraphy of mare basalts in Oceanus Procellarum, Mare Nubium, Mare Cognitum, and Mare Insularum. *Journal of Geophysical Research*, 108(E7), 5065.

Hiesinger, H., Head III, J., Wolf, U., Jaumann, R., Neukum, G., 2010. Ages and stratigraphy of lunar mare basalts in Mare Frigoris and other nearside maria based on crater size-frequency distribution measurements. *J. Geophys. Res.: Plan* 115 (E3).

Hiesinger, H., Head III, J.W., Wolf, U., Jaumann, R., Neukum, G., 2003. Ages and stratigraphy of mare basalts in Oceanus Procellarum, mare Nubium, mare Cognitum, and mare

- Insularum. *J. Geophys. Res.*: Plan 108 (E7).
- Hiesinger, H., Head, J., 2006. New views of lunar geoscience: an introduction and overview. *Reviews in Mineralogy and Geochemistry* 60, 1–81.
- Hiesinger, H., Head, J.W., Wolf, U., Jaumann, R., Neukum, G., 2011. Ages and stratigraphy of lunar mare basalts: a synthesis. *Recent Advances and Current Research Issues in Lunar Stratigraphy* 477, 1–51.
- Hiesinger, H., Jaumann, R., Neukum, G. and Head, J.W., 2000. Ages of mare basalts on the lunar nearside. *Journal of Geophysical Research: Planets*, 105(E12), pp.29239-29275.
- Hill, R., and Roeder, P., 1974. The crystallization of spinel from basaltic liquid as a function of oxygen fugacity. *The Journal of Geology*, 82(6), pp.709-729.
- Hirata, M. Ohtake, T. Hiroi, Y. Yokota, 2013. A new type of pyroclastic deposit on the Moon containing Fe-spinel and chromite, *Geophys. Res. Lett.* 40, 4549–4554.
- Holsapple K. A. and Schmidt R. M., 1986. Point source solutions and coupling parameters in cratering mechanics. *J. Geophys. Res.*, 92, 6350–6376.
- Horgan, B. H. N., Cloutis, E. A., Mann, P., & Bell, J. F., 2014. Near-infrared spectra of ferrous mineral mixtures and methods for their identification in planetary surface spectra. *Icarus*, 234, 132–154.
- Hörz, F., Grieve, R., Heiken, G., Spudis, P. and Binder, A., 1991. Lunar surface processes. *Lunar sourcebook*, pp.61-120.
- Hörz, F., Ostertag, R. and Rainey, D.A., 1983. Bunte Breccia of the Ries: Continuous deposits of large impact craters. *Reviews of Geophysics*, 21(8), pp.1667-1725.
- Howard, K.A., 1974. Fresh lunar impact craters - Review of variations with size. In *Lunar and Planetary Science Conference Proceedings (Vol. 5, pp. 61-69)*.
- Huguenin, R.L. and Jones, J.L., 1986. Intelligent information extraction from reflectance spectra: Absorption band positions. *Journal of Geophysical Research: Solid Earth*, 91(B9), pp.9585-9598.
- Hunt, J.C. Wynn, 1979. Visible and near-infrared spectra of rocks from chromium-rich areas, *Geophysics* 44, 820–825.
- Hunt, 1970. Visible and near-infrared spectra of minerals and rocks: I silicate minerals, *Modern Geol.* 1, 283–300.
- Inoue, T., Rapp, R.P., Zhang, J., Gasparik, T., Weidner, D.J. and Irifune, T., 2000. Garnet

fractionation in a hydrous magma ocean and the origin of Al-depleted komatiites: melting experiments of hydrous pyrolite with REEs at high pressure. *Earth and Planetary Science Letters*, 177(1-2), pp.81-87.

Irvine, 1965. Chromian spinel as a petrogenetic indicator: Part 1. Theory, *Canadian Journal of Earth Sciences* 2 (6) 648–672.

Irvine, 1967. Chromian spinel as a petrogenetic indicator: Part 2 Petrologic applications, *Can. J. Earth Sci.* 4, 71–103.

Isaacson P. J., Petro N. E., Pieters C. M., Besse S., Boardman J. W., Clark R. N., Green R. O., Lundeen S., Malaret E., and McLaughlin S., 2013. Development, importance, and effect of a ground truth correction for the Moon Mineralogy Mapper reflectance data set. *Journal of Geophysical Research: Planets* 118:369–381.

Isaacson P. J., Pieters C. M., Besse S., Clark R. N., Head J. W., Klima R. L., Mustard J. F., Petro N. E., Staid M. I., and Sunshine J. M., 2011. Remote compositional analysis of lunar olivine-rich lithologies with moon mineralogy mapper (M3) spectra. *Journal of Geophysical Research: Planets* 116:E00G11.

Isaacson, J.J. Gillis-Davis, C. Jackson, T.C. Prissel, S. Parman, K. Donaldson Hanna, L. Cheek, 2014. Experimental weathering of synthetic spinels, LPSC 45, #1612.

Jackson, L.C. Cheek, K.B. Williams, K.D. Hanna, C.M. Pieters, S.W. Parman, R.F. Cooper, M.D. Dyar, M. Nelms, M.R. Salvatore, 2014. Visible-infrared spectral properties of iron-bearing aluminite spinel under lunar-like redox conditions, *Am. Mineral.* 99 (10), 1821–1833.

Eckert Jr, J.O., Taylor, L.A. and Neal, C.R., 1991, March. Spinel troctolite from Apollo 17 breccia 73215: Evidence for petrogenesis as deep-seated lunar crust. In *Lunar and Planetary Science Conference (Vol. 22)*.

Janardhanan, B.E. Leake, 1975. The origin of the meta-anorthositic gabbros and garnetiferous granulites of the Sittampundi Complex, Madras, India, *Journal of Geological Society of India* 16, 391–408.

Jappji, M., Thesniya, P.M. and Rajesh, V.J., 2021, March. Morphology of the Copernican Das Crater on the Farside of the Moon. In *Lunar and Planetary Science Conference (No. 2548, p. 2260)*.

Jaumann, R., Hiesinger, H., Anand, M., Crawford, I.A., Wagner, R., Sohl, F., Jolliff, B.L., Scholten, F., Knapmeyer, M., Hoffmann, H. and Hussmann, H., 2012. Geology, geochemistry, and geophysics of the Moon: Status of current understanding. *Planetary*

- and Space Science, 74(1), pp.15-41.
- John D. Winter, 2001. An introduction to igneous and metamorphic petrology, Prentice Hall, New Jersey, United States p.15 – 45
- John, S. Balakrishnan, B.K. Bhadra, 2005. Contrasting metamorphism across Cauvery shear zone, south India, J. Earth Syst. Sci. 114, 143.
- Jolliff, B.L., Gillis, J.J., Haskin, L.A., Korotev, R.L. and Wieczorek, M.A., 2000. Major lunar crustal terranes: Surface expressions and crust-mantle origins. Journal of Geophysical Research: Planets, 105(E2), pp.4197-4216.
- Jozwiak, L. M., Head, J. W., & Wilson, L., 2016. An analysis of eruption styles in lunar floor-fractured craters. In Lunar and Planetary Science Conference (Vol. 47, 1169 pp.).
- Jozwiak, L. M., Head, J. W., Zuber, M. T., Smith, D. E., & Neumann, G. A., 2012. Lunar floor-fractured craters: Classification, distribution, origin and implications for magmatism and shallow crustal structure. Journal of Geophysical Research, 117, E11005.
- Jozwiak, L. M., Head, J.W. I., Neumann, G. A., & Wilson, L., 2016. Observational constraints on the identification of shallow lunar magmatism: Insights from floor-fractured craters. Icarus, 0, 1–8.
- Kalynn, J., Johnson, C.L., Osinski, G.R. and Barnouin, O., 2011, March. Topographic characterization of complex lunar craters with LOLA data. In Lunar and Planetary Science Conference (Vol. 42, p. 1514).
- Karmakar, S. Mukherjee, S. Sanyal, P. Sengupta, 2017. Origin of peraluminous minerals (corundum, spinel, and sapphirine) in a highly calcic anorthosite from the Sittampundi Anorthosite Complex, Tamil Nadu, India, Contr. Mineral. Petrol. 172, 67.
- Kato, M., Sasaki, S. and Takizawa, Y., 2010. The Kaguya mission overview. Space Science Reviews, 154(1-4), pp.3-19.
- Kato, M., Sasaki, S., Tanaka, K., Iijima, Y. and Takizawa, Y., 2008. The Japanese lunar mission SELENE: Science goals and present status. Advances in Space Research, 42(2), pp.294-300.
- Kato, M., Takizawa, Y., Sasaki, S., & SELENE Project Team, 2006. SELENE, The Japanese lunar orbiting satellites mission: Present status and science goals. Paper presented at the 37th Lunar and Planetary Science Conference, Lunar and Planetary Institute, Houston, TX.
- Kato, S., Morota, T., Yamaguchi, Y., Watanabe, S.I., Otake, H. and Ohtake, M., 2017. Magma

source transition of lunar mare volcanism at 2.3 Ga. *Meteoritics & Planetary Science* 52(9), pp.1899-1915

Kaur, P. and Chauhan, P., 2014, March. Detection of spinels exposures from some near side locations of the Moon. In *Lunar and Planetary Science Conference* (Vol. 45, p. 2059).

Kaur, P., Bhattacharya, S., Chauhan, P., Kumar, A.K., 2013a. Mineralogy of mare Serenitatis on the near side of the moon based on Chandrayaan-1 moon mineralogy mapper (M3) observations. *Icarus* 222 (1), 137–148.

Kaur, P., Chauhan, P. and Ajai., 2013b. Exposures of Mg-spinel on an evolved silicic lithology Hansteen Alpha on the Moon. In *Lunar and Planetary Science Conference* (Vol. 44, p. 1348).

Kaur, P., Chauhan, P. and Ajai., 2013c. Detection of Mg-spinel exposures from the anorthositic terrain surrounding Mare Ingenii on the far side of the Moon. In *Lunar and Planetary Science Conference* (Vol. 44, p. 1547).

Kaur, P., Chauhan, P., Bhattacharya, S. and Kumar, A.S.K., 2012, March. Compositional Diversity at Tycho Crater: Mg-Spinel Exposures Detected from Moon Mineralogical Mapper (M³) Data. In *Lunar and Planetary Science Conference* (Vol. 43).

Kepezhinskas, M.J. Defant, M.S. Drummond, 1995. Na metasomatism in the island-arc mantle by slab melt-peridotite interaction: evidence from mantle xenoliths in the North Kamchatka Arc, *J. Petrol.* 36 (6), 1505–1527.

Kesson S., 1975. Mare basalts-melting experiments and petrogenetic interpretations. *Lunar and Planetary Science Conference Proceedings* 921–944.

Kesson S. E. and Ringwood A. E., 1976. Mare basalt petrogenesis in a dynamic Moon. *Earth and Planetary Science Letters* 30:155–163.

King T. V. and Ridley W. I., 1987. Relation of the spectroscopic reflectance of olivine to mineral chemistry and some remote sensing implications. *Journal of Geophysical Research: Solid Earth* 92:11457–11469.

Klima R. L., Dyar M. D., and Pieters C. M., 2011. Nearinfrared spectra of clinopyroxenes: Effects of calcium content and crystal structure. *Meteoritics and Planetary Science* 46:379–395.

Klima R., and Pieters C., and the M3 Team., 2010. The colorful Moon: Science discoveries from the Moon Mineralogy Mapper on Chandrayaan-1. In *Annual Meeting of the Lunar Exploration Analysis Group*.

- Klima, C.M. Pieters, M.D. Dyar, 2008. Characterization of the 1.2 μm M1 pyroxene band: Extracting cooling history from near-IR spectra of pyroxenes and pyroxene-dominated rocks, *Meteorit. Planet. Sci.* 43, 1591–1604.
- Klima, C.M. Pieters, M.D. Dyar, 2007. Spectroscopy of synthetic Mg-Fe pyroxenes I: Spin-allowed and spin-forbidden crystal field bands in the visible and near-infrared, *Meteorit. Planet. Sci.* 42, 235–253.
- Klima, R.L., Dyar, M.D. and Pieters, C.M., 2011. Near-infrared spectra of clinopyroxenes: Effects of calcium content and crystal structure. *Meteoritics & Planetary Science*, 46(3), pp.379-395.
- Klima, R.L., Pieters, C.M. and Dyar, M.D., 2007. Spectroscopy of synthetic Mg-Fe pyroxenes I: Spin-allowed and spin-forbidden crystal field bands in the visible and near-infrared. *Meteoritics & Planetary Science*, 42(2), pp.235-253.
- Klima, R.L., Pieters, C.M., Dyar, M.D., 2008. Characterization of the 1.2 μm M1 pyroxene band: extracting cooling history from near-IR spectra of pyroxenes and pyroxene dominated rocks. *Meteoritics Planet Sci.* 43 (10), 1591–1604.
- Kordas, J.F., Lewis, I.T., Priest, R.E., White, W.T., Nielsen, D.P., Park, H.S., Wilson, B.A., Shannon, M.J., Ledebuhr, A.G. and Pleasance, L.D., 1995, June. UV/visible Camera for the Clementine Mission. In *Space Telescopes and Instruments (Vol. 2478, pp. 175-187)*. International Society for Optics and Photonics.
- Kreslavsky, M.A., Head, J.W., Neumann, G.A., Rosenburg, M.A., Aharonson, O., Smith, D.E. and Zuber, M.T., 2013. Lunar topographic roughness maps from Lunar Orbiter Laser Altimeter (LOLA) data: Scale dependence and correlation with geologic features and units. *Icarus*, 226(1), pp.52-66.
- Krüger, T., Hergarten, S. and Kenkmann, T., 2018. Deriving Morphometric Parameters and the Simple-to-Complex Transition Diameter from a High-Resolution, Global Database of Fresh Lunar Impact Craters ($D \geq \sim 3$ km). *Journal of Geophysical Research: Planets*, 123(10), pp.2667-2690.
- Krüger, T., van Der Bogert, C.H. and Hiesinger, H., 2016. Geomorphologic mapping of the lunar crater Tycho and its impact melt deposits. *Icarus*, 273, pp.164-181.
- Kuiper, G.P., 1959. The exploration of the moon. *Vistas in astronautics*, 2, pp.273-313.
- Kumar, A.K. and Chowdhury, A.R., 2005. Terrain mapping camera for Chandrayaan-1. *Journal of earth system science*, 114(6), pp.717-720.

- Kumar, A.K., Chowdhury, A.R., Banerjee, A., Dave, A.B., Sharma, B.N., Shah, K.J., Murali, K.R., Mehta, S., Joshi, S.R. and Sarkar, S.S., 2009. Hyper spectral imager for lunar mineral mapping in visible and near infrared band. *Current Science*, pp.496-499.
- Kumar, A.S., Chowdhury, A.R., Banerjee, A., Dave, A.B., Sharma, B.N., Shah, K.J., Murali, K.R., Joshi, S.R., Sarkar, S.S. and Patel, V.D., 2009. Terrain Mapping Camera: A stereoscopic high-resolution instrument on Chandrayaan-1. *Current Science* (00113891), 96(4).
- Kumar, P.S., Kumar, A.S., Keerthi, V., Goswami, J.N., Krishna, B.G. and Kumar, A.K., 2011. Chandrayaan-1 observation of distant secondary craters of Copernicus exhibiting central mound morphology: Evidence for low velocity clustered impacts on the Moon. *Planetary and Space Science*, 59(9), pp.870-879.
- Kumar, P.S., Sruthi, U., Krishna, N., Lakshmi, K.J.P., Menon, R., Krishna, B.G., Kring, D.A., Head, J.W., Goswami, J.N. and Kumar, A.K., 2016. Recent shallow moonquake and impact-triggered boulder falls on the Moon: New insights from the Schrödinger basin. *Journal of Geophysical Research: Planets*, 121(2), pp.147-179.
- Lafuente, R. Downs, H. Yang, N. Stone, 2015. The power of databases: the RRUFF project, in: T. Armbruster, R.M. Danisi (Eds.), *Highlights in mineralogical crystallography*, 1, W. De Gruyter, Berlin, Germany, p. 30.
- Lakshmi, K.J.P. and Kumar, P.S., 2020. Physical properties of basalt ejecta boulders at Lonar crater, India: Insights into the target heterogeneity and impact spallation processes in basalt with application to Mars. *Journal of Geophysical Research: Planets*, 125(10), p.e2020JE006593.
- Lal, D., Chauhan, P., Shah, R.D., Bhattacharya, S. and Kumar, A.K., 2012. Detection of Mg spinel lithologies on central peak of crater Theophilus using Moon Mineralogy Mapper (M₃) data from Chandrayaan-1. *Journal of earth system science*, 121(3), pp.847-853.
- Lemelin, M., Lucey, P. G., Song, E., & Taylor, G. J., 2015. Lunar central peak mineralogy and iron content using the Kaguya Multiband Imager: Reassessment of the compositional structure of the lunar crust. *Journal of Geophysical Research: Planets*, 120, 869–887.
- Lemelin, M., Lucey, P., Gaddis, L., Hare, T., Ohtake, M., 2016. Global map products from the Kaguya multiband imager at 512 ppp: Minerals, FeO, and OMAT. *Lunar Planet Sci. Conf.*, 2994
- Lenaz, V. Lughì, 2013. Raman study of MgCr₂O₄-Fe²⁺Cr₂O₄ and MgCr₂O₄-MgFe₂O₄ synthetic series: the effects of Fe²⁺ and Fe³⁺ on Raman shifts, *Phys. Chem.*

- Miner. 40, 491–498.
- Li, B., Ling, Z.C., Zhang, J., Chen, J., Liu, C.Q. and Bi, X.Y., 2017. Geological mapping of lunar crater lalande: topographic configuration, morphology and cratering process. *International Archives of the Photogrammetry, Remote Sensing & Spatial Information Sciences*, 42.
- Li, R.E. Milliken, 2016. An empirical thermal correction model for Moon Mineralogy Mapper data constrained by laboratory spectra and Diviner temperatures, *Journal of Geophysical Research: Planets* 121 (10) 2081–2107.
- Lin, Y., Tronche, E. J., Steenstra, E. S., & van Westrenen, W., 2017. Evidence for an early wet Moon from experimental crystallization of the lunar magma ocean. *Nature Geoscience*, 10(1), 14–18.
- Lindsley D. H, and Munoz J. L., 1969. Subsolidus relations along the join hedenbergite-ferrosilite. *American Journal of Science* 267:295–324.
- Lindsley D. H. and Andersen D. J., 1983. A two-pyroxene thermometer. *Journal of Geophysical Research: Solid Earth* 88:A887–A906.
- Lindsley D. H. and Burnham C. W., 1970. Pyroxferroite: Stability and X-ray crystallography of synthetic $\text{Ca}_0.15\text{Fe}_0.85\text{SiO}_3$ pyroxenoid. *Science* 168:364–367.
- Lindsley D. H., Papike J. J., and Bence A. E., 1972. Pyroxferroite: Breakdown at low pressure and high temperature. *Proceedings, 3rd Lunar Science Conference*.p. 483.
- Lindsley, D.H., 1983. Pyroxene thermometry. *American Mineralogist*, 68(5-6), pp.477-493.
- Lindsley, D.H., Andersen, D.J., 1983. A two-pyroxene thermometer. *J. Geophys. Res.: Solid Earth* 88 (S02), A887–A906.
- Lindsley, D.H., Munoz, J.L., 1969. Subsolidus relations along the join hedenbergiteferrosilite. *Am. J. Sci.* 267, 295–324. Schairer Volume.
- Longhi J., 1992. Origin of picritic green glass magmas by polybaric fractional fusion. *Proceedings, 22nd Lunar and Planetary Science Conference*. pp.
- Longhi, J., 1980. Lunar Crust, Achondrites. *Geotimes* 25, 19–20.
- Lucey P. G., Blewett D. T., and Hawke B. R., 1998. Mapping the FeO and TiO₂ content of the lunar surface with multispectral imagery. *Journal of Geophysical Research Planets* 103:3679–3699.
- Lucey P. G., Blewett D. T., and Jolliff B. L., 2000. Lunar iron and titanium abundance

- algorithms based on final processing of Clementine ultraviolet-visible images. *Journal of Geophysical Research: Planets* 105:20,297–20,305.
- Lucey P. G., Taylor G. J., and Malaret E., 1995. Abundance and distribution of iron on the Moon. *Science* 268:1150–1153.
- Lucey, P. G., Blewett, D. T., Taylor, G. J., & Hawke, B. R., 2000. Imaging of lunar surface maturity. *Journal of Geophysical Research: Planets*, 105(E8)
- Lucey, P.G., Blewett, D.T. and Jolliff, B.L., 2000. Lunar iron and titanium abundance algorithms based on final processing of Clementine ultraviolet-visible images. *Journal of Geophysical Research: Planets*, 105(E8), pp.20297-20305.
- Lucey, P.G., Spudis, P.D., Zuber, M., Smith, D. and Malaret, E., 1994. Topographic-compositional units on the Moon and the early evolution of the lunar crust. *Science*, 266(5192), pp.1855-1858.
- Lucey, P.G., Taylor, G.J. and Malaret, E., 1995. Abundance and distribution of iron on the Moon. *Science*, 268(5214), pp.1150-1153.
- Lyon, Analysis of rocks by spectral infrared emission (8 to 25 microns), *Economic Geology* 60 (4) (1965) 715–736.
- Lyon, 1963. E.A. Burns, Analysis of rocks and minerals by reflected infrared radiation, *Econ. Geol.* 58, 274–284.
- Lyon, 1964. Evaluation of infrared spectrophotometry for compositional analysis of lunar and planetary soils. part ii-rough and powdered surfaces.
- Ma M.-S., Schmitt R. A., Taylor G. J., Warner R. D., and Keil K., 1981. Chemical and petrographic study of spinel troctolite in 67435: Implications for the origin of Mg-rich plutonic rocks (abstract). In *Lunar and Planetary Science X11*, pp. 640–642. Lunar and Planetary Institute, Houston.
- Malézieux, B. Piriou, 1988. Relation entre la composition chimique et le comportement vibrationnel de spinelles de synthèse et de chromites naturelles en microspectrométrie Raman, *Bull. Minér.* 111, 649–669.
- Malézieux, J. Barbillat, B. Cerveille, J.P. Coutures, M. Couzi, B. Piriou, 1983. Étude de spinelles de synthèse de la série Mg (Cr x Al 2-x) O 4 et de chromites naturelles par microsonde Raman-Laser, *Tschermaks Mineralogische und Petrographische Mitteilungen* 32, 171–185.
- Mao, P.M. Bell, 1975. Crystal-field effects in spinel: oxidation states of iron and chromium,

- Geochim. Cosmochim. Acta 39, 866–867.
- Mason, B., Melson, W.G. and Nelen, J., 1972, January. Spinel and hornblende in Apollo 14 fines. In Lunar and Planetary Science Conference (Vol. 3, p. 512). Maxwell D. E. (1977) Simple Z model of cratering, ejection and the overturned flap. In Impact and Explosion Cratering (D. J. Roddy, R. O. Pepin, and R. B. Merrill, eds.), pp. 1003–1008. Pergamon, New York.
- May T. W., 1976. Holographic analysis and interpretation of the 5 megahertz radar imagery of the Apollo Lunar Sounder experiment in Maria Serenitatis and Crisium. M.Sc. thesis, Univ. of Utah. 91 pp.
- McCallister R. H. and Taylor L. A., 1973. Kinetics of ulvöspinel reduction—synthetic study and applications to lunar rocks. *Earth Planet. Sci. Lett.*, 17, 357–364.
- McCauley J. F., 1973. Geologic map of the Grimaldi quadrangle of the Moon. Scale 1:1,000,000, Map I-740. USGS. Washington, D.C.: Department of the Interior.
- McCord, T.B., Clark, R.N., Hawke, B., McFadden, L.A., Owensby, P.D., Pieters, C.M. and Adams, J.B., 1981. Moon: Near-infrared spectral reflectance, a first good look. *Journal of Geophysical Research: Solid Earth*, 86(B11), pp.10883-10892.
- McCord, T.B., Taylor, L.A., Combe, J.P., Kramer, G., Pieters, C.M., Sunshine, J.M. and Clark, R.N., 2011. Sources and physical processes responsible for OH/H₂O in the lunar soil as revealed by the Moon Mineralogy Mapper (M3). *Journal of Geophysical Research: Planets*, 116(E6).
- McEwen A. S., Robinson M. S., Eliason E. M., Lucey P. G., Duxbury T. C., and Spudis P. D., 1994. Clementine observations of the Aristarchus region of the Moon. *Science* 266:1858–1862.
- McEwen, A.S. and Robinson, M.S., 1997. Mapping of the Moon by Clementine. *Advances in Space Research*, 19(10), pp.1523-1533.
- McEwen, A.S., and Shoemaker, E.M., 1995. Two classes of impact basins on the Moon. In *Lunar and Planetary Science Conference (Vol. 26)*.
- McEwen, A.S., Becker, T.L., Robinson, M.S., Klaasen, K.P., Heffernan, C. and Sunshine, J.M., 1993, January. Lunar multispectral mosaics from Galileo's second Earth-Moon flyby. In *Lunar and Planetary Inst., Twenty-Fourth Lunar and Planetary Science Conference. Part 2: GM*.
- McLeod, C. and Krekeler, M., 2017. Sources of extraterrestrial rare earth elements: to the moon

- and beyond. *Resources*, 6(3), p.40.
- McMillan, A.M. Hofmeister, 1988. Spectroscopic methods in mineralogy and geology, Infrared and Raman Spectroscopy, *Rev. Mineral.* 18, 99–159.
- McMillan, M. Akaogi, 1987. Raman spectra of beta-Mg₂SiO₄ (modified spinel) and gamma-Mg₂SiO₄ (spinel), *Am. Mineral.* 72, 361–364.
- McMillan, 1985. Vibrational spectroscopy in the mineral sciences, *Microscop. Macroscop.* 9–63.
- Mehta, N., Shaik, S., Devireddy, R. and Gartia, M.R., 2018. Single-Cell Analysis Using Hyperspectral Imaging Modalities. *Journal of biomechanical engineering*, 140(2), p.020802.
- Meißner, P. Deters, C. Srikantappa, H. Köhler, 2002. Geochronological evolution of the Moyar, Bhavani and Palghat shear zones of southern India: implications for east Gondwana correlations, *Precamb. Res.* 114, 149–175.
- Melosh H. J., 1977. Crater modification by gravity: A mechanical analysis of slumping. In *Impact and Explosion Cratering* (D. J. Roddy, R. O. Pepin, and R. B. Merrill, eds.), pp. 1245–1260. Pergamon, New York.
- Melosh H. J., 1982, A schematic model of crater modification by gravity. *J. Geophys. Res.*, 87, 371–380
- Melosh H., Freed A. M., Johnson B. C., Blair D. M., Andrews-Hanna J. C., Neumann G. A., Phillips R. J., Smith D. E., Solomon S. C., and Wieczorek M. A., 2013. The origin of lunar mascon basins. *Science* 340:1552–1555.
- Melosh, H.J. and Ivanov, B.A., 1999. Impact crater collapse. *Annual Review of Earth and Planetary Sciences*, 27(1), pp.385-415.
- Melosh, H.J., 1989. *Impact cratering: A geologic process*. Research supported by NASA. New York, Oxford University Press (Oxford Monographs on Geology and Geophysics, No. 11), 1989, 253 p., 11.
- Melosh, H.J., 2011. *Planetary surface processes* (Vol. 13). Cambridge University Press. (Merrill, eds.), pp. 907–918. Pergamon, New York.
- Metzger A. E. and Parker R. E., 1979. The distribution of titanium on the lunar surface. *Earth Planet. Sci. Lett.*, 45, 155–171.
- Michael, G. G., & Neukum, G., 2010. Planetary surface dating from crater size-frequency distribution measurements: Partial resurfacing events and statistical age uncertainty.

- Earth and Planetary Science Letters, 294(3–4), 223–229.
- Milliken, R.E. and Li, S., 2017. Remote detection of widespread indigenous water in lunar pyroclastic deposits. *Nature geoscience*, 10(8), pp.561-565.
- Milton, D.J., Glikson, A.Y., Manwaring, E.A., Moss, F.J., Sedmik, E.C.E., Van Son, J., Barlow, B.C., Brett, R. and Young, G.A., 1972. Gosses Bluff Impact Structure, Australia: Geological and geophysical techniques establish the origin of an analog of lunar craters. *Science*, 175(4027), pp.1199-1207.
- Miura, R.A. Graham, 1994. Shock metamorphism on the surface of the Moon, *Shock Waves* 3 (4), 293–298.
- Miura, T. Kato, 1992. Shock metamorphism on the Moon, in: *Dynamics and Evolution of Minor Bodies with Galactic and Geological Implications*, Springer, Dordrecht, pp. 245–248.
- Moore, H.J., Hodges, C.A. and Scott, D.H., 1974. Multiringed basins-illustrated by Orientale and associated features. In *Lunar and Planetary Science Conference Proceedings (Vol. 5, pp. 71-100)*.
- Morota, T., Haruyama, J., Ohtake, M., Matsunaga, T., Honda, C., Yokota, Y., Kimura, J., Ogawa, Y., Hirata, N., Demura, H., Iwasaki, A., 2011. Timing and characteristics of the latest mare eruption on the Moon. *Earth Planet Sci. Lett.* 302 (3–4), 255–266.
- Morse, Z.R., Osinski, G.R. and Tornabene, L.L., 2018a. New morphological mapping and interpretation of ejecta deposits from Orientale Basin on the Moon. *Icarus*, 299, pp.253-271.
- Morse, Z.R., Osinski, G.R. and Tornabene, L.L., 2018b. Morphologic Mapping and Analysis of Tsiolkovsky Crater Ejecta. In *Lunar and Planetary Science Conference (Vol. 49)*.
- Morse, Z.R., Osinski, G.R., Tornabene, L.L. and Neish, C.D., 2021. Morphologic mapping and interpretation of ejecta deposits from Tsiolkovskiy crater. *Meteoritics & Planetary Science*, 56(4), pp.767-793.
- Mukhopadhyay, M.K. Bose, 1994. Transitional granulite-eclogite facies metamorphism of basic supracrustal rocks in a shear zone complex in the Precambrian shield of south India, *Mineralogical Magazine* 58 (390), 97–118.
- Mukhopadhyay, P.S. Kumar, R. Srinivasan, T. Bhattacharya, 2003. Nature of the Palghat-Cauvery lineament in the region South of Namakkal, Tamil Nadu: Implications for terrane assembly in the South Indian granulite Province, *Memoirs-Geol. Soc. India*, 279–

- Muller P. M. and Sjogren W. L., 1968. Mascons: Lunar mass concentrations. *Science* 161:680–684.
- Mustard J. F., Pieters C. M., Isaacson P. J., Head J. W., Besse S., Clark R. N., Klima R. L., Petro N. E., Staid M. I., and Sunshine J. M., 2011. Compositional diversity and geologic insights of the Aristarchus crater from moon mineralogy mapper data. *Journal of Geophysical Research: Planets* 116:E00G12.
- Mustard, C.M. Pieters, 1989. Photometric phase functions of common geologic minerals and applications to quantitative analysis of mineral mixture reflectance spectra, *J. Geophys. Res. Solid Earth* 94, 13619–13634.
- Mustard, J.F., Pieters, C.M., Isaacson, P.J., Head, J.W., Besse, S., Clark, R.N., Klima, R.L., Petro, N.E., Staid, M.I., Sunshine, J.M., 2011. Compositional diversity and geologic insights of the Aristarchus crater from Moon Mineralogy Mapper data. *J. Geophys. Res.: Plan* 116 (E6).
- N.L. Ross, A. Navrotsky, 1987. The Mg₂GeO₄ olivine-spinel phase transition, *Phys. Chem. Miner.* 14, 473–481.
- Naganjaneyulu, M. Santosh, 2010. The Cambrian collisional suture of Gondwana in southern India: a geophysical appraisal, *J. Geodyn.* 50, 256–267.
- Nagasawa H., Schreiber H. D., and Blanchard D. P., 1976. Partition coefficients of REE and Sc in perovskite, melilite, and spinel and their implications for Allende inclusions (abstract). In *Lunar Science VII*, pp. 588–590. The Lunar Science Institute, Houston.
- Nasdala, D.C. Smith, R. Kaindl, M.A. Ziemann, 2004. Raman spectroscopy: analytical perspectives in mineralogical research, *Spectrosc. Meth. Mineral.* 6, 281–343.
- Nash, J.E. Conel, 1974. Spectral reflectance systematics for mixtures of powdered hypersthene, labradorite, and ilmenite, *J. Geophys. Res.* 79, 1615–1621.
- Naveen, T. Sarkar, N. Kumar, D. Ray, S. Bhattacharya, A.D. Shukla, H. Moitra, A. Dagar, P. Chauhan, K. Sen, S. Das, 2019. Mineralogy and spectroscopy (VIS near infrared and micro-Raman) of chromite from Nidar ophiolite complex, SE Ladakh, India: Implications for future planetary exploration., *Planetary and Space Science* 165, 1–9.
- Neal, C.R. and Taylor, L.A., 1992, December. Using Apollo 17 high-Ti mare basalts as windows to the lunar mantle. In *Lunar Science Inst., Workshop on Geology of the Apollo 17 Landing Site*.

- Nehru C. E., Prinz M., Dowty E., and Keil K., 1974. Spinel group minerals and ilmenite in Apollo 15 rock samples. *Am. Mineral.*, 59, 1220–1234.
- Nehru, R.D. Warner, K. Keil, 1976. Electron Microprobe Analyses of Opaque Mineral Phases from Apollo 11 Basalts. Univ. of New Mexico Spec. Publ. 17, Albuquerque.
- Neukum G., 1983. Meteorite bombardment and dating of planetary surfaces. Habilitation Thesis for Faculty Membership, University of Munich, Munich, Germany.
- Neukum G. and Ivanov B., 1994. Crater size distributions and impact probabilities on Earth from lunar, terrestrial planet, and asteroid cratering data. *Hazards due to Comets and Asteroids* 1:359–416.
- Neukum G., Ivanov B. A., and Hartmann W. K., 2001. Cratering records in the inner solar system in relation to the lunar reference system. *Space Science Reviews* 96:55–86.
- Neukum, G., 1983. Meteorite Bombardment and Dating of Planetary Surfaces. Habilitation Thesis for Faculty Membership, University of Munich, 186.
- Neukum, G., Horn, P., 1976. Effects of lava flows on lunar crater populations. *Moon* 15 (3–4), 205–222.
- Neukum, G., Ivanov, B., 1994. Crater size distributions and impact probabilities on Earth from lunar, terrestrial-planet, and asteroid cratering data. In: *Hazards Due to Comets and Asteroids*, vol. 1, pp. 359–416.
- Neukum, G., K€onig, B., Fechtig, H., Storzer, D., 1975. Cratering in the Earth-Moon system- Consequences for age determination by crater counting. In: *Lunar and Planetary Science Conference Proceedings*, pp. 2597–2620.
- Neumann, G.A., Zuber, M.T., Smith, D.E. and Lemoine, F.G., 1996. The lunar crust: Global structure and signature of major basins. *Journal of Geophysical Research: Planets*, 101(E7), pp.16841-16863.
- Nozette, S., Rustan, P., Pleasance, L.P., Kordas, J.F., Lewis, I.T., Park, H.S., Priest, R.E., Horan, D.M., Regeon, P., Lichtenberg, C.L. and Shoemaker, E.M., 1994. The Clementine mission to the Moon: Scientific overview. *Science*, 266(5192), pp.1835-1839.
- Nyquist, L.E., Shih, C.Y., 1992. The isotopic record of lunar volcanism. *Geochem. Cosmochim. Acta* 56 (6), 2213–2234.
- O’Keefe, J. D., and T. J. Ahrens, 1977. Impact-induced energy partitioning, melting, and vaporization on terrestrial planets. *Proc. Lunar Planet. Sci Conf.* 8th, 3357–3374.

- Oberbeck, V.R., 1975. The role of ballistic erosion and sedimentation in lunar stratigraphy. *Reviews of Geophysics*, 13(2), pp.337-362.
- Öhman, T. and Kring, D.A., 2012. Photogeologic analysis of impact melt-rich lithologies in Kepler crater that could be sampled by future missions. *Journal of Geophysical Research: Planets*, 117(E12).
- Ohtake, M., Matsunaga, T., Haruyama, J., Yokota, Y., Morota, T., Honda, C., Josset, J.-L., 2009. The global distribution of pure anorthosite on the Moon. *Nature*, 461(7261), 236–240.
- Ohtani, E., Moriyama, J. and Kawabe, I., 1988. Majorite garnet stability, and its implication for genesis of komatiite magmas. *Chemical Geology*, 70(1-2), p.147.
- Hawthorne, F.C. ed., 2018. *Spectroscopic methods in mineralogy and geology* (Vol. 18). Walter de Gruyter GmbH & Co KG.
- Orphal D. L., 1977. Calculations of explosive cratering—II: Cratering mechanics and phenomenology. In *Impact and Explosion Cratering* (D. J. Roddy, R. O. Pepin, and R. B.
- Osinski, G. R., 2004. Impact melt rocks from the Ries structure, Germany: An origin as impact melt flows? *Earth and Planetary Science Letters*, 226(3–4), 529–543
- Osinski, G.R., Silber, E.A., Clayton, J., Grieve, R.A., Hansen, K., Johnson, C.L., Kalynn, J. and Tornabene, L.L., 2019. Transitional impact craters on the Moon: Insight into the effect of target lithology on the impact cratering process. *Meteoritics & Planetary Science*, 54(3), pp.573-591.
- Osinski, G.R., Tornabene, L.L. and Grieve, R.A., 2011. Impact ejecta emplacement on terrestrial planets. *Earth and Planetary Science Letters*, 310(3-4), pp.167-181.
- Papike J. J. and Vaniman D. T., 1978. The lunar mare basalt suite. *Geophysical Research Letters* 5:433–436.
- Papike J. J., Bence A. E., Brown G. E., Prewitt C. T., and Wu C. H., 1971. Apollo 12 clinopyroxenes: Exsolution and epitaxy. *Earth and Planetary Science Letters* 10:307–315.
- Papike J., Taylor L., and Simon S., 1991. Lunar minerals. In *Lunar sourcebook: A user's guide to the Moon*, edited by Heiken G. H., Vaniman D. T., and French B. M. Cambridge: Cambridge University Press. pp. 121–181.
- Papike, J.J., Hodges, F.N., Bence, A.E., Cameron, M., Rhodes, J.M., 1976. Mare basalts:

- crystal chemistry, mineralogy, and petrology. *Rev. Geophys.* 14 (4), 475–540.
- Papike, J.J., Ryder, G., Shearer, C.K., 1998. Lunar Samples In: Papike, J.J. (Ed.), *Planetary Materials*. Min. Soc. of Am., Washington, D.C., USA, pp. 1–234.
- Papike, J.J., Vaniman, D.T., 1978. The lunar mare basalt suite. *Geophys. Res. Lett.* 5 (6), 433–436.
- Pearce, S.J. and Melosh, H.J., 1986. Terrace width variations in complex lunar craters. *Geophysical Research Letters*, 13(13), pp.1419-1422.
- Peterson C., Hawke B., Lucey P., Coombs C., and Spudis P., 1995. Spectral reflectance studies of the Grimaldi region of the Moon. *Geophysical Research Letters* 22:3055–3058.
- Peterson, C.A., Hawke, B.R., Lucey, P.G., Taylor, G.J., Blewett, D.T., Spudis, P.D., 1993. Spectral reflectance studies of the Humorum Basin region. In: *Lunar and Planetary Science Conference*, vol. 24.
- Pierazzo, E. and Melosh, H.J., 2000. Understanding oblique impacts from experiments, observations, and modeling. *Annual Review of Earth and Planetary Sciences*, 28(1), pp.141-167.
- Pierazzo, E. and Melosh, H.J., 2000. Melt production in oblique impacts. *Icarus*, 145(1), pp.252-261.
- Pieters C. M., 1998. Lunar materials from the visible to mid infrared: The effects of space weathering. *International Geology Review* 40:981–989.
- Pieters C. M., Boardman J., Buratti B., Chatterjee A., Clark R., Glavich T., Green R., Head J. III, Isaacson P., and Malaret E., 2009. The moon mineralogy mapper (M3) on chandrayaan-1. *Science* 326:568–572.
- Pieters C. M., Fischer E. M., Rode O., and Basu A., 1993. Optical effects of space weathering: The role of the finest fraction. *Journal of Geophysical Research* 98:20,817–20,824.
- Pieters C. M., Head J. W., Adams J. B., McCord T. B., Zisk S. H., and Whitford-Stark J. L., 1980. Late high-titanium basalts of the western maria: Geology of the flamsteed region of oceanus procellarum. *Journal of Geophysical Research: Solid Earth* 85:3913–3938.
- Pieters C. M., Taylor L. A., Noble S. K., Keller L. P., Hapke B., Morris R. V., Allen C. C., McKay D. S., and Wentworth S., 2000. Space weathering on airless bodies: Resolving a mystery with lunar samples. *Meteoritics & Planetary Science* 35:1101–1107.
- Pieters, C. M., Besse, S., Boardman, J., Buratti, B., Cheek, L., Clark, R. N., Whitten, J., 2011. Mg-spinel lithology: A new rock type on the lunar farside. *Journal of Geophysical*

Research, 116, E00G08.

- Pieters, C. M., Boardman, J., Buratti, B., Chatterjee, A., Clark, R., Glavich, T., White, M., 2009. The Moon Mineralogy Mapper (M3) on Chandrayaan-1. *Current Science*, 96(4), 500–505.
- Pieters, C. M., Donaldson Hanna, K., Cheek, L., Deepak, D., Prissel, T., Jackson, C., Taylor, L. A., 2014. The distribution of Mg-spinel across the Moon and constraints on crustal origin. *American Mineralogist*, 99, 1893–1910.
- Pieters, C. M., Head, J. W., Gaddis, L., Jolliff, B. and Duke, M., 2001. Rock types of South Pole Aitken basin and extent of basaltic volcanism. *Jour. Geophys. Res., Planets* (1991–2012), v.106 (E11), pp.28001–28022.
- Pieters, C., McCord, T.B., 1976. Characterization of lunar mare basalt types. I-A remote sensing study using reflection spectroscopy of surface soils. In: *Lunar and Planetary Science Conference Proceedings*, vol. 7, pp. 2677–2690.
- Pieters, C., McCord, T.B., 1978. Distribution of basalt types on the front side of the moon. In: *Lunar and Planetary Science Conference*, vol. 9, pp. 898–900.
- Pieters, C.M., Boardman, J., Buratti, B., Chatterjee, A., Clark, R., Glavich, T., Green, R., Head III, J., Isaacson, P., Malaret, E., 2009. The moon mineralogy mapper (M3) on Chandrayaan-1. *Curr. Sci.* 500–505.
- Pieters, C.M., Hanna, K.D., Cheek, L., Dhingra, D., Prissel, T., Jackson, C., Moriarty, D., Parman, S. and Taylor, L.A., 2014. The distribution of Mg-spinel across the Moon and constraints on crustal origin. *American Mineralogist*, 99(10), pp.1893-1910.
- Pieters, C.M., Head, J.W., Gaddis, L., Jolliff, B., Duke, M., 2001. Rock types of South Pole-Aitken basin and extent of basaltic volcanism. *J. Geophys. Res.: Plan* 106 (E11), 28001–28022.
- Pieters, S. Besse, J. Boardman, B. Buratti, L. Cheek, R.N. Clark, J.P. Combe, D. Dhingra, J.N. Goswami, R.O. Green, 2011. Mg-spinel lithology: A new rock type on the lunar farside, *J. Geophys. Res. Planets* 116.
- Pieters, S.K. Noble, 2016. Space weathering on airless bodies, *J. Geophys. Res.* 121, 1865–1884.
- Pike R. J., 1980. Geometric interpretation of lunar craters. USGS Professional Paper
- Pike, R.J., 1974. Depth/diameter relations of fresh lunar craters: Revision from spacecraft data. *Geophysical Research Letters*, 1(7), pp.291-294.

- Pike, R.J., 1980. Control of crater morphology by gravity and target type—Mars, Earth, Moon. In *Lunar and Planetary Science Conference Proceedings* (Vol. 11, pp. 2159-2189).
- Pike, R.J., 1988. *Geomorphology of impact craters on Mercury*. Mercury, University of Arizona Press, pp.165-273.
- Pike, R.J., Spudis, P.D., 1987. Basin-ring spacing on the moon, mercury, and mars. *Earth Moon Planets* 39 (2), 129–194.
- Preudhomme, P. Tarte, 1971. Infrared studies of spinels—I: a critical discussion of the actual interpretations, *Spectrochim. Acta, Part A* 27, 961–968.
- Preudhomme, P. Tarte, 1971. Infrared studies of spinels—II: The experimental bases for solving the assignment problem, *Spectrochim. Acta, Part A* 27, 845–851.
- Prinz M., Dowty E., Keil K., and Bunch T. E., 1973. Spinel troctolite and anorthosite in Apollo 16 samples. *Science*, 179, 74–76.
- Prinz, M., Dowty, E., Keil, K. and Bunch, T.E., 1973. Spinel troctolite and anorthosite in Apollo 16 samples. *Science*, 179(4068), pp.74-76.
- Martinot, M., Flahaut, J., Besse, S., Quantin, C., Van Westrenen, W., Donaldson Hanna, K. L., & Blanchette Guertin, J.-F. (2017). Lunar crustal composition in the Humboldt crater region. In *Lunar and Planetary Science Conference* (Vol. 48).
- Prissel, S.W. Parman, C.R.M. Jackson, M.J. Rutherford, P.C. Hess, J.W. Head, L. Cheek, D. Dhingra, C.M. Pieters, 2014. Pink Moon: The petrogenesis of pink spinel anorthosites and implications concerning Mg-suite magmatism, *Earth Planet. Sci. Lett.* 403, 144–156.
- Proenza, F. Ortega-Gutiérrez, A. Camprubí, J. Tritlla, M. Elías-Herrera, M. Reyes-Salas, 2004. Paleozoic serpentinite-enclosed chromitites from Tehuizingo (Acatlán Complex, southern Mexico): a petrological and mineralogical study, *Journal of South American Earth Sciences* 16 (8), 649–666.
- Raith, S. Brandt, P. Sengupta, J. Berndt, T. John, C. Srikantappa, 2016. Element mobility and behaviour of zircon during HT metasomatism of ferroan basic granulite at Ayyarmalai, South India: Evidence for polyphase Neoproterozoic crustal growth and multiple metamorphism in the Northeastern Madurai Province, *J. Petrol.* 57, 1729–1774.
- Ramadurai, S. Ta, W. Bf, 1975. The stratigraphy and structure of the Sittampundi complex, Tamil Nadu, India.
- Raman, 1928. A new radiation, *Indian J. Phys.* 2, 387–398.
- Raman, K.S. Krishnan, 1928. A new type of secondary radiation, *Nature* 121, 501–502.

- Rao, K. Sain, P.R. Reddy, W.D. Mooney, 2006. Crustal structure and tectonics of the northern part of the Southern Granulite Terrane, India, *Earth and Planetary Science Letters* 251 (1–2), 90–103.
- Rao, M. Santosh, K. Sajeev, B.F. Windley, 2013. Chromite–silicate chemistry of the Neoproterozoic Sittampundi Complex, southern India: Implications for subduction-related arc magmatism, *Precamb. Res.* 227, 259–275.
- Rao, T.R.K. Chetty, A.S. Janardhan, K. Gopalan, 1996. Sm-Nd and Rb-Sr ages and PT history of the Archean Sittampundi and Bhavani Anorthosite meta anorthosite complexes in Cauvery shear zone, South India: evidence for Neoproterozoic reworking of Archean crust, *Contrib. Mineral. Petrol.* 125, 237–250.
- Reddy, R.L. Frost, 2005. Spectroscopic characterization of chromite from the Moa Baracoa ophiolitic massif, Cuba, *Spectrochim. Acta Part A: Mol. Biomol. Spectrosc.* 61, 1721–1728.
- Reddy, V., Nathues, A., Gaffey, M.J. and Schaeff, S., 2011. Mineralogical characterization of potential targets for the ASTEX mission scenario. *Planetary and Space Science*, 59(8), pp.772-778.
- Reid J. B., 1971. Apollo 12 spinels as petrogenetic indicators. *Earth Planet. Sci. Lett.*, 10, 351–356.
- Rhodes J. M., Adams J. B., Blanchard D. P., Charette M. P., Rodgers K. V., Jacobs J. W., Brannon J. C., and Haskin L. A., 1975. Chemistry of agglutinate fractions in lunar soils. *Proc. Lunar Sci. Conf. 6th*, pp. 2291–2307.
- Robinson, M.S., Brylow, S.M., Tschimmel, M., Humm, D., Lawrence, S.J., Thomas, P.C., Denevi, B.W., Bowman-Cisneros, E., Zerr, J., Ravine, M.A. and Caplinger, M.A., 2010. Lunar reconnaissance orbiter camera (LROC) instrument overview. *Space science reviews*, 150(1-4), pp.81-124.
- Roedder E. and Weiblen P. W., 1972. Occurrence of chromian, hercynitic spinel (“pleonaste”) in Apollo 14 samples and its petrologic implications. *Earth Planet. Sci. Lett.*, 15, 376–402.
- Roeder, P.L. and Reynolds, I., 1991. Crystallization of chromite and chromium solubility in basaltic melts. *Journal of Petrology*, 32(5), pp.909-934.
- Roeder, P.L., 1994. Chromite; from the fiery rain of chondrules to the Kilauea Iki lava lake. *The Canadian Mineralogist*, 32(4), pp.729-746.

- Rollinson, C. Reid, B. Windley, 2010. Chromitites from the Fiskenæsset anorthositic complex, West Greenland: clues to late Archaean mantle processes, Geological Society, London, Special Publications 338 (1) 197–212.
- Ross M., Bence A. E., Dwornik E. J., Clark J. R., and Papike J. J., 1970. Lunar clinopyroxenes: Chemical composition, structural state, and texture. *Science* 167:628–630.
- Roush, T.L. and Singer, R.B., 1986. Gaussian analysis of temperature effects on the reflectance spectra of mafic minerals in the 1- μ m region. *Journal of Geophysical Research: Solid Earth*, 91(B10), pp.10301-10308.
- Ryder, G., Spudis, P., 1980. Volcanic rocks in the lunar highlands. In: *Lunar Highlands Crust*, pp. 353–375.
- Sack, M.S. Ghiorso, 1991. Chromian spinels as petrogenetic indicators: Thermodynamics and petrological applications, *American Mineralogist* 76 (5–6) 827–847.
- Sack, 1982. Spinel as petrogenetic indicators: activity-composition relations at low pressures, *Contrib. Miner. Petrol.* 79, 169–186.
- Saitoh, T. Tsunogae, M. Santosh, T.R.K. Chetty, K. Horie, 2011. Neoproterozoic high-pressure metamorphism from the northern margin of the Palghat–Cauvery Suture Zone, southern India: Petrology and zircon SHRIMP geochronology, *Journal of Asian Earth Sciences* 42 (3) 268–285.
- Santosh, K. Sajeev, 2006. Anticlockwise evolution of ultrahigh-temperature granulites within continental collision zone in southern India, *Lithos* 92, 447–464.
- Santosh, S. Maruyama, K. Sato, 2009. Anatomy of a Cambrian suture in Gondwana: Pacific-type orogeny in southern India?, *Gondwana Res* 16, 321–341.
- Santosh, W.J. Xiao, T. Tsunogae, T.R.K. Chetty, T. Yellappa, 2012. The Neoproterozoic subduction complex in southern India: SIMS zircon U–Pb ages and implications for Gondwana assembly, *Precambrian Research* 192, 190–208.
- Sasaki, S., Kato, M., Takizawa, Y., 2010. KAGUYA (SELENE) Science Mission. In *Transactions of the Japan Society for Aeronautical and Space Sciences, Space Technology Japan*.
- Sato, H., Hiesinger, H., Jolliff, B. L., Sandra, A. W., Lawrence, S.J., & Tran, T. N., et al., 2011. Non-mare silicivolcanism on the lunar farside at Compton-belkovich. *Nature Geoscience*, 4(2011-07-24), 566-571.
- Sato, H., Robinson, M.S., Hapke, B., Denevi, B.W. and Boyd, A.K., 2014. Resolved Hapke

- parameter maps of the Moon. *Journal of Geophysical Research: Planets*, 119(8), pp.1775-1805.
- Sato, H., Robinson, M.S., Lawrence, S.J., Denevi, B.W., Hapke, B., Jolliff, B.L., Hiesinger, H., 2017. Lunar mare TiO₂ abundances estimated from UV/Vis reflectance. *Icarus* 296, 216–238.
- Sato, N.L. Hickling, J.E. McLane, 1973. Oxygen fugacity values of Apollo 12, 14, and 15 lunar samples and reduced state of lunar magmas. *Proc. Lunar Sci. Conf.* 4th, 1061–1079.
- Sato, 1978. Oxygen fugacity of basaltic magmas and the role of gas forming elements, *Geophys. Res. Lett.* 5, 447–449.
- Scholten F., Oberst J., Matz K. D., Roatsch T., Wählisch M., Speyerer E., and Robinson M., 2012. GLD100: The near global lunar 100 m raster DTM from LROC WAC stereo image data. *Journal of Geophysical Research: Planets* 117: E00H17.
- Schultz P.H., 1999. Ejecta distribution from oblique impacts into particulate targets. *Lunar Planet. Sci. Conf.* 30, Abstr. #1919. Houston: Lunar Planet. Inst. (CD-ROM)
- Schultz, P. H., & Spudis, P. D., 1983. The beginning and end of lunar volcanism. *Nature* 302, 33-236.
- Schultz, P. H., 1976. Floor-fractured lunar craters, *Moon*, 15, 241-273.
- Schultz, P. H., 1992, Atmospheric effects on ejecta emplacement and crater formation on Venus: *Journal of Geophysical Research*, v. 97, p. 16183–16248.
- Schultz, P. H., and Gault, D. E., 1990. Prolonged global catastrophes from oblique impacts, in Sharpton, V. L., and Ward, P. D., eds., *Global catastrophes in Earth history, An interdisciplinary conference on impacts, volcanism, and mass mortality: Geological Society of America Special Paper 247*, p. 239–261.
- Schultz, P.H. and D'Hondt, S., 1996. Cretaceous-Tertiary (Chicxulub) impact angle and its consequences. *Geology*, 24(11), pp.963-967.
- Scott D. H., McCauley J. F., and West Mareta N., 1977. *Geologic map of the west side of the Moon*. Reston, Virginia: US Geological Survey, Citeseer.
- Sengupta, M.M. Raith, E. Kooijman, M. Talukdar, P. Chowdhury, S. Sanyal, K. Mezger, D. Mukhopadhyay, 2015. Provenance, timing of sedimentation and metamorphism of metasedimentary rock suites from the Southern Granulite Terrane, India, *Geol. Soc., London, Memoirs* 43, 297–308.
- Sengupta, U. Dutta, U.K. Bhui, D. Mukhopadhyay, 2009. Genesis of wollastonite and grandite-

- rich skarns in a suite of marble-calc-silicate rocks from Sittampundi, Tamil Nadu: constraints on the P-T–fluid regime in parts of the Pan-African mobile belt of South India, *Mineral. Petrol.* 95, 179.
- Sengupta, U.K. Bhui, I. Braun, U. Dutta, D. Mukhopadhyay, 2009. Chemical substitutions, paragenetic relations, and physical conditions of formation of hognomite in the Sittampundi Anorthosite anorthosite complex, South India, *Am. Mineral.* 94, 1520–1534.
- Shankland, A.G. Duba, A. Woronow, 1974. Pressure shifts of optical absorption bands in iron-bearing garnet, spinel, olivine, pyroxene, and periclase, *J. Geophys. Res.* 79, 3273–3282.
- Shearer C. K., Hess P. C., Wieczorek M. A., Pritchard M. E., Parmentier E. M., Borg L. E., Longhi J., Elkins-Tanton L. T., Neal C. R., and Antonenko I., 2006. Thermal and magmatic evolution of the Moon. *Reviews in Mineralogy and Geochemistry* 60:365–518.
- Shearer, C.K. and Newsom, H.E., 2000. W-Hf isotope abundances and the early origin and evolution of the Earth-Moon system. *Geochimica et Cosmochimica Acta*, 64(20), pp.3599-3613.
- Shearer, C.K., Hess, P.C., Wieczorek, M.A., Pritchard, M.E., Parmentier, E.M., Borg, L.E., Longhi, J., Elkins-Tanton, L.T., Neal, C.R., Antonenko, I. and Canup, R.M., 2006. Thermal and magmatic evolution of the Moon. *Reviews in Mineralogy and Geochemistry*, 60(1), pp.365-518.
- Shimpo, T. Tsunogae, M. Santosh, 2006. First report of garnet–corundum rocks from southern India: implications for prograde high-pressure (eclogite facies?) metamorphism, *Earth Planet. Sci. Lett.* 242, 111–129.
- Shkuratov, Y., Kaydash, V., & Videen, G., 2012. The lunar crater giordano bruno as seen with optical roughness imagery. *Icarus*, 218(1), 525-533.
- Shoemaker E. M., 1972. Cratering history and early evolution of the Moon (abstract). In *Lunar Science III*, pp. 696–698. The Lunar Science Institute, Houston
- Shoemaker E. M., 1977. Why study impact craters? In *Impact and Explosion Cratering* (D. J. Roddy, R. O. Pepin, and R. B. Merrill, eds.), pp. 1–10. Pergamon, New York.
- Shoemaker E. M. and Hackman R. J., 1962. Stratigraphic basis for a lunar time scale. In *The Moon* (Z. Kopal, ed.), pp. 289–300. Academic, New York.
- Shoemaker, E.M., 1962. Interpretation of lunar craters. In *Physics and Astronomy of the Moon*

(pp. 253-359)

- Shoemaker, E.M., Robinson, M.S. and Eliason, E.M., 1994. The south-pole region of the Moon as seen by Clementine. *Science*, 266(5192), pp.1851-1854.
- Šilhavý, J., Minár, J., Mentlík, P. and Sládek, J., 2016. A new artefacts resistant method for automatic lineament extraction using Multi-Hillshade Hierarchic Clustering (MHHC). *Computers & geosciences*, 92, pp.9-20.
- Simpson, R.A. and Tyler, G.L., 1999. Reanalysis of Clementine bistatic radar data from the lunar south pole. *Journal of Geophysical Research: Planets*, 104(E2), pp.3845-3862.
- Singer, R.B., 1981. Near-infrared spectral reflectance of mineral mixtures: Systematic combinations of pyroxenes, olivine, and iron oxides. *Journal of Geophysical Research: Solid Earth*, 86(B9), pp.7967-7982.
- Singh, T. and Srivastava, N., 2020. Geology of Grimaldi Basin on the Moon: Evidence for volcanism and tectonism during the Copernican period. *Icarus*, 351, p.113921.
- Sio C. K., Borg L. E., and Cassata W. S., 2020. The timing of lunar solidification and mantle overturn recorded in ferroan anorthosite 62237. *Earth and Planetary Science Letters* 538:116,219.
- Slack, F.S. Ham, R.M. Chrenko, 1966. Optical Absorption of Tetrahedral Fe²⁺(3 d 6) in Cubic ZnS, CdTe, and Mg Al₂ O₄, *Phys. Rev.* 152, 376.
- Smith D. and Lindsley D. H., 1971. Stable and metastable augite crystallization trends in a single basalt flow. *American Mineralogist: Journal of Earth and Planetary Materials* 56:225–233.
- Smith J., Anderson A., Newton R., Olsen E., Crewe A., Isaacson M., Johnson D., and Wyllie P., 1970. Petrologic history of the Moon inferred from petrography, mineralogy and petrogenesis of Apollo 11 rocks. *Geochimica et Cosmochimica Acta Supplement* 1:897.
- Smith, D. E., Zuber, M. T., Neumann, G. A., Lemoine, F. G., Mazarico, E., Torrence, M. H., Bartels, A. E., 2010. Initial observations from the Lunar Orbiter Laser Altimeter (LOLA). *Geophysical Research Letters*, 37, L18204.
- Smith, D., Lindsley, D.H., 1971. Stable and metastable augite crystallization trends in a single basalt flow. *Am. Mineral.* 56 (1–2), 225–233.
- Smith, E.I. and Sanchez, A.G., 1973. Fresh lunar craters: Morphology as a function of diameter, a possible criterion for crater origin. *Modern Geology*, 4, pp.51-59.
- Smith, E.I., 1973. Identification, distribution and significance of lunar volcanic domes. *The*

- moon, 6(1), pp.3-31.
- Smith, G. and Strens, R.G.J., 1976. Intervalence transfer absorption in some silicate, oxide and phosphate minerals. *The Physics of Minerals and Rocks*, pp.583-612.
- Snyder G. A., Taylor L. A., and Neal C. R., 1992. A chemical model for generating the sources of mare basalts: Combined equilibrium and fractional crystallization of the lunar magmasphere. *Geochimica et Cosmochimica Acta* 56:3809–3823.
- Solomon S., 1975. Mare volcanism and lunar crustal structure. *Proceedings, 6th Lunar Science Conference*. Pp. 1021–1042.
- Solomon S. C. and Longhi J., 1977. Magma oceanography I. Thermal evolution. *Proceedings, 8th Lunar Science Conference*. pp. 8:583–599.
- Speyerer, E., Robinson, M., Denevi, B., 2011. Lunar reconnaissance orbiter camera global morphological map of the moon. In: *Lunar and Planetary Science Conference*, 2387.
- Spinella, G.A. Baratta, G. Strazzulla, 1991. An apparatus for in situ Raman spectroscopy of ion-irradiated frozen targets, *Rev. Sci. Instrum.* 62, 1743–1745.
- Spudis, P. D., and Bussey, D. B. J., 1997. *Clementine Explores the Moon*, 2nd ed, LPI Contrib. 929, Lunar and Planetary Institute, Houston, Texas
- Spudis, P.D. and Davis, P.A., 1986. A chemical and petrological model of the lunar crust and implications for lunar crustal origin. *Journal of Geophysical Research: Solid Earth*, 91(B13), pp.E84-E90.
- Spudis, P.D., Gillis, J.J. and Reisse, R.A., 1994. Ancient multiring basins on the Moon revealed by Clementine laser altimetry. *Science*, 266(5192), pp.1848-1851.
- Spudis, P.D., Hawke, B.R., Lucey, P.G., Taylor, G.J., Peterson, C.A., 1992. Geology and deposits of the Humorum basin. *Lunar Planet. Sci.* XXIII, 1345–1346.
- Sridharan, R., Ahmed, S.M., Das, T.P., Sreelatha, P., Pradeepkumar, P., Naik, N. and Supriya, G., 2010. The sunlit lunar atmosphere: A comprehensive study by CHACE on the Moon Impact Probe of Chandrayaan-1. *Planetary and Space Science*, 58(12), pp.1567-1577.
- Srivastava, N. and Gupta, R.P., 2012, July. Compositional diversity inside Lowell Crater, Orientale Basin: Evidences for extensive spinel rich deposits. In *Second Conference on the Lunar Highlands Crust (Vol. 1677, pp. 55-56)*.
- Srivastava, N. and Gupta, R.P., 2013. Spatial distribution of spinel in the Orientale Basin: New insight from M3. In *Lunar Planetary Science Conference 44th (Abstract 1509)*.

- Srivastava, N. and Varatharajan, I., 2016. Geomorphology of Lowell crater region on the Moon. *Icarus*, 266, pp.44-56.
- Sruthi, U. and Kumar, P.S., 2014. Volcanism on farside of the Moon: New evidence from Antoniadi in South Pole Aitken basin. *Icarus*, 242, pp.249-268.
- Stöffler D., Ryder G., Ivanov B. A., Artemieva N. A., Cintala M. J., and Grieve R. A., 2006. Cratering history and lunar chronology. *Reviews in Mineralogy and Geochemistry* 60:519–596.
- Staid M. I. and Pieters C. M., 2000. Integrated spectral analysis of mare soils and craters: Applications to eastern nearside basalts. *Icarus* 145:122–139.
- Staid M., and Besse S., 2013. Spectral and stratigraphic mapping of lava flows in Mare Imbrium. 44th Lunar and Planetary Science Conference, p. 2661
- Staid, M.I., Pieters, C.M., 2000. Integrated spectral analysis of mare soils and craters: Applications to eastern nearside basalts. *Icarus* 145 (1), 122–139.
- Staid, M.I., Pieters, C.M., Besse, S., Boardman, J., Dhingra, D., Green, R., Head, J., Isaacson, P., Klima, R., Kramer, G., 2011. The mineralogy of late stage lunar volcanism as observed by the Moon Mineralogy Mapper on Chandrayaan-1. *J. Geophys. Res.: Plan* 116 (E6).
- Stanojević, N. Romčević, B. Stojanović, 2007. Spectroscopic study of spinel ZnCr₂O₄ obtained from mechanically activated ZnO–Cr₂O₃ mixtures, *J. Eur. Ceram. Soc.* 27, 903–907.
- Stevens, 1944. Composition of some chromites of the western hemisphere, *Am. Mineral.: J. Earth Planet. Mater.*
- Stöffler D., Gault D. E., Wedekind J., and Polkowski G., 1975. Experimental hypervelocity impact into sand: Distribution and shock metamorphism of ejecta. *J. Geophys. Res.*, 80, 4062–4077.
- Stöffler, D., Grieve, R.A.F., 2007. Impactites. In: Fettes, D., Desmons, J. (Eds.), *Metamorphic Rocks*. Cambridge University Press, Cambridge, pp. 82–92.
- Storm, R. G., and Fielder, G., 1968. Multiphase development of lunar crater Tycho. *Nature*, 217, 611–615.
- Stowe, 1994. Compositions and tectonic settings of chromite deposits through time, *Economic Geology* 89, 528–546.
- Strom, R.G., 1964. Analysis of lunar lineaments, I: Tectonic maps of the Moon.

- Communications of the Lunar and Planetary Laboratory, 2, pp.205-216.
- Subramaniam, 1956. Mineralogy and petrology of the Sittampundi complex, Salem district, Madras State, India, Geological Society of America Bulletin 67 (3) 317–390.
- Sunshine, C.M. Pieters, 1993. Estimating modal abundances from the spectra of natural and laboratory pyroxene mixtures using the modified Gaussian model, J. Geophys. Res. Planets 98, 9075–9087.
- Sunshine, J. M., and Pieters, C. M., 1998. Determining the composition of olivine from reflectance spectroscopy. Journal of Geophysical Research, 103, 675–688.
- Sunshine, J.M., Farnham, T.L., Feaga, L.M., Groussin, O., Merlin, F., Milliken, R.E. and A’Hearn, M.F., 2009. Temporal and spatial variability of lunar hydration as observed by the Deep Impact spacecraft. Science, 326(5952), pp.565-568.
- Sunshine, J.M., Pieters, C.M. and Pratt, S.F., 1990. Deconvolution of mineral absorption bands: An improved approach. Journal of Geophysical Research: Solid Earth, 95(B5), pp.6955-6966.
- Sunshine, N. Petro, S. Besse, L.R. Gaddis, 2014. Widespread exposures of small scale spinel-rich pyroclastic deposits in Sinus Aestuum, Lunar Planet. Sci. Conf. 45, Abstract 1777.
- Takano, Y., Takizawa, Y. and Sasaki, S., 2005. The SELENE project and Japanese future lunar exploration. Acta Astronautica, 57(2-8), pp.112-115.
- Takeda H., Miyamoto M., Ishii T., and Lofgren G. E., 1975. Relative cooling rates of mare basalts at the Apollo 12 and 15 sites as estimated from pyroxene exsolution data. Proceedings, 6th Lunar Science Conference. pp. 17–21.
- Talukdar, S. Sanyal, P. Sengupta, 2017. Metasomatic alteration of chromite from parts of the late Archaean Sittampundi Anorthosite Magmatic Complex (SLC), Tamil Nadu, India, Ore Geol. Rev. 90, 148–165.
- Taylor L. A. and McCallister R. H., 1972. Experimental investigation of significance of zirconium partitioning in lunar ilmenite and ulvöspinel. Earth Planet. Sci. Lett., 17, 105–111.
- Taylor L. A., Williams R. J., McCallister R. H., 1972. Stability relations of ilmenite and ulvöspinel in the Fe-Ti-O system and application of these data to lunar mineral assemblages. Earth Planet. Sci. Lett., 16, 282–288.
- Taylor S. R., 1982. Planetary science: A lunar perspective. Houston, Texas: Lunar and Planetary Institute. p. 3303.

- Taylor S. R. and Jakes P., 1974. The geochemical evolution of the Moon. Proceedings, 5th Lunar Science Conference. Pp. 5:1287–1305.
- Taylor, F. Lu, 1964. The formation of ore mineral deposits on the Moon: A feasibility study, in: W.W. Mendell (Ed.), The Second Conference on Lunar Bases and Space Activities of the 21st Century, Univelt, San Diego.
- Taylor, G. Kullerud, W.B. Bryan, 1971. Opaque mineralogy and textural features of Apollo 12 samples and a comparison with Apollo 11 rocks. Proc. Lunar Sci. Conf. 2nd, 855–871.
- Taylor, L.A., Longi, J., 1991. Workshop on mare volcanism and basalt petrogenesis: astounding fundamental concepts (AFC) developed over the last fifteen years. In: Taylor, L.A. (Ed.), Mare Volcanism and Basalt Petrogenesis: Astounding Fundamental Concepts.
- Taylor, S.R., 1982. Lunar and terrestrial crusts: a contrast in origin and evolution. Physics of the Earth and Planetary Interiors, 29(3-4), pp.233-241.
- Terada, K., Anand, M., Sokol, A.K., Bischoff, A. and Sano, Y., 2007. Cryptomare magmatism 4.35 Gyr ago recorded in lunar meteorite Kalahari 009. Nature, 450(7171), p.849.
- Terada, T. Maekawa, 1964. The infrared absorption spectra of several chromites, Trans. Jpn. Inst. Met. 5, 205–206.
- Thesniya P. M. and Rajesh V. J. 2020a. Pyroxene chemistry and crystallization history of basaltic units in the Mare Humorum on the nearside Moon: Implications for the volcanic history of the region. Planetary and Space Science 193:105093.
- Thesniya P. M. Rajesh V. J., 2020b. Lunar Crust, Chemical Composition Book: Encyclopedia of Lunar Science (Living edition). Publisher: Springer Nature Switzerland AG 2020. ISBN: 978-3-319 05546-6, pp. 1-21.
- Thesniya P. M. Rajesh V. J., 2020c. Lunar Crust, Morphology Book: Encyclopedia of Lunar Science (Living edition). Publisher: Springer Nature Switzerland AG 2020. ISBN: 978-3-319 05546-6, pp. 1-15.
- Thesniya P. M., Rajesh V. J., and Flahaut J. 2020a. High titanium olivine-rich basalts from the Grimaldi basin on the nearside of the Moon: Implications for the volcanic history of the basin. (abstract #3069). 51st Lunar and Planetary Science Conference. CD-ROM.
- Thesniya P. M., Rajesh V. J., and Flahaut J., 2020b. Ages and chemistry of mare basaltic units in the Grimaldi basin on the nearside of the Moon: Implications for the volcanic history of the basin. Meteoritics & Planetary Science 55, Nr 11, 2375–2403. 13579.

<http://dx.doi.org/10.1111/maps.13579>.

- Thesniya P. M., Rajesh, V. J., and J. Flahaut, 2020c. Evidence for Late-Imbrian and Eratosthenian Mare Volcanism from the Grimaldi basin on the Nearside of the Moon: Implications for the Lunar Mantle Heterogeneity and Thermal Evolution. Proceedings of the 6th Shear Zones and Crustal Blocks of southern India conference, 05 Nov 2020. Organized by Department of Geology, University of Kerala, Thiruvananthapuram.
- Thesniya P. M., Rajesh, V. J., and Saranya R., 2021a. Spectrochemical Characteristics of Chromium Spinels from the Sittampundi Anorthosite Complex, Southern India: Implications for Remote Identification of Lunar Spinels. In Abstracts of the 52nd Lunar and Planetary Science Conference, held virtually on March 15–19, 2021.
- Thesniya P. M., Saranya R., and Rajesh V. J., 2021b. Compositional and Spectrochemical Analysis of Cr-spinels in the Sittampundi Anorthosite Complex, Southern India: Implications for Remote Observation of Spinels on the Moon. *Spectrochimica Acta Part A: Molecular and Biomolecular Spectroscopy* 255, p.119677.
- Tompkins, S., Pieters, C.M., 1999. Mineralogy of the lunar crust: Results from Clementine. *Meteoritics Planet Sci.* 34 (1), 25–41.
- Tooley, C.R., Houghton, M.B., Saylor, R.S., Peddie, C., Everett, D.F., Baker, C.L. and Safdie, K.N., 2010. Lunar Reconnaissance Orbiter mission and spacecraft design. *Space Science Reviews*, 150(1-4), pp.23-62.
- Turkevich, A.L., 1971. Comparison of the analytical results from the Surveyor, Apollo, and Luna missions. In *Lunar and Planetary Science Conference Proceedings (Vol. 2, p. 1209)*.
- Ullrich G. W., Roddy D. J., and Simmons G., 1977. Numerical simulations of a 20-ton TNT detonation at the earth's surface and implications concerning the mechanics of central uplift formation. In *Impact and Explosion Cratering (D. J. Roddy, R. O. Pepin, and R. B. Merrill, eds.)*, pp. 959– 982. Pergamon, New York
- Urey, H.C. and MacDonald, G.J.F., 1962. Origin and History of the Moon. *Physics and Astronomy of the Moon*, 1, p.481.
- Varatharajan, I., Srivastava, N. and Murty, S.V., 2014. Mineralogy of young lunar mare basalts: Assessment of temporal and spatial heterogeneity using M3 data from Chandrayaan-1. *Icarus*, 236, pp.56-71.
- Vaughan, W. M., Head, J.W., Wilson, L., and Hess, P. C., 2013. Geology and petrology of enormous volumes of impact melt on the Moon: A case study of the Orientale basin

- impact melt sea. *Icarus*, 223(2), 749–765.
- Venugopal, K. Muthukkumaran, M. Annadurai, T. Prabu, S. Anbazhagan, 2020. Study on geomechanical properties of lunar soil simulant (LSS-ISAC-1) for chandrayaan mission, *Adv. Space Res.* 66 (11) 2711–2721.
- Venugopal, T. Prabu, K. Muthukkumaran, M. Annadurai, 2020. Development of a novel lunar highland soil simulant (LSS-ISAC-1) and its geotechnical properties for Chandrayaan missions, *Planet. Space Sci.* 194, 105116.
- Vondrak, R., Keller, J., Chin, G. and Garvin, J., 2010. Lunar Reconnaissance Orbiter (LRO): observations for lunar exploration and science. *Space science reviews*, 150(1-4), pp.7-22.
- Vorburger, A., Wurz, P., Barabash, S., Wieser, M., Futaana, Y., Holmström, M., Bhardwaj, A. and Asamura, K., 2014. First direct observation of sputtered lunar oxygen. *Journal of Geophysical Research: Space Physics*, 119(2), pp.709-722.
- Wagner R., Speyerer E., and Robinson M. and the LROC team., 2015. New mosaicked data products from the LROC team (abstract #1473). 46th In Lunar and
- Wang, C. Xu, G. Wang, Y. Liu, C. Zheng, 2002. Synthesis and Raman scattering study of rutile SnO₂ nanowires, *J. Appl. Phys.* 92, 2740–2742.
- Wang, K.E. Kuebler, B.L. Jolliff, L.A. Haskin, 2004. Raman spectroscopy of Fe-Ti-Oxides, case study: Martian meteorite EETA79001, *Am. Mineral.* 89, 665–680.
- Warner R. D., Barkley J. L., Manaker W. L., Warren R G., and Keil K., 1976. Electron Microprobe Analyses of Spinel, Ferric Oxides, and Metal from Apollo 17 Rake Sample Mare Basalts. *Inst. of Meteoritics Spec. Publ.* 16, Univ. of New Mexico, Albuquerque. 114 pp. page no. 199
- Warren P. H. and Wasson J. T., 1979. The origin of KREEP. *Rev. Geophys. Space Phys.*, 17, 73–88.
- Warren, P.H., 1985. The magma ocean concept and lunar evolution. *Annual Review of Earth and Planetary Sciences*, 13(1), pp.201-240.
- Weitz, M.I. Staid, L.R. Gaddis, S. Besse, J.M. Sunshine, 2017. Investigation of lunar spinels at Sinus Aestuum, *J. Geophys. Res. Planets* 122, 2013–2033.
- White, B.A. DeAngelis, 1967. Interpretation of the vibrational spectra of spinels, *Spectrochim. Acta, Part A* 23, 985–995.
- Whitten J., Head J. W., Staid M., Pieters C. M., Mustard J., Clark R., and Taylor L., 2011.

- Lunar mare deposits associated with the Orientale impact basin: New insights into mineralogy, history, mode of emplacement, and relation to Orientale basin evolution from Moon Mineralogy Mapper (M3) data from Chandrayaan-1. *Journal of Geophysical Research: Planets* 116:E00G09.
- Wieczorek M. A. and Phillips R. J., 2000. The “Procellarum KREEP Terrane”: Implications for mare volcanism and lunar evolution. *Journal of Geophysical Research: Planets* 105:20,417–20,430.
- Wieczorek M. A., Neumann G. A., Nimmo F., Kiefer W. S., Taylor G. J., Melosh H. J., Phillips R. J., Solomon S. C., Andrews-Hanna J. C., and Asmar S. W., 2013. The crust of the Moon as seen by GRAIL. *Science* 339:671–675.
- Wieczorek M. A., Zuber M. T., and Phillips R. J., 2001. The role of magma buoyancy on the eruption of lunar basalts. *Earth and Planetary Science Letters* 185:71–83.
- Wieczorek, M. A., and Zuber, M. T., 2001. The composition and origin of the lunar crust: Constraints from central peaks and crustal thickness modeling. *Geophysical Research Letters*, 28(21), 4023–4026.
- Wieczorek, M.A. and Phillips, R.J., 1999. Lunar multiring basins and the cratering process. *Icarus*, 139(2), pp.246-259.
- Wieczorek, M.A., Jolliff, B.L., Khan, A., Pritchard, M.E., Weiss, B.P., Williams, J.G., Hood, L.L., Richter, K., Neal, C.R., Shearer, C.K. and McCallum, I.S., 2006. The constitution and structure of the lunar interior. *Reviews in mineralogy and geochemistry*, 60(1), pp.221-364.
- Wieczorek, M.A., Phillips, R.J., 2000. The “Procellarum KREEP Terrane”: implications for mare volcanism and lunar evolution. *J. Geophys. Res.: Plan* 105 (E8), 20417–20430.
- Wilhelms D. E., John F., and Trask N. J., 1987. The geologic history of the Moon. U.S. Geological Survey Special Paper 1348. <https://doi.org/10.3133/pp1348>
- Wilhelms, D. E., 1970. Summary of lunar stratigraphy--Telescopic observations, *Geol. Surv. Prof. Pap.* 599-F, 1-47.
- Wilhelms, D. E., and El-Baz, F., 1977. Geological Map of the East Side of the Moon.
- Wilhelms, D.E., John, F., Trask, N.J., 1987. The Geologic History of the Moon. Professional Paper, US Geological Survey, Reston VA, 1348.
- Williams, C.R.M. Jackson, L.C. Cheek, K.L. Donaldson-Hanna, S.W. Parman, C.M. Pieters, M.D. Dyar, T.C. Prissel, 2016. Reflectance spectroscopy of chromium bearing spinel

- with application to recent orbital data from the Moon, *Am. Mineral.* 101, 726–734.
- Wilson L. and Head J. W. III, 1981. Ascent and eruption of basaltic magma on the Earth and Moon. *Journal of Geophysical Research: Solid Earth* 86:2971–3001.
- Windley, F.C. Bishop, J.V. Smith, 1981. Metamorphosed Anorthosite igneous complexes in Archean granulite-gneiss belts, *Annu. Rev. Earth Planet. Sci.* 9, 175–196.
- Windley, B.F. and Selvan, T.A., 1975. Anorthosites and Associated Rocks of Tamilnadu Southern India. *Journal of Geological Society of India* (Online archive from Vol 1 to Vol 78), 16(2), pp.209-215.
- Wohler C., Lena R., Lazzarotti P., Phillips J., Wirths M., Pujic Z., and the Geologic Lunar Research (GLR) Group., 2006. A combined spectrophotometric and morphometric study of the lunar mare dome fields near Cauchy, Arago, Hortensius, and Milichius. *Icarus* 183:237–264.
- Wöhler, C., Grumpe, A., Berezhnoy, A.A. and Shevchenko, V.V., 2017. Time-of-day–dependent global distribution of lunar surficial water/hydroxyl. *Science advances*, 3(9), p.e1701286.
- Wood C. A., 2004. Astonishing megadome. *Lunar Photo of the Day*. <http://www.lpod.org/archive/LPOD-2004-09-26.htm>
- Wood J., 1975. Lunar petrogenesis in a well-stirred magma ocean. *Proceedings, 6th Lunar Science Conference*. Pp. 1087–1102.
- Wood J. A., 1972. Thermal history and early magmatism in the Moon. *Icarus* 16:229–240.
- Wood J. A., 1983. The lunar magma ocean, thirteen years after Apollo 11. *Workshop on Pristine Highlands Rocks and the Early History of the Moon*, 87.
- Wood J. A., Dickey J. S. Jr, Marvin U. B., and Powell B., 1970. Lunar anorthosites and a geophysical model of the Moon. *Geochimica et Cosmochimica Acta Supplement* 1:965.
- Xiao, Z., Zeng, Z., Li, Z., Blair, D.M. and Xiao, L., 2014. Cooling fractures in impact melt deposits on the Moon and Mercury: Implications for cooling solely by thermal radiation. *Journal of Geophysical Research: Planets*, 119(7), pp.1496-1515.
- Yamamoto, S., Nakamura, R., Matsunaga, T., Ogawa, Y., Ishihara, Y., Morota, T. Haruyama, J., 2010. Possible mantle origin of olivine around lunar impact basins detected by SELENE. *Nature Geoscience*, 3(8), 533–536.
- Yamamoto, S., Nakamura, R., Matsunaga, T., Ogawa, Y., Ishihara, Y., Morota, T., Hirata, N., Ohtake, M., Hiroi, T., Yokota, Y. and Haruyama, J., 2015. Global occurrence trend of

- high-Ca pyroxene on lunar highlands and its implications. *Journal of Geophysical Research: Planets*, 120(5), pp.831-848.
- Yamanaka, M. Ishii, 1986. Raman scattering and lattice vibrations of Ni₂SiO₄ spinel at elevated temperature, *Phys. Chem. Miner.* 13, 156–160.
- Yue Z., Yang M., Jia M., Michael G., Di K., Gou S., and Liu J., 2020. Refined model age for Orientale Basin derived from zonal crater dating of its ejecta. *Icarus* 346:113804.
- Zanetti, M. R., 2015. Investigating the complexity of impact crater ejecta. PhD thesis for 539 Washington University, St. Louis. pp 218.
- Zhang F., Zhu M.-H., and Zou Y., 2016. Late-stage Imbrium volcanism on the Moon: Evidence for two source regions and implications for the thermal history of Mare Imbrium. *Earth and Planetary Science Letters* 445:13–27.
- Zhang F., Zou Y., Zheng Y., Fu X., and Zhu Y., 2014. Lunar mare basalts in the Aristarchus region: Implications for the stratigraphic sequence from Clementine UVVIS data. *Icarus* 227:132–151.
- Zhang N., Parmentier E. M., and Liang Y., 2013. A 3-D numerical study of the thermal evolution of the Moon after cumulate mantle overturn: The importance of rheology and core solidification. *Journal of Geophysical Research: Planets* 118:1789–1804.
- Zhang, W. and Bowles, N.E., 2013, September. Mapping lunar TiO₂ and FeO with M3 data. In *European Planetary Science Congress* (Vol. 8, p. 374).
- Zhong Z., Yan J., Rodriguez J. A. P., and Dohm J. M., 2018. Ancient selenophysical structure of the Grimaldi basin: Constraints from GRAIL gravity and LOLA topography. *Icarus* 309:411–421.
- Zhu, M.H., Chang, J., Ma, T., Ip, W.H., Fa, W., Wu, J., Cai, M., Gong, Y., Hu, Y., Xu, A. and Tang, Z., 2013. Potassium map from Chang'E-2 constraints the impact of Crisium and Orientale basin on the Moon. *Scientific reports*, 3(1), pp.1-6.
- Zhu, P. Ni, J.-Y. Ding, D.-Z. Wang, Y. Ju, N. Kang, G.-G. Wang, 2017. Petrography, chemical composition, and Raman spectra of chrome spinel: Constraints on the diamond potential of the No. 30 pipe kimberlite in Wafangdian, North China Craton, *Ore Geol. Rev.* 91, 896–905.
- Zuber, M.T., Smith, D.E., Lemoine, F.G. and Neumann, G.A., 1994. The shape and internal structure of the Moon from the Clementine mission. *Science*, 266(5192), pp.1839-1843.

List of Publications

Refereed Journals

1. Thesniya P. M., Saranya R., and Rajesh V. J., 2021. Compositional and Spectrochemical Analysis of Cr-spinels in the Sittampundi Anorthosite Complex, Southern India: Implications for Remote Observation of Spinels on the Moon. *Spectrochimica Acta Part A: Molecular and Biomolecular Spectroscopy* 255, p.119677. <https://doi.org/10.1016/j.saa.2021.119677>.
2. Thesniya P. M., Rajesh V. J., and Flahaut J., 2020. Ages and chemistry of mare basaltic units in the Grimaldi basin on the nearside of the Moon: Implications for the volcanic history of the basin. *Meteoritics & Planetary Science* 55, Nr 11, 2375–2403. 13579. <http://dx.doi.org/10.1111/maps.13579>.
3. Thesniya P. M. and Rajesh V. J. 2020. Pyroxene chemistry and crystallization history of basaltic units in the Mare Humorum on the nearside Moon: Implications for the volcanic history of the region. *Planetary and Space Science* 193:105093. 10.1016/j.pss.2020.105093.
4. Thesniya P. M. Rajesh V. J., 2020. Lunar Crust, Morphology Book: Encyclopedia of Lunar Science (Living edition). Publisher: Springer Nature Switzerland AG 2020. ISBN: 978-3-319 05546-6, pp. 1-15.
5. Thesniya P. M. Rajesh V. J. , 2020. Lunar Crust, Chemical Composition Book: Encyclopedia of Lunar Science (Living edition). Publisher: Springer Nature Switzerland AG 2020. ISBN: 978-3-319 05546-6, pp. 1-21.

Refereed Conferences

1. Thesniya P. M., Jappji Meher, and Rajesh, V. J., 2021. Morphology and ejecta emplacement dynamics of the Das crater on the lunar farside: Insights into the impact

- dynamics and cratering mechanics of the Moon. MetMeSS, 29-30 Nov 2021.
2. Thesniya P. M., Rajesh, V. J., and Saranya R., 2021. Spectrochemical Characteristics of Chromium Spinels from the Sittampundi Anorthosite Complex, Southern India: Implications for Remote Identification of Lunar Spinels. In Abstracts of the 52nd Lunar and Planetary Science Conference, held virtually on March 15–19, 2021.
 3. Jappji Meher, Thesniya P. M., Rajesh, V. J., 2021. Morphology of the Copernican Das Crater on the Farside of the Moon. In Abstracts of the 52nd Lunar and Planetary Science Conference, held virtually on March 15–19, 2021.
 4. Thesniya P. M., Rajesh, V. J., and Saranya R., 2021. Spectral and compositional analyses of chromium spinels from the Sittampundi Anorthosite Complex, southern India. In abstracts of the Indian Planetary Science Conference 2021, held at Physical Research Laboratory, Ahmedabad, during 25-26 Feb' 2021.
 5. Deepchand, A. Haritha, P. M. Thesniya, V. J. Rajesh, R. B. Binoj Kumar. Comparative chemical and spectral characterization of chromites in Nuggihalli schist belt, western Dharwar craton (southern India). In abstracts of the Indian Planetary Science Conference 2021, held at Physical Research Laboratory, Ahmedabad, during 25-26 Feb' 2021.
 6. Thesniya P. M., Rajesh, V. J., and J. Flahaut, 2020. Evidence for Late-Imbrian and Eratosthenian Mare Volcanism from the Grimaldi basin on the Nearside of the Moon: Implications for the Lunar Mantle Heterogeneity and Thermal Evolution. Proceedings of the 6th Shear Zones and Crustal Blocks of southern India conference, 05 Nov 2020. Organized by Department of Geology, University of Kerala, Thiruvananthapuram.
 7. Thesniya, P.M., Rajesh, V. J., and J. Flahaut, 2020. High-titanium olivine-rich basalts from the Grimaldi basin on the nearside of the moon: Implications for the volcanic history of the basin. In: abstracts of the 51st Lunar and Planetary Science Conference, 16-21 March 2020. Abstract No. #3069.
 8. Thesniya, P. M., Jappji Meher, Rajesh, V.J., 2020. Unravelling the stratigraphy and geological history of das crater on the farside of the moon based on morphology, mineralogy, and ejecta emplacement dynamics. In: abstracts of the Indian Planetary Science Conference (IPSC) held at Physical Research Laboratory, Ahmedabad during 19-21 February 2020.
 9. Thesniya, P. M., Sai Neelu Harishchandran, Rajesh, V.J., 2020. Pyroxene Chemistry and Ages of Basaltic Units in the Mare Humorum on the Nearside of the Moon: Implications for the Interior Composition of the Earth's Moon. In: abstracts of the 'Kerala Science Congress 2020', held at Yuvakshetra Institute of Management Studies, Mundoor, Palakkad during 25-27th January 2020.

10. Thesniya, P.M., Rajesh, V. J., 2020. Ages and chemistry of Maria basaltic units in the Grimaldi basin on the nearside of the Earth's Moon: Implications for the volcanic history of the basin. In: abstracts of the 'International Geological Congress 2020', held at New Delhi, India, 20 Mar' 2020.
11. Thesniya, P.M., Saranya R. Chandran, Rajesh, V.J., 2020. Spectral and chemical characteristics of the chromites associated with Sittampundi Anorthosite Complex, Southern India: Implications for the similar spinel compositions on Moon. In: abstracts of the 'International Geological Congress 2020', held at New Delhi, India, 20 Mar' 2020.
12. Saranya R. Chandran, Thesniya, P.M., Rajesh, V.J., 2020. Compositional variations of magmatic spinels on Moon. In: abstracts of the 'International Geological Congress 2020', held at New Delhi, India, 20 Mar' 2020.
13. Deepchand, B., Haritha, A., Thesniya, P.M., and Binoj Kumar, 2020. Chemical and Spectral Characterization of Chromites in Nuggehulli Schist Belt, Western Dharwar Craton, Southern India: Implications for the Remote Observation of Spinel on the Moon. In: abstracts of the 'International Geological Congress 2020', held at New Delhi, India, 20 Mar' 2020.
14. Thesniya, P.M., Sai Neelu Harishchandran and Rajesh, V. J., 2019. Pyroxene chemistry of basaltic units in the Mare Humorum on the nearside of the Moon using Chandrayaan-1 data. In: abstracts of the European and Planetary Science Conference, to be held at Centre International de Conférences de Genève (CICG) Geneva, Switzerland, 5-20 Sept' 2019, EPSC-DPS2019. Abstract No. #1836.
15. Thesniya, P.M., Rajesh, V. J., and Juda Benhur, I. S., 2019. Evidences for late-stage volcanic activity from the Ohm crater on the farside of the Moon. In: Proceedings of the 50th Lunar and Planetary Science Conference, held at Hotel Marriott Convention Centre, The Woodlands Waterway, The Woodlands, Texas, U. S., 18-22 March 2019. Abstract No. #2624.
16. Thesniya, P.M., Rajesh, V. J., 2019. Deriving the Chemical History of Maria Basaltic units in the Grimaldi Basin on the Nearside of the Moon using Chandrayaan-1 data. In: abstracts of the 'NSSS (National Space Science Symposium) 2019', pp.433, held at Savitribai Phule University, Pune, India, 29-31 Jan' 2019
17. Thesniya, P.M., I. S. Juda Benhur and Rajesh, V. J., 2019. Chemistry and morphology of olivine occurrences from the Ohm crater on the farside of the Moon: Insight into their origin. In: abstracts of the 2nd international conference on 'GEM 2019 (Geology: Emerging Methods and Applications)', pp.71, held at Department of Earth and Environmental Sciences, Christ College, Thrissur, Kerala, India, 17-19 Feb' 2019.

18. Thesniya, P.M., Rajesh, V. J., 2019. Earth's Moon: Geology and research highlights. In: abstracts of the 2nd international conference on 'GEM 2019 (Geology: Emerging Methods and Applications)', pp.111, held at Department of Earth and Environmental Sciences, Christ College, Thrissur, Kerala, India, 17-19 Feb' 2019.
19. Jappji, M., Thesniya, P.M and Rajesh, V. J., 2019. Morphological and Mineralogical Characterization of Das crater on the Farside of the Moon. In: abstracts of the 2nd international conference on 'GEM 2019 (Geology: Emerging Methods and Applications)', pp.29, held at Department of Earth and Environmental Sciences, Christ College, Thrissur, Kerala, India, 17-19 Feb' 2019.
20. Jappji, M., Thesniya, P.M and Rajesh, V. J., 2019. Characterization of Morphology, Mineralogy, and Ejecta Emplacement of Das crater on the lunar farside. In: abstracts of the European and Planetary Science Conference, to be held at Centre International de Conférences de Genève (CICG) Geneva, Switzerland, 5-20 Sept' 2019, Abstract ID: EPSC-DPS2019, #1842.
21. Deepchand, B., Haritha, A., Thesniya, P.M., and Binoj Kumar, 2019. Chemical and Spectral Characterization of Chromites in Nuggehulli Schist Belt, Western Dharwar Craton, Southern India: Implications for the Remote Observation of Spinel on the Moon. In: abstracts of the National Seminar on 'Advances in Earth and Environmental Sciences', pp.20, held at Dept. of Geology, the University of Kerala, India, 20 Sept' 2019.
22. Saranya R. Chandran, Thesniya, P.M. and Rajesh V.J., 2019. Chemical and spectral characterization of Sittampundi chromites, Tamil Nadu, India. In: abstracts of the National Seminar on 'Advances in Earth and Environmental Sciences', pp.20, held at Dept. of Geology, University of Kerala, India, 20 Sept' 2019.
23. Thesniya, P. M., Rajesh, V. J., 2018. Olivine rich exposures in the Grimaldi basin on the nearside of the Moon: Implications for lunar endogenic processes. In: abstracts of the 42nd COSPAR Scientific Assembly, held at Pasadena, California, U.S., July 14-22, 2018.
24. Thesniya, P. M., Rajesh, V. J., 2018. Compositional mapping of a previously unidentified localized pyroclastic deposit in the Grimaldi basin. In: Abstracts of the 30th Kerala Science Congress, pp. 121-122, held at Brennan College, Kannur, Kerala, India, 28-30 January 2018.
25. Thesniya, P. M., Rajesh, V. J., 2018. Detection of primary mineral assemblages in Grimaldi basin on the nearside of the Moon: Implications for the evolution of the lunar crust. In: Proceedings of the 5th UGC-SAP-DRS II (2013-18) conference, vol. 5, pp. 13-19, held at Dept. of Geology, University of Kerala, India, 15-16 Feb' 2018.

26. Thesniya, P.M., Rajesh, V. J., 2018. Remote spectral and chemical characterization of Mare basalts in the Grimaldi basin on the nearside of the Moon. In: abstracts of the National Seminar on ‘Advances in Earth and Environmental Sciences’, pp.20, held at Dept. of Geology, the University of Kerala, India, 15 Oct’ 2018.
27. Saranya, R. C., Thesniya, P. M., Rajesh, V. J. and Sajeev Krishnan, 2018. Chemical and Spectral characterization of chromites from Sittampundi Anorthosite Complex, South India: Implications for remote observations of spinels on Moon. In: abstracts of the NIPR (the Ninth Symposium on Polar Science) 2018, held at National Institute of Polar Research, Tokyo, Japan, 4-7 Dec’ 2018.
28. Saranya, R. C., Thesniya, P. M., Rajesh, V. J., Ajith, G., 2018. Compositional diversity of lunar magmatic spinels: Implications for endogenic processes. In: Proceedings of the 5th UGC-SAP-DRS II (2013-18) conference, vol. 5, pp. 24-27, held at Dept. of Geology, University of Kerala, India, 15-16 Feb’ 2018.
29. Jappji, M., Thesniya, P.M and Rajesh, V. J., 2018. Morphological and mineralogical characterization of Das crater on the farside of the Moon. In: abstracts of the National Seminar on ‘Advances in Earth and Environmental Sciences’, pp.22, held at Dept. of Geology, the University of Kerala, India, 15 Oct’ 2018.
30. Thesniya, P. M., Rajesh, V. J., 2017. Characterization of Localized pyroclastic deposits in the Grimaldi basin. In: abstracts of the Brainstorming session on ‘Vision and Explorations for Planetary Sciences in Decades 2020-2060’. This was organized by Physical Research Laboratory, Ahmedabad, India, 8-10 Nov’ 2017.

Others

Manuscripts ‘under review’ in journals

1. Thesniya P. M., Jappji Meher, and Rajesh V. J., 2022. Morphology and ejecta distribution of the Das crater on the lunar farside: Insights into cratering mechanics of the Moon. *Icarus*, ICARUS-D-22-00039.
2. Hariitha A., V. J. Rajesh, Sanjeev Kumar, M. Santosh, and P. M. Thesniya, 2021. Spectrochemical and stable isotopic characteristics of magnesite deposits from Salem, southern India: CO₂ repository through supergene processes. *Ore Geology Reviews*. Under review, ORGEO-D-21-00885.

Manuscripts under preparation/to be submitted to journals

1. Thesniya P. M., Rajesh V. J., Amit Basu Sarbadhikari, 2022. Compositional variations in spinels on the Moon: Insights into genesis of lunar spinels.
2. Deepchand, A. Haritha, P. M. Thesniya, V. J. Rajesh, R. B. Binoj Kumar, 2021. Spectroscopic characteristics of chromite in relation to its textural variations and chemistry: A case study from Nuggihalli Schist Belt, southern India.

Awards/achievements

1. Awarded the Second best poster prize for the poster titled 'Characterization of Localized pyroclastic deposits in the Grimaldi basin' presented at a Brainstorming session on 'Vision and Explorations for Planetary Sciences in Decades 2020-2060'. This was organized by Physical Research Laboratory, Ahmedabad, on 8-10 Nov 2017.